

Supramolecular Self-assembly of Low Molecular Weight Receptors: Aggregation, Chemosensing and Gelation Study

A Dissertation

*Submitted in the partial fulfillment for the degree of
Doctor of Philosophy*



RUBI MORAL

(Roll No. 216122043)

Thesis Supervisor: Prof. Gopal Das

**Department of Chemistry
Indian Institute of Technology Guwahati
India-781039**

Supramolecular Self-assembly of Low Molecular Weight Receptors: Aggregation, Chemosensing and Gelation Study

A Dissertation

*Submitted in the partial fulfillment for the degree of
Doctor of Philosophy*



Rubi Moral

(Roll No. 216122043)

Thesis Supervisor: Prof. Gopal Das

Department of Chemistry

Indian Institute of Technology Guwahati

India-781039

The logo of the Indian Institute of Technology Guwahati is a circular emblem. It features a central stylized figure with three rounded shapes, possibly representing a person or a symbol. The text "Indian Institute of Technology Guwahati" is written in English around the bottom half of the circle, and its Assamese equivalent "সংগীতীয় প্ৰৌছোগিকী সংস্থান গুৱাহাটী" is written along the top half. Two horizontal blue lines are drawn across the page, one above and one below the central text.

Dedicated to my Parents



INDIAN INSTITUTE OF TECHNOLOGY GUWAHATI

Department of Chemistry

STATEMENT

I do hereby declare that the matter embodied in this thesis is the result of investigations carried out by me in the Department of Chemistry, Indian Institute of Technology Guwahati, India, under the guidance of Prof. Gopal Das, Department of Chemistry, Indian Institute of Technology Guwahati, India.

In keeping with the general practice of reporting scientific observations, due acknowledgements have been made wherever this work is based on the findings of other investigators.

2nd March, 2026

IIT Guwahati

Rubi Moral



INDIAN INSTITUTE OF TECHNOLOGY GUWAHATI

Department of Chemistry

CERTIFICATE

This is to certify that Ms. Rubi Moral has been working under my supervision since July, 2021 as a regular registered Ph.D. student. Her thesis, entitled “**Supramolecular Self-assembly of Low Molecular Weight Receptors: Aggregation, Chemosensing and Gelation Study**”, is an authentic record of the results obtained from the research work carried out under my supervision in the Department of Chemistry, Indian Institute of Technology Guwahati, Assam, India. I am forwarding her thesis to submit for the award of degree of Doctor of Philosophy, from this institute. I hereby certify that she has fulfilled all the requirements, according to the rules of this institute regarding the investigations embodied in her thesis, and this work has not been submitted elsewhere for a degree.

Prof. Gopal Das
(Thesis Supervisor)

Professor
Department of Chemistry
IIT Guwahati
Assam - 781039, India

ACKNOWLEDGEMENT

“Gratitude is an opener of locked-up blessings.” — Marianne Williamson

At the very onset, I would like to express my earnest gratitude to my supervisor Prof. Gopal Das, for his persistent motivation and constant support regarding my research work during my entire PhD journey. His visionary leadership has always prompted me to think and work freely towards new innovative ideas. I have deepest respect for his discipline and sincerity towards work, professionalism, wisdom, generosity and kindness. I will always look forward to his guidance in future expedition as well.

I would like to take the opportunity to express my sincere gratitude towards my doctoral committee members Prof. Sandip Paul, Prof. A. S. Achalkumar and Prof. Shyam Prosad Biswas for their careful evaluation of my research work, valuable suggestions and feedbacks that certainly helped me improving my thesis work. I am also thankful to the heads of our department during my PhD tenure, Prof. Gopal Das, Prof. Aditya Narayan Panda and Prof. Biplab Mondal for their help and support during my PhD journey. Nevertheless, I would also like to thank the staff members, Mr. Imdadul Islam, Mr. Diganta Kumar Hira, Mr. Aniruddha Gogoi, Mr. Michael Deka, Mr. Shyamal Kumar Mondal, Ms. Sayanee Mukherjee, Mrs. Abhilasa M. Baruah, Mrs. Lipika Nath, Dr. Kula Kamal Senapati, Dr. Babulal Das, for their support. I honestly acknowledge the instrument facilities of the department of chemistry as well as CIF, IIT Guwahati for necessary instrument facilities required for the experiments. I am grateful towards the Government of India for the prestigious PMRF fellowship for the smooth conduction of my research works.

I am profoundly thankful to all my lab seniors and lab mates Dr. Asesh, Dr. Debojit, Dr. Megha, Dr. Sagnik, Dr. Debolina, Pampi, Oiyao Appun, Neha, Bikram, Sulekha, Akash, Jumi, Sanjana, Sudip, Protyakshi and Maharshi for their valuable supports during my PhD tenure. I also extend my sincere appreciation to Mr. Amarjit Pandey (Chemical Engineering Department, IIT Guwahati) for his unconditional help during my research journey.

During my PhD journey sports has become an inseparable part and helped me with physical and mental well-being. Hence, here I would like to thank all my badminton playing partners especially, Oiyao Appun, Tejaswini, Nishan, Rantu, Sreeram, Jyotiprakash as well as Prof. Charudatt Y. Kadolkar for making my mornings very productive and memorable.

“Friends are the family you choose.” – Jess C. Scott. The acknowledgement section is incomplete without mentioning the name of my best friend, Mr. Oiyao Appun Pegu. During my whole PhD journey, being a labmate, he has become my consistent support system during all my ups and downs. We have helped each other in every possible way and have worked towards our mutual growth. He is a persistent cheerer of all my achievements making all my moments a cherishable one. I admire his commitment, passion, observation skill and discipline towards his works and I am forever grateful towards him for being a constant motivator during my whole PhD tenure.

Finally, coming to the moment to acknowledge the people who are very precious to my life. My father Mr. Chakra Dhar Moral and my mother Mrs. Golapi Moral are the reasons, I am standing here today and I am blessed to have them in my life. Their hard works and sacrifices have always motivated me to bring best out of myself. My younger brother Mr. Dimple Kumar Moral has always got my back and has always stood as the pillar of my strength. As a sibling, we have always shared our moments of happiness and sorrows with each other and still holds each other’s hands during any difficult phase of life. The love and care they have given to me have always taught me to remain grounded in my life and I am beyond grateful to have them as my family.

I bow down to the almighty in gratitude for the journey of life and hope his blessings continues.....!



Rubi

The synopsis report entitled “**Supramolecular Self-assembly of Low Molecular Weight Receptors: Aggregation, Chemosensing and Gelation Study**” has been divided into seven chapters, detailing the outcomes and results of the experimental work conducted during the research tenure.

Chapter 1: Introduction and Literature Survey

Molecular self-assembly is a spontaneous process in which molecules form ordered aggregates through various non-covalent interactions such as H-bonding, π - π interactions, hydrophobic interactions, solvophobic interactions, host-guest, charge-transfer, metal coordination, etc. Self-assembly is more than a process to be studied as most of the biological macromolecules are the outcome of self-assembly process, examples including formation of DNA double helix, protein folding, formation of polysaccharides, etc. Scientists have borrowed this astonishing idea from nature and exploiting nature’s assembly principle, scientists are now enthusiastic to create artificial materials with hierarchical structures and tailored properties for the construction of advanced materials. Self-assembled systems are promising in nanotechnology, drug delivery, tissue engineering and also in sensing and detection of biologically and environmentally important analytes. Self-assembling low molecular weight systems can show fast response to external stimuli. These systems reveal distinct response towards spectroscopic signals between their self-assembled and dis-assembled stages thus can be used as tool for chemosensing applications. Rationale designing of such self-assembled systems may include integration of fluorescent dyes for better spectroscopic responses. Self-assembled systems can be applied for the detection of enzymes, metal ions, anions, proteins, harmful molecules etc. based on the properties of dis-assembly triggered fluorescence turn on of conventional dyes, aggregation-induced emission dyes (AIE) or environment change-induced fluorescence turn on. Hence, self-assembly is providing a route to fabricate complex supramolecular architecture and is gaining considerable attention among researchers worldwide to create some novel molecules with unique properties [1-12].

Supramolecular gels, self-assembled from low-molecular-weight gelators (LMWGs), have drawn immense research interest in recent years owing to their promising applications in diverse areas like chemosensors, drug delivery, biomaterials, biosensors, tissue engineering, hybrid functional materials etc. The dynamic and reversible nature of the non-covalent interactions of the gel network gives them inherent ability to respond to external stimuli such as temperature, pH, solvent, light, and redox reactions. Supramolecular metallogel results when metal centres are incorporated into organic-based gelators that can integrate the interesting and unique

properties of metal complexes into gelator molecules. In recent years, metallogels are receiving substantial attention owing to their promising application in material science which can be attributed to their fascinating redox, optical, electronic, and magnetic properties [13-20].

This thesis explores the design and preparation strategy of different types of self-assembled systems derived from low molecular weight compounds with a particular emphasis on environmental applications such as in sensing/detection of pollutants like nitro-aromatic compounds; heavy metals like Zn^{2+} , Cd^{2+} and Hg^{2+} ; biologically important anions such as SO_4^{2-} / HSO_4^- and some harmful dye molecules like methyl orange and bromophenol blue. In the first chapter, the self-systems obtained from 4-(dimethylamino)cinnamaldehyde based receptors displayed Solvent polarity dependent morphological alteration. The second chapter reported a self-aggregated system prepared from benzimidazole-based urea receptors that showed aggregation induced emission behaviour (AIE) or aggregation caused quenching (ACQ) behaviour depending on the terminal substitutions. In the following chapters, organohydrogels as well as metallogels were prepared from self-assembled low molecular weight gelator (LMWG) compounds of tripodal acylhydrazone based gelators and adipic dihydrazide based gelators functionalized with quinoline and pyridine respectively and they possessed fascinating properties. In the last chapter, interestingly, a rare anion driven supramolecular gel system was also prepared via rationale designing of the gelator molecule having guanidium as the core and three arms fabricated with indole moieties. The synthesized supramolecular gel matrixes demonstrated diverse applications including absorption of harmful dyes, spontaneous in-situ metal nanoparticle formation which could show antioxidant and antibacterial activities, and also heavy metal ion detection via gelation process. Nonetheless, the guanidium based gelator molecule could show solid-state anion exchange phenomena.

Chapter 2: Experimental methods and characterization

In this chapter, a detailed and comprehensive report of the various materials used in the synthesis of low molecular weight self-assembled systems is documented. The chapter outlines the design and preparation strategies employed, along with specifications of analytical instruments used in material characterization. In addition to this, detailed reports of the results are thoroughly represented.

Chapter 3: Probing the effect of different aromatic core substitution in the aggregation potential and picric acid recognition aptitude in a series of cinnamaldehyde-based receptors (*Dyes Pigm.*, 2023, 218, 111502)

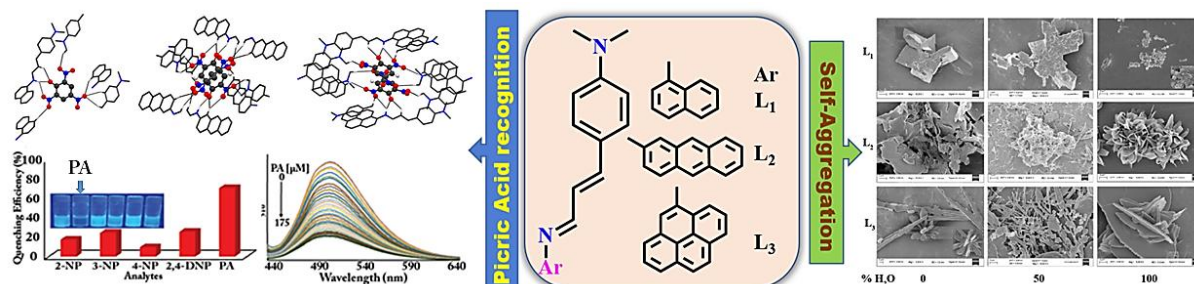


Figure 1. Pictorial representation of key findings of the research work included in Chapter 3.

In this chapter, three 4-(dimethylamino)cinnamaldehyde-based Schiff base receptors (**L₁₋₃**) with different fluorophore molecules were prepared to get insight into the functional integration of varying fluorophores in the aspect of the self-assembly phenomenon. Three different potential fluorophores, naphthalene (**L₁**), anthracene (**L₂**), and pyrene (**L₃**) were used as the aromatic core for a strong fluorescence response. Also, incorporation of both donor and acceptor sites through Schiff base linkage in a single molecule could impart ICT prospect to the receptors. The chapter presents comparative study on the impact of changing the aromatic core on their self-aggregation as well as small molecule recognition potential in the solid and solution phase. The UV-Vis spectra of the three receptors (10 μ M) in pure acetonitrile (ACN) showed a regular fall of the sharp absorbance and a visible upliftment of the baseline region with the incremental addition of water (H₂O), suggesting formation of aggregated species in the aqueous medium. However, the effect was more prominent in **L₃**. The formation of aggregates was further validated by DLS and FESEM analysis. The π electron-rich and strongly emissive nature of self-assembled receptors were applied for studying the interaction with different nitro phenols such as 2-nitrophenol, 3-nitrophenol, 4-nitrophenol, 2,4-dinitrophenol, and picric acid (PA) in the aqueous medium via fluorescence spectroscopy. PA being the most electron-deficient among different nitro phenols results in the highest quenching in the fluorescence intensity upon interaction with the electron-rich **L₁**, **L₂**, and **L₃**, thus giving selective sensing of PA. The highest selectivity was observed with **L₃**, as it was the most electron-rich among the three, while **L₁** displayed almost no selectivity. The analytical utility of the receptors was also demonstrated via the detection of PA in various real water samples as well as through paper strips. Moreover, all three receptors **L₁**, **L₂**, and **L₃** could recognize picric acid in the solid state.

Chapter 4: Exploring the effect of terminal substituent on aggregation and sensing properties of neutral benzimidazole-based urea receptors (*New J. Chem.*, 2023, 47, 19625-19632)

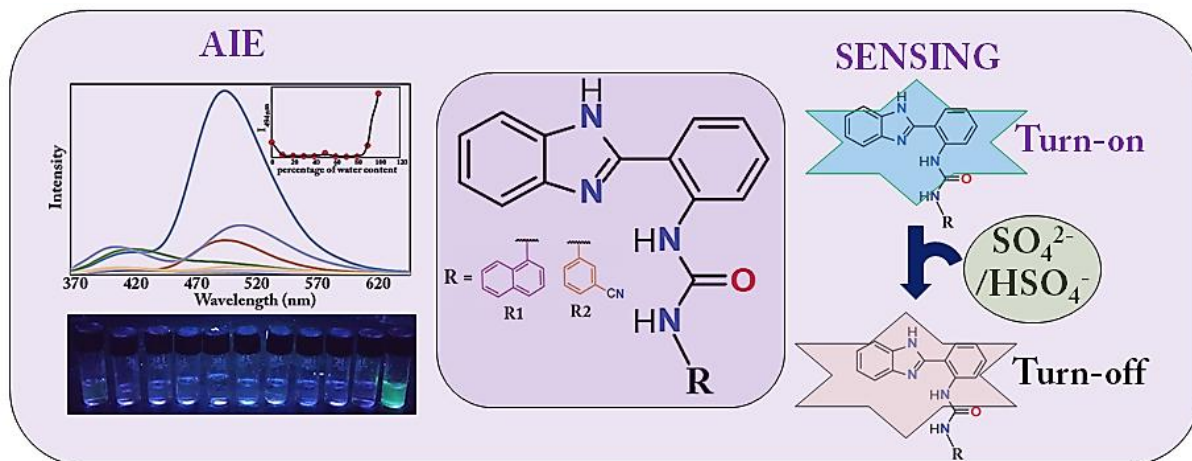


Figure 2. Pictorial representation of the research work included in chapter 4.

In this chapter, two unsymmetrical urea-based receptors **R1** and **R2** were prepared, containing benzimidazole fluorophore part as a constant unit in one arm while varying the other arm, fabricated with a naphthyl and 3-cyanophenyl moiety in **R1** and **R2**, respectively. The naphthalene moiety could act as an electron-rich fluorophore; on the other hand, the 3-cyanophenyl moiety had electron-withdrawing tendency. This comparative design was followed to realize the role of changing the terminal substituent towards the aggregation aptitude, different photophysical aspects as well as sensing behaviour. The aggregation properties of **R1** and **R2** were investigated by UV-Vis absorption and fluorescence spectroscopy in acetonitrile (ACN)/water (H₂O) binary solvent systems. A comparison of the absorption spectra for **R1** and **R2** revealed that the aggregation capacity of **R1** in water was five times the capacity of **R2**. Aggregation behaviour of the receptors was further supported by FESEM and DLS studies. Moreover, while **R1** displayed aggregation-induced emission (AIE) behaviour, **R2**, on the other hand, showed typical aggregation-caused quenching (ACQ) behaviour. The anion binding properties of receptors **R1** and **R2** (10 μM) towards various anions such as SO₄²⁻, HSO₄⁻, CN⁻, F⁻, Cl⁻, Br⁻, I⁻, ClO₄⁻, OH⁻, AcO⁻, and NO₃⁻ were also investigated. While **R1** exhibited excellent optical sensing properties towards only SO₄²⁻ and HSO₄⁻ through both colorimetric and fluorometric responses in aqueous medium; **R2** on the other contrary was not that selective towards SO₄²⁻ and HSO₄⁻. Encapsulation of HSO₄⁻ inside the cation-sealed cavity of receptor **R1** and n-TBA via both classical and non-classical hydrogen bonding interactions was reported via SCXRD analysis. The easily synthesized model paper strips were utilized to show real-life

applications of the receptors via the detection of $\text{SO}_4^{2-}/\text{HSO}_4^-$. This study suggested that tailoring functional groups within the molecular framework can provide contrasting aggregation and sensing behaviour.

Chapter 5: Tripodal acylhydrazone-based probe for turn-on Zn^{2+} sensing in HEPES buffer: investigation of gelation and AIE property (Soft Matter, 2024, 20, 7668-7677)

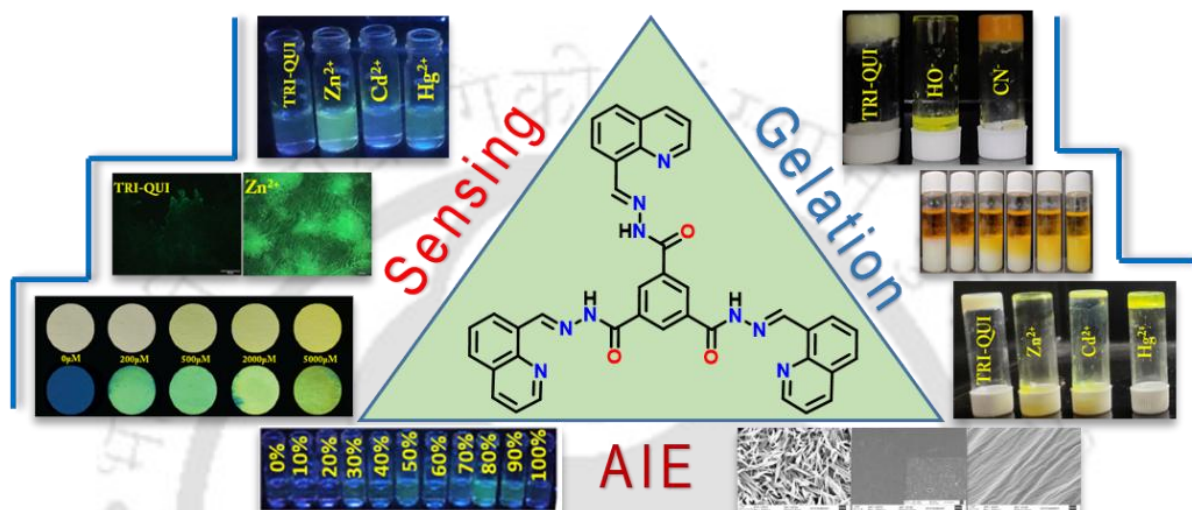


Figure 3. Pictorial representation of the findings of the research work included in chapter 5.

In this work, along with solution state aggregation as well as sensing properties, we also explored the supramolecular self-assembly phenomena in terms of supramolecular gelation. Two C_3 -symmetric acylhydrazone-based AIE active probes, **TRI-QUI** and **TRI-NAP**, were synthesized with different peripheral substituents to investigate the difference in response towards solution phase aggregation along with sensing of metal ions as well as towards supramolecular gelation as a consequence of structural change. The same acylhydrazone skeleton was utilized for the probes but peripheral substituents were altered by incorporating a quinoline moiety in **TRI-QUI** and a naphthalene moiety in **TRI-NAP**. The aggregation properties of both **TRI-QUI** and **TRI-NAP** were investigated in aqueous medium, 0.1 M HEPES buffer as well as in *N,N*-dimethylformamide (DMF) solvent via UV-Vis absorption and fluorescence spectroscopic studies. In UV-Vis spectra, sharp absorption of both the probes in pure DMF showed a regular fall along with broadening and a bathochromic shift with the gradual addition of water/HEPES buffer. An upliftment of the baseline with the increase in the water/HEPES buffer percentage for both cases was also observed suggesting formation of aggregates in water. Fluorescence spectroscopy confirmed that both probes were AIE active. **TRI-QUI** showed turn-on

fluorescence response only in the presence of Zn^{2+} along with a ~ 35 nm red shift of the spectral peak position in HEPES buffer medium out of all selected cations. Complexation with Zn^{2+} resulted in the chelation-induced enhanced fluorescence (CHEF) effect, thereby leading to a significant enhancement of fluorescence intensity. The real-world applicability of our designed probe was demonstrated via Zn^{2+} sensing in real water samples as well as via paper strip experiments. Important to mention here that no sensing phenomena was observed by the probe **TRI-NAP** in aqueous medium. Moreover, **TRI-QUI** (5 mg mL^{-1}) could form a gel in a DMSO: H_2O (2: 3, v/v) mixture. The minimum gelation concentration of the gel was found to be as low as 0.5 mg mL^{-1} . The gelator could interact with anions and metal cations in the gel phase, leading to intriguing morphological changes. CN^- could lead to gel-to-gel transition as the colour of the gel changed from creamy white to bright orange. However, **TRI-NAP** could only form a gel at a very high concentration of 20 mg mL^{-1} in a DMSO: H_2O (2: 3, v/v) mixture. Furthermore, **TRI-QUI** gel could adsorb small molecules like methyl orange and bromophenol blue, with an uptake efficiency of 63% and 60%, respectively, thus making the probe a multifunctional smart material. So, expansion of the self-assembly phenomena to supramolecular gel formation opened up more scope in terms of real-life applications.

Chapter 6: Positional Isomerism Driven Differential Metallogelation: Biological Application and Naked Eye Detection of Cd^{2+} ion (*Manuscript submitted*)

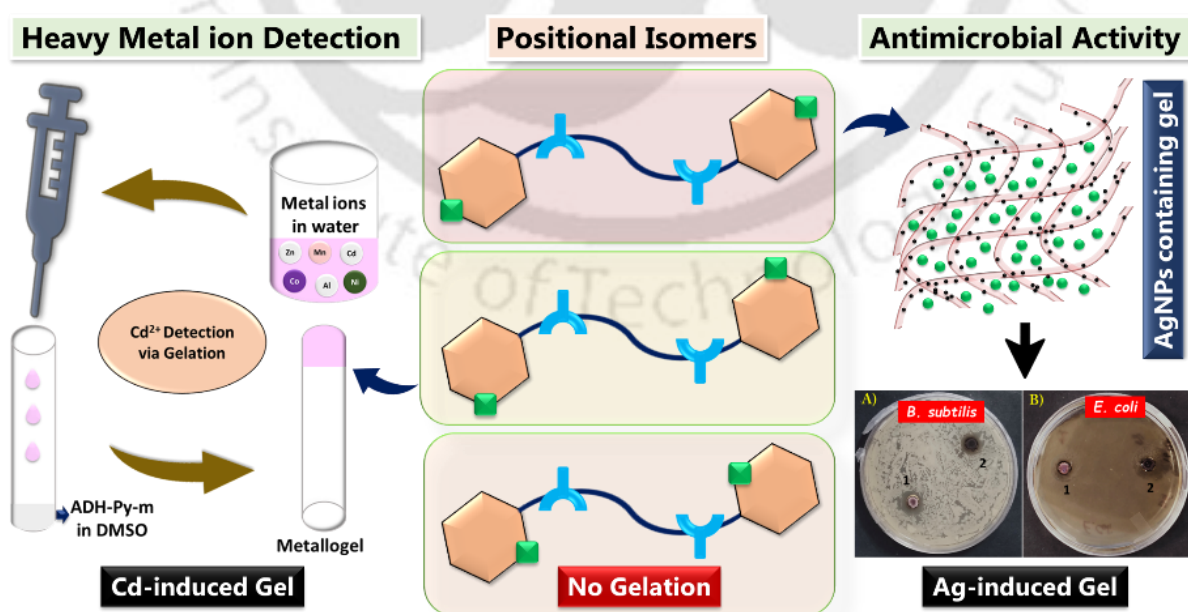


Figure 4. Pictorial representation of the findings of the research work included in chapter 6.

To explore some more aspects of supramolecular gelation, in this chapter, we focused on designing of receptors for metallogelation to understand the structure-function relationships for the same. We have synthesized four adipic dihydrazide-based LMWG molecules, **ADH-Py-o**, **ADH-Py-m**, **ADH-Py-p**, and **ADH-Ph** functionalized with -o, -m, -p amino pyridine and phenyl groups at the terminal positions, respectively. We explored the effect of positional isomerism on metallogelation behaviours. The presence of 'pyridine -N' in **ADH-Py-p**, **ADH-Py-m** and **ADH-Py-o** provided metal ion coordination sites which might facilitate the formation of a 3-dimensional supramolecular network structure. The acylhydrazone unit on the other hand, is well known for its typical role in supramolecular gelation. Thus, hierarchical self-assembly formation along with metal ion coordination might favor metallogelation. **ADH-Ph** was synthesized as a control compound, where both arms of the adipic dihydrazide were fabricated with phenyl units instead of the pyridine motif. The gelation behaviour of all the receptors was investigated in presence of different metal salts, viz. $\text{AlCl}_3 \cdot 6\text{H}_2\text{O}$, $\text{MnCl}_2 \cdot 4\text{H}_2\text{O}$, $\text{CdCl}_2 \cdot \text{H}_2\text{O}$, $\text{CuCl}_2 \cdot 2\text{H}_2\text{O}$, ZnCl_2 , $\text{NiCl}_2 \cdot 6\text{H}_2\text{O}$, $\text{CoCl}_2 \cdot 6\text{H}_2\text{O}$, $\text{FeCl}_3 \cdot 6\text{H}_2\text{O}$, $\text{Pb}(\text{NO}_3)_2$, PdCl_2 , HgCl_2 and AgNO_3 . It was interesting to see that selective metallogelation was observed only for the receptors, **ADH-Py-p** and **ADH-Py-m** with AgNO_3 (**P-Ag-G**) and $\text{CdCl}_2 \cdot \text{H}_2\text{O}$ (**M-Cd-G**) respectively. While the gel **P-Ag-G** formed irrespective of the counter anion of silver salts; **M-Cd-G** gel formed specifically only in presence of $\text{CdCl}_2 \cdot \text{H}_2\text{O}$. This difference in gelation behavior suggested different underlying mechanism for metallogel formation. From IR and NMR analysis of the **P-Ag-G** and **M-Cd-G** gels and xerogels, it was hypothesized that Ag^+ binds to the pyridine -N, leading to polymeric network formation and ultimately leading to gel formation. Cd^{2+} on the other hand, bind to the acylhydrazone unit rather than the pyridine -N. **P-Ag-G** facilitated the formation of AgNPs inside the gel matrix, The gel nanocomposite showed antibacterial activity against the bacterial strains *B. subtilis* and *E. Coli*. Nevertheless, the idea of selective metallogelation of **ADH-Py-m** only in presence of $\text{CdCl}_2 \cdot \text{H}_2\text{O}$ was further exploited for visual detection of Cd^{2+} in different real water samples in presence of various competitive metal chloride salts through gelation process. Important to mention here is that no metallogel formation was observed for **ADH-Py-o** and **ADH-Ph** with any of the metal ions studied for our work under the identical conditions, which clearly stated the importance of proper positioning of pyridine -N to form a polymeric network through coordination of metal ion. Hence, the presence of the pyridine unit, as well as the positioning of the -N atom in pyridine, governed the metallogel formation ability of all our reported receptors.

Chapter 7: Anion Induced Supramolecular Gel for Visual Detection of Picric Acid and in situ Formation of Gel Nanocomposites: Solid-State Anion Exchange of Guanidinium based receptor (*Nanoscale*, 2025, 17, 26845-26854)

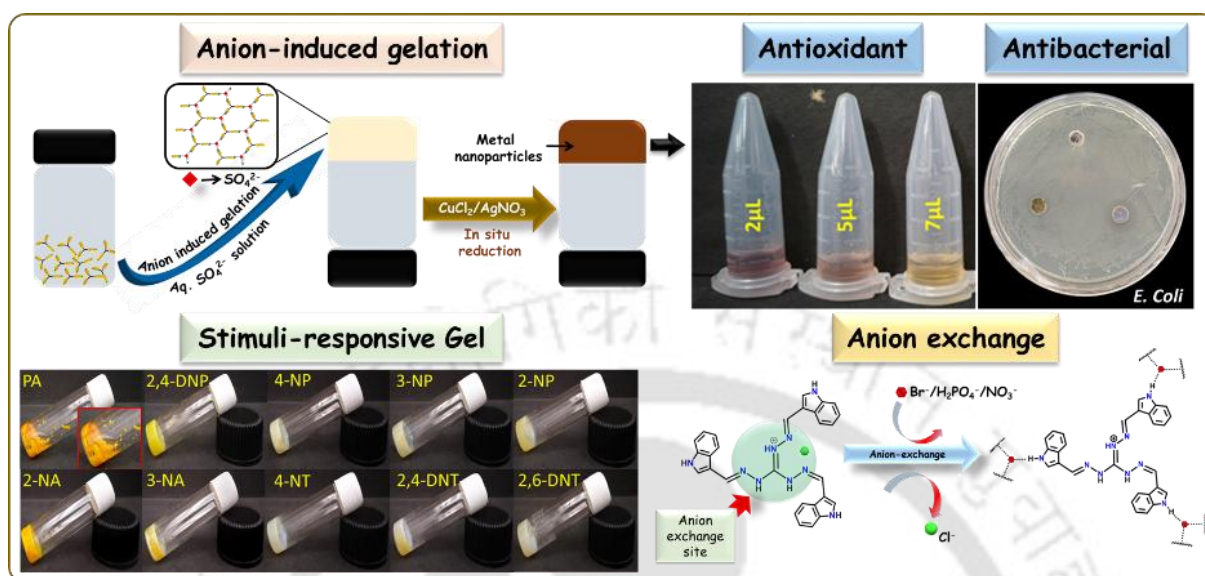


Figure 5. Pictorial representation of the research work included in chapter 7.

In recent years, metallogels are receiving substantial attention owing to their promising application in material science. However, to date, only a handful of examples report the preparation of anion-driven supramolecular gels, as designing such compounds is tricky and challenging, although the lower toxicity of metal-free systems may be advantageous for both environmental and biological applications. To explore anion induced supramolecular gel formation, receptor **GUA-IND** was designed using guanidinium hydrazide as the core, and its three arms were functionalized with three indole moieties. It was anticipated that the receptor would coordinate with anions (especially oxoanions) by virtue of coulombic interactions of the guanidinium core and hydrogen bonding interactions with the indole $-NH$ groups, which were at the periphery. This self-assembled system, formed from the receptor and anions, may lead to the formation of a supramolecular gel. Moreover, replacement of the counter anion Cl^- in the crystal structure of the receptor by anions of different sizes and shapes may provide another dimension to the present work. The gelation study of **GUA-IND** was performed in the presence of TBA salts of different anions in DMSO- H_2O (1 : 4, v/v). However, gelation was observed only in the presence of SO_4^{2-} and HSO_4^- and partial gelation was observed in the presence of $H_2PO_4^-$. With the rest of the anions, no gelation was observed under the identical conditions. The **GI-G** gel exhibited excellent stimulus-responsive properties towards PA among different nitroaromatic compounds. The significance of this finding lies in the fact that, the sensing of PA that could be

easily visualised through the naked eye as gel to sol transition occurred in presence of PA. Besides, **GI-G** gel formed nanocomposites, **GI-Cu-G** and **GI-Ag-G**, in the presence of Cu and Ag metal ions via spontaneous in situ reduction of precious metal salts like Cu and Ag into their nanoparticles, which, along with **GI-G**, could exhibit antioxidant and antimicrobial activities. Moreover, **GUA-IND** exhibited a phenomenon of anion exchange where the counter anion (Cl^-) of **GUA-IND** was replaced by different anions such as Br^- , NO_3^- , and H_2PO_4^- during the process of crystallization. This research work paves the way for advanced materials with tailored functionalities.

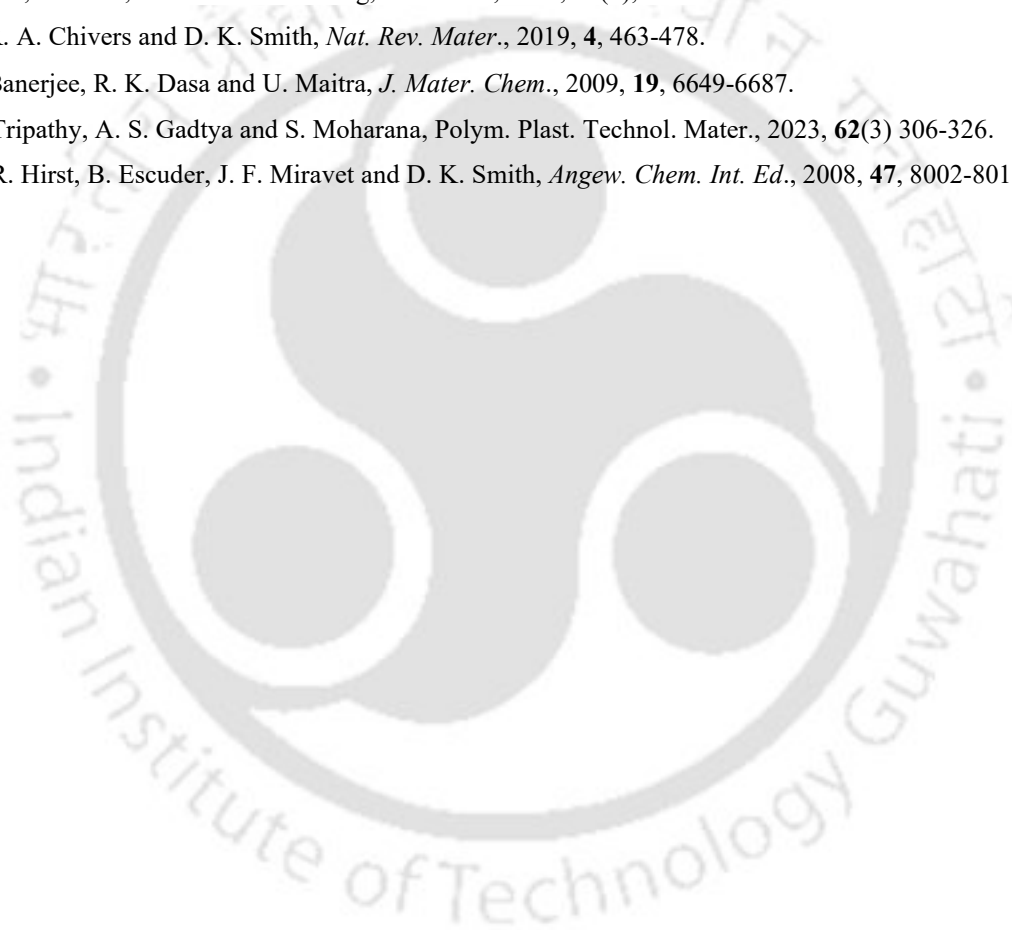
Conclusions

In summary, small molecule-based probes/receptors can demonstrate exciting photophysical properties in aggregated state and they can be very advantageous in terms of chemosensing of various important analytes because of their easy chemical modification to interact selectively with specific analytes. The thesis discusses effect of different peripheral substituents on the photophysical as well as chemosensing applications of small molecule-based receptors keeping the core skeleton intact. Moreover, the thesis also emphasizes on synthesis of low molecular weight supramolecular gels/metallogels/anion-driven gels derived from the self-assembly of small molecules. The supramolecular gels very attractive and they find application in diverse fields. The thesis explores some real-life applications of supramolecular gels, like removal of harmful analytes through adsorption, gel-sol transition based visual detection of analytes, facilitation of in situ formation of metal nanoparticles etc. The thesis also elucidates on rare anion-induced supramolecular gelation providing a future prospective for rational designing of more such gelator molecules. Thus, this research lays a strong foundation for the development of small molecule with captivating aggregation properties and contributes towards advancement of this research area.

REFERENCES

1. V. K. Praveen, B. Vedhanarayanan, A. Mal, R. K. Mishra, and A. Ajayaghosh, *Acc. Chem. Res.*, 2020, **53**(2), 496–507.
2. Y. Mai, Z. An, and S. Liu, *Macromol. Rapid Commun.*, 2022, **43**, 2200481.
3. Y. Su, Y. Liu, Y. Zhong, S. Ma, Q. Ouyang, X. Chen, Y. Li, E. Xiong, Z. Zou, and J. Liu, *Coord. Chem. Rev.*, 2025, **527**, 216403.
4. D. Lombardo, P. Calandra, L. Pasqua, and S. Magazù, *Materials*, 2020, **13**(5), 1048.
5. D. I. Ugwu, J. Conradie, *Chem. Soc. Rev.*, 2023, **1293**, 136275.
6. V. B. Kumar, B. Ozguney, A. Vlachou, Y. Chen, E. Gazit, P. Tamamis, *J. Phys. Chem. B*, 2023, **127**(9) 1857–1871.

7. H. K. Mirzahosseini, M. Sheikhi, F. Najmeddin, M. Shirangi and M. Mojtahedzadeh, *Drug Metab. Rev.*, 2023, **55**, 140–162.
8. Y. Sasaki, T. Minamiki, S. Tokitob and T. Minami, *Chem. Commun.*, 2017, **53**, 6561-6564.
9. C. Ren, J. Zhang, M. Chenb and Z. Yang, *Chem. Soc. Rev.*, 2014, **43**, 7257-7266.
10. X. Yan, P. Zhua and J. Li, *Chem. Soc. Rev.*, 2010, **39**, 1877-1890.
11. X. Zhao, F. Pan, H. Xu, M. Yaseen, H. Shan, C. A. E. Hauser, S. Zhang and J. R. Lu, *Chem. Soc. Rev.*, 2010, **39**, 3480-3498.
12. L. Li, R. Sun, and R. Zheng, *Mater. Des.*, 2021, **197**, 109209.
13. D. K. Smith, *Soft Matter*, 2024, **20**, 10-70.
14. G. Yu, X. Yan, C. Hana and F. Huang, *Chem. Soc. Rev.*, 2013, **42**, 6697-6722.
15. A. Y.-Y. Tama and V. W.-W. Yam, *Chem. Soc. Rev.*, 2013, **42**, 1540-1567.
16. Z. Liu, X. Zhao, X. Zhao and Yu Feng, *Molecules*, 2023, **28**(5), 2274.
17. P. R. A. Chivers and D. K. Smith, *Nat. Rev. Mater.*, 2019, **4**, 463-478.
18. S. Banerjee, R. K. Dasa and U. Maitra, *J. Mater. Chem.*, 2009, **19**, 6649-6687.
19. D. Tripathy, A. S. Gadtya and S. Moharana, *Polym. Plast. Technol. Mater.*, 2023, **62**(3) 306-326.
20. A. R. Hirst, B. Escuder, J. F. Miravet and D. K. Smith, *Angew. Chem. Int. Ed.*, 2008, **47**, 8002-8018.



Chapter 1: Introduction

1.1. Supramolecular self-assembly: An Introduction	1
1.2. Self-assembly of small molecules	2
1.3. AIE active small molecular probes for chemosensing application	3
1.3.1. AIE probes for sensing of small organic molecules	4
1.3.2. AIE probes for sensing of metal ions	6
1.3.3. AIE probes for sensing of anions	7
1.4. Supramolecular gels	9
1.4.1. Visual detection of biologically and environmentally important Analytes	11
1.4.2. Removal of toxic analytes from wastewater	12
1.4.3. Gel-nanoparticle hybrid materials	13
1.5. Summary of Literature Review and Research Gaps	15
1.6. Objectives of the Thesis	16

Chapter 2: Experimental and Characterization Details

2.1. General Information and Materials	19
2.2. Synthetic procedure and characterization of the all the probes/receptors	20
2.2.1. Synthesis of L₁ , L₂ and L₃	20
2.2.2. Synthesis of R1 and R2	21
2.2.3. Synthesis of TRI-NH₂ , TRI-QUI and TRI-NAP	22
2.2.4. Synthesis of ADH-Py-p , ADH-Py-m , ADH-Py-o and ADH-Ph	24
2.2.5. Synthesis of GUA , GUA-IND and GUA-NAP	26
2.3. Synthetic Procedure of Metallogels viz. P-Ag-G , P-Ag-G (B) and M-Cd-G	27
2.4. Synthetic Procedure for formation of supramolecular gel GI-G	28
2.5. Rheological Experimental Details	28
2.6. UV-Vis and Fluorescence Spectral Studies	29
2.7. Estimation of the Apparent Binding Constant	30
2.8. Detection limit (LOD)	30
2.9. Stern-Volmer Plot	31
2.10. Dynamic light scattering measurement	31
2.11. Measurement of fluorescence lifetime	31
2.12. Theoretical investigations (DFT study)	31
2.13. Quantum yield measurement	31
2.14. Time response study and rate constant determination	32
2.15. ¹ H NMR titration experiments of R1 and R2	32
2.16. Field Emission Scanning Electron Microscope (FESEM) Studies	32
2.17. Field Emission Transmission Electron Microscopy (FETEM) Analysis	33
2.18. Determination of DPPH (Radical Scavenging Assay)	33

2.19. Antibacterial studies	33
2.19.1. Evaluation of Zone of Inhibition by Well-Diffusion Method	34
2.20. Anion exchange study	34
2.21. Crystallographic Refinement Details	34
References	35
Annexure 2	36

Chapter 3: Probing the effect of different aromatic core substitution in the aggregation potential and picric acid recognition aptitude in a series of cinnamaldehyde-based receptors

3.1. Background and Focus of the Chapter	63
3.2. Objective of the Chapter	64
3.3. Results and Discussion	64
3.3.1. Design principle of the receptors	64
3.3.2. Self-assemble potential of the receptors	65
3.3.3. Interaction of the receptors with picric acid	68
3.4. Conclusions	74
References	74
Annexure 3	77

Chapter 4: Exploring the effect of terminal substituent on aggregation and sensing properties of neutral benzimidazole-based urea receptors

4.1. Background and Focus of the Chapter	83
4.2. Objective of the Chapter	84
4.3. Results and Discussion	84
4.3.1. The rationale behind designing the receptors	84
4.3.2. Structural analysis of the receptors	85
4.3.3. Exploring the self-aggregation potential of R1 and R2	86
4.3.4. Selective UV and fluorescence response towards SO_4^{2-} and HSO_4^-	89
4.3.5. Structural analysis of R1.HSO₄	91
4.3.6. Interference test	92
4.3.7. Probing the mechanism of sensing	93
4.3.8. DFT studies of receptors and their SO_4^{2-} adduct	94
4.3.9. Paper-based detection of $\text{SO}_4^{2-}/\text{HSO}_4^-$	95
4.4. Conclusions	95
References	95
Annexure 4	97

Chapter 5: Tripodal acylhydrazone-based probe for turn-on Zn^{2+} sensing in HEPES buffer: investigation of gelation and AIE property

5.1. Background and Focus of the Chapter	103
5.2. Objective of the Chapter	105
5.3. Results and Discussion	105
5.3.1. Design of probes TRI-QUI and TRI-NAP	105
5.3.2. Solid-state self-assembly of the probe TRI-QUI	105
5.3.3. Exploring the self-aggregation potential of probes TRI-QUI and TRI-NAP	106
5.3.4. Selective fluorescence turn-on response towards Zn^{2+}	108
5.3.5. Microscopic study	110
5.3.6. Mechanism of sensing	111
5.3.7. Applications	113
5.3.8. Interaction of TRI-QUI with anions in the solution phase	113
5.3.9. Gelation properties of TRI-QUI	114
5.3.10. The effect of metal ions and anions in gel formation	116
5.3.11. Rheological properties	117
5.3.12. Encapsulation of small molecules	118
5.4. Conclusions	119
References	120
Annexure 5	122

Chapter 6: Positional Isomerism Driven Differential Metallogelation: Biological Application and Naked Eye Detection of Cd^{2+} ion

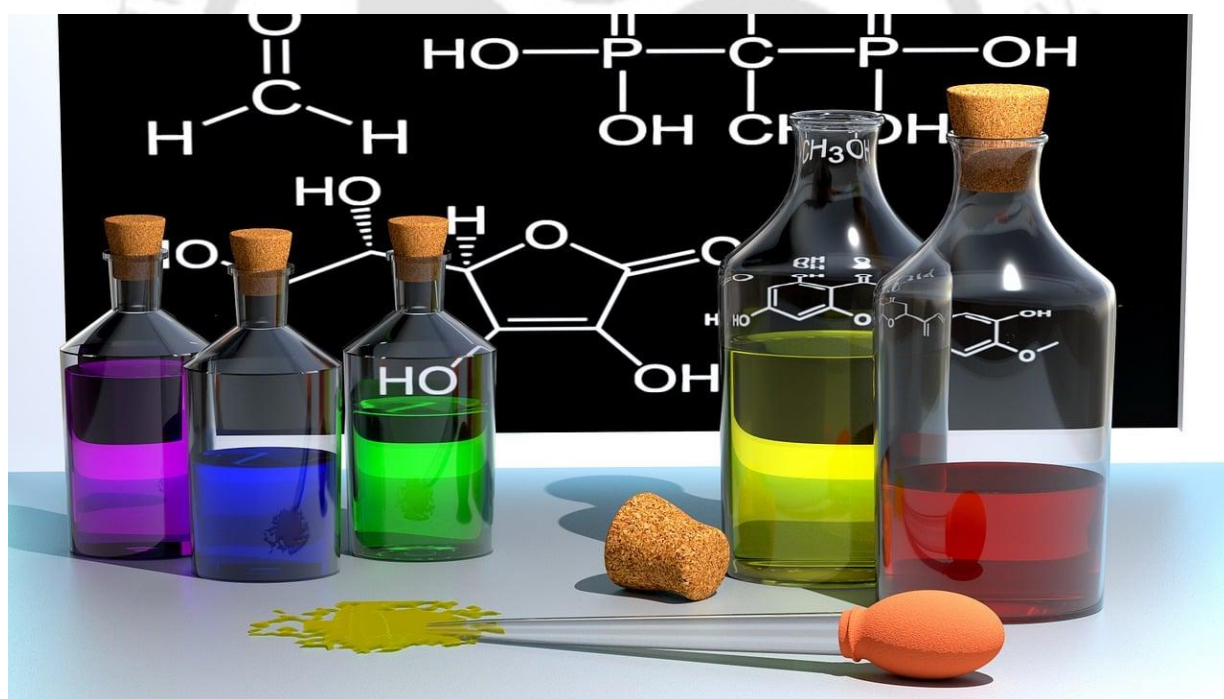
6.1. Background and Focus of the Chapter	133
6.2. Objective of the Chapter	134
6.3. Results and Discussion	135
6.3.1. Design Rationale of the Receptors ADH-Py-p , ADH-Py-m , ADH-Py-o and ADH-Ph	135
6.3.2. Solid State Self-Assembly of the Receptors ADH-Py-p and ADH-Py-m	136
6.3.3. Insights into the Gelation Behaviour of the Receptors	137
6.3.4. Formation of AgNPs Inside Gel Matrix	141
6.3.5. Investigation of Gelation Mechanism	143
6.3.6. Visual Detection of Cadmium in Real Water Samples	147
6.4. Conclusions	148
References	149
Annexure 6	151

Chapter 7: Anion Induced Supramolecular Gel for Visual Detection of Picric Acid and in situ Formation of Gel Nanocomposites: Solid-State Anion Exchange of Guanidium based receptor

7.1. Background and Focus of the Chapter	161
7.2. Objective of the Chapter	163
7.3. Results and Discussion	164
7.3.1. Design rationale of receptor GUA-IND	164
7.3.2. Solid-state self-assembly in GUA-IND	164
7.3.3. Anion coordination-induced gelation	165
7.3.4. Sensing of PA by the GI-G gel	169
7.3.5. <i>In situ</i> reduction of metal salts into nanoparticles within the gel matrix	170
7.3.6. Application of GI-G and nanocomposite gels (GI-Cu-G and GI-Ag-G)	173
7.3.7. Solid-state anion exchange	175
7.4. Conclusions	177
References	178
Annexure	181
Conclusion and Future Perspective	196
Curriculum Vitae	199

Chapter 1

Introduction



1.1. Supramolecular self-assembly: An Introduction

Supramolecular self-assembly refers to spontaneous association of molecular building blocks to produce nano/micro-aggregates of desired properties. Self-assembly is abundant in nature, formation of which includes various non-covalent interactions including hydrogen bonds, π - π stacking interactions, van der Waals forces, electrostatic interactions, hydrophobic interactions, etc. Biological macromolecules like proteins, nucleic acids, lipids are classic examples of functional nanostructures formed by hierarchical self-assembly process. Self-assembly is emerging as a platform for the synthesis of functional materials [1.1-1.5].

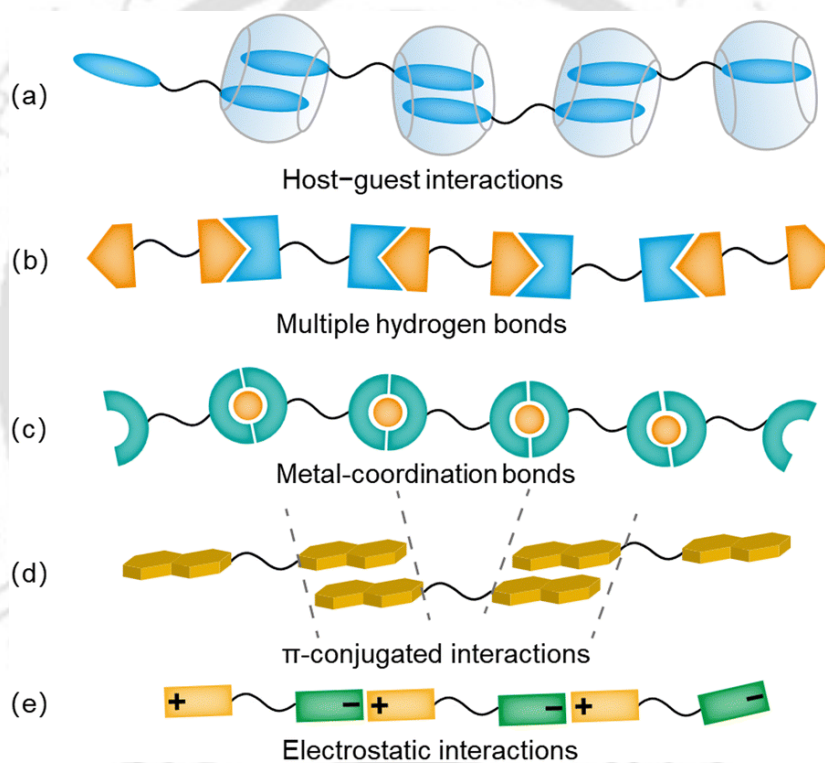


Figure 1.1: Schematic diagrams of supramolecular assembly formation via various noncovalent forces. (adapted from [1.13])

Self-assembly has turned out to be a useful tool to craft new paradigms for chemistry and material science, where numerous, typically nanometer-sized, architectures with well-defined sizes, shapes, and morphologies serve as “meta-atoms” for hierarchically assembled functional materials. While atoms assemble to form molecules which have properties drastically different from the atomic constituents; similarly, self-assembly of “meta-atoms” can generate “meta-molecules”. Eventually, self-assembly strategies should come up with advances in material design for real-

world applications. Hydrogen bonds, Host-guest interactions, π -conjugated interaction, metal-coordination bonds, electrostatic interactions etc. assist as impetus for the supramolecular self-assembly (Scheme 1.1). Self-assembly may lead to the formation of precise macroscopic systems like gel, micelle, vesicles, host-guest composite, quantum dots, etc. with definite microscopic architectures (Scheme 1.2), which find applications in various fields like sensing, drug delivery, tissue engineering, bioimaging, etc. Self-assembled molecular systems derived from low molecular weight compounds are particularly interesting in this regard as their optical properties can be tuned by modulating molecular packing via non-covalent interactions. The optically tunable self-assemblies of small molecules can further be utilized as stimuli-responsive tools to develop sensor materials. On the other hand, supramolecular gels obtained from low molecular weight compounds are another fascinating and useful class of soft materials finding applications in a wide range of fields [1.6-1.12].

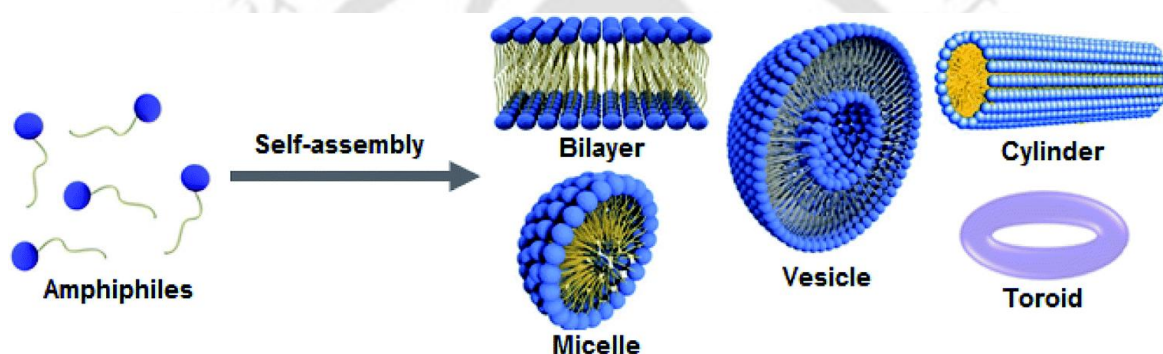


Figure 1.2: Hierarchical self-assembly of amphiphiles to form functional materials of different shapes. (adapted from [1.14])

1.2. Self-assembly of small molecules

Nano-materials designed by the self-assembly of small molecules are very promising in terms of various applications, especially detection of important analytes, as they have fast response to external stimuli. Self-assembly of small molecules integrated with fluorescent dyes can display distinct differences in their fluorescence signals between their self-assembled and disassembled states. Hence, immense research efforts have been put forwarded to explore the sensing applications via changes in fluorescence signal instigated from the controlled self-assembly of small molecule probes, including aggregation caused quenching (ACQ), aggregation induced emission (AIE), and the tunable monomer-excimer transition (Figure 1.3). Important to mention here that within the squad of fluorescent sensors, those appended with a donor and an acceptor unit can show Fluorescence/Förster Resonance Energy Transfer (FRET), photoinduced electron transfer (PET), intramolecular charge transfer (ICT) behaviour and have seen widespread

applicability. On the other hand, self-assembly of small molecules may also lead to supramolecular gelation, where gel-sol/sol-gel phase transitions offer another way for easy naked eye detection of biologically and environmentally important analytes [1.13-1.18].

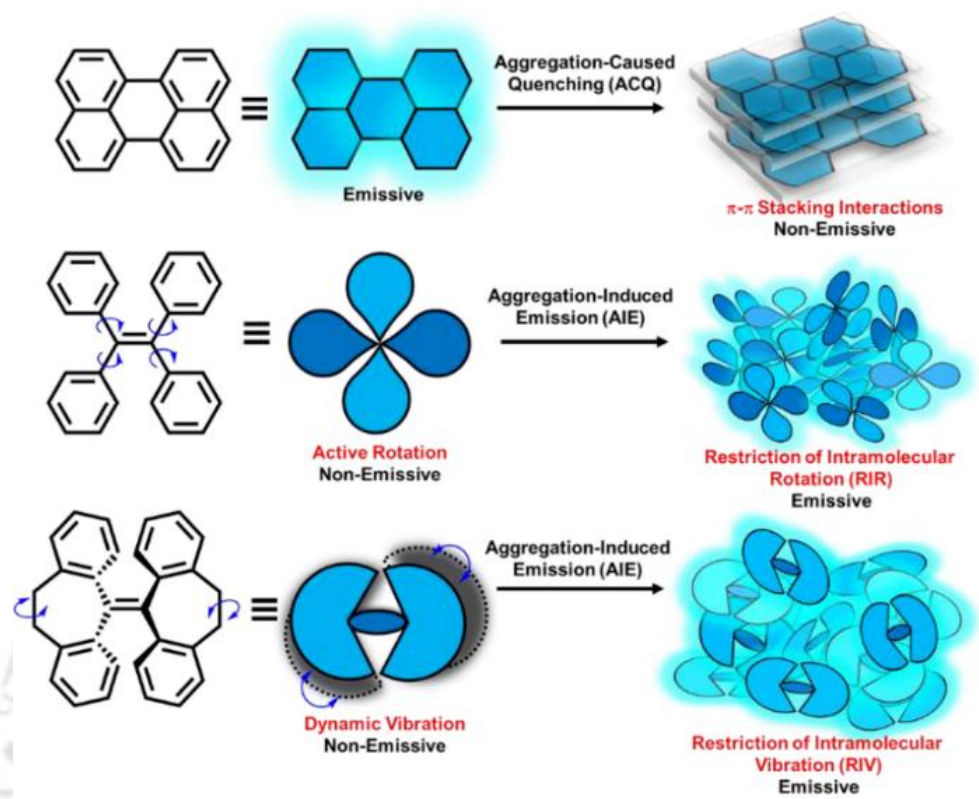


Figure 1.3: Schematics showing the general self-assembly mechanism of ACQ and AIE. (*adapted from [1.23]*)

1.3. AIE active small molecular probes for chemosensing application

The AIE behaviour was first reported by Ben Zhong Tang's research team in 2001. In contrast to the conventional ACQ property of organic small molecules, the discovery of AIE luminogens have emerged as breakthrough materials by opening up new possibilities for real-life applications. Restriction of intramolecular motion (RIM) has been proposed to be the mechanism of AIE phenomena. Contrary to traditional organic luminophores such as perylene having conjugated planar structures, AIEgens typically have twisted conformations, such as tetraphenylethylene (TPE), hexaphenylsilole (HPS), and 9,10-distyrylanthracene (DSA), which minimizes strong π - π interactions. However, in the course of time, more compounds have been found to display AIE properties. To date, myriads of AIE-based fluorescent chemosensors have been reported, which are capable of detecting varied analytes including organic small molecules, macromolecules, metal ions, anions etc. The mechanism of sensing by AIE probes may vary based on the chemical structures and photophysical properties of the analytes. For example, mechanism for sensing of

organic small molecules (including nitroaromatics, VOCs, antibiotics, biomolecules etc.) may include (although not restricted to) modulation of photophysical properties for instance introduction or inhibition of photoinduced electron transfer (PET), intramolecular charge transfer (ICT), Förster resonance energy transfer (FRET), inner filter effect (IFE) and excited state intramolecular proton transfer (ESIPT). Alteration of optical properties and/ or solubility of the AIEgens can also be achieved through chemical reaction/ supramolecular host guest chemistry between the analyte and the sensor, which can impact optical properties, or can lead to further aggregation or disaggregation. The AIE chemosensors for detection of cations commonly relies on the chelation-enhanced fluorescence (CHEF) and chelation-enhanced quenching (CHEQ) mechanism. The metal ion chemosensors contain functional groups that can coordinate with cations, thus forming insoluble coordination complexes or coordination polymers, which can form aggregate and thus giving turn on emission response. Metal-ligand interaction may induce or hinder photophysical processes such as PET, ICT, ESIPT, FRET, metal-to-ligand charge transfer (MLCT) or ligand-to-metal charge transfer (LMCT), which can lead to emission quenching, enhancement or colour change. Nevertheless, irreversible chemical reaction between the sensor and cationic analyte may also change the chemical structure of the probe, subsequently altering the emission response. On the other hand, most of the AIE fluorescent probes for anions depend on chemical reactions between electrophilic functional groups and nucleophilic anions, leading to change in the chemical structure resulting in either aggregation/disaggregation/decrease in the degree of electronic conjugation. Some anions may preferentially act as a base which can deprotonate the acidic protons from the fluorescent sensor thus changing the solubility. Moreover, some anions may also engage in anion- π and host-guest interactions with the sensor. In recent years an ample number of AIE-based chemosensors have been reported for detection of biologically and environmentally important analytes [1.19-1.23].

1.3.1. AIE probes for sensing of small organic molecules

In 2020, Lin *et al.* synthesized (Figure 1.4) a novel tripodal naphthalimide-based chemosensor (**TNQ**) which could self-assemble into a supramolecular system (**S-TNQ**) and demonstrated strong light blue AIE in DMF-H₂O binary solvent system. The bright blue fluorescence of **S-TNQ** was quenched in presence of PA. The **S-TNQ** showed sensitive and selective response for PA with limit of detection (LOD) of 4.73×10^{-8} M. The recognition mechanism is based on competitive binding of PA with the **TNQ**, which led to the destruction of the self-assembly and AIE of the **S-TNQ**. Additionally, the solid powder of the **TNQ** could be utilized as material for direct visual

detection of PA. Hence, the rational introduction of AIE in fluorescent sensors provided a new strategy for detection of explosives [1.24].

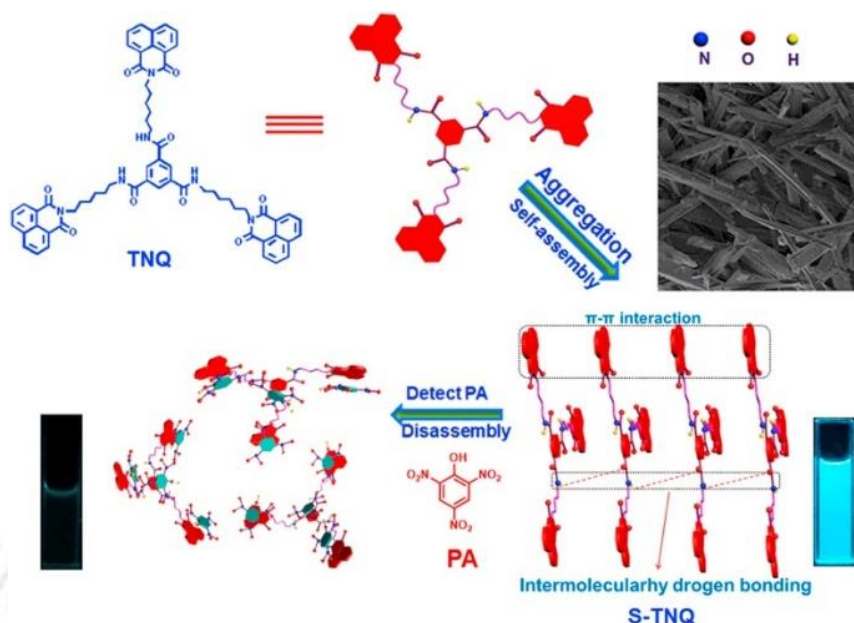


Figure 1.4: The structure of TNQ and the proposed recognition mechanism for detection of PA. (adapted from [1.24])

Tang and his group in 2015 developed a fluorescent sensor **HPQ-Ac** which could detect amine vapors (Figure 1.5) based on the fluorogen of 2-(2-hydroxyphenyl)quinazolin-4(3H)-one (**HPQ**). **HPQ** demonstrated typical AIE behaviour by virtue of excited state intramolecular proton transfer (ESIPT) and restriction of intramolecular motion (RIM) mechanisms.

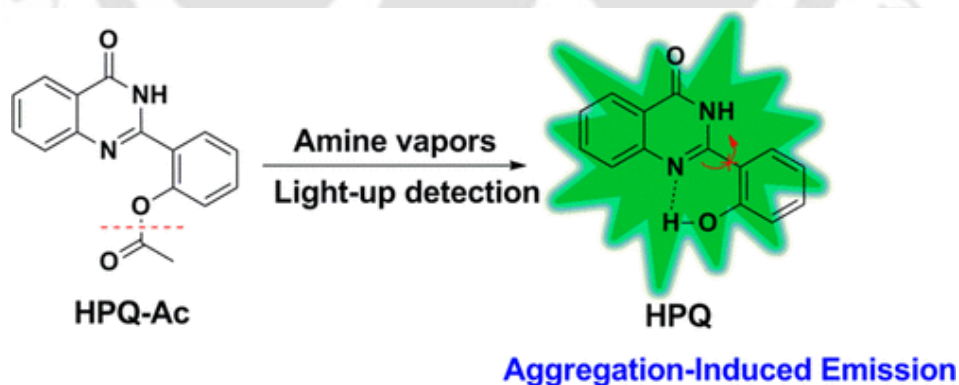


Figure 1.5: Design strategy of **HPQ-Ac** for Light-Up Detection of Amine Vapors. (adapted from [1.25])

The AIE property of both **HPQ** and **HPQ-Ac** was investigated in H₂O/THF (99:1, v/v) mixture. **HPQ-Ac** showed negligible fluorescence, while **HPQ** showed an intense fluorescence with maximum emission at 492 nm. Upon exposure to amine vapors, the fluorescence intensity of **HPQ-Ac** increased rapidly as the amine vapors could cleavage of the O-acetyl bond to yield highly

emissive **HPQ** product. Furthermore, the **HPQ-Ac** sensor was used for food spoilage monitoring by detection of volatile amines generated in food spoilage. It could also be used as fluorescent invisible ink displayed only when treated with ammonia vapor and UV light [1.25].

1.3.2. AIE probes for sensing of metal ions

Tian *et al.* synthesized fluorescent sensor **TPE-HB** containing TPE unit (Figure 1.6). **TPE-HB** exhibited AIE property when investigated in THF-H₂O system and showed strong yellow light in a 95% water solution. When Cu²⁺ was added to a solution of **TPE-HB** in THF/H₂O (v/v) = 1: 9 at pH = 7.3, the fluorescence emission was immediately quenched. It was hypothesized that the molecular structure of **TPE-HB-Cu²⁺** complex became planar because of the chelation effect between **TPE-HB** and Cu²⁺, which led to the stacking of molecules, resulting in fluorescence “turn-off” [1.26].

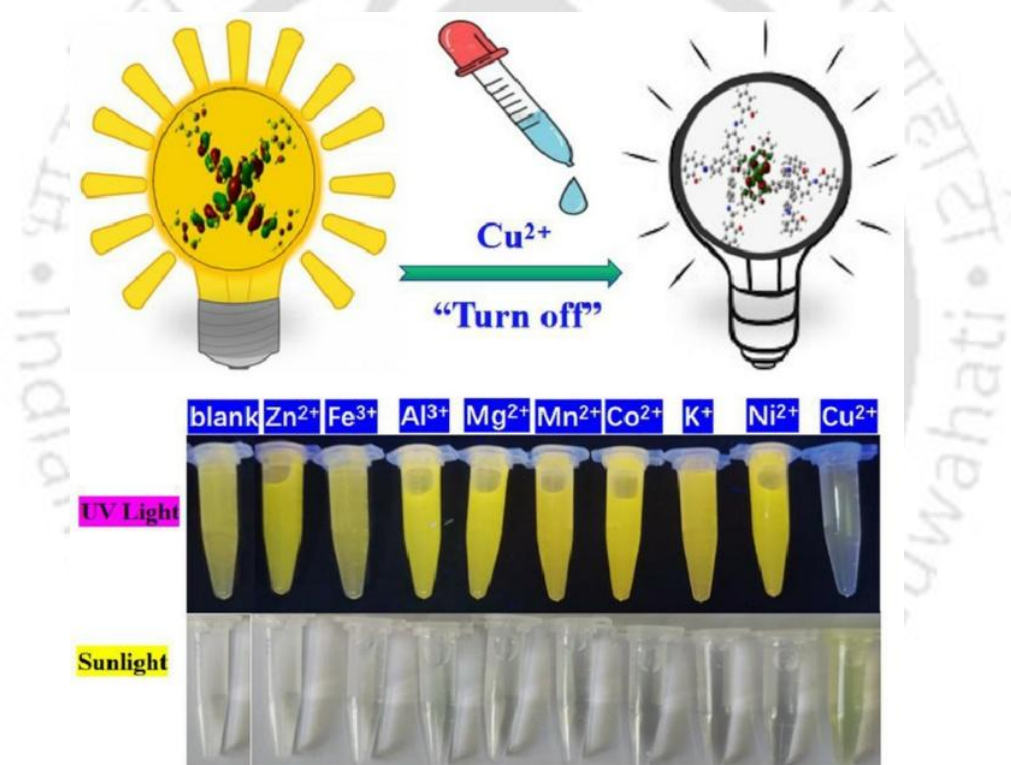


Figure 1.6: The structure of **TPE-HB** and turn off sensing of Cu²⁺. (adapted from [1.26])

In 20215, Zhao *et al.* reported an AIE-active fluorescent probe **TPE-COOH** (Figure 1.7). The probe itself is nonfluorescent in solution, however, upon complexation with Al³⁺, blue fluorescence was switched on with a 52-fold enhanced fluorescence intensity at 470 nm. The limit of detection was determined to be 21.6 nM for Al³⁺ quantitation. The nanoaggregate formation was clearly observed by transmission electron microscopy (TEM) after addition of Al³⁺. The

outcome suggested that Al^{3+} ions initiated the aggregation of **TPE-COOH**, leading to AIE effect and thus resulted in the significant fluorescence emission [1.27].

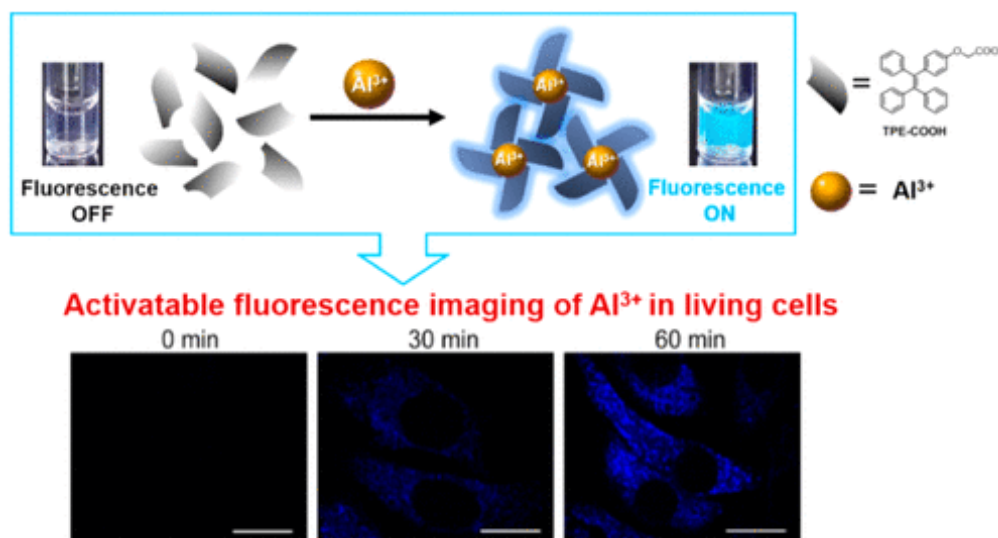


Figure 1.7: The proposed mechanism for fluorescence response of **TPE-COOH** to Al^{3+} . (adapted from [1.27])

1.3.3. AIE probes for sensing of anions

In 2017, Qu and his group designed a novel AIE active probe **1** from 2-benzothiazoleacetonitrile and 4-(diphenylamino)-benzaldehyde (Figure 1.8).

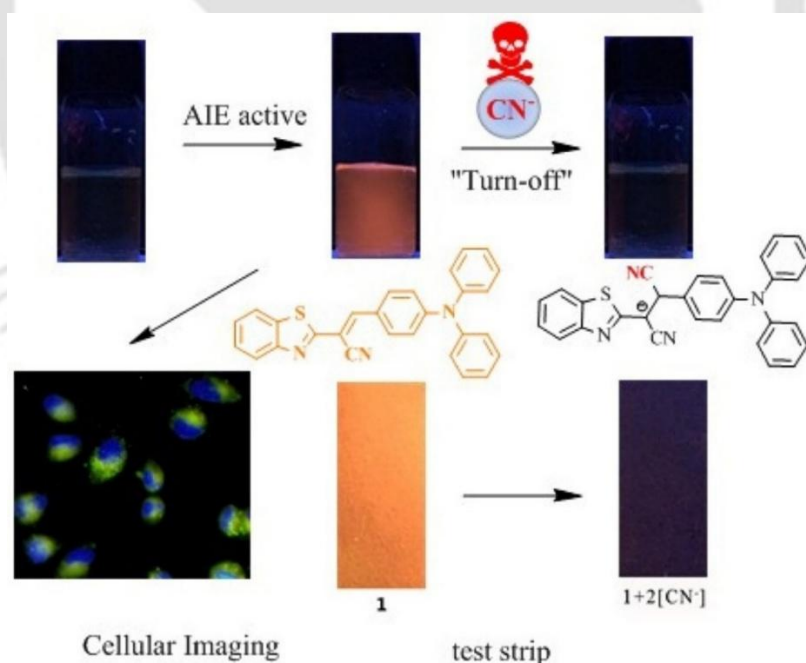


Figure 3.3: A) UV-Vis spectra of **L1**, **L2**, and **L3** in the mixed solvent system by varying solvent fraction and B) UV-Vis spectra of **L1**, **L2**, **L3** in aqueous medium of varying concentration. (adapted from [1.28])

The AIE behaviour of **1** was studied in acetonitrile/water binary solvent system. Orange fluorescence was observed when high quantity of water ($f_w > 80$ vol%) were added to acetonitrile

solution of **1**. It could detect toxic CN^- with very high selectivity and high sensitivity as the fluorescence intensity of **1** decreased 99% in presence of CN^- in almost 100% aqueous solution with a detection limits of 9.44 ppm. The fluorescent response to CN^- was ascribed to the nucleophilic addition of CN^- to the vinyl group of **1** which led to the breaking of the conjugation. Furthermore, prototype device based on test strips prepared by utilizing **1** could also detect CN^- conveniently [1.28].

Yan *et al.* in 2024, developed a novel fluorescent probe **TPA-Y**, which contained Triphenylamine (TPA) as the fluorophore unit (Figure 1.9). **TPA-Y** showed AIE behaviour when investigated in DMF/HEPES system and showed red fluorescence when water content was high ($f_w > 60\%$). Upon addition of HSO_3^- , there was visible colour change of **TPA-Y** from orange to colourless and also, there was fluorescence colour change of **TPA-Y** from red to blue. The LOD value was calculated to be 47.1 nM. The HSO_3^- induced obvious spectral changes of **TPA-Y**, might due to the Michael addition reaction of HSO_3^- with the probe, which broke the conjugated system and resulted in UV-vis/fluorescence spectra blue shift. The mechanism for HSO_3^- induced obvious spectral changes was hypothesized to be due to the Michael addition reaction of HSO_3^- with the probe, which led to the breaking of the conjugation and thus resulted in blue shift of UV-vis/fluorescence spectra. However, the original **TPA-Y** could be reverted via oxidation of **TPA-Y-HSO}_3^-** by H_2O_2 . Furthermore, **TPA-Y** could quantitatively detect HSO_3^- in water and food samples along with portable paper-based test strips applications [1.29].



Figure 1.9: The structure of **TPA-Y**, recognition mechanism for $\text{HSO}_3^-/\text{H}_2\text{O}_2$ and applications of **TPA-Y**. (adapted from [1.29])

1.4. Supramolecular gels

Pushing the limits of supramolecular assembly to form hierarchically dynamic and smart functional materials is a great challenging task for supramolecular chemists. In this regard, supramolecular gels can provide a platform for the fabrication supramolecular smart material via modulation and fine-tuning the gel properties. Supramolecular gels are constructed from self-assembly of organic compounds, termed as low molecular weight gelators (LMWG) exploiting non-covalent interactions. The self-assembly of these LMWG can be triggered by a number of ways depending on the chemical structure of the compound, however, the most common method includes simple heating and cooling. Heating leads to the dissolution of the LMWG, with cooling resulting in the molecules becoming insoluble. The designing of LMMG must be effective to prefer gelation over crystallization or precipitation. It is believed that the gelation presumably proceeds through the following three steps (Figure 2.0): 1. one-dimensional self-assembly of the LMWG leads to the formation of so-called supramolecular polymers; 2. the hierarchical assembly of these supramolecular polymers results in mesoscopic fibers; 3. the entanglement of these fibers leads to a three-dimensional network with solvent molecules immobilized within the network. Since supramolecular gels are formed with the help of supramolecular interactions such as hydrogen bonding, π - π stacking, hydrophobic interactions, van der Waals interactions, charge-transfer interactions, etc., which are reversible in nature, consequently, the gels are highly sensitive to different external stimuli and thus making those gels highly dynamic in nature.

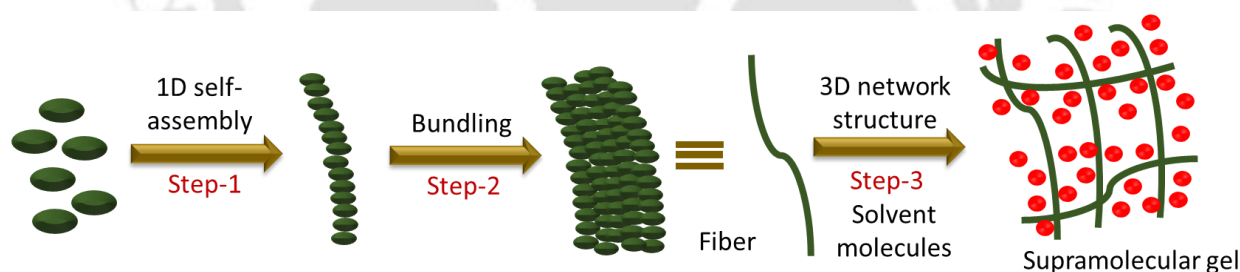


Figure 2.0: The schematic for formation of supramolecular gel.

Depending upon the solvent in which the gel is formed, the supramolecular gels can be termed as hydrogels, organogels, organohydrogels and aero/xerogels (Figure 2.1). Organogels contain organic solvents as the fluid phase. Supramolecular hydrogels on the other hand are prepared from hydrophilic molecules, comprising of water as the fluid phase. Aerogels and xerogels are basically dried gels where the liquid from the gel is extracted and they differ in their drying process. Both organogel and hydrogels have advantages and disadvantages in terms of their applications in different fields. However, this thesis highlights the importance of organohydrogels and possibility

to use them as the multifunctional smart materials. Organohydrogels are emerging class of soft materials composed of immiscible hydrophilic and hydrophobic counterparts having excellent advantages in environmental adaptability, switchable mechanical properties, adjustable wettability, etc. The thesis will mainly focus on organohydrogels comprising of binary solvent systems, including organic solvent and water. The preparation strategy for synthesis of such organohydrogel includes dissolution of the organic gelator molecule in a suitable organic solvent, followed by rapid addition of water in it.

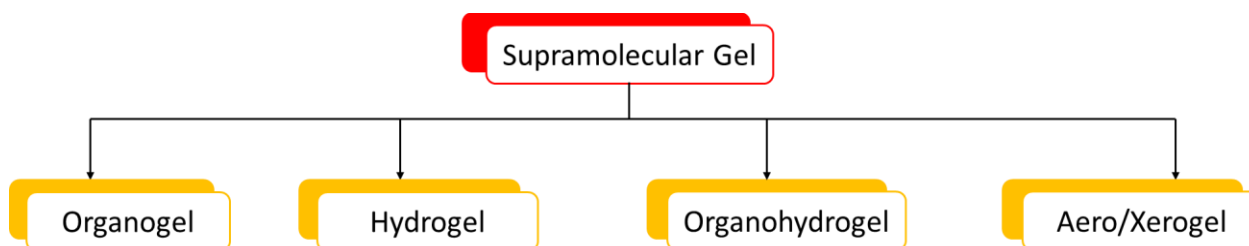


Figure 2.1: Different types of supramolecular gels depending upon the solvent medium.

Important to mention here about the supramolecular metallogels, which result when metal ions interact with the gelator. This particular field has received substantial attention as the presence of metals has been shown to be very advantageous in providing the gels with enhanced properties including fascinating redox, optical, electronic, and magnetic properties. This thesis not only reports metallogelators for various applications but also tried to understand the structure-function relationship for effective designing of metallogelators. Although, recent research has highlighted metallogelators and their applications in numerous fields, however, to date, only a handful of examples have been reported regarding the synthesis of anion-induced self-assemblies into supramolecular gels. The design rationale of such gelator is tricky and challenging, while the lower toxicity of such metal-free systems may be beneficial for both environmental and biological applications. The thesis thus tried to shed lights on synthesis of anion induced gel and explored their real-life applications.

Supramolecular gels due to their versatile nature applications in various fields. The gels can help naked detection of biologically and environmentally important analytes via gel to sol transitions. Conversely, gelation can be triggered only in the presence of some specific analytes. This way can also help detection of analytes through naked eye. The gels can find applications in waste water remediation by sequestration of the harmful substrates including toxic heavy metal ions, anions, or some dye molecules. Apart from these, the gel matrix can facilitate the in-situ synthesis and stabilization of metal nanoparticles, thus helping formation gel-nanocomposite materials, which can find applications in fields like catalysis along with biological applications [1.30-1.37].

1.4.1. Visual detection of biologically and environmentally important analytes

In 2019 Ghosh *et al.* designed a Cholesterol-appended benzothiazole based gelator **1** which could form gel in different solvents viz. nitrobenzene, benzene, toluene and DMF etc (Figure 2.2). The gelation of **1** in nitrobenzene was also investigated in the presence of nitrophenols and phenols. Interestingly, only in presence of picric acid (PA) gel formation was prohibited. In contrast, nitrobenzene gel of **1**, transformed to a yellow-colored sol upon addition of PA in nitrobenzene on the top of the gel. It was hypothesized that PA being strongly acidic could protonate the benzothiazole nitrogen, leading to a charge transfer complex formation with the protonated benzothiazole ultimately disrupting the gel. Additionally, the nitrobenzene gel of **1** could also detect Hg^{2+} and Ag^+ as there was a gel-to-sol phase transformation upon addition of these two ions. It was presumed that the binding interaction of these two thiophilic ions with sulfur of the benzothiazole unit led to the rupture of the gel network to give the sol [1.38].

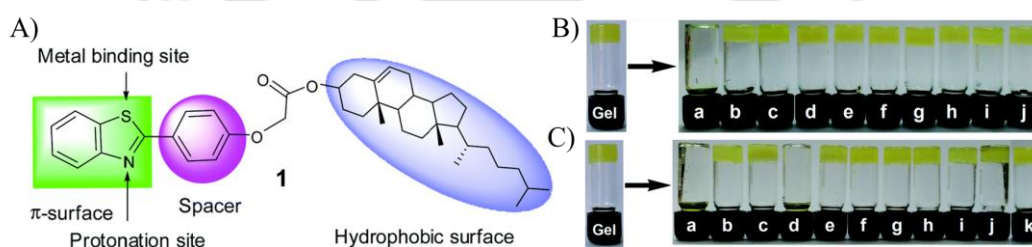


Figure 2.2: A) The structure of compound **1**, recognition mechanism for $\text{HSO}_3^-/\text{H}_2\text{O}_2$ and applications of TPA-Y, B) Images showing the phase changes of nitrobenzene gel of **1** (20 mg mL^{-1}) in the presence of a 1 equiv. amount of (a) picric acid, (b) o-nitrophenol, (c) p-nitrophenol, (d) 2,4-dinitrotoluene, (e) m-dinitrobenzene, (f) p-cresol, (g) o-chlorophenol, (h) benzoic acid, (i) acetic acid and (j) trifluoroacetic acid after 2 h, C) Images showing the phase changes of nitrobenzene gel **1** (20 mg mL^{-1}) in presence of 1 equiv. amounts of (a) Hg^{2+} , (b) Al^{3+} , (c) Fe^{3+} , (d) Ag^+ , (e) Cu^{2+} , (f) Fe^{2+} , (g) Zn^{2+} , (h) Co^{2+} , (i) Ni^{2+} , (j) Cd^{2+} and (k) Cu^+ after 2 h. (adapted from [1.38])

McNeil *et al.* in 2014, reported synthesis of nine Hg-containing compounds (**1-5**). Initial gel screening of **1-5** revealed that the compounds **1a**, **2b**, **2c**, **3a**, and **3b** could gelate at least one solvent system. As such the remediation potential of four gelators namely, **1a**, **2c**, **3a** and **3b** was scrutinized. Instantaneous gelation was observed when Hg-contaminated water was added to a MeOH solution containing each of the gelators at the suitable concentration (Figure 2.3). The gelators exhibited high Hg^{2+} remediation abilities (>98%). The gelation was observed to be highly selective for Hg^{2+} over other metal ions, which was assumed to be because of the linear geometries of these complexes, thus facilitating 1D intermolecular interactions. The gel formation was also observed in different environmentally relevant water sources (bottled water, tap water, and Huron River water) in presence of added $\text{Hg}(\text{OAc})_2$, thus proving the robustness of this sensing platform [1.39].

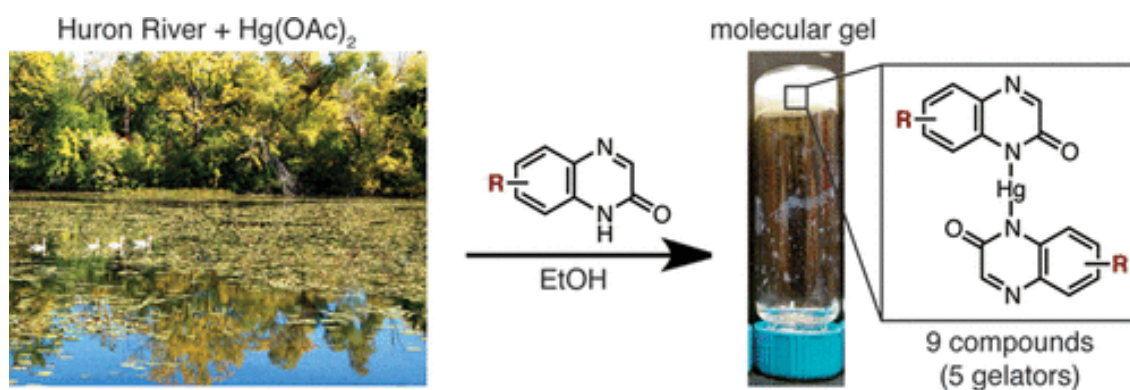


Figure 2.3: Gel formation in Huron River water in presence of $\text{Hg}(\text{OAc})_2$ by the gelators. (adapted from [1.39])

1.4.2. Removal of toxic analytes from wastewater

In 2018, Mondal *et al.* developed a novel pyridine-pyrazole-based gelator molecule **BP3D** (Figure 2.4). It could form a transparent colorless hydrogel, **G-L** in the dimethyl sulfoxide (DMSO)/water solvent mixture. To investigate the toxic heavy metal sequestration from polluted water, metal solutions of known concentration of Pb, Cd and Hg were added on top of the hydrogel column of 2 mL and 1 wt % concentration.

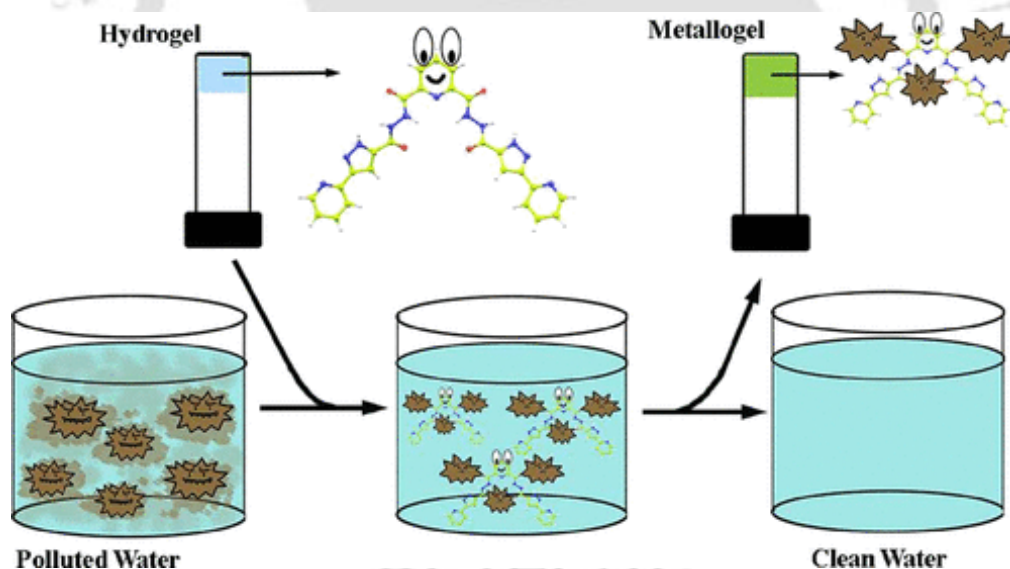


Figure 2.4: Wastewater purification by the hydrogel **G-L**. (adapted from [1.40])

Thereafter, the aliquots from the top of the gel were taken from time to time and measured for metal concentrations. The sequestration rate for Cd was observed to be slow. However, concentration of Pb showed a decreased from an initial 301.5 to 205.1 mg/L after 15 days to an impressive 43.34 mg/L (85.63% removal) within 3 months. Similar was the case for Hg with a decrease in concentration from 24.12 to 12.27 mg/L after first 15 days and as low as 0.011 mg/L

(99.95% removal) within 3 months. There was a distinct change in the colour of the gel, as the decrease in metal concentration on the upper solution layer implied the gain in the lower gel state. The lesser concentration of metal suggested lesser amount of toxic metals in the residual water and consequently suggested that the hydrogel column could be used for water purification [1.40].

Yamanaka *et al.* in 2017, synthesized an amphiphilic tris-urea gelator **1** which was capable of forming supramolecular hydrogels via hierarchical self-assembly process (Figure 2.5). The mixing of **1** and NaOH solution formed a viscous solution. The addition of HCl or CaCl₂ to this solution produced supramolecular hydrogels (**1-HCl** gel or **1-CaCl₂** gel). The hydrogels were employed to investigate the adsorption of organic dyes and it was observed that cationic organic dyes were adsorbed efficiently. The extent of methylene blue adsorption was as high as 4.19 mol equiv compared to **1**. Luminescence spectroscopy and fluorescence microscopy analyses revealed that adsorption proceeded gradually by two modes, occurring initially on the fibers and later in the aqueous spaces of the supramolecular hydrogel [1.41].

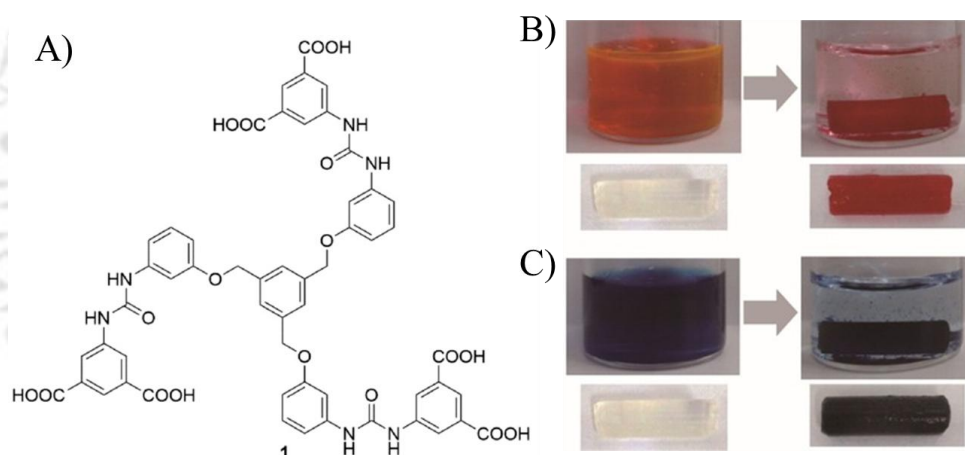


Figure 2.5: A) Structure of amphiphilic tris-urea **1**, Pictures showing adsorption of B) rhodamine 6G (Rh6G) and C) methylene blue (MB) by **1-HCl** gel. The smaller photographs show the gels before and after adsorption. (*adapted from [1.41]*)

1.4.3. Gel-nanoparticle hybrid materials

In 2024, Banerjee and his group developed an amphiphilic peptide **P1** (Figure 2.6). It was found that **P1** itself did not form gel, however, metallogelation was observed at a 1:2 (metal: **P1**) ratio in phosphate buffer at pH 7.46 by encapsulating metal (Co²⁺ or Ni²⁺ or Ag⁺) ions inside the cross-linked nanofibrillar network structure. The white colour of the silver metallogel (**Ag-Gel**) changed to brown due to reduction of silver upon exposure to sunlight, generating a hydrogel infused with silver nanoparticles (**AgNP-Gel**). The silver nanoparticles (AgNPs) thus generated by amphiphilic

peptide finds immense interest due to their ease of functionality. The AgNP-Gel was further used as catalysts for electrochemical hydrogen generation [1.42].

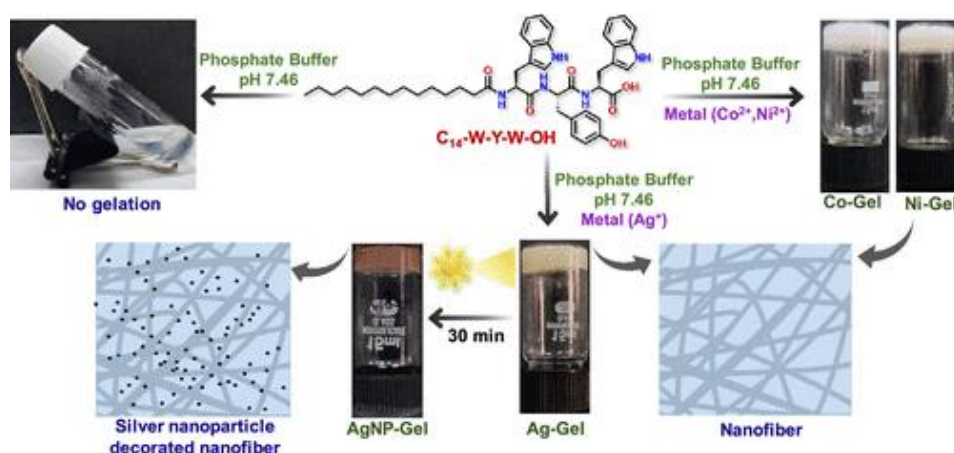


Figure 2.6: Schematic diagram of the formation of the peptide amphiphile-based metallogels and silver nanoparticle-loaded metallogels. (adapted from [1.42])

In 2020, Das and his co-workers reported boronate ester directed G-quadruplex hydrogels as a template for in situ synthesis of metal NPs without using any external reducing and stabilizing agents (Figure 2.7). The use of guanosine (G) functionalized dynamic G-TBA based soft G-quadruplex hydrogel as template for the synthesis of NPs might provide a greenery approach due to their biodegradable nature.

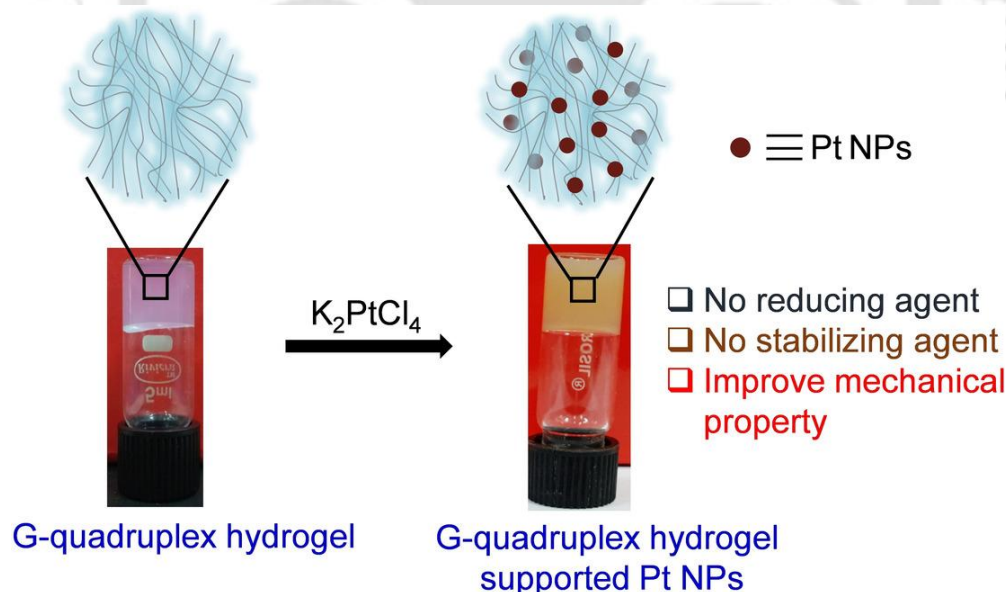


Figure 2.7: Schematic illustration of in situ synthesis of Pt NPs in G-quadruplex hydrogel network. (adapted from [1.43])

The G-TBA hydrogel nanofibrillar network behaved as a nanoreactor for the nucleation and growth of NPs. Das *et al.* reported the G-quadruplex hydrogel as nanoreactor for in situ synthesis

of Pt NPs. 0.2 mL of K_2PtCl_4 (0.1 M) was added during the synthesis of hydrogel (2 mL) and the solution was kept in a dark place. The change in colour of the gel initially hinted towards the formation of Pt NPs, which was further confirmed by the TEM and XPS results. The Pt NPs thus synthesized were then used as effective reusable catalyst for the hydrogenation reaction of nitroarenes [1.43].

1.5. Summary of Literature Review and Research Gaps

A comprehensive literature review highlighted the role of low molecular weight molecular probe as promising materials for various multifunctional applications. Small molecule-based probes/receptors can be rationally designed and fine-tuned its properties via modification of substituents keeping the core skeleton intact. Detection of various important analytes via these molecular receptors relies on the fact that the recognition is followed by some readable responses, including optical (change of fluorescence or colour) or sol-gel transition, hence confirming the presence of that particular analyte. For synthesis of optical sensors, receptor molecule containing the recognition site is connected with a chromophore and/or fluorophore unit, called as the signalling unit that responds to various stimuli through noticeable as well as measurable colorimetric or fluorometric changes. Consequently, optical sensors provide a detection method having advantages like low-cost, fast response, easy sample preparation and simple handling. The general sensing mechanism of fluorescent sensors includes aggregation-induced emission (AIE), photoinduced electron transfer (PET), fluorescence resonance energy transfer (FRET), chelation induced enhanced fluorescence (CHEF), metal-ligand charge transfer (MLCT), intramolecular charge transfer (ICT), twisted intramolecular charge transfer (TICT) etc. Nevertheless, receptors fabricated with conventional fluorophores often meet drawbacks like aggregation-caused quenching effect causing fluorescence quenching at high concentrations and thus, limiting its real-world sensing applications as sensitivity is compromised. Hence, the thesis stressed on improved design rationale of fluorescent probes to mitigate the quenching effect.

Low molecular weight supramolecular gels are on the other hand, a class of multifunctional smart materials getting boost in recent times. These gelators are advantageous over the traditional polymeric gels due to the dynamic nature of the non-covalent interactions present in them which makes them stimuli-responsiveness to environmental changes such as pH, heat, light, enzymes etc. They are capable of providing a platform for naked eye detection of analytes via gel to sol transformation or vice-versa without using any sophisticated instrumentations. However, these gelators are inherently difficult to design and as such understanding of structure-function relationship for synthesis of such system is important. This thesis in this regard, presented design

rationale for different gelator molecules including anion induced and metal induced gelator molecules. A diverse range of practical applications of these soft materials were then explored in this thesis.

1.6. Objectives of the Thesis

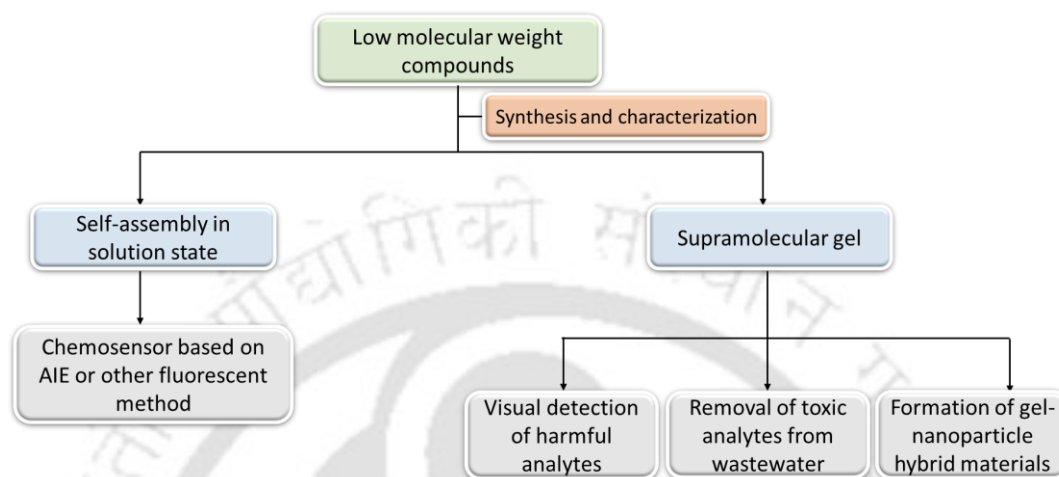
The present thesis highlights the importance of small molecule-based probes for development of aggregated species having fascinating photophysical properties and further utilizes these systems as sensing tools for different biologically and environmentally important analytes. Moreover, small molecular receptors were also exploited for the synthesis of supramolecular gels via hierarchical self-assembly formation, which were then used as multifunctional smart materials.

The thesis hence, aims to focus on the following critical areas:

- Synthesis of self-assembled system capable of showing interesting photophysical properties in solution state
- Utilizing these self-assembled systems for chemosensing of harmful anions, cations or organic small molecules
- Hierarchical self-assembly formation of these molecules to form supramolecular gels
- Exploitation of the supramolecular gels for various real-life applications

Emphasis was given on synthesis of low molecular weight receptors because of their small size, easy chemical modification, and biocompatibility. Schiff base, urea and amide based small molecular probes fabricated with different fluorophore moieties were designed rationally because of their easy synthesis process and their ability to show interesting self-aggregation as well as sensing behaviour. Interesting solution state aggregation properties such as AIE were explored along with stimuli responsive properties towards various solvents, pH, temperature and important analytes. Depending on the design strategy, the self-assembled systems were capable of sensing different analytes including toxic heavy metals, anions, explosives like picric acid etc. The fluorescence-based techniques were primarily used for the solution state sensing of these analytes. Nevertheless, the thesis also highlights on synthesis of low molecular weight organohydrogels. The design rationale for the gelator basically comprised of inclusion of groups having multiple hydrogen bond donor and acceptors such as acylhydrazone units, π - π stacking units or coordination sites for metals/anions to form extended polymeric networks. The synthesis steps were simple yet effective and supramolecular gels thus synthesized were utilized for visual detection of analytes via gel to sol transition or triggering of gelation selectively in presence of a specific analyte. The gels were also used for the adsorption of harmful dye molecule from contaminated water.

Furthermore, gel-nanocomposite hybrid materials were also synthesized which found applications in antioxidant/ antibacterial study. The thesis represented that tailoring the probes/receptors with substituents of interest can offer desired property for controlled self-assembly formation. The objectives of the thesis work are broadly divided into two objectives, which are pictorially represented in the form of a flow chart in scheme 1.1.



Scheme 1.1: Thesis Objectives.

References

- [1.1] D. Pochan and O. Scherman, *Chem. Rev.*, 2021, **121**(22), 13699-13700.
- [1.2] J. Zhang, S. Qi, C. Zhang, W. Wang, Q. Ding, H. Zhang and Z. Dong, *Chem. Commun.*, 2021, **57**, 6272-6275.
- [1.3] A. C. Mendes, E. T. Baran, R. L. Reis and H. S. Azevedo, *WIREs Nanomed Nanobiotechnol.*, 2013, **5**, 582-612.
- [1.4] N. Stephanopoulos, J. H. Ortony, S. I Stupp, *Acta Mater.*, 2013, **61**(3), 912-930.
- [1.5] N. Stephanopoulos, *Chem*, 2020, **6**, 364-405.
- [1.6] D. V. Talapin, M. Engel and P. V. Braun, *MRS Bulletin*, 2020, **45**, 799-806.
- [1.7] J. Yin, L. Huang, L. Wu, J. Li, T. D. James and W. Lin, *Chem. Soc. Rev.*, 2021, **50**, 12098-12150.
- [1.8] B. Parshad, S. Prasad, S. Bhatia, A. Mittal, Y. Pan, P. K. Mishra, S. K. Sharma and L. Fruk, *RSC Adv.*, 2020, **10**, 42098-42115.
- [1.9] Y. Hou, L. Zou, Q. Li, M. Chen, H. Ruan, Z. Sun, X. Xu, J. Yang and G. Ma, *Mater. Today Bio*, 2022, **15**, 100327.
- [1.10] S. Varughese, *J. Mater. Chem. C*, 2014, **2**, 3499-3516.
- [1.11] V. K. Praveen, B. Vedhanarayanan, A. Mal, R. K. Mishra and A. Ajayaghosh, *Acc. Chem. Res.*, 2020, **53**, 2, 496-507.
- [1.12] E. R. Draper and D. J. Adams, *Chem.*, 2017, **3**, 390-410.
- [1.13] B. Wang, Y. Liu, X. Chen, X.-T. Liu, Z. Liu and C. Lu, *Chem. Soc. Rev.*, 2024, **53**, 10189-10215.
- [1.14] B. Parshad, S. Prasad, S. Bhatia, A. Mittal, Y. Pan, P. K. Mishra, S. K. Sharma and L. Fruk, *RSC Adv.*, 2020, **10**, 42098-42115.
- [1.15] C. Ren, J. Zhang, M. Chen and Z. Yang, *Chem. Soc. Rev.*, 2014, **43**, 7257-7266.

- [1.16] Y. Li, H. Zhou, J. Chen, S. A. Shahzad and C. Yu, *Biosens. Bioelectron.*, 2016, **76**, 38-53.
- [1.17] L. Wu, C. Huang, B. P. Emery, A. C. Sedgwick, S. D. Bull, X.-P. He, H. Tian, J. Yoon, J. L. Sessler and T. D. James, *Chem. Soc. Rev.*, 2020, **49**, 5110-5139.
- [1.18] J. Yin, L. Huang, L. Wu, J. Li, T. D. James and W. Lin, *Chem. Soc. Rev.*, 2021, **50**, 12098-12150.
- [1.19] J. Luo, Z. Xie, J. W. Y. Lam, L. Cheng, H. Chen, C. Qiu, H. S. Kwok, X. Zhan, Y. Liu, D. Zhuc and B. Z. Tang, *Chem. Commun.*, 2001, 1740-1741.
- [1.20] M. H. Chua, B. Y. K. Hui, K. L. O. Chin, Q. Zhu, X. Liu and J. Xu, *Mater. Chem. Front.*, 2023, **7**, 5561-5660.
- [1.21] Y. Luo, L. K. E. A. Abdelmohsen, J. Shao, J. C. M. van Hest, *Small Struct.*, 2025, **6**, 2500387.
- [1.22] M. H. Chua, H. Zhou, Q. Zhu, B. Z. Tang and J. W. Xu, *Mater. Chem. Front.*, 2021, **5**, 659-708.
- [1.23] M. H. Chua, K. W. Shah, H. Zhou and J. Xu, *Molecules*, 2019, **24**, 2711.
- [1.24] Y.-J. Li, Y.-F. Zhang, Y.-M. Zhang, Z.-H. Wang, H.-L. Yang, H. Yao, T.-B. Wei and Q. Lin, *Dyes pigm.*, 2020, **181**, 108563.
- [1.25] M. Gao, S. Li, Y. Lin, Y. Geng, X. Ling, L. Wang, A. Qin and B. Z. Tang, *ACS Sens.*, 2016, **1**(2), 179-184.
- [1.26] X. Niu, H. Zhang, X. Wu, S. Zhu, Y. Liu and M. Tian, *J. Mol. Struct.*, 2022, **1264**, 133294.
- [1.27] S. Gui, Y. Huang, F. Hu, Y. Jin, G. Zhang, L. Yan, D. Zhang and R. Zhao, *Anal. Chem.*, 2015, **87**(3), 1470-1474.
- [1.28] X. Chen, L. Wang, X. Yang, L. Tang, Y. Zhou, R. Liu and J. Qu, *Sens. Actuator. B Chem.*, 2017, **241**, 1043-1049.
- [1.29] X. Yao, Y. Li, Y. Guo, K. Zhong, L. Tang and X. Yan, *J. Photochem. Photobiol. A-Chem.*, 2024, **446**, 115116.
- [1.30] Y. Wang, J. Xiong, F. Peng, Q. Li and M.-H. Zeng, *Colloids Surf. A: Physicochem. Eng. Asp.*, 2022, **640**, 128445.
- [1.31] S. Kimura, K. Adachi, Y. Ishii, T. Komiyama, T. Saito, N. Nakayama, M. Yokoya, H. Takaya, S. Yagai, S. Kawai, T. Uchihashi and M. Yamanaka, *Nat. Commun.*, 2025, **16**, 3758.
- [1.32] D. J. Adams, *J. Am. Chem. Soc.*, 2022, **144**(25), 11047-11053.
- [1.33] M. A. Kuzina, D. D. Kartsev, A. V. Stratonovich and P. A. Levkin, *Adv. Funct. Mater.*, 2023, **33**, 2301421.
- [1.34] X. Le, H. Shang and T. Chen, *Macromol. Chem. Phys.*, 2024, **225**, 2300377.
- [1.35] L. Casimiro, F. Volatron, G. Boivin, B. Abécassis, S. Alves, D. Brouri, D. Montero, J.-M. Guigner, L.-M. Chamoreau, G. Gontard, D. Portehault, Y. Li, A. Proust, R. Lescouëzec, G. Ducouret, A. S.-Daura, P. Davidson, T. Merland and G. Izzet, *JACS Au*, 2024, **4**(12), 4948-4956.
- [1.36] Z. Kokan, M. D. Smrčková and V. Šindelář, *Chem*, 2021, **7**, 2473-2490.
- [1.37] B. Pramanik and S. Ahmed, *Gels*, 2022, **8**(9), 533.
- [1.38] S. Mondal, R. Raza and K. Ghosh, *New J. Chem.*, 2019, **43**, 10509.
- [1.39] K. K. Carter, H. B. Rycenga and A. J. McNeil, *Langmuir*, 2014, **30**(12), 3522-352.
- [1.40] A. De and R. Mondal, *ACS Omega*, 2018, **3**(6), 6022-6030.
- [1.41] J. Takeshita, Y. Hasegawa, K. Yanai, A. Yamamoto, A. Ishii, M. Hasegawa, M. Yamanaka, *Chem. Asian J.*, 2017, **12**, 2029-2032.
- [1.42] T. Mondal, S. Patra, B. Mondal, P. Ghosh, I. W. Hamley and A. Banerjee, *ACS Appl. Polym. Mater.*, 2024, **6**(18), 11383-11391.
- [1.43] T. Ghosh, A. Biswas, S. Bhowmik and A. K. Das, *Chem Asian J.*, 2021, **16**, 215-223.

Chapter 2

Experimental & Characterization Details



2. Experimental Details and Characterization

This chapter provides thorough descriptions of the various chemicals/materials and procedures used in the synthesis and characterisation of the involved probes/receptors (**L₁₋₃**, **R1**, **R2**, **TRI-QUI**, **TRI-NAP**, **ADH-Py-o**, **ADH-Py-m**, **ADH-Py-p**, **ADH-Ph**, **GUA-IND** and **GUA-NAP**). It also outlines the specifications of the analytical tools utilised, as well as the various experimental setups and computations needed to observe the aggregation/disaggregation behaviour of analytes, photophysical properties, and interactions with cationic, anionic or neutral analytes. Moreover, procedures for supramolecular gel formation as well as their characterizations are also provided.

2.1. General Information and Materials

All the reagents, starting materials, solvents, fine chemicals and different metal salts; were procured from commercial sources and were used as received. All were of reagent grade. The solvents used were HPLC grade. For NMR analyses, deuterated solvent [(CD₃)₂SO and CDCl₃] was purchased from Sigma-Aldrich. The UV-Visible or absorption spectra were recorded on a Perkin-Elmer Lambda-750 UV-Vis spectrophotometer using 10 mm path length quartz cuvettes in 250-700 nm wavelengths. Baseline correction was applied for all spectra. Fluorescence emission spectra were recorded on a Horiba Fluoromax-4 spectrofluorometer using a 1 cm path length of quartz cuvettes at 298 K. High-resolution mass spectrometry of all probes were carried out on a Waters Q-ToF Premier mass spectrometer. The solution-phase ¹H and ¹³C Nuclear Magnetic Resonance spectra were recorded using Bruker Advances 600 MHz, 500 MHz and 400 MHz NMR instruments. The chemical shifts were reported in parts per million (ppm) with the deuterated solvents. The following abbreviations are used to delineate spin multiplicities in ¹H NMR spectra: s = singlet; d = doublet; t = triplet; q = quartet, m = multiplet. Rheological measurements were performed using a Thermo Scientific Rheometer (HAAKE MARS iQ Air) equipped with a 35 mm parallel plate arrangement. Experiments were carried out on freshly prepared gels. Linear viscoelastic regions of the samples were determined by measuring the storage modulus, G' (associated with energy storage), and the loss modulus G'' (associated with the loss of energy) as a function of the stress amplitude. The gel-sol transitions were monitored over different shear strains with a fixed frequency at 1 Hz. As the storage modulus(G') starts to decrease after a 1% shear strain, we decided on a shear strain of 0.1 % to measure the frequency-dependent rheological behaviors of the gels.

2.2. Synthetic procedure and characterization of the all the probes/receptors

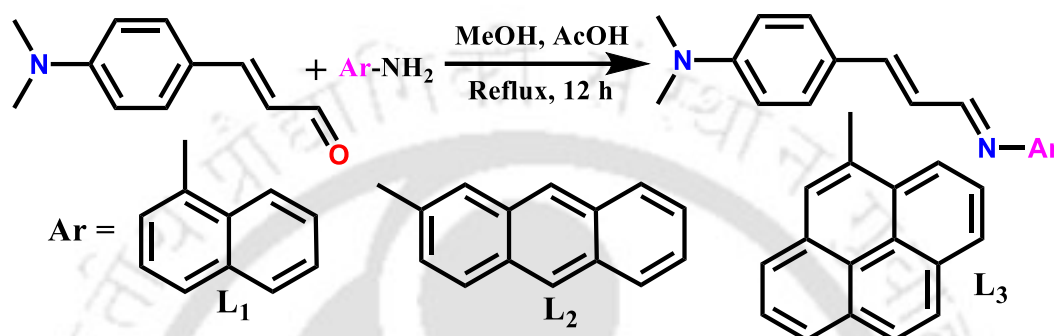
2.2.1. Synthesis of L₁ [*N,N*-dimethyl-4-((1*E*,3*E*)-3-(naphthalen-1-ylimino)prop-1-en-1-yl)aniline], L₂ [4-((1*E*,3*E*)-3-(anthracen-2-ylimino)prop-1-en-1-yl)-*N,N* dimethylaniline] and L₃ [*N*-((1*E*,3*E*)-4-(4-(dimethylamino)phenyl)buta-1,3-dien-1-yl)pyren-1-amine]

Receptors L₁ have been synthesized by adding 4-Dimethylcinnamaldehyde (305.94mg, 1.74 mmol) into a dehydrated methanolic solution of 1-Naphthylamine (250mg, 1.75mmol). 1-2 drops of glacial acetic acid were added to the methanolic solution and refluxed overnight at 60 ° C. Orange crystalline solid product was obtained. The product was then filtered, washed several times with methanol, and dried in a desiccator to obtain the pure product. Calculated yield was found to be 70%. ¹H NMR (600 MHz, Chloroform-*d*) δ 8.34 (d, *J* = 8.9 Hz, 1H), 8.31 (d, *J* = 7.6 Hz, 1H), 7.86 (d, *J* = 8.7 Hz, 1H), 7.70 (d, *J* = 8.9 Hz, 1H), 7.52 (dd, *J* = 13.1, 6.5 Hz, 6H), 7.47 (t, *J* = 7.7 Hz, 1H), 7.13 (d, *J* = 10.0 Hz, 2H), 7.02 (d, *J* = 7.2 Hz, 1H), 6.75 (d, *J* = 8.5 Hz, 1H), 3.07 (s, 6H), ¹³C NMR (151 MHz, CDCl₃) δ 162.98, 151.37, 149.94, 145.01, 133.95, 129.15 (×2C, Ar-C), 128.78, 127.60, 126.28, 126.08, 125.62, 125.23, 124.11, 123.98, 123.65, 112.94, 112.04 (×2C, Ar-C), 40.23 (×2C, N(CH₃)₂), HRMS (*m/z*): calculated for C₂₁H₂₀N₂ [M+H]⁺: 301.1626; found: 301.1707; FT-IR (KBr pellets, cm⁻¹): 1583.84 (C=N), melting point: 112°C. (Scheme 2.2.1)

Receptors L₂ have been synthesized by adding 4-Dimethylcinnamaldehyde (226.7mg, 1.29 mmol) into a dehydrated methanolic solution of 2-Aminoanthracene (250mg, 1.75mmol). 1-2 drops of glacial acetic acid were added to the methanolic solution and refluxed overnight at 60 ° C. Greenish yellow crystalline solid product was obtained. The product was then filtered, washed several times with methanol, and dried in a desiccator to obtain the pure product. Calculated yield was found to be 85%. ¹H NMR (600 MHz, Chloroform-*d*) δ 8.47 (d, *J* = 9.0 Hz, 1H), 8.46 (s, 2H), 8.02 (t, *J* = 9.6 Hz, 3H), 7.72 (s, 1H) 7.49 (dt, *J* = 15.1, 7.7 Hz, 5H), 7.18 (d, *J* = 15.7 Hz, 1H), 7.06 (dd, *J* = 15.7, 9.0 Hz, 1H), 6.75 (d, *J* = 8.5 Hz, 2H), 3.07 (s, 6H), ¹³C NMR (151 MHz, CDCl₃) δ 162.26, 151.40, 149.07, 145.23, 144.23, 132.38, 132.12, 131.36, 130.37, 129.28, 129.20 (×2C, Ar-C), 128.26, 127.97, 126.15, 126.03, 125.54, 125.11, 124.02, 123.69, 121.83, 117.40, 112.05 (×2C, Ar-C), 40.22 (×2C, N(CH₃)₂), HRMS (*m/z*): calculated for C₂₅H₂₂N₂[M+H]⁺: 351.1783; found: 351.1870, FT-IR (KBr pellets, cm⁻¹): 1589.84 (C=N), melting point: 230°C. (Scheme 2.2.1)

Receptors L₃ have been synthesized by adding 4-Dimethylcinnamaldehyde (202mg, 1.15 mmol) into a dehydrated methanolic solution of 1-Aminopyrene (250mg, 1.15mmol). 1-2 drops of glacial acetic acid were added to the methanolic solution and refluxed overnight at 60 ° C. Dark red crystalline solid product was obtained. The product was then filtered, washed several times with methanol, and dried in a desiccator to obtain the pure product. Calculated yield was found

to be 80%. ^1H NMR (600 MHz, Chloroform-*d*) δ 8.65 (d, $J = 9.1$ Hz, 1H), 8.49 (dd, $J = 5.1, 2.6$ Hz, 1H), 8.18 (t, $J = 6.0$ Hz, 3H), 8.12 (d, $J = 9.1$ Hz, 1H), 8.06 (d, $J = 8.9$ Hz, 1H), 8.02 (dd, $J = 13.2, 5.9$ Hz, 2H), 7.69 (d, $J = 8.0$ Hz, 1H), 7.55 (d, $J = 8.5$ Hz, 2H), 7.23 (s, 2H), 6.77 (d, $J = 8.4$ Hz, 2H), 3.08 (s, 6H), ^{13}C NMR (151 MHz, CDCl_3) δ 163.44, 151.41, 146.61, 145.21, 131.64, 131.60, 129.23 ($\times 2\text{C}$, Ar-C), 129.18, 127.34, 126.92, 126.39, 126.03, 125.57, 125.33, 125.03, 125.00, 124.76, 124.74, 124.41, 123.75, 123.38, 115.70, 112.07 ($\times 2\text{C}$, Ar-C), 40.24 ($\times 2\text{C}$, $\text{N}(\text{CH}_3)_2$), HRMS (m/z): calculated for $\text{C}_{27}\text{H}_{22}\text{N}_2[\text{M}+\text{H}]^+$: 375.1783; found: 375.1825, FT-IR (KBr pellets, cm^{-1}): 1595.39(C=N), melting point: 185°C. (Scheme 2.2.1)



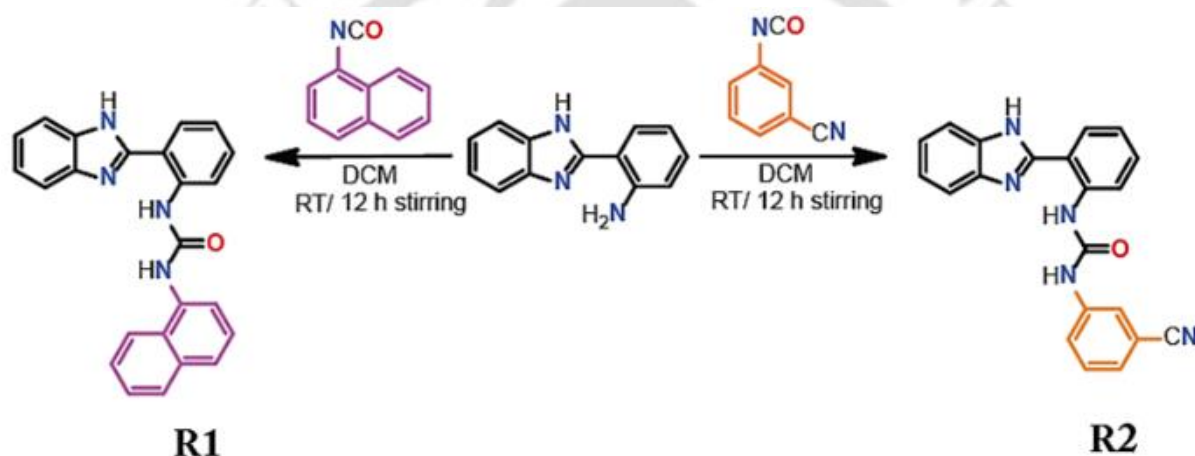
Scheme 2.2.1: Preparation of **L1-3**.

2.2.2. Synthesis of **R1** [1-(2-(1H-benzo[d]imidazol-2-yl)phenyl)-3-(naphthalen-1-yl)urea] and **R2** [1-(2-(1H-benzo[d]imidazol-2-yl)phenyl)-3-(3-cyanophenyl)urea]

2-(1H-benzimidazol-2-yl)aniline (500 mg, 2.39 mmol, 1 equiv.) was placed in a 50 mL round-bottomed flask and dissolved in dichloromethane (DCM) (15 mL). A solution of naphthyl isocyanate (340 mg, 2.39 mmol, 1 equiv.) was added into the flask in dropwise manner. The reaction was stirred at room temperature for 12 hours. The precipitates were separated by filtration and washed with DCM (30 mL) and diethyl ether (30 mL). The obtained white powder was further dried over vacuum and isolated as compound **R1**. Yield, 90%. ^1H NMR (500 MHz, $\text{DMSO-}d_6$) δ 12.97 (s, 1H), 12.01 (s, 1H), 9.42 (s, 1H), 8.48 (d, $J = 8.4$ Hz, 1H), 8.15 (d, $J = 8.2$ Hz, 1H), 7.99 (t, $J = 8.2$ Hz, 2H), 7.85 (d, $J = 8.2$ Hz, 1H), 7.65 (d, $J = 7.3$ Hz, 1H), 7.58-7.50 (m, 4H), 7.42 (dt, $J = 15.3, 7.9$ Hz, 2H), 7.24 (t, $J = 7.4$ Hz, 1H), 7.20-7.12 (m, 2H). ^{13}C NMR (500 MHz, DMSO) δ 154.68, 151.29, 142.66, 139.98, 134.60, 134.44, 133.99, 130.71, 129.68, 128.58, 127.78, 126.52, 126.37, 126.34, 125.93, 123.55, 123.52, 123.50, 122.21, 121.71, 120.72, 119.21, 115.72, 111.67. FT-IR spectra (KBr pellet used): 3226 cm^{-1} vs (urea N-H), 3000 cm^{-1} vs (aromatic C-H), 1653 cm^{-1} vs (urea C=O). ESI-MS (positive mode, m/z): calculated for $\text{C}_{24}\text{H}_{18}\text{N}_4\text{O}$: 378.1481. Found: 379.3227 $[\text{M} + \text{H}]^+$. m.p: 193°C. (Scheme 2.2.2)

R2: 2-(1H-benzimidazol-2-yl)aniline (500 mg, 2.39 mmol, 1 equiv.) was placed in a 50 mL round-bottomed flask and dissolved in dichloromethane (DCM) (15 mL). A solution of 3-

cyanophenyl isocyanate (344.4 mg, 2.39 mmol, 1 equiv.) was added into the flask in dropwise manner. The reaction was stirred at room temperature for 12 hours. The precipitates were separated by filtration and washed with DCM (30 mL) and diethyl ether (30 mL). The obtained white powder was further dried over vacuum dried and isolated as compound **R2**. Yield: 80%. $^1\text{H NMR}$ (600 MHz, $\text{DMSO-}d_6$) δ 13.10 (s, 1H), 12.22 (s, 1H), 10.08 (s, 1H), 8.39 (s, 1H), 8.10 - 8.04 (m, 2H), 7.82 (d, $J = 8.0$ Hz, 2H), 7.60 (s, 1H), 7.55 - 7.50 (m, 1H), 7.49-7.44 (m, 2H), 7.30 (s, 2H), 7.23-7.18 (m, 1H). $^{13}\text{C NMR}$ (600 MHz, DMSO) δ 153.08, 151.37, 141.36, 140.73, 139.36, 130.81, 130.70, 130.59, 127.79, 126.20, 125.95, 124.03, 123.69, 122.21, 122.03, 121.60, 120.92, 119.39, 115.88, 112.11, 111.96. **FT-IR** spectra (KBr pellet used): 3338 cm^{-1} vs (urea N-H), 3291 cm^{-1} vs (aromatic C-H), 2256 cm^{-1} ($-\text{C}\equiv\text{N}$) 1688 cm^{-1} vs (urea $\text{C}=\text{O}$). **ESI-MS** (positive mode, m/z): calculated for $\text{C}_{21}\text{H}_{15}\text{N}_5\text{O}$: 353.1277. Found: 354.2478 $[\text{M} + \text{H}]^+$, m.p: 172°C . (Scheme 2.2.2)



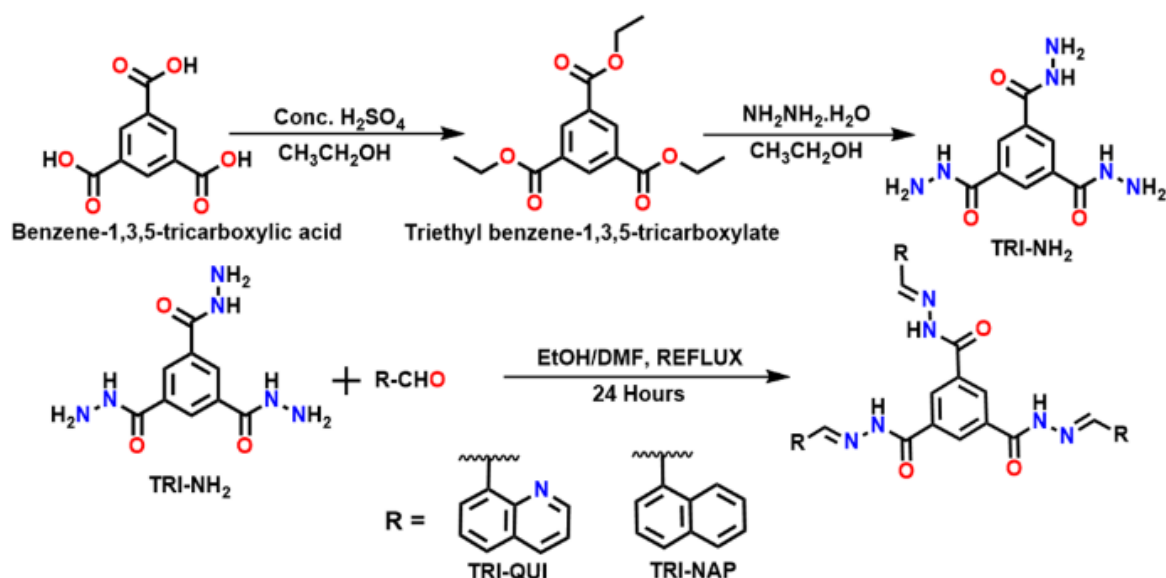
Scheme 2.2.2: Preparation of **R1** and **R2**.

2.2.3. Synthesis of TRI-NH₂ [*benzene-1,3,5-tricarbohydrazide*], TRI-QUI [*N^1, N^3, N^5 -tris((*E*)-quinolin-8-ylmethylene)benzene-1,3,5-tricarbohydrazide*] and TRI-NAP [*N^1, N^3, N^5 -tris((*E*)-naphthalen-1-ylmethylene)benzene-1,3,5-tricarbohydrazide*]

Benzene-1,3,5-tricarboxylic acid (1g) was placed in a 50 mL round-bottomed flask and dissolved in ethanol (EtOH) (30 mL). A few drops of concentrated H_2SO_4 were added to the flask. The reaction was refluxed at 74°C for 48 hours. The precipitates were separated by filtration and washed with EtOH (30 mL). The obtained white crystalline product (500 mg) was dried and taken in a round-bottomed flask for further reaction with an excess amount of hydrazine hydrate ($\text{NH}_2\text{NH}_2\cdot\text{H}_2\text{O}$). The reaction was refluxed at 74°C for 24 hours. The white precipitates were separated by filtration washed with EtOH (30 mL) and vacuum dried to obtain **TRI-NH₂**. $^1\text{H NMR}$ [600 MHz, $\text{DMSO-}d_6$, δ (ppm)]: $3\times[9.85$ (s, 1H), 8.32 (s, $J = 2.2$ Hz, 1H), 4.58 (s, 2H)]. $^{13}\text{C NMR}$ [151 MHz, $\text{DMSO-}d_6$, δ (ppm)] 165.47×3 , 134.31×3 , 128.51×3 . (Scheme 2.2.3)

TRI-NH₂ (200 mg, 0.793 mmol, 1 equiv.) was placed in a 50 mL round-bottomed flask and dissolved in ethanol (EtOH) (10 mL). 8-quinoline carboxaldehyde (436 mg, 2.80 mmol, 3.5 equiv.) was added and the reaction was refluxed at 74 °C for 24 hours. The precipitates were separated by filtration and washed with EtOH (30 mL). The obtained white amorphous product was further vacuum-dried and isolated as compound **TRI-QUI**. It was further crystallized from DMSO and a suitable single crystal was isolated for SC-XRD analysis. Calculated yield: 95%. ¹H NMR [600 MHz, DMSO-*d*₆, δ (ppm)]: 3×[12.49 (s, 1H), 9.88 (s, 1H), 9.03 (d, J = 3.9 Hz, 1H), 8.85 (s, 1H), 8.51-8.45 (m, 2H), 8.15 (d, J = 7.8 Hz, 1H), 7.78 (t, J = 7.5 Hz, 1H), 7.67 (dd, J = 8.2, 4.0 Hz, 1H)]. ¹³C NMR [151 MHz, DMSO-*d*₆, δ (ppm)]: 3×[162.41, 150.97, 146.01, 145.90, 137.24, 134.47, 131.50, 130.79, 130.62, 128.57, 127.13, 126.32, 122.47]. ESI-MS (positive mode, m/z) calculated for C₃₉H₂₇N₉O₃: 669.2237, found: 670.2327 [M + H]⁺. Empirical formula C₃₉H₂₉N₉O₄, Mw: 687.71, T = 297 K, triclinic, space group: P-1, a = 8.3334 (12) Å, b = 11.9948 (17) Å, c = 16.823 (2) Å, α = 94.916 (4)°, β = 99.085 (4)°, γ = 94.038(4)°, V = 1648.3 (4) Å³, Z = 2, Dx (g cm⁻³) = 1.386, F(000) = 716.0, total no. of reflections/no. of independent reflections/no. of observed reflections = 38298/5791/3398, R1, I > 2σ(I) = 0.0824 (3398), wR2, I > 2σ(I) = 0.2981 (5791), GOF (F2) = 1.107. CCDC:: 2363554. (Scheme 2.2.3)

TRI-NAP was synthesized with a similar procedure as to that of **TRI-QUI**, where, **TRI-NH₂** (200 mg, 0.793 mmol, 1 equiv.) was placed in a 50 mL round-bottomed flask and dissolved in N,N-Dimethylformamide (DMF) (10 mL). 1-naphthaldehyde (436 mg, 2.80 mmol, 3.5 equiv.) was added and the reaction was refluxed at 60 °C for 24 hours. The clear yellow solution was poured into ice-cold water and the white precipitates obtained were separated by filtration and washed with distilled water (30 mL). The obtained white powder product was further vacuum-dried and isolated as compound **TRI-NAP**. Calculated yield: 80%. ¹H NMR [600 MHz, DMSO-*d*₆, δ (ppm)]: 3×[12.36 (s, 1H), 9.22 (s, 1H), 8.88 (d, J = 8.4 Hz, 1H), 8.80 (s, 1H), 8.07 (dd, J = 14.1, 8.6 Hz, 2H), 8.02 (d, J = 7.1 Hz, 1H), 7.75 – 7.70 (m, 1H), 7.65 (m, J = 12.0, 7.9 Hz, 2H)]. ¹³C NMR [151 MHz, DMSO-*d*₆, δ (ppm)]: 3×[162.51, 148.90, 134.77, 134.04, 131.30, 130.76, 130.39, 129.90, 129.36, 128.35, 127.95, 126.85, 126.13, 124.59]. ESI-MS (positive mode, m/z) calculated for C₄₂H₃N₆O₃: 666.2379, found: 667.2453 [M + H]⁺. (Scheme 2.2.3)



Scheme 2.2.3: Preparation of TRI-NH₂, TRI-QUI and TRI-NAP.

2.2.4. Synthesis of ADH-Py-p [*N*¹,*N*⁶-bis((*E*)-pyridin-4-ylmethylene)adipohydrazide], ADH-Py-m [*N*¹,*N*⁶-bis((*E*)-pyridin-3-ylmethylene)adipohydrazide], ADH-Py-o [*N*¹,*N*⁶-bis((*E*)-pyridin-2-ylmethylene)adipohydrazide] and ADH-Ph [*N*¹,*N*⁶-di((*E*)-benzylidene)adipohydrazide]

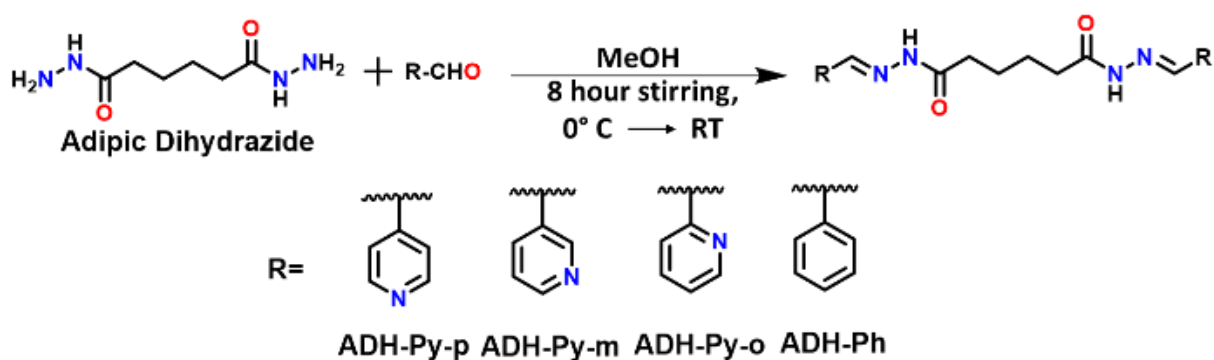
Adipic Dihydrazide (1g, 5.7mmol, 1 equiv.) was placed in a 250 mL round-bottomed flask and dissolved in methanol (MeOH) (30 mL). 4-pyridine carboxaldehyde (1.4mL, 14.3mmol, 2.5 equiv.) was added and the reaction was stirred at 0° C for 12 hours. The precipitates were separated by filtration and washed with MeOH (30 mL). The obtained white amorphous product was further vacuum-dried and isolated as compound **ADH-Py-p**. It was further crystallized from MeOH-H₂O and a suitable single crystal was isolated for SC-XRD analysis. Calculated yield: ~94%. ¹H NMR (600 MHz, DMSO-*d*₆) δ 11.58 (d, *J* = 69.6 Hz, 2H), 8.63 – 8.56 (m, 4H), 8.15 (s, 1H), 7.94 (s, 1H), 7.62 – 7.57 (m, 4H), 2.73 – 2.66 (m, 2H), 2.30 – 2.24 (m, 2H), 1.70 – 1.59 (m, 4H). ¹³C NMR (151 MHz, DMSO-*d*₆) δ 175.14, 169.44, 4×150.66, 2×143.81, 141.95, 140.44, 2×121.38, 2×121.09, 34.50, 32.08, 25.08, 24.35. ESI-MS (positive mode, *m/z*) calculated for C₁₈H₂₀N₆O₂: 352.1648, found: 353.1705 [M+H]⁺. FT-IR spectra (KBr pellet used): 3083 cm⁻¹ vs (Amide N-H), 2944 cm⁻¹ vs (aromatic C-H), 1676 cm⁻¹ vs (Amide C=O), 1595 cm⁻¹ (imine C=N). (Scheme 2.2.4)

Adipic Dihydrazide (1g, 5.7mmol, 1 equiv.) was placed in a 250 mL round-bottomed flask and dissolved in methanol (MeOH) (30 mL). 3 -pyridine carboxaldehyde (1.3mL, 14.3mmol, 2.5 equiv.) was added and the reaction was stirred at 0° C for 12 hours. The precipitates were separated by filtration and washed with MeOH (30 mL). The obtained white amorphous product was further vacuum-dried and isolated as compound **ADH-Py-m**. It was further crystallized from

DMSO and a suitable single crystal was isolated for SC-XRD analysis. Calculated yield: ~90%. ^1H NMR (600 MHz, DMSO- d_6) δ 11.56 – 11.37 (m, 2H), 8.80 (d, $J = 7.4$ Hz, 2H), 8.62 – 8.51 (m, 2H), 8.21 (s, 1H), 8.06 (t, $J = 7.8$ Hz, 2H), 8.00 (s, 1H), 7.43 (dq, $J = 20.6, 6.5, 5.7$ Hz, 2H), 2.72 – 2.64 (m, 2H), 2.29 – 2.22 (m, 2H), 1.70 – 1.58 (m, 4H). ^{13}C NMR (151 MHz, DMSO- d_6) δ 174.92, 169.19, 150.96, 150.70, 2 \times 149.08, 2 \times 148.75, 143.54, 140.06, 133.80, 133.55, 130.72, 124.39, 34.51, 32.13, 25.21, 24.45. ESI-MS (positive mode, m/z) calculated for $\text{C}_{18}\text{H}_{20}\text{N}_6\text{O}_2$: 352.1648, found: 353.1705 $[\text{M}+\text{H}]^+$. FT-IR spectra (KBr pellet used): 3203 cm^{-1} vs (Amide N-H), 3048 cm^{-1} vs (aromatic C-H), 1659 cm^{-1} vs (Amide C=O), 1549 cm^{-1} (imine C=N). (Scheme 2.2.4)

Adipic Dihydrazide (1g, 5.7mmol, 1 equiv.) was placed in a 250 mL round-bottomed flask and dissolved in methanol (MeOH) (30 mL). 2-pyridine carboxaldehyde (1.4mL, 14.3mmol, 2.5 equiv.) was added and the reaction was stirred at 0° C for 12 hours. The precipitates were separated by filtration and washed with MeOH (30 mL). The obtained white amorphous product was further vacuum-dried and isolated as compound **ADH-Py-o**. Calculated yield: ~80%. ^1H NMR (600 MHz, DMSO- d_6) δ 11.52 (d, $J = 85.8$ Hz, 2H), 8.58 (d, $J = 7.8$ Hz, 2H), 8.18 (s, 1H), 8.03 (s, 1H), 7.90 (t, $J = 10.0$ Hz, 2H), 7.85 (q, $J = 8.2$ Hz, 1H), 7.79 (t, $J = 7.8$ Hz, 1H), 7.42 – 7.35 (m, 2H), 2.70 (d, $J = 7.4$ Hz, 2H), 2.28 (d, $J = 7.0$ Hz, 2H), 1.66 (d, $J = 26.0$ Hz, 4H). ^{13}C NMR (151 MHz, DMSO) δ 175.15, 175.08, 171.97, 169.49, 169.44, 150.64, 143.90, 143.86, 142.08, 141.96, 140.52, 140.46, 121.38, 121.08, 34.50, 32.08, 25.08, 24.35. ESI-MS (positive mode, m/z) calculated for $\text{C}_{18}\text{H}_{20}\text{N}_6\text{O}_2$: 352.1648, found: 353.1702 $[\text{M}+\text{H}]^+$. FT-IR spectra (KBr pellet used): 3240 cm^{-1} vs (Amide N-H), 2956 cm^{-1} vs (aromatic C-H), 1664 cm^{-1} vs (Amide C=O), 1553 cm^{-1} (imine C=N). (Scheme 2.2.4)

Adipic Dihydrazide (1g, 5.7mmol, 1 equiv.) was placed in a 250 mL round-bottomed flask and dissolved in methanol (MeOH) (30 mL). Benzaldehyde (1.4mL, 14.3mmol, 2.5 equiv.) was added and the reaction was stirred at 0° C for 12 hours. The precipitates were separated by filtration and washed with MeOH (30 mL). The obtained white amorphous product was further vacuum-dried and isolated as compound **ADH-Ph**. Calculated yield: 84%. ^1H NMR (600 MHz, DMSO- d_6) δ 11.28 (d, $J = 84.3$ Hz, 2H), 8.17 (s, 1H), 7.99 (s, 1H), 7.73 – 7.62 (m, 4H), 7.42 (dd, $J = 18.0, 11.5$ Hz, 6H), 2.72 – 2.64 (m, 2H), 2.30 – 2.21 (m, 2H), 1.72 – 1.59 (m, 4H). ^{13}C NMR (151 MHz, DMSO- d_6) δ 174.76, 169.03, 2 \times 146.27, 142.93, 134.85, 2 \times 130.08, 4 \times 129.26, 2 \times 127.42, 2 \times 127.07, 34.54, 32.16, 25.29, 24.49. ESI-MS (positive mode, m/z) calculated for $\text{C}_{20}\text{H}_{22}\text{N}_4\text{O}_2$: 350.1743, found: 351.1817 $[\text{M}+\text{H}]^+$. FT-IR spectra (KBr pellet used): 3182 cm^{-1} vs (Amide N-H), 3025 cm^{-1} vs (aromatic C-H), 1664 cm^{-1} vs (Amide C=O), 1648 cm^{-1} (imine C=N). (Scheme 2.2.4)



Scheme 2.2.4: Preparation of ADH-Py-p, ADH-Py-m, ADH-Py-o and ADH-Ph.

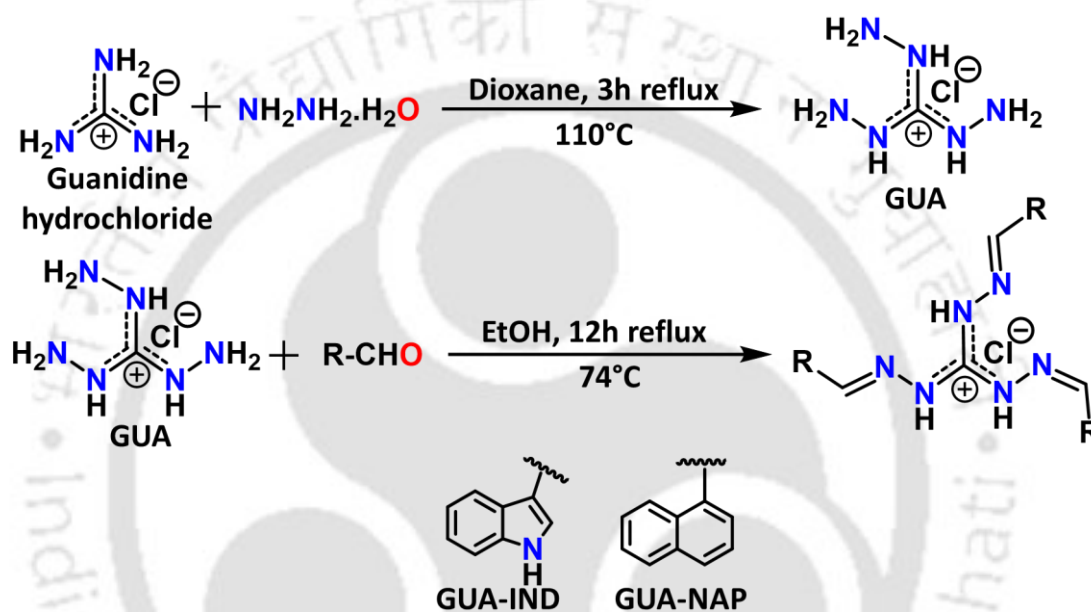
2.2.5. Synthesis of GUA [(*E*)-1-((1 λ^4 -diazanylidene)(hydrazinyl)methyl)hydrazin-1-ium chloride], **GUA-IND** [(*E*)-2-((1*H*-indol-3-yl)methylene)-1-((*E*)-((*E*)-(1*H*-indol-3-yl)methylene)-1 λ^4 -diazanylidene)(2-((*E*)-(1*H*-indol-3-yl)methylene)hydrazinyl)methyl)hydrazin-1-ium chloride], and **GUA-NAP** [(*E*)-2-(naphthalen-1-ylmethylene)-1-((*E*)-((*E*)-naphthalen-1-ylmethylene)-1 λ^4 -diazanylidene)(2-((*E*)-naphthalen-1-ylmethylene)hydrazinyl)methyl)hydrazin-1-ium chloride]

Guanidinium chloride (20 mmol, 1.911 g) was placed in a 250 ml round-bottom flask and dissolved in 50 ml 1,4-dioxane. An excess of hydrazine monohydrate (150 mmol, 7.3 ml) was added to it while stirring. The reaction mixture was heated at 110 °C for 3 hours under refluxing conditions. After 3 hours, the reaction mixture was cooled to room temperature, and the solid precipitate was filtered and washed with 1,4-dioxane and then dried in a vacuum desiccator. The yield obtained for **GUA** was ~ 98%. (Scheme 2.2.5)

GUA (1g, 237.1 mM, 1 equiv.) was placed in a 250 mL round-bottomed flask and dissolved in ethanol (EtOH) (30 mL). Indole-3-carboxaldehyde (4.6g, 2.80 mmol, 3.5 equiv.) was added, and the reaction was refluxed at 74 °C for 12 hours. The precipitates were separated by filtration and washed with EtOH (30 mL). The obtained pale-yellow amorphous product was further vacuum-dried and isolated as compound **GUA-IND**. It was further crystallized from DMSO, and a suitable single crystal was isolated for SC-XRD analysis. Calculated yield: 85%. ¹H NMR (600 MHz, DMSO-*d*₆) δ 11.95 (s, 3H), 11.34 (s, 3H), 8.88 (s, 3H), 8.42 (d, *J* = 7.4 Hz, 3H), 8.08 (d, *J* = 2.8 Hz, 3H), 7.52 (d, *J* = 7.4 Hz, 3H), 7.30-7.24 (m, 6H). ¹³C NMR (151 MHz, DMSO-*d*₆) δ 148.71, 3×[148.10, 137.61, 132.63, 124.64, 123.34, 122.68, 121.31, 112.49, 111.07]. ESI-MS (positive mode, *m/z*) calculated for C₂₈H₂₄N₉⁺: 486.2149, found: 486.2172. FT-IR spectra (KBr pellet used): 3514 cm⁻¹ vs (Indole N-H), 3314 cm⁻¹ vs (Guanidine N-H), 3097 cm⁻¹ vs (aromatic C-H), 1638 cm⁻¹ (imine C=N), 1596 cm⁻¹ (aromatic C=C). (Scheme 2.2.5)

GUA (100mg, 0.71 mmol, 1 equiv.) was placed in a 250 mL round-bottomed flask and dissolved in ethanol (EtOH) (30 mL). 1-naphthaldehyde (388.9mg, 2.9 mmol, 3.5 equiv.) was added, and

the reaction was refluxed at 74 °C for 12 hours. The precipitates were separated by filtration and washed with EtOH (30 mL). The obtained pale-yellow amorphous product was further vacuum-dried and isolated as compound **GUA-NAP**. Calculated yield: 82%. ¹H NMR (600 MHz, DMSO-*d*₆) δ 12.39 (s, 1H), 9.74 (s, 1H), 8.56 (d, *J* = 7.2 Hz, 1H), 8.46 (d, *J* = 8.5 Hz, 1H), 8.19 (d, *J* = 8.1 Hz, 1H), 8.10 (d, *J* = 8.2 Hz, 1H), 7.76 (q, *J* = 8.5 Hz, 3H), 7.68 (t, *J* = 7.4 Hz, 1H). ¹³C NMR (151 MHz, DMSO) δ 150.19, 3×[149.55, 133.90, 132.07, 131.44, 129.49, 128.94, 128.05, 126.93, 126.70, 126.08, 123.20]. ESI-MS (positive mode, *m/z*) calculated for C₃₄H₂₇N₆⁺: 519.2292, found: 519.2292. FT-IR spectra (KBr pellet used): 3047 cm⁻¹ vs (aromatic C-H), 1621 cm⁻¹ (imine C=N), 1513 cm⁻¹ (aromatic C=C). (Scheme 2.2.5)



Scheme 2.2.5: Preparation of **GUA-IND** and **GUA-NAP**.

2.3. Synthetic Procedure of Metallogels viz. **P-Ag-G**, **P-Ag-G (B)** and **M-Cd-G**

A supramolecular metallogel (**P-Ag-G**) of silver nitrate with **ADH-Py-p**, utilized as the LMWG, was achieved under laboratory conditions. Here, **ADH-Py-p** (10 mg per ml, 0.28 mM) was dissolved in 400 μL of DMSO and silver nitrate (9.6 mg per ml, 0.056 mM) was dissolved in 600 μL of H₂O in two separate glass vials and one-shot mixing of the above mentioned two solutions helped to form a white-colored stable metallogel (i.e., **P-Ag-G**). The stability of the synthesized **P-Ag-G** metallogel is shown by the retention of inverted glass vial characteristic against gravitational force. The organohydrogel remained stable for more than 6 months. However, the white colour of the gel becomes reddish black within ~2 months to form metallogel **P-Ag-G (B)**. Nevertheless, the receptor itself cannot form a gel in the absence of silver ion under the same conditions. The metallogel **M-Cd-G** is also synthesized using the same procedure as is used for the synthesis of the metallogel **P-Ag-G**. **ADH-Py-m** (10 mg per ml,

28.4mM) was dissolved in 400 μL of DMSO and cadmium chloride (11.4 mg per ml, 0.056 M) was dissolved in 600 μL of H_2O in two separate glass vials and one-shot mixing of the above mentioned two solutions helped to form a white-colored stable metallogel (i.e., **M-Cd-G**). The organohydrogel remained stable for more than 6 months. Important to mention here that the receptor **ADH-Py-m** also cannot form a gel in the absence of cadmium ion under the same conditions. Both the Gels **P-Ag-G** and **M-Cd-G** maintaining different pH was prepared by dissolving the respective receptors in DMSO while dissolving/ dispersing the respective metal ions in water maintaining different pH.

2.4. Synthetic Procedure for formation of supramolecular gel GI-G

Supramolecular gels are composed of the **GUA-IND** receptor and sulfate (or bisulfate) salts. The gel **GI-G** was prepared by dissolving **GUA-IND** (5mg per ml) in DMSO, followed by rapid addition of an aqueous solution of $(\text{TBA})_2\text{SO}_4$ salt (1 equivalent of the receptor) in a 1:4 ratio, respectively. The receptor itself cannot form a gel in the absence of the anion under the same conditions. The minimum gelling concentration for sulfate salt was found to be 0.5 equivalent of the receptor. The prepared organohydrogels were opaque, and the gelation was confirmed by the absence of flow upon vial inversion. The organogel with $(\text{TBA})_2\text{SO}_4$ was stable up to 48-72 hours. However, the gel formed from TBAHSO_4 remained stable for only 3-4 hours. Various metal sulfate salts (Na^+ , Mg^{2+} , Al^{3+} , K^+ , Ca^{2+} , Mn^{2+} , Fe^{2+} , Fe^{3+} , Co^{2+} , Ni^{2+} , Zn^{2+}) successfully formed organohydrogels. The metal sulfate gels were stable up to 10-12 hours.

2.5. Rheological Experimental Details

Measurements were performed using a Thermo Scientific Rheometer (HAAKE MARS iQ Air) equipped with a 35 mm parallel plate arrangement. Experiments were carried out on freshly prepared gel from **TRI-QUI** (5 mg mL^{-1}), metallogel **ADH-Ag-G** (10 mg mL^{-1}) and anion induced supramolecular gel **GI-G** (5 mg mL^{-1}) Linear viscoelastic regions of the samples were determined by measuring the storage modulus, G' (associated with energy storage), and the loss modulus G'' (associated with the loss of energy) as a function of the stress amplitude. The gel-sol transitions were monitored over different shear strains with a fixed frequency at 1 Hz. As the storage modulus(G') starts to decrease after a 1% shear strain, we decided on a shear strain of 0.1 % to measure the frequency-dependent rheological behaviors of the gels.

2.6. UV-Vis and Fluorescence Spectral Studies

Stock solutions of different analytes (nitroaromatics, anions, metals $50 \times 10^{-3} \text{ mol L}^{-1}$) were prepared preferably in water or DMSO depending on solubility. Stock solution of probes **L1-3**, **R1**, **R2**, **TRI-QUI**, **TRI-NAP**, **ADH-Py-o**, **ADH-Py-m**, **ADH-Py-p**, **ADH-Ph**, **GUA-IND** and **GUA-NAP** ($5 \times 10^{-3} \text{ mol L}^{-1}$) were prepared in DMSO.

For different photophysical experiments including solvatochromism and solution state aggregation study for the probes **L1-3** performed via both UV-Vis and fluorescence experiments, the stock solutions of probes ($5 \times 10^{-3} \text{ mol L}^{-1}$) were diluted to $5 \times 10^{-6} \text{ mol L}^{-1}$ or $10 \times 10^{-6} \text{ mol L}^{-1}$ by taking only 4 μL of stock solution and making the final volume upto 2 mL. The fluorescence selectivity experiments of the probes **L1-3** towards different nitroaromatic compounds were performed with a 10 μM solution of the receptors in 100% aqueous medium. In fluorescence titration experiments, a quartz optical cell of 10 mm pathlength was filled with a 2.0 mL solution of receptors to which various NAC's stock solutions were gradually added using a micropipette. For all the fluorescence experiments, excitation wavelengths were fixed at 320 nm, 420 nm, and 380 nm for **L1**, **L2** and **L3** respectively. In case of **R1** and **R2** also, solution state aggregation and sensing study of SO_4^{2-} and HSO_4^- was performed via both UV-Vis and fluorescence experiments where the stock solutions of two probes ($5 \times 10^{-3} \text{ mol L}^{-1}$) were diluted to $10 \times 10^{-6} \text{ mol L}^{-1}$. For the case of **TRI-QUI** and **TRI-NAP**, stock solutions of all the metal ions (using acetate, chloride, and nitrate salts) (50mM) were prepared in water. Stock solutions of all the anions (using *n*-Tetrabutylammonium salts of the corresponding anions) (50mM) were prepared in DMSO. Stock solutions of **TRI-QUI** ($5 \times 10^{-3} \text{ mol L}^{-1}$) and **TRI-NAP** ($5 \times 10^{-3} \text{ mol L}^{-1}$) were prepared in DMSO and then diluted to $10 \times 10^{-6} \text{ mol L}^{-1}$ for various spectral studies. In the fluorescence/UV-Vis sensing experiment, the test samples were prepared by placing the appropriate amounts of the stock solutions of the respective metal ions into 2.0 mL of probe solution (containing $10 \times 10^{-6} \text{ mol L}^{-1}$ of probe and 0.2% DMSO). For fluorescence titration experiments, $5 \times 10^{-3} \text{ mol L}^{-1}$ stock solution of $\text{Zn}(\text{OAc})_2 \cdot 2\text{H}_2\text{O}$ (zinc acetate dihydrate), $\text{Cd}(\text{OAc})_2 \cdot 2\text{H}_2\text{O}$ (cadmium acetate dihydrate), and HgCl_2 (mercuric chloride) was prepared in DMSO, then it was gradually added into a 2.0 mL of probe solution (containing $10 \times 10^{-6} \text{ mol L}^{-1}$ of probe and 0.2% DMSO). Fluorescence spectra of the **TRI-QUI** gel prepared in the fluorescence cuvette was also recorded in the presence and absence of CN^- . The UV-Vis spectra of the receptor **GUA-IND** in the presence of different nitroaromatic compounds were also performed with $10 \times 10^{-6} \text{ mol L}^{-1}$ of the receptor in 2 mL of water.

2.7. Estimation of the Apparent Binding Constant

Probes **L₂**, **L₃** with a sufficient concentration of 10 μM in water was titrated with varying picric acid concentrations, while probes **R1**, **R2** with a sufficient concentration of 10 μM in water was titrated with varying SO₄²⁻/HSO₄⁻ concentrations. Thus, the apparent binding constants for forming the Probe -analyte complex for the above-mentioned probes were assessed utilizing the Benesi-Hildebrand (B-H) plot (Equation 1).

$$1/(I-I_0) = 1/\{K(I_{max}-I_0) C\} + 1/(I_{max}-I_0) \dots (1)$$

I_0 is the emission intensity of probes at maximum (λ_{max}), and I is the recorded emission intensity at that particular wavelength in the presence of a specific concentration of the analyte (C). I_{max} is the maximum emission intensity value obtained at λ_{max} during titration with varying analyte concentrations. K is the apparent binding constant (M^{-1}) and was determined from the linear plot's slope.

2.8. Detection limit (LOD)

The detection limit (**L₂**, **L₃**, **R1**, **R2**, **TRI-QUI**, **TRI-NAP**) was evaluated based on the fluorescence titration changes. The fluorescence emission spectrum of respective probe was computed ten times, and the standard deviation of the blank measurement was estimated. To measure the slope, the fluorescence emission at respective wavelength was plotted as a function of the concentration of analyte from the titration experiment. The detection limits were calculated using the following equation:

$$\text{Detection limit} = 3\sigma/k \dots (2)$$

Where σ is the standard deviation of blank measurement, and k is the slope between the fluorescence emission intensity versus [analyte].

In case of the receptor **GUA-IND**, we reported visual detection of picric acid via gel to sol conversion of **GI-G** gel, where we calculated the minimum amount of PA required for disruption of the gel **GI-G**. However, it was difficult to weigh very small amount of PA and hence to maintain the proper concentration we made PA solution (3 equivalent of the receptor concentration) in DMSO by calculating the required amount and then diluted it to prepare 2, 1, 0.5 and 0.25 equivalent (compared to the receptor) of PA solutions. We added 100 μL of each of these PA solutions on the top the **GI-G** gels prepared in different glass vials. Important to mention here that, the equivalents of PA compared to the receptor was calculated considering a total of 600 μL volume of solvent (500 μL in the gel and 100 μL for preparation of PA solution).

2.9. Stern-Volmer Plot

The quenching behaviour of **L2** and **L3** in presence of picric acid was studied by Stern-Volmer equation,

$$I_0 / I = 1 + K_{sv} [Q],$$

where I_0 , I are the fluorescence intensities before and after addition of the quencher, K_{sv} is the Stern- Volmer quenching rate constant and $[Q]$ is the concentration of the quencher.

2.10. Dynamic light scattering measurement

Dynamic light scattering (DLS) experiments were carried out in Malvern Zetasizer Nano ZS instrument equipped with a 4.0 mW He-Ne laser running at a wavelength of 633 nm. The samples and the background were measured at room temperature (25 °C). DLS experiments were executed with optically clear solutions of respective probes (**L2**, **L3**, **R1**, **R2**, **TRI-QUI**, **TRI-NAP**) (10 μ M) in water and in different solvents as well as of the probe **TRI-QUI** in presence of 50 equivalents of Zn^{2+} , Cd^{2+} and Hg^{2+} in water. The solutions were equilibrated for 120 minutes before taking the measurements.

2.11. Measurement of fluorescence lifetime

Fluorescence lifetimes were assessed using the time-correlated single-photon counting (TCSPC) method in the Edinburgh Instrument Life-Spec II spectrometer. The samples (**L2** and **L3**) and picric acid were excited at respective excitation wavelengths or required experimental conditions, keeping the emission wavelength fixed as mentioned earlier using a pulsed diode laser. The fluorescence decays were surveyed by the re-convolution method using the FAST software provided by Edinburgh Instruments.

2.12. Theoretical investigations (DFT study)

DFT optimizations of **L2**, **L3**, **R1** and **R2** and analytes interaction were accomplished with the B3LYP/6-31 G (d, p) basis set using the Gaussian 09 program, while using water as a solvent through CPCM solvent model.

2.13. Quantum yield measurement

We have utilized the **Parker-Rees method** [2.1] to calculate the quantum yield of the prepared luminescent materials, using a **0.5 M H₂SO₄** solution of quinine sulphate as a standard reference.

The formula for this calculation is provided as follows:

$$\Phi_s = (A_r F_s n_s^2 / A_s F_r n_r^2) \Phi_r$$

In this equation, Φ_r represents the quantum yield of the quinine sulfate reference solution, while Φ_s represents the quantum yield of the samples (**L1-L3 and R1, R2**). The absorbance maxima were kept under 0.1 to minimize the reabsorption of fluorescent light that passed through the materials. The values of A_r and A_s correspond to the absorbance of the reference and samples, respectively, whereas F_r and F_s refer to the integrated area of fluorescence intensity for the reference and sample, respectively. The refractive indices of the reference and samples are represented by n_r and n_s , respectively [2.2].

2.14. Time response study and rate constant determination

Response time is a crucial factor for the practical application of a sensor. To do so, the receptor **R1** (10 μ M) was exposed towards $\text{SO}_4^{2-}/\text{HSO}_4^-$ (10 μ M) for 20 min and the emission intensity at 494 nm was recorded. Considering, pseudo-first-order kinetics, the reaction rate constants of **R1** with $\text{SO}_4^{2-}/\text{HSO}_4^-$ anion were determined from the time-dependent fluorescence spectra. The rate constants were experimentally evaluated from the following equation: $\ln(F_t - F_{\min})/F_{\min} = -k't$ where F_t and F_{\min} were the corresponding fluorescence intensities at time t and the end of the reactions, respectively, and k' is the rate constant.

2.15. ^1H NMR titration experiments of R1 and R2

The ^1H NMR (600 MHz) titrations of the receptors were performed with the tetrabutylammonium sulphate/bisulfate salts, in $\text{DMSO-}d_6$ at 298K. The preliminary concentrations of the hosts and the guests were, $[\text{receptor}]_0 = 50\text{mM}$, and $[\text{SO}_4^{2-}/\text{HSO}_4^-]_0 = 500\text{mM}$ respectively. All the titrations were performed by 10-16 measurements at room temperature, and the peak of $\text{DMSO-}d_6$ (at 2.5ppm) was used for an internal reference.

2.16. Field Emission Scanning Electron Microscope (FESEM) Studies

Size and Morphology of **L1-3, R1, R2, TRI-QUI, TRI-NAP, ADH-Py-o, ADH-Py-m, ADH-Py-p, ADH-Ph, GUA-IND and GUA-NAP** were imaged separately using Gemini 300 FESEM (Carl Zeiss) and Sigma 300 FESEM (10000KX) instrument. The morphology of the aggregated/disaggregated species was investigated by using FESEM imaging studies by the drop (~ 1 mM) cast method on glass plates covered with Al-foil. To investigate the morphology of the gel samples, they were vacuum dried to form xerogels and then analyzed through by FESEM imaging studies.

The changes in morphology with changes in solvent fraction for the probes **L1-3** was acquired from FESEM imaging studies. FESEM analysis were also conducted to investigate the variation in surface morphology of self-assembled receptors in the absence and presence of PA to get an

insight into the assembly/disassembly process. The changes in size and morphology of the probes **R1** and **R2** changing solvent fraction was also investigated through FESEM. For the receptor **GUA-IND** as well, the morphological alteration with changing solvent fractions along with aggregation/disaggregation study after addition of metal salts were analysed through FESEM analysis. Moreover, the morphology of **GI-G** xerogel in presence and absence of different metal ions and anions were investigated through FESEM analysis. The morphology of the crude powder of **ADH-Py-p** and **ADH-Py-m** as well as the vacuum-dried xerogel of **P-Ag-G**, **P-Ag-G (B)** and **M-Cd-G** were assessed through FESEM experiment. Similarly, the morphology of the crude powder of **GUA-IND** and of the xerogel **GI-G** was conceived via FESEM analysis.

2.17. Field Emission Transmission Electron Microscopy (FETEM) Analysis

AgNPs formation was visualised via FETEM, where small portions of **ADH-Ag-G (B)** gels were scooped out and smeared on carbon-coated copper grids (400 meshes) and dried in vacuum. Whereas, small portions of **GI-Cu-G** and **GI-Ag-G** gels were scooped out and smeared on carbon-coated copper grids (400 meshes) and dried in vacuum to visualize formation of CuNPs and AgNPs.

2.18. Determination of DPPH (Radical Scavenging Assay)

2,2-diphenyl-1-picrylhydrazyl (DPPH) assay, a spectrophotometric technique, is employed for quantifying the antioxidant activity of antioxidants. The DPPH solution was prepared by dissolving in methanol (4 mg in 100 mL), and 3 mL of this deep purple coloured solution was added to 1 mL of methanolic solution of gels (**GI-G**, **GI-Cu-G**, and **GI-Ag-G**). Then these solutions were kept in the dark at room temperature for 30 min. MeOH was used for the baseline correction and finally, the absorbance was measured at 517 nm. The concentration of the **GI-G** gel and nanocomposite gels **GI-Cu-G** and **GI-Ag-G** were varied by pipetting out different amounts, viz. 2 μ L, 5 μ L and 7 μ L and then dissolved in 1ml of methanol. Radical scavenging activity was expressed as the inhibition percentage and was calculated using the following formula,

$$\text{DPPH scavenging activity (\%)} = \frac{\text{Abs}_{\text{DPPH}} - \text{Abs}_{\text{Sample}}}{\text{Abs}_{\text{DPPH}}} \times 100$$

2.19. Antibacterial studies

The antibacterial performance of the organohydrogels was evaluated against gram-positive (*B. subtilis* MTCC 441) and gram-negative (*E. coli* DH5 α MTCC 433) strains by zone inhibition test.

2.19.1. Evaluation of Zone of Inhibition by Well-Diffusion Method

The antibacterial properties of the **ADH-Ag-G**, **ADH-Ag-G (B)**, **GI-G**, **GI-Cu-G**, and **GI-Ag-G** were ascertained by the determination of zone of inhibition by the well-diffusion method. Firstly, the respective bacterial lawn was prepared in sterile nutrient agar media plates using sterile cotton swab sticks. 10^6 CFU/ml cultures of freshly overnight-grown bacterial suspensions of representative gram-positive (*B. subtilis*) and gram-negative (*E. coli*) bacterial strains were used to prepare the lawn culture on the plates. Following this, wells of approximately 5mm in diameter were made, and 100 μ L of gel samples were added to the wells. The plates were then kept for incubation at 37°C, overnight [2.3].

2.20. Anion exchange study

Powder sample of **GUA-IND** was dissolved in DMSO and placed in separate vials. Different TBA salts were added to the DMSO solution of **GUA-IND** placed in individual vials and kept it undisturbed for one week. Crystals appeared in the vials were analysed and Cl^- anion of **GUA-IND** was found to be exchanged with anions like Br^- , NO_3^- and H_2PO_4^- in the crystal structures.

2.21. Crystallographic Refinement Details

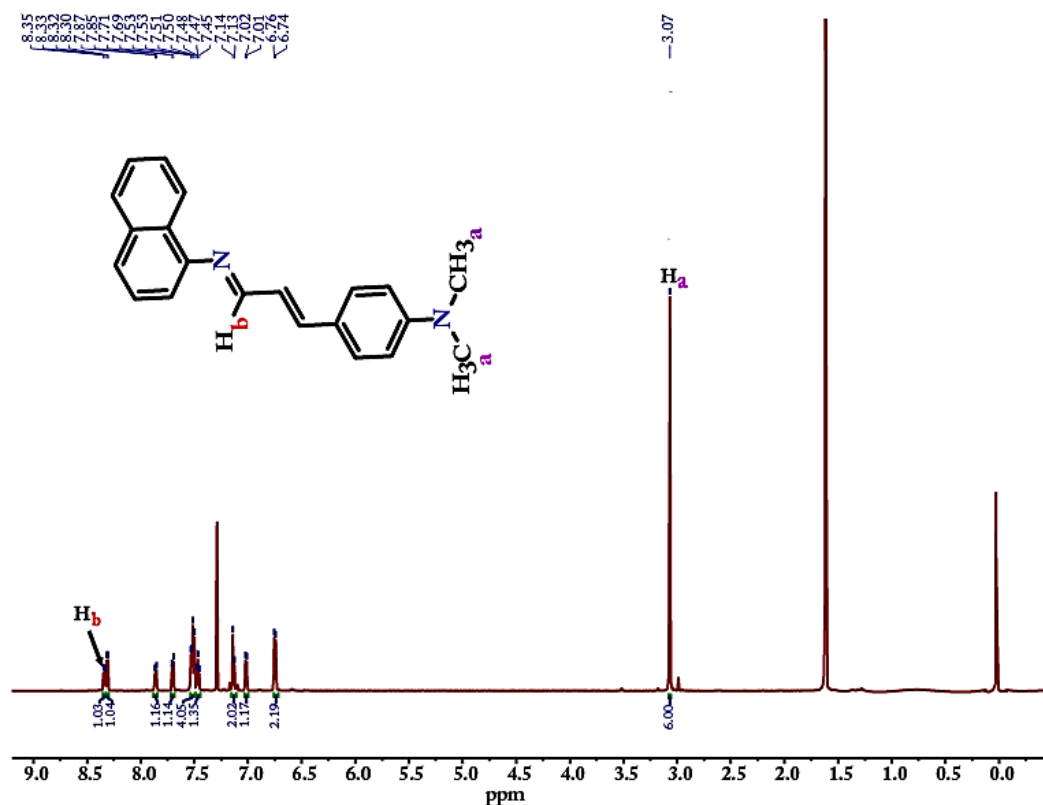
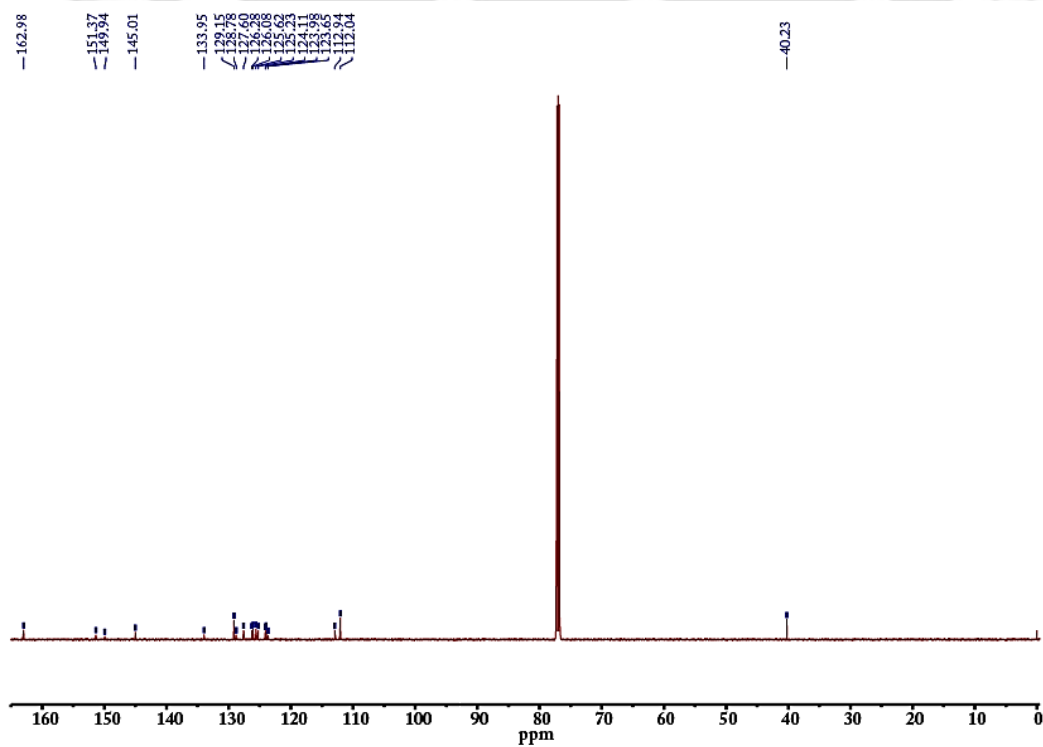
Single crystals of proper size were chosen for all the crystals and were dipped into silicon oil prior to mounting into a glass fibre tube. Supernova (a single source at an offset) Eos diffractometer with Mo $K\alpha$ radiation ($\lambda = 0.71073 \text{ \AA}$) source, connected with a CCD region detector was used to collect the X-ray intensity data, and with the help of APEX 4 all the data refinement and cell reduction were done [2.4,2.5]. Using a narrow-frame algorithm and XPREP, the frames were combined with the Bruker SAINT software kit [2.6], and data were corrected for absorption effects using the multi-Scan process (SADABS) [2.7]. Using direct methods in XT, version 2014/15, all of the structures were solved, and after that, refinement was done using the full-matrix least-squares technique in the SHELXL-2016 and 2018 software packages on F2 [2.8]. The positions of the hydrogen atoms were fixed. MERCURY 4.2.0 for windows was used for creating structural drawings [2.9]. The hydrogen atoms were found on a separate Fourier map and refined where it was most advantageous. For all non-hydrogen atoms Anisotropic refinement was employed. All the details of the refinement parameters of crystallographic data collection, and the detailed data on hydrogen bonding distances, and bond angles are furnished in the annexures of the respective chapters. Moreover, all the alerts wherever applicable have been explained in the annexures of the respective chapters. All the crystallographic data have been submitted to CCDC. The CCDC numbers assigned to the crystal structures of the probes and their respective picric acid complexes **L₁**, **L₂**, **L₃**, **L₁.PA**, **L₂.PA** and **L₃.PA** are 2244703, 2244704,

2244705, 2244706, 2244707 and 2244708 respectively. The CCDC numbers of the receptors **R1**, **R2** and the anionic complex **R1.HSO₄** are 2285005, 2285016 and 2285018 respectively. On the other hand, CCDC of the probe **TRI-QUI** is 2363554. The CCDC of the receptors **ADH-Py-p** and **ADH-Py-m** are 2515769 and 2515774. Moreover, the CCDC of the receptor **GUA-IND** as well as of **[GUA-IND.Br]⁻**, **[GUA-IND.NO₃]⁻**, **[GUA-IND.H₂PO₄]⁻** are 2419337, 2419425, 2419339, 2419341 respectively.

References

- [2.1] C. A. Parker and W. T. Rees, S. Mishra, M.Z. Siddiqui, *Analyst*, 1960, **85**(1013), 587-600.
- [2.2] A. Rana, C. Gogoi, S. Ghosh, S. Nandi, S. Kumar, U. Manna and S. Biswas, *New J. Chem.*, 2021, **45**(43), 20193-20200.
- [2.3] J. Yoonus, R. Resmi and B. Beena, *Mater. Today: Proc.*, 2021, **46**, 2969-2974.
- [2.4] Apex 3; Bruker AXS Inc.: 2016.
- [2.5] Apex 4. Bruker AXS Inc.; 2016.
- [2.6] SMART, SAINT, and XPREP; Siemens Analytical X-ray Instruments Inc.: 1995.
- [2.7] G. M. Sheldrick, SADABS, Program for Area Detector Adsorption Correction; Institute for Inorganic Chemistry, University of Göttingen: 1996.
- [2.8] G. M. Sheldrick, Crystal structure refinement with SHELXL. *Acta Crystallogr., Sect. C: Struct. Chem.*, 2015, **71**, 3.
- [2.9] C. F. Macrae, I. Sovago, S. J. Cottrell, P. T. A. Galek, P. McCabe, E. Pidcock, M. Platings, G. P. Shields, J. S. Stevens, M. Towler and P. A. Wood, *J. Appl. Crystallogr.*, 2020, **53**, 226.

Annexure 2

Figure A2.1: 1H NMR of L_1 in chloroform-d at room temperature.Figure A2.2: ^{13}C NMR of L_1 in chloroform-d at room temperature.

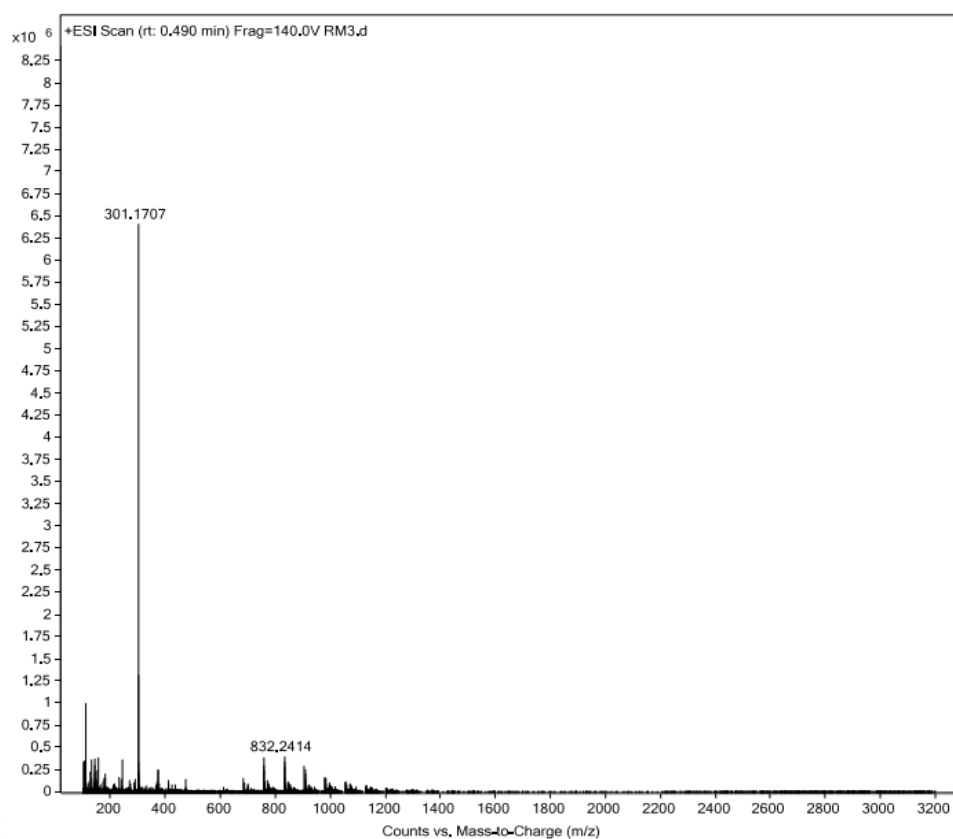


Figure A2.3: HRMS spectra of L₁ in acetonitrile in positive ionization mode.

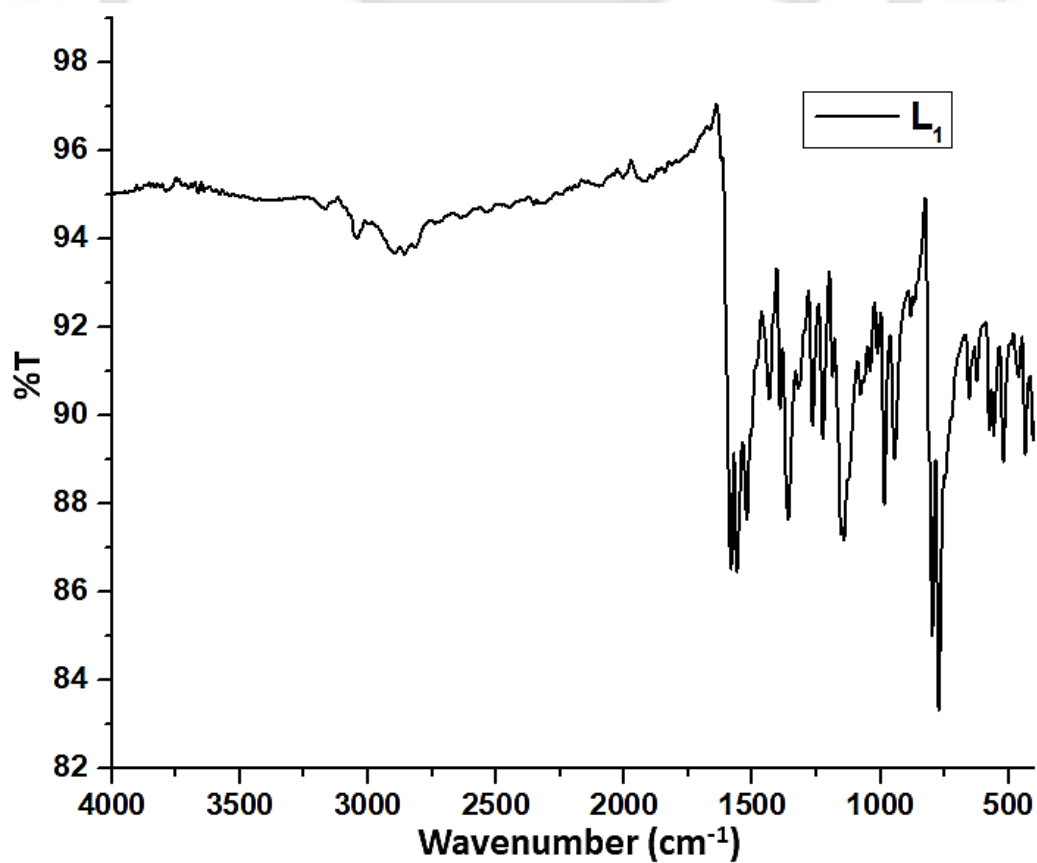


Figure A2.4: FTIR spectrum of L₁ recorded in KBr pellet at room temperature.

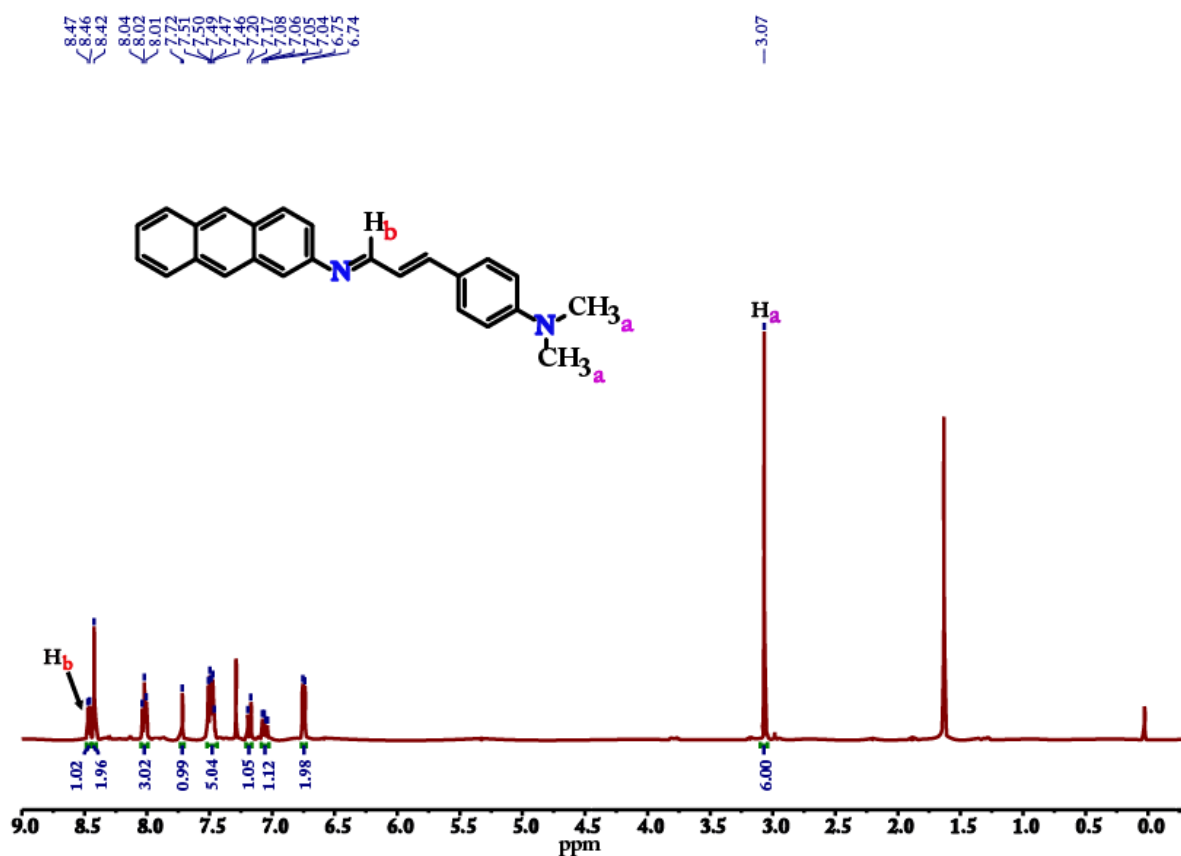


Figure A2.5: 1H NMR of L_2 in chloroform- d at room temperature.

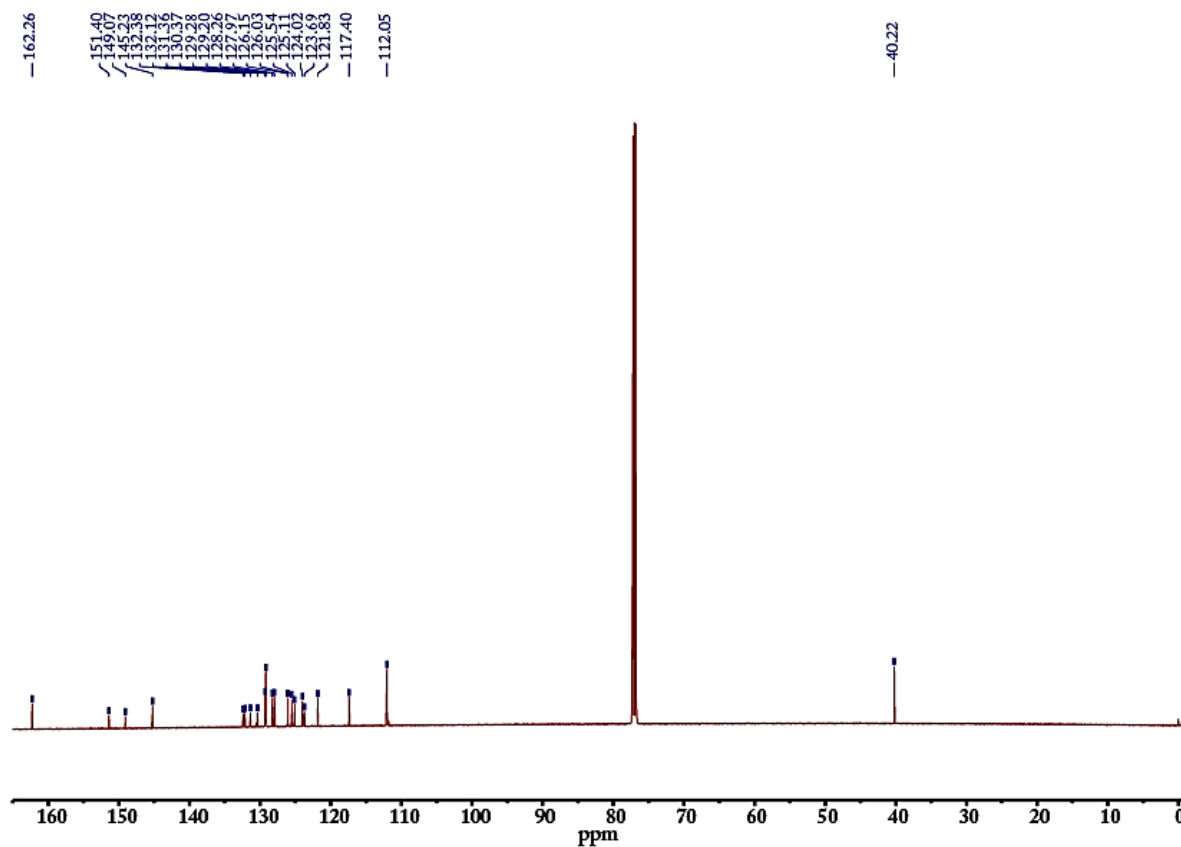


Figure A2.6: ^{13}C NMR of L_2 in chloroform- d_6 at room temperature.

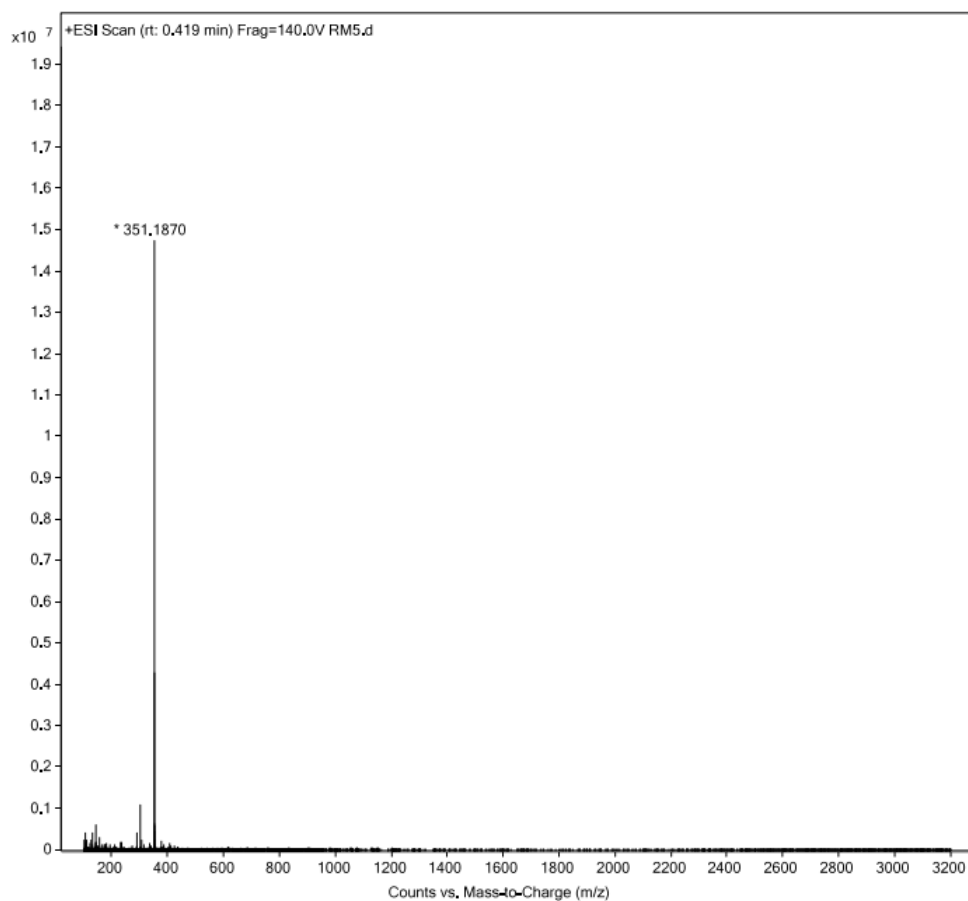


Figure A2.7: HRMS spectra of L₂ in acetonitrile in positive ionization mode.

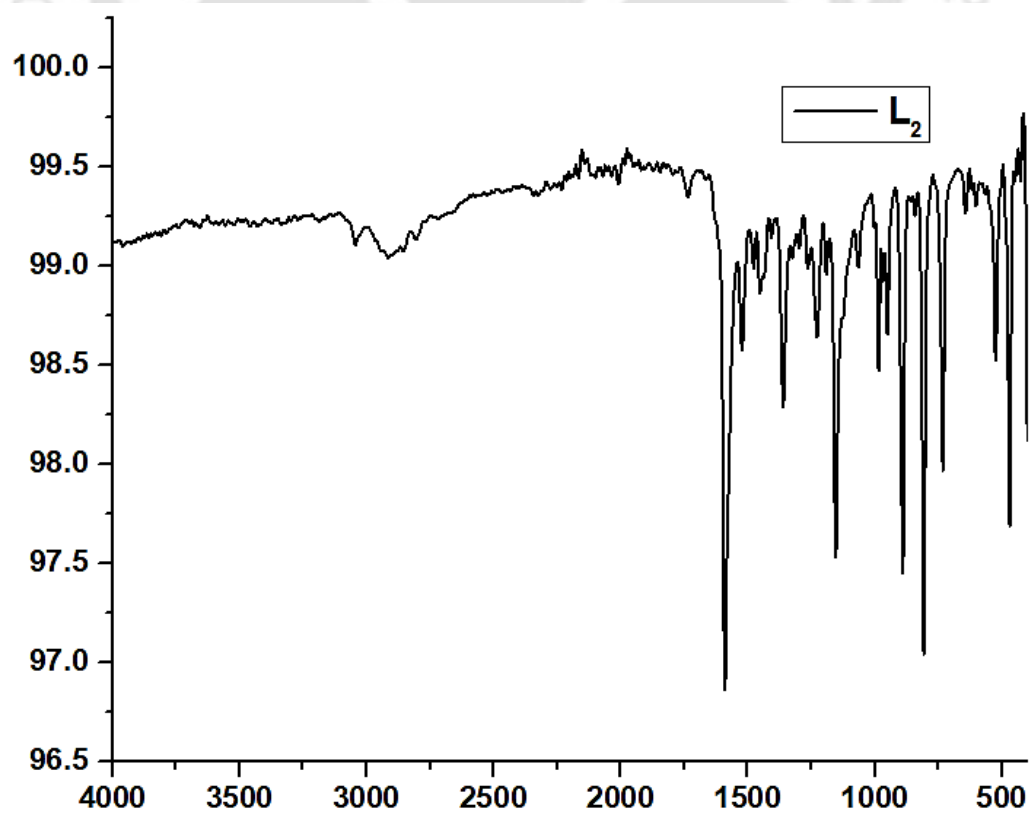


Figure A2.8: FTIR spectrum of L₂ recorded in KBr pellet at room temperature.

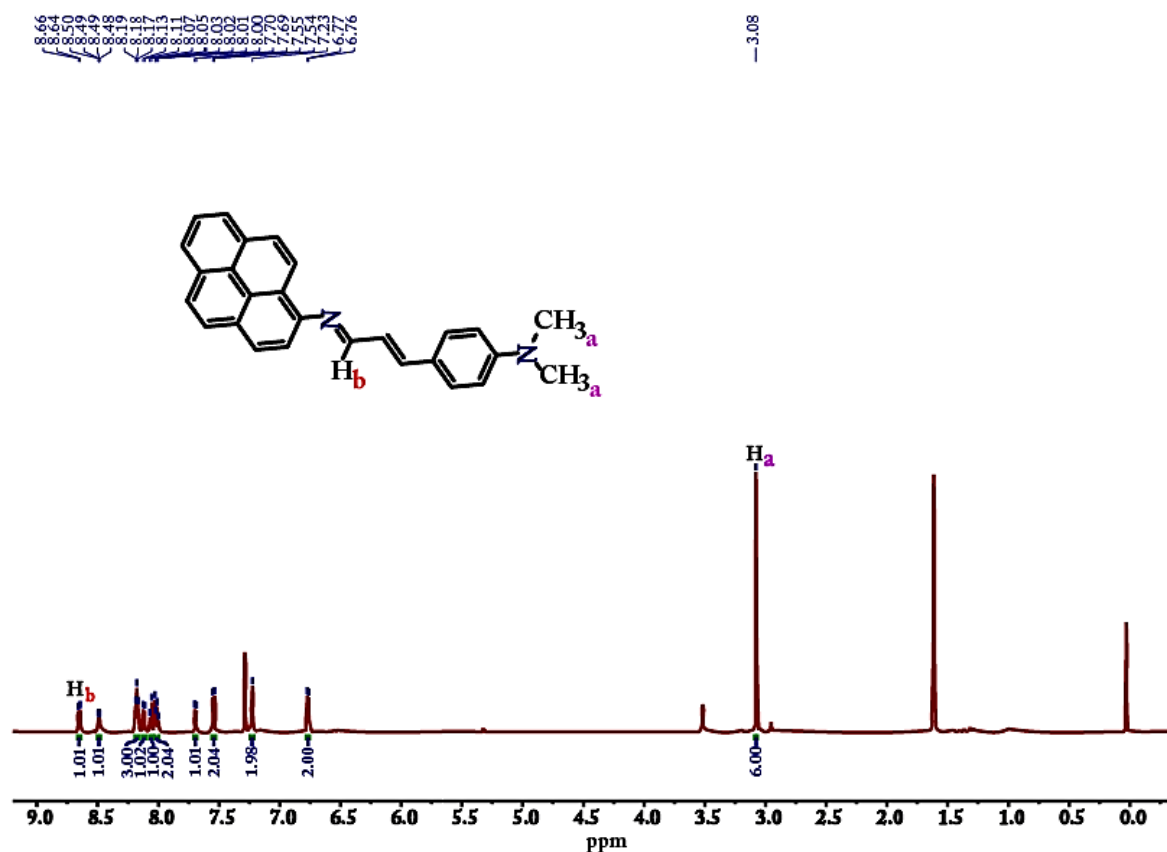


Figure A2.9: ¹H NMR of L₃ in chloroform-d at room temperature.

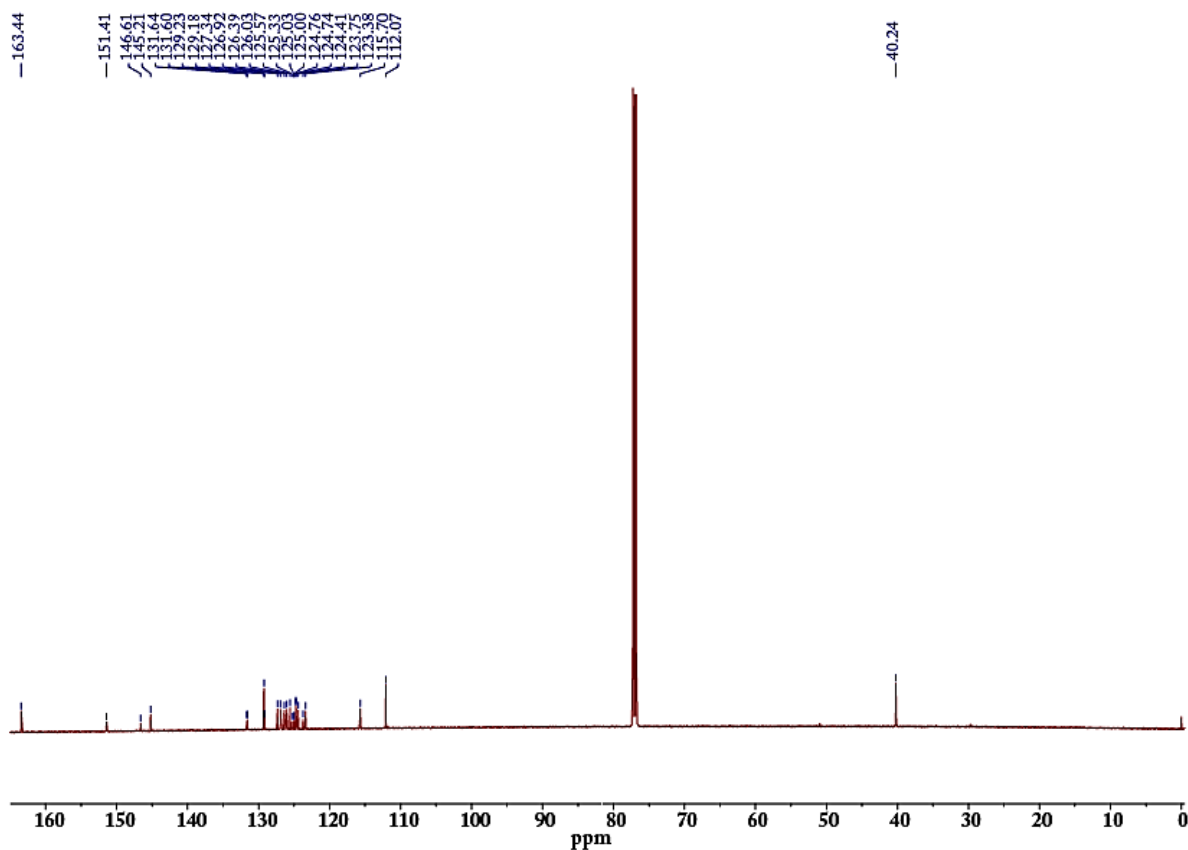


Figure A2.10: ¹³C NMR of L₃ in chloroform-d at room temperature.

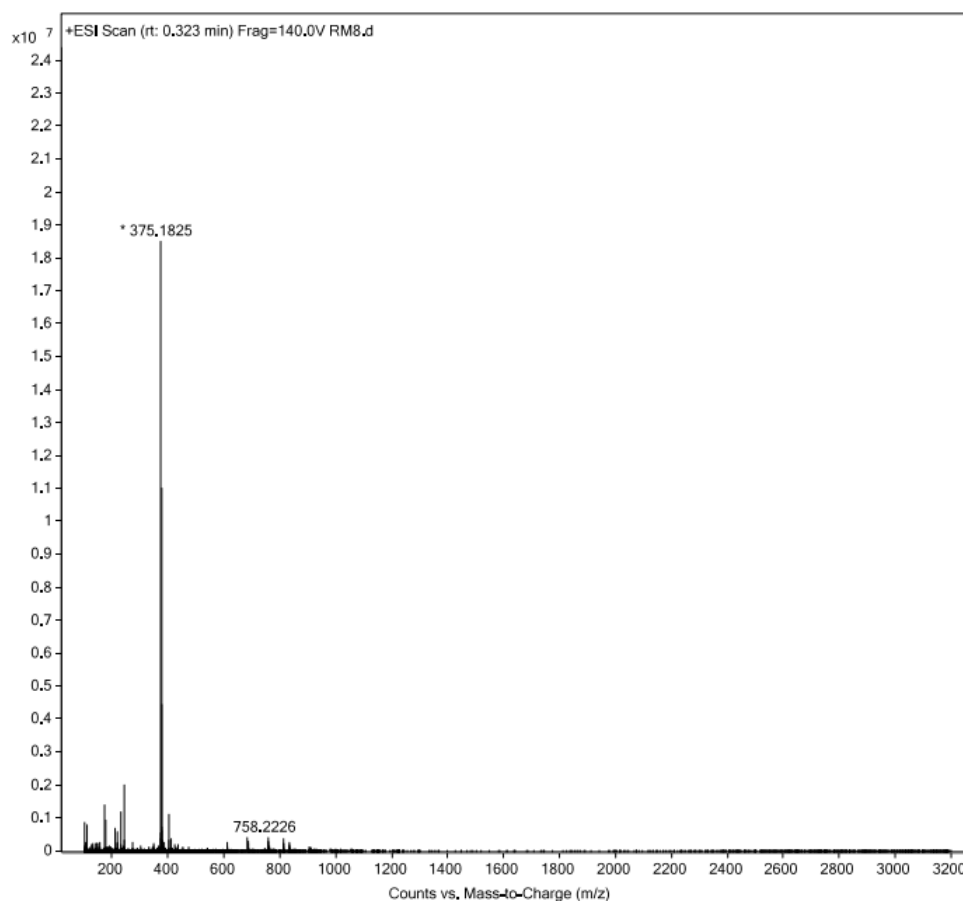


Figure A2.11: HRMS spectra of L_3 in acetonitrile in positive ionization mode.

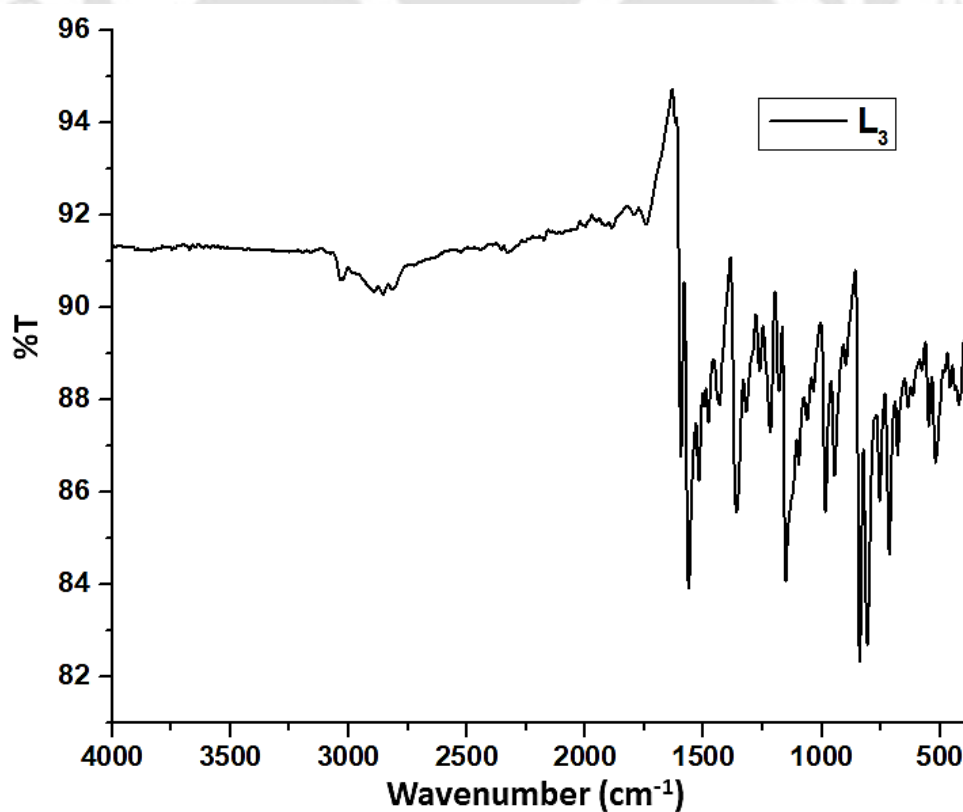


Figure A2.12: FTIR spectrum of L_3 recorded in KBr pellet at room temperature.

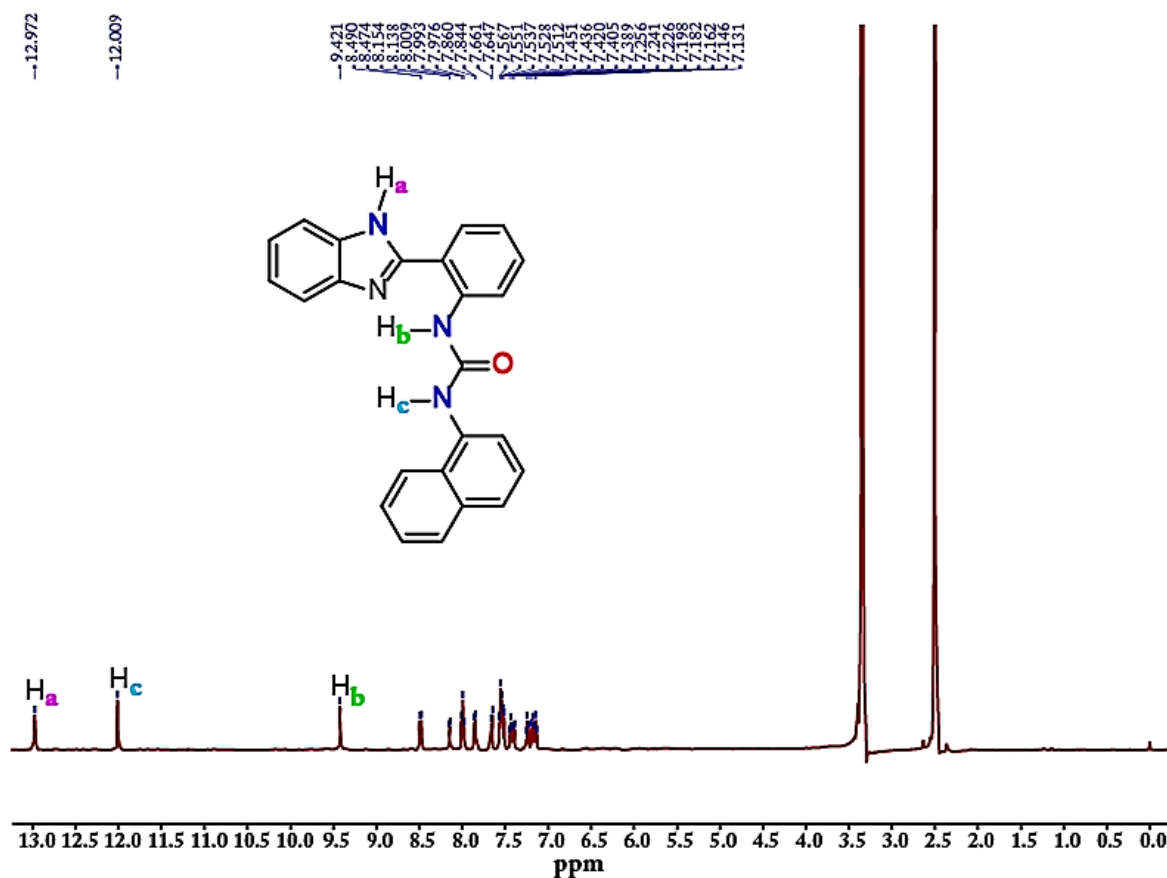


Figure A2.13: ¹H NMR of R1 in DMSO-*d*₆ at room temperature.

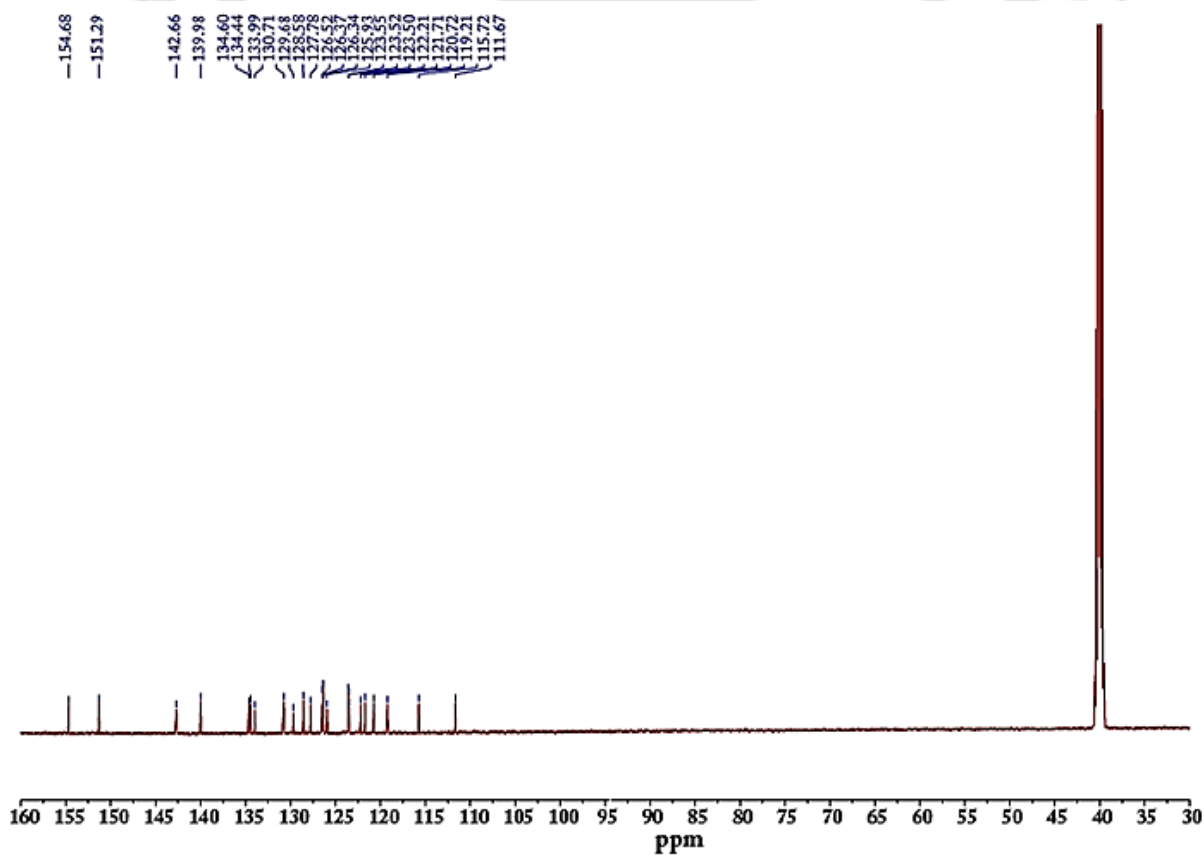


Figure A2.14: ¹³C NMR of R1 in DMSO-*d*₆ at room temperature.

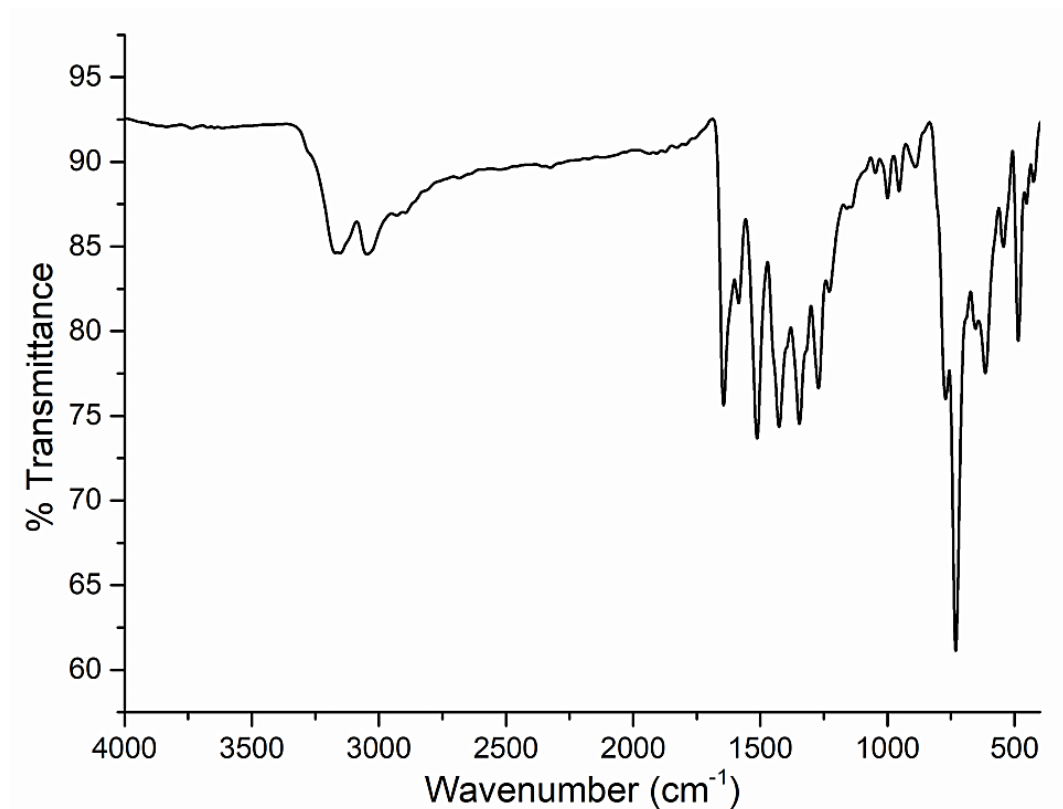


Figure A2.15: FT-IR spectra of R1.

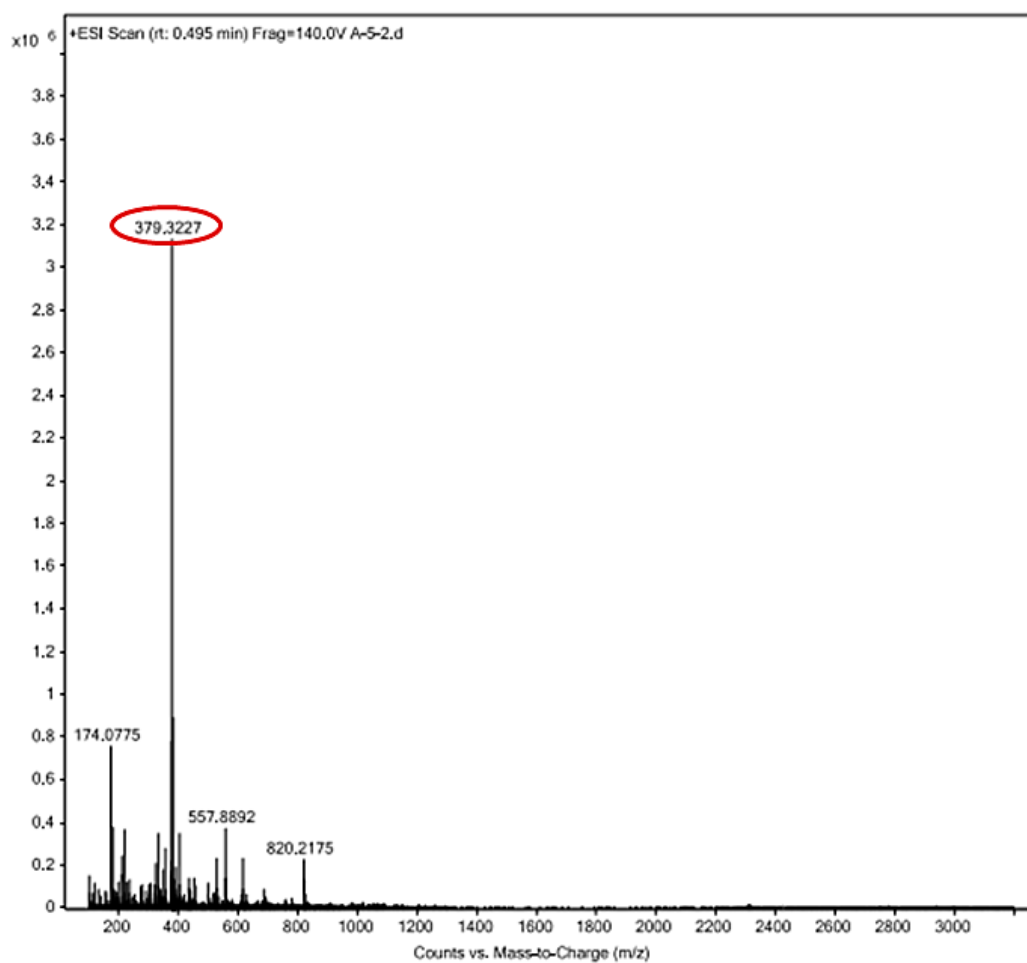


Figure A2.16: HRMS spectra of R1 in acetonitrile in positive ionization mode.

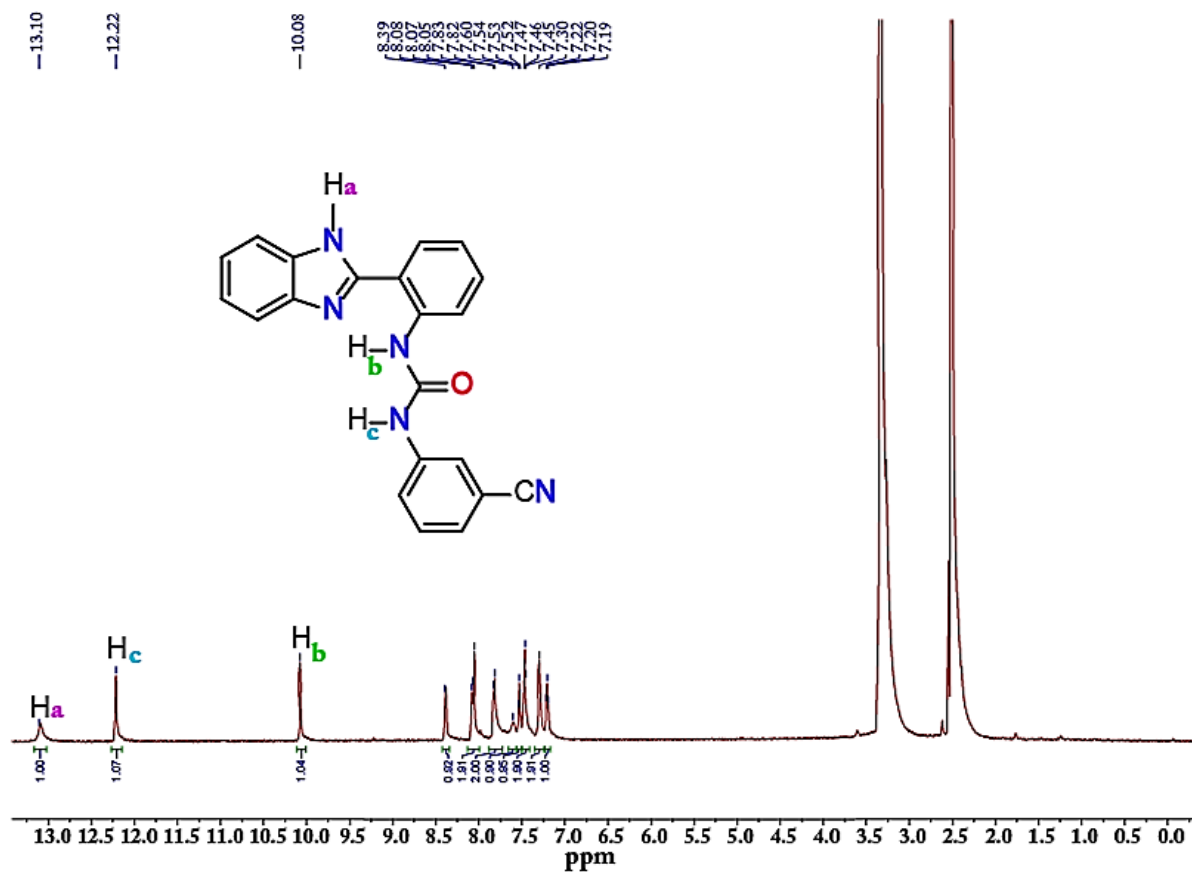


Figure A2.17: ¹H NMR of R2 in DMSO-*d*₆ at room temperature.

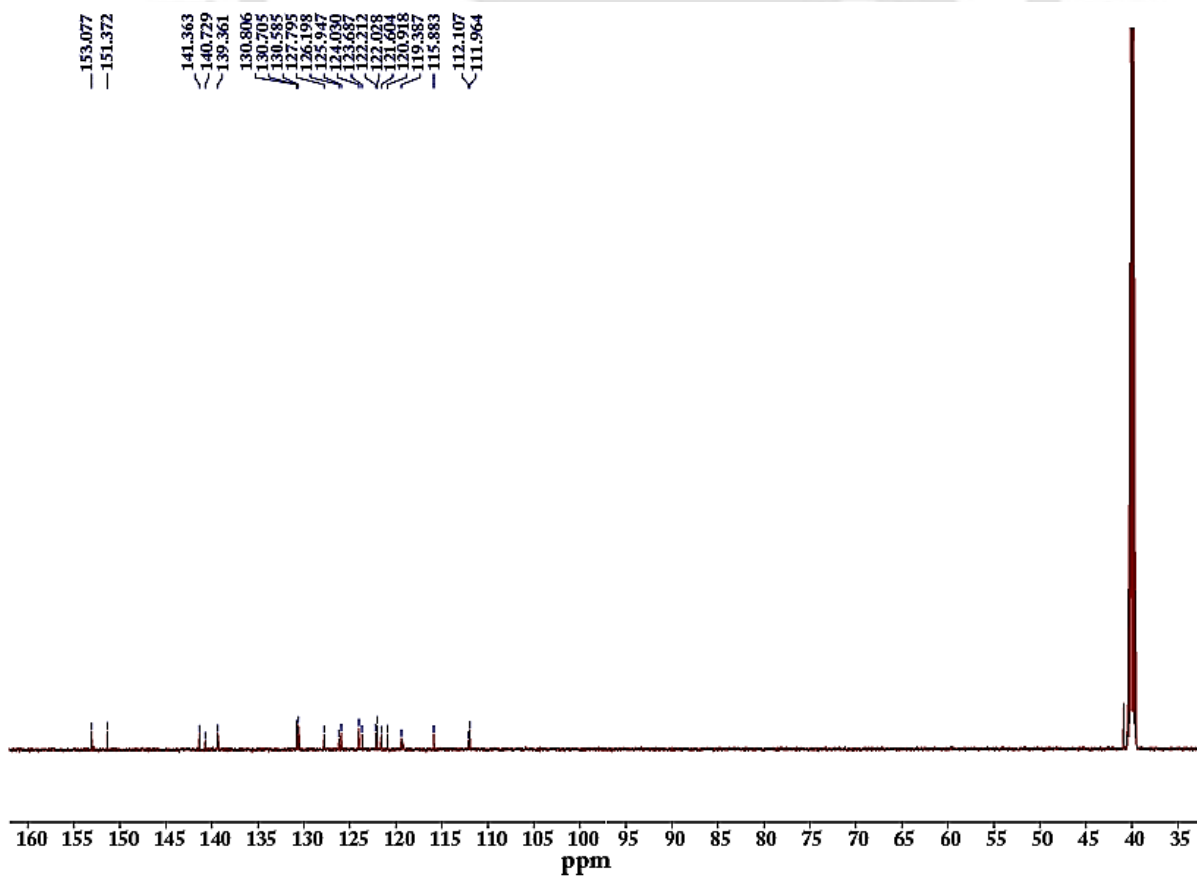


Figure A2.18: ¹³C NMR of R1 in DMSO-*d*₆ at room temperature.

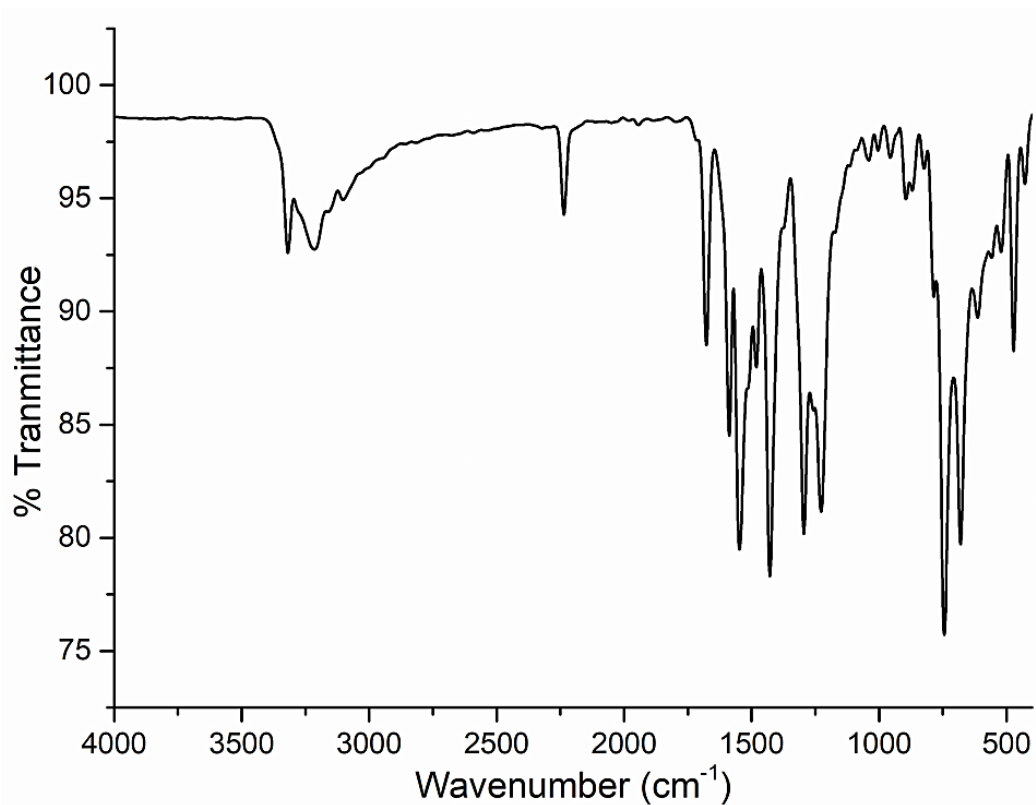


Figure A2.19: FT-IR spectra of R2.

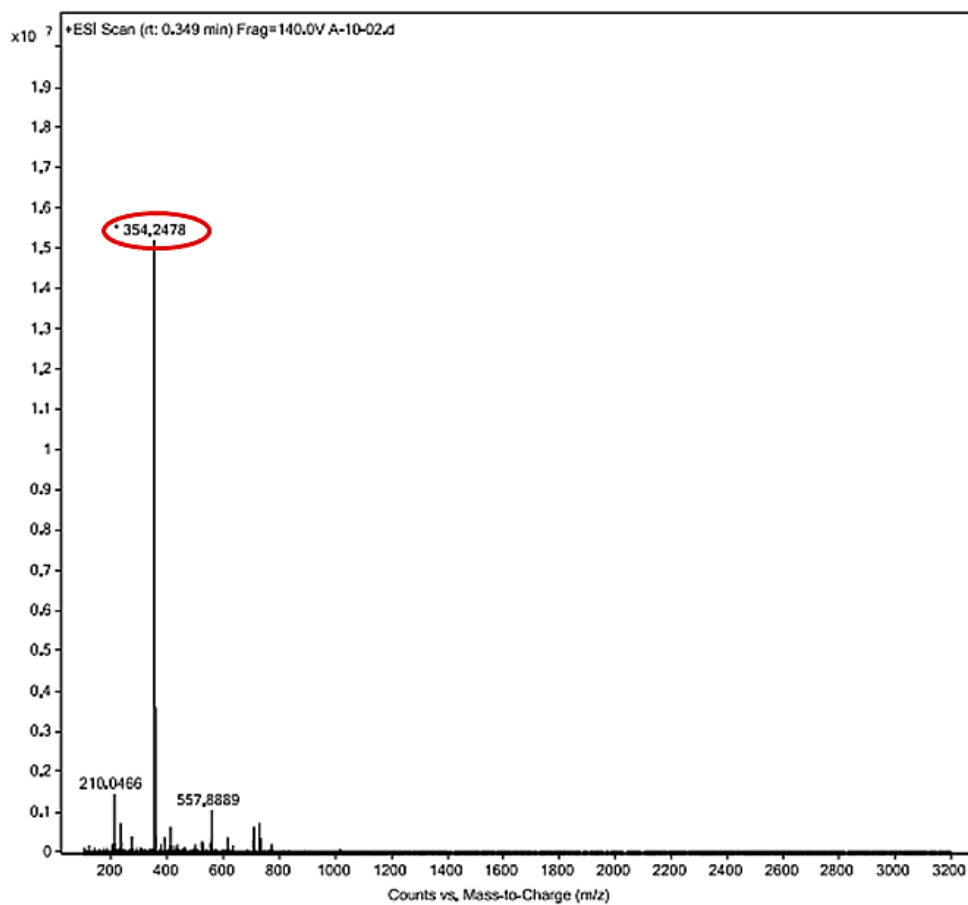


Figure A2.20: HRMS spectra of R2 in acetonitrile in positive ionization mode.

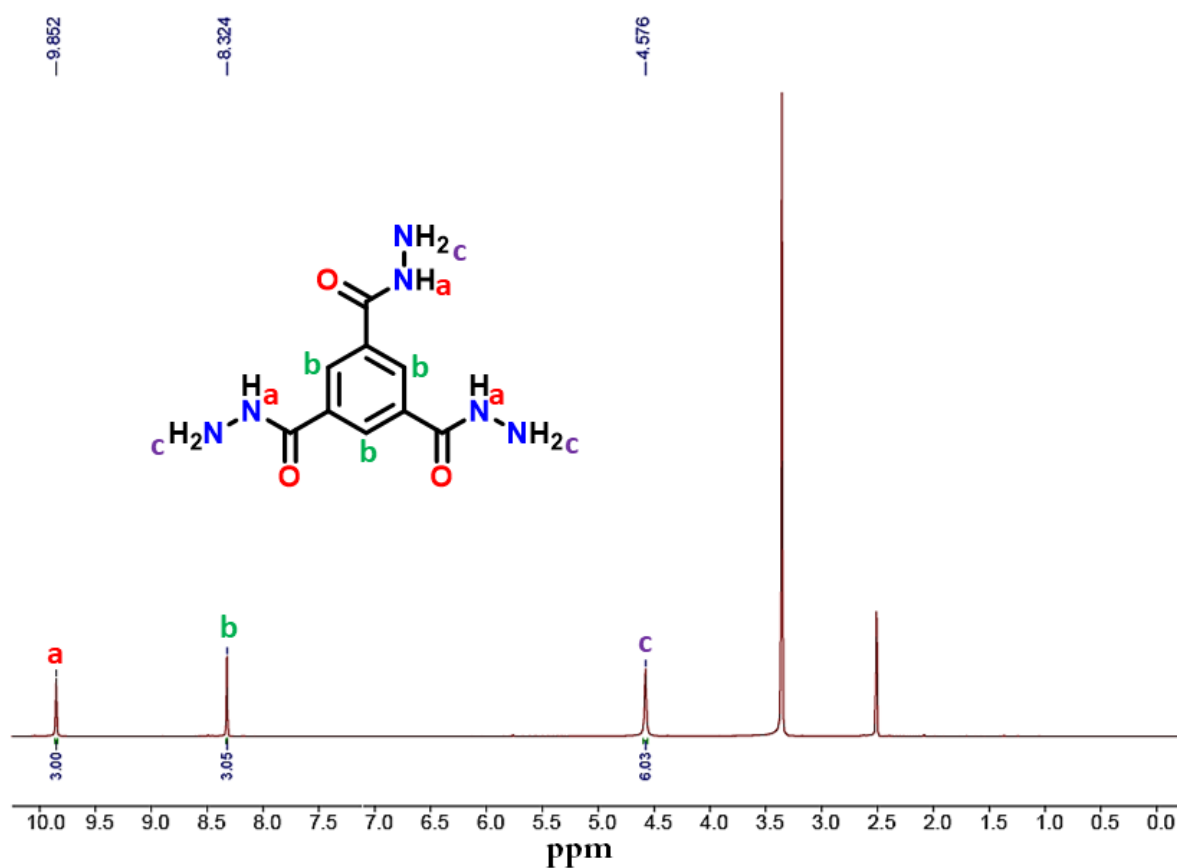


Figure A2.21: ¹H NMR spectrum of TRI-NH₂ in DMSO-*d*₆.

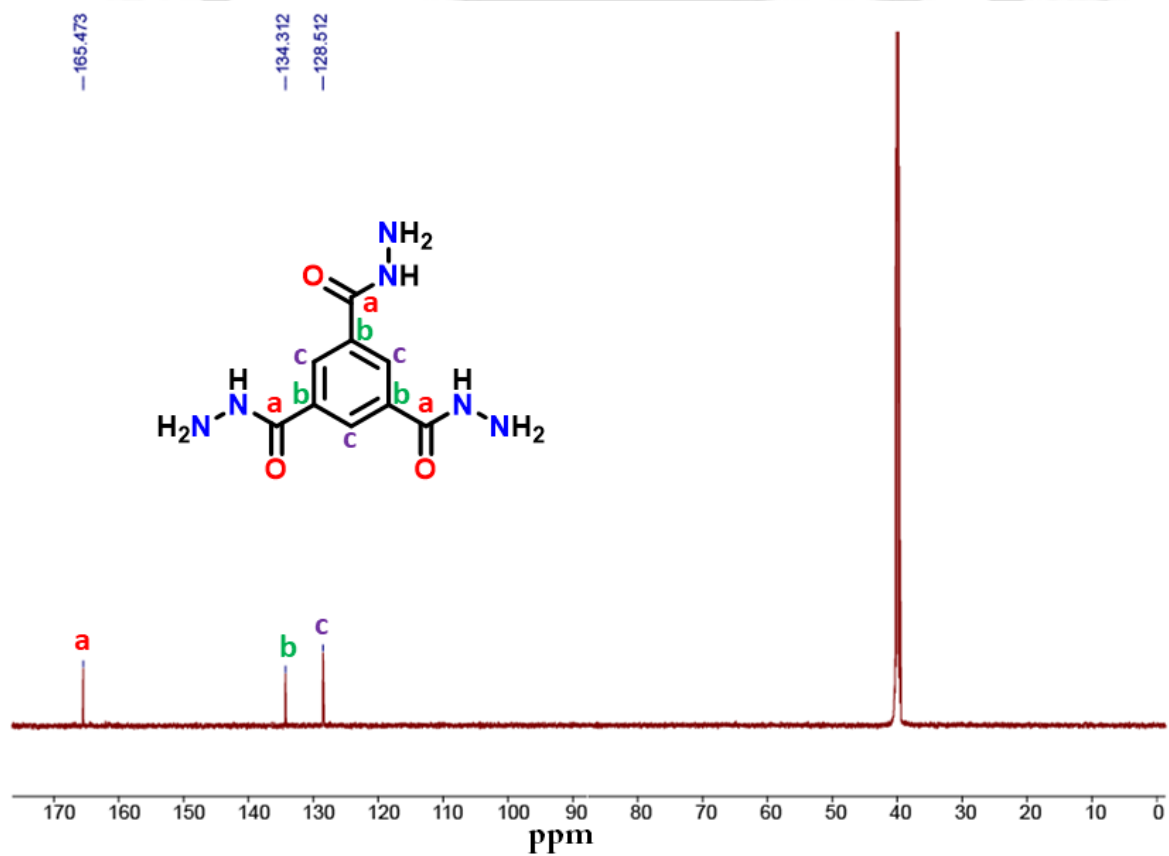


Figure A2.22: ¹³C NMR spectrum of TRI-NH₂ in DMSO-*d*₆.

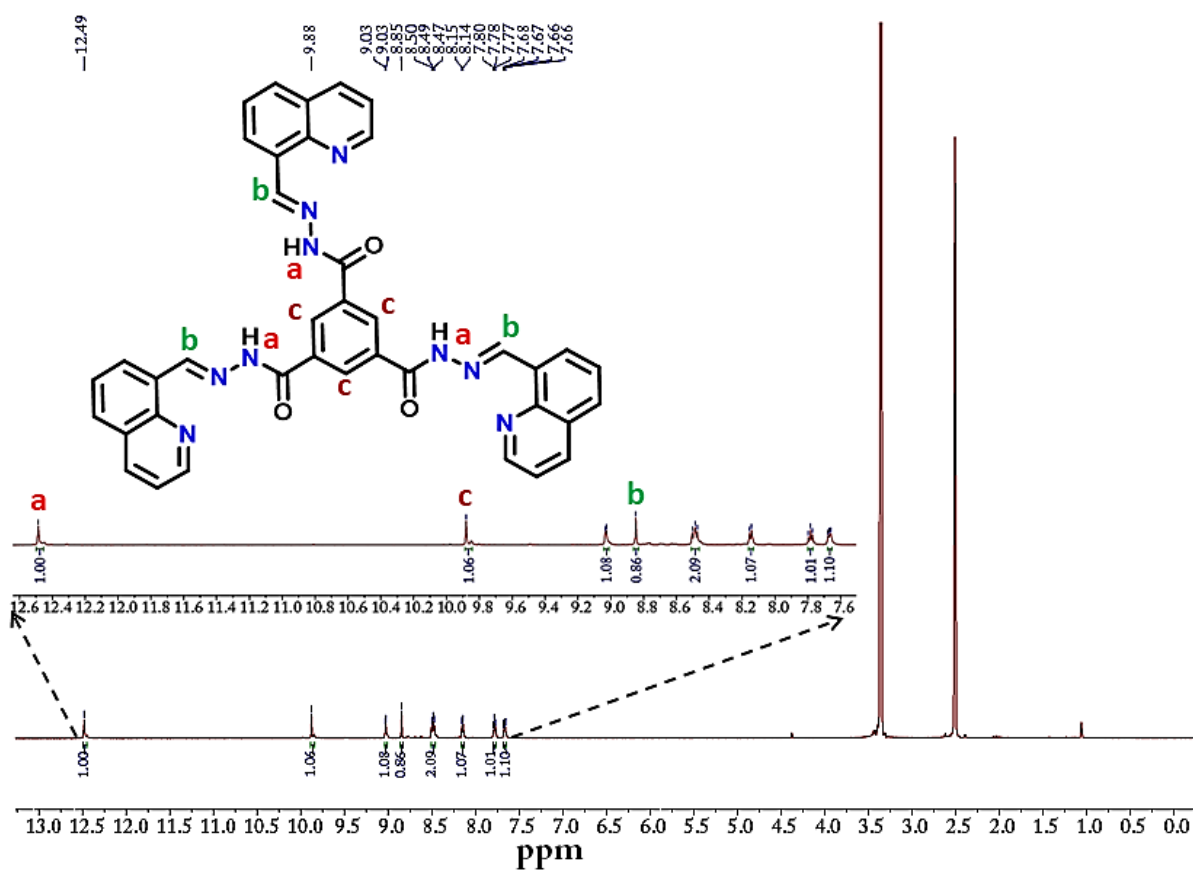


Figure A2.23: ^1H NMR spectrum of TRI-QUI in $\text{DMSO-}d_6$.

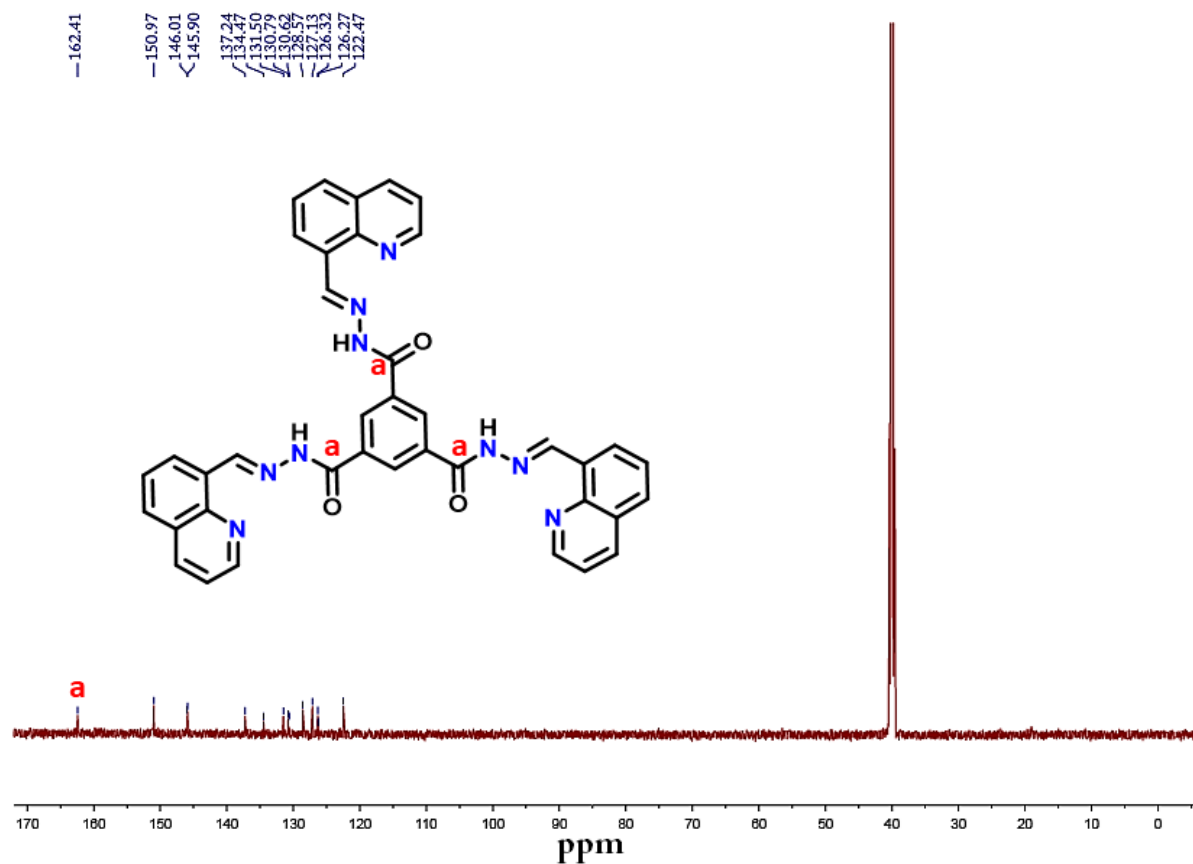


Figure A2.24: ^{13}C NMR spectrum of TRI-QUI in $\text{DMSO-}d_6$.

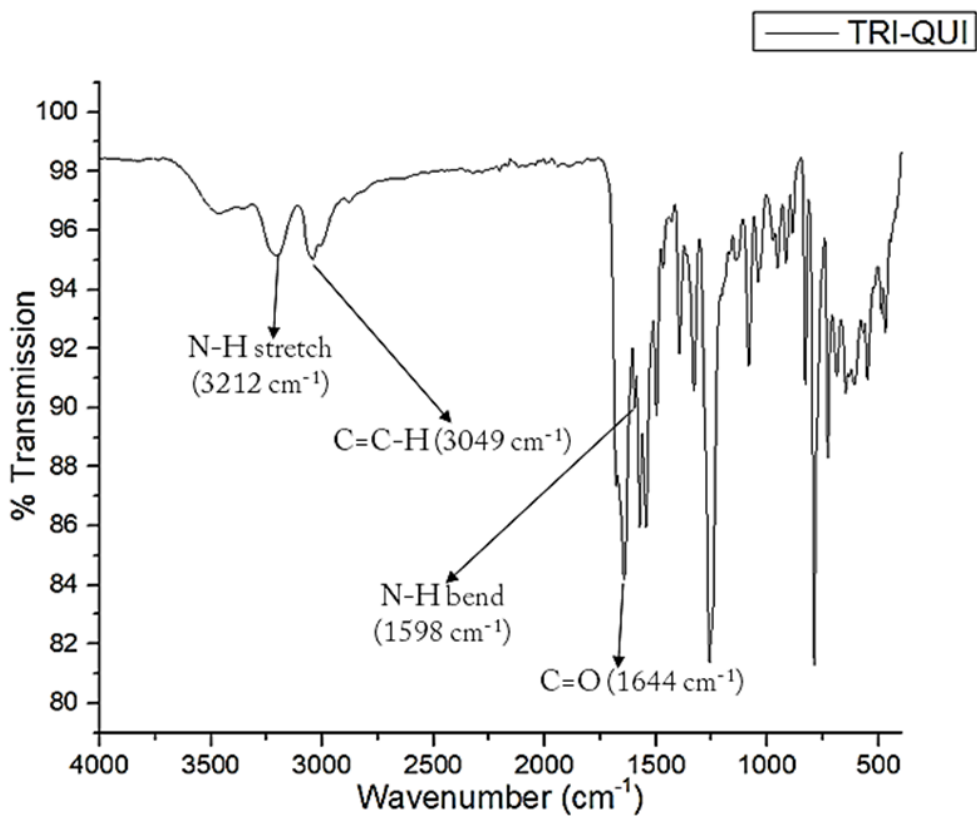


Figure A2.25: FTIR spectra of TRI-QUI.

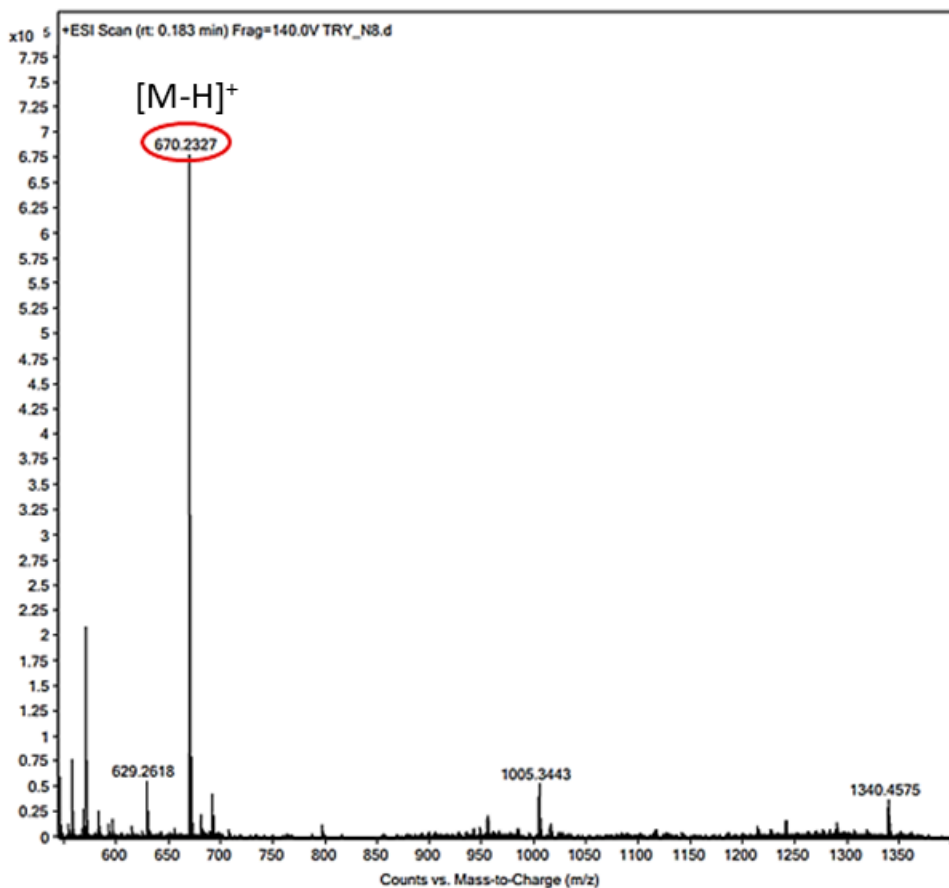


Figure A2.26: HRMS of TRI-QUI.

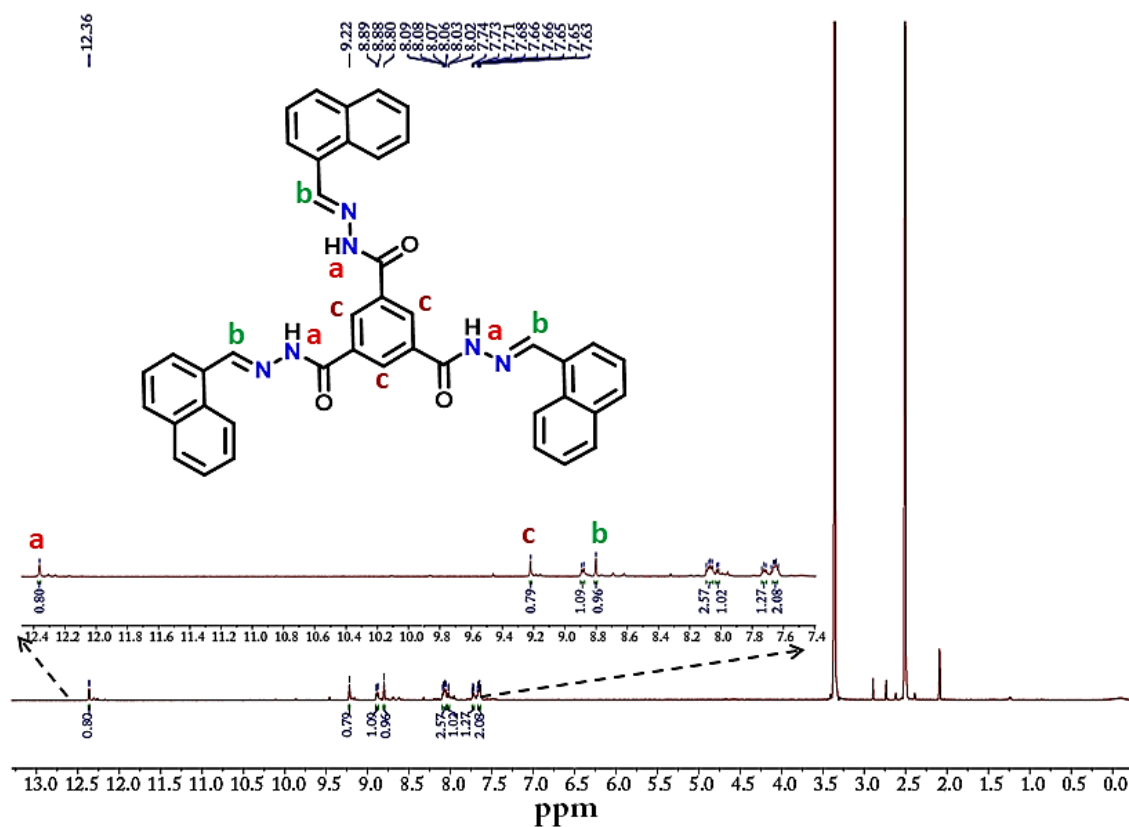


Figure A2.27: ^1H NMR spectrum of TRI-NAP in $\text{DMSO-}d_6$.

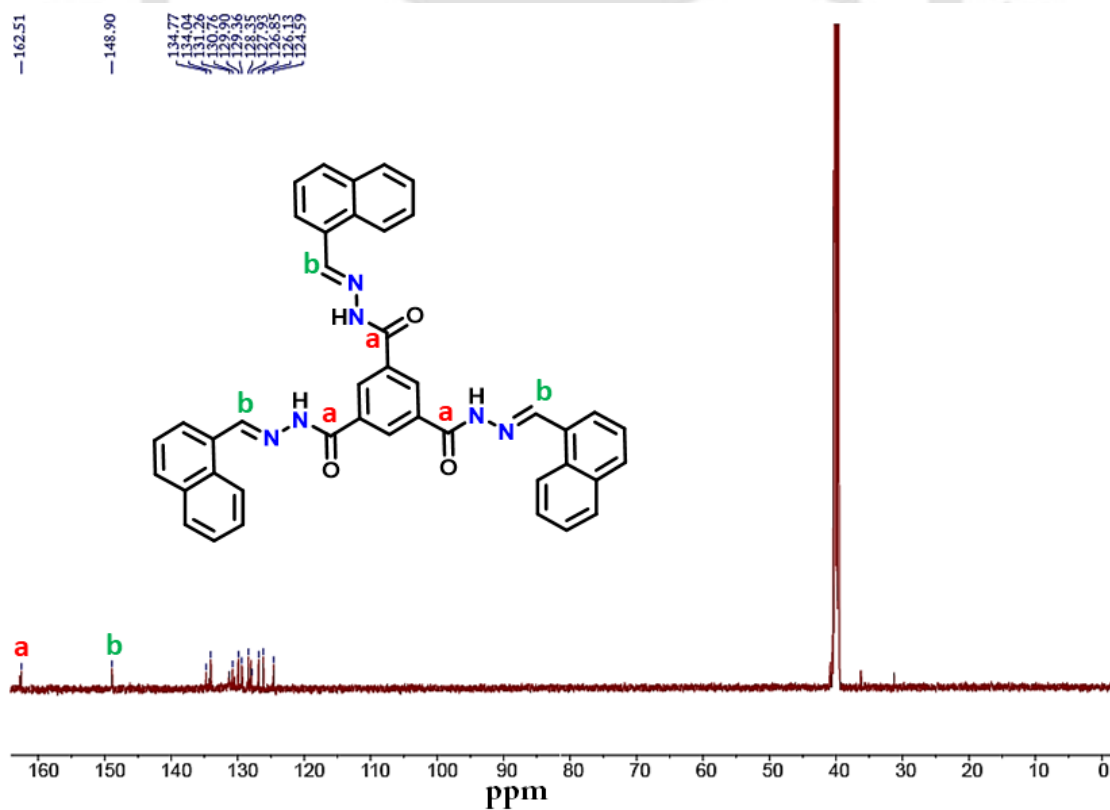


Figure A2.28: ^{13}C NMR spectrum of TRI-NAP in $\text{DMSO-}d_6$.

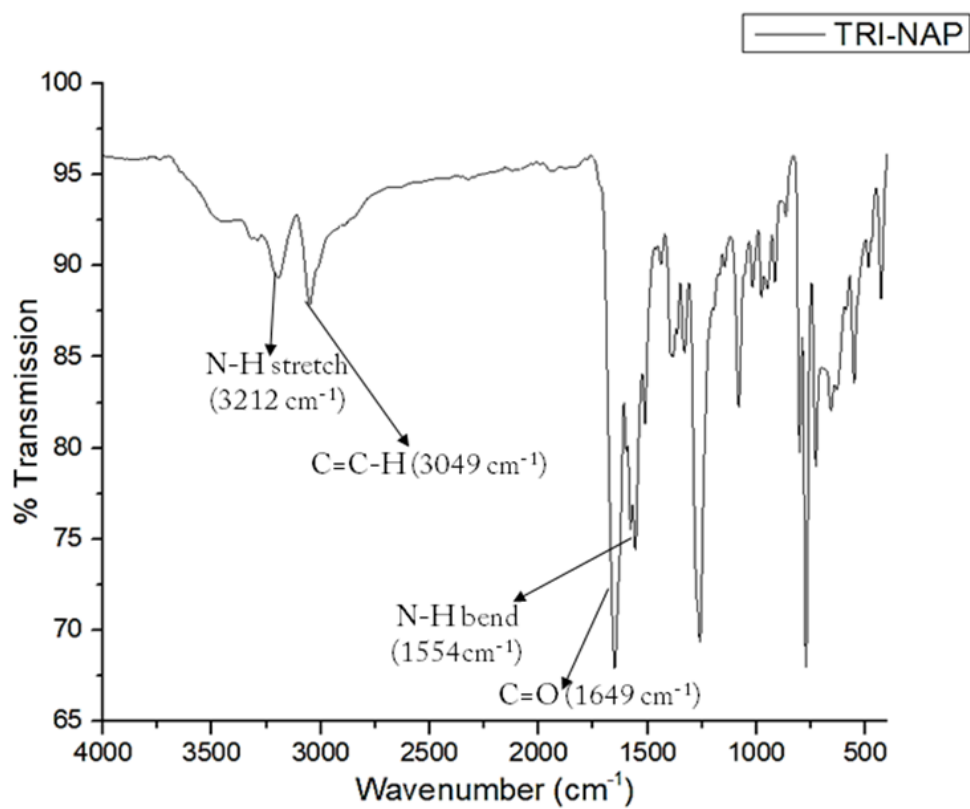


Figure A2.28: FTIR spectra of TRI-NAP.

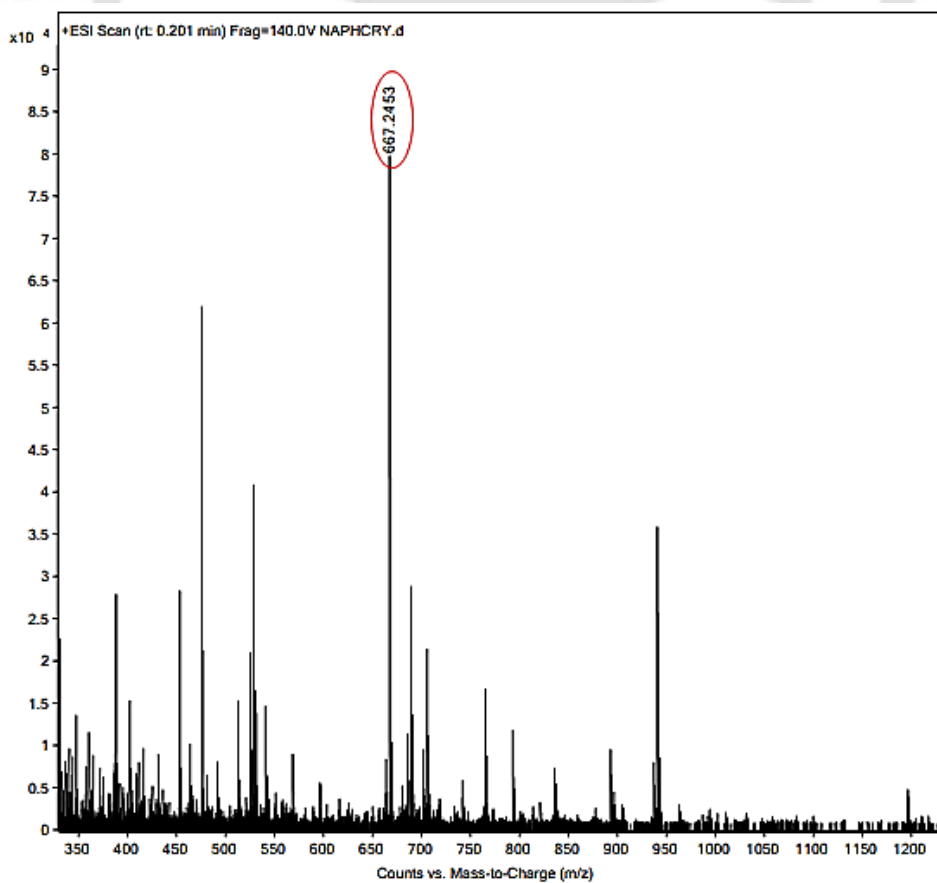


Figure A2.29: HRMS of TRI-NAP.

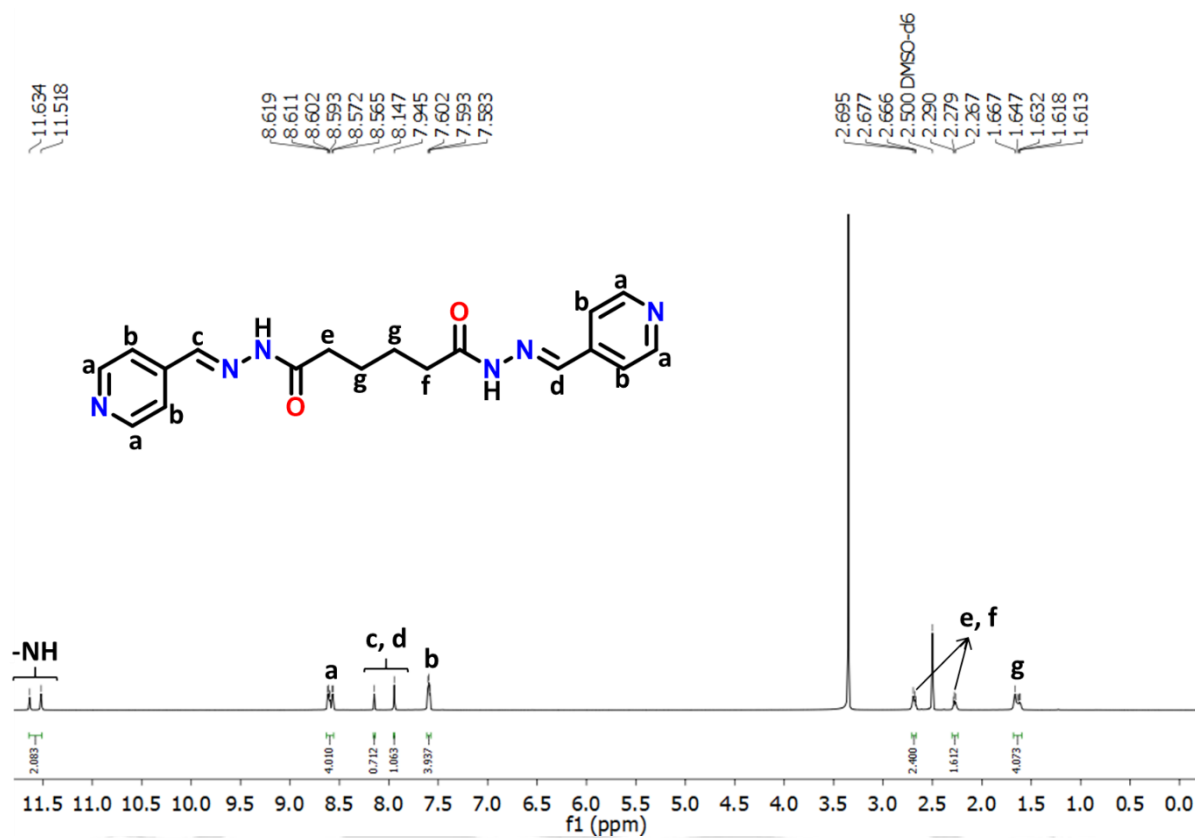


Figure A2.30: ^1H NMR of ADH-Py-p DMSO- d_6 .

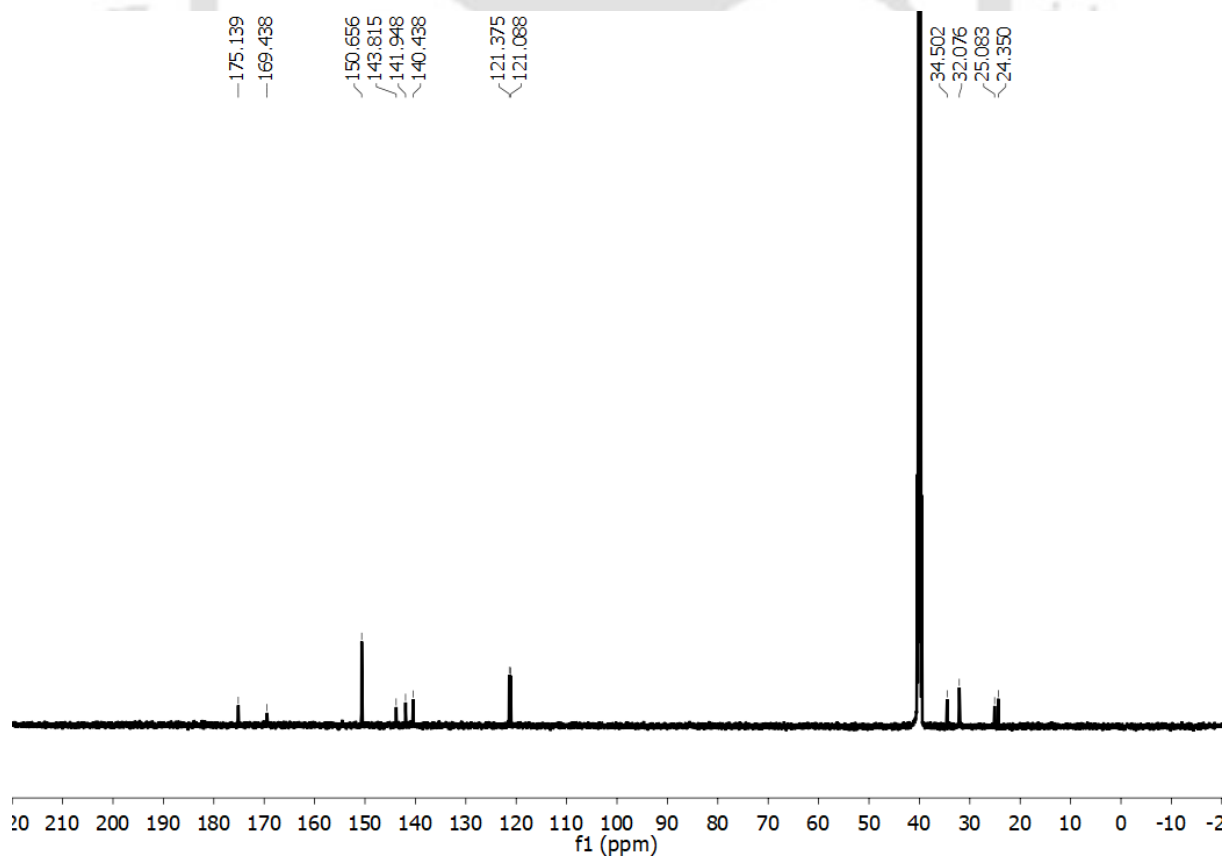


Figure A2.31: ^{13}C NMR of ADH-Py-p DMSO- d_6 .

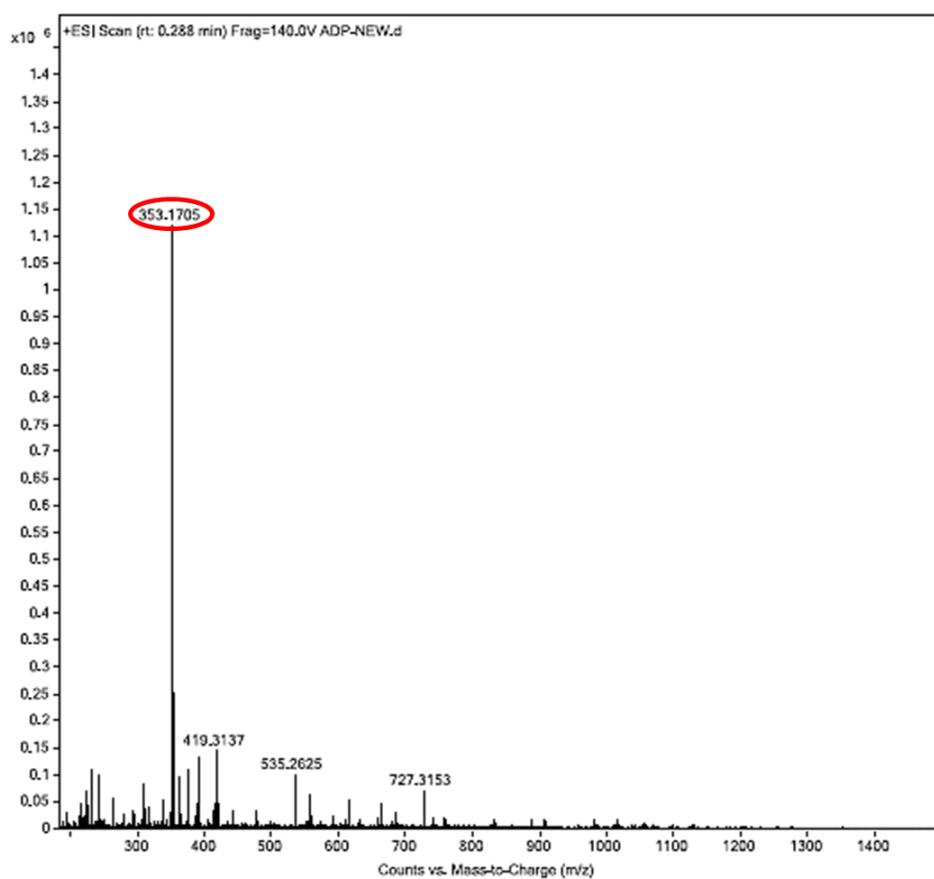


Figure A2.32: HRMS of ADH-Py-p.

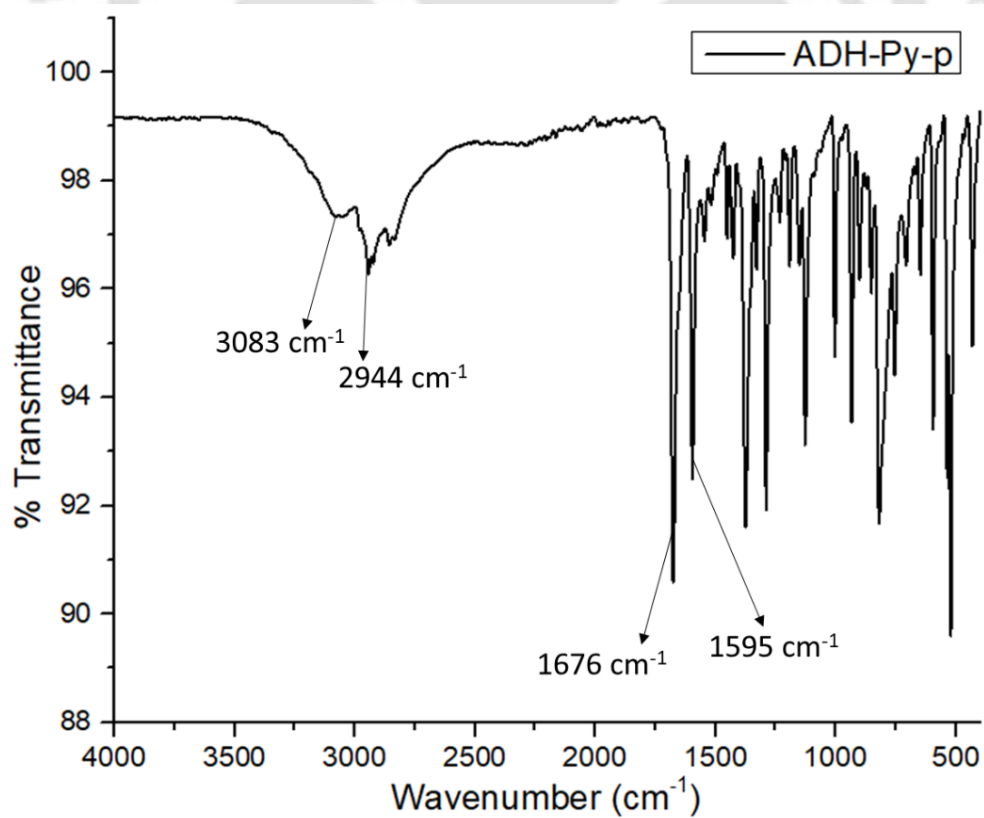


Figure A2.33: IR of ADH-Py-p.

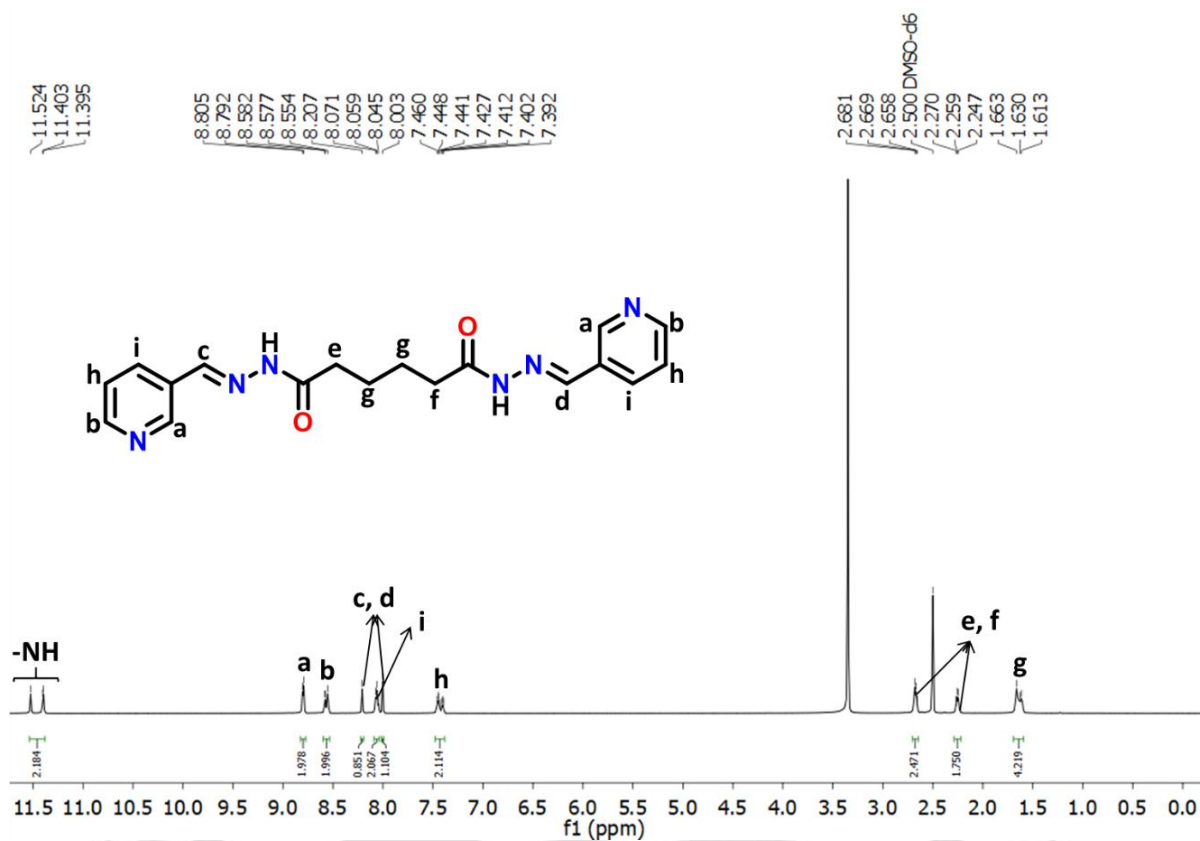


Figure A2.34: ¹H NMR of ADH-Py-m DMSO-*d*₆.

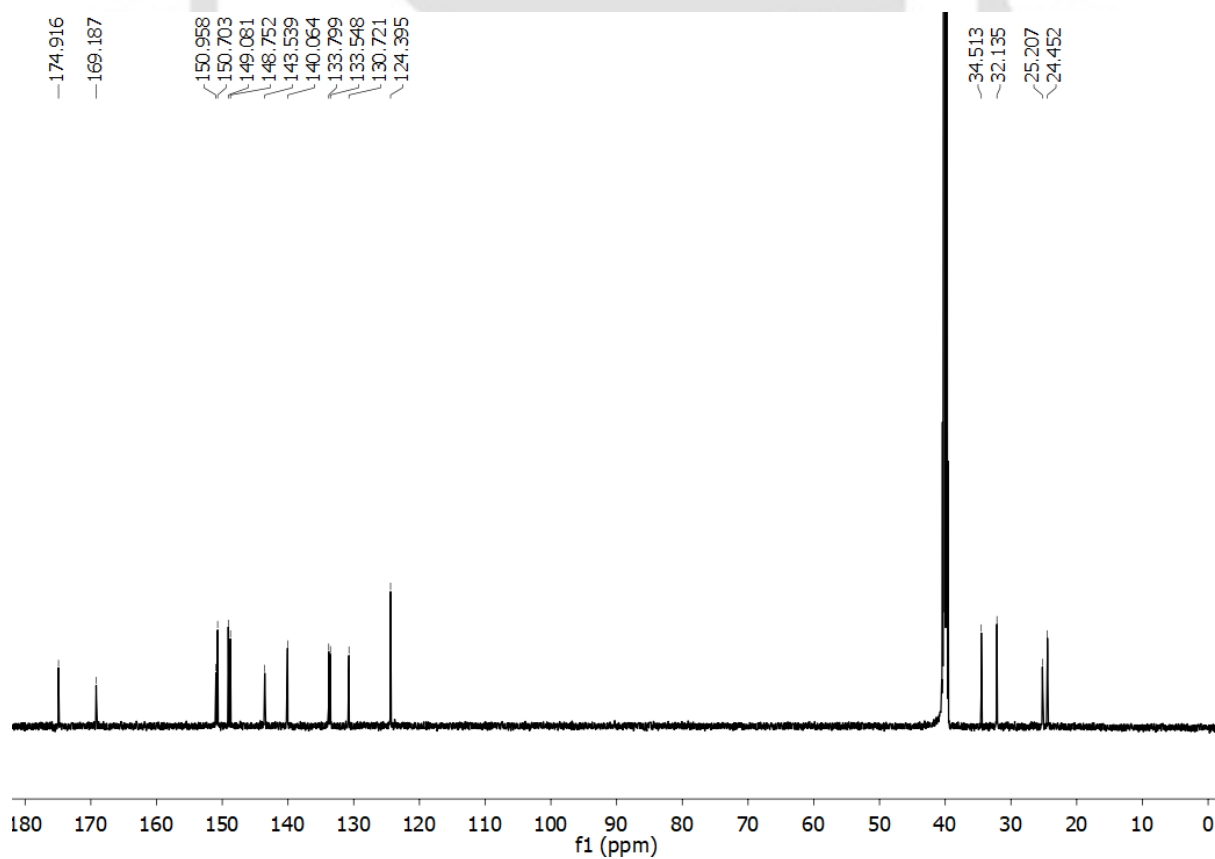


Figure A2.35: ¹³C NMR of ADH-Py-m DMSO-*d*₆.

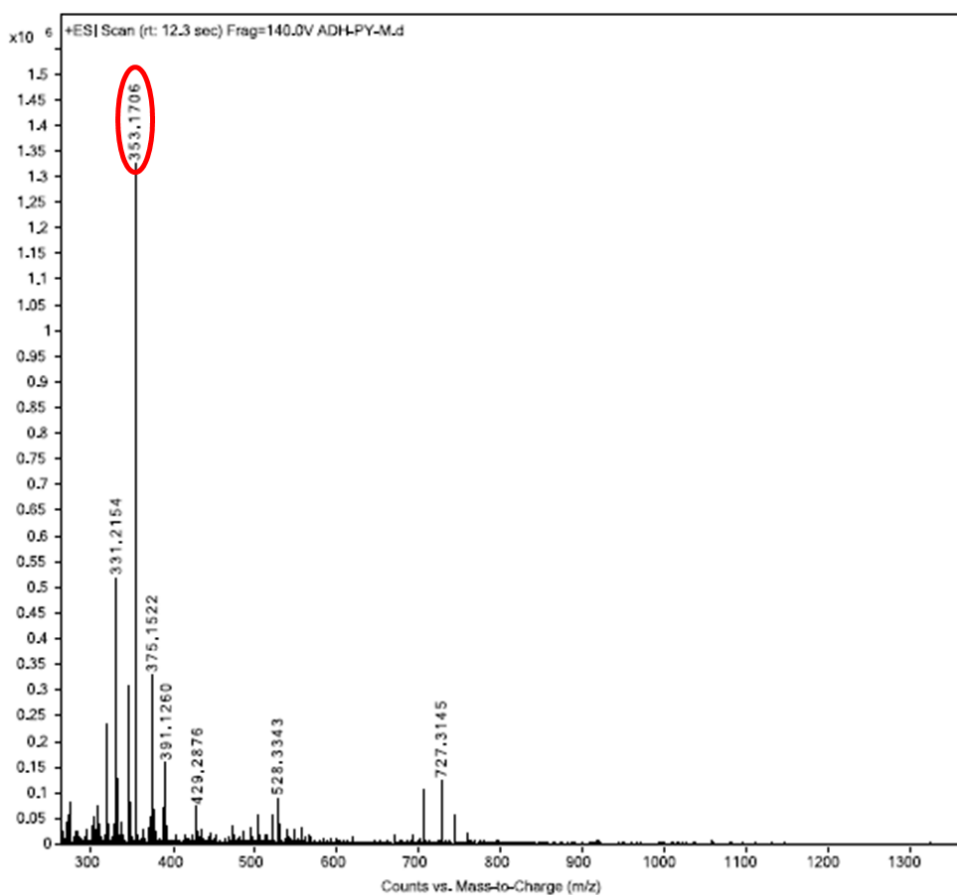


Figure A2.35: HRMS of ADH-Py-m.

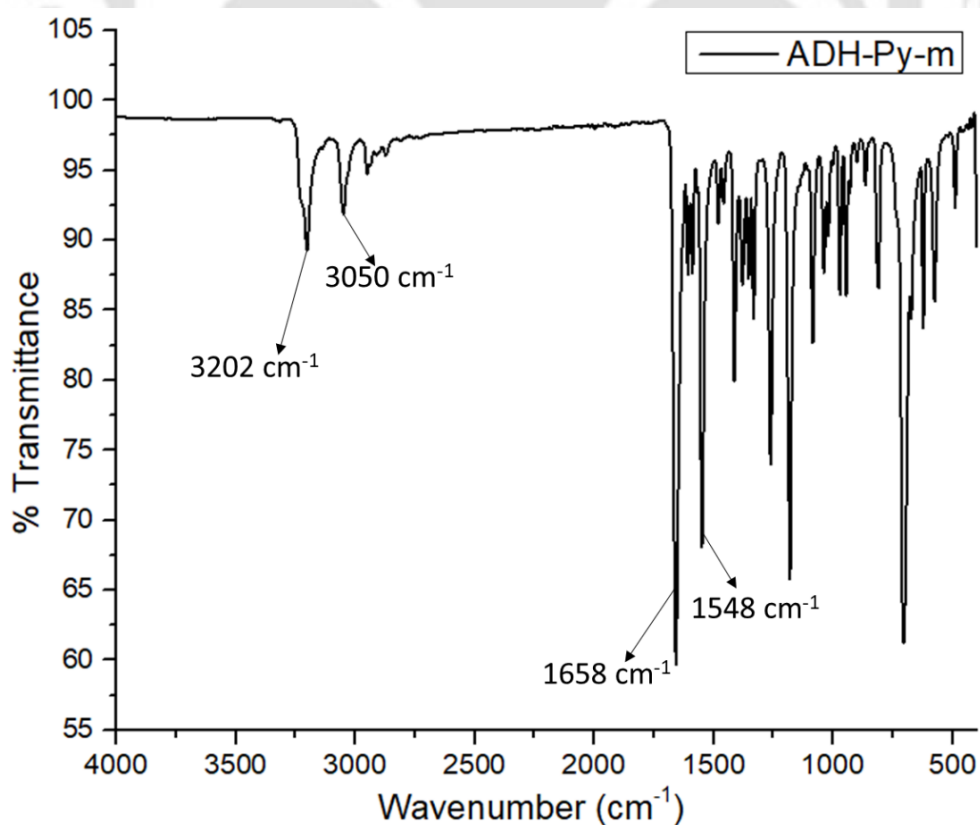


Figure A2.36: IR of ADH-Py-m.

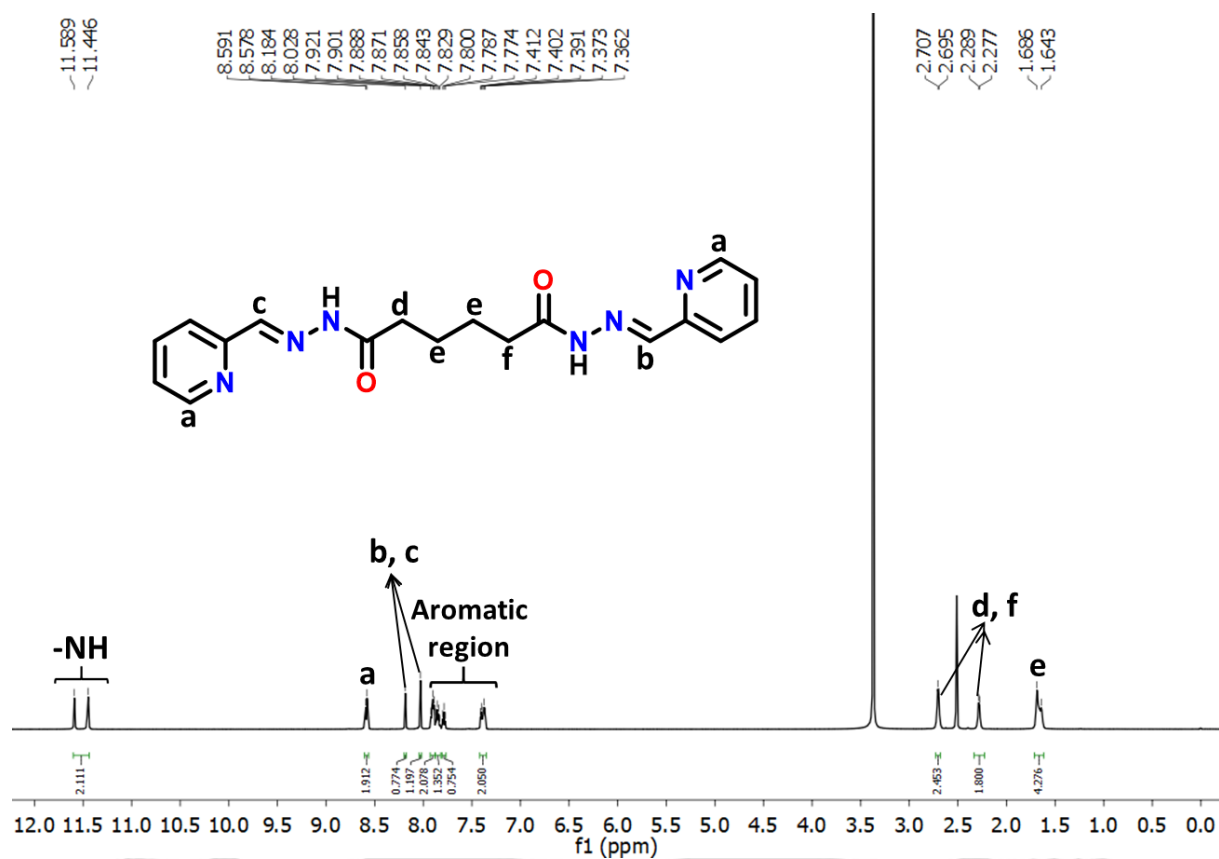


Figure A2.37: ^1H NMR of ADH-Py-o $\text{DMSO-}d_6$.

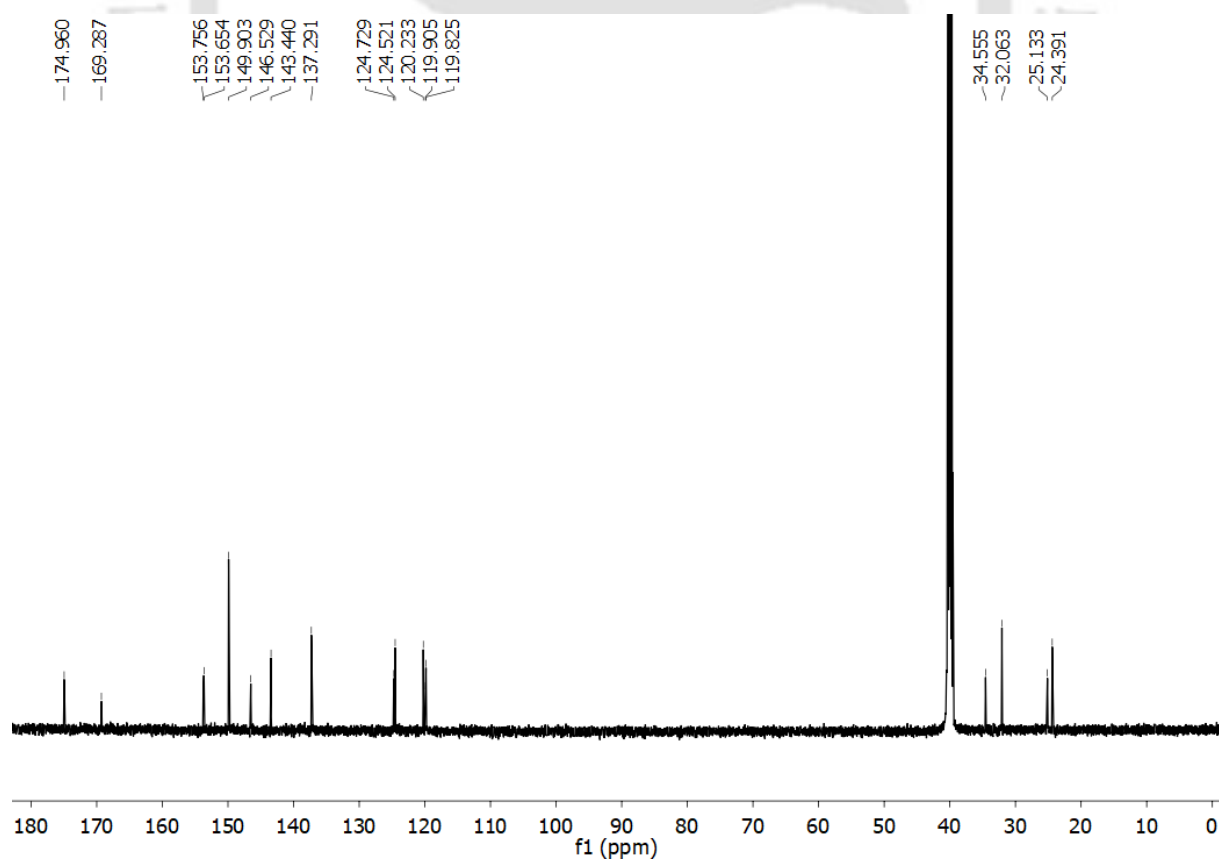


Figure A2.38: ^{13}C NMR of ADH-Py-o $\text{DMSO-}d_6$.

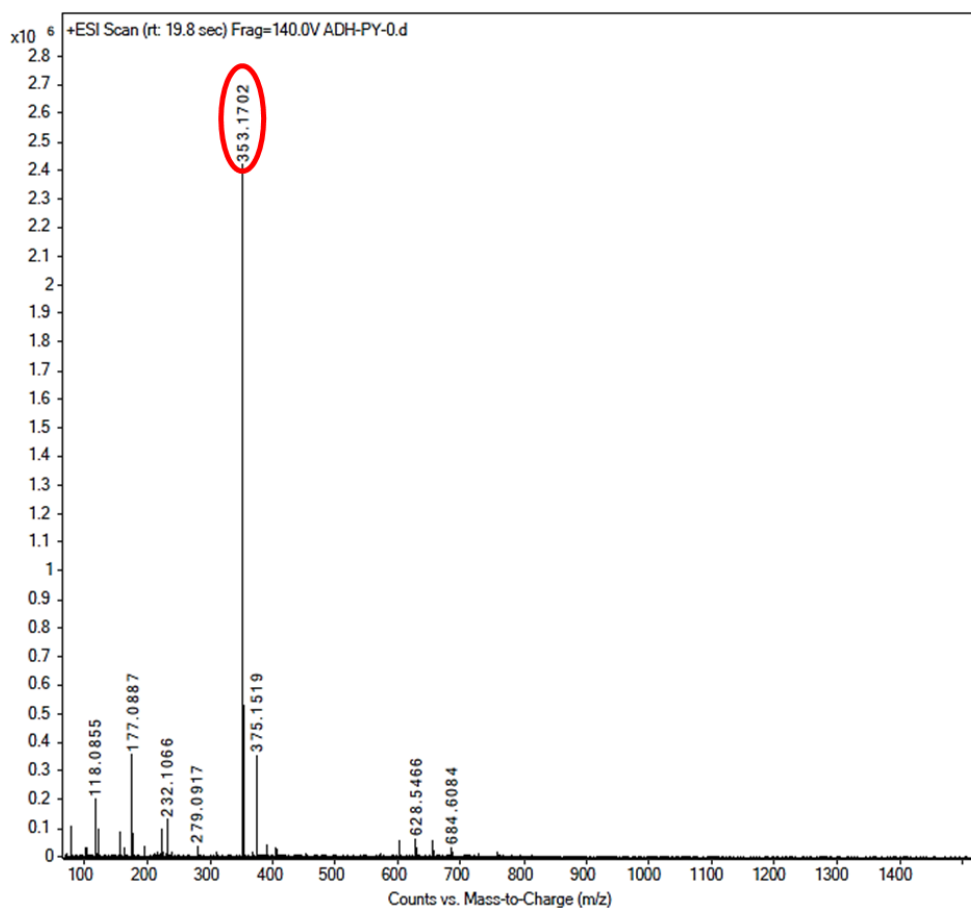


Figure A2.39: HRMS of ADH-Py-o.

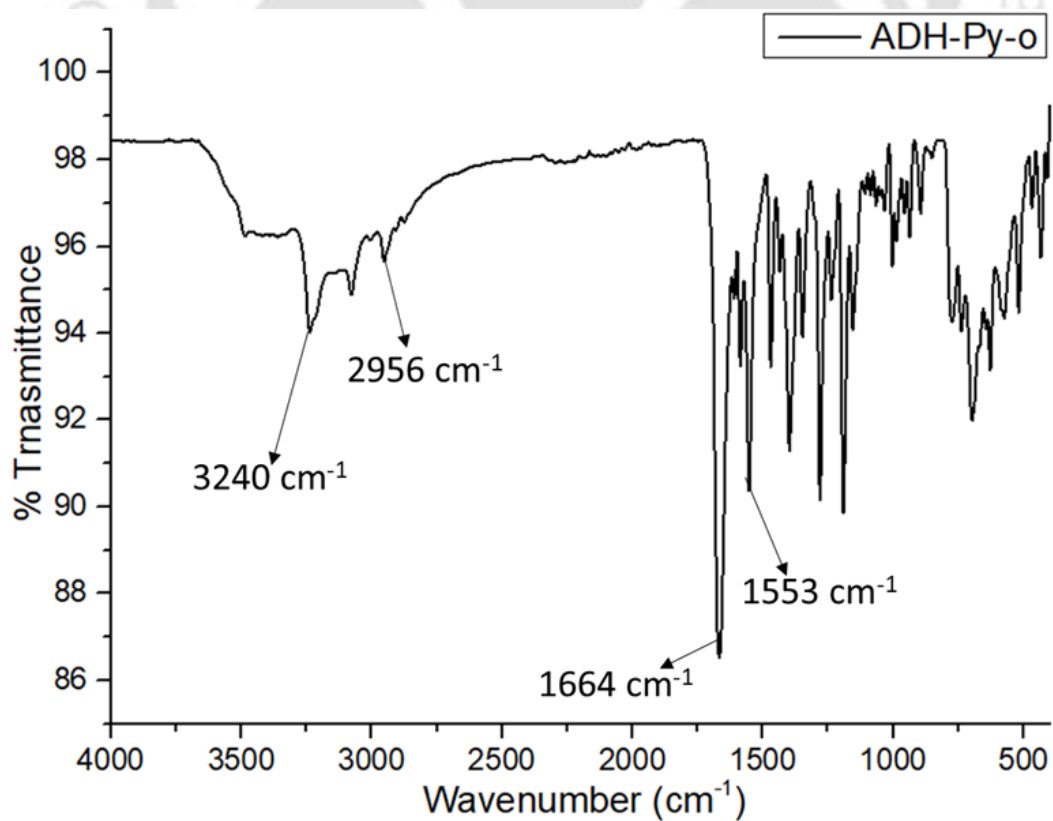
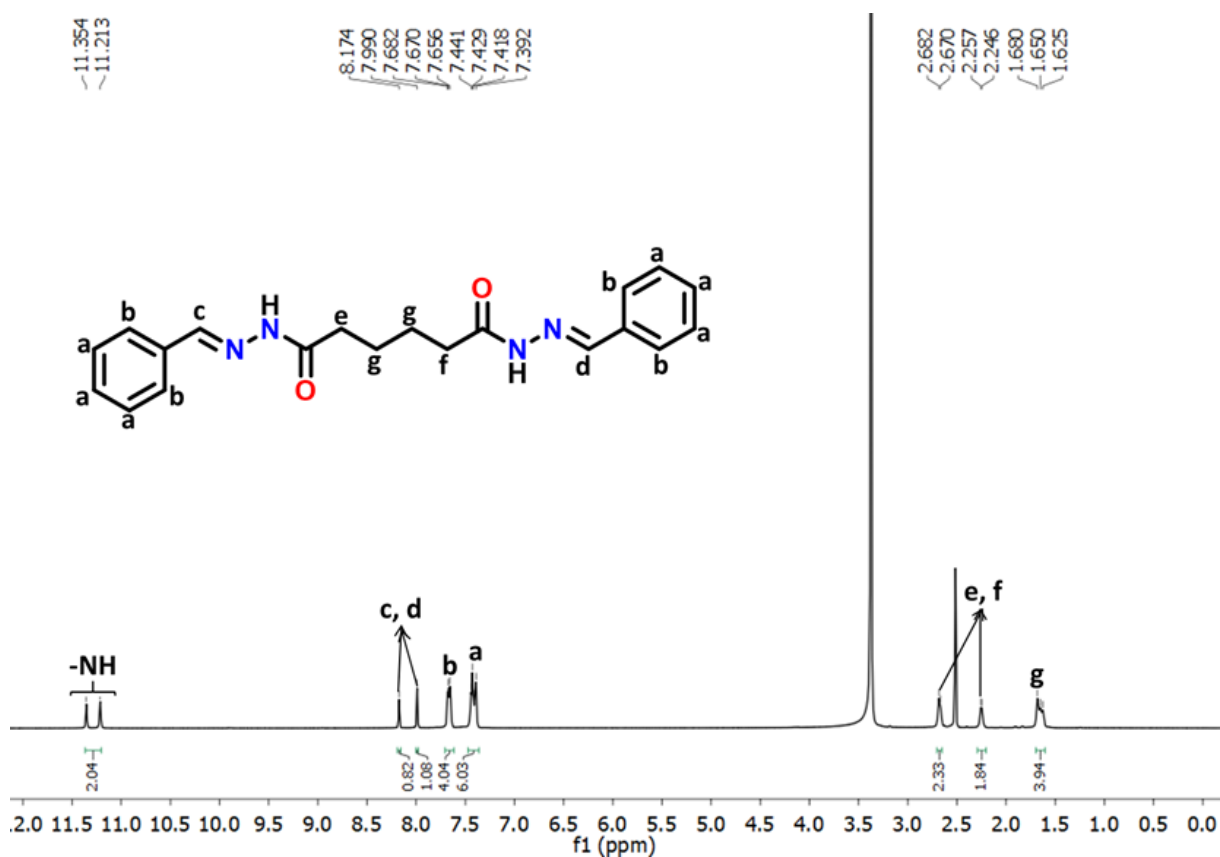
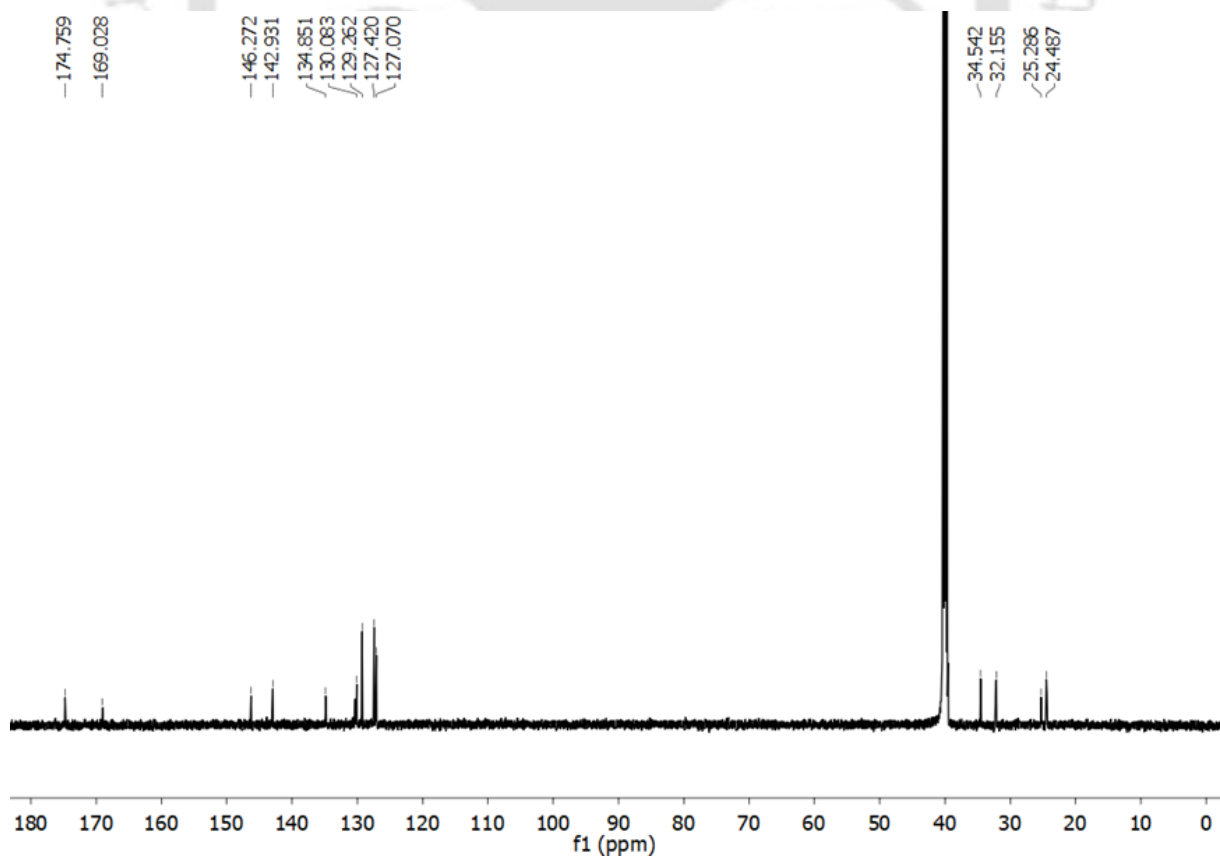


Figure A2.40: IR of ADH-Py-o.

Figure A2.41: ^1H NMR of ADH-Ph $\text{DMSO-}d_6$.Figure A2.42: ^{13}C NMR of ADH-Ph $\text{DMSO-}d_6$.

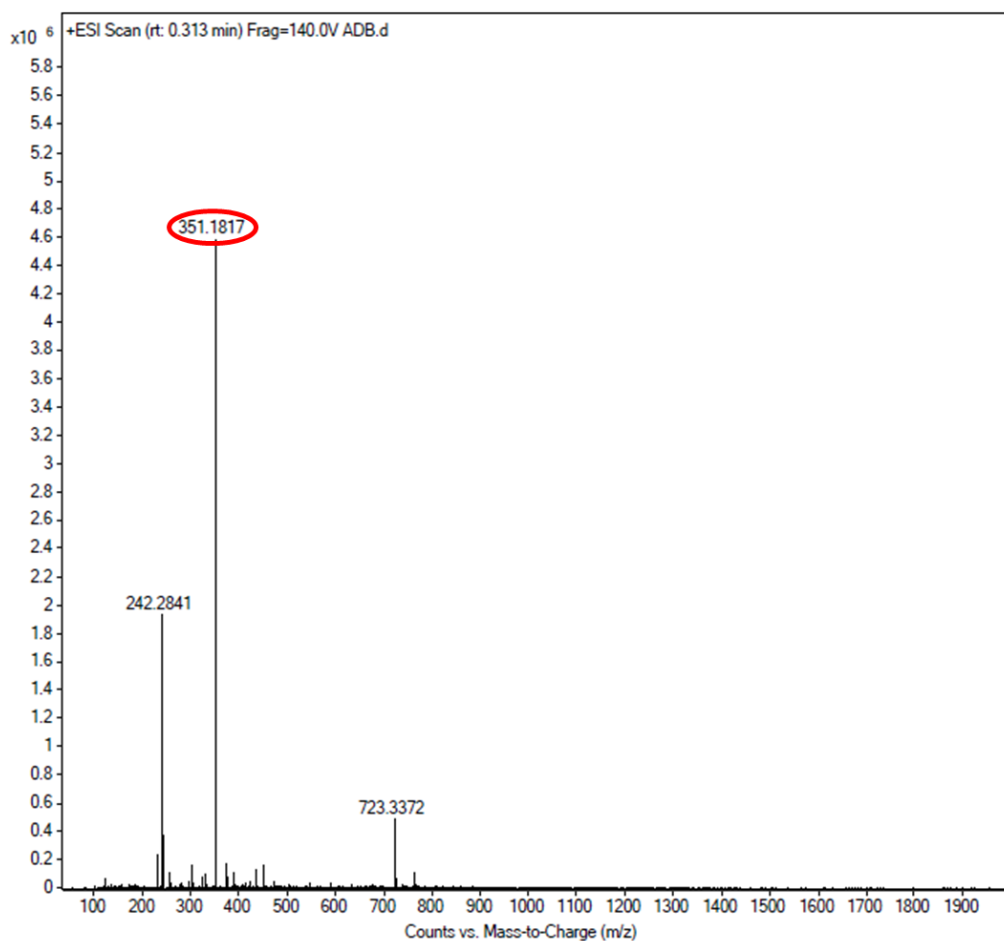


Figure A2.43: HRMS of ADH-Ph.

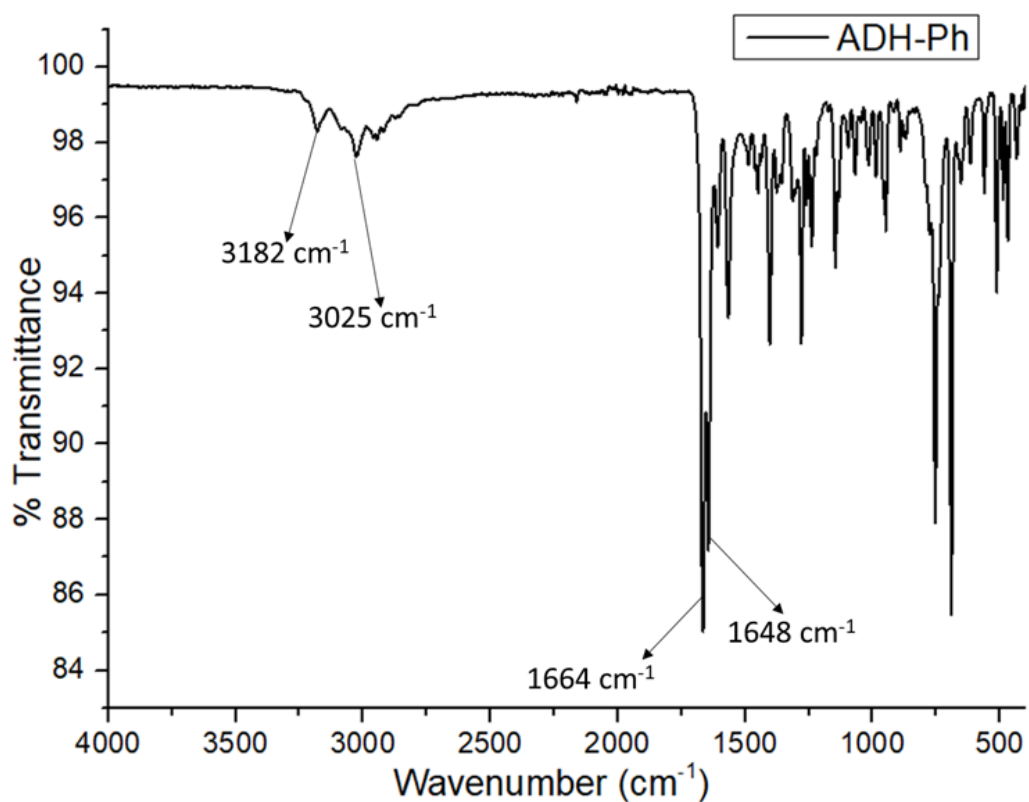


Figure A2.44: IR of ADH-Ph.

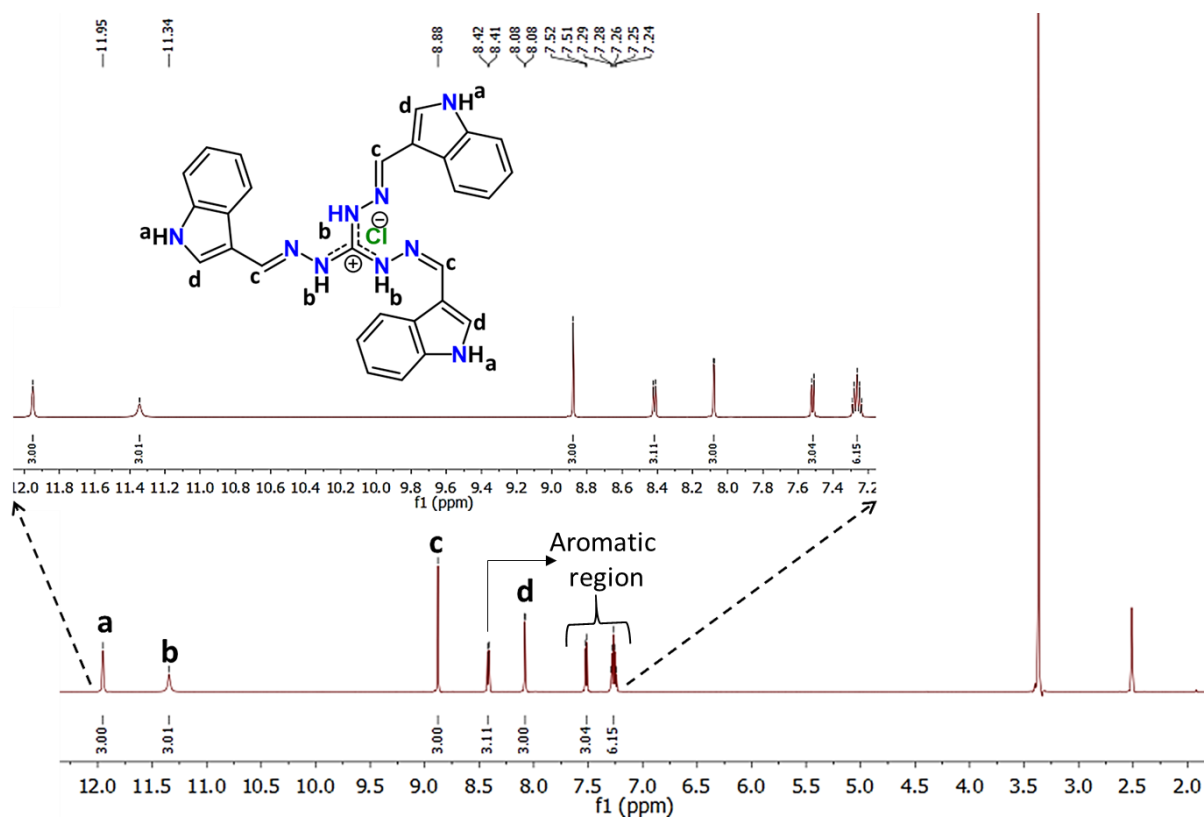


Figure A2.45: ^1H NMR spectrum of GUA-IND in $\text{DMSO-}d_6$.

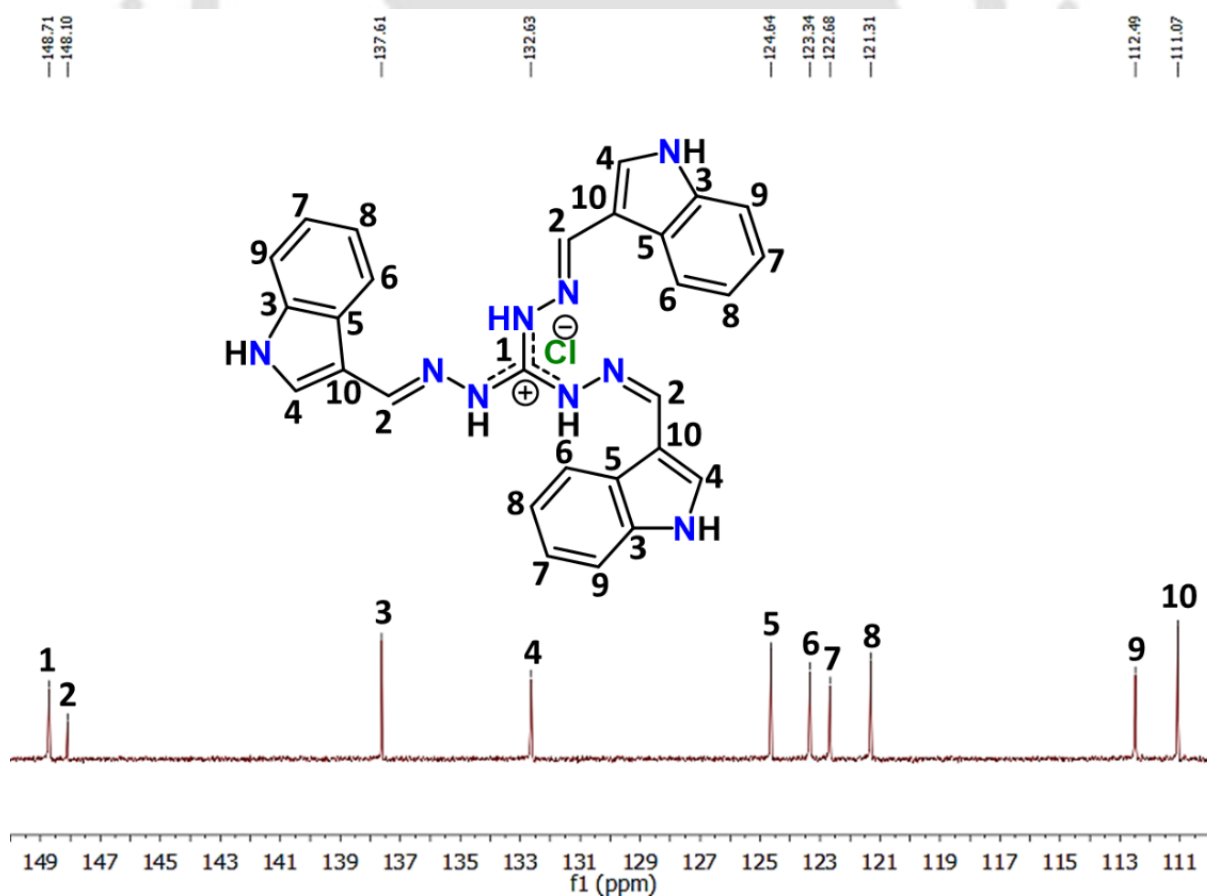


Figure A2.46: ^{13}C NMR spectrum of GUA-IND in $\text{DMSO-}d_6$.

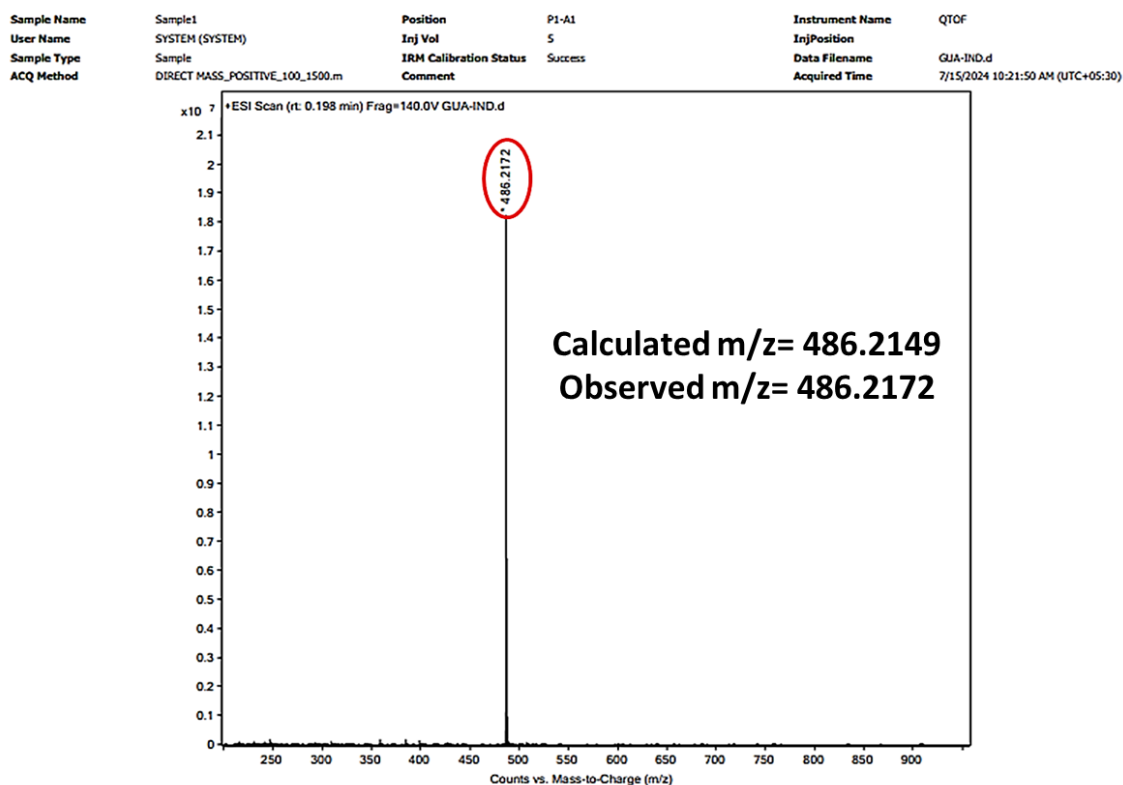


Figure A2.47: HRMS of GUA-IND.

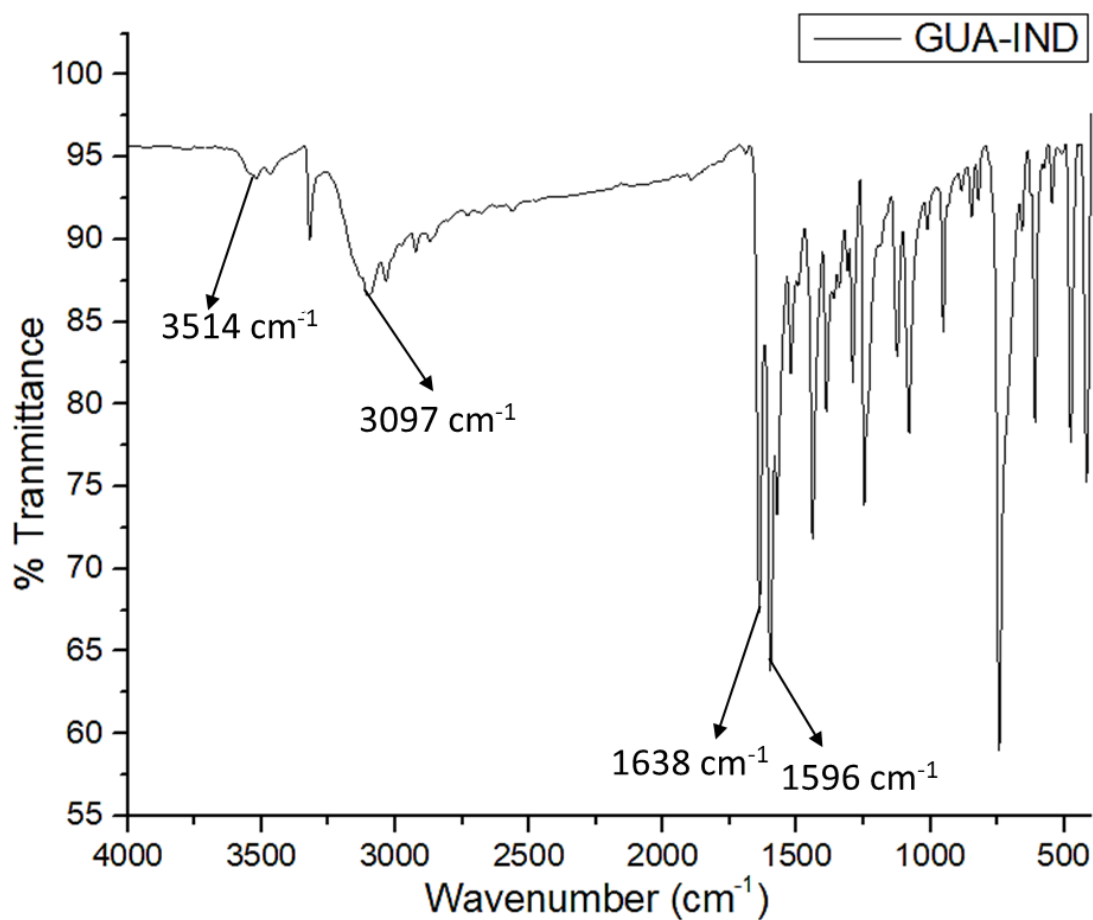


Figure A2.48: FT-IR spectrum of GUA-IND.

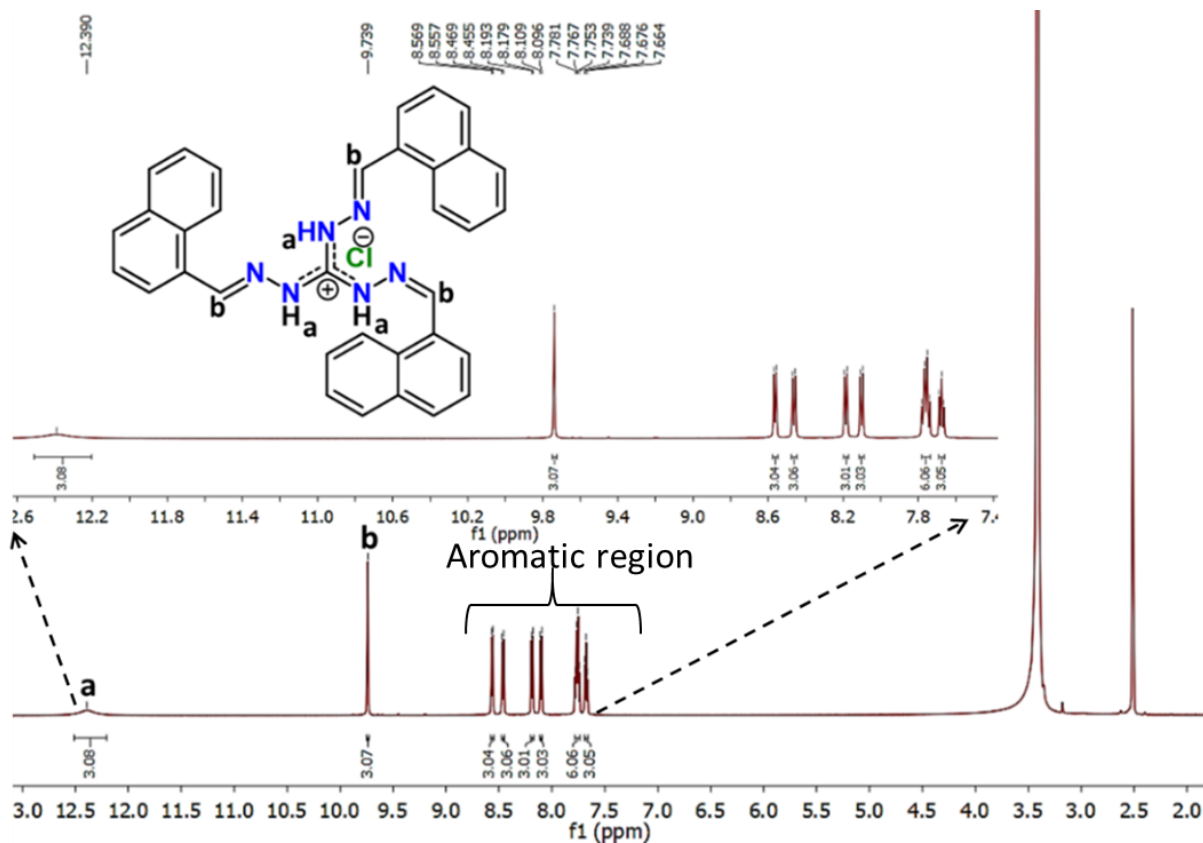


Figure A2.49: ^1H NMR spectrum of GUA-NAP in $\text{DMSO-}d_6$.

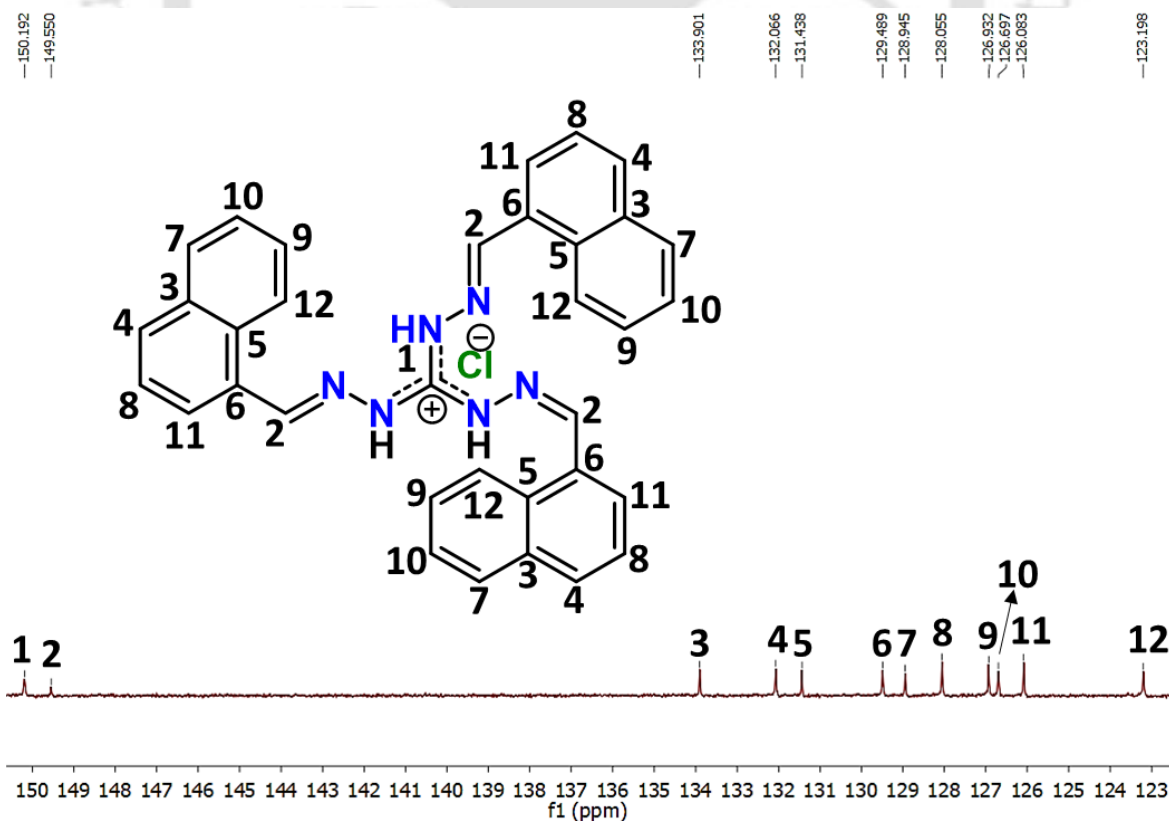


Figure A2.50: ^{13}C NMR spectrum of GUA-NAP in $\text{DMSO-}d_6$.

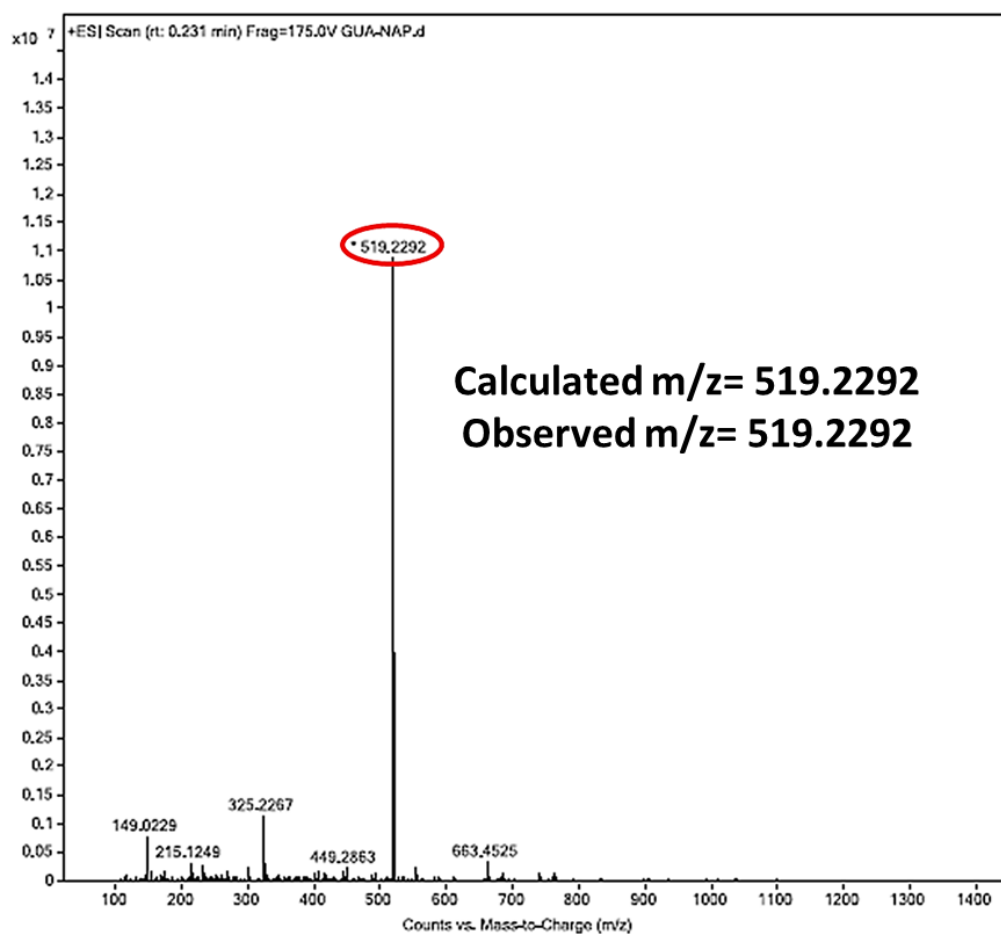


Figure A2.50: HRMS of GUA-NAP.

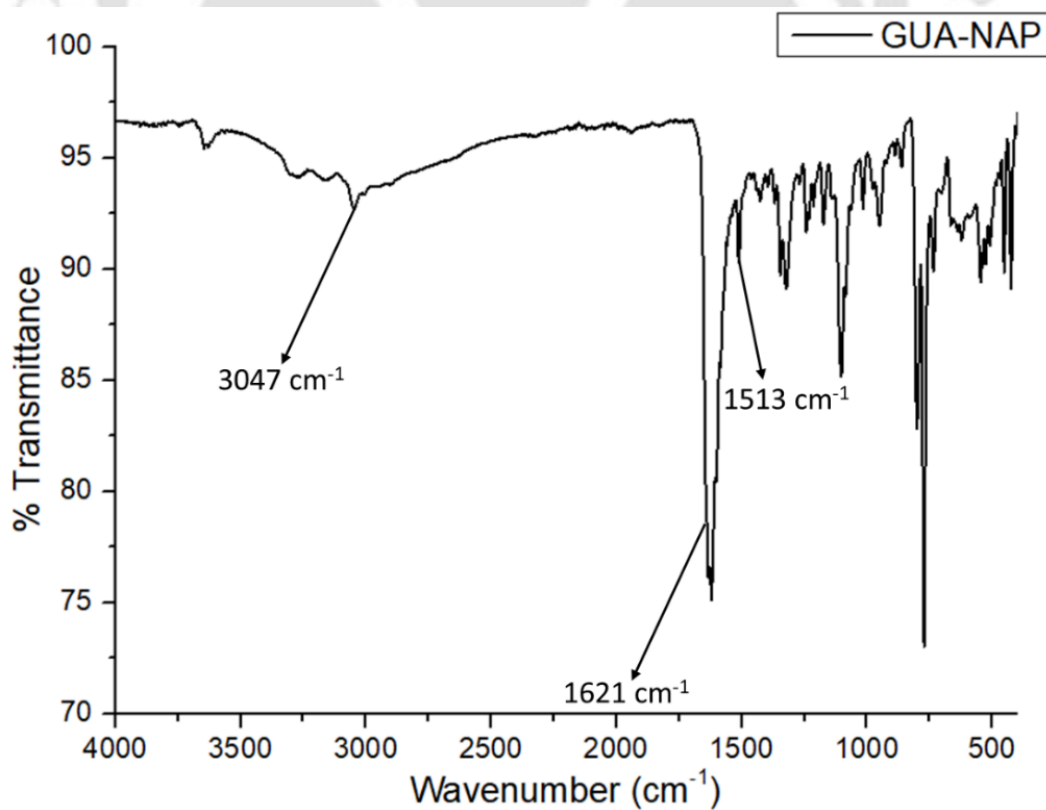


Figure A2.51: FT-IR spectrum of GUA-NAP.

Chapter 3

Probing the effect of different aromatic core substitution in the aggregation potential and picric acid recognition aptitude in a series of cinnamaldehyde-based receptors



3.1. Background and Focus of the Chapter

The term 'molecular self-assembly' portrays the spontaneous association of molecules to generate well-ordered aggregates as a result of various non-covalent interactions [3.1-3.3]. The concept of self-assembly is borrowed from nature, which helps in the execution of complex processes, which are impossible to execute through a monomeric version [3.4]. The controlled self-assembly of molecular receptors comprising a variety of fluorophores leads to the fluorescence signal alteration, between the aggregated state and the probe monomer. Molecules can form larger supramolecular hierarchical architectures which can present diverse morphologies at the micro- or nano-level in countless areas [3.5-3.6]. However, it is challenging to design, and modify the molecular superstructures to attain controlled photoluminescence properties and fascinating morphology in the presence or absence of external stimuli [3.7-3.10]. The combination of controlled self-assembly of small molecules and modern bio-analytical techniques have opened the way for a dynamic and highly growing field for developing fascinating supramolecular architectures [3.11-3.14]. Tailor-made molecular receptors containing several non-covalent interaction sites emerging for neutral molecular recognition receive special attention because of their significance to biological and environmental sciences [3.15].

Detection of trace-explosive chemicals is drawing substantial attention to mitigate counter-terrorism and improve national security [3.16-3.17]. Among various chemical explosives, selective and sensitive detection of nitroaromatic compounds (NACs) has become a major research focus in recent times as they are highly energetic explosives. Picric acid (PA) is one such strong explosive and it was widely used as an explosive until World War I [3.18-3.22]. PA finds extensive applications in batteries, matches, and leather manufacturing units, rocket fuels processing, textile, fireworks, and dye industries as well [3.23-3.26]. Nevertheless, PA holds serious health effects as it is a strong irritant to the skin/eye and may cause damage to the respiratory system. Besides, PA is highly soluble in water, and hence, it may easily contaminate soil and groundwater when exposed [3.27-3.29]. For effective detection of PA, different methodologies such as gas chromatography [3.30], surface Plasmon resonance [3.31], thermal neutron analysis [3.32], SERS [3.33-3.34], and X-ray imaging [3.35], have been reported. However, time-consuming procedures, high costs of sophisticated instruments, and complex operation of precision instruments limit the practical applicability of these techniques [3.36]. In this aspect, self-assembled fluorescent sensors

have advantages over the conventional methods because of their high fluorescence quantum yield, cost efficiency, easy sample preparation, enhanced sensitivity, and quick response [3.37-3.38]. The donor-acceptor interaction between electron-rich fluorescent receptors and electron poor nitro explosives leads to luminescence quenching of the fluorescent probes and hence, provides a sensing platform [3.39-3.40]. Our prime motive is to have a comparative study to investigate the effect of changing fluorophore moiety in a simple Schiff base receptor towards aggregation and recognition potential. Herein, we report the synthesis of three novel 4-(dimethylamino)cinnamaldehyde constituted Schiff base receptors furnished with different fluorophore molecules intending to increase the ring size alongside the π -conjugation of the fluorophores. These fluorophores fabricated with donor-acceptor groups are capable of showing selective recognition of PA in both solid as well as in solution states besides providing fascinating photophysical properties. The result may offer more insight into the functional integration of varying fluorophores/aromatic cores in the aspect of the self-assembly phenomenon.

3.2. Objective of the Chapter

Three receptors (**L**₁₋₃) based on 4-(dimethylamino)cinnamaldehyde-based were prepared to study the effects of aromatic core substitution on the self-assembly behavior. All three receptors demonstrated different types of micro/nano-structure depending on the solvent polarities and their hydrogen-bonding abilities, which can dramatically influence the supramolecular self-assembly process. Selective sensing of picric acid (PA) among various nitroaromatic compounds was achieved by receptors **L**₂ and **L**₃ via quenching of fluorescence and their mechanistic details has been investigated thoroughly. Furthermore, the solid-state recognition of PA among different nitrophenols was also explored via SCXRD study. To evaluate the real-world efficacy of our study, herein we have demonstrated PA detection by the receptors **L**₁₋₃ in real water samples along with very economical yet efficient paper-strip applications.

3.3. Results and Discussion

3.3.1. Design principle of the receptors

Our prime objective behind the synthesis of the three rationally designed Schiff base receptors was to investigate their potential to confer self-aggregation property and simultaneous recognition of small molecules in solid as well as in solution state. To achieve the aforementioned objective, we have synthesized **L**₁, **L**₂, and **L**₃ (Scheme 2.2.1 of Chapter 2), taking into consideration the following vital factors: (i) the use of three different potential fluorophores, naphthalene, anthracene, and pyrene as the aromatic core for a strong fluorescence response (ii) incorporation

of both donor and acceptor sites through Schiff base linkage in a single molecule for crafting the ICT prospect (iii) to have a comparative study on the impact of changing the aromatic core on their self-aggregation as well as small molecule recognition potential in the solid and solution phase. This comparative study was undertaken to distinguish the effect of an aromatic core substitution on their aggregation ability and the aggregated system was further employed as a sensing tool.

3.3.2. Self-assemble potential of the receptors

Structural analysis of the receptors

The crystal structure of **L1** (CCDC no: 2244703) displays the presence of two symmetry-independent molecules in the unit cell. Two molecules orient themselves in different planes. One of them has both intramolecular ($N3 \cdots H28 = 2.483 \text{ \AA}$) as well as intermolecular hydrogen ($N3 \cdots H19 = 2.690 \text{ \AA}$) bonding interactions and the other one involves only intramolecular hydrogen bonding interaction ($N1 \cdots H1 = 2.503 \text{ \AA}$). Additional $C-H \cdots \pi$ ($dC-H \cdots \pi = 2.792-2.897 \text{ \AA}$) interactions were also responsible for the stabilization of the overall self-assembled network formed by **L1** (Figure 3.1 A, D).

On the other hand, **L2** (CCDC no: 2244704) does not exhibit any intermolecular hydrogen bonding interactions in the solid state. However, it exhibits similar intramolecular hydrogen bonding interaction ($N1 \cdots H13 = 2.530 \text{ \AA}$) like **L1**. Additionally, the hydrogen atom ($H25A$) of the methyl group undergoes $CH \cdots \pi$ interaction with its nearby pyrene ring ($dC-H \cdots \pi = 2.880 \text{ \AA}$), thus facilitating a one-dimensional self-assembled network of **L2** (Figure 3.1 B, E).

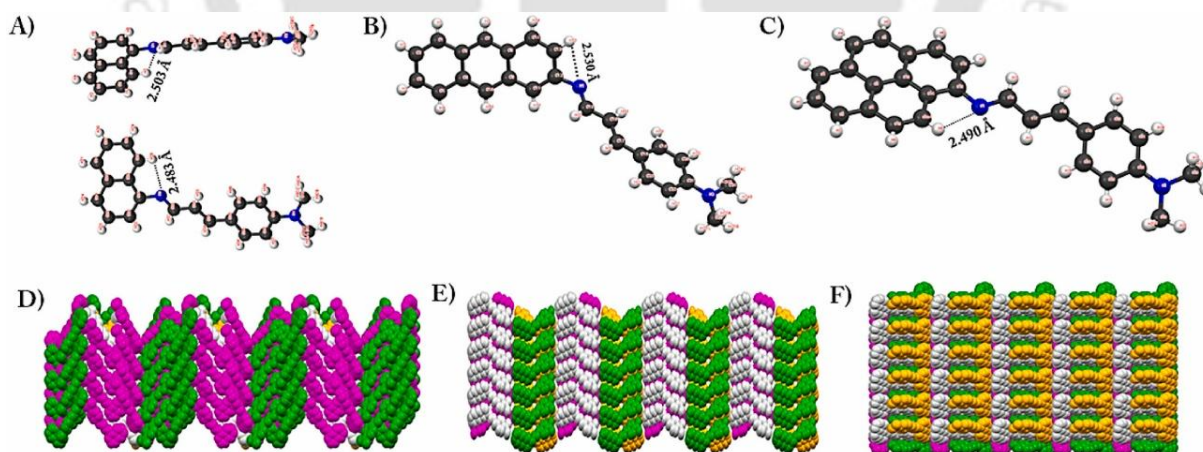


Figure 3.1: (A-C) Crystal structures and (D-F) packing diagram of **L1**, **L2**, and **L3**.

Crystal structure analysis of **L3** (CCDC no: 2244705) reveals that the imine nitrogen atom ($N1$) forms intramolecular as well as intermolecular hydrogen bonding interactions with the aromatic hydrogen atoms $H8$ ($N1 \cdots H8 = 2.490 \text{ \AA}$) and $H13$ ($N1 \cdots H13 = 2.478 \text{ \AA}$) respectively. The

intermolecular hydrogen bonding assisted by CH- π interactions ($\text{Ar-H7}\cdots\pi = 3.361 \text{ \AA}$; $\text{Ar-H10}\cdots\pi = 3.147 \text{ \AA}$ and $\text{Ar-H12}\cdots\pi = 3.034 \text{ \AA}$, 3.346 \AA) helps in forming 1D self-assembled polymeric architecture of **L**₃ (Figure 3.1 C, F).

Photophysical investigation

The photophysical properties of **L**₁, **L**₂, and **L**₃ were explored in various solvents at room temperature. A 5.0 mM stock solution of all three compounds was prepared in dimethyl sulfoxide (DMSO) and diluted consequently with the experimental solutions. The presence of both donor and acceptor units in the receptors suggested the possibility of a typical solvatochromism [3.41-3.42] (Figure 3.2). In hexane **L**₁, **L**₂, and **L**₃ (10 μM) show absorption bands around 376 nm, 370/406 nm, and 400 nm, respectively. However, in a highly polar solvent (DMSO) these bands gradually shifted to longer wavelength regions. This polarity-dependent redshift of the spectral peak position was also observed in the fluorescence, the excitation wavelength being 320 nm, 420 nm, and 380 nm, respectively. These results certainly confirmed the ICT along the D- π -A track for all three compounds.

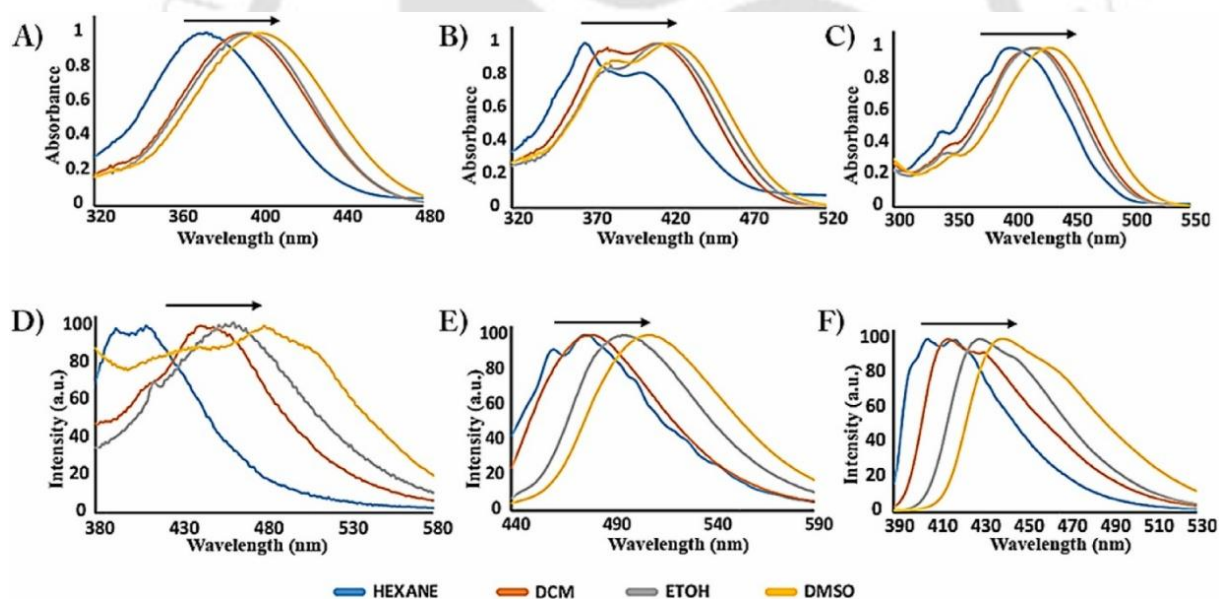


Figure 3.2: (A-C) Normalized UV-Vis spectra and (D-F) normalized fluorescence spectra of **L**₁, **L**₂, and **L**₃ in solvents with different polarities.

To have an insight into the aggregation features in the aqueous medium, UV-Vis spectra of the receptors (10 μM) in pure acetonitrile (ACN) with the incremental addition of water (H_2O) were recorded. A regular fall of the sharp absorbance maximum around 392 nm, 378/412 nm, and 422 nm (Figure 3.3 A) accompanied by a visible upliftment of the baseline was observed. There is also a generation of a broad band in the longer wavelength region around 515 nm, 555 nm, and 530 nm

with an increase in water percentages, maximum absorption being at water fraction (f_w) = 80%, 50%, and 70% for **L**₁, **L**₂, and **L**₃ respectively, probably due to Mie scattering [3.43]. The effect is very pronounced in the case of **L**₃, suggesting prominent aggregation with the increase in aromatic ring size. This observation supports the existence of molecular aggregates in the mixed solvent system. Further analysis regarding aggregation was carried out by recording the absorbance spectra with the incremental addition of the respective compound separately in water. The proper systematic growth in the absorbance value along with the elevated baseline in the tail region of UV-Vis spectra for all three compounds was observed as the concentration increased from 5 μ M to 35 μ M (Figure 3.3 B) which corroborated the formation of aggregated species in the aqueous medium. It was observed that spectral response increases from **L**₁ to **L**₃, supporting more aggregation potential in the case of **L**₃. Furthermore, to validate the formation of aggregates, DLS and FESEM studies were also pursued in acetonitrile and aqueous medium.

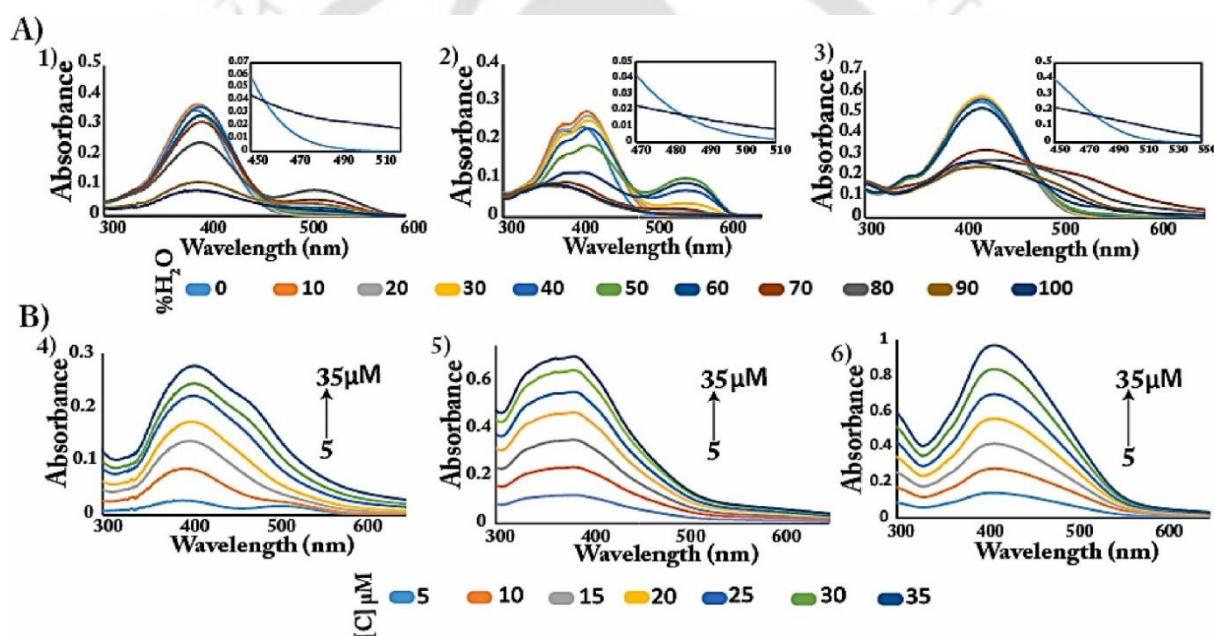


Figure 3.3: A) UV-Vis spectra of **L**₁, **L**₂, and **L**₃ in the mixed solvent system by varying solvent fraction and B) UV-Vis spectra of **L**₁, **L**₂, **L**₃ in aqueous medium of varying concentration.

Microscopic imaging studies of the receptors

The evidence for changes in morphology with changes in solvent fraction has been acquired from FESEM imaging studies (Figure 3.4). All receptors showed apparent sensitivity toward changes in the respective solvent fractions. The block-shaped morphology of **L**₁ in 100% ACN got changed to a coral shape in 100% H₂O. **L**₂ showed flake-shaped morphology in 100% ACN while flower-like morphology in 100% H₂O. **L**₃, however, showed flower-like and leaf-like morphology in 100% ACN and 100% H₂O respectively. It may be mentioned here that owing to the inherent

difference in the aromatic core, molecular aggregation is induced in the presence of the different solvent fractions in diverse ways giving rise to contrasting molecular superstructures. Dynamic light scattering experiments were performed to determine the hydrodynamic size of L_1 , L_2 , and L_3 (Figure A3.2).

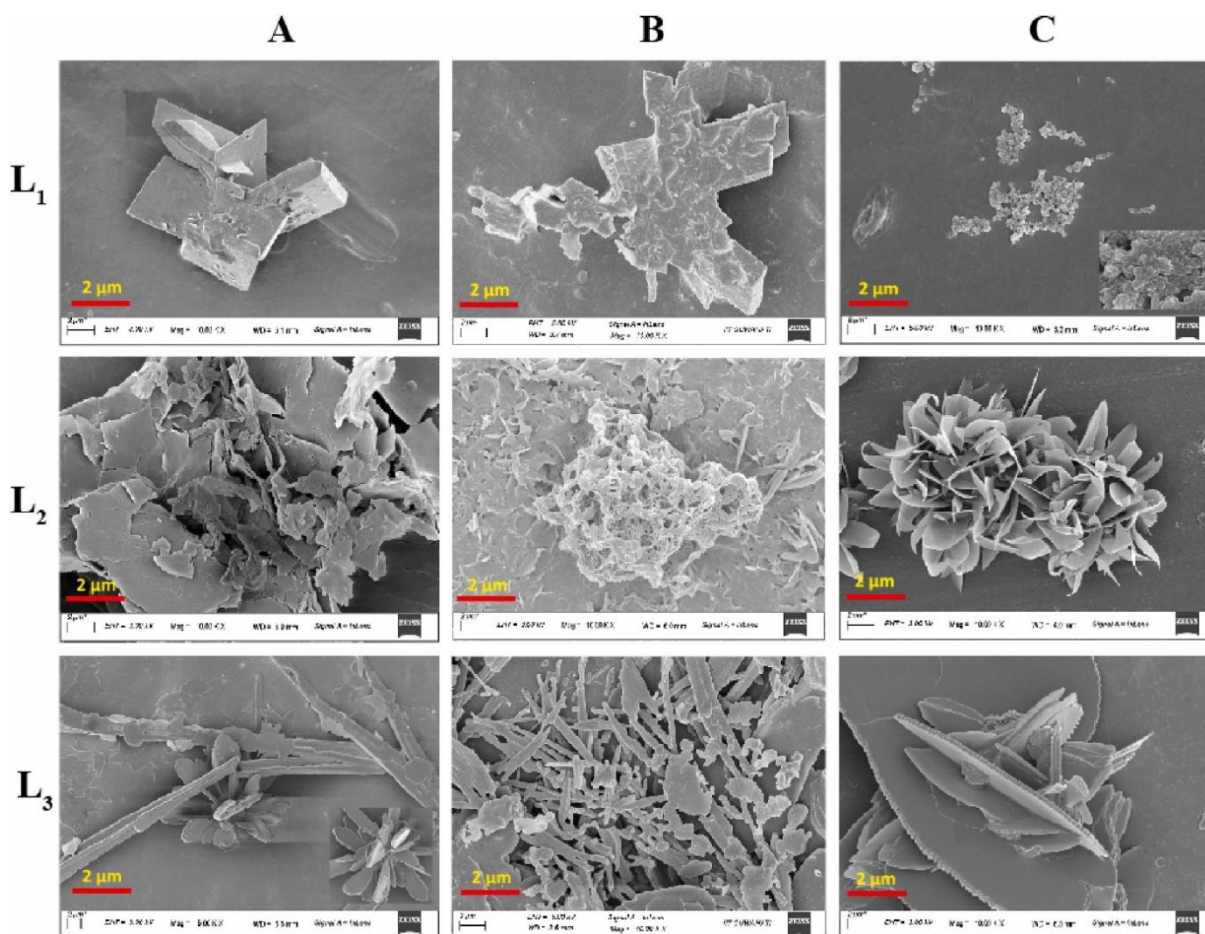


Figure 3.4: (A-C) FESEM images of L_1 , L_2 , and L_3 by varying the solvent fractions.

3.3.3. Interaction of the receptors with picric acid

Structural analysis of the picric acid complex

A block-shaped tiny single crystal was isolated for the L_1 .PA (CCDC no: 2244706) complex. SCXRD analysis reveals the efficient entrapment of PA through various non-covalent interactions majorly, hydrogen bonding interaction. The oxygen atom, O6 of the PA undergoes rare trifurcated hydrogen bonding interaction with H5, H9 and H21 ($O6 \cdots H5 = 2.679 \text{ \AA}$, $O6 \cdots H9 = 2.648 \text{ \AA}$ and $O6 \cdots H21 = 2.673 \text{ \AA}$). Bifurcated hydrogen bonding interaction is also prevalent in the self-assembled system, where the oxygen atom, O7 exhibits hydrogen bonding interactions with H1 and H10 with a hydrogen bonding distance of 1.783 \AA and 2.578 \AA respectively. The oxygen atoms viz. O1, O3, and O4 undergo intermolecular hydrogen bonding interactions with the nearby hydrogen bond donor sites ($O1 \cdots H2B = 2.670 \text{ \AA}$, $O3 \cdots H1 = 2.512 \text{ \AA}$ and $O4 \cdots H15 = 2.462 \text{ \AA}$).

O2 of PA is involved in intramolecular hydrogen bonding interactions with one of its neighboring hydrogen atoms labeled as H25 ($O2 \cdots H25 = 2.322 \text{ \AA}$) (Figure 3.5 A, D).

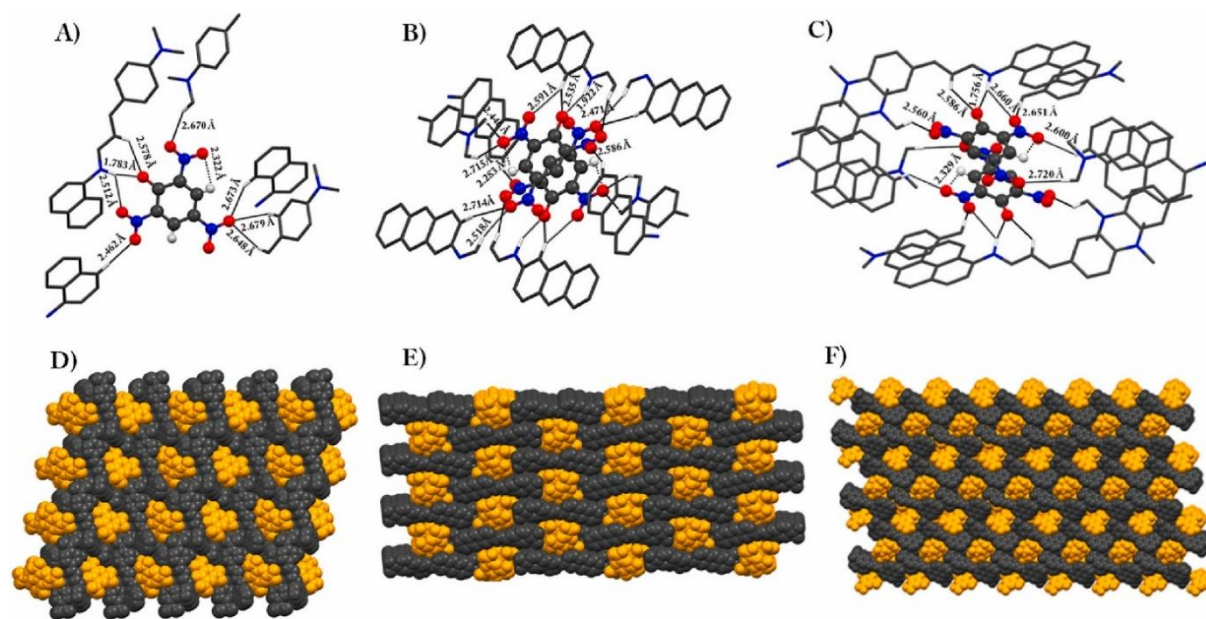


Figure 3.5: (A-C) Crystal structures and (D-F) space-filled model of L1, L2, and L3 with picric acid depicting various interactions.

Crystal structure analysis of L2.PA (CCDC no: 2244707) reveals the encapsulation of PA within the self-assembled network of L2, as supported by hydrogen bonding as well as $\pi \cdots \pi$ interactions. The deprotonated phenyl oxygen atom (O1) and all the NO₂-oxygen atoms of PA except O5 undergo intermolecular hydrogen bonding interactions with the neighboring hydrogen bond donor sites, where, two oxygen atoms of PA (O1 and O4) exhibit bifurcated hydrogen bonding interactions ($O1 \cdots H2N = 1.992 \text{ \AA}$, $O1 \cdots H1 = 2.535 \text{ \AA}$ and $O4 \cdots H3A = 2.714 \text{ \AA}$, $O4 \cdots H15 = 2.518 \text{ \AA}$) and one oxygen atom O3 exhibits trifurcated hydrogen bonding interaction which includes one intramolecular hydrogen bonding interaction ($O3 \cdots H24B = 2.715 \text{ \AA}$, $O3 \cdots H25B = 2.446 \text{ \AA}$, $O3 \cdots H29 = 2.283 \text{ \AA}$). Remaining all the other oxygen atoms act as a single hydrogen bond acceptor site ($O2 \cdots H1 = 2.591 \text{ \AA}$, $O6 \cdots H13 = 2.586 \text{ \AA}$ and $O7 \cdots H16 = 2.471 \text{ \AA}$). In addition to the hydrogen bonding interactions, PA undergoes $\pi \cdots \pi$ interactions ($d\pi \cdots \pi = 3.575 \text{ \AA}$) with another nearby PA unit, thus facilitating the self-assembly of the overall complex system (Figure 3.5 B, E).

SCXRD analysis of the L3.PA (CCDC no: 2244708) complex unveils the involvement of various weak non-covalent interactions such as hydrogen bonding (H-bonding) and $\pi \cdots \pi$ interactions in the encapsulation process of PA within the self-assembled polymeric architecture of L3. All the oxygen atoms of picric acid (O2, O3, O4, O5, and O7) except O1 and O6 are involved in hydrogen bonding interactions with the neighboring hydrogen bond donor sites. The oxygen atoms O4 and

the deprotonated phenolic oxygen O5 of PA undergoes bifurcated hydrogen bonding interaction ($O4\cdots H9 = 2.651 \text{ \AA}$, $O4\cdots H2N$ (protonated imine) = 2.660 \AA and $O5\cdots H2N$ (protonated imine) = 1.756 \AA , $O5\cdots H10 = 2.586 \text{ \AA}$). O3 also undergoes bifurcated hydrogen bonding interaction, where both intermolecular as well as intramolecular hydrogen bonding interactions are present involving, H27 and H29 respectively ($O3\cdots H27 = 2.600 \text{ \AA}$ and $O3\cdots H29 = 2.329 \text{ \AA}$). In addition to these, two neighboring picric acids are interconnected by hydrogen bonding ($O2\cdots H1B = 2.720 \text{ \AA}$) as well as $\pi\cdots\pi$ (4.615 \AA) interactions providing stability to the self-assembled architecture (Figure 3.5 C, F).

Structural analysis of the picric acid complex

The π electron-rich and strongly emissive nature of self-assembled receptors were then applied for studying the interaction with different nitro phenols such as 2-nitrophenol (2-NP), 3-nitrophenol (3-NP), 4-nitrophenol (4-NP), 2,4-dinitrophenol (2,4-DNP), and PA in the aqueous medium. The electron transfer from fluorescent receptors to electron-poor NACs should result in the receptor's rapid fluorescence quenching. The solution state recognition potential of the receptors was studied with a $10 \text{ }\mu\text{M}$ solution of the receptors in a 100% aqueous medium. PA being the most electron-deficient among different nitro phenols results in the highest quenching in the fluorescence intensity upon interaction with the electron-rich **L1**, **L2**, and **L3**, (quantum yield of **L1**, **L2**, **L3** = 0.056, 0.062, 0.069 respectively) however, other nitrophenols lead to minimal changes in the emission intensity of the receptors, thus giving selective sensing of PA (Figure 3.6 A, D). Also, the highest selectivity is observed with **L3**, as it is the most electron-rich among the three, while **L1** displays almost no selectivity (Figure A3.3). Since PA displayed substantial quenching among all other nitrophenols, the quantitative behavior of the compounds **L2** and **L3** was also evaluated by adding different concentrations of the PA in the aqueous solution of the receptors ($10 \text{ }\mu\text{M}$) under the optimized conditions. The quenching efficiency was found to be $\sim 71\%$ and $\sim 92\%$ for **L2** and **L3** (Figure 3.6 B, E) respectively. The fluorescence quenching of both compounds depended on the concentrations of PA. Upon successive incremental addition of PA, the fluorescence spectrum of the two compounds showed a gradual decrease in emission intensity at 510 nm and 440 nm when excited at 420 nm and 380 nm respectively (Figure 3.6 C, F). The limit of detection (LOD) for PA was calculated to be $4.32 \text{ }\mu\text{M}$ and $4.15 \text{ }\mu\text{M}$ respectively (Figure A3.4). The binding constants were calculated to be $4.64 \times 10^8 \text{ M}^{-1}$ and $5.17 \times 10^8 \text{ M}^{-1}$ (Figure A3.5) respectively. The quenching mechanism was also evaluated by Stern-Volmer (SV) equation. The Stern-Volmer constant K_{sv} and LOD obtained for the receptors for PA detection in the current

study compares well with previous reports (Table A3.5). The SV plot was found to be linear with Stern-Volmer constants (K_{sv}) of $10.5 \times 10^3 \text{ M}^{-1}$ and $29.4 \times 10^3 \text{ M}^{-1}$ (Figure A3.6) respectively. The linear response may be ascribed to static quenching. To investigate the reason behind the highly selective fluorescence emission quenching of **L2** and **L3** by PA, the change in the absorbance and emission profile was studied carefully. Spectral overlap between the absorption spectrum of PA with the emission band of **L2** and **L3** (Figure A3.7 A and B) was observed although **L3** shows prominent overlap compared to **L2**, suggesting that the quenching of **L2** and **L3** fluorescence can take place via the fluorescence resonance energy transfer (FRET), Inner filter effect (IFE) and photoinduced electron transfer (PET) process. To illustrate the mechanistic aspect of fluorescence quenching, time-resolved fluorescence spectra of **L2** and **L3** (10 μM) in an aqueous medium were recorded before and after the addition of PA. The fluorescence lifetime of **L2** and **L3** showed negligible change (Figure A3.19 C and D) in both the presence (23.065 ns, 5.396 ns) and absence (21.058 ns, 5.293 ns) of PA (Table A3.3) under a pulsed excitation of 405 nm, 375 nm respectively (λ_{em} 510 nm and 440 nm respectively), the decay curves were fitted biexponentially as shown. The above result discards the involvement of FRET in the process of quenching. Thus, IFE and PET can be the probable mechanism for fluorescence quenching.

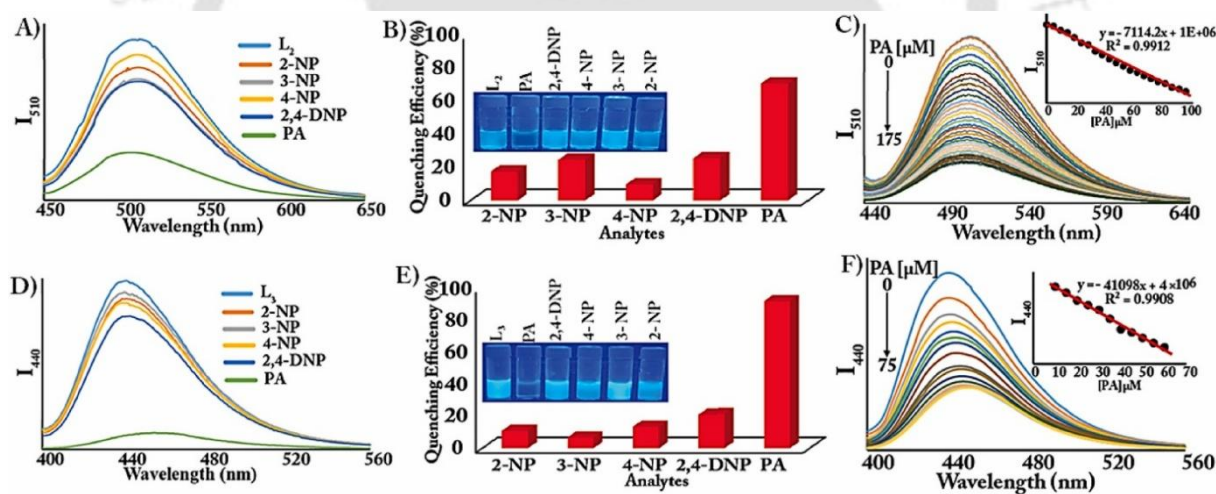


Figure 3.6: (A, D) Interaction of **L2** (10.0 μM , λ_{ex} = 420 nm) and **L3** (10.0 μM , λ_{ex} = 380 nm) with different nitrophenols. (B, E) Fluorescence quenching efficiency of **L2** and **L3** in the presence of various analytes (50 Equiv.) in water. Inset: Visual change of **L2** and **L3** observed under UV light upon the addition of different analytes. (C, F) Change in fluorescence intensity of **L2** and **L3** upon incremental addition of PA.

FESEM analysis studies were conducted to conceive the variation in surface morphology of self-assembled receptors in the absence and presence of PA. Self-assembled receptors **L1**, **L2**, and **L3** which exhibited coral, flower, and leaf-like morphology in 100% water, became disaggregate upon interaction with PA, giving an insight into the assembly/disassembly process.

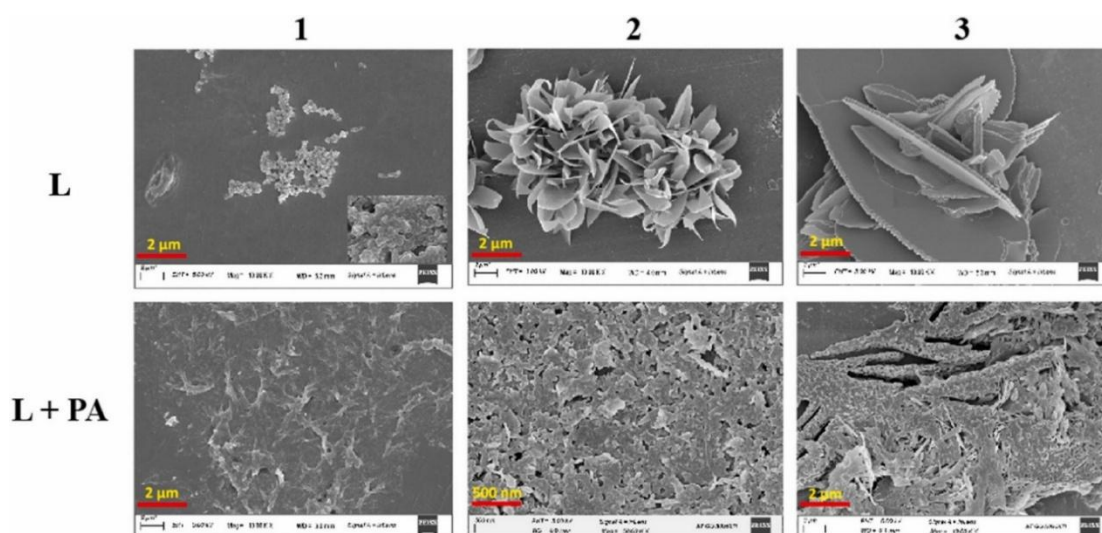


Figure 3.7: FESEM images of L_1 , L_2 , and L_3 before and after the addition of PA in the aqueous medium.

Plausible mechanism of PA recognition

To investigate the fluorescence “turn-off” mechanism of L_1 , L_2 , and L_3 with PA, density functional theory (DFT) calculations were accomplished with the B3LYP/6–31 G (d, p) method basis set using the Gaussian 09 program while using water as a solvent through CPCM solvent model. In general, the interaction of an electron-rich fluorophore with an electron-deficient species leads to facile photoinduced electron transfer (PET) from the lowest unoccupied molecular orbital (LUMO) of the excited fluorophore to the LUMO of the NACs followed by reverse electron transfer to the HOMO of the receptors in a non-radiative process leading to the extinction of the emission intensity of the fluorophore. Hence the DFT results confirmed that there is a probability of PET from LUMO (-0.07593 eV and -0.07931 eV) of L_2 and L_3 respectively to the LUMO (-0.14806 eV) of PA (Figure 3.8).

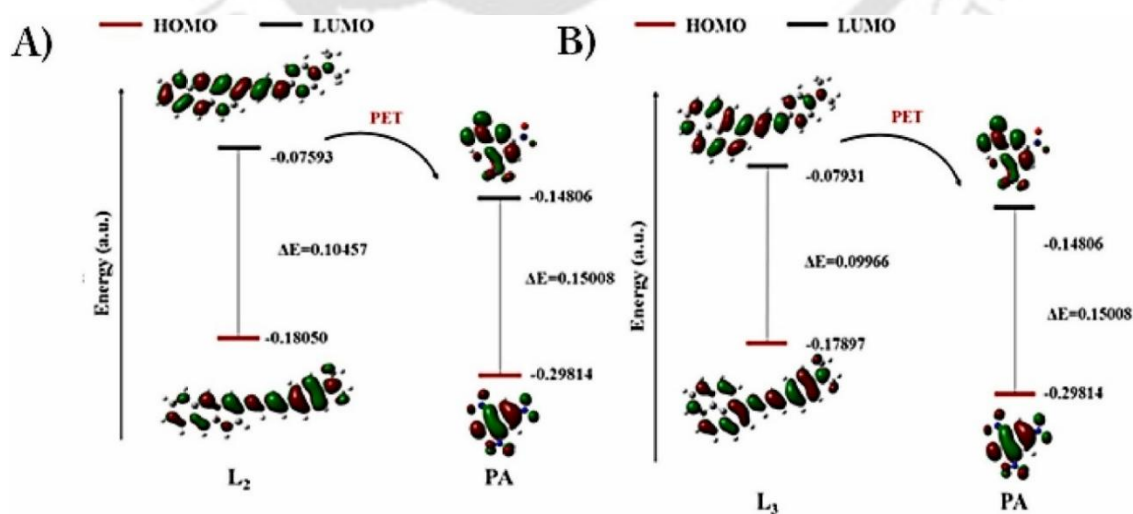


Figure 3.8: Graphical representation of the suggested photoinduced electron transfer (PET) from LUMO of receptors (A) L_2 (A) and (B) L_3 to LUMO of PA.

Detection of PA in natural water samples

To realize the ability of **L₂** and **L₃** in the real spectrum, the detection of PA in different water sources was carried out. Lake water and river water specimens were brought from the Serpentine lake (IIT Guwahati Campus) and Brahmaputra River (near IIT Guwahati Campus, Assam, India). Distilled and tap water was available in the laboratory. A known concentration of PA (100 μM) was added into the experimental medium (i.e., collected water sample), and **L₂** and **L₃** (10 μM) were added. The fluorescence spectra of **L₂** and **L₃** (10.0 μM) displayed emission maxima at 510 nm and 440 nm respectively in real water samples. The quenching efficiency in the case of **L₂** (Figure 3.9 A) is significant in distilled water compared to other water samples taken, however, in the case of **L₃** (Figure 3.9 B) quenching efficiency is approximately similar in all the water samples taken. The results of the quantitative recovery of spiked specimens of analyte are shown in Table A3.2.

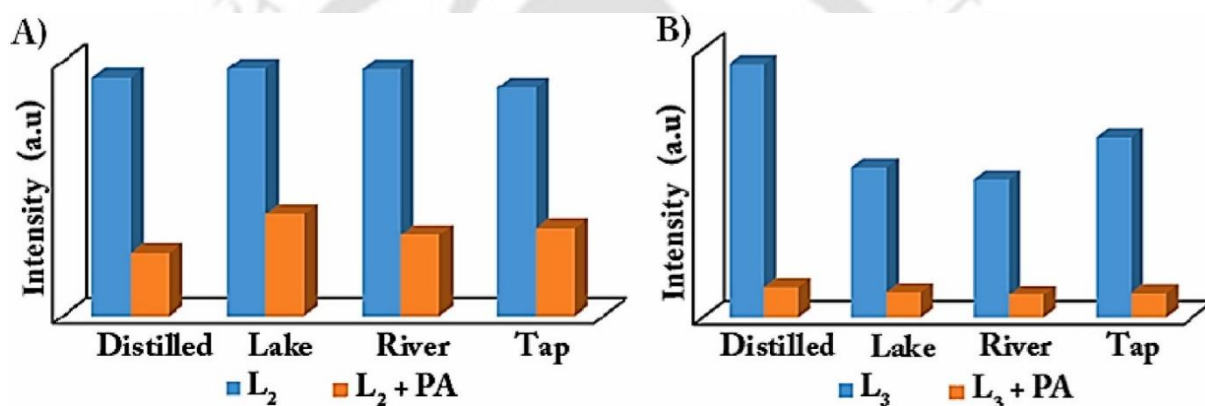


Figure 3.9: Changes in emission intensity of A) **L₂** (10.0 μM) in the presence of PA (100 μM) at 510 nm and B) **L₃** (10.0 μM) at 440 nm in the presence of PA (100 μM) in natural sources of water.

Paper-based detection of PA

Following the solution-phase detection of PA successfully, PA sensing by simple methods in its contact mode through solid support has also been investigated. Whatman paper being economically cheap, simple, easy handling solid based material, has been chosen for this purpose. Whatman filter paper has been dip-coated in 1×10^{-4} M aqueous solutions of **L₂** & **L₃** and dried. A small amount of freshly prepared aqueous PA solution (10^{-3} M) was applied to the test strips and visualized under a hand-held 365 nm UV light ($\lambda_{\text{ex}} = 365$ nm). The unaided eye visualization reveals that the luminescent strip becomes non-luminescent in the presence of PA. The entire detection system was made with water, making it more environmental-friendly (see Figure 3.10).

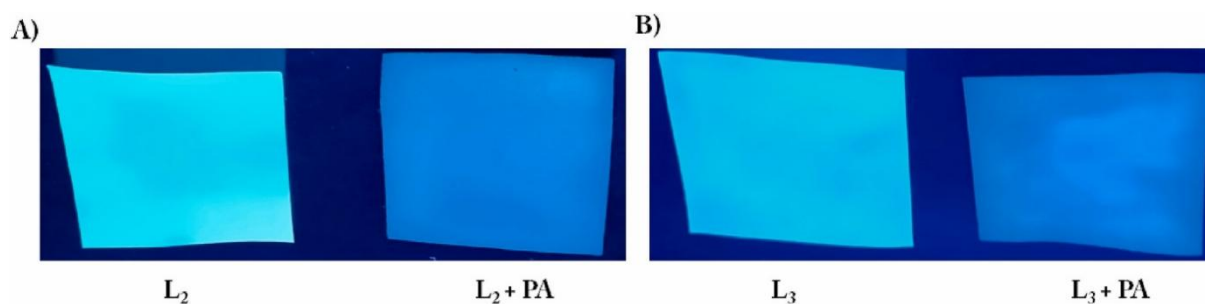


Figure 3.10: Photographs of the test strips under a UV lamp (irradiation of 365 nm) for visual detection of both A) L_2 and B) L_3 in the presence and absence of PA.

3.4. Conclusions

In summary, we report the synthesis of three 4-(dimethylamino)cinnamaldehyde constituted Schiff base receptors with different aromatic cores to have a comparative analysis of their aggregation potential with the help of spectral studies along with microscope imaging. Based on the outcomes of the analysis, it can be concluded that with an increase in water percentages all three compounds form aggregates, however, the effect is more prominent in L_3 . Furthermore, all three receptors L_1 , L_2 , and L_3 could recognize picric acid in the solid state. Also, in the solution phase, L_2 and L_3 containing more electron-rich fluorophores could give selective sensing of picric acid among different nitrophenols. The quenching efficiency was $\sim 71\%$ and $\sim 92\%$ for L_2 and L_3 respectively in water. Disaggregation of the self-assembled sensor as evidenced by FESEM imaging, as well as IFE and PET are concomitantly responsible for the discriminative detection of PA in water with high selectivity and sensitivity. The analytical utility of the receptors has also been demonstrated via the detection of PA in various real water samples as well as through paper strips.

References

- [3.1] S. Halder, U. Manna and G. Das, *New J. Chem.*, 2019, **43**, 14112.
- [3.2] X. Yan, P. Zhu and J. Li, *Chem. Soc. Rev.*, 2010, **39**, 1877-1890.
- [3.3] X. Zhao, F. Pan, H. Xu, M. Yaseen, H. Shan, C.A.E. Hauser, S. Zhang and J.R. Lu, *Chem. Soc. Rev.*, 2010, **39**, 3480-3498.
- [3.4] S. De and G. Das, *Dyes Pigm.*, 2021, **195**, 109659.
- [3.5] K. Chen, T. Jiao, J. Li, D. Han, R. Wang, G. Tian and Q. Peng, *Langmuir*, 2019, **35**(9), 33370-3345.
- [3.6] H. Ma and M. Cao, *Langmuir*, 2022, **38**, 13627-13634.
- [3.7] S. Halder, B. Nayak, B. Bhattacharjee, A. Ramesh and G. Das, *J. Mater. Chem. C*, 2021, **9**, 8596.
- [3.8] Z. Zeng, J. Wu, Q. Chen, Y. Shi, J. Zheng and C. Xu, *Dyes Pigm.*, 2019, **170**, 107649.
- [3.9] Y. Kimura and T. Terashima, *Eur. Polym. J.*, 2020, **139**, 110001.
- [3.10] H. Zhang, X. Fan, R. Suo, H. Li, Z. Yang, W. Zhang, Y. Bai, H. Yao and T. Wei, *Chem. Commun.*, 2015, **51**, 15366-15369.

- [3.11] L. Peng, Y.N. Chen, Y.Q. Dong, C. He and H. Wang, *J. Mater. Chem. C.*, 2017, **5**, 557-565.
- [3.12] H. Huang, D. Xu, M. Liu, R. Jiang, L. Mao, Q. Huang, Q. Wan, Y. Wen, X. Zhang and Y. Wei, *Mater. Sci. Eng. C*, 2017, **78**, 862-867.
- [3.13] L. Zhang, K. Liang, Yang P. Dong, Y. Li, X. Feng, J. Zhi, J. Shi, B. Tong and Y. Dong, *New J. Chem.*, 2017, **41**, 8877-8884.
- [3.14] J. Han, Y. Li, J. Yuan, Z. Li, R. Zhao, T. Han and T. Han, *Sens. Actuators. B Chem.*, 2018, **258**, 373-380.
- [3.15] J. Pitchaimani, A. Kundu, S. Karthikeyan, S.P. Anthony, D. Moon and V. Madhu, *Cryst. Eng. Comm.*, 2017, **19**, 3557.
- [3.16] S. Shanmugaraju and P.S. Mukherjee, *Chem. Eur. J.*, 2015, **21**, 6656-6666.
- [3.17] a) D. Banerjee and Z. Hu, *Dalton Trans.*, 2014, **43**, 10668-10685, b) A.W. Czarnik, *Nature*, 1998, **394**, 417-418.
- [3.18] B. Roy, A.K. Bar, B. Gole and P.S. Mukherjee, *J. Org. Chem.*, 2013, **78**, 1306-1310.
- [3.19] J. Akhavan, (*second ed.*), *Royal Society of Chemistry, London*, 2004.
- [3.20] P. Cooper, *Wiley-VCH, New York*, 1996, 33.
- [3.21] S.S.R. Dasary, A.K. Singh, K.S. Lee, H. Yu and P.C. Ray, *Sens. Actuator B Chem.*, 2018, **255**, 1646- 1654.
- [3.22] H. Muthurajan, R. Sivabalan, M.B. Talawar and S.N. Asthana, *J. Hazard. Mater.*, 2004, **A112**, 17-33.
- [3.23] K. Acharyya and P.S. Mukherjee, *Chem. Commun.*, 2014, **50**, 15788-15791.
- [3.24] Y. Xu, B. Li, W. Li, J. Zhao, S. Sun and Y. Pang, *Chem. Commun.*, 2013, **49**, 4764-4766.
- [3.25] R. Guo, T. Jiao, R. Li, Y. Chen, W. Guo, L. Zhang, J. Zhou, Q. Zhang and Q. Peng, *ACS Sustain. Chem. Eng.*, 2018, **6**, 1279-1288.
- [3.26] R. Geng, R. Chang, Q. Zou, G. Shen, T. Jiao and X. Yan, *Small*, 2021, **17**, Article 2008114.
- [3.27] a) Safety data sheet for picric acid, Resource of National Institute of Health, b) M. Cameron
Picric acid hazards, American Industrial Hygiene Association: Fairfax, VA (1995).
- [3.28] P.C. Ashbrook and T.A. Houts, *ACS Div. Chem. Health Safety*, 2003, **10**, 27.
- [3.29] M.E. Wals, *Talanta*, 2001, **54**, 427-438.
- [3.30] C. Qian, R. Wang, M. Li, X. Li, B. Ge, Z. Bai and T. Jiao, *Colloids Surf. A: Physicochem. Eng. Asp.*, 2021, **608**, 125616.
- [3.31] C. Byram, S.S.B. Moram, A.K. Shaik and V.R. Soma, *Chem Phys Lett*, 2017, **685**, 103-107.
- [3.32] G. Vourvopoulos and P.C. Womble, *Talanta*, 2001, **54**, 459-468.
- [3.33] A. Hakonen, F. Wang, P.O. Andersson, H. Wingfors, T. Rindzevicius, M.S. Schmidt, V.R. Soma, S. Xu, Y. Li, A. Boisen and H. Wu, *ACS Sens.*, 2017, **2**, 198-202.
- [3.34] R. Wang, X. Yan, B. Ge, J. Zhou, M. Wang, L. Zhang and T. Jiao, *ACS Sustainable Chem. Eng.*, 2020, **8**(11), 4521-4536.
- [3.35] K.E. Brown, M.T. Greenfield, S.D. McGrane and D.S. Moore, *Anal. Bioanal. Chem.*, 2016, **408**, 35-47.
- [3.36] W. Zheng, Y. Zhao, X. Lin, Q. Zhang, K. Xiao, N. Cheng, X. Mei, Y. Lu and Z. Ya, *Dyes Pigm.*, 2022, **207**, 110761.
- [3.37] S. Nath, S.K. Pathak, B. Pradhan, R.K. Gupta, K.A. Reddy, G. Krishnamoorthy and A.S. Achalkumar, *New J. Chem.*, 2018, **42**, 5382.

- [3.38] K. Sheng, H. Lu, A. Sun, Y. Wang, Y. Liu, F. Chen, W. Bian, Y. Li, R. Kuang and D. Sun, *Chin Chem Lett*, 2019, **30**, 895-898.
- [3.39] T. Liu, L. Ding, K. Zhao, W. Wang and Y. Fang, *J. Mater. Chem.*, 2012, **22**, 1069-1077.
- [3.40] X.P. Wang, L.L. Han, Z. Wang, L.Y. Guo, D. Sun, *J. Mol. Struct.*, 2016, **1107**, 1-6.
- [3.41] K. Anandhan, M. Ceron, V. Perumal, P. Ceballos, P. Gordillo-Guerra, E. Perez-Gutierrez, A.E. Castillo, S. Thamotharanb and M.J. Percino, *RSC Adv.*, 2019, **9**, 12085-12096.
- [3.42] Y. Niko, Y. Cho, S. Kawauchia and G. Konishi, *RSC Adv.*, 2014, **4**, 36480-36484.
- [3.43] M. Basak, B. Bhattacharjee, A. Ramesh and G. Das, *Dyes Pigm.*, 2021, **196**, 109779.



Annexure 3

Table A3.1: Crystal parameters and refinement data of the free receptors as well as their PA complexes

Parameters	L ₁	L ₂	L ₃	L ₁ .PA	L ₂ .PA	L ₃ .PA
formula	C ₂₁ H ₂₀ N ₂	C ₂₅ H ₂₂ N ₂	C ₂₇ H ₂₂ N ₂	C ₂₇ H ₂₃ N ₅ O ₇	C ₃₁ H ₂₅ N ₅ O ₇	C ₃₃ H ₂₅ N ₅ O ₇
fw	300.39	350.44	374.46	529.50	579.56	603.58
cryst syst	orthorhombic	monoclinic	monoclinic	monoclinic	monoclinic	monoclinic
space group	P b c a	P 21/c	P 21/c	P 21/c	P 21/c	P 21/n
a (Å)	25.297(4)	6.041(9)	19.221(2)	12.8301(11)	7.3828(12)	16.289(5)
b (Å)	7.2717(13)	42.17(6)	7.9954(9)	8.0820(7)	30.815(5)	7.977(2)
c (Å)	37.125(7)	7.515(9)	13.5818(15)	24.945(2)	11.9609(19)	21.855(7)
α (deg)	90	90	90	90	90	90
β (deg)	90	95.47(3)	106.851(3)	102.407(2)	97.044(4)	97.925(9)
γ (deg)	90	90	90	90	90	90
V (Å ³)	6829(2)	1906(5)	1997.7(4)	2526.2(4)	2700.6(7)	2812.7(15)
Z	16	4	4	4	4	4
DC (g cm ⁻³)	1.169	1.221	1.245	1.392	1.425	1.425
μ (Mo Kα) (mm ⁻¹)	0.069	0.071	0.073	0.103	0.103	0.102
F (000)	2560.0	744.0	792.0	1104.0	1208.0	1256.0
T (K)	297 K	297 K	297 K	297 K	297 K	297 K
θmax (deg)	20.957	20.740	23.280	21.984	23.295	23.267
total no. of rflns	130984	12568	35500	57152	58822	48218
no. of indep rflns	3622	1938	2872	3091	3893	4027
no. of obsd rflns	1941	931	1474	1951	1662	2256
no. of params refined	420	247	264	359	394	413
R ₁ , I > 2σ(I)	0.0800 (1941)	0.1777 (931)	0.0908 (1474)	0.0661 (1951)	0.0707 (1662)	0.0778 (2256)
wR ₂ , I > 2σ(I)	0.2836 (3622)	0.3522 (1938)	0.2699 (2872)	0.2567 (3091)	0.2588 (3893)	0.1696 (4027)
GOF (F ₂)	1.198	1.532	1.354	1.277	1.162	1.148
CCDC no.	2244703	2244704	2244705	2244706	2244707	2244708

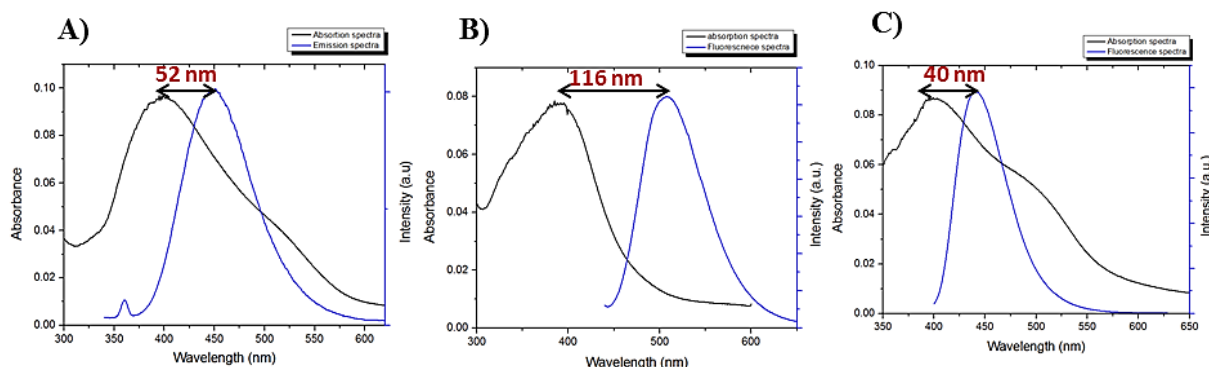


Figure A3.1: Absorption and emission spectra of A) L₁, B) L₂ and C) L₃ in water.

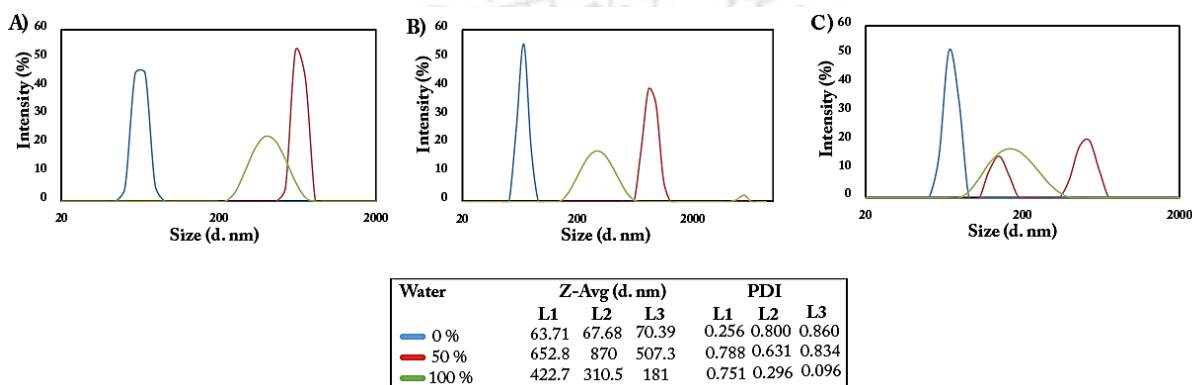


Figure A3.2: DLS output of (A) L₁, (B) L₂ & (C) L₃.

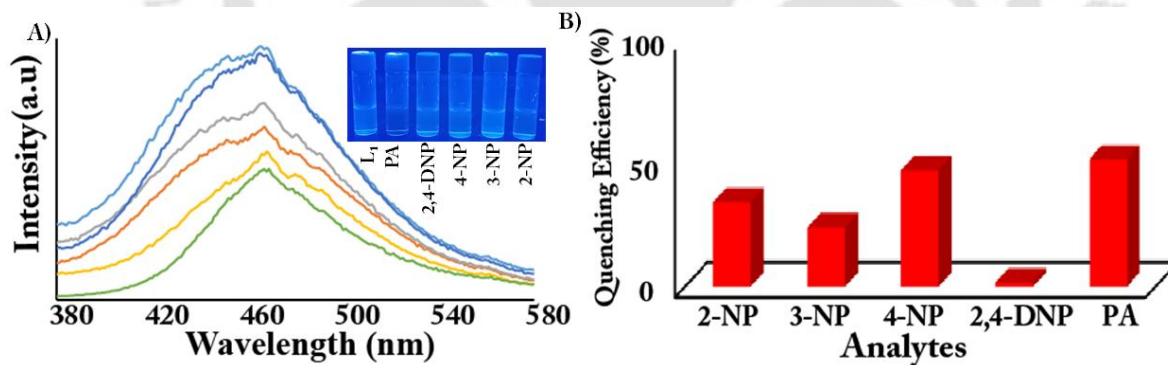


Figure A3.3: A) Interaction of L₁ with different nitrophenols; Inset: Visual changes in fluorescence intensity of L₁ observed under UV light upon the addition of different nitrophenols. B) Fluorescence quenching efficiency ($\lambda_{ex} = 320$ nm) of L₁ (10.0 μ M) in water in the presence of various analytes (50 Equiv.).

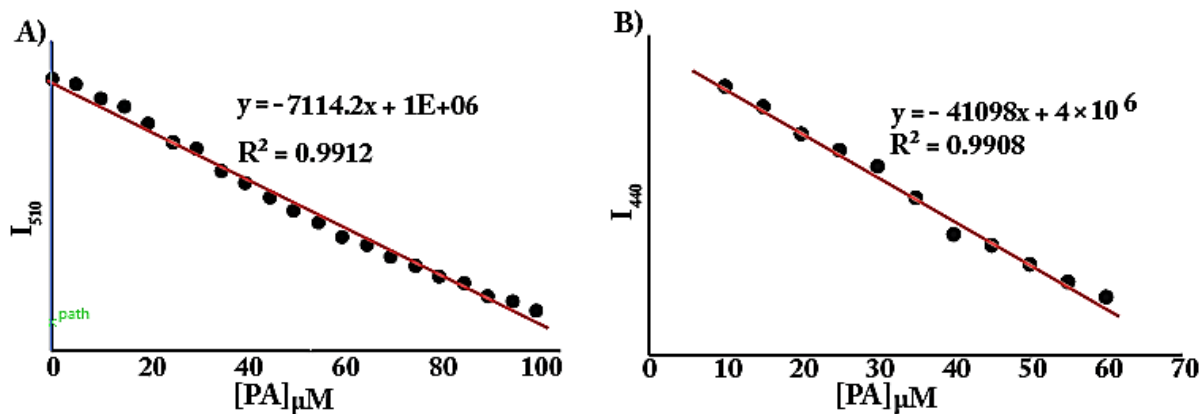


Figure A3.4: Fluorescence emission intensity of A) L₂ at 510 nm vs. PA concentration A) L₃ at 440 nm vs. PA concentration to calculate the limit of detection (LOD).

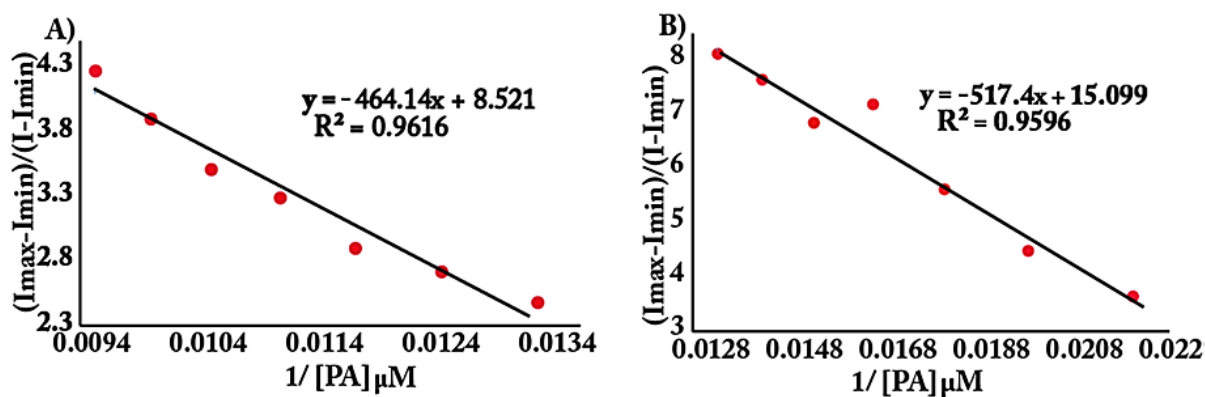


Figure A3.5: Benesi-Hildebrand plot for determination of binding constant of A) L₂ and PA, B) L₃ and PA.

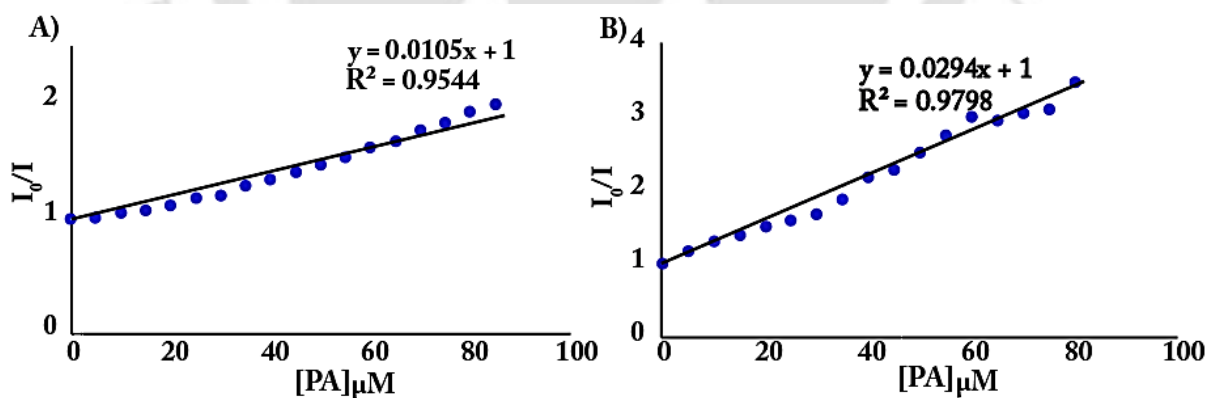


Figure A3.6: Stern-Volmer plot: I_0/I vs. $[PA]$ of A) L₂ B) L₃.

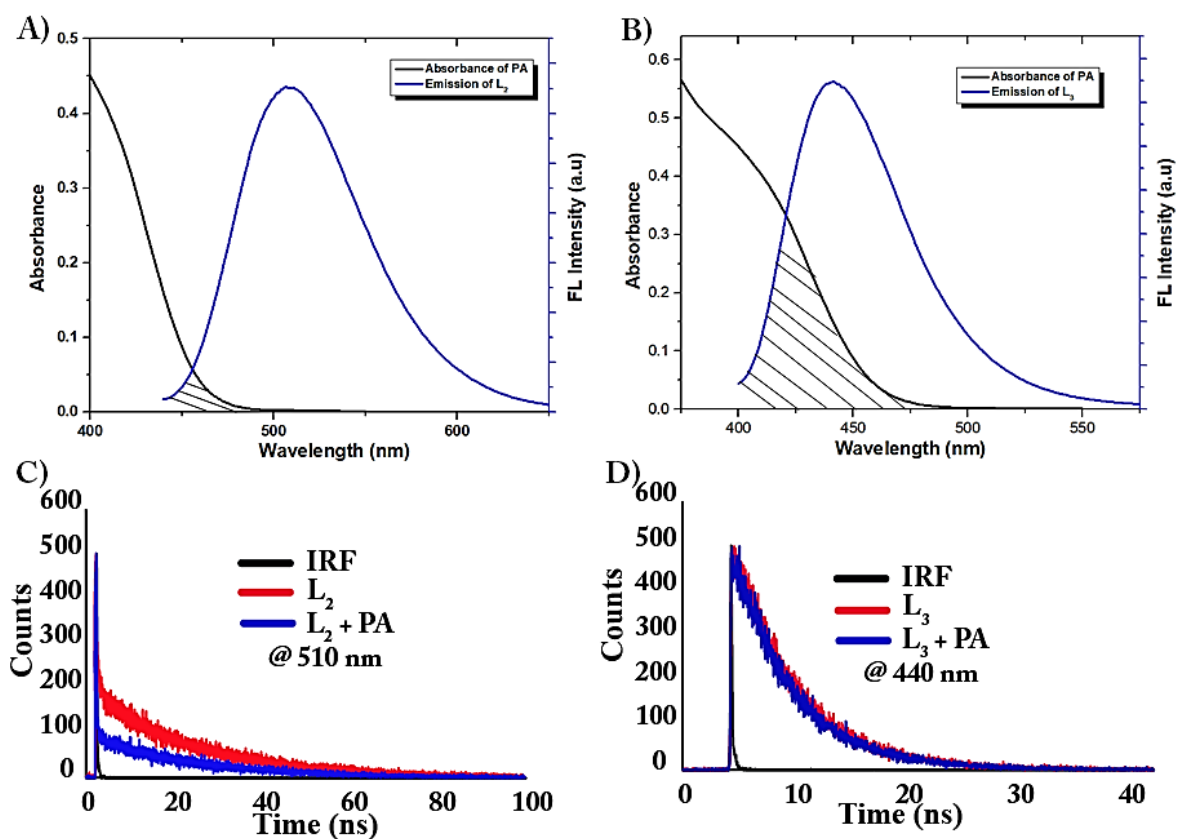


Figure A3.7: Spectral overlap of the emission spectra of A) L₂ (blue line) and the absorption spectra of PA (black line), B) L₃ (blue line) and the absorption spectra of PA (black line) in the aqueous medium. Time-resolved fluorescence spectra of C) L₂ (10.0 μM, red line) and in the presence of PA (blue line), D) L₃ (10.0 μM, red line) and in the presence of PA (blue line).

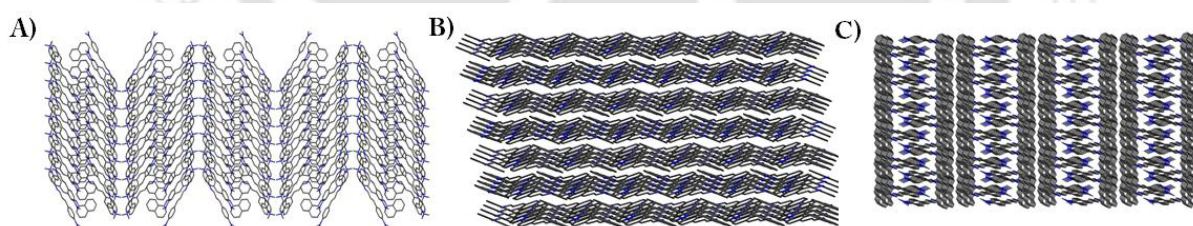


Figure A3.8: Packing arrangement of the receptors (A) L₁, (B) L₂ & (C) L₃.

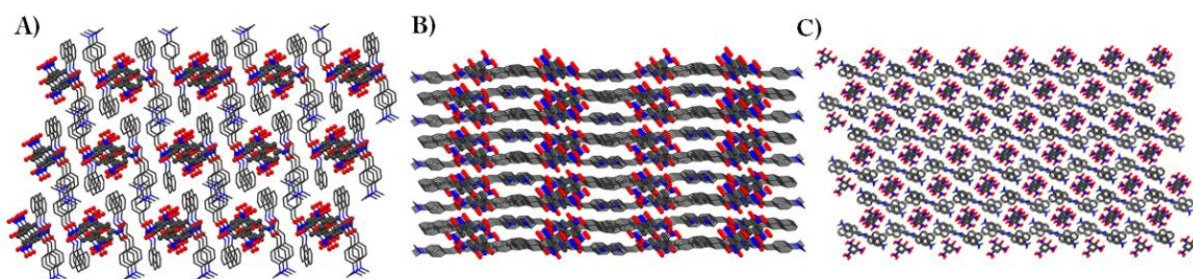


Figure A3.9: PA encapsulated within the self-assembled architecture of receptors (A) L₁, (B) L₂ & (C) L₃.

Table A3.2: Detection of PA in natural water samples.

Sl no.	Water Sample	Added PA(μM)	Recovery (%)	
			L ₂	L ₃
1.	Lake	100	58.82	82.74
2.	River	100	67.15	83.48
3.	Tap	100	61.58	86.14

Table A3.3: Fluorescence lifetime values of L₂ (10 μM) & L₂.PA and L₃ (10 μM) & L₃.PA in an aqueous medium.

Sample	B _i	ΔB_i	f _i (%)	Δf_i (%)	t _i (ns)	Δt_i (ns)
L ₂	0.0337	0.0026	100.000	7.801	23.065	0.0003
L ₂ + PA	0.0201	0.0023	100.000	11.329	21.058	0.0007
L ₃	0.1359	0.0007	100.000	0.501	5.396	0.0005
L ₃ + PA	0.1322	0.0068	100.000	5.120	5.293	0.0006

Table A3.4: Hydrogen bonding distances and angles of the receptors as well as their PA complexes.

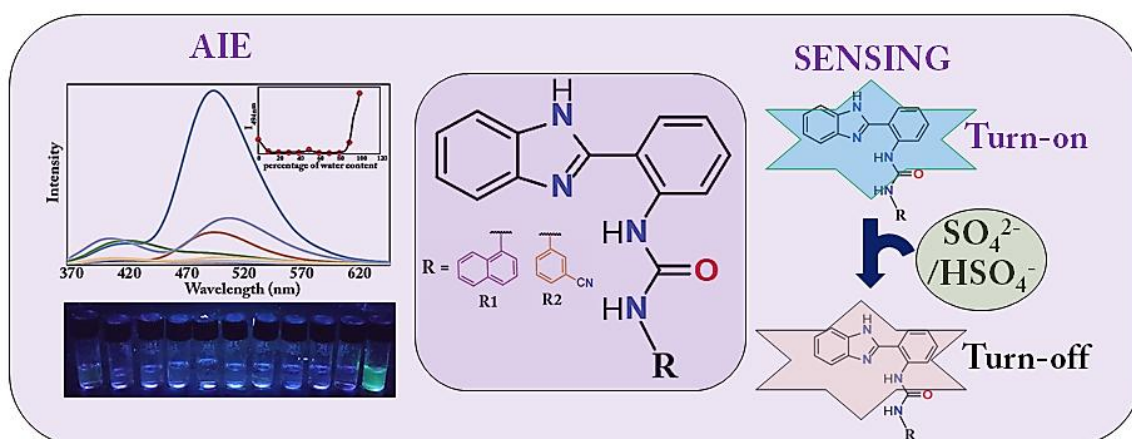
Ligand/Complex	D-H...A	d(D...H)/Å	d(H...A)/Å	d(D...A)/Å	<D-H...A/°	Symmetry codes
L ₁	C1-H1...N1	0.93	2.50	2.816 (12)	100	x, y, z
	C28-H28...N3	0.93	2.48	2.806 (8)	101	x, y, z
L ₃	C00A-H8...N1	0.93	2.49	2.815 (7)	101	x, y, z
	C20-H13...N1	0.93	2.48	3.378 (7)	163	x, 3/2-y, 1/2+z
L ₁ .PA	N2-H1...O3	0.96 (5)	2.51 (5)	3.101 (7)	120 (4)	1-x, 1-y, -z
	N2-H1...O7	0.96 (5)	1.78 (5)	2.719 (6)	165 (4)	1-x, 1-y, -z
	C10-H10...O7	0.93	2.58	3.238 (6)	128	1-x, 1-y, -z
	C15-H15...O4	0.93	2.46	3.374 (8)	166	-1+x, -1+y, z
	C21-H21...N2	0.93	2.55	2.866 (7)	100	x, y, z
	C25-H25...O2	0.93	2.32	2.643 (7)	100	x, y, z
L ₂ .PA	N2-H2N...O1	1.03 (9)	1.92 (9)	2.896 (7)	156 (8)	x, y, z
	C1-H1...O1	0.93	2.53	3.295 (7)	139	x, y, z
	C1-H1...O2	0.93	2.59	3.441 (8)	152	x, y, z
	C13-H13...O6	0.93	2.59	3.377 (8)	143	1-x, -1/2+y, 1/2-z
	C15-H15...O4	0.93	2.52	3.424 (8)	165	1+x, y, 1+z
	C16-H16...O7	0.93	2.47	3.261 (8)	143	x, y, z
	C25-H25B...O3	0.96	2.45	3.351 (8)	157	1-x, 1/2+y, 1/2-z
	C29-H29...O3	0.93	2.28	2.619 (8)	101	x, y, z
L ₃ .PA	N2-H2N...O5	1.00 (6)	1.76 (7)	2.745 (6)	168 (5)	1/2-x, -1/2+y, 1/2-z
	C2-H2B...O7	0.96	2.56	3.151 (9)	120	-1/2+x, 1/2-y, 1/2+z
	C10-H10...O5	0.93	2.59	3.236 (6)	127	1/2-x, -1/2+y, 1/2-z
	C27-H27...O3	0.93	2.60	3.294 (7)	132	1+x, -1+y, z
	C29-H29...O3	0.93	2.33	2.648 (6)	100	x, y, z

Table A3.5: A representative comparison of K_{SV} values and the detection limits along with the receptor and solvent system used for the detection of PA.

Sl. No.	References	Receptors	Solvent system	LOD (μM)	K_{SV} (M^{-1})
1.	Present work	Pyrene and anthracene-based probe	100% water	4.32 and 4.15	10.5×10^3 and 29.4×10^3
2.	Journal of Molecular Liquids 2018, 261, 446–455	9-Anthraldehyde-based AIE sensor	hydrosol	8.07	1.89×10^5
3.	Spectrochimica Acta Part A: Molecular and Biomolecular Spectroscopy, 2019, 223, 117201	Coumarin based probe	Acetonitrile/water (1:9) mixture	9.5	2.21×10^5
4.	Anal. Chem., 2019, 91, 13,675-13680	BODIPY probe	Acetonitrile/water (8:2) mixture	0.44	Not reported
5.	Dyes and Pigments, 2020, 181, 108563	Tripodal naphthalimide derivative	DMF/H ₂ O (1: 9, v/v) solution	4.73×10^{-2}	73.6×10^3
6.	New J. Chem., 2020, 44, 20092	Phenanthroimidazole derivatives	Ethanol	2.8, 2.3, 4.6 (0.64, 0.53, 1.05 ppm)	8.62×10^4 , 1.45×10^5 , 8.53×10^4
7.	Sensors and Actuators: B. Chemical., 2021, 330 129,287	Polyaromatic-based imidazolium	Aqueous medium	5	9.57×10^6
8.	Journal of Molecular Structure, 2022, 1249, 131619	Pyranone based Schiff base	Methanol	6.92×10^{-1}	Not reported
9.	Journal of Solid State Chemistry, 2022, 316, 123561	Ca(II)- organic framework	Ethanol	19.06	6.7×10^3
10.	ACS Appl. Mater. Interfaces 2023, 15, 14575-14586	Ni-MOF	Water	0.29	3.45×10^5

Chapter 4

Exploring the effect of terminal substituent on aggregation and sensing properties of neutral benzimidazole-based urea receptors



4.1. Background and Focus of the Chapter

Anions performing vital functions in diverse fields which include biological sciences, chemistry, environmental sciences, etc. that are closely related to people's lives [4.1-4.3]. Hence, their detection has gained substantial attention worldwide. In the past 25 years, much effort has been devoted to designing receptors for anion complexing and sensing. Small molecule anion sensors developed strategically based on well-established anion sensing mechanisms are attractive for this purpose [4.4]. Neutral anion receptors bearing amide or urea/thiourea have been exploited for anion binding via favorable hydrogen bonding [4.5-4.6]. However, the recognition event employing such inherently weak interactions is difficult owing to the effective competitiveness of solvent molecules towards both the receptor (host) and anion (guest) [4.7]. Also, recognition of anions in water is one of the key challenges in modern anion supramolecular chemistry owing to the strong hydration, resulting in an additional energetic barrier due to desolvation during host-guest binding although it is essential to be applicable for biology, healthcare, and environmental monitoring purposes [4.8]. The literature reports the domination of highly charged polycationic receptors for anion binding in water utilizing electrostatic attractions [4.9-4.15]. Scarce examples of low charge or neutral receptors have recently been reported that can operate in 100% water including cyclopeptide macrocycles, [4.16-4.17] bambus[6]urils, [4.18-4.19] biotin[6]urils, [4.20-4.21] and indolocarbazoles [4.22] for preferential recognition of weakly hydrated chaotropic anions (e.g., PF_6^- , SCN^- , and ClO_4^-). However, reports portraying aqueous medium sensing of the highly hydrophilic SO_4^{2-} anion by neutral receptors are not very common in the literature. Designing a receptor capable of SO_4^{2-} binding is very important as sulfate is present in all freshwater and marine environments and is reduced to toxic and corrosive hydrogen sulfide by anaerobic bacteria [4.23]. Moreover, SO_4^{2-} is one of the most abundant anions in human plasma [4.24] and has been regarded as an end metabolite of cysteine and methionine [4.25]. Since cationic receptors are likely to be too toxic [4.26] to be used in biological applications, neutral receptors for sulfate anions in aqueous solution are of particular interest for modern supramolecular chemistry.

Since being proposed by Tang's research team in 2001 [4.27], the aggregation-induced emission (AIE) property has evolved as a perfect solution to the very common ACQ (Aggregation-caused quenching) issue [4.28-4.31]. The ubiquitous ACQ phenomenon limits the practical applications

of traditional organic luminophores [4.32]. The emergence of the AIE concept has brought huge opportunities for the analysis of bioactive species as well as the monitoring of complicated biological processes [4.33]. However, upon rational design by the introduction of adequate aromatic (phenyl) rotors on the periphery, the normal ACQ luminogens with a big and planar π structure could be converted to an AIE or AEE (aggregation enhanced emission) one as a result of the twisted conformation and suppressed π - π stacking [4.34].

Our persistent effort to explore the fascinating supramolecular self-assembly behaviour of small molecules [4.35-4.37] as well as to employ the system as an excellent sensing tool has led us to develop two benzimidazole-based urea receptors **R1** and **R2**, differing in the terminal substituents, to have a comparative study regarding aggregation as well as sensing potential. One of them is tailored with a naphthyl fluorophore, while the other contains a meta-cyanophenyl group, both attached to 2-(1H-benzimidazol-2-yl)aniline through a urea linkage. A small change in the electronic properties of the receptors results in differential aggregation as well as sensing abilities. Herein, we have tuned the functional group attached to the molecular frameworks, which not only varied the optical features but could also be used in analytical applications.

4.2. Objective of the Chapter

Two neutral benzimidazole-based urea receptors **R1** and **R2** with varying terminal substituents led to changes in aggregation as well as chemosensing properties. While **R1** displayed aggregation-induced emission (AIE) properties by showing the highest emission in water against binary solvent switching, **R2**, on the other hand, exhibited typical aggregation-caused quenching (ACQ) behaviour. Both **R1** and **R2**, however, could sense $\text{SO}_4^{2-}/\text{HSO}_4^-$ in an aqueous medium although with different binding affinities, the mechanistic details of which are investigated with the help of different spectroscopic, microscopic, and theoretical approaches.

4.3. Results and Discussion

4.3.1. The rationale behind designing the receptors

We have rationally designed two unsymmetrical urea-based receptors **R1** and **R2**, where in both the receptors we have purposefully incorporated a benzimidazole fluorophore part as a constant unit in one arm while varying the other arm, fabricated with a naphthyl and 3-cyanophenyl moiety in **R1** and **R2**, respectively. The naphthalene moiety will act as an electron-rich fluorophore; on the contrary, the 3-cyanophenyl moiety will have an electron-withdrawing tendency. In both the receptors, the urea and the benzimidazole subunits act as both H-bond donor/acceptor sites, thus facilitating the self-assembly and anion recognition process, which is quite evident from the

electrostatic potential map (Figure 4.1) and SCXRD analysis. In the electrostatic potential mapping, the blue regions are mostly localized on the aforementioned hydrogen atoms indicating the highest electrostatic potential in those regions, signifying them as the most probable hydrogen bonding interaction sites, allowing anion coordination through hydrogen bonding interactions. This comparative design was followed to realize the role of changing the terminal substituent in one arm towards the aggregation aptitude, with different photophysical aspects as well as sensing behaviour.

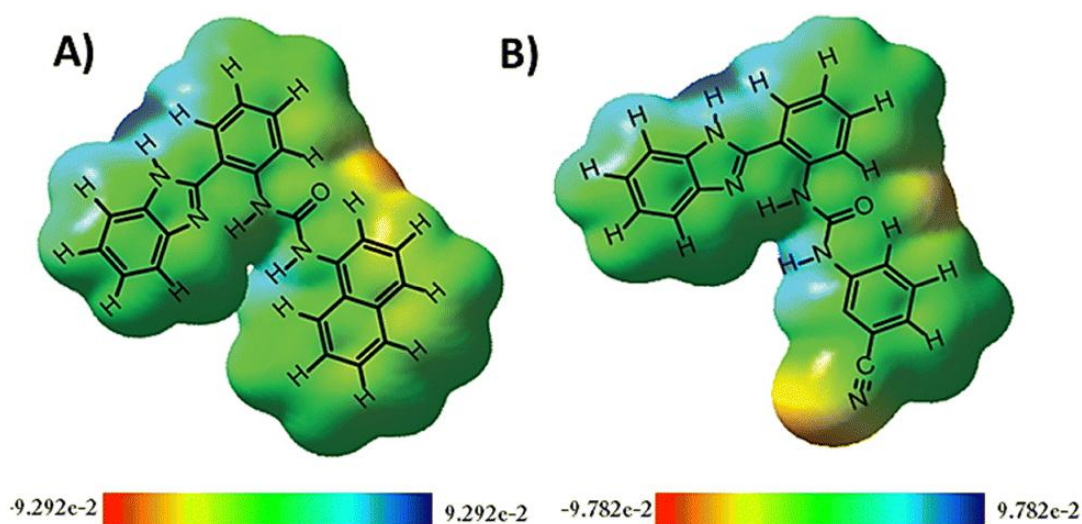


Figure 4.1: Calculated electrostatic potential map (DFT, B3LYP/6-31+G(d)) depicting electronic distribution of (A) **R1** and (B) **R2**.

4.3.2. Structural analysis of the receptors

Successful crystallization of receptor **R1** was achieved through slow evaporation of a DMSO/DMF (1: 1) solution of **R1**, where it crystallizes in triclinic space group P-1. Crystal structure analysis of **R1** unveils that the primary anion receptor sites, that is the urea hydrogen atoms, are oriented in an anti-fashion, where one of the hydrogen atoms (H3N) is forming an intramolecular hydrogen bonding interaction with its neighboring benzimidazole nitrogen atom (N2), where, $d(N3 \cdots N2) = 2.7834(19) \text{ \AA}$. Two of the **R1** receptors self-assemble to form a pseudocapsular cavity as facilitated by two hydrogen bonding interactions involving a urea oxygen atom (O1) and a benzimidazole hydrogen atom (H1N) with $d(N1 \cdots O1) = 2.8632(18) \text{ \AA}$, and such two nearby pseudocapsular cavities are interconnected via hydrogen bonding interactions involving a urea oxygen atom (O1) and a urea hydrogen atom (H4N), where $d(N4 \cdots O1) = 2.8707(17) \text{ \AA}$, thus facilitating the formation of a 1D self-assembled network (Figure 4.2 and Figure A4.8 A, Annexure 4).

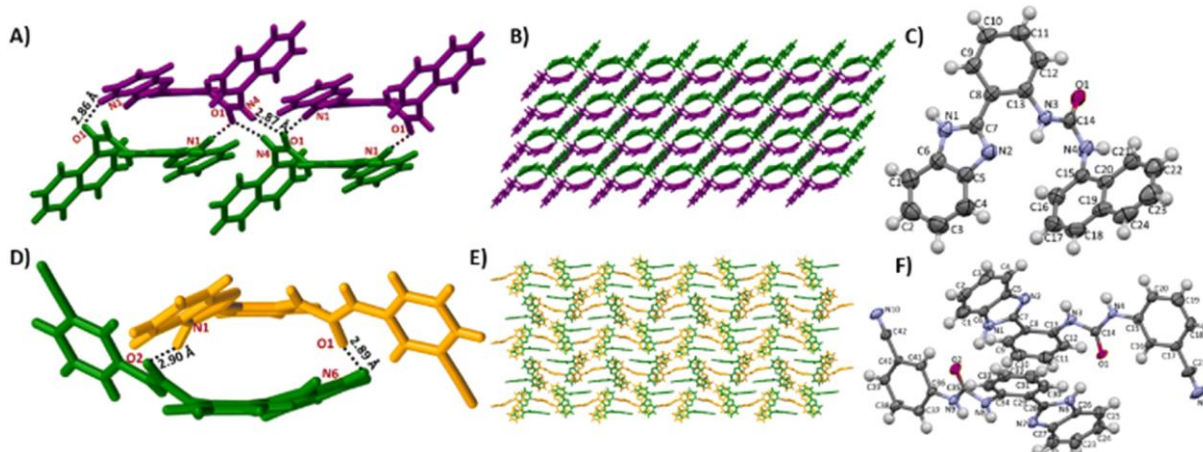


Figure 4.2: Depicting hydrogen bonding interactions, (A) in receptor **R1** and (D) in receptor **R2**; 3D packing with (B) in receptor **R1** and (E) in receptor **R2**; ORTEP diagram of (C) receptor **R1** and (F) receptor **R2** (ellipsoids drawn at 50% probability).

Receptor **R2** crystallizes in orthorhombic space group P212121. The urea hydrogen atoms are observed to be oriented in a syn-fashion in the case of receptor **R2**, unlike receptor **R1**, where the anti-arrangement of the same was observed, which is quite evident from crystal structure analysis. As observed earlier in the case of **R1**, a quite similar self-assembled pseudocapsular cavity formation has been observed to be prevalent in **R2** as facilitated by two hydrogen bonding interactions involving the urea oxygen atom (O1 and O2) and benzimidazole hydrogen atom (H6N and H1N) with a slight increase in the hydrogen bonding distances, with $d(\text{N6}\cdots\text{O1}) = 2.886(9) \text{ \AA}$ and $d(\text{N1}\cdots\text{O2}) = 2.901(9) \text{ \AA}$. Two nearby pseudo capsular cavities are interconnected via $\pi\cdots\pi$ stacking interactions involving the terminal cyanophenyl rings (the distance between the centroids of the two cyanophenyl rings was observed to be 4.213\AA), which ultimately led to the formation of a self-assembled architecture as depicted in Figure 4.2 and Figure A4.8 B, Annexure 4).

4.3.3. Exploring the self-aggregation potential of R1 and R2

The photophysical properties of **R1** and **R2** were investigated by UV-Vis absorption and fluorescence emission studies in acetonitrile (ACN)/water (H₂O) binary solvent systems. The absorbance spectra of **R1** and **R2** (10 μM) in pure ACN medium displayed two absorption bands around 294/330 nm and 266/330 nm respectively (Figure 4.3 A and B). Changing the solvent from ACN to water led to a noticeable change in the absorption profile for both cases. While **R1** gives an absorption band at ~ 290 nm and a shoulder peak at ~ 350 nm, for **R2**, two absorption bands at 260 nm and 290 nm were observed. The absorption bands at lower wavelength regions are presumably due to intra-molecular $\pi\text{-}\pi^*$ transition, whereas the bands at higher wavelength

regions are owing to the ICT (intra-molecular charge transfer) transitions for both **R1** and **R2**. The upliftment of the baseline observed in both cases indicated the probability of the formation of aggregates in water. A comparison of the absorption spectra at 600 nm for **R1** and **R2** revealed that the aggregation capacity of **R1** in water was five times the capacity of **R2** (Figure 4.3 E).

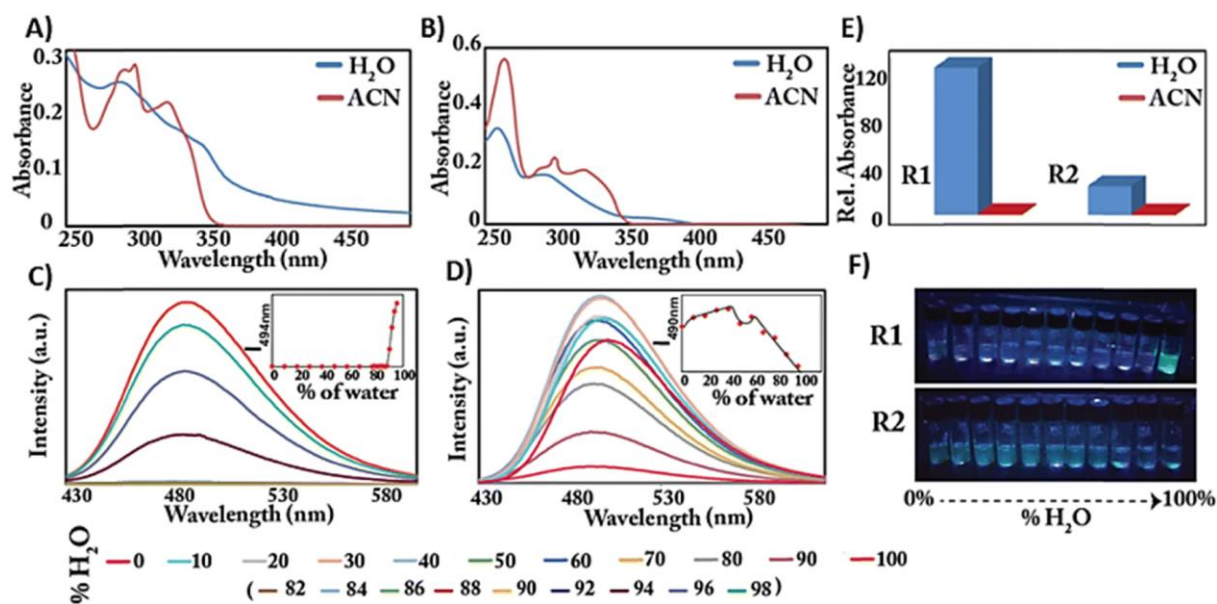


Figure 4.3: Absorbance spectrum of (A) **R1**, and (B) **R2** in ACN and water. Emission spectroscopy with increasing water percentages in ACN of (C) **R1**, and (D) **R2**. (E) Plot of relative absorbance for **R1** and **R2**. (F) Visual illustration of the AIE activity of **R1** and **R2** (10 μM) under a 365 nm UV lamp.

R1 reveals reasonable fluorescence intensity at ~506 nm in 100% acetonitrile medium; however, a ~4-fold increase in emission intensity at ~494 nm was observed upon altering to 100% water medium (Figure 4.3 C). Interestingly, in a mixed aqueous solvent (CH₃CN/H₂O) system, the fluorescence intensity of **R1** becomes very weak. The emission intensity of **R1** was recorded with increasing water fraction (additional measurements between 80-100% H₂O content have been performed for **R1**) in the mixed (CH₃CN/H₂O) solvent system keeping the concentration of the receptor 10 μM. So, the bright fluorescence of the receptor was observed in 100% water (Figure 4.3 F). Thus, by restricting the intramolecular rotational motions of the molecule, the receptor displays probable aggregation-induced emission properties, which resulted in an aggregation-triggered enhancement in fluorescence. However, in contrast, **R2** shows typical aggregation-caused quenching phenomena in the CH₃CN/H₂O mixed solvent system (Figure 4.3 D). A slight blue shift from 495 nm to 490 nm was observed while switching the solvent from ACN to H₂O. A small manipulation of the terminal substituent in the benzene moiety caused changes in the aggregation behaviour. The disparity regarding aggregation of the two structurally similar yet terminal substituent varied molecules **R1** and **R2** is probably due to the difference of

conformations in solution, which is quite evident from SCXRD structural analysis. Whereas **R1** exhibits a highly twisted conformation around urea linkage resulting in the prohibition of π - π stacking of the benzimidazole moiety, making it self-assembled to emit bright greenish yellow emission in 100% water medium. While the comparatively more planar conformation of **R2** facilitates π - π stacking interactions, which results in aggregation-caused quenching. The concentration-dependent fluorescence spectra of **R1** and **R2** also validated the formation of self-assembly in water. The concentration of the receptors was increased from 1.25 μM to greater than 10 equivalents. The systematic growth of the emission intensity with an increase in concentration eventually, abruptly broke giving a critical aggregation constant (CAC) of each receptor at specific concentrations. The measured CAC values for **R1** and **R2** were found to be 6.25 μM and 8.75 μM , respectively (Figure A4.1, Annexure 4).

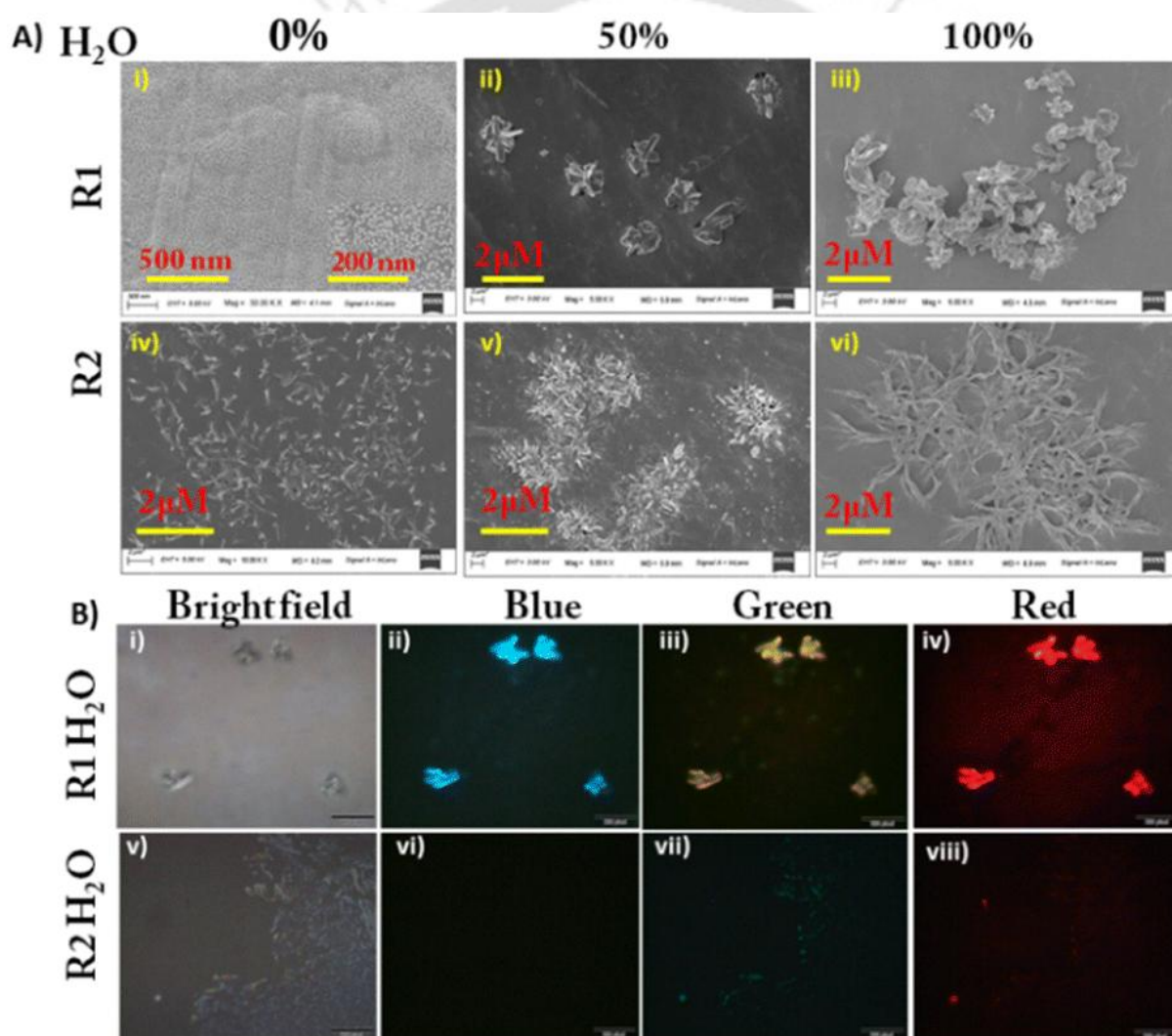


Figure 4.4: (A) FESEM images of **R1** (i)-(iii) and **R2** (iv)-(vi) with increasing water percentages. (B) Bright field as well as fluorescence microscope images of **R1** (i)-(iv) and **R2** (v)-(viii).

Aggregation was further corroborated by FESEM and DLS studies. The average particle size of **R1** (20 μM) increased from 77 nm to 263 nm upon increasing the water fractions from 0-100% in the acetonitrile medium in DLS studies (Figure A4.2 A, Annexure 4). A similar effect was observed in the case of **R2** (20 μM), where the average particle size increased to 170 nm in 100% water fraction compared to 58 nm in 100% ACN medium, thus confirming the formation of larger aggregates in water (Figure A4.2 B, Annexure 4). The FESEM study indicated that **R1** (100 μM) which exhibited spherical shapes of an average 14 nm diameter in pure ACN medium, self-assembled to generate flower-like aggregates of larger size (average diameter 43 nm) in pure water (Figure 4.4 A(i), (ii), (iii)). Whereas, **R2** (100 μM) showed rice grain-like morphology (average diameter 12 nm) in ACN medium, however self-assembled to give ribbon-like aggregates of average diameter 32 nm in pure water (Figure 4.4 A(iv), (v), (vi)). The fluorescence microscope images of self-assembled **R1** in 100% water (Figure 4.4 B(i), (ii), (iii), (iv)) showed intense fluorescence in all channels while minimal fluorescence intensity was observed in the case of **R2** (Figure 4.4 B(v), (vi), (vii), (viii)).

4.3.4. Selective UV and fluorescence response towards SO_4^{2-} and HSO_4^-

The anion binding properties of receptors **R1** and **R2** (10 μM) towards various biologically important anions such as SO_4^{2-} , HSO_4^- , CN^- , F^- , Cl^- , Br^- , I^- , ClO_4^- , OH^- , AcO^- , and NO_3^- were studied.

R1 exhibited excellent optical sensing properties towards only SO_4^{2-} and HSO_4^- through both colorimetric and fluorometric responses in an aqueous medium (Figure 4.5 A and B); **R2** on the other hand is not that selective towards SO_4^{2-} and HSO_4^- (Figure 4.5 C and D). Figure 4.5 A displays that only the addition of SO_4^{2-} and HSO_4^- caused a significant spectral shift, whilst the addition of other selected anions has no effect in the case of **R1**. The absorption band at ~ 290 nm slightly blue shifted to 285 nm. Also the ICT band at longer wavelength vanished. For **R2**, there was no noticeable spectral change with all the tested anions. The results obtained from UV-Vis studies provided us with an impetus to study the fluorometric responses of the receptors towards anions. The emission intensity of receptor **R1** (10 μM) at 494 nm (quantum yield = 6.4%) was completely quenched (98.95 and 99.78%) in the presence of 10 equivalents of SO_4^{2-} (quantum yield = 1.9%) and HSO_4^- (quantum yield = 0.8%) (Figure 4.5 E). Whereas other anions caused negligible changes to the emission profile of the receptor. The quenching of the emission intensity of **R2** (quantum yield = 3.9%) by SO_4^{2-} (quantum yield = 1.5%) and HSO_4^- (quantum yield = 0.9%) on the other hand was poor (70.25 and 77.33%) compared to **R1** (Figure 4.5 F). The titration

experiments with increasing concentrations of SO_4^{2-} and HSO_4^- ions were then conducted in aqueous medium for both **R1** and **R2** (Figure 4.6). Incremental addition of SO_4^{2-} and HSO_4^- ions caused an orderly decrease of the fluorescence emission intensity at 494 nm and 490 nm, respectively, until saturation is reached for both **R1** and **R2**.

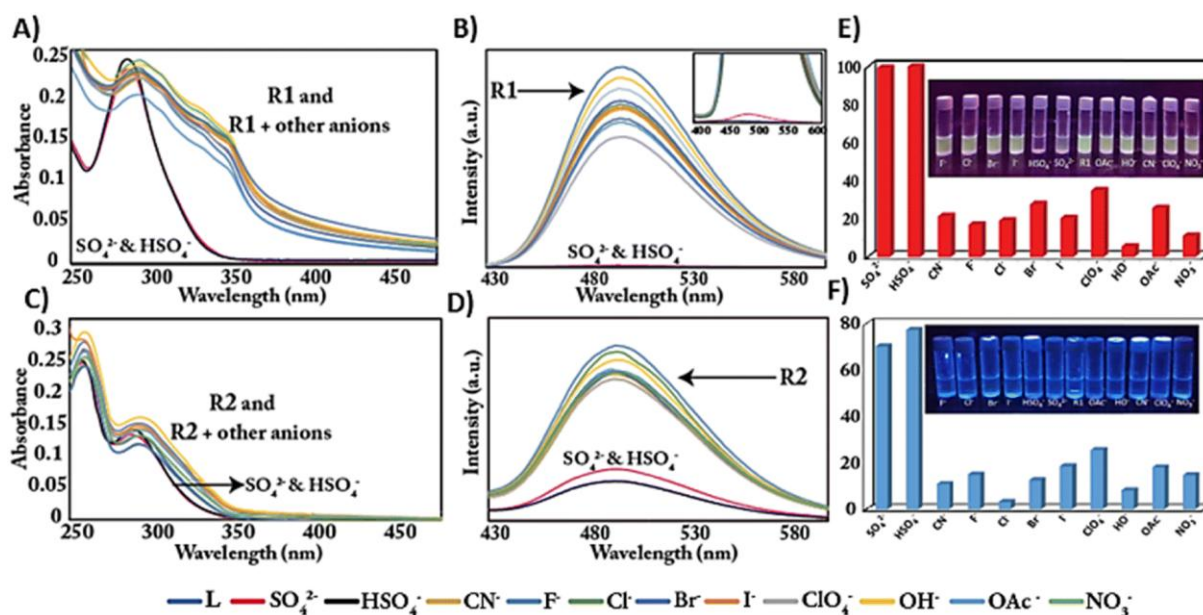


Figure 4.5: Absorption and fluorescence spectra of **R1** [A) and B)] and **R2** [C) and D)] in the presence of various anions [**R1** ($\lambda_{\text{ex}} = 350 \text{ nm}$) and **R2** ($\lambda_{\text{ex}} = 320 \text{ nm}$)] in water; Bar diagram representing the % quenching of emission intensity of E) **R1** and F) **R2** after the addition of anions in water.

The results obtained can be attributed to the prohibition of ICT as well as the facilitation of PET (Photoinduced electron transfer) from the benzimidazole part to the naphthyl/cyanophenyl moiety as a result of coordination of SO_4^{2-} and HSO_4^- to the receptors through H-bonding interactions. For **R1**, the LOD was calculated to be $1.74 \mu\text{M}$ and $1.76 \mu\text{M}$ while for **R2**, $1.09 \mu\text{M}$ and $0.93 \mu\text{M}$ for SO_4^{2-} and HSO_4^- , respectively (Figure A4.3, Annexure 4). The LOD value estimated based on the intensity at 494 nm and 490 nm was found to be one of the lowest, in comparison with any other fluorescent probes reported in the literature (Table A4.1, Annexure 4). Also, the binding constant calculated for our receptors was very high. The binding constants obtained from the Benesi-Hildebrand (B-H) plot for the $\text{SO}_4^{2-}/\text{HSO}_4^-$ complex for **R1** were found to be $14.31 \times 10^8 \text{ M}^{-1}$ and $14.85 \times 10^8 \text{ M}^{-1}$ while for **R2**, $1.57 \times 10^8 \text{ M}^{-1}$ and $1.12 \times 10^8 \text{ M}^{-1}$, respectively (Figure A4.4, Annexure 4). Although the LOD values of **R1** and **R2** for $\text{SO}_4^{2-}/\text{HSO}_4^-$ were comparable, the binding constant value of **R1** for SO_4^{2-} complexation is ~ 9 times and for HSO_4^- complexation is ~ 13 times compared to that of **R2**.

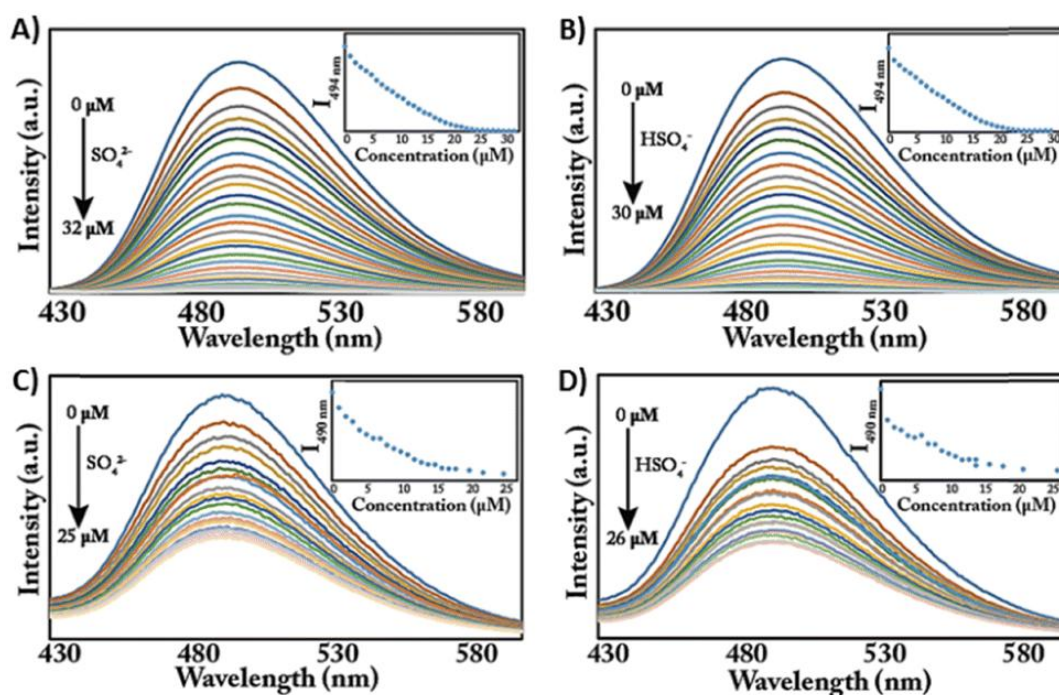


Figure 4.6: Absorption and fluorescence spectra of **R1** [A) and B)] and **R2** [C) and D)] in the presence of various anions [**R1** ($\lambda_{\text{ex}} = 350 \text{ nm}$) and **R2** ($\lambda_{\text{ex}} = 320 \text{ nm}$)] in water; Bar diagram representing the % quenching of emission intensity of E) **R1** and F) **R2** after the addition of anions in water.

4.3.5. Structural analysis of **R1.HSO₄**

Encapsulation of HSO_4^- inside the cation-sealed cavity of receptor **R1** and n-TBA via both classical and non-classical hydrogen bonding interactions has been reported. It is quite interesting to note that the anti-arrangement of the urea hydrogen atoms that existed earlier in the free receptor **R1** reorients into the syn-arrangement to facilitate HSO_4^- anion recognition. The total number of hydrogen bonding interactions in this recognition process is observed to be eight involving strong hydrogen bonding interactions, where both the urea hydrogen atoms ($d(\text{N}3 \cdots \text{O}4) = 3.316(7) \text{ \AA}$ and $d(\text{N}4 \cdots \text{O}4) = 2.901(7) \text{ \AA}$) along with the benzimidazole hydrogen atoms ($d(\text{N}1 \cdots \text{O}3) = 2.796(8) \text{ \AA}$ and $d(\text{O}2 \cdots \text{N}2) = 2.661(8) \text{ \AA}$) are acting as classical hydrogen bond donor sites; additionally, the involvement of non-classical hydrogen bond donor sites such as $\text{C-H}_{\text{TBA}} \cdots \text{O}$ and $\text{C-H}_{\text{phenyl}} \cdots \text{O}$ is also quite prevalent in this recognition process. All of those hydrogen bonding interactions result in a 1D self-assembled polymeric chain as assisted by HSO_4^- anion coordination, as depicted in Figure 4.7 and Figure A4.8 C, Annexure 4).

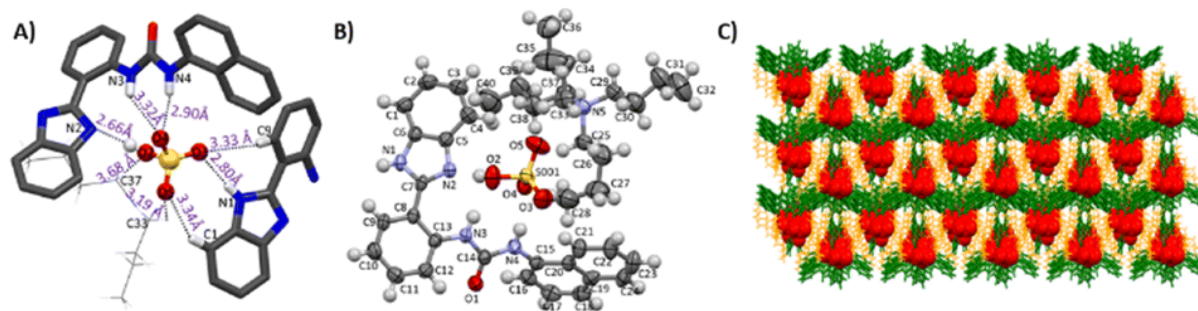


Figure 4.7: (A) Encapsulation of HSO₄⁻ by receptor **R1** and the n-TBA cation through hydrogen bonding interactions (depicting donor to acceptor distance, $d(D\cdots A)$); (B) ORTEP diagram of **R1**·HSO₄ (ellipsoids drawn at the 50% probability); (C) 3D packing arrangement of the **R1**·HSO₄ complex.

4.3.6. Interference test

Minimal external interference from any competing agents helps make a sensor more reliable and usable for further application. The selectivity of our receptors was tested by adding 10 equivalents of SO₄²⁻/HSO₄⁻ ions to each of the receptors in the presence of the same equivalents of other competing anions such as CN⁻, F⁻, Cl⁻, Br⁻, I⁻, ClO₄⁻, AcO⁻, OH⁻, OAc⁻, and NO₃⁻ in the aforementioned test solutions (Figure 4.8). The interference from the foreign analytes in the original fluorescence intensity obtained from the addition of SO₄²⁻/HSO₄⁻ was observed to be negligible.

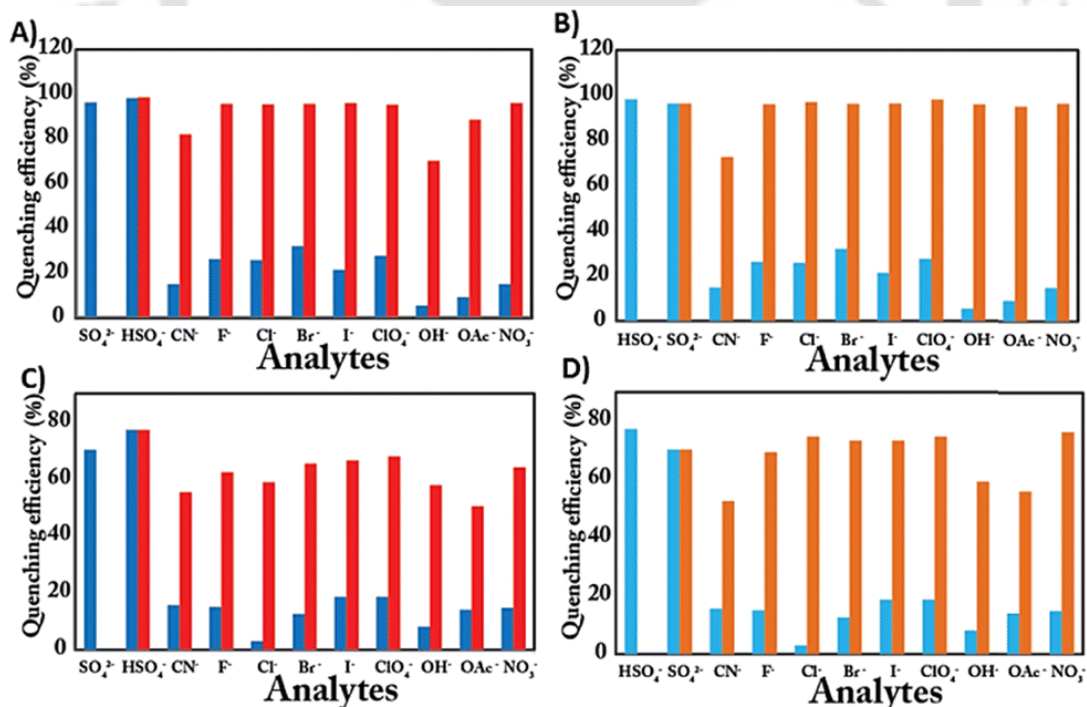


Figure 4.8: (A), (B) and (C), (D) Depict the interference study of receptor **R1** and **R2** (10 μM) in the presence of various competitive anions (100 μM) such as F⁻, Cl⁻, Br⁻, I⁻, ClO₄⁻, OH⁻, AcO⁻, and NO₃⁻ alongside the SO₄²⁻/HSO₄⁻ anion. The blue bar indicates receptor **R1/R2** + anions and the red/orange bar shows **R1/R2** + anions + SO₄²⁻/HSO₄⁻.

4.3.7. Probing the mechanism of sensing

To understand the reaction mechanism, ^1H NMR titration analysis was performed in the absence and presence of $\text{SO}_4^{2-}/\text{HSO}_4^-$ in $\text{DMSO-}d_6$ (Figure 4.9). The titration profile of **R1** and **R2** suggested that the NH_a , NH_b , and NH_c are the primary sites of hydrogen-bonding interactions as prominent broadening/shifting of these peaks is only observed for those protons on the addition of $\text{SO}_4^{2-}/\text{HSO}_4^-$. The peak intensity at 12.97 ppm of **R1** corresponding to NH_a , gradually decreased and finally completely vanished, suggesting a strong H-bond interaction/H-bond induced rapid dynamic effect upon the addition of both $\text{SO}_4^{2-}/\text{HSO}_4^-$. Concurrently, the peak due to urea $-\text{NH}$ protons H_c close to the naphthalene moiety at 12.00 ppm underwent systematic upfield shifting, while H_b at 9.42 ppm, close to the benzimidazole fluorophore, showed downfield shifting upon gradual addition of SO_4^{2-} . However, in the case of HSO_4^- addition, negligible shifting of the H_b and H_c peaks was observed, although the peak intensity decreased gradually. Similar results were observed in the case of **R2**. The downfield shift with concomitant broadening of the H_b results due to H-bonding interaction with SO_4^{2-} , which ultimately alters the electronic environment of the nearby naphthalene/cyanophenyl ring, leading to upfield shifting of H_c .

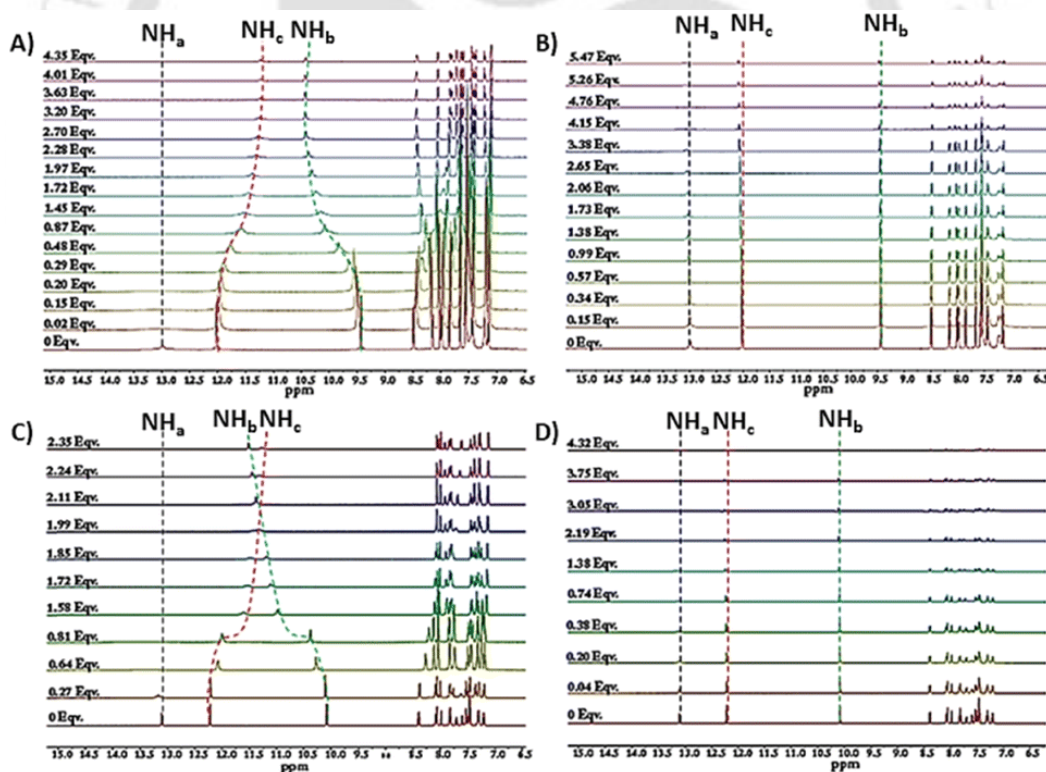


Figure 4.9: The change in the ^1H NMR spectra of **R1** [A) and B)] and of **R2** [C) & D)] upon incremental addition of $\text{SO}_4^{2-}/\text{HSO}_4^-$ in $\text{DMSO-}d_6$.

The FT-IR analysis of the receptors as well as their $\text{SO}_4^{2-}/\text{HSO}_4^-$ complexes corroborates very well with the observations obtained from the ^1H NMR titration study. The characteristic stretching

frequency corresponding to the urea hydrogen atoms is observed to be slightly shifted in the presence of $\text{SO}_4^{2-}/\text{HSO}_4^-$, indicating hydrogen bonding interactions involving the same, as depicted in Figure A4.6 and A4.7, Annexure 4.

4.3.8. DFT studies of receptors and their SO_4^{2-} adduct

To understand the photophysical behaviour of the receptors (**R1** and **R2**) towards SO_4^{2-} binding, we performed DFT [b3lyp/6–31 g (d)] calculations (Figure 4.10). The HOMO-LUMO of the optimized structure of **R1** shows clear charge separation indicating the prevalence of ICT operating from urea nitrogen (nearest to the spacer phenyl ring) to the benzimidazole ring. After SO_4^{2-} binding, blockage of the ICT process might have occurred, thus leading to quenching of the emission intensity, which is quite evident from the changes in electronic distribution after SO_4^{2-} complexation through DFT calculation. In addition to that, SO_4^{2-} complexation also facilitates PET phenomena from the naphthyl moiety to the benzimidazole part. Hence, the cumulative effect of both ICT inhibition as well as PET can be ascribed to the fluorescence turn-off mechanism. On the other hand, unlike **R1**, in the case of **R2**, initially both the HOMO-LUMO were distributed all over the molecule, and upon complexation with SO_4^{2-} , the LUMO was observed to be completely localized over the cyanophenyl-part, suggesting PET phenomena operating from the electron-rich benzimidazole to the electron-deficient cyanophenyl moiety thus leading to the quenching of the emission intensity of **R2**.

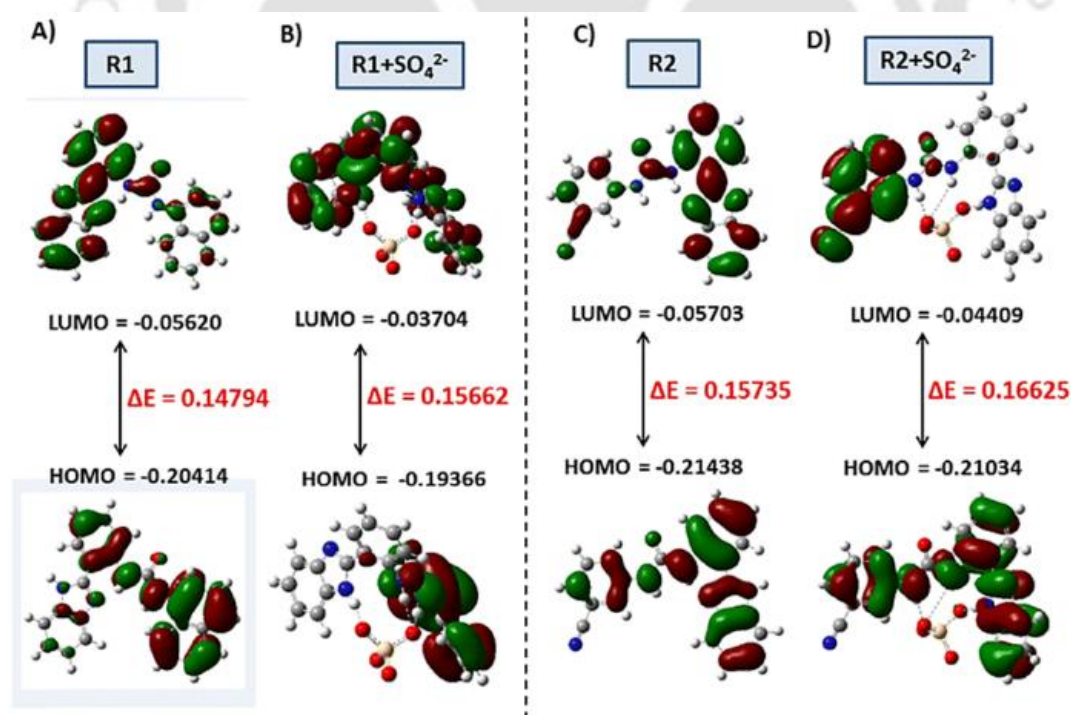


Figure 4.10: The DFT optimized geometries of the most stable form of (A) **R1** and (C) **R2**, and (B) and (D) their corresponding complex with SO_4^{2-} .

4.3.9. Paper-based detection of $\text{SO}_4^{2-}/\text{HSO}_4^-$

Paper strip experiments were performed to demonstrate the practical utility of the sensing system (Figure 4.11). Whatman filter paper was cut out to prepare the model paper strips and dried in air for a few hours after dipping it into the receptor solution of **R1** and **R2**. Afterward excess $\text{SO}_4^{2-}/\text{HSO}_4^-$ solution was loaded on them. When visualized under a hand-held 365 nm UV light, prominent fluorescence variations were perceptible.

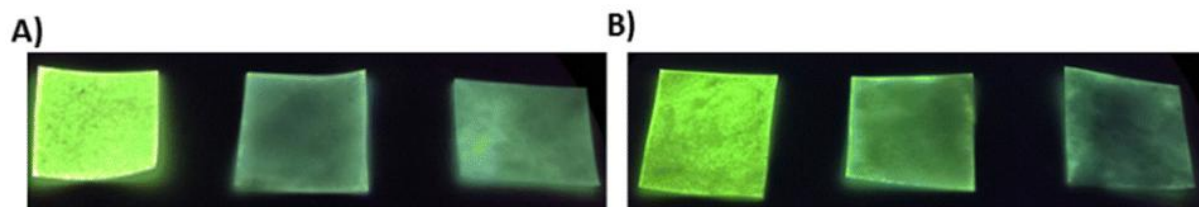


Figure 4.11: Photographs of the test strips under a UV lamp (irradiation of 365 nm) for visual detection of both A) **R1** and B) **R2** in the presence and absence of $\text{SO}_4^{2-}/\text{HSO}_4^-$

4.4. Conclusion

In a nutshell, we have systematically studied the consequences of varying terminal substituents on the aggregation as well as the sensing properties of two benzimidazole-based urea derivatives through spectroscopic as well as microscopic analysis. Based on the outcomes, it can be concluded that tailoring functional groups within the molecular framework can provide contrasting aggregation and sensing behaviour. The incorporation of the naphthyl group in **R1** led to the formation of an emissive aggregated state while **R2** with a cyanophenyl group formed an aggregated state with weakly emissive properties. Both the receptors displayed the potential of sensing highly hydrated $\text{SO}_4^{2-}/\text{HSO}_4^-$ in 100% aqueous medium, although differing in their binding constant values. Theoretical investigation through DFT reveals the prohibition of ICT as well as the facilitation of PET as the probable mechanism of sensing. The easily synthesized model paper strips have been utilized to demonstrate real-life applications of the receptors via the detection of $\text{SO}_4^{2-}/\text{HSO}_4^-$.

References

- [4.1] J. Wu, C. Li, Q. Chen and J. Zhao, *Dyes Pigm.*, 2021, **195**, 109709.
- [4.2] N. Kaur, G. Kaur, U. A. Fegade, A. Singh, S. K. Sahoo, A. S. Kuwar and N. Singh, *Trends Anal. Chem.*, 2017, **95**, 86-109.
- [4.3] F. Li, J. H. Wang, F. Wang and Y. B. Jiang, *Chem. Soc. Rev.*, 2010, **39**, 3729-3745.
- [4.4] P. A. Gale and C. Caltagirone, *Chem. Soc. Rev.*, 2015, **44**, 4212.
- [4.5] C. Caltagirone and P. A. Gale, *Chem. Soc. Rev.*, 2009, **38**, 520-563.
- [4.6] P. A. Gale, S. E. G. Garrido and J. Garric, *Chem. Soc. Rev.*, 2008, **37**, 15-190.

- [4.7] T. Gunnlaugsson, P. E. Kruger, P. Jensen, J. Tierney, H. D. P. Ali and G. M. Hussey, *J. Org. Chem.*, 2005, **70**, 10875-10878.
- [4.8] A. Borissov, I. Marques, J. Y. C. Lim, V. Fe'lix, M. D. Smith and P. D. Beer, *J. Am. Chem. Soc.*, 2019, **141**, 4119-4129.
- [4.9] F. P. Schmidtchen, *Angew. Chem., Int. Ed. Engl.*, 1977, **16**, 720-721.
- [4.10] J. M. Lehn, *Pure Appl. Chem.*, 1978, **50**, 871-892.
- [4.11] B. Dietrich, D. L. Fyles, T. M. Fyles and J. M. Lehn, *Helv. Chim. Acta*, 1979, **62**, 2763-2787
- [4.12] M. W. Hosseini and J. M. Lehn, *Helv. Chim. Acta*, 1988, **71**, 749-756.
- [4.13] I. Alfonso, B. Dietrich, F. Rebolledo, V. Gotor and J. M. Lehn, *Helv. Chim. Acta*, 2001, **84**, 280-295.
- [4.14] F. P. Schmidtchen and M. Berger, *Chem. Rev.*, 1997, **97**, 1609-1646.
- [4.15] F. P. Schmidtchen, *Chem. Soc. Rev.*, 2010, **39**, 3916-3935.
- [4.16] S. Kubik, R. Kirchner, D. Nolting and J. Seidel, *J. Am. Chem. Soc.*, 2002, **124**, 12752-12760.,
- [4.17] A. Schaly, R. Belda, E. G. Espan˜a and S. Kubik, *Org. Lett.*, 2013, **15**, 6238-6241.
- [4.18] V. Havel, J. Svec, M. Wimmerova, M. Dusek, M. Pojarova and V. Sindelar, *Org. Lett.*, 2011, **13**, 4000-4003.
- [4.19] M. A. Yawer, V. Havel and V. Sindelar, *Angew. Chem., Int. Ed.*, 2015, **54**, 276-279.
- [4.20] M. Lisbjerg, B. E. Nielsen, B. O. Milhøj, S. P. A. Sauer and M. Pittelkow, *Org. Biomol. Chem.*, 2015, **13**, 369-373.
- [4.21] M. Lisbjerg, H. Valkenier, B. M. Jessen, H. Al-Kerdi, A. P. Davis and M. Pittelkow, *J. Am. Chem. Soc.*, 2015, **137**, 4948-4951.
- [4.22] J. Suk, M. K. Chae and K. S. Jeong, *Pure Chem. Appl.*, 2012, **84**, 953-964.
- [4.23] U. Marzocchi and N. P. Revsbech, *Limnol. Oceanogr.:Methods*, 2022, **20**, 674-681.
- [4.24] Y. C. He, Y. M. Yan, H. B. Tong, Z. X. Ren, J. H. Wang, Y. B. Zhang, J. B. Chao and M. L. Wang, *Chem. Commun.*, 2020, **56**, 9364.
- [4.25] D. Markovich, *Phys. Rev.*, 2001, **81**, 1499.
- [4.26] M. A. Mintzer and M. W. Grinstaff, *Chem. Soc. Rev.*, 2011, **40**, 173-190.
- [4.27] J. Luo, Z. Xie, J. W. Lam, L. Cheng, H. Chen, C. Qiu, H. S. Kwok, X. Zhan, Y. Liu, D. Zhu and B. Z. Tang, *Chem. Commun.*, 2001, 1740-1741.
- [4.28] D. D. La, S. V. Bhosale, L. A. Jones and S. V. Bhosale, *ACS Appl. Mater. Interfaces*, 2018, **10**, 12189-12216.
- [4.29] G. Qian, Z. Zhong, M. Luo, D. Yu, Z. Zhang, Z. Y. Wang and D. Ma, *Adv. Mater.*, 2009, **21**, 111-116.
- [4.30] J. Luo, Z. Xie, J. W. Y. Lam, L. Cheng, B. Z. Tang and H. Chen, *Chem. Commun.*, 2001, 1740-1741.
- [4.31] C. Ma, Z. Li, C. Zhang, G. Xie, Y. Wu, Y. Zhang, J. Mo, X. Liu, K. Wang, D. Xie and Y. Li, *Front. Chem.*, 2021, **9**, 727631.
- [4.32] Y. Hong, J. W. Y. Lam and B. Z. Tang, *Chem. Soc. Rev.*, 2011, **40**, 5361-5388.
- [4.33] C. Zhu, R. T. K. Kwok, J. W. Y. Lam and B. Z. Tang, *ACS Appl. Bio Mater.*, 2018, **1**, 1768-1786.
- [4.34] L. Zong, Y. Xie, C. Wang, J. R. Li, Q. Li and Z. Li, *Chem. Commun.*, 2016, **52**, 11496-11499.
- [4.35] S. Halder, S. Samanta and G. Das, *Analyst*, 2019, **144**, 2696-2703.
- [4.36] S. Halder, U. Manna and G. Das, *New J. Chem.*, 2019, **43**, 14112-14119.
- [4.37] S. Halder, B. Nayak, B. Bhattacharjee, A. Ramesh and G. Das, *J. Mater. Chem. C*, 2021, **9**, 8596-8605.

Annexure 4

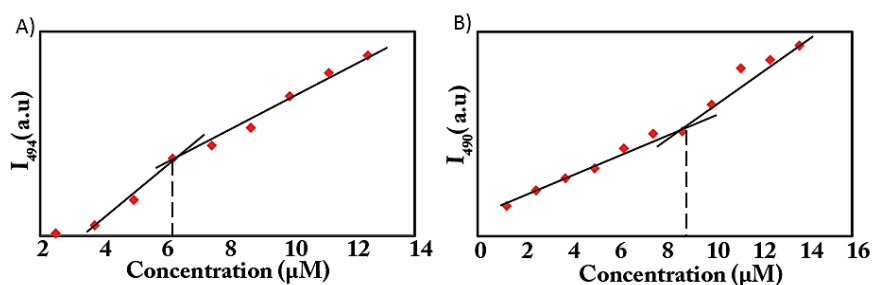


Figure A4.1: Critical aggregation constant of A) R1 and B) R2.

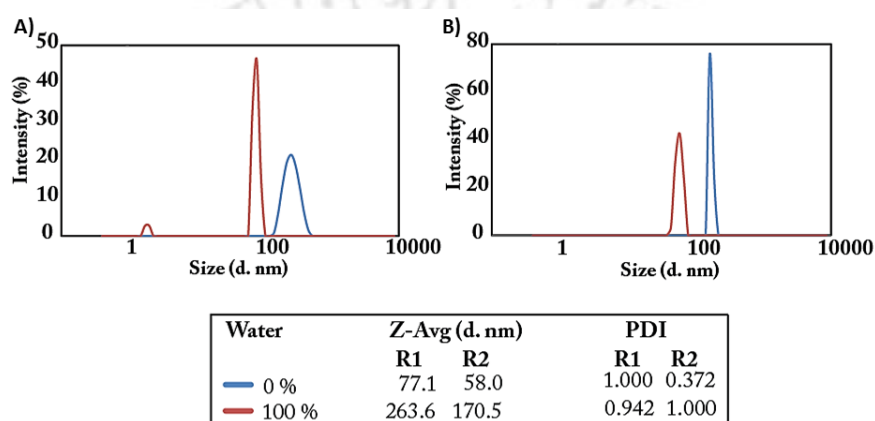


Figure A4.2: DLS output of A) R1 and B) R2.

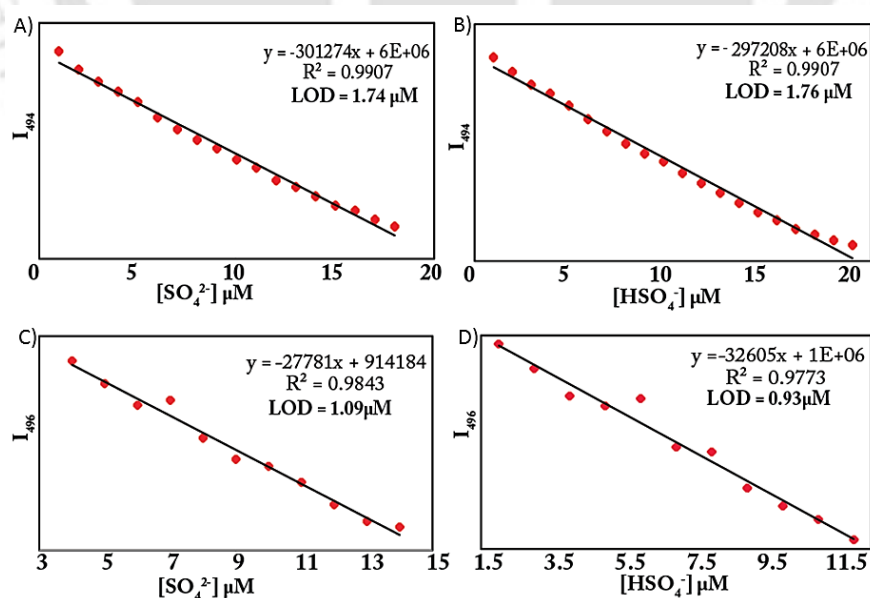


Figure A4.3: Fluorescence emission intensity of A) R1 at 494 nm vs. SO_4^{2-} concentration B) R1 at 494 nm vs. HSO_4^- concentration C) R2 at 490 nm vs. SO_4^{2-} concentration D) R2 at 490 nm vs. HSO_4^- concentration to calculate the limit of detection (LOD).

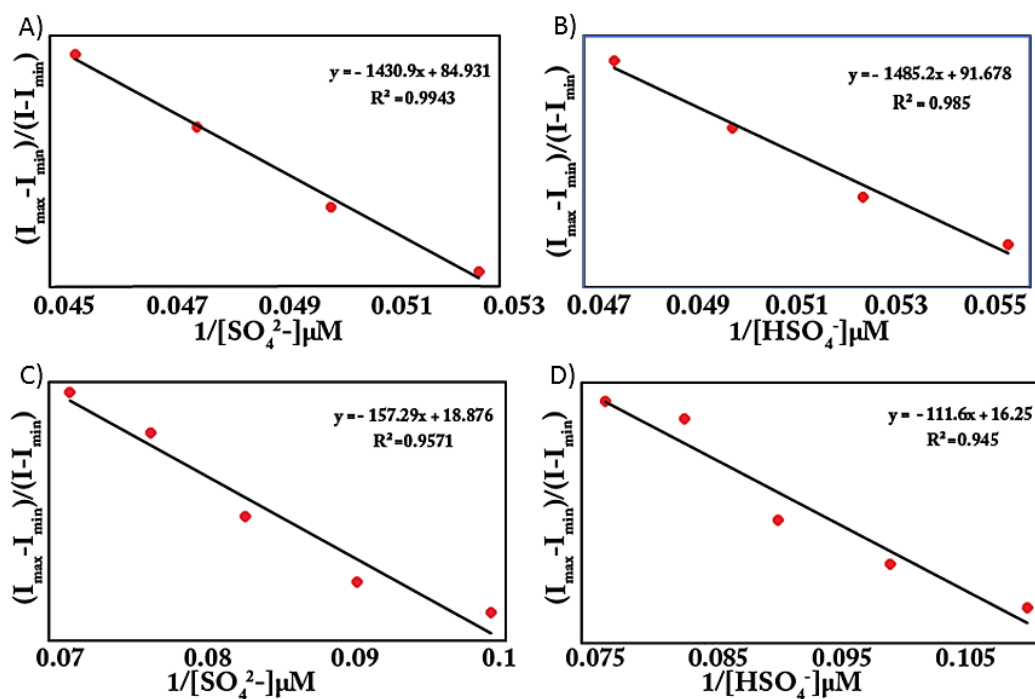


Figure A4.4: Benesi-Hildebrand plot for determination of binding constant of A) R1 and SO_4^{2-} , B) R1 and HSO_4^- , C) R2 and SO_4^{2-} , D) R2 and HSO_4^- .

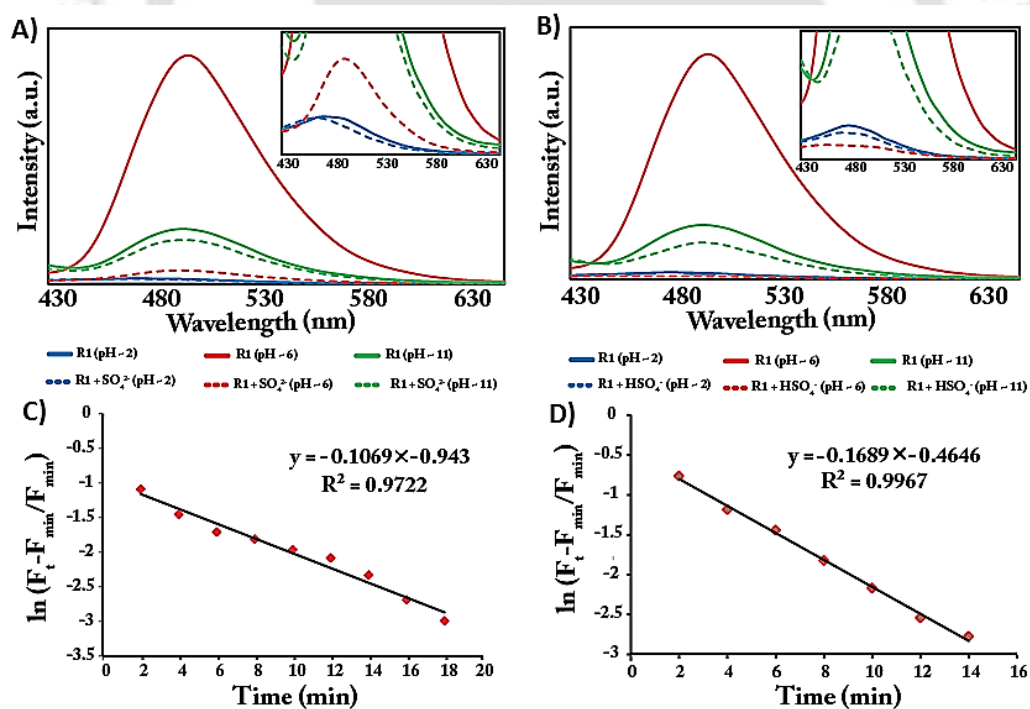


Figure A4.5: Fluorescence response of the probe R1 (10 μM) in the absence or presence of A) SO_4^{2-} , B) HSO_4^- (100 μM) upon variation of pH in experimental solution and Fluorescence intensity vs time (min), plotted using the first-order rate equation for R1 recorded at 494 nm in presence of C) SO_4^{2-} , D) HSO_4^- (10 μM).

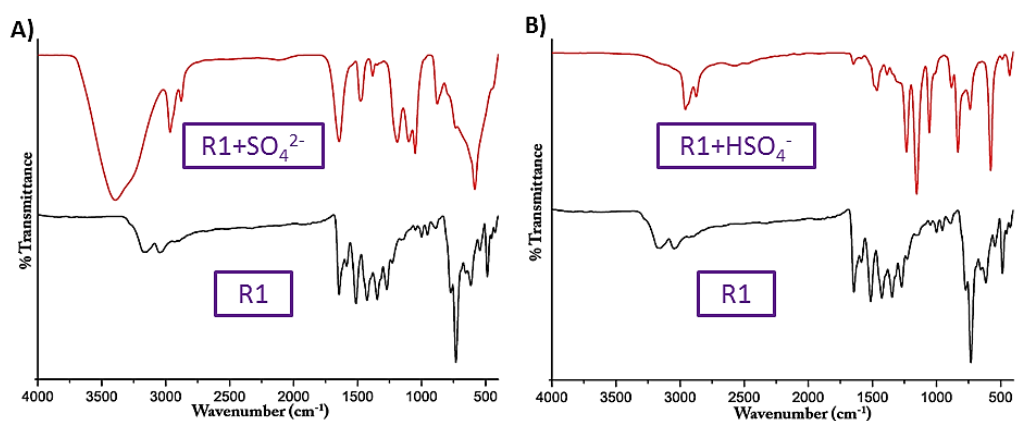


Figure A4.6: Comparison of FT-IR spectra of A) R1 and R1+ SO₄²⁻, B) R1 and R1+ HSO₄⁻.

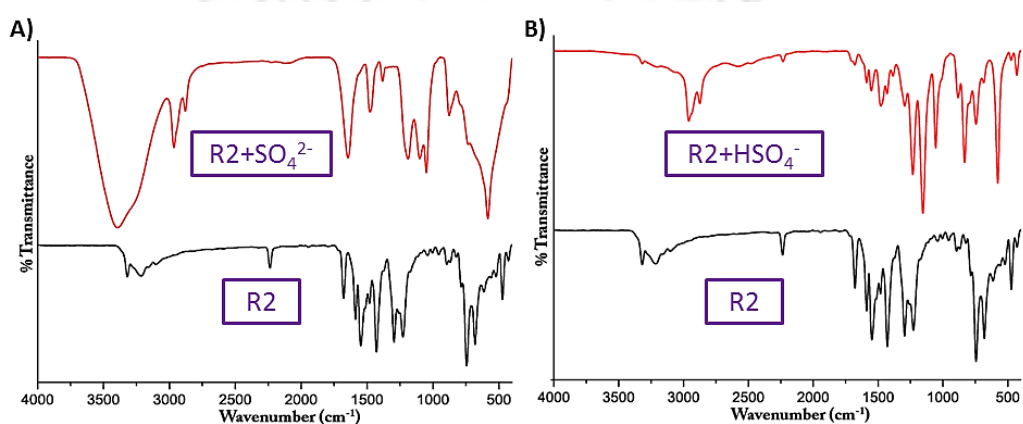


Figure A4.7: Comparison of FT-IR spectra of A) R2 and R2+ SO₄²⁻, B) R2 and R2+ HSO₄⁻.

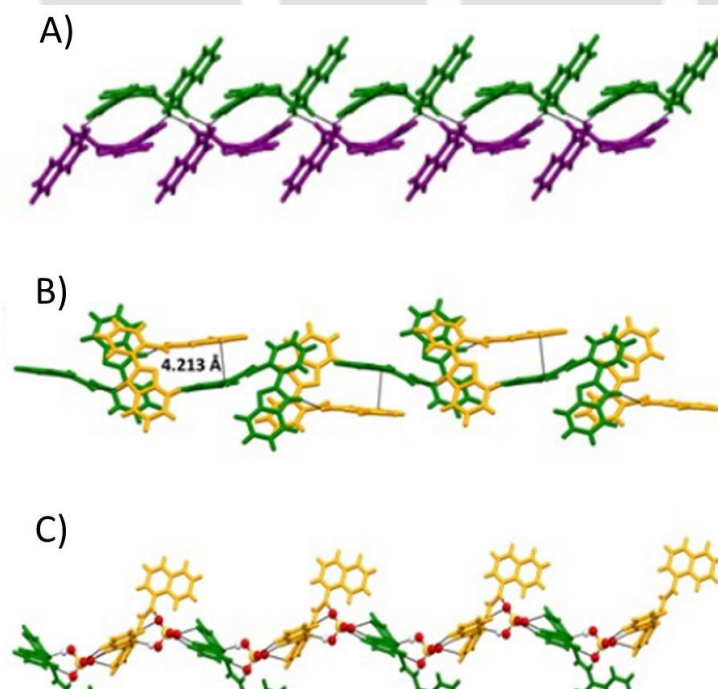


Figure A4.8: Self-assembled architecture of A) receptor R1, B) receptor R2, and c) complex R1.HSO₄.

Table A4.1: A representative comparison of the detection limits and binding constant values along with the receptor and solvent system used for the detection of $\text{SO}_4^{2-}/\text{HSO}_4^-$.

Sl. no.	References	Receptors	Solvent system	LOD (μM)	Binding Constant (M^{-1})
1.	Present work	neutral benzimidazole based urea receptors	100% water	1.74/1.76 and 1.09/0.93	$14.31 \times 10^8 / 14.85 \times 10^8$ and $1.57 \times 10^8 / 1.12 \times 10^8$
2.	Chemical Communications, 2009, 7128-7130	coumarin-based derivative	aqueous solution	3.75	4.86×10^4
3.	Organic letters, 2011, 13, 24, 6432–6435	bisferrocene-benzobisimidazole triad	Ethanol	6.58	3.95×10^5
4.	Analytical Methods, 2014,6, 9030-9036	Fluorescent organic nanoparticles of tripodal receptor	Aqueous medium	1.12	6.68×10^7
5.	RSC Advances, 2015, 5, 50532	copper(II) complex of quinazoline based ligand	water : DMSO (9 : 1, v/v)	3.18×10^{-1}	1.4×10^5
6.	Spectrochimica Acta Part A: Molecular and Biomolecular Spectroscopy, 2017, 180, 44–50	rhodamine 6G hydrazide receptor	Methanol	3.72	5353
7.	Journal of Photochemistry & Photobiology A: Chemistry 2019, 376, 146–154	oxindole-based probes	$\text{CH}_3\text{CN}/\text{H}_2\text{O}$ (7:3:v:v)	8.9	1.21×10^5
8.	Spectrochimica Acta Part A: Molecular and Biomolecular Spectroscopy, 2019, 213, 73–82	Azaindole-BODIPYs	acetonitrile	75.6 and 44.27	1.87×10^5 and 6.13×10^5
9.	Inorganica Chimica Acta, 2020, 511, 119794	dinuclear Zn (II) complex	3:2 v/v MeOH/water in HEPES buffer	Not reported	1.85×10^5
10.	New Journal of Chemistry, 2022,46, 18973-18983	diindolylarylmethane (DIAM)-based probes	Aqueous medium	6.2 ppb	Not reported

Table A4.2: Crystallographic parameters and refinement data of the free receptors and the anionic complex.

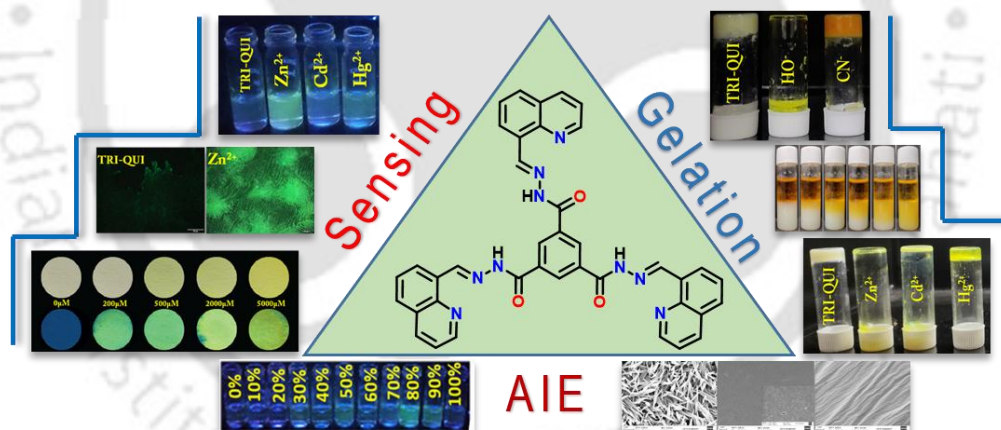
Parameters	R1	R2	R1.HSO ₄
formula	C ₂₄ H ₁₈ N ₄ O	C ₂₁ H ₁₅ N ₅ O	C ₄₀ H ₅₅ N ₅ O ₅ S
fw	378.42	353.38	717.95
cryst syst	triclinic	orthorhombic	orthorhombic
space group	P -1	P 21 21 21	P c a 21
a (Å)	7.602(2)	16.878(9)	18.1980(14)
b (Å)	10.285(3)	24.478(13)	11.6386(9)
c (Å)	12.821(4)	8.566(5)	18.3823(14)
α (deg)	88.415(8)	90	90
β (deg)	87.473(8)	90	90
γ (deg)	73.566(8)	90	90
V (Å ³)	960.4(5)	3539(3)	3893.4(5)
Z	2	8	4
DC (g cm ⁻³)	1.309	1.326	1.225
μ (Mo Kα) (mm ⁻¹)	0.083	0.086	0.132
F (000)	396.0	1472.0	1544.0
T (K)	296 K	297 K	295 K
θ _{max} (deg)	24.995	24.995	24.999
total no. of rflns	16242	51084	99620
no. of indep rflns	3333	6226	6855
no. of obsd rflns	2818	4974	5128
no. of params refined	266	495	472
R1, I > 2σ(I)	0.0413(2818)	0.0809(4974)	0.0628(5128)
wR2, I > 2σ(I)	0.1553(3333)	0.2132(6226)	0.1875(6855)
GOF (F ²)	1.149	1.074	1.165
CCDC no.	2285005	2285016	2285018

Table A4.3: Hydrogen bonding distances (Å) and Bond angles (°) in the neutral receptors and the anionic complex.

Ligand/Complex	D-H...A	d(D...H)/Å	d(H...A)/Å	d(D...A)/Å	<D-H...A/°	Symmetry codes
R1	N1-H1N...O1	0.99 (2)	1.88 (2)	2.8621 (19)	176.1 (19)	-x, 1-y, 1-z
	N3-H3N...N2	0.86	2.29	2.7834 (19)	117	x, y, z
	N4-H4N...O1	0.86	2.05	2.8716 (18)	160	-x, 2-y, 1-z
	C12-H12...O1	0.93	2.59	2.898 (2)	100	x, y, z
	C21-H21...N4	0.93	2.55	2.871 (2)	100	x, y, z
R2	N1-H1N...O2	1.04 (12)	1.98 (12)	2.901 (9)	145 (9)	x, y, z
	N3-H3N...N2	0.86	2.22	2.787 (9)	124	x, y, z
	N4-H4N...N5	0.86	2.24	3.087 (9)	170	x, y, 1+z
	N6-H6N...O1	0.94 (5)	2.00 (5)	2.886 (9)	157 (4)	x, y, z
	N8-H8N...N7	0.86	2.21	2.734 (9)	119	x, y, z
	N9-H9N...N10	0.86	2.15	2.995 (9)	167	x, y, -1+z
	C12-H12...O1	0.93	2.49	2.896 (9)	107	x, y, z
	C16-H16...O1	0.93	2.20	2.802 (9)	122	x, y, z
	C30-H30...N6	0.93	2.60	2.909 (11)	100	x, y, z
	C33-H33...O2	0.93	2.53	2.898 (9)	104	x, y, z
	C41-H41...O2	0.93	2.35	2.870 (9)	115	x, y, z
R1.HSO₄	N1-H1N...O3	0.76 (7)	2.04 (7)	2.796 (8)	172 (6)	x, y, z
	O2-H2O...N2	0.78 (9)	1.88 (9)	2.661 (8)	177 (9)	1/2-x, y, -1/2+z
	N3-H3N...N2	0.86	2.26	2.892 (7)	131	x, y, z
	N3-H3N...O4	0.86	2.58	3.316 (7)	144	1/2-x, y, 1/2+z
	N4-H4N...O4	0.86	2.05	2.901 (7)	170	1/2-x, y, 1/2+z
	C1-H1...O5	0.93	2.51	3.342 (9)	149	x, y, z
	C12-H12...O1	0.93	2.34	2.851 (9)	114	x, y, z
	C16-H16...O1	0.93	2.53	2.915 (8)	105	x, y, z
	C21-H21...N4	0.93	2.58	2.883 (9)	100	x, y, z
	C23-H23...O1	0.93	2.56	3.448 (8)	159	-x, -y, 1/2+z
	C34-H34B...O1	0.97	2.54	3.464 (11)	159	-x, -y, -1/2+z

Chapter 5

Tripodal acylhydrazone-based probe for turn-on Zn^{2+} sensing in HEPES buffer: investigation of gelation and AIE property



5.1. Background and Focus of the Chapter

Self-assembly is a ubiquitous process in nature leading to the formation of highly functional complex macromolecular systems, exploiting supramolecular interactions from monomeric building blocks, which are crucial for life [5.1-5.2]. Inspired by these sophisticated macro/nanostructures, materials scientists have developed synthetic supramolecular self-assembled functional systems promising for drug delivery, development of optoelectronic devices, environmental remediation, and detection of important analytes via fast response to external stimuli [5.3]. Organic small molecular receptors capable of forming self-assembled supramolecules are particularly exciting for their astonishing photophysical properties [5.4]. Although the commonly observed aggregation-caused quenching (ACQ) of organic luminophores limits their practical applications, the emergence of aggregation-induced emission (AIE) phenomena by Tang's research team in 2001 [5.5] has enabled one to utilize the aggregation process to foster light emission [5.6], thus paving the way for important developments in luminogen research. Nevertheless, suitable strategies and appropriate selection of luminophores as well as substituents are pivotal for designing an AIE system [5.7]. Moreover, over the last two decades, the evolution of supramolecular self-assembled systems and the development of sensing strategies have facilitated the creation of excellent multifunctional sensing platforms for sensing metal cations, anions, neutral molecules, etc. [5.8] Particularly, fluorescence sensing technology has gained extensive attention due to its quick response, cost efficiency, easy sample preparation, visualization, and high sensitivity [5.9]. Moreover the molecular self-assembly leading to supramolecular gel formation by specific low-molecular-weight gelators (LMWGs) have drawn immense research interest in recent years owing to their promising applications in diverse areas like chemosensors, drug delivery, biomaterials, biosensors, tissue engineering, hybrid functional materials, etc.[5.10-5.12] Because of the weak non-covalent interaction driven self-assembly formation, these soft materials are extremely sensitive to external stimuli, including pH, light, ions, redox agents, etc.[5.13] Such responsive systems, for example, metal ion/anion recognition, are highly advantageous for the development of sensor devices [5.14].

Detection of transition metals via fluorescence technique is an active area of research as they can have acute biological effects on animals and the environment even at extremely low concentrations [5.15]. In this regard, sensing of Zn^{2+} has attracted a great deal of attention [5.16-5.17] as it is the

second most abundant element in the human body, after iron, and plays various key roles in biological systems, including neural signal transmission [5.18], enzyme regulation [5.19], apoptosis [5.20], and gene transcription [5.21]. The imbalance of Zn^{2+} may lead to adverse effects, viz. night blindness, weight loss, emotional disturbance, elevated blood ammonia levels, and less growth in the human body [5.22]. Furthermore, Cd^{2+} and Hg^{2+} ions in the same group of the periodic table as Zn^{2+} often exhibit a similar fluorescence response to Zn^{2+} [5.23]. and the detection of these metal ions is also important as exposure of an individual to cadmium exerts toxic effects on the kidneys, the skeletal system and the respiratory system and cadmium is classified as a human carcinogen [5.24]., while mercury poisoning can cause serious damage to the brain, kidneys, and nervous system [5.25].

Application of 8-aminoquinoline derivatives in the detection of metal ions, especially zinc ions, has been well reported in the literature as they are exciting compounds with low initial fluorescence and they can show enhanced fluorescence emission upon interaction with metal ions when chosen as fluorophores [5.26-5.28]. A few years back, Ghosh et al. [5.29] designed a quinoline-based C_3 -symmetric fluorescent probe that can selectively detect Zn^{2+} in a 50% aqueous buffer (10 mM HEPES, pH = 7.4) acetonitrile medium. Song et al. [5.30] reported the synthesis of a novel quinoline-based acyl hydrazone probe for selective sensing of Zn^{2+} in DMSO. Recently, Li et al. [5.31] synthesized a quinoline-based fluorescent probe for selective and sensitive detection of Zn^{2+} in DMSO/HEPES buffer solution (v/v = 3/2, HEPES, 10 mM, pH 7.4). On the other hand, the C_3 -symmetric acylhydrazone-derived building block has aroused great interest as an ideal block in the formation of supramolecular LMWGs over the past decade [5.32-5.33]. C_3 -symmetric geometry makes them particularly efficient for triggering the self-assembly of molecular units into supramolecular gels; also, the acylhydrazone groups may act as anion recognition sites [5.34].

Our continuous attempt to prepare solid/solution state supramolecular self-assembled systems from small organic compounds and utilize their fascinating photophysical properties for different applications along with the chemosensing of metals/anions or neutral molecules [5.35-5.41] has led to the preparation of two C_3 -symmetric acylhydrazone based probes **TRI-QUI** and **TRI-NAP**, differing in the peripheral substitution. Both compounds have the same skeleton; however, **TRI-QUI** contains a quinoline group and **TRI-NAP** contains a naphthalene group at the periphery to investigate their difference in response to aggregation as well as sensing phenomena. The probes **TRI-QUI** and **TRI-NAP** can show fascinating aggregation properties in both solid and solution phases. Also, **TRI-QUI** containing a quinoline moiety in its structure exhibits a selective turn-on response towards Zn^{2+} in 0.1 M HEPES buffer (0.2% DMSO). **TRI-QUI** can not only self-assemble to form a supramolecular gel but also interact with metal ions/anions in the gel phase

with alterations in morphological behavior as evident from FESEM studies. Encapsulation of small molecules such as methyl orange and bromophenol blue has been successfully carried out, making them supramolecular gel-based multifunctional smart materials.

5.2. Objective of the Chapter

Two C_3 -symmetric acylhydrazone-based AIE active probes, **TRI-QUI** and **TRI-NAP**, were synthesized which differed in the peripheral substituents. The probe containing a quinoline moiety in the periphery displayed a selective turn-on response towards Zn^{2+} in HEPES buffer, with a calculated detection limit of 6.45 μM . The probe **TRI-QUI** was also recognized as a supergelator as it formed a gel in DMSO- H_2O (2:3, v/v) with a minimum gelation concentration of 0.5 mg mL^{-1} . The gelator could interact with various metal ions or anions in the gel phase. Furthermore, the gelator could encapsulate small molecules like methyl orange and bromophenol blue, making the probe a multifunctional smart material.

5.3. Results and discussion

5.3.1. Design of probes TRI-QUI and TRI-NAP

Probes **TRI-QUI** and **TRI-NAP** were designed to investigate the difference in response towards solution phase aggregation along with sensing of metal ions as well as towards supramolecular gelation as a consequence of structural change. We utilised the same acylhydrazone skeleton but altered the peripheral substituents by incorporating a quinoline moiety in **TRI-QUI** and a naphthalene moiety in **TRI-NAP**. The quinoline moiety, well known for its metal ion complexation properties, may help in selective solution phase sensing of metal ions coupled with the fact that tripodal building blocks can provide efficient coordination to a metal center. Both probes contain multiple potential hydrogen bond donor and acceptor sites which might be of great use in the supramolecular self-aggregation process for gelation and multiple coordination sites for anions/metal ions which can provide strong coordination interactions between metal ions/anions and acylhydrazone groups in the gel phase (Scheme 2.2.3 of chapter 2) [5.42-5.43].

5.3.2. Solid-state self-assembly of the probe TRI-QUI

The solid-state self-assembly behavior of **TRI-QUI** was investigated through SC-XRD analysis. **TRI-QUI** was observed to be involved in various non-covalent interactions such as hydrogen bonding interaction ($N-H\cdots O$, $C-H\cdots O$, $O-H\cdots N$, etc.), π - π stacking interaction, etc. Active participation of the acylhydrazone unit in the hydrogen bonding interaction along with the π - π stacking interaction between two nearby quinoline rings plays an indispensable part in the self-

assembly formation of **TRI-QUI**. Water molecules crystallize with **TRI-QUI**, which further helps in the cross-linking formation between two of the nearby **TRI-QUI** units through hydrogen bonding interactions, thus contributing extensively to solid-state self-assembly formation. **TRI-QUI** is slightly propeller-shaped as evident from SC-XRD structural analysis, and molecules with such characteristic shapes in the aggregated state are expected to possess some fascinating photophysical properties such as AIE behavior. Moreover, the three arms of **TRI-QUI** are observed to be involved in the three-dimensional network formation via various non-covalent interactions, mainly through hydrogen bonding interactions, which provided an opportunity to further explore its applicability as a soft functional material.

So, the solid-state study guided us to explore the different functionalities of **TRI-QUI**, which covers photophysical and soft functional material perspectives (Figure 5.1).

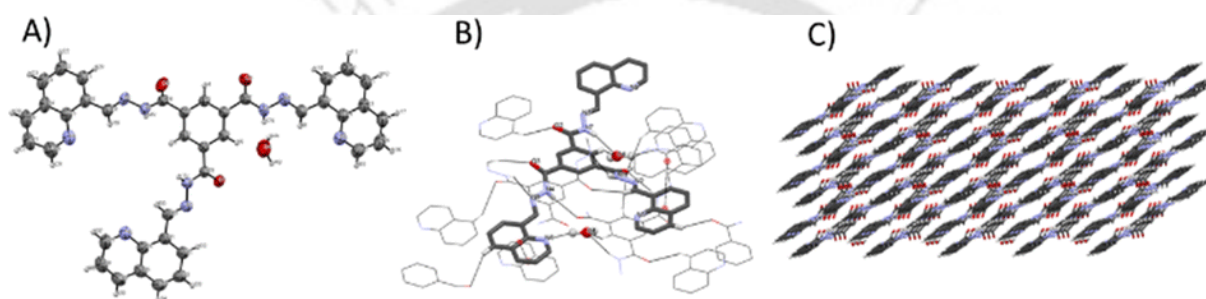


Figure 5.1: (A) ORTEP diagram of **TRI-QUI** at the 50% probability level, (B) ligand–ligand interactions through various non-covalent interactions, and (C) self-assembled packing pattern of **TRI-QUI**.

5.3.3. Exploring the self-aggregation potential of probes **TRI-QUI** and **TRI-NAP**

The photophysical properties of **TRI-QUI** and **TRI-NAP** were investigated by UV-Vis absorption and fluorescence emission studies in aqueous medium, 0.1 M HEPES buffer as well as in N, N-dimethylformamide (DMF) solvent. In UV-Vis spectra, the absorption behavior in water and 0.1 M HEPES remains the same for both probes, the absorption maxima being ~ 355 nm and ~ 350 nm for **TRI-QUI** and **TRI-NAP**, respectively, probably due to the π - π^* transition of the conjugated molecular backbone [5.32].

While in pure DMF a sharp absorption was observed at ~ 345 nm and ~ 340 nm, respectively, for **TRI-QUI** and **TRI-NAP**, a regular fall along with broadening and a bathochromic shift in the absorption spectra was observed with the gradual addition of water/HEPES buffer. We also observed an upliftment of the baseline with the increase in the water/HEPES buffer percentage for both cases. All these events support light scattering due to the formation of aggregates in water [5.44] [Figure 5.2 A and D]/HEPES buffer [Figure A5.1 A and D, Annexure 5].

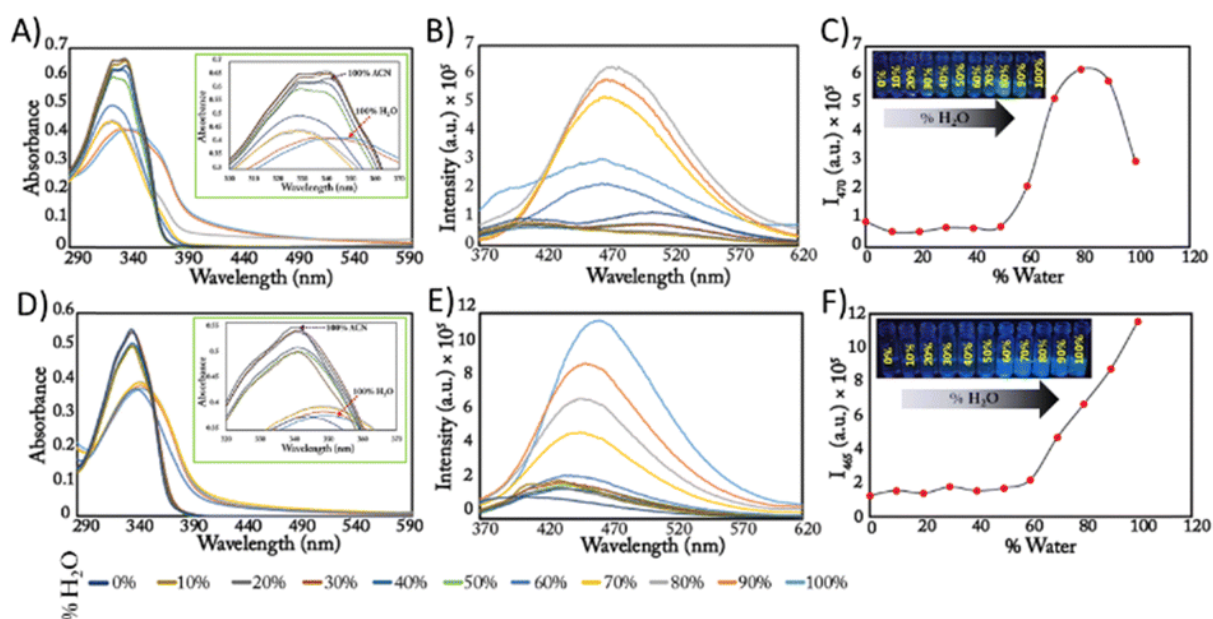


Figure 5.2: Absorption spectra of (A) **TRI-QUI** and (D) **TRI-NAP** in DMF and water (inset: enlarged view of the spectra). Emission spectroscopy with increasing water percentages in DMF of (B) **TRI-QUI** and (E) **TRI-NAP**. Plot of the percentage of water vs. emission intensity of (C) **TRI-QUI** and (F) **TRI-NAP** [inset: visual illustration of the AIE activity of **TRI-QUI** (20 μ M) and **TRI-NAP** (20 μ M) under a 365 nm UV lamp].

Both **TRI-QUI** and **TRI-NAP** were weakly emissive in pure DMF medium. However, the fluorescence emission intensity increases with the addition of the poor solvent water/HEPES buffer. The emission intensity was observed to be maximum at 80% water and HEPES buffer fractions for **TRI-QUI** with the respective \sim 7-fold and \sim 5-fold enhancements in emission intensity, while for **TRI-NAP** the highest emission intensity was observed at 100% water and HEPES buffer fractions with \sim 14-fold and \sim 18-fold increases in emission intensity, respectively, as compared to that of pure DMF [Figure 5.2 B, E and Figure A5.1, Annexure 5]. Hence, both probes are confirmed to be AIEgens. The aggregation-induced emission (AIE) behavior of the probes is probably owing to their propeller shape¹⁰ and π - π stacking interactions leading to the uniform aggregate formation and hence restricting intramolecular rotation (RIR), as evident from the crystal structure and DFT analysis of the probes (Fig. A5.1, Annexure 5). **TRI-QUI** displays a drop in the emission intensity for water fractions $>$ 80%, probably because aggregated matter show insolubility in higher aqueous fractions.⁴⁵ The increase in emission intensity in water was accompanied by a red shift of the spectra by \sim 30 nm for both cases suggesting a probability of aggregation [5.10]. The maximum emission intensities of the probes were also visualized through their colorimetric analysis of vial images under UV irradiation 365 nm; insets of Figure 5.2 C and F. The concentration-dependent fluorescence spectra of **TRI-QUI** and **TRI-NAP** also validated the formation of self-assembly in water and HEPES (Figure A5.3, Annexure 5) as evident from

the systematic growth of the emission intensity with an increase in concentration, which eventually broke abruptly, giving a critical aggregation constant (CAC) of each receptor at specific concentrations. The CAC was calculated to be $\sim 15 \mu\text{M}$ for both probes in water as well as in HEPES.

Field emission scanning electron microscopy (FESEM) and dynamic light scattering experiments were carried out to inquire further into the morphology and size of the aggregates. FESEM analysis revealed that dispersed small spherical-shaped particles of both probes in 100% DMF form larger aggregates in 80% H₂O for **TRI-QUI** [Figure 5.3 A and B] and in pure water for **TRI-NAP** [Figure 5.3 D and E]. The fluorescence microscopy images of **TRI-QUI** in 80% water fraction [Figure 5.3 C] and **TRI-NAP** in 100% water fraction [Figure 5.3 D] displayed bright green emission validating the formation of emissive aggregates in the respective water fractions. The DLS findings revealed the hydrodynamic radius of the respective aggregate in 80% and 100% water fractions to be 1303 nm and 155.9 nm for **TRI-QUI** and **TRI-NAP**, respectively (Figure A5.4, Annexure 5).

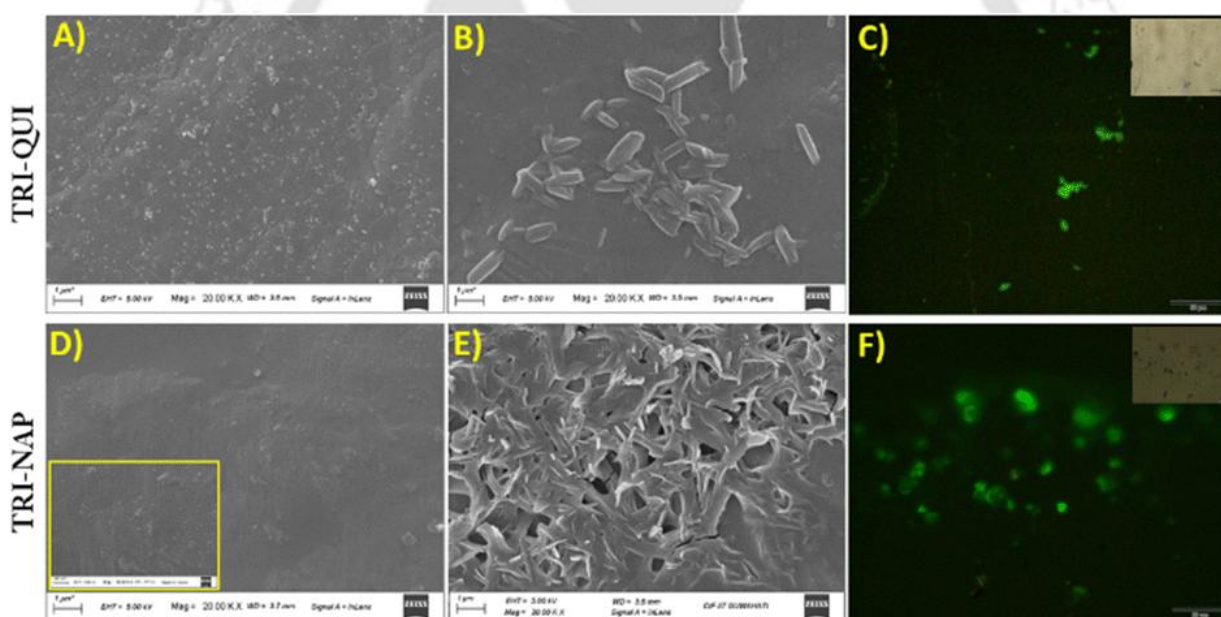


Figure 5.3: FESEM and fluorescence microscopy images of **TRI-QUI** (A) in 100% DMF and (B) and (C) in 80% water and of **TRI-NAP** (D) in 100% DMF, and (E) and (F) in 100% water.

5.3.4. Selective fluorescence turn-on response towards Zn^{2+}

Sensing of metal ions was performed in aqueous medium as well as in 0.1 M HEPES buffer. In aqueous medium, out of all selected cations, i.e. Zn^{2+} , Cd^{2+} , Hg^{2+} , Pb^{2+} , Cu^{2+} , Ni^{2+} , Co^{2+} , Fe^{2+} , Mn^{2+} , Cr^{3+} , Al^{3+} , Ag^+ (acetate salts of Zn^{2+} , Cd^{2+} , Ni^{2+} , and Mn^{2+} , chloride salts of Hg^{2+} , Cu^{2+} , Co^{2+} , and Cr^{3+} , nitrate salts of Pb^{2+} , Al^{3+} , and Ag^+ and sulfate salt of Fe^{2+}), a selective turn-on

response was observed only with Zn^{2+} and Cd^{2+} along with spectral shifts [Figure 5.4 A]. However, the selectivity increases in the HEPES buffer medium, where turn-on fluorescence response was observed only in the presence of Zn^{2+} [Figure 5.4 D]. In a pure aqueous medium, the weak fluorescence emission intensity of **TRI-QUI** was enhanced in the presence of Zn^{2+} . A noticeable ~ 4.5 -fold increase in the fluorescence intensity along with a significant ~ 40 nm red shift of the spectral peak position was observed. With Cd^{2+} , there was a ~ 3 -fold increase in the emission intensity along with a ~ 35 nm red shift in the spectral peak position. With Hg^{2+} , however, no turn-on response was perceived, although a ~ 40 nm red shift of the spectral peak position was observed. On the other hand, in 0.1 M HEPES buffer, the probe displayed more selectivity towards Zn^{2+} with a ~ 3 -fold increase in emission intensity along with a ~ 35 nm red shift of the spectral peak position. A slight red shift of 10 nm in the spectral peak position of the probe was observed with Cd^{2+} (Figure A5.5, Annexure 5). Also, only a shift in the spectral peak position of ~ 35 nm was observed with Hg^{2+} . The non-emissive nature of **TRI-QUI** in water/HEPES might be attributed to the photo-induced electron transfer (PET) process from the lone pair electrons of Schiff base nitrogen atoms to the quinoline rings [5.31]. Complexation with Zn^{2+} results in the chelation-induced enhanced fluorescence (CHEF) effect, thus suppressing or eliminating PET, thereby leading to a significant enhancement of fluorescence intensity [5.46-5.48]. The CHEF effect leads to turn-on fluorescence response in the presence of Zn^{2+} and Cd^{2+} ; however, alterations in the extent of the CHEF effect because of the difference in radius between Cd^{2+} (0.96 Å) and Zn^{2+} (0.74 Å) lead to a difference in fluorescence intensity. Also, the spin-orbit quenching mechanism associated with the heavy metals may lead to quenching of fluorescence intensity in the presence of Hg^{2+} [5.49]. The interference test was performed by adding 10 equivalents of Zn^{2+} ions to **TRI-QUI** in water as well as in HEPES in the presence of the same equivalents of other competing cations such as Cd^{2+} , Hg^{2+} , Pb^{2+} , Cu^{2+} , Ni^{2+} , Co^{2+} , Fe^{2+} , Mn^{2+} , Cr^{3+} , Al^{3+} and Ag^{+} in the aforementioned test solutions. Interference from Hg^{2+} , Cu^{2+} , Co^{2+} , and Fe^{2+} was observed in both water and HEPES which might be due to their strong quenching characteristics to fluorescence [5.31]. The reversibility of emission intensity of **TRI-QUI** was investigated by the addition of EDTA. The alternative addition of zinc and EDTA showed fluorescence turn-on or turn-off up to two cycles (Figure A5.6, Annexure 5). Titration experiments with increasing concentrations of Zn^{2+} , Cd^{2+} , and Hg^{2+} were also conducted in water and HEPES (Figure A5.7, Annexure 5). Incremental addition of Zn^{2+} and Cd^{2+} ions caused an orderly increase, while in the case of Hg^{2+} there was an orderly decrease of the fluorescence emission intensity of **TRI-QUI** until saturation was reached. The LOD value was estimated based on the intensity at 510 nm (Zn^{2+} and Hg^{2+}) and 505 nm (Cd^{2+}) (Table A5.2,

Annexure 5). The probe shows LOD values (Figure A5.8, Annexure 5) of 1.61 μM and 6.45 μM for the detection of Zn^{2+} in water and HEPES which is far below the World Health Organization guideline (76 μM).¹⁶ Although LOD values for Cd^{2+} and Hg^{2+} were found to be too high, it is comparable for Zn^{2+} with other quinoline-based fluorescent probes reported in the literature (Table A5.3, Annexure 5). Moreover, Job's plot in both water and HEPES exhibited a maximum at a 0.5 mol fraction for Zn^{2+} , Cd^{2+} , and Hg^{2+} indicating a 1:1 complex formation (Figure A5.7 and A5.8, Annexure 5). The red shifted emission spectra suggested complexation of **TRI-QUI** with Zn^{2+} , Cd^{2+} , and Hg^{2+} that led to ligand-to-metal charge transfer (LMCT) and a decreased ICT energy gap [5.50]. We recorded UV-Vis spectra as well for the sensing study of **TRI-QUI** in H_2O and HEPES with different metal ions, but no noticeable changes in the spectra were observed (Figure A5.9, Annexure 5).

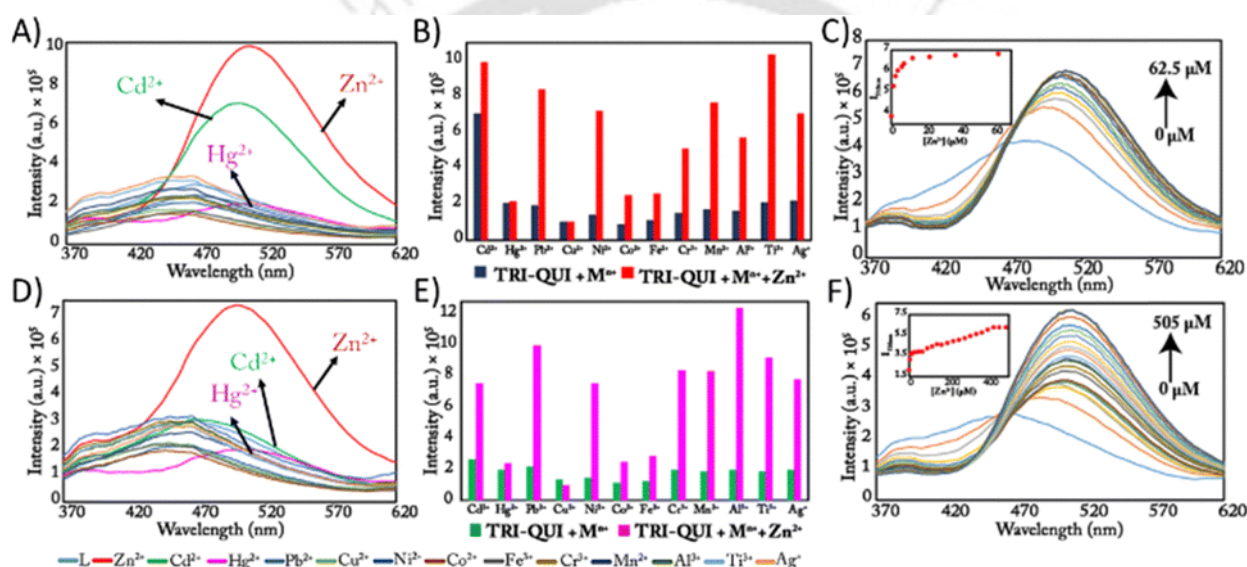


Figure 5.4: Fluorescence spectra ($\lambda_{\text{ex}} = 320 \text{ nm}$) of **TRI-QUI** (10 μM) in the presence of different metal ions (A) in water (0.2% DMSO) and (D) in HEPES (0.1 M); interference test of **TRI-QUI** in the presence of various competitive metal ions (100 μM) such as Cd^{2+} , Hg^{2+} , Pb^{2+} , Cu^{2+} , Ni^{2+} , Co^{2+} , Fe^{3+} , Mn^{2+} , Cr^{3+} , Al^{3+} , and Ag^+ along with Zn^{2+} (B) in water and (E) in HEPES (0.1 M). The blue/green bar indicates probe **TRI-QUI** + metal ions and the red/pink bar represents **TRI-QUI** + metal ions + Zn^{2+} ; emission intensity profiles depicting the titration of **TRI-QUI** with Zn^{2+} (C) in water and (F) in HEPES (0.1 M).

5.3.5. Microscopic study

FESEM measurements and fluorescence microscopic analyses were carried out to figure out if there was any kind of variation in the surface morphology of the probe **TRI-QUI** before and after the addition of Zn^{2+} , Cd^{2+} , and Hg^{2+} in water (Figure 5.5). The aggregated rice grain-like morphology of only the probe in 100% H_2O forms somewhat smaller cubic and spherical aggregates in the presence of Zn^{2+} , Cd^{2+} , and Hg^{2+} . Hence, FESEM results indicate metal

complexation induced smaller emissive aggregate formation. A clearer picture of the drop in particle size was obtained from the dynamic light scattering (DLS) experiment (Figure A5.10, Annexure 5), where the particle size of the aggregates of **TRI-QUI** in water ($Z_{\text{average}} = 828.9 \text{ nm}$) and HEPES ($Z_{\text{average}} = 907.2 \text{ nm}$) becomes somewhat smaller upon interaction with Zn^{2+} ($Z_{\text{average}} = 462.7 \text{ nm}$ and 641.7 nm in H_2O and HEPES, respectively), Cd^{2+} ($Z_{\text{average}} = 483.6 \text{ nm}$ in H_2O), and Hg^{2+} ($Z_{\text{average}} = 419.6 \text{ nm}$ and 509.9 nm in H_2O and HEPES, respectively).

Further, fluorescence microscopy imaging studies of **TRI-QUI** revealed intense green fluorescence in the presence of Zn^{2+} and Cd^{2+} in H_2O only in the presence of Zn^{2+} in HEPES correlating with the vial images where a bright greenish yellow emission of **TRI-QUI** was observed with Zn^{2+} and Cd^{2+} in H_2O and with only Zn^{2+} in HEPES among all tested metal ions (Figure A5.11, Annexure 5).

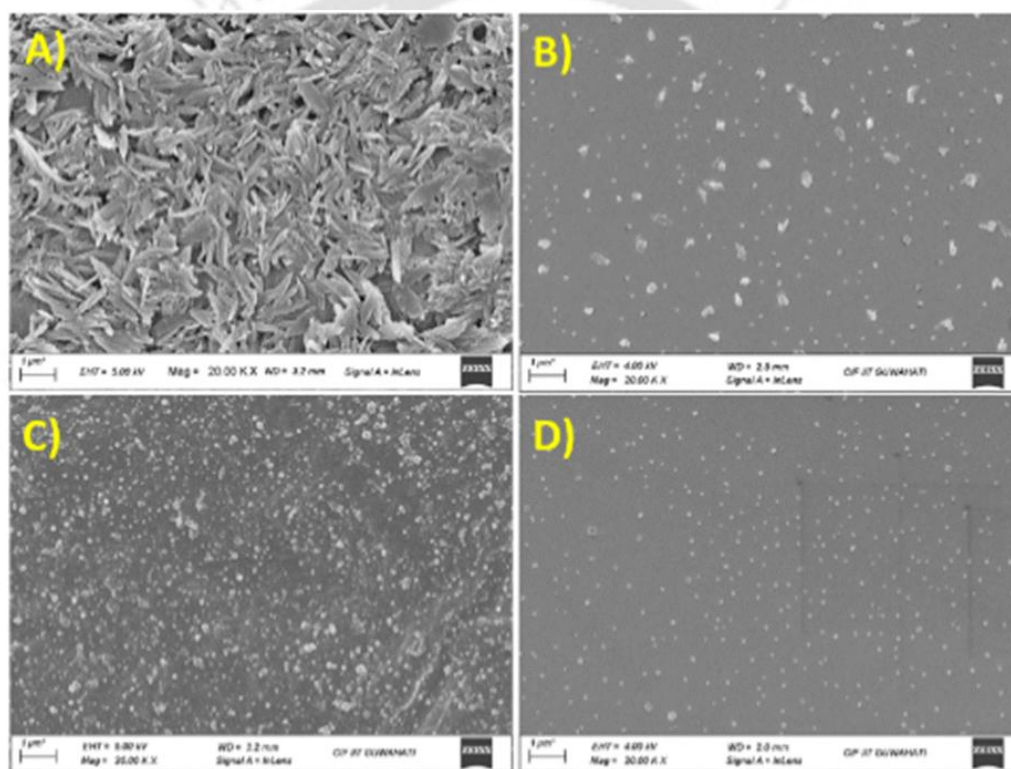


Figure 5.5: FESEM images of (A) **TRI-QUI**, (B) **TRI-QUI** + Zn^{2+} , (C) **TRI-QUI** + Cd^{2+} , and (D) **TRI-QUI** + Hg^{2+} in water.

5.3.6. Mechanism of sensing

To understand the mechanism of sensing, we performed ^1H NMR titration of **TRI-QUI** in the presence of $\text{Zn}(\text{OAc})_2 \cdot 2\text{H}_2\text{O}$ in $\text{DMSO}-d_6$. As shown in Figure 5.6, with the gradual addition of Zn^{2+} ions, the peak corresponding to the amide proton (a) at 12.47 ppm shifts downfield and disappears slowly, indicating that the amide $-\text{NH}-\text{C}(=\text{O})-$ is deprotonated and enolized to

coordinate with Zn^{2+} . The precipitation starts after the addition of 0.5 equiv. of Zn^{2+} in the process of NMR titration and the creamy white solution of the probe in $\text{DMSO-}d_6$ at the end of the titration turned bright yellow. The precipitate formation might be attributed to the complexation of the probe **TRI-QUI** with Zn^{2+} . Also, the NMR peak at 9.88 ppm corresponding to protons of the central benzene ring shifts downfield and broadens. No significant shift of the remaining peaks was observed. FT-IR spectral analysis of the probe in the presence of Zn^{2+} (Figure A5.12, Annexure 5) also showed that the bands at 3212 cm^{-1} correspond to an N–H frequency shift to a lower wavenumber (3061 cm^{-1}), while the C=O stretching frequency at 1644 cm^{-1} almost disappears suggesting strong interactions of these groups with Zn^{2+} . We also performed a pH-dependent fluorescence study (Figure A5.13, Annexure) of the probe **TRI-QUI** in the aqueous medium. **TRI-QUI** was found to be sensitive towards changes in the pH of the medium as, upon decreasing the pH value to as low as 2, the spectra showed a prominent red shift from 470 nm to 530 nm, suggesting the fact that, in the acidic medium, the quinoline nitrogen atoms get protonated, leading to a shift in the spectral peak position.

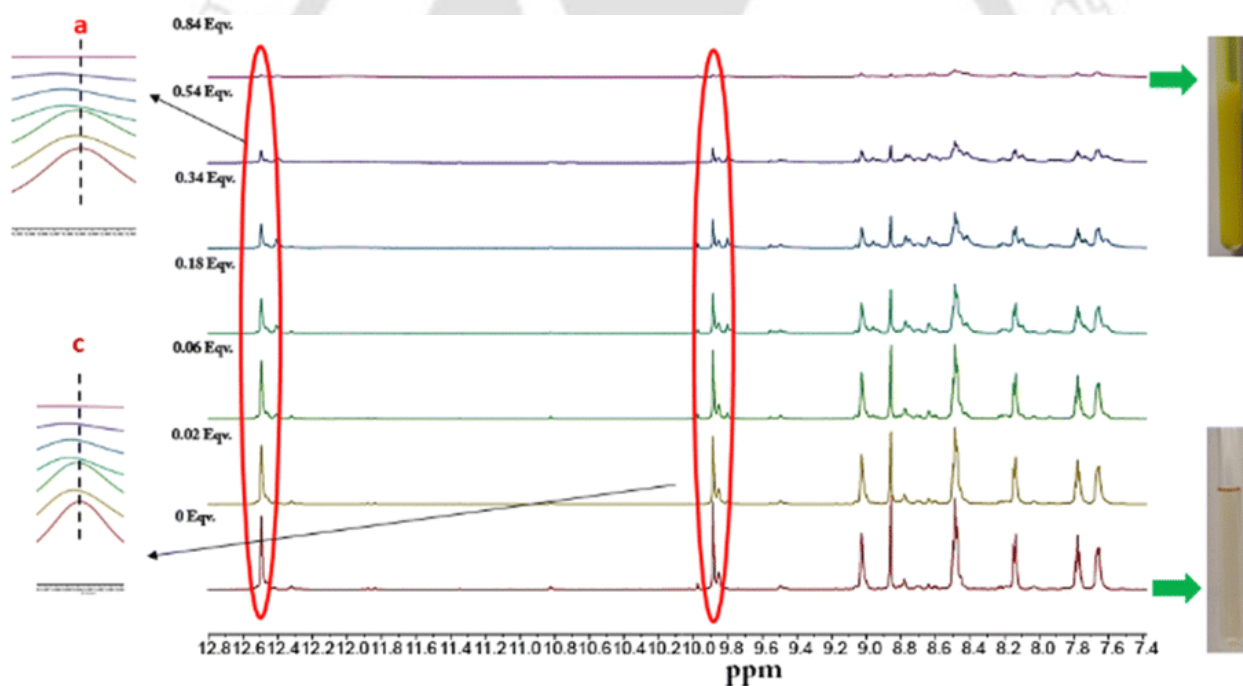


Figure 5.6: NMR titration of **TRI-QUI** with Zn^{2+} in $\text{DMSO-}d_6$.

Density functional theory (DFT) calculations were accomplished with the B3LYP/6-31G(d,p) basis set using the Gaussian 16 program while using water as a solvent through the CPCM solvent model to understand the mechanism of detection of Zn^{2+} (Figure A5.14, Annexure 5). The HOMO of **TRI-QUI** is distributed over the imine linkage as well as the quinoline ring, while the electron density in the case of the LUMO is also around the same region, suggesting the possibility of PET

phenomena occurring from imine N to the quinoline moiety which is well established in the literature [5.31]. In the case of coordination with Zn^{2+} , however, although the HOMO is over the quinoline ring and acylhydrazone part, in the LUMO there is a lower electron density on the quinoline moiety compared to the LUMO of **TRI-QUI**, and also a large part of electron density shifts towards Zn^{2+} , suggesting a combined process of the prevention of the PET and CHEF effects. The energy gap between the HOMO and LUMO also decreases in the **TRI-QUI**- Zn^{2+} complex (0.11 eV) compared to the probe **TRI-QUI** (0.14 eV), correlating well with the red shift of the fluorescence spectra of **TRI-QUI** in the presence of Zn^{2+} .

5.3.7. Applications

We investigated the real-world applicability of our designed probes towards Zn^{2+} sensing in real water samples as well as via paper strip experiments. **TRI-QUI** could be employed for Zn^{2+} detection in various natural water sources such as Milli-Q water, drinking water, and tap water (a red shift of 15 nm in the presence of Zn^{2+} ; Figure A5.15, Annexure 5). Turn-on fluorescence response along with a red shift in the spectra was observed with Zn^{2+} . Moreover, paper strip applications were performed to investigate the applicability of **TRI-QUI** for the detection of Zn^{2+} in the solid state. To investigate the same, we prepared test strips of the probe by immersing a few filter papers in the THF solution of **TRI-QUI** (10 μ M solution) for 15 min and then drying them in air. Various concentrations of Zn^{2+} ions spiked in Milli-Q water were applied onto the surface of the filter papers using capillary tubes; the greenish-yellow colour of the filter papers intensified with increasing concentrations of Zn^{2+} in the probe. This result demonstrates a prototype device using **TRI-QUI** for real-world application.

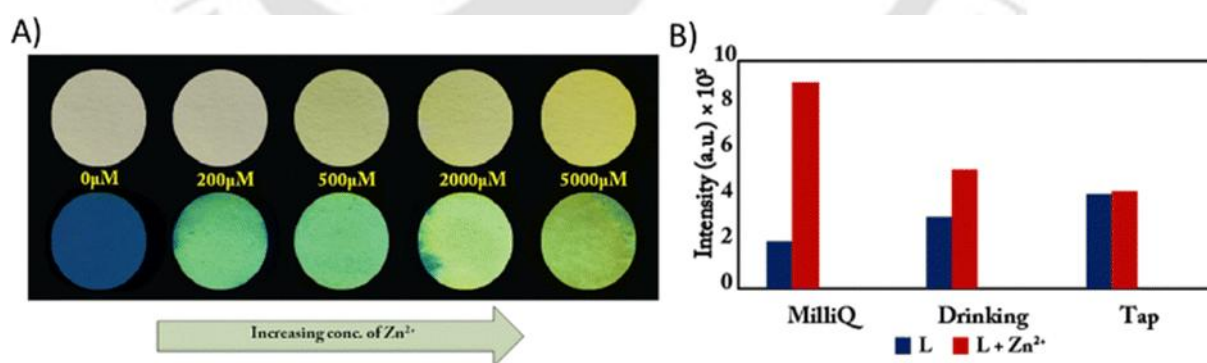


Figure 5.7: Zn^{2+} sensing by using paper strips loaded with **TRI-QUI** and (B) Zn^{2+} sensing in real-life water samples.

5.3.8. Interaction of **TRI-QUI** with anions in the solution phase

The anion binding properties of the probe **TRI-QUI** (10 μ M) in aqueous medium towards various biologically important anions such as F^- , Cl^- , Br^- , I^- , CN^- , OH^- , NO_3^- , SO_4^{2-} , HSO_4^- , AcO^- , $H_2PO_4^-$

and ClO_4^- (tetrabutylammonium salts) were also studied (Figure A5.16, Annexure 5). No distinguishable change in the presence of any anions was observed except CN^- and OH^- , with which a ~ 20 nm red shift of the spectra along with a slight turn-on in the emission intensity (~ 1.5 -fold increase with CN^- and ~ 1.3 -fold increase with OH^-) was observed probably due to deprotonation. We recorded the ^1H NMR spectrum of **TRI-QUI** (Figure A5.17, Annexure 5) in the presence of an excess amount of tetrabutyl-ammonium cyanide (TBACN). It was observed that the peak corresponding to the amide proton (a) at 12.47 ppm completely vanished, while all the remaining peaks shifted upfield except that the peak at 8.86 ppm corresponding to imine protons shifted slightly downfield.

We also investigated the sensing of metal cations and anions using the probe **TRI-NAP**. However, no sensing was observed by the probe in aqueous medium (Figure A5.18, Annexure 5).

5.3.9. Gelation properties of TRI-QUI

The gelation ability of **TRI-QUI** in a series of organic solvents and H_2O was systematically investigated via the typical 'inversion test' method. The probe **TRI-QUI** was not soluble in most of the organic solvents and was soluble in DMSO and DMF only. No gelation was observed for **TRI-QUI** in the organic solvents used in this work or water. Interestingly, **TRI-QUI** could form a gel in a DMSO: H_2O (2:3, v/v) mixture. A stable creamy white gel can be formed instantly with the rapid addition of water in the DMSO solution of the probe (5 mg mL^{-1}) without heating. However, the gel became transparent white as we decreased the concentration from 5 mg mL^{-1} to 0.5 mg mL^{-1} , and also it took about 3-4 hours for the formation of gel when the concentration was decreased to 0.5 mg mL^{-1} (Figure 5.8). The minimum gelation concentration of the gel was found to be as low as 0.5 mg mL^{-1} , appropriate to be termed a supergelator [5.13]. Below this concentration no gelation was observed. **TRI-QUI** could also form a gel in DMF- H_2O (2:3, v/v) mixed solvent. The gel-to-sol transition temperature (T_{gel}) of the **TRI-QUI** gel formed in DMSO- H_2O (2:3, v/v) increased from ~ 55 °C to ~ 75 °C as the **TRI-QUI** concentration increased from 0.5 mg mL^{-1} to 5 mg mL^{-1} . From the results of T_{gel} , a relatively high temperature (55 °C) was required for the gel to be converted into a solution even at the minimum gelation concentration (0.5 mg mL^{-1}), indicating that the prepared gel had good stability in a normal environment. The stable period for the **TRI-QUI** gel was found to be more than 1 month. Moreover, the ligand **TRI-NAP** was also tested for the gelation. Unlike **TRI-QUI**, the probe **TRI-NAP** could only form a gel at a very high concentration of 20 mg mL^{-1} only in a DMSO: H_2O (2: 3, v/v) mixture. It takes around 2-3 hours for the formation of gel in the case of **TRI-NAP**. This result is a clear indication

of the fact that the gelation abilities of gelators depend strongly on their molecular structures. Although both compounds contain acylhydrazone units, compared to **TRI-NAP**, **TRI-QUI** has more H-bond acceptor sites because of the quinoline N-atom which helps to induce self-assembly of the ligand **TRI-QUI** through H-bonding in the presence of water, along with π - π stacking between the benzene and quinoline moieties as evident from SC-XRD analysis. Therefore, the existing H-bonding in **TRI-NAP** is not enough for molecular gelation at low concentrations. Nevertheless, the presence of a naphthyl ring can induce π - π stacking providing gelation properties at high concentrations.

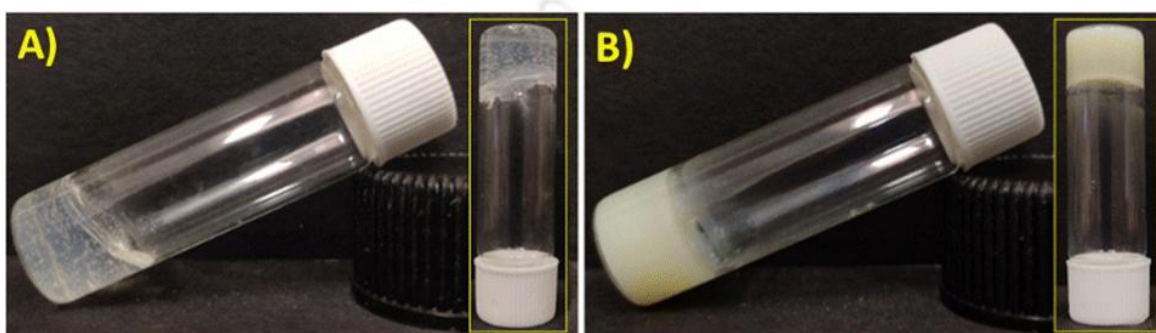


Figure 5.8: **TRI-QUI** forming a gel at a concentration of (A) 0.5 mg per mL and (B) 5 mg per mL in DMSO-H₂O (2: 3, v/v).

Furthermore, to analyze the ordered stacking in the gel of **TRI-QUI**, a powder X-ray diffraction (PXRD) study was performed. From Figure A5.19, Annexure 5, a peak at $2\theta = 10.66^\circ$ with a d-spacing value of 0.83 nm suggested diminished intermolecular distances.¹⁰ The peaks at $2\theta = 25.44$ and 26.69 with the d spacing values of 0.35 nm and 0.34 nm, respectively, indicated π - π stacking interactions between the aromatic rings.³² The spectra also showed two peaks at $2\theta = 21.02$ and 21.56 corresponding to the d spacing values of 0.42 nm and 0.41 nm, signifying a 2D network forming the assembly [5.51]. To further investigate the mechanism behind the gelation, we recorded the FT-IR spectra of the xerogel (Figure A5.20, Annexure 5) of **TRI-QUI** which shows that the crucial vibration peak for -NH stretching at a wavenumber of 3213 cm^{-1} shifts to a lower wavenumber of 3188 cm^{-1} , while the vibration peak at 1644 cm^{-1} for -C=O stretching broadens after gelation, indicating the network formation due to intermolecular hydrogen bonding interactions [5.32].

The driving force in the self-assembly process of **TRI-QUI** was also examined by ¹H NMR experiments (Figure A5.21, Annexure 5). With increasing content of D₂O in DMSO-*d*₆, the resonance signal corresponding to the amide proton (a) at 12.47 ppm shifted downfield to 12.48 ppm and broadened, which was ascribed to proton exchange [5.32]. All the remaining protons

including the protons of the aromatic regions shifted upfield, implying the presence of π -stacking between the molecules of **TRI-QUI** in the gel state [5.52]

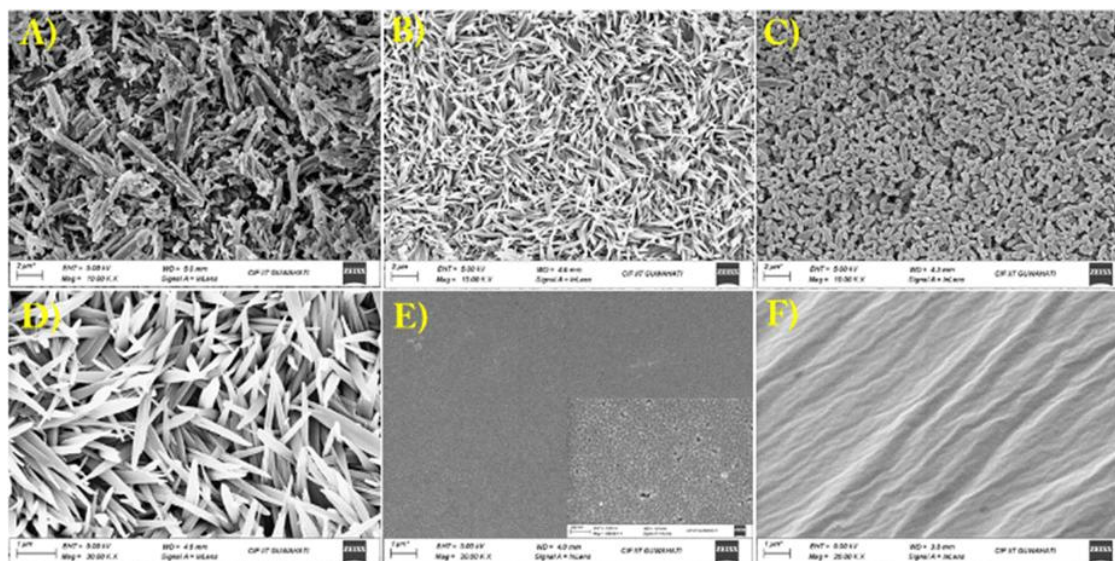


Figure 5.9: FESEM images of (A) **TRI-QUI** powder, (B) **TRI-QUI** xerogel obtained from DMSO-H₂O (2: 3, v/v), (C) **TRI-QUI** xerogel obtained from DMF-H₂O (2: 3, v/v), (D) magnified image of the **TRI-QUI** xerogel obtained from DMSO-H₂O (2: 3, v/v), (E) **TRI-QUI**+ Hg²⁺ xerogel obtained from DMSO-H₂O (2: 3, v/v), and (F) the **TRI-QUI**+ CN⁻ xerogel obtained from DMSO-H₂O (2: 3, v/v).

The variation in the morphology of the xerogels of **TRI-QUI** was investigated by FESEM analysis. As shown in Figure 5.9, when the xerogel of **TRI-QUI** formed in DMSO-H₂O (2: 3, v/v) was analyzed via FESEM, it was observed that the rod-like morphology of the powder form of **TRI-QUI** became grass-like and more compact. Also, the morphology of the xerogel of **TRI-QUI** formed in DMF-H₂O (2: 3, v/v) was distinctly different from that of the DMSO-H₂O (2: 3, v/v) xerogel, appearing like small rice grain-like structures, implying the solvent driven morphological alteration of the gel structures.

5.3.10. The effect of metal ions and anions in gel formation

The results obtained from solution state sensing of metals as well as anions by **TRI-QUI** prompted us to perform the sensing study in the gel phase as well. We tried to study the effect of the addition of metal ions in the process of gel formation (5 mg mL⁻¹ in 2: 3, v/v ratio of DMSO: H₂O). It was observed that the addition of 3 equivalents of metal ions other than Hg²⁺, Pb²⁺, Cr³⁺, Al³⁺, and Ag⁺ has a destructive effect on the gelation process (Figure A5.22, Annexure 5). However, the sensing result unlike in the solution phase was not selective. The FESEM images of the gel incorporated with 3 equivalents of Hg²⁺ and Ag⁺ showed complete alteration of the grass-like morphology of

the native gel to spheres of a ~ 35 nm average diameter in the case of Hg^{2+} [Figure 5.9 E] and ~ 200 nm in the case of Ag^{2+} [Figure A5.23 B, Annexure 5].

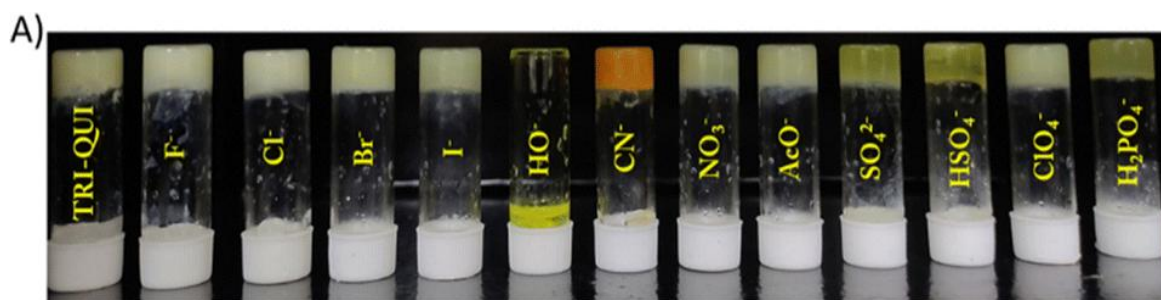


Figure 5.10: TRI-QUI gel formed in DMSO- H_2O (2: 3, v/v) in the presence of different anions in normal light.

We also tried to inquire about the effect of the addition of 3 equivalents of anions in the gelation process of TRI-QUI (5 mg mL^{-1} in 2: 3, v/v ratio of DMSO: H_2O). It was observed that only the presence of OH^- ions hampered the formation of a gel. In the case of CN^- , a gel-to-gel transition was observed as the color of the gel changed from creamy white to bright orange probably due to deprotonation of TRI-QUI (Figure 5.10). We investigated the morphological changes of TRI-QUI in the presence of anions (CN^- , SO_4^{2-}) via FESEM analysis. However, in the process of drying the anion-incorporated gels to form xerogels, they formed thin film-like structures in glass slides which was also evident from the FESEM images. We recorded the fluorescence spectra of the TRI-QUI gel in the presence and absence of CN^- (Figure A5.24, Annexure 5). Upon excitation at 400 nm, the gelator displayed a fluorescence peak at ~ 485 nm; however, the same excitation gelator TRI-QUI in the presence of CN^- displayed a red-shifted spectrum with an emission maximum of ~ 580 nm with a much lower emission intensity.

5.3.11. Rheological properties

Rheological measurements were employed to investigate the viscoelastic behavior and provide quantitative information about the mechanical strength of TRI-QUI and TRI-NAP gels. As shown in Figure 5.11, the results of the frequency sweep test of rheology for the organogel indicated that the TRI-QUI gel exhibits a higher elastic storage modulus (G') and a lower loss modulus (G''), demonstrating the authenticity of gelation judgment [5.53-5.54]. The damping factor or $\tan \delta = G''/G'$ depicted a value of $\tan \delta \ll 1$, assuring a solid-like state of the organogels. Moreover, no crossover point between G' and G'' was obtained for TRI-QUI indicating the mechanical stability of the gel [5.10]. Upon addition of CN^- into the TRI-QUI organogel, G' is still higher than G'' , thereby confirming the elastic properties of the gel. However, interestingly, the TRI-QUI gel in the presence of CN^- showed a decreased storage modulus compared to the native gel leading to

lower strength. On the other hand, for **TRI-NAP** (Figure A5.25, Annexure 5) as well, the storage modulus was greater than the loss modulus, confirming the elastic properties of the gel. However, in comparison to **TRI-QUI**, **TRI-NAP** exhibited a much lower storage modulus indicating very weak gel formation.

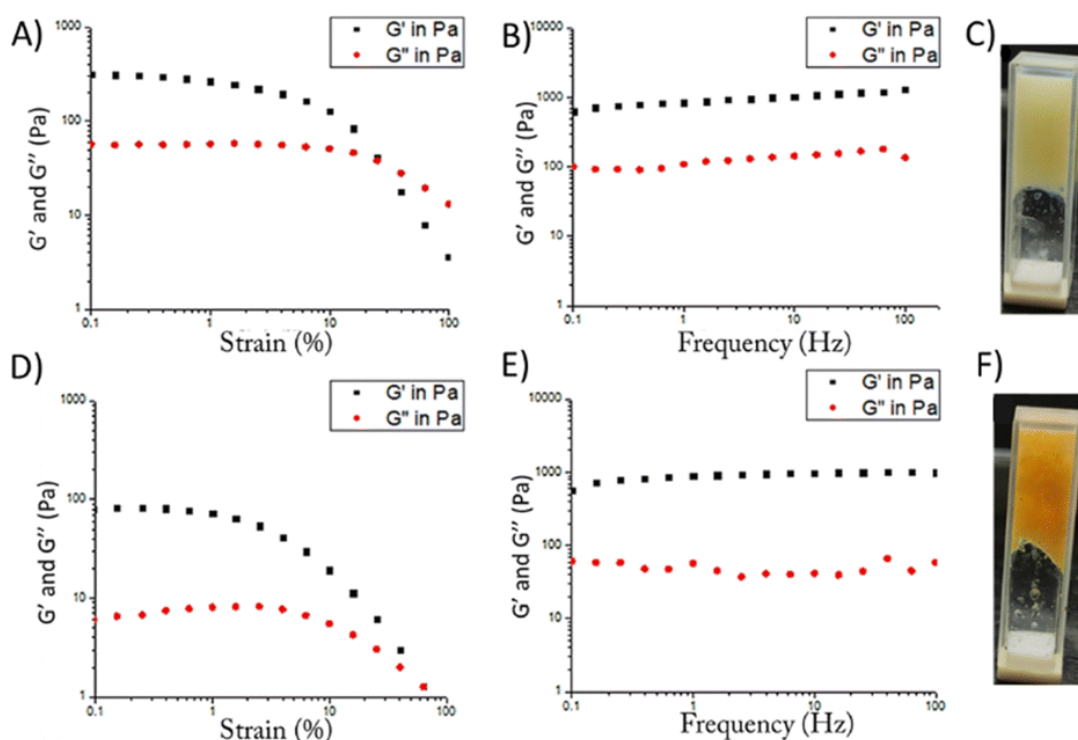


Figure 5.11: (A) Amplitude sweep and (B) frequency sweep of the **TRI-QUI** organogel, (C) gel formation by (A) **TRI-QUI**, (D) amplitude sweep and (E) frequency sweep of the **TRI-QUI+ CN⁻** organogel, and (F) the gel-to-gel transition of **TRI-QUI** in the presence of **CN⁻**.

5.3.12. Encapsulation of small molecules

We explored the possibility of utilizing our **TRI-QUI** gelator for the uptake of dye molecules since encapsulation of small molecules is one of the most important applications for supramolecular gel systems [5.32]. To test the ability of the **TRI-QUI** gel to store small molecules, two hydrophilic dye molecules, methyl orange and bromophenol blue, were selected as the guest molecular models. At first, the **TRI-QUI** (5 mg per mL) gel was formed in a DMSO: H₂O (2: 3, v/v) mixture in 2 separate glass vials. 2 mL aqueous solutions of the two dyes, methyl orange of 250 mM initial concentration and bromophenol blue of 150 mM initial concentration, were placed on the gels in the two respective vials. As expected, layering of the respective dye solutions on gels resulted in a gradual yet visible colour change of the native creamy white gel indicating uptake of the dye molecules into the **TRI-QUI** gel. Based on these qualitative observations, a quantitative characterization of dye molecule uptake was tested by UV-Vis absorbance measurements, by

plotting the % uptake of the two dyes methyl orange ($\lambda_{\text{abs}} = 470 \text{ nm}$) and bromophenol blue ($\lambda_{\text{abs}} = 592 \text{ nm}$), respectively, as a function of time. Based on the relationship between % uptake and the time of uptake (hour), the amount of dye adsorbed by the **TRI-QUI** gel was calculated. The total amounts of methyl orange and bromophenol blue that could get adsorbed were calculated to be 63.33% and 60%, respectively, in 60 hours. The results suggested that the presently studied **TRI-QUI** gel system could encapsulate small molecules within the gel network under suitable conditions (Figure 5.12).

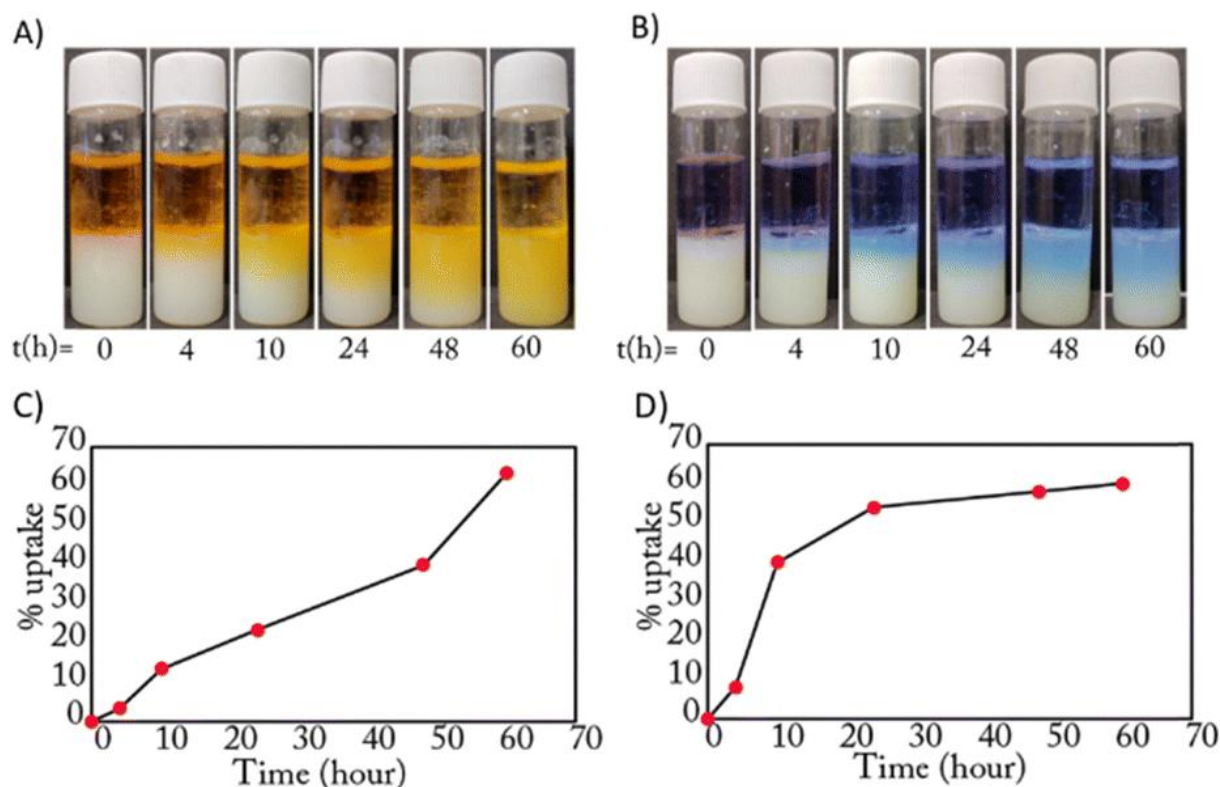


Figure 5.12: Photos of the uptake of small molecules by the **TRI-QUI** gel (DMSO-H₂O = 2: 3, v/v) at room temperature: (A) methyl orange (left) and (B) bromophenol blue (right); plots of the uptake percentage of (C) methyl orange measured at 470 nm and (D) bromophenol blue measured at 592 nm versus time.

5.4. Conclusion

In summary, we have synthesized two new acylhydrazone-based probes, **TRI-QUI** and **TRI-NAP**, containing quinoline and naphthalene at their peripheries, respectively. **TRI-QUI** responds selectively to Zn²⁺ in 0.1 M HEPES, with an LOD value of 6.45 μM . The increased emission spectra in the presence of Zn²⁺ are likely due to the PET process being prevented from the lone pair electrons of Schiff base nitrogen atoms to the quinoline rings after complexation with Zn²⁺. **TRI-QUI** can be used for real-world applications, such as Zn²⁺ sensing via paper strips and natural water samples. Additionally, **TRI-QUI** can form a stable supramolecular gel in a DMSO: H₂O (2:

3 v/v) solution through interconnected network formation driven by H-bonding and π - π stacking interactions. The gelator can also interact with anions and metal cations in the gel phase, leading to intriguing morphological changes. Upon interaction with CN^- , a gel-to-gel transition results in a change from creamy white to bright orange, as evidenced by a 95 nm red shift in the fluorescence spectra. Notably, the **TRI-QUI** gel can adsorb small molecules like methyl orange and bromophenol blue, with an uptake efficiency of 63% and 60%, respectively. This work opens the door to developing a multifunctional probe useful for sensing harmful metal ions in solution and creating soft materials applicable in real-life scenarios.

References

- [5.1] Y. Wang, J. Weng, X. Wen, Y. Hu and D. Ye, *Biomater. Sci.*, 2021, **9**, 406.
- [5.2] C. Ren, J. Zhang, M. Chen and Z. Yang, *Chem. Soc. Rev.*, 2014, **43**, 7257-7266
- [5.3] L. Li, R. Sun and R. Zhen, *Mater. Des.*, 2021, **197**, 109209.
- [5.4] S. De, D. Ghosh and G. Das, *Chem. – Asian J.*, 2024, e202400148
- [5.5] J. Luo, Z. Xie, J. W. Y. Lam, L. Cheng, H. Chen, C. Qiu, H. S. Kwok, X. Zhan, Y. Liu, D. Zhuc and B. Z. Tang, *Chem. Commun.*, 2001, 1740–1741.
- [5.6] Kenry, B. Z. Tang and B. Liu, *Catalysis*, 2020, **6**, 1195-1198.
- [5.7] M. Huang, H. Lu, K. Wang, B. Liu, M. Wang, X. Qiao and J. Yang, *Dyes Pigm.*, 2021, **186**, 108992
- [5.8] V. K. Praveen, B. Vedhanarayanan, A. Mal, R. K. Mishra and A. Ajayaghosh, *Acc. Chem. Res.*, 2020, **53**, 496-507.
- [5.9] C. Zhou, J. Ma and D. W. Sun, *Trends Food Sci.*, 2023, **134**, 232-246.
- [5.10] S. Sharma, M. Kumari and N. Singh, *Soft Matter*, 2020, **16**, 6532.
- [5.11] X. Ma, Z. Zhang, H. Xie, Y. Ma, C. Liu, S. Liua and M. Liu, *Chem. Commun.*, 2018, **54**, 13674.
- [5.12] X. Yu, L. Chen, M. Zhanga and T. Yi, *Chem. Soc. Rev.*, 2014, **43**, 5346–5371.
- [5.13] A. Ghosh, P. Das, R. Kaushik, K. K. Damodaranc and D. A. Jose, *RSC Adv.*, 2016, **6**, 83303-83311
- [5.14] N. Malviya, M. Das, P. Mandala and S. Mukhopadhyay, *Soft Matter*, 2017, **13**, 6243-6249.
- [5.15] Z. Yan, Y. Cai, J. Zhang and Y. Zhao, *Measurement*, 2022, 187, 110355.
- [5.16] Y. W. Choi, J. J. Lee and C. Kim, *RSC Adv.*, 2015, **5**, 60796-60803
- [5.17] H. M. Liu, P. Venkatesan and S. P. Wu, *Sens. Actuators, B*, 2014, **203**, 719-725.
- [5.18] E. L. Que, D. W. Domaille and C. J. Chang, *Chem. Rev.*, 2008, **108**, 1517-1549.
- [5.19] W. Maret and Y. Li, *Chem. Rev.*, 2009, **109**, 4682-4707.
- [5.20] P. D. Zalewski, I. J. Forbes and W. H. Betts, *Biochem. J.*, 1993, **296**, 403-408.
- [5.21] K. H. Falchuk, *Mol. Cell. Biochem.*, 1998, **188**, 41-48.
- [5.22] S. Dey, S. Ghosh, A. Das, R. N. Yadav, R. Chakrabarty, S. Pradhan, D. Saha, A. K. Srivastava and Md. F. Hossain, *J. Fluoresc.*, 2024, **34**, 1829-1840.
- [5.23] X. Liu, N. Zhang, J. Zhou, T. Chang, C. Fangab and D. Shangguan, *Analyst*, 2013, **138**, 901-906.
- [5.24] J. Charoensuk, J. Thonglao, B. Wichaiyo, K. Mukdasai, Y. Santaladchayakit, S. Srijaranai and S. Mukdasai, *Microchem. J.*, 2021, **160**, 105666.

- [5.25] H. Shuai, C. Xiang, L. Qian, F. Bin, L. Xiaohui, D. Jipeng, Z. Chang, L. Jiahui and Z. Wenbin, *Dyes Pigm.*, 2021, **187**, 109125.
- [5.26] N. S. Mohamad, N. H. Zakaria, N. Daud, L. L. Tan, G. C. Ta, L. Y. Heng and N. I. Hassan, *Sensors*, 2021, **21**, 311.
- [5.27] H. Liu, Y. Dong, B. Zhang, F. Liu, C. Tan, Y. Tan and Y. Jiang, *Sens. Actuators, B*, 2016, **234**, 616-624.
- [5.28] G. Wua, Q. Gao, M. Li, X. Tang, K. W. C. Laib and Q. Tong, *J. Photochem. Photobiol., A*, 2018, **355**, 487-495.
- [5.29] S. Sinha, B. Chowdhury, N. N. Adarsh and P. Ghosh, *Dalton Trans.*, 2018, **47**, 6819-683.
- [5.30] H. J. Cho, T. W. Kim, H. Kim and C. Song, *Sensors*, 2020, **20**, 600.
- [5.31] J. T. Wang, Y. Y. Pei, M. Y. Yan, Y. G. Li, G. G. Yang, C. H. Qu, W. Luo, J. Wang and Q. F. Li, *Microchem. J.*, 2021, **160**, 105776.
- [5.32] Y. Liu, Y. Tan, Z. Liuc and G. Che, *Soft Matter*, 2021, **17**, 7227-7235
- [5.33] X. Cao, A. Gao, J. Hou and T. Yi, *Coord. Chem. Rev.*, 2021, **434**, 213792.
- [5.34] B. Wang, J. Li, S. Shuia and J. Xu, *New J. Chem.*, 2021, **45**, 1899-1903.
- [5.35] R. Moral, O. A. Pegu and G. Das, *Dyes Pigm.*, 2023, **218**, 111502.
- [5.36] O. A. Pegu, A. Das and G. Das, *J. Mol. Struct.*, 2023, **1294**, 136427.
- [5.37] O. A. Pegu, R. Moral and G. Das, *Cryst. Growth Des.*, 2023, **23**, 8370-838.
- [5.38] R. Moral, O. Appun Pegu and G. Das, *New J. Chem.*, 2023, **47**, 19625-19632.
- [5.39] O. A. Pegu and Gopal Das, *J. Mater. Chem. C*, 2024, **12**, 6519-6527.
- [5.40] S. De and G. Das, *Soft Matter*, 2023, **19**, 6116-6121
- [5.41] S. De, O. A. Pegu and G. Das, *Langmuir*, 2023, **39**, 2444-2449.
- [5.42] Q. Wang, H. Wu, A. Gao, X. Ge, X. Chang and X. Cao, *Chin. Chem. Lett.*, 2023, **34**, 107644.
- [5.43] X. Cao, N. Zhao, H. Lv, Q. Ding, A. Gao, Q. Jing and T. Yi, *Langmuir*, 2017, **33**, 7788-7798.
- [5.44] S. Halder, U. Manna and G. Das, *New J. Chem.*, 2019, **43**, 14112-14119.
- [5.45] M. Yang, D. Xu, W. Xi, L. Wang, J. Zheng, J. Huang, J. Zhang, H. Zhou, J. Wu and Y. Tian, *J. Org. Chem.*, 2013, **78**(20), 10344-1035.
- [5.46] Y. Dong, R. Fan, W. Chen, P. Wang and Y. Yang, *Dalton Trans.*, 2017, **46**, 6769-6775.
- [5.47] H. Liu, Y. Tan, Q. Daic, H. Liang, J. Song, J. Qua and W.-Y. Wong, *Dyes Pigm.*, 2018, **158**, 312-318.
- [5.48] K. Rout, A. K. Manna, M. Sahu and G. K. Patra, *Inorg. Chim. Acta*, 2019, **486**, 733-741.
- [5.49] Y. Mikata, Y. Sato, S. Takeuchi, Y. Kuroda, H. Konno and S. Iwatsuki, *Dalton Trans.*, 2013, **42**, 9688.
- [5.50] X. Ma, S. Liu, Z. Zhang, Y. Niua and J. Wu, *Soft Matter*, 2017, **13**, 8882-8885.
- [5.51] C. Po, Z. Ke, A. Y.-Y. Tam, H.-F. Chow and V. W.-W. Yam, *Chem. – Eur. J.*, 2013, **19**, 15735-15744.
- [5.52] A. Dawn and H. Kumari, *Chem. – Eur. J.*, 2018, **24**, 762-776.
- [5.45] L. Liao, X. Jia, H. Lou, J. Zhong, H. Liu, S. Ding, C. Chen, S. Hong and X. Luo, *RSC Adv.*, 2021, **11**, 11519-11528.
- [5.46] D. Ghosh, M. Basak, D. Deka and G. Das, *J. Mol. Liq.*, 2022, **363**, 11981.

Annexure 5

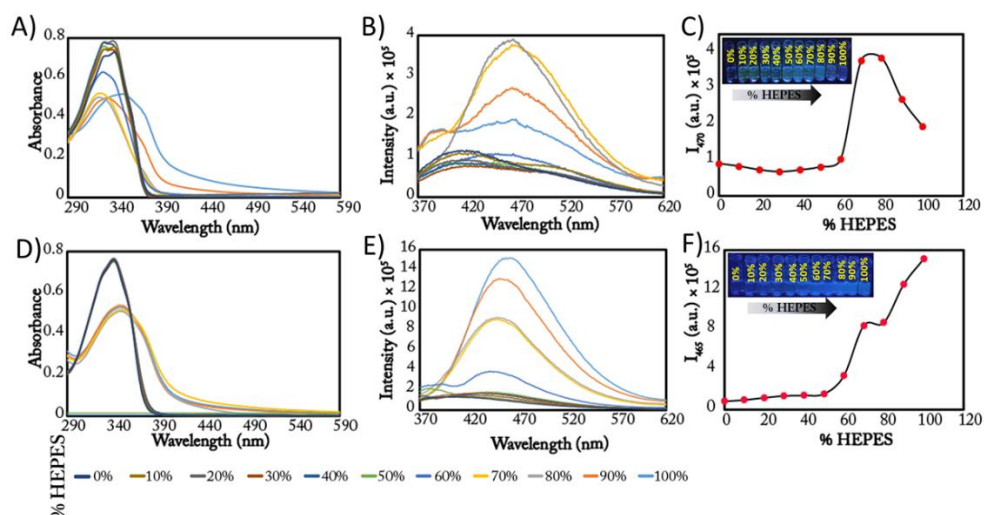


Figure A5.1: Absorbance spectrum of (A) TRI-QUI, and (D) TRI-NAP in DMF and HEPES. Emission spectroscopy with increasing percentages of HEPES in DMF of (B) TRI-QUI, and (E) TRI-NAP. Plot of percentage of water vs emission intensity of (C) TRI-QUI and (F) TRI-NAP [INSET: Visual illustration of the AIE activity of TRI-QUI (20 μ M) and TRI-NAP (20 μ M) under a 365 nm UV lamp].

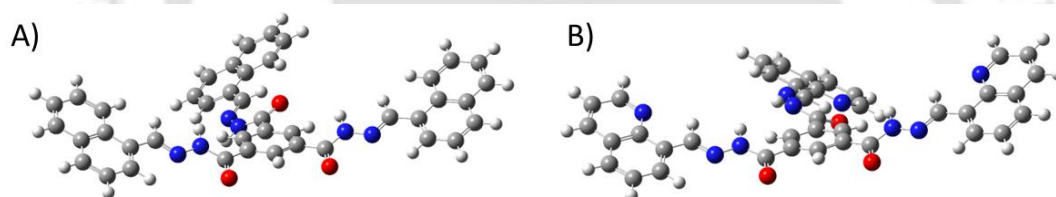


Figure A5.2: DFT optimized structures of both the probes.

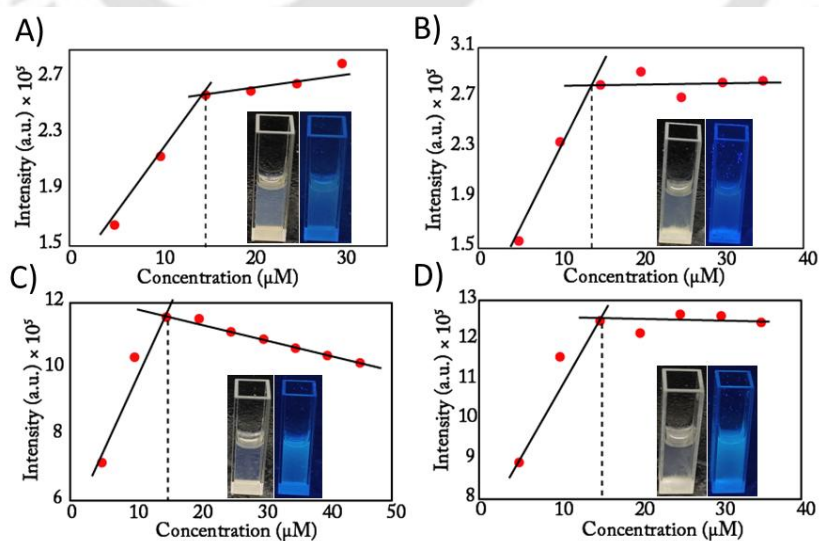
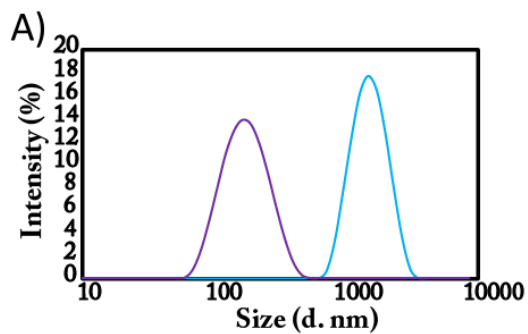


Figure A5.3: Critical aggregation constant of TRI-QUI in A) H₂O, B) HEPES, and of TRI-NAP in C) H₂O, D) HEPES.



SAMPLES	H ₂ O	
	Z-Avg (d. nm)	PDI
■ TRI-QUI	1303	0.164
■ TRI-NAP	155.9	0.143

Figure A5.4: DLS output of TRI-QUI in 80% H₂O and TRI-NAP in 100% H₂O.

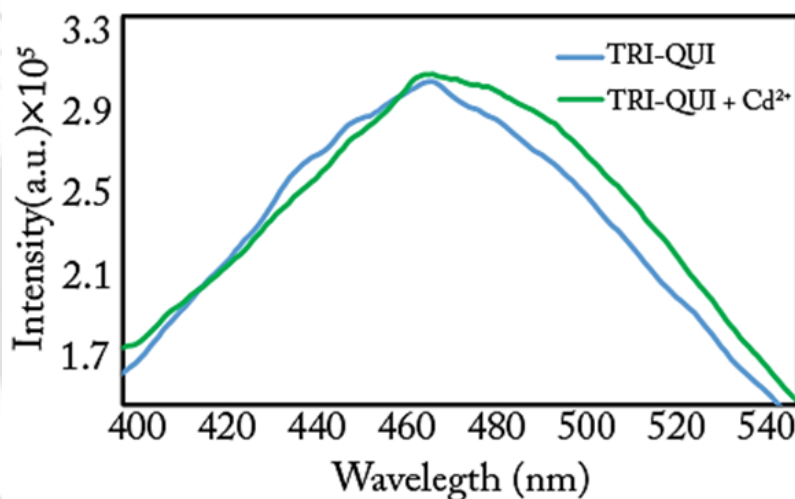


Figure A5.5: Sensing of Cd²⁺ by TRI-QUI in HEPES (enlarged view).

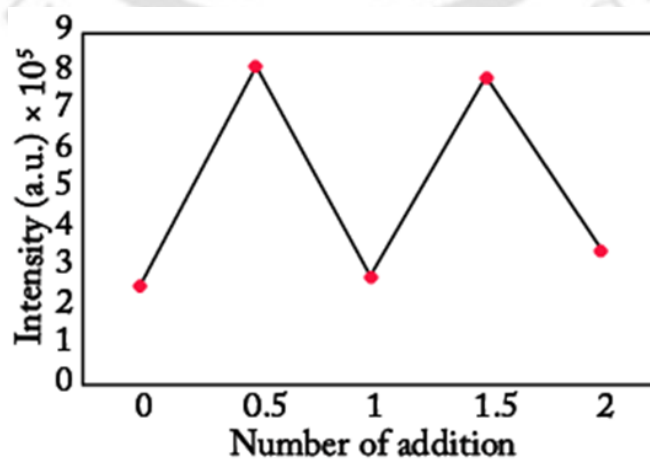


Figure A5.6: Sensing of Cd²⁺ by TRI-QUI in HEPES (enlarged view).

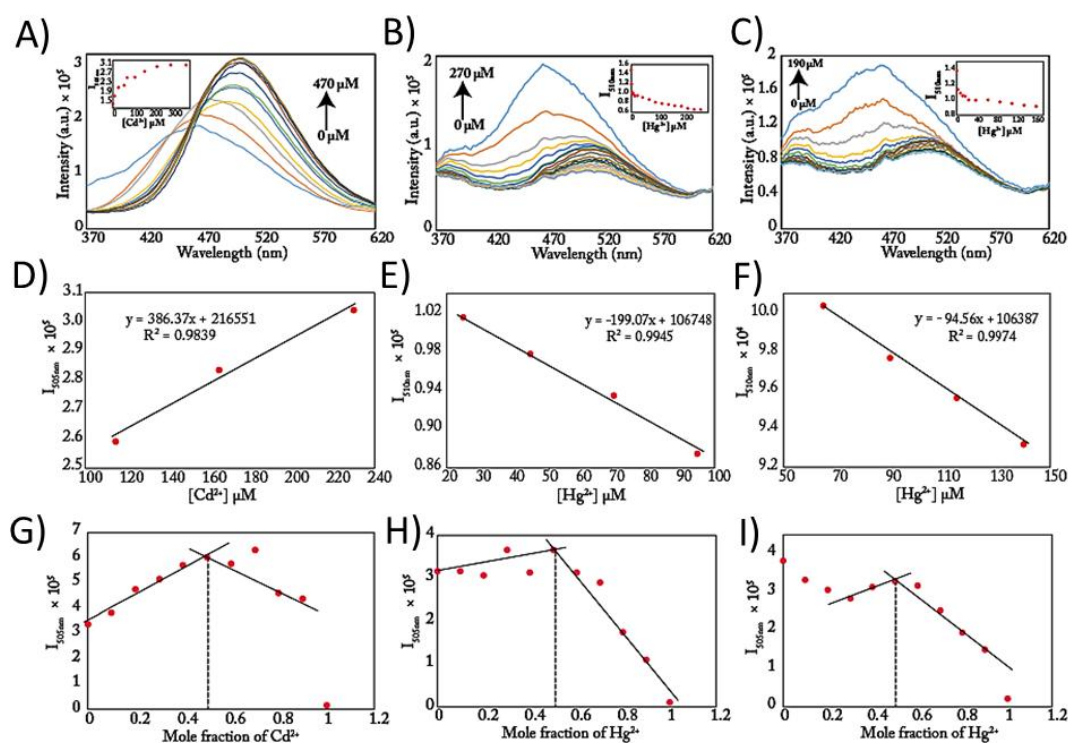


Figure A5.7: Emission intensity profile depicting the titration of TRI-QUI with Cd²⁺ A) in water, with Hg²⁺ B) in H₂O and C) in HEPES, fluorescence emission intensity of TRI-QUI vs. D) Cd²⁺ concentration E), F) Hg²⁺ concentration to calculate the limit of detection (LOD), Job's plot of TRI-QUI with G) Cd²⁺ H), I) Hg²⁺.

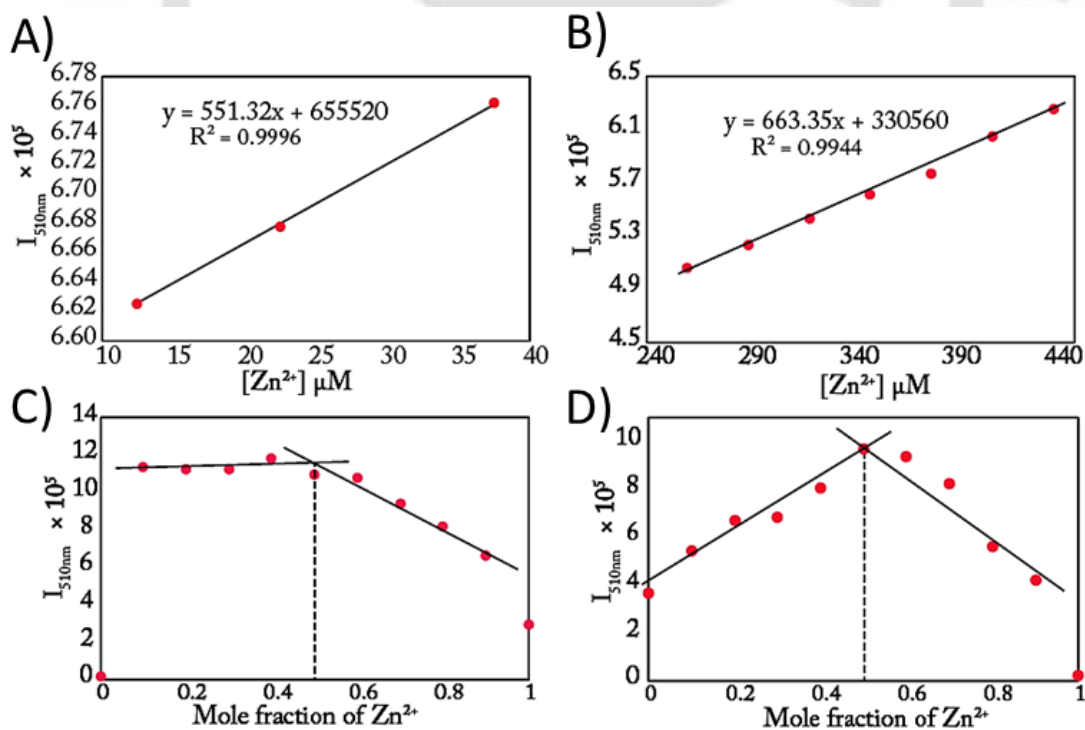


Figure A5.8: The fluorescence emission intensity of TRI-QUI vs. Zn²⁺ concentration A) in water and B) in HEPES to calculate the limit of detection (LOD), Job's plot of TRI-QUI with mole fraction of Zn²⁺ C) in water and D) in HEPES.

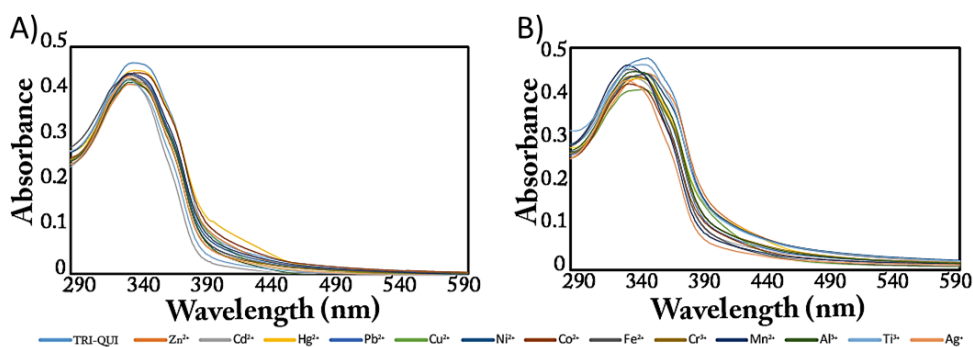
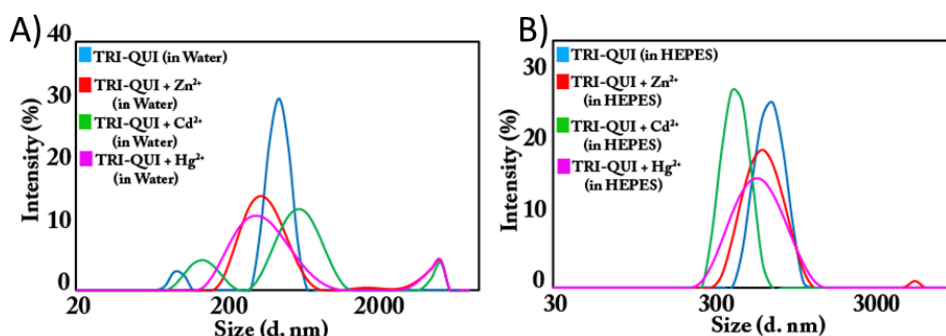


Figure A5.9: UV-Vis Sensing of metal ions by TRI-QUI A) in water and B) in HEPES.



SAMPLES	H ₂ O		HEPES	
	Z-Avg (d. nm)	PDI	Z-Avg (d. nm)	PDI
TRI-QUI	828.9	0.802	907.2	0.519
TRI-QUI + Zn ²⁺	462.7	0.398	641.7	0.249
TRI-QUI + Cd ²⁺	483.6	0.708	703.8	0.651
TRI-QUI + Hg ²⁺	419.6	0.409	509.9	0.270

Figure A5.10: DLS output of TRI-QUI in the presence of Zn²⁺, Cd²⁺, and Hg²⁺ A) in water and B) in HEPES.

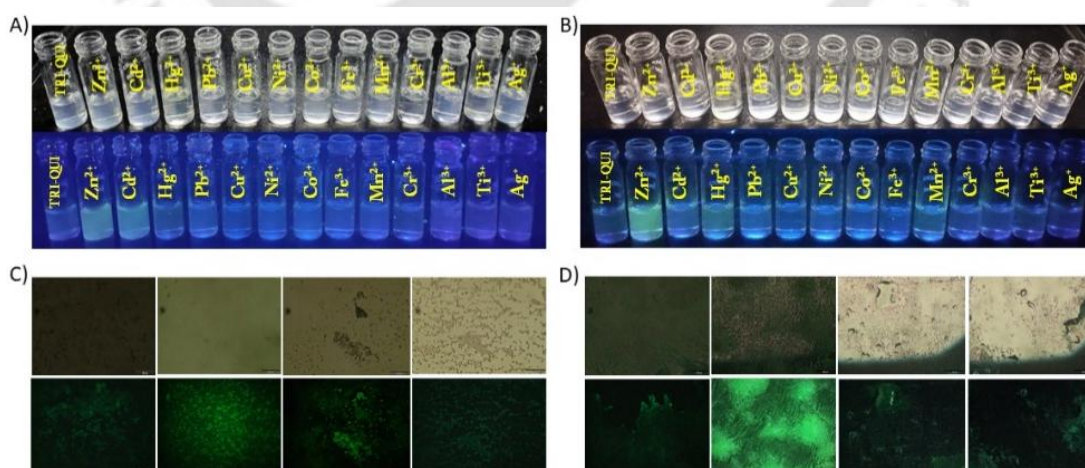


Figure A5.11: Vial images of TRI-QUI in the presence of different metal ions A) in water, B) in HEPES, and fluorescence microscope images of TRI-QUI in the presence of Zn²⁺, Cd²⁺, and Hg²⁺ respectively C) in water and D) in HEPES.

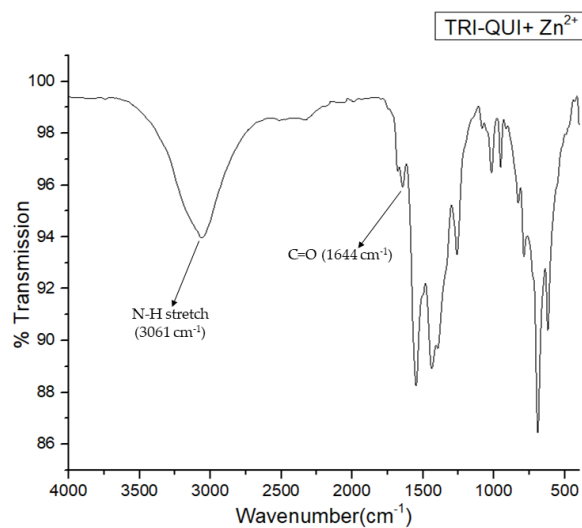


Figure A5.12: FT-IR spectra of TRI-QUI in the presence of Zn²⁺.

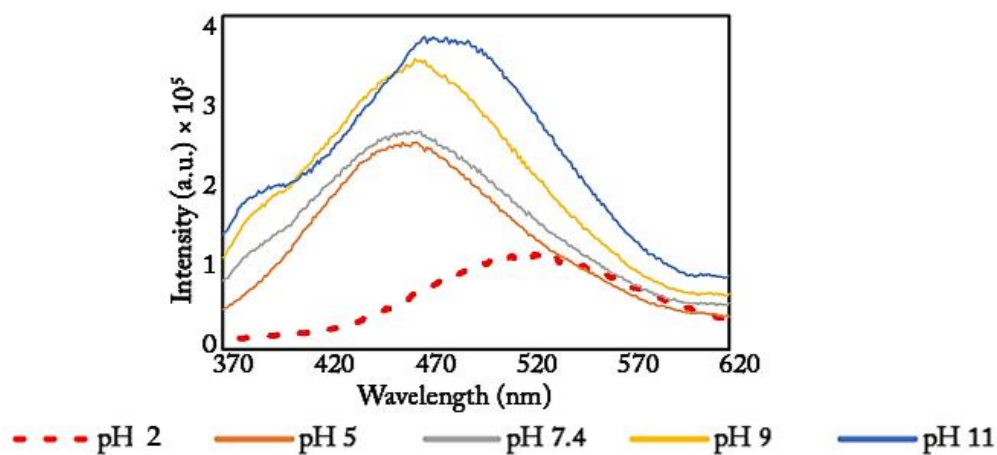


Figure A5.13: Fluorescence spectra of TRI-QUI in different pH.

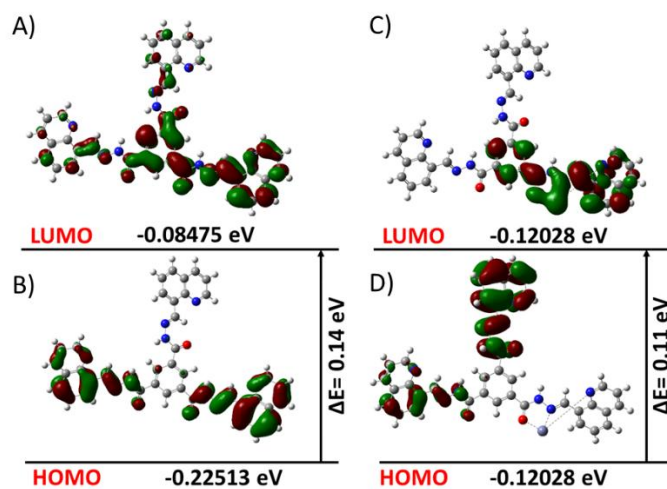


Figure A5.14: HOMO and LUMO of TRI-QUI in absence A), B) and in presence C), D) of Zn²⁺.

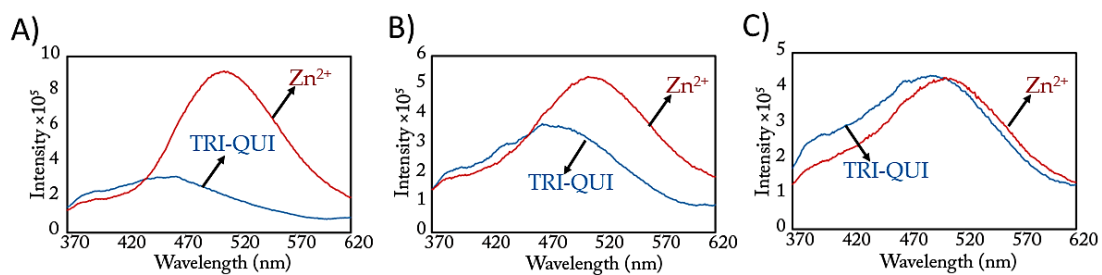


Figure A5.15: Sensing of Zn^{2+} in real water samples A) milli Q water B) drinking water and C) tap water.

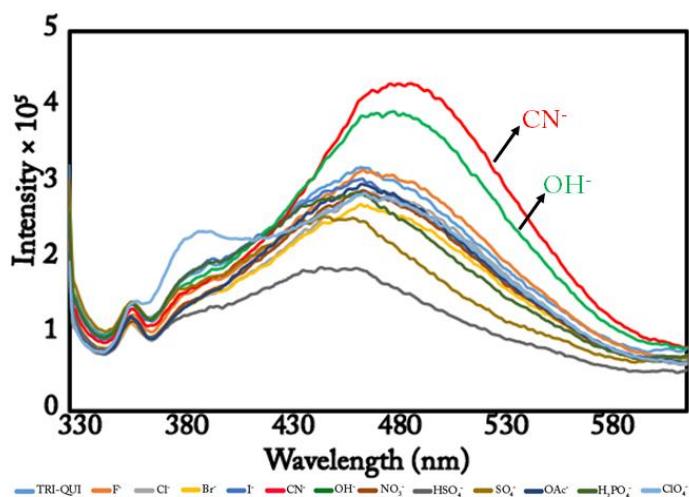


Figure A5.16: Anion sensing by TRI-QUI in water.

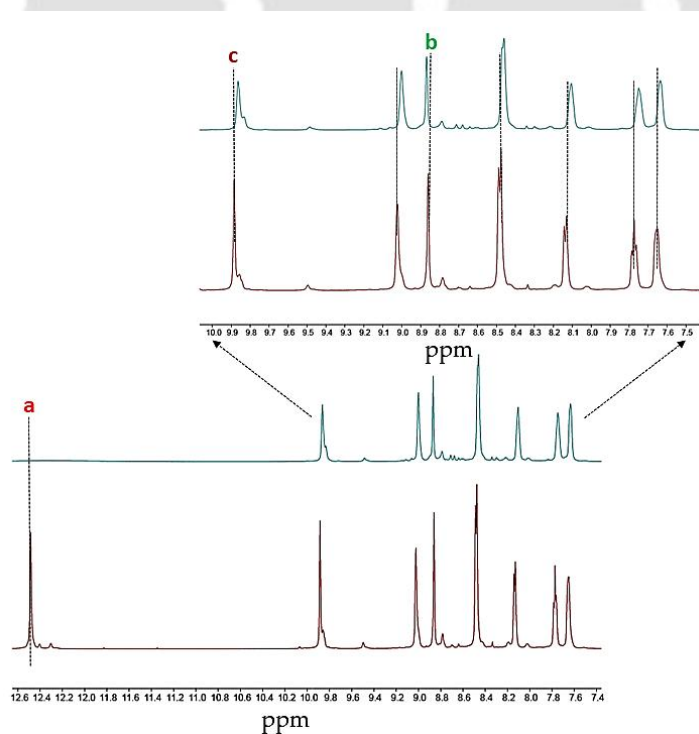


Figure A5.17: 1H NMR spectra of TRI-QUI in the presence of excess of CN^- .

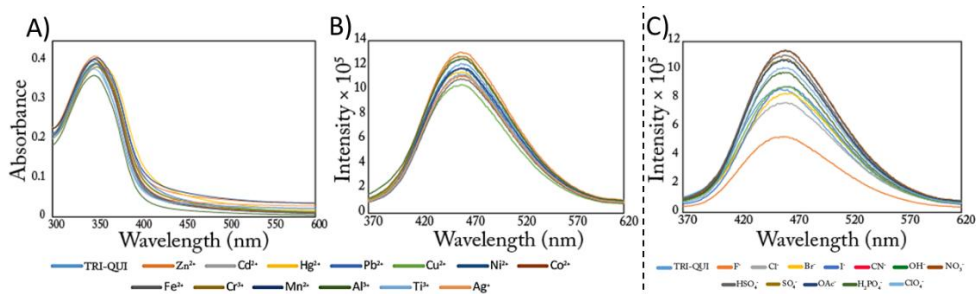


Figure A5.18: A) UV-Vis sensing of metal ions, B) fluorescence sensing of metal ions, and C) fluorescence sensing of anions by TRI-NAP in water.

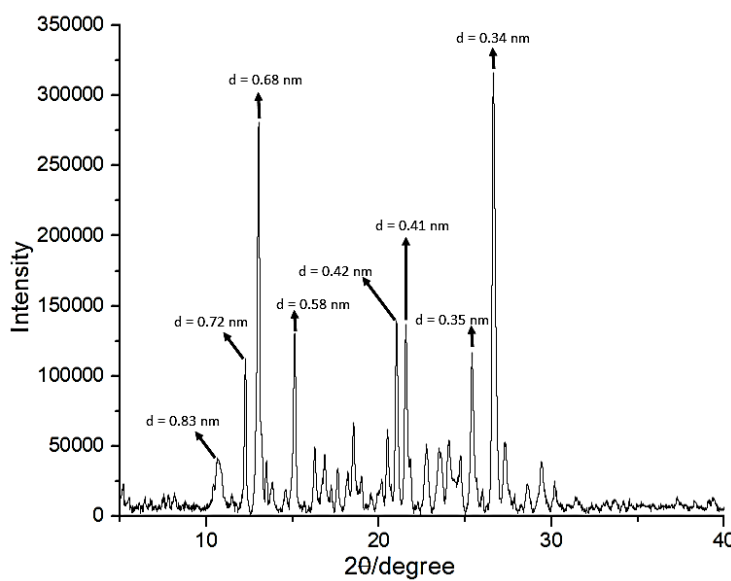


Figure A5.19: Powder XRD spectra of xerogel TRI-QUI.

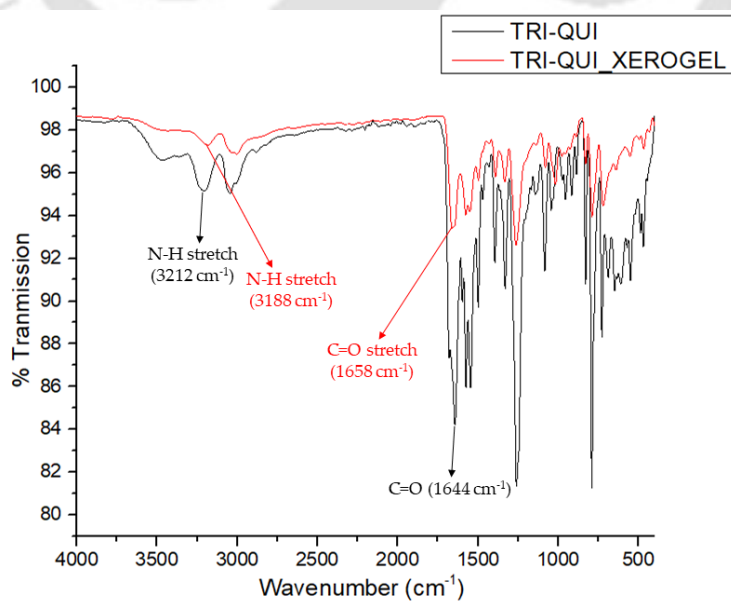


Figure A5.20: FT-IR spectra of xerogel TRI-QUI.

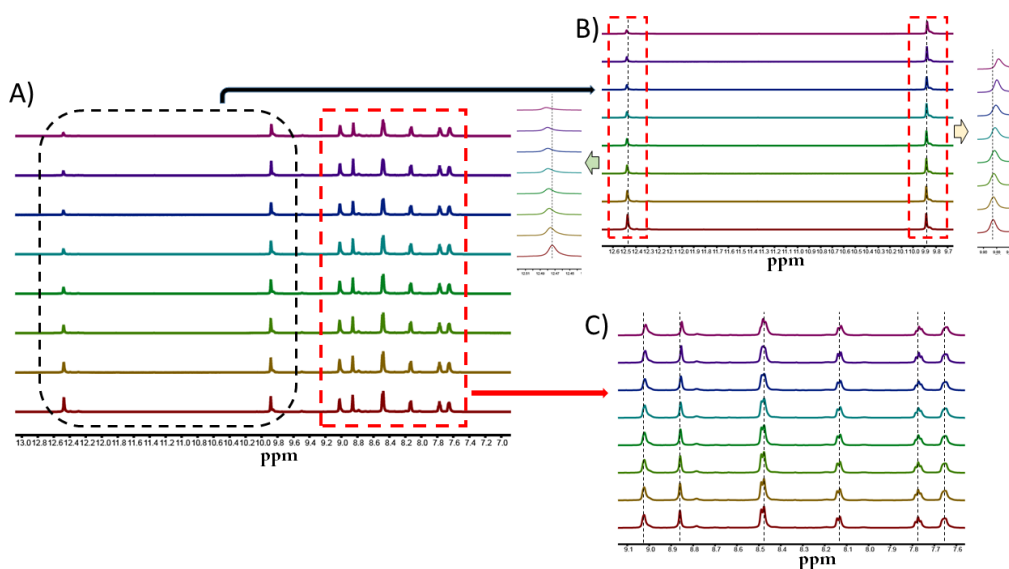


Figure A5.21: ^1H NMR spectra of TRI-QUI in $\text{DMSO-}d_6$ with increasing content of D_2O .

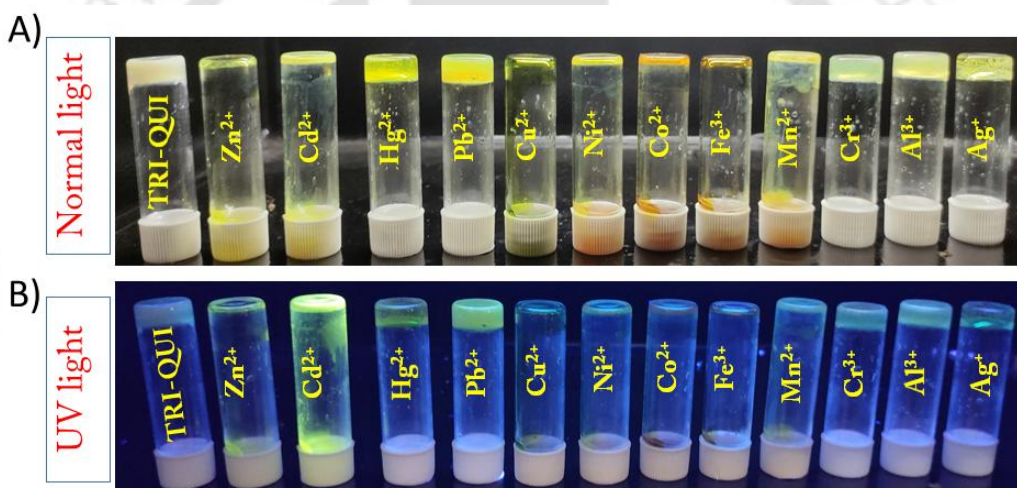


Figure A5.22: TRI-QUI gel formed in $\text{DMSO-H}_2\text{O}$ (2: 3, v/v) in the presence of different metal ions A) in normal light and B) in UV light.

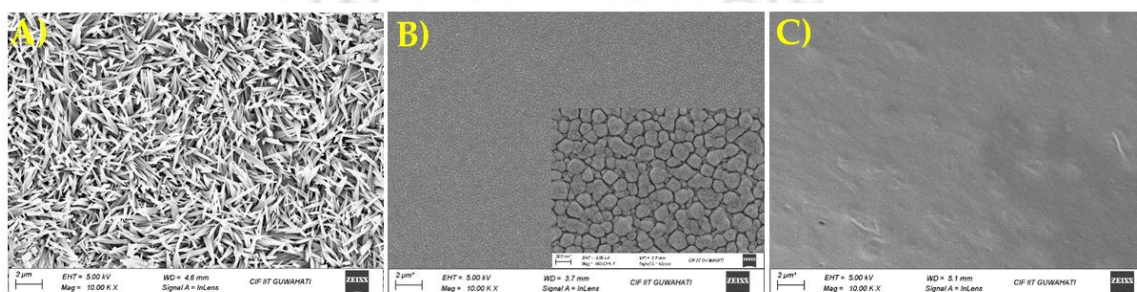


Figure A5.23: FESEM images of A) TRI-QUI xerogel obtained from $\text{DMSO-H}_2\text{O}$ (2: 3, v/v), B) TRI-QUI+ Ag^{2+} xerogel obtained from $\text{DMSO-H}_2\text{O}$ (2: 3, v/v), F) TRI-QUI+ SO_4^{2-} xerogel obtained from $\text{DMSO-H}_2\text{O}$ (2: 3, v/v).

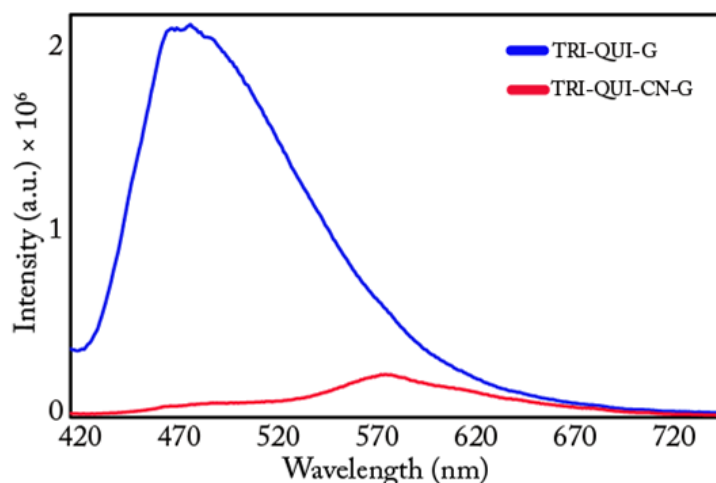


Figure A5.24: Fluorescence spectra of TRI-QUI gel formed in DMSO-H₂O (2: 3, v/v) and TRI-QUI gel formed in DMSO-H₂O (2: 3, v/v) formed in the presence of CN⁻.

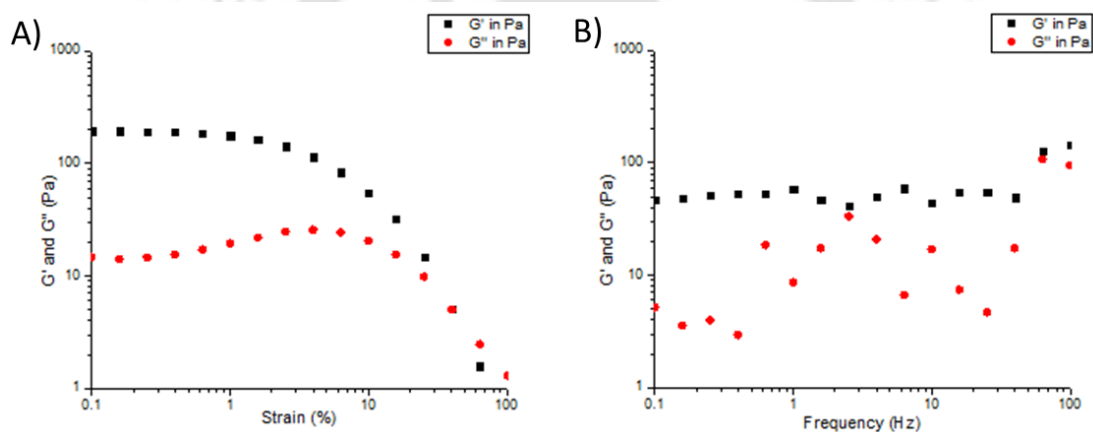


Figure A5.25: A) Amplitude sweep and B) Frequency sweep of TRI-NAP organogel DMSO-H₂O (2: 3, v/v).

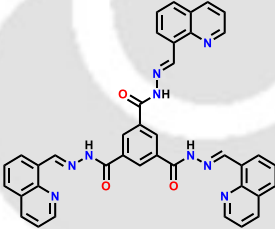
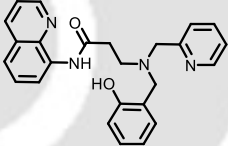
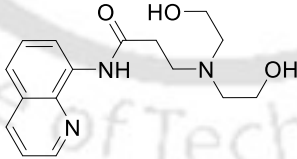
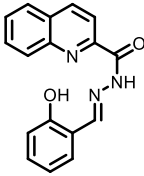
Table A5.1 Hydrogen bonding distances (Å) and Bond angles (°) in TRI-QUI.

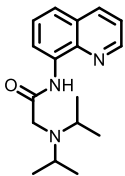
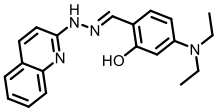
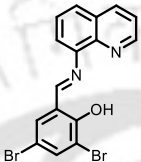
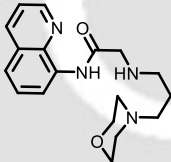
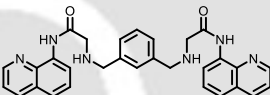
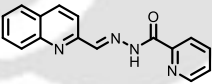
Ligand	D-H...A	d(D...H)/Å	d(H...A)/Å	d(D...A)/Å	<D-H...A/°	Symmetry codes
TRI-QUI	N1-H1N...N5	0.79 (4)	2.51 (4)	3.189 (5)	145 (4)	-x, 1-y, 1-z
	O4-H4B...N6	1.02 (10)	2.07 (10)	3.065 (6)	165 (8)	x, y, z
	N4-H4N...O1	0.74 (4)	2.21 (4)	2.931 (5)	164 (4)	1-x, 1-y, 1-z
	N7-H7N...O4	0.82 (5)	2.27 (5)	3.055 (6)	162 (5)	1-x, 1-y, 1-z
	C6-H6...O4	0.93	2.60	3.354 (6)	139	1-x, 1-y, 1-z
	C23-H23...O1	0.93	2.56	3.369 (5)	146	-1+x, 1+y, z
	C30-H30...O3	0.93	2.52	3.426 (6)	164	-x, 1-y, 1-z
	C39-H39...O2	0.93	2.48	3.337 (6)	154	x, y, -1+z

Table A5.2 Table for LOD and binding constant calculation in H₂O and HEPES.

Metal	MEDIUM	LOD	BINDING STOICHIOMETRY
Zn ²⁺	H ₂ O	14.33 μM	1:1
	HEPES	6.45 μM	1:1
Cd ²⁺	H ₂ O	20.44 μM	1:1
Hg ²⁺	H ₂ O	39.68 μM	1:1
	HEPES	45.26 μM	1:1

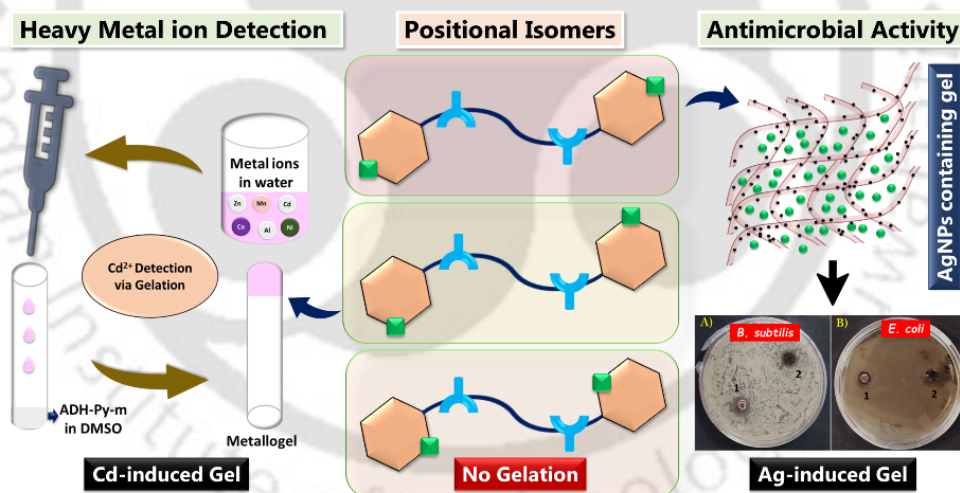
Table A5.3 Table for LOD and binding constant calculation in H₂O and HEPES.

Sl. No.	References	Structure of probe	Solvent system	LOD (μM)
1.	Present work		0.1M HEPES buffer	6.45
2.	Sensors and Actuators B: Chemical, 2015, 213, 268-275		10 mM HEPES, pH 7.4, 1:1 acetonitrile/buffer	8.14×10^{-3}
3.	RSC Advances, 2015, 5, 60796-60803		10 mM bis-tris buffer	4.48
4.	Sensors and Actuators B 2016, 234, 616-624		MeOH-HEPES buffer (3/7, v/v, pH 7.4)	2.1×10^{-2}

5.	Dyes and Pigments 2018, 158, 312-318		MeOH-Tris buffer (1/1, v/v, pH 7.2)	4.1×10^{-2}
6.	New J. Chem., 2019,43, 7320-7328		buffer/DMF mixture (7:3)	0.08
7.	Dalton Transaction, 2020, 49, 4758-4773		10 mM HEPES buffer	1.39×10^{-1}
8.	New Journal of Chemistry, 2020, 44, 442-449		bis-tris buffer	0.29
9.	Journal of Fluorescence, 2020, 30, 347-356		DMSO/bis-tris buffer (1:1)	0.53
10.	Microchemical Journal 2021, 160, 105776		DMSO/HEPES buffer solution (v/v = 3/2, HEPES 10 mM, pH 7.4)	72×10^{-3}

Chapter 6

Positional Isomerism Driven Differential Metallogelation: Biological Application and Naked Eye Detection of Cd²⁺ ion



6.1. Background and Focus of the Chapter

Metallogels in gel research have revealed a huge opportunity, as these smart materials can integrate the distinctive features of metals into gelator molecules [6.1-6.4]. These versatile classes of materials are designed by the incorporation of metal ions with appropriate LMWG to create a 3D network structure [6.5]. Metal-ligand coordination interaction, with the proper choice of coordinating ligand and metal ion, plays a vital role in the formation of metallogels [6.6]. Supramolecular metallogels find applications in diverse fields of materials science, including drug delivery, cell culturing, biomineralization, tissue engineering, optical activity, catalysis, conductivity, actuators, redox responsiveness, chemosensors, optoelectronic devices, nanoscience and nanoelectronics etc. [6.7-6.11]. Supramolecular gel as a class of supramolecular architecture is attractive material that can serve as a medium which can direct the in-situ synthesis of the nanosized materials with the ability to control the shape and properties of nanomaterials [6.12-6.14]. Nanomaterials are versatile and impactful in different day-to-day applications, and the synthesis of nanoparticles is in high demand [6.15]. Silver nanoparticles (AgNPs) are particularly fascinating due to their strong surface plasmon resonance (SPR), high optical and catalytic properties, and remarkable potential applications in sensing and biomedicine, along with their significance as effective antimicrobial agents against various microorganisms [6.16-6.17]. Silver nanoparticle embedded silver metallogels are a flourishing class of hybrid materials, leveraging silver's well-known antibacterial properties [6.18-6.19]. Further, gel-based adsorption of toxic heavy metals for example Cd^{2+} , Hg^{2+} , Pb^{2+} , etc., is becoming an emerging area of research for environmental remediation applications [6.20-6.22]. The metals do not leave their sites under ambient conditions in metallogels because of strong metal-ligand coordination bonds, and thus, can lead to a highly stable toxic metal capturing process with improved wastewater purification [6.23-6.25]. If the ligand demonstrates binding specificity towards any particular metal ion, then the gelation process becomes metal ion specific [6.26].

It is important to note that the proper design of the organic ligand and finding its perfect metal ion counterpart is always critical to accomplish metallogelation. The structural tunability of the ligand molecule also provides us with an opportunity to modulate the different properties of such metallogels as well. Mentionable in this regard are the positional isomers, which may demonstrate different interactions with the same/different metal ions, that could result in different

supramolecular complexations and gel properties [6.27]. Supramolecular metallogels find application in numerous fields such as catalysis, pollutant remediation, gas absorption, and molecular sensing [6.28-6.30]. In literature, most of the LMWGs reported are serendipitous discoveries because of the difficulties in predicting gelation properties in terms of the molecular structure [6.31-6.32]. Specially in the case of metallogelators, diversity in the molecular structure of the ligands and metal ions makes it extremely difficult to put forward a general design strategy [6.33]. Nevertheless, researchers have adopted some rational approaches towards designing metallogelators by exploiting some already known gelator moiety to an organometallic moiety/coordination complex or by using a supramolecular synthon [6.34-6.37]. However, the effect of positional isomers on metallogelation behaviour has been rarely explored in the literature, although it can be very helpful to understand the structure-function relationships. In the previous reports from our group, we have emphasised the structure-function relationship for the designing of the low molecular weight gelator molecules [6.38-6.40].

Considering all those factors into account, in this work, we have synthesized four adipic dihydrazide-based LMWG molecules, **ADH-Py-o**, **ADH-Py-m**, **ADH-Py-p**, and **ADH-Ph** functionalized with -o, -m, -p amino pyridine and phenyl groups at the terminal positions, respectively and explored their metallogelation behaviours. Interestingly, **ADH-Py-p** and **ADH-Py-m** formed a metallogel out of all four compounds and biological applications in terms of antimicrobial activity of the same have been demonstrated. Moreover, we have utilized the idea of selectivity in metallogelation for the detection of toxic heavy metal ions in the presence of other competitive metal ions, and also in different real water samples.

6.2. Objective of the Chapter

Three adipic dihydrazide-based receptors fabricated with a pyridine moiety were synthesized by changing the positions of 'pyridine-N'. Also, one more receptor was fabricated as a control compound appended with phenyl moieties in the two arms instead of pyridine. The motive behind this was to investigate positional isomeric effects on the metallogelation behaviour. Receptors **ADH-Py-p** and **ADH-Py-m**, functionalised with pyridine-N at the para and meta positions, respectively, were found to exhibit selective metallogelation behaviour in the presence of Ag^+ (**P-Ag-G**) and Cd^{2+} (**M-Cd-G**), respectively, out of all the metal ions undertaken for our study. Additionally, the metallogel, **P-Ag-G**, formed in the presence of Ag^+ eventually led to the spontaneous in situ formation of AgNP inside the gel matrix. **P-Ag-G** and its nanocomposite were further utilized for antibacterial study. The idea of selective metallogelation behaviour of the receptor **ADH-Py-m** in the presence of toxic Cd^{2+} was then exploited for the detection of Cd^{2+} in

the presence of other competitive metal ions in different real water samples through the naked eye, thus circumventing the need for any sophisticated instrumentation.

6.3. Results and discussion

6.3.1. Design Rationale of the Receptors ADH-Py-p, ADH-Py-m, ADH-Py-o and ADH-Ph

ADH-Py-p, ADH-Py-m, ADH-Py-o and ADH-Ph. Both arms of adipic dihydrazide were fabricated with ortho, meta and para-pyridine carboxaldehyde to study the effect of positional isomerism on metallogelation properties. The acylhydrazone unit is well known for its typical role in supramolecular gelation owing to the presence of multiple hydrogen bond donor and acceptor sites. The presence of 'pyridine -N' in ADH-Py-p, ADH-Py-m and ADH-Py-o imparted metal ion coordination sites which could facilitate the formation of a 3-dimensional supramolecular network structure (Figure 6.1). Thus, hierarchical self-assembly formation along with metal ion coordination might contribute to metallogelation. To further evaluate the role played by the 'pyridine -N' on the metallogel formation, we additionally synthesized a control compound ADH-Ph, where both arms of the adipic dihydrazide were fabricated with phenyl units instead of the pyridine motif.

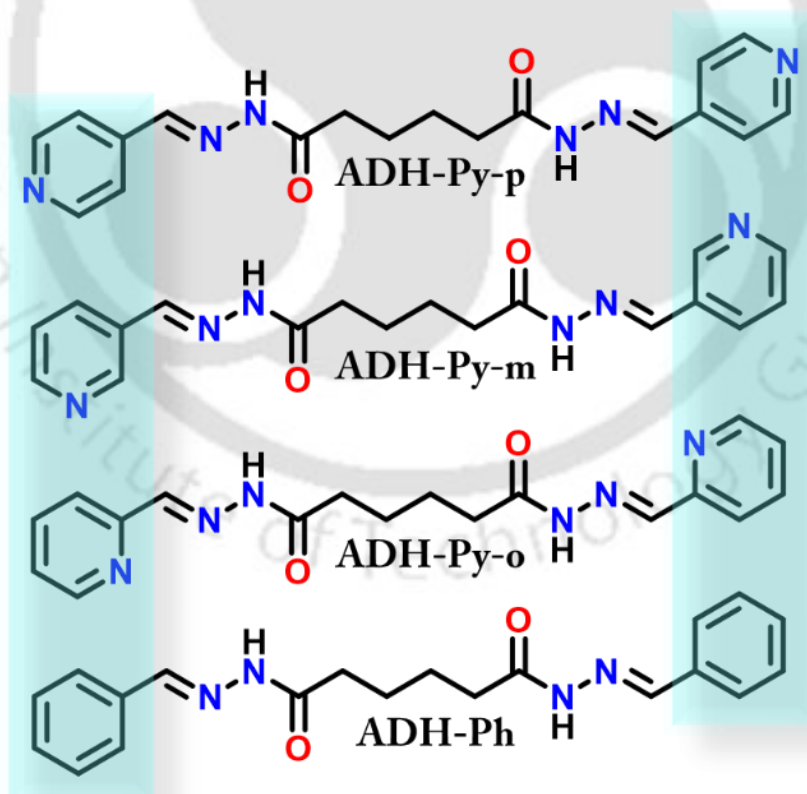


Figure 6.1. Structural presentation of ADH-Py-p, ADH-Py-m, ADH-Py-o and ADH-Ph.

6.3.2. Solid State Self-Assembly of the Receptors ADH-Py-p and ADH-Py-m

We could isolate mountable single crystals for both **ADH-Py-p** and **ADH-Py-m**, which were analysed through a single crystal X-ray diffraction (SCXRD) study, where the asymmetric unit of **ADH-Py-p** contained half of the receptor along with two water molecules, and in **ADH-Py-m**, only half of the receptor was evident as an asymmetric unit (Figure A6.1, Annexure 6). The water molecules helped in the formation of a kind of complex self-assembled pattern in **ADH-Py-p** with the help of hydrogen bonding interactions. **ADH-Py-p** formed one dimensional (1-D) self-assembly with the help of water molecules, where each arm of **ADH-Py-p** coordinated with its nearby receptor molecule via four water molecules via hydrogen bonding interactions [O1...H3B (water) = 2.26 Å, N2...H3B (water) = 2.55 Å, O3 (water)...H2 (pyridine) = 2.50 Å, O3 (water)...H2B (water) = 1.79 Å, and N1 (pyridine)...H2A (water) = 1.93 Å] (Figure 6.2 A and B). The water molecules further helped in expanding such 1-D self-assembly into 2-D space via hydrogen bonding interaction involving O2 (water)...H3A (water) = 2.04 Å (Figure 6.2 A and B).

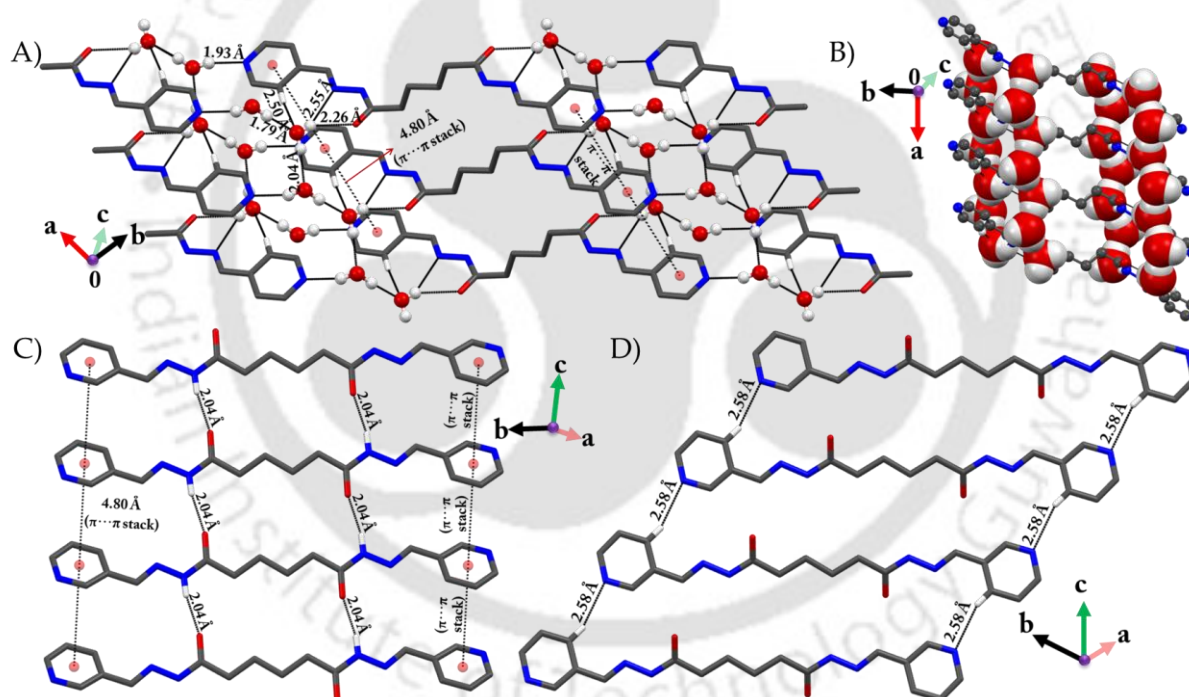


Figure 6.2: A) Representing 3-D Self- assembled network formation in **ADH-Py-p** with the help of hydrogen bonding, facilitated via water molecules, and $\pi \cdots \pi$ stacking interactions. B) Depicting the entrapment of the **ADH-Py-p** receptor molecules via water molecules. C) Demonstrating hydrogen bonding (facilitated by acylhydrazone unit) and $\pi \cdots \pi$ stacking interaction driven self-assembly formation in **ADH-Py-m**. D) Representing pyridine unit facilitated hydrogen bonding driven self-assembly formation in **ADH-Py-m**.

Moreover, weak $\pi \cdots \pi$ stacking interaction between the two nearby pyridine units also helped in such a self-assembly process where, π (pyridine) $\cdots \pi$ (pyridine) = ~ 4.80 Å (Figure 6.2 A and B).

The N-H of acylhydrazone unit further assisted in expanding such an assembly into 3-D self-assembled architecture through hydrogen bonding interaction involving O2 (water)···H3N = 1.99 Å (Figure A6.2). However, in **ADH-Py-m**, the absence water molecule resulted in a simpler self-assembly pattern. SCXRD revealed that two nearby **ADH-Py-m** receptor molecules are interconnected via hydrogen bonding and π ··· π stacking interactions involving O1···H3N = 2.04 Å, and π (pyridine)··· π (pyridine) = \sim 4.80 Å, respectively (Figure 6.2 C). Furthermore, the pyridine nitrogen and hydrogen atom also helped in expanding the self-assembly process via hydrogen bonding interactions, which involved N1 (pyridine)···H3(pyridine) = 2.58 Å (Figure 6.2 D). So, the hydrogen bonding interactions, majorly facilitated by the acylhydrazone unit, and the π ··· π stacking interactions enabled by the pyridine unit helped in the formation of a 3-D supramolecular self-assembled architecture in both the receptor molecules.

6.3.3. Insights into the Gelation Behaviour of the Receptors

Owing to the presence of metal coordination sites, metallogel formation ability of **ADH-Py-p**, **ADH-Py-m** and **ADH-Py-o** were tested with various metals in different organic solvents, as well as different aqueous-organic solvent mixtures.

Study of the Metal-Induced Gelation in **ADH-Py-p**

As per our design strategy, we investigated the gelation behaviour of **ADH-Py-p** in the presence of different metal salts, viz. AlCl₃·6H₂O, MnCl₂·4H₂O, CdCl₂·H₂O, CuCl₂·2H₂O, ZnCl₂, NiCl₂·6H₂O, CoCl₂·6H₂O, FeCl₃·6H₂O, Pb(NO₃)₂, PdCl₂, HgCl₂ and AgNO₃ (Figure A6.3, Annexure 6). However, selective gelation was observed only in the presence of AgNO₃ (**P-Ag-G**) in DMSO-H₂O (2:3, v/v). The gelation study was performed in different ratios of DMSO: H₂O, viz. 1:4, 2:3, 1:1, 3:2 and 4:1 (Figure A6.4, Annexure 6). Except DMSO: H₂O ratios of 1:4 and 4:1, gelation was observed in the other above-mentioned ratios (partial gelation was observed in DMSO: H₂O ratio of 3:2). However, we decided to proceed with maximum water content i.e. DMSO: H₂O ratio of 2:3. The concentration of the receptor was kept constant at 10 mg/ml, while minimum AgNO₃ concentration required for the gelation was 2 equivalents of the receptor, below which no gelation was observed. Also, below 10 mg per ml of receptor concentration, no metallogelation was observed; instead, gelatinous precipitate formation was observed even after the addition of an excess of AgNO₃ (Figure A6.5, Annexure 6). Gelation study of **ADH-Py-p** with AgNO₃ was also performed in different organic solvents and water mixtures in a ratio of 2:3, respectively (Figure A6.6, Annexure 6), such as dimethylformamide-water (DMF-H₂O), methanol-water (MeOH-H₂O), ethanol-water (EtOH-H₂O), ethyl acetate-water (EA-H₂O),

acetonitrile-water (ACN-H₂O) and tetrahydrofuran-water (THF-H₂O). The gel formation was observed in the case of DMF-H₂O, while precipitate formation was observed in the case of MeOH-H₂O and EtOH-H₂O mixtures. **ADH-Py-p** was insoluble in EA, ACN and THF, and as such, no gelation was observed in the presence of silver in these solvent mixtures. The white coloured metallogel thus formed remained stable for more than 6 months; however, it changed its colour from white to red to reddish black, probably because of in-situ silver nanoparticles (AgNPs) formation inside the gel matrix, which have been discussed later in this manuscript. Hence, we decided to proceed by taking 2 equivalents of AgNO₃ concentration compared to that of the receptor, where the receptor concentration was fixed at 10 mg/ml. The gel nature of the resulting gel was initially proven by the lack of flow, followed by the inversion of the vial (Figure 6.3 A) and subsequently by rheological characterization (Figure 6.3 C). Rheological measurements were employed to investigate the viscoelastic behavior and provided quantitative information about the mechanical strength of **P-Ag-G** gel. As shown in Figure 6.3 C and Figure A6.7 of Annexure 6, the results of the amplitude sweep and frequency sweep test of rheology for metallogel indicated that **P-Ag-G** gel exhibited a higher elastic storage modulus (G') and a lower loss modulus (G''), demonstrating the authenticity of gelation judgment [6.12]. The receptor itself was not capable of gelation under these conditions, indicating that the metal-ligand interactions were necessary for the gelation. We hypothesized that the coordination of Ag⁺ by the 'Pyridine -N' might have facilitated coordination polymer formation, and additionally, the H-bonding from the acylhydrazone units led to hierarchical self-assembly formation, leading to supramolecular metallogel formation. The gel-to-sol transition temperature (T_{gel}) of **P-Ag-G** gel formed in DMSO-H₂O (2:3, v/v) was calculated to be ~95 °C (Figure A6.8, Annexure 6). A relatively high T_{gel} value (95 °C) indicated that the prepared gel had good stability in a normal environment. Field emission scanning electron microscopic (FESEM) images revealed a dense fibrous network structure of **P-Ag-G** gel (Figure 6.3 B). Noticeably, the colour of the gel changed to light brown from white as it converted to a sol upon heating. This led to the breaking of the gel network, as Ag⁺, which was involved in the gel network formation, might have come out as Ag⁰, making the gelation process irreversible. With the rest of the metal salts, however, solution or precipitate formation was observed under the same conditions (Figure A6.3, Annexure 6). The metallogelation was also observed with AgClO₄·xH₂O and AgBF₄, suggesting silver was solely responsible for gelation behaviour. However, an interesting thing to note here is that the gels did not show any significant changes in their colours compared to their initial white colours; in fact, even after 2 weeks, the colour remained the same (Figure A6.9, Annexure 6). Hence, we did not carry out further investigations for these two Ag⁺ metallogels regarding nanoparticle formation. The gelation was

also tested with AgOAc; however, it was poorly soluble in water. The gelation was hence tested with sparingly soluble AgOAc, which resulted in precipitate formation with the receptor dissolved in DMSO (Figure A6.10, Annexure 6). Also, AgSO₄ was not soluble in water, and hence we did not proceed for gelation with the same. To further prove that silver has the predominant role in gelation irrespective of the anion, we performed the gelation study with 2 equivalents of TBA salts of different anions compared to the receptor, including NO₃⁻, ClO₄⁻ and OAc⁻ ions (Figure A6.11, Annexure 6). No gelation was observed; instead, clear solution was obtained in the presence of all the selected anions. We also investigated the pH effect on the gelation process. The metallogel formation was observed in a pH range from ~2 to ~12 (Figure A6.12, Annexure 6). However, the colour of the gel in basic conditions (pH ~ 12) was blackish in colour, probably because of deprotonation.

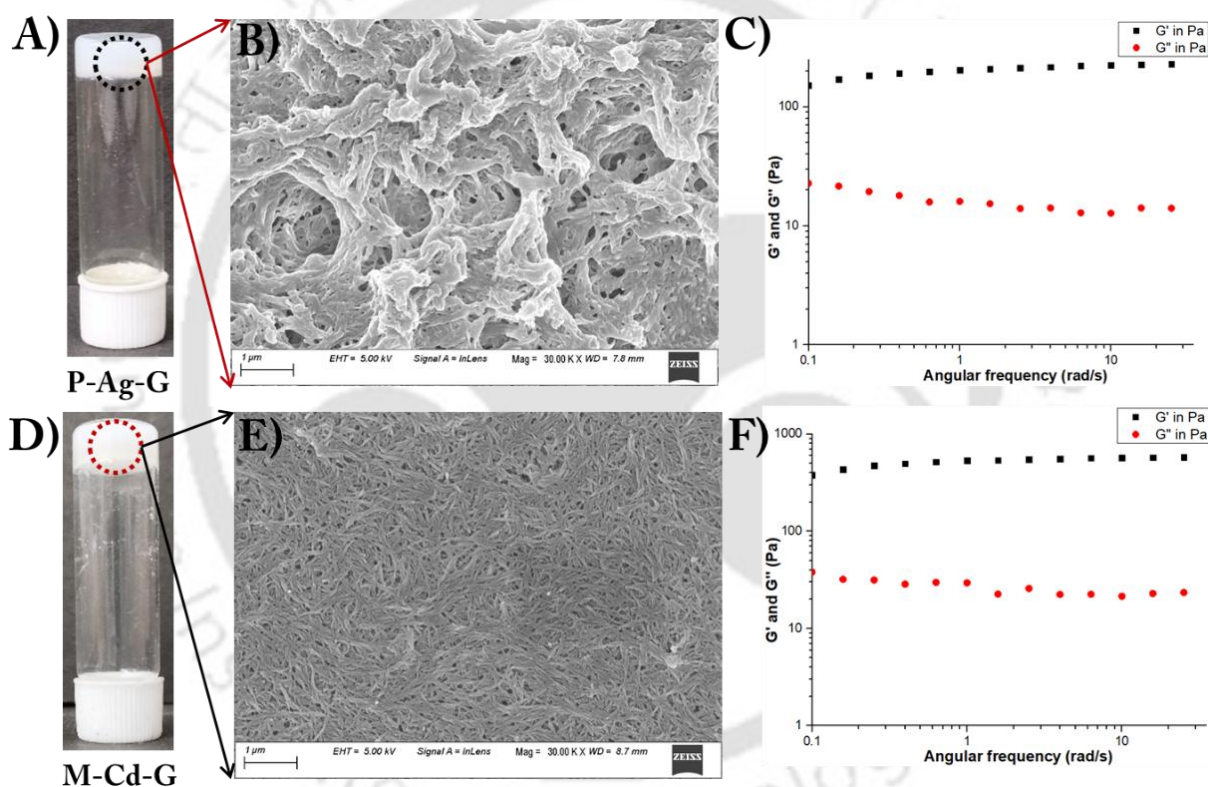


Figure 6.3: A) P-Ag-G gel, B) FESEM image of P-Ag-G xerogel, C) frequency sweep study of the gel P-Ag-G, D) M-Cd-G gel, E) FESEM image of M-Cd-G xerogel, F) frequency sweep study of the gel M-Cd-G.

Study of the Metal-Induced Gelation in ADH-Py-m

Metallogelation behaviour of the receptor **ADH-Py-m** was also investigated with all the above-mentioned metal ions (Figure A6.13, Annexure 6). For the case of **ADH-Py-m**, selective gelation was observed only in the presence of CdCl₂•H₂O (**M-Cd-G**) in DMSO-H₂O (2:3, v/v). Gelation with CdCl₂•H₂O was investigated in different ratios of DMSO: H₂O, like 1:4, 2:3, 1:1, 3:2 and 4:1.

Except DMSO: H₂O ratio of 4:1, metallogelation was observed in all the other above-mentioned ratios (Figure A6.14, Annexure 6). However, for this study, we decided to proceed with a DMSO: H₂O ratio of 2:3, like in the case of **P-Ag-G** gel, to keep the experimental parameters the same for both the gels, i.e **P-Ag-G** and **M-Cd-G**, for comparative analysis. The minimum gelation concentration of CdCl₂•H₂O required for gelation was 2 equivalents of the receptor, keeping the receptor concentration fixed at 10mg/ml. When 1 equivalent of CdCl₂•H₂O compared to the receptor concentration, precipitate formations were observed. Also, below 10 mg/ml of receptor concentration, partial gelation was observed, even after the addition of an excess of CdCl₂•H₂O (Figure A6.15, Annexure 6). Hence, we proceeded by taking 2 equivalents of CdCl₂•H₂O concentration compared to that of the receptor, keeping the receptor concentration fixed at 10 mg/ml. Gelation was observed in DMF-H₂O mixture, maintaining a ratio of 2:3, respectively. However, no gelation was observed in 2:3 ratio of MeOH-H₂O, EtOH-H₂O, EA-H₂O, ACN-H₂O and THF-H₂O (Figure A6.16, Annexure 6). The metallogel formation was observed in a pH range from ~2 to ~12 (Figure A6.17, Annexure 6) under the same conditions. It is important to mention here that the receptor itself was not capable of gel formation under the identical conditions, indicating that the metal-ligand interactions were necessary for the metallogel formation. The gel-to-sol transition temperature (T_{gel}) of **M-Cd-G** gel formed in DMSO-H₂O (2:3, v/v) was investigated. It was observed that the metallogel required a very high temperature of about ~115 °C, at which the gel started to melt and gel converted to sol at a temperature of ~125 °C (Figure A6.18, Annexure 6). FESEM images revealed an entangled ribbon-like morphology of **M-Cd-G** gel (Figure 6.3 E). The results of the amplitude sweep (Figure A6.19, Annexure 6) and frequency sweep test of rheology for organohydrogel **M-Cd-G** indicated the formation of a gel as the G' is greater than the G'' throughout the frequency range (Figure 6.3 F). Metallogel formation was not observed for the rest of the metal ions undertaken for this study with the receptor **ADH-Py-m**. Also, the receptor **ADH-Py-m** did not form gel with any of the anions (TBA salts), including Cl⁻ ion, when using 2 equivalents compared to that of the receptor (Figure A6.20, Annexure 6), suggesting cadmium has the predominant role in gelation irrespective of the anions. Interestingly, **ADH-Py-m** did not form gel in the presence of other salts of cadmium, such as 3CdSO₄•8H₂O, Cd(CH₃COO)₂•H₂O, Cd(ClO₄)₂•H₂O and Cd(NO₃)₂•4H₂O, indicating gelation was extremely selective towards CdCl₂•H₂O, unlike the **P-Ag-G** gel (Figure A6.21, Annexure 6). We hypothesized that, Cl⁻ being smaller in radius compared to SO₄²⁻, ClO₄⁻, NO₃⁻ and CH₃COO⁻ ions, it could fit well into the cavity formed by **ADH-Py-m** and Cd²⁺. The bigger anions did not fit well into the cavity and hence, hindered the metallogelation behaviour.

Important to mention here is that metallogelation was not observed for **ADH-Py-o** (Figure A6.22, Annexure 6) and **ADH-Ph** (Figure A6.23, Annexure 6) with any of the metal ions studied for our work under the identical conditions. Moreover, none of the receptors showed gelation ability in DMSO: H₂O ratio of 2:3 in the absence of any metal ions (Figure A6.24, Annexure 6). In addition, we investigated the gelation capability of the receptors **ADH-Py-m**, **ADH-Py-o** and **ADH-Ph** in the presence of AgNO₃ in different DMSO: H₂O ratios, viz. 1:4, 2:3, 1:1, 3:2 and 4:1, nevertheless, no gelation was observed (Figure A6.24, Annexure 6). Similarly, gelation capability of the receptor **ADH-Py-p**, **ADH-Py-o** and **ADH-Ph** in the presence of CdCl₂.H₂O in different DMSO: H₂O ratios, viz. 1:4, 2:3, 1:1, 3:2 and 4:1 was also checked. No gelation was observed in these cases as well (Figure A6.25, Annexure 6). The lack of metal coordination sites might have inhibited the metallogel formation in **ADH-Ph**. Nonetheless, no metallogelation behaviour in the case of **ADH-Py-o**, unlike **ADH-Py-p** and **ADH-Py-m**, clearly stated the importance of proper positioning of pyridine -N to form a polymeric network through coordination of metal ion. From all the above studies, we could conclude that the presence of the pyridine unit, as well as the positioning of the -N atom in pyridine, governed the metallogel formation ability of all our reported receptors.

6.3.4. Formation of AgNPs Inside Gel Matrix

The **P-Ag-G** gel had a remarkable stability of more than 6 months. However, we observed slow but visible colour changes of the gel from pure white to red to reddish black (Figure 6.4 A). The gel became almost reddish in colour within 1 week and then gradually became dark brown-red in colour within 1 month and then changed completely to reddish black (**P-Ag-G (B)**) within ~ 2 months (Figure 6.4 A). This colour change gave us the initial hints of the formation of silver nanoparticles inside the gel matrix. We then proceeded to further characterize the silver nanoparticles.

We initially recorded UV-Vis spectra of the receptor **ADH-Py-p** (10 μM) and gel samples **P-Ag-G** and **P-Ag-G (B)** dissolved in DMSO. **ADH-Py-p** showed absorbance ~ 293 nm in DMSO. All the gel samples also showed absorbance maxima ~ 293 nm recorded in DMSO. Only, **ADH-Ag-G (B)** revealed the appearance of a broad absorption band at ~ 440 nm as a shoulder peak along with the characteristic peak of the receptor at 293 nm, corresponding to the surface plasmon resonance (SPR) band of AgNPs as depicted in Figure 6.4 B, confirming formation of AgNPs inside gel matrix. Field Emission Transmission Electron Microscope (FETEM) analysis revealed the size range of spherical-shaped AgNPs to be from 14.86 nm to 28.22 nm (Figure 6.4 C and D).

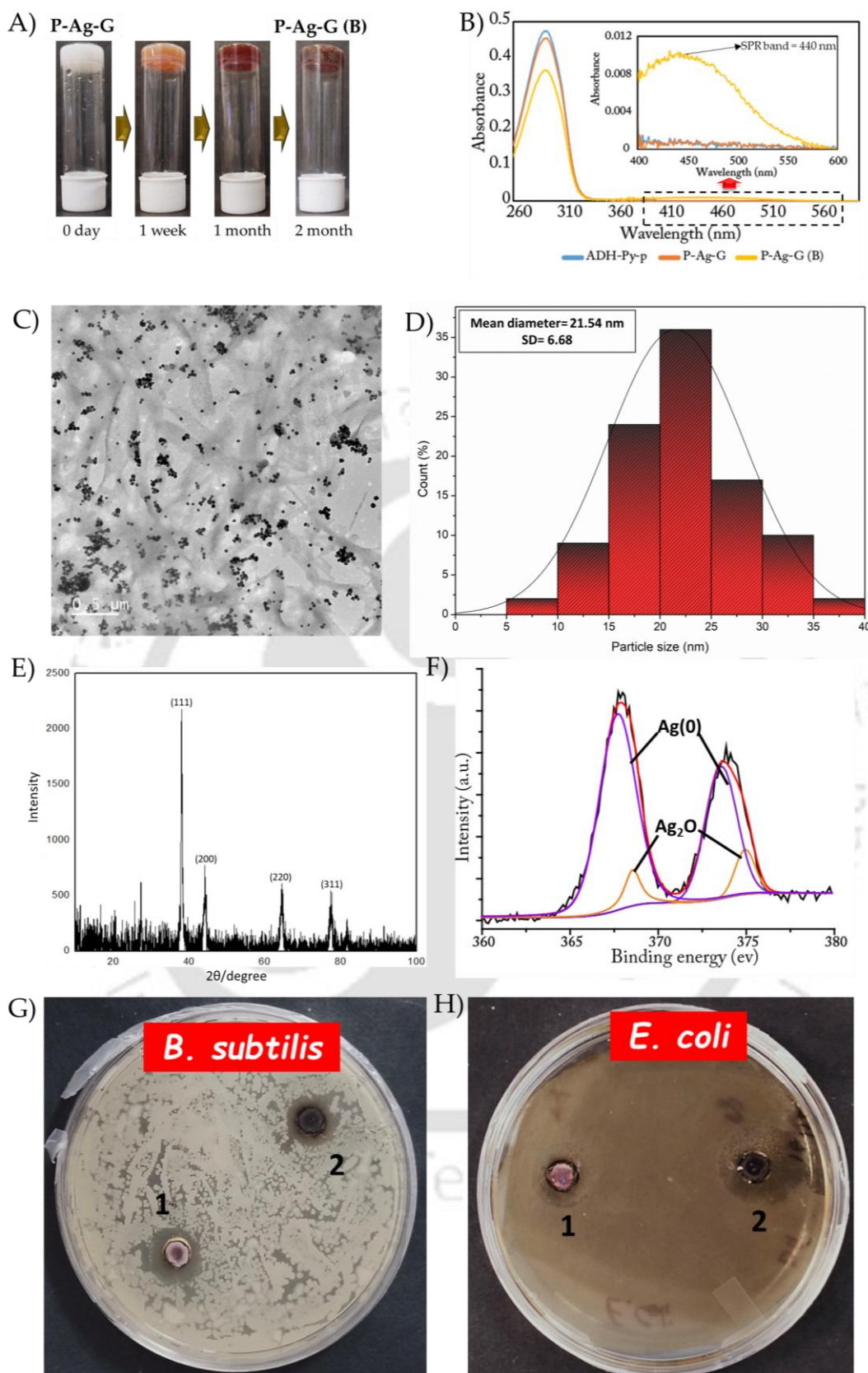


Figure 6.4. A) AgNPs formation inside gel matrix, B) SPR band of AgNP recorded in DMSO, C) FETEM images of P-Ag-G gel containing AgNPs residing on the gel nanofibers, D) particle size distributions of AgNPs obtained from FETEM, E) PXRD spectra of P-Ag-G xerogel, F) XPS spectra of P-Ag-G xerogel.

Further, XPS analysis revealed binding energies of Ag 3d_{5/2} and 3d_{3/2} at 368.1 eV and 374.1 eV, along with the weak satellite peaks at 368.9 eV and 374.8 eV, thus confirming the presence of both Ag₀ and Ag₂O (Figure 6.4 F). The analysis of the AgNPs was also carried out by PXRD (Figure 6.4 E). The number of Bragg reflections with 2θ values of 38.53°, 44.67°, 65.08° and 78.06° corresponding to (1 1 1), (2 0 0), (2 2 0) and (3 1 1) respectively indicated that the AgNPs were spherical structured and crystalline in nature (JCPDS card no: 65-2871) [6.41].

As silver is well-known for its strong antimicrobial properties [6.42], and to explore the antimicrobial potential of our organohydrogels **P-Ag-G** and **P-Ag-G (B)**, a zone inhibition assay was performed with Gram-negative representative bacteria, *Escherichia coli* (DH5α) and Gram-positive representative bacteria, *Bacillus subtilis*. The results were impressive for both the Gram-positive and Gram-negative representative groups, as a diameter of 15 mm was observed in the case of **P-Ag-G** gel for both *B. subtilis* and *E. Coli*, respectively.

However, a relatively high effect was evident for the gel **P-Ag-G (B)** as a diameter of 15 mm and 20 mm was observed in the case of *B. subtilis* and *E. Coli*, respectively (Figure 6.4 G and 6.4 H). It has been reported that the Ag⁺ cations can be responsible for the antimicrobial activity because Ag⁺ cations have been found to disrupt the bacterial cell membranes and inhibit the enzymatic activity of bacterial cells [6.43]. Also, in the last decade, AgNPs have become known as an effective antimicrobial agent owing to their ability to kill bacteria with complex mechanisms.

6.3.5. Investigation of Gelation Mechanism

In view of the fact that receptors **ADH-Py-p** and **ADH-Py-m** formed metallogel with silver and cadmium, respectively, while **ADH-Py-o** and **ADH-Ph** did not show metallogelation property, this confirmed the critical role of 'pyridine -N' for the self-assembly formation with metal ions, along with its position in the ligand.

The ¹H NMR spectra of both the receptors, **ADH-Py-p** and **ADH-Py-m**, along with their respective xerogels (**P-Ag-G**, **P-Ag-G(B)** and **M-Cd-G**) were recorded by dissolving (dispersing in case of **P-Ag-G(B)**) 3mg of each sample in 400 μL of DMSO-*d*₆ in separate NMR tubes. From comparison of the spectra of **ADH-Py-p**, **P-Ag-G**, and **P-Ag-G(B)**, it was observed that the ¹H NMR peaks corresponding to acylhydrazide -NH₁ and -NH₂ in **ADH-Py-p** got downfield shifted by 0.040 ppm and 0.032 ppm, respectively, in **P-Ag-G** (Figure 6.5 A). On the other hand, both the imine protons (H_c and H_d) showed average downfield shifting of ~ 0.009 ppm in the xerogel of **P-Ag-G** compared to that of **ADH-Py-p**. The aromatic protons H_b also showed a downfield shift of 0.042 ppm in **P-Ag-G** as compared to that of **ADH-Py-p**. Mentionable in this regard is that, peak positions of xerogels of **P-Ag-G** and **P-Ag-G(B)** overlapped. The downfield shifting of the

aromatic region protons suggested binding of Ag^+ to the pyridine -N, leading to the deshielding effect. Intermolecular H-bonding between the acylhydrazone -NH and -C=O was probably the reason for the downfield shifting of the rest of the protons in the solution state.

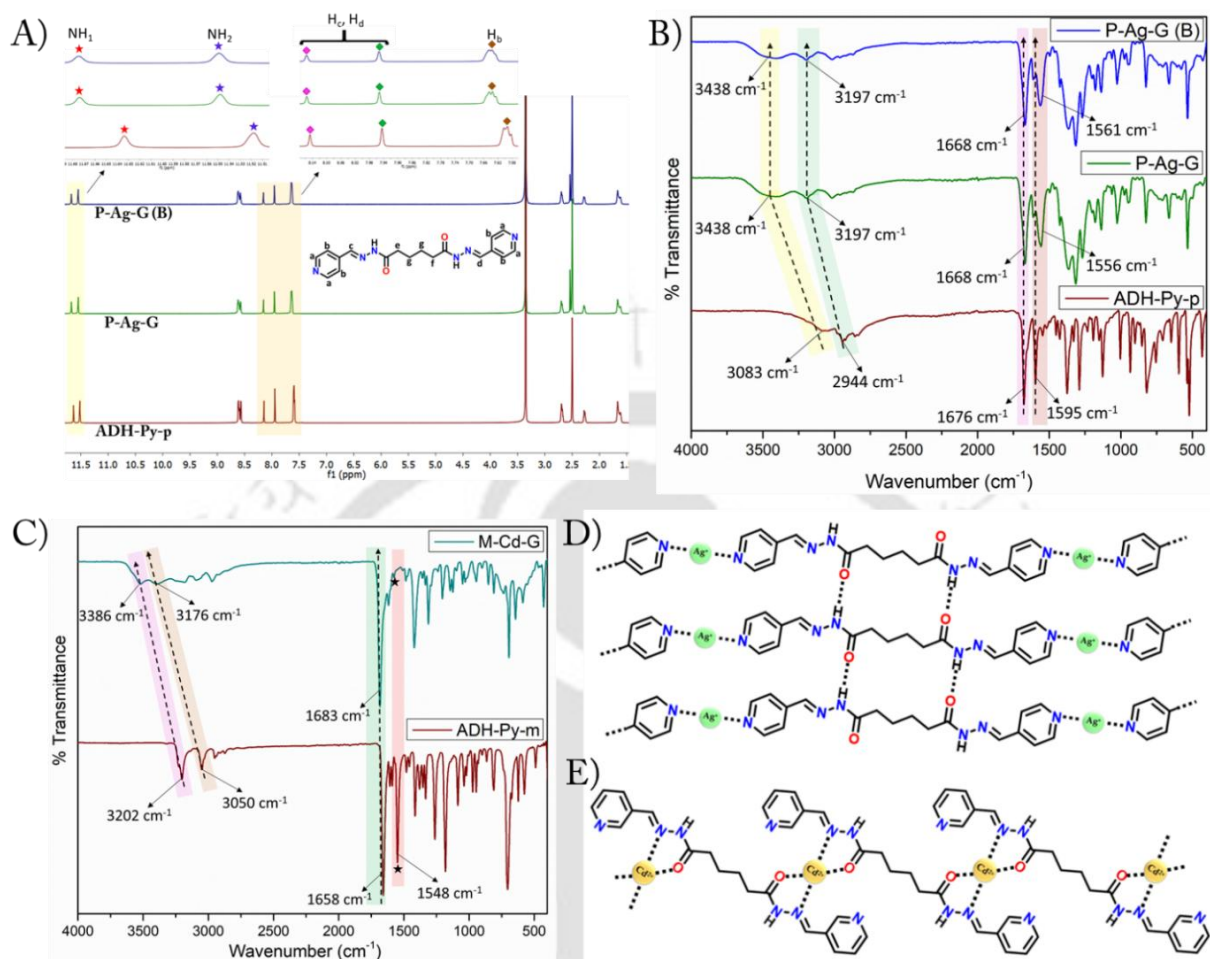


Figure 6.5. A) Stacked ^1H NMR spectra of ADH-Py-p, P-Ag-G and P-Ag-G (B), B) Stacked FTIR-ATR spectra of ADH-Py-p, P-Ag-G and P-Ag-G (B), C) Stacked FTIR-ATR spectra of ADH-Py-m, and M-Cd-G, pictorial depiction of the plausible metal ion coordination driven self-assembly in D) P-Ag-G gel and E) M-Cd-G gel.

The FTIR-ATR spectra of ADH-Py-p, P-Ag-G and P-Ag-G (B) were also recorded (Figure 6.5 B). The stretching frequency corresponding to acylhydrazone -NH at 3083 cm^{-1} of ADH-Py-p showed a significant shifting of 355 cm^{-1} towards the higher wavenumber region in the case of both xerogels. The aromatic -CH stretching frequency of ADH-Py-p at 2944 cm^{-1} also showed a shift of 253 cm^{-1} towards the higher wavenumber region for both the xerogels. Conversely, the -C=O stretching frequency of ADH-Py-p at 1676 cm^{-1} exhibited a slight shifting of 8 cm^{-1} towards the lower wavenumber region in the case of both xerogels. The imine -C=N stretching frequency of ADH-Py-p at 1595 cm^{-1} demonstrated shifting of 39 cm^{-1} and 34 cm^{-1} towards lower wavenumber regions in the case of P-Ag-G and P-Ag-G (B), respectively. The shifting of the

stretching frequency of acylhydrazide –NH to the higher wavenumber region in **P-Ag-G** and **P-Ag-G-(B)** suggested the alteration of hydrogen bonding interactions after metal coordination, thereby changing the packing arrangement in the xerogel state as compared to the one which earlier existed in the solid powder of **ADH-Py-p**. The binding of Ag^+ to pyridine-N imparts electron withdrawing effect from the same, thereby leading to charge redistribution of the entire aromatic ring system, which might have caused shifting of the aromatic –CH stretching frequency to a higher wavenumber region. Compared to –NH and –CH, minimal shiftings were observed for –C=O and –C=N stretching frequencies. The hypothetical binding mode of Ag^+ to **ADH-Py-p** (Figure 6.5 D).

On the other hand, comparison of the ^1H NMR spectra of **ADH-Py-m** and **M-Cd-G** revealed that, unlike the case of **ADH-Py-p** and its xerogels, the peak positions of **M-Cd-G** xerogel showed negligible shifting compared to those of **ADH-Py-m** (Figure A6.27, Annexure 6). Hence, the binding mode of $\text{CdCl}_2 \cdot \text{H}_2\text{O}$ to **ADH-Py-m** was inconclusive from the ^1H NMR spectra. However, comparison of FTIR-ATR spectra of **ADH-Py-m** and **M-Cd-G** provided a much clearer picture of the binding mechanism (Figure 6.5 C). The stretching frequencies corresponding to acylhydrazide –NH at 3202 cm^{-1} and aromatic –CH at 3050 cm^{-1} of **ADH-Py-m** showed shifting of 184 cm^{-1} and 126 cm^{-1} towards higher wavenumber regions in the case of **M-Cd-G**. Interesting to note here was that, unlike the case of **ADH-Py-p**, the –C=O stretching frequency of **ADH-Py-m** at 1658 cm^{-1} displayed shifting of 25 cm^{-1} towards the higher wavenumber region in the case of the xerogel. Furthermore, the imine –C=N stretching frequency of **ADH-Py-m** at 1548 cm^{-1} almost vanished in the xerogel state. The distinct difference observed for –C=O and –C=N stretching frequencies in the FTIR-ATR spectra suggested different metal binding modes for the receptors **ADH-Py-p** and **ADH-Py-m**. The almost disappearance of the imine –C=N stretching frequency of **ADH-Py-m** in the **M-Cd-G** xerogel hinted towards the binding of Cd^{2+} by the acylhydrazide group rather than the pyridine -N, which led to the change in overall electronic environment of the acylhydrazide group, thus justifying the shifting in the –C=O stretching frequency. The metal coordination in **M-Cd-G** faded the already existing intermolecular hydrogen bonding network between the acylhydrazide -NH and -C=O in **ADH-Py-m**, thus leading to shifting of the acylhydrazide -NH stretching frequency to the higher wavenumber region. The tentative model of binding of Cd^{2+} to the receptor **ADH-Py-m** is shown in Figure 6.5 E.

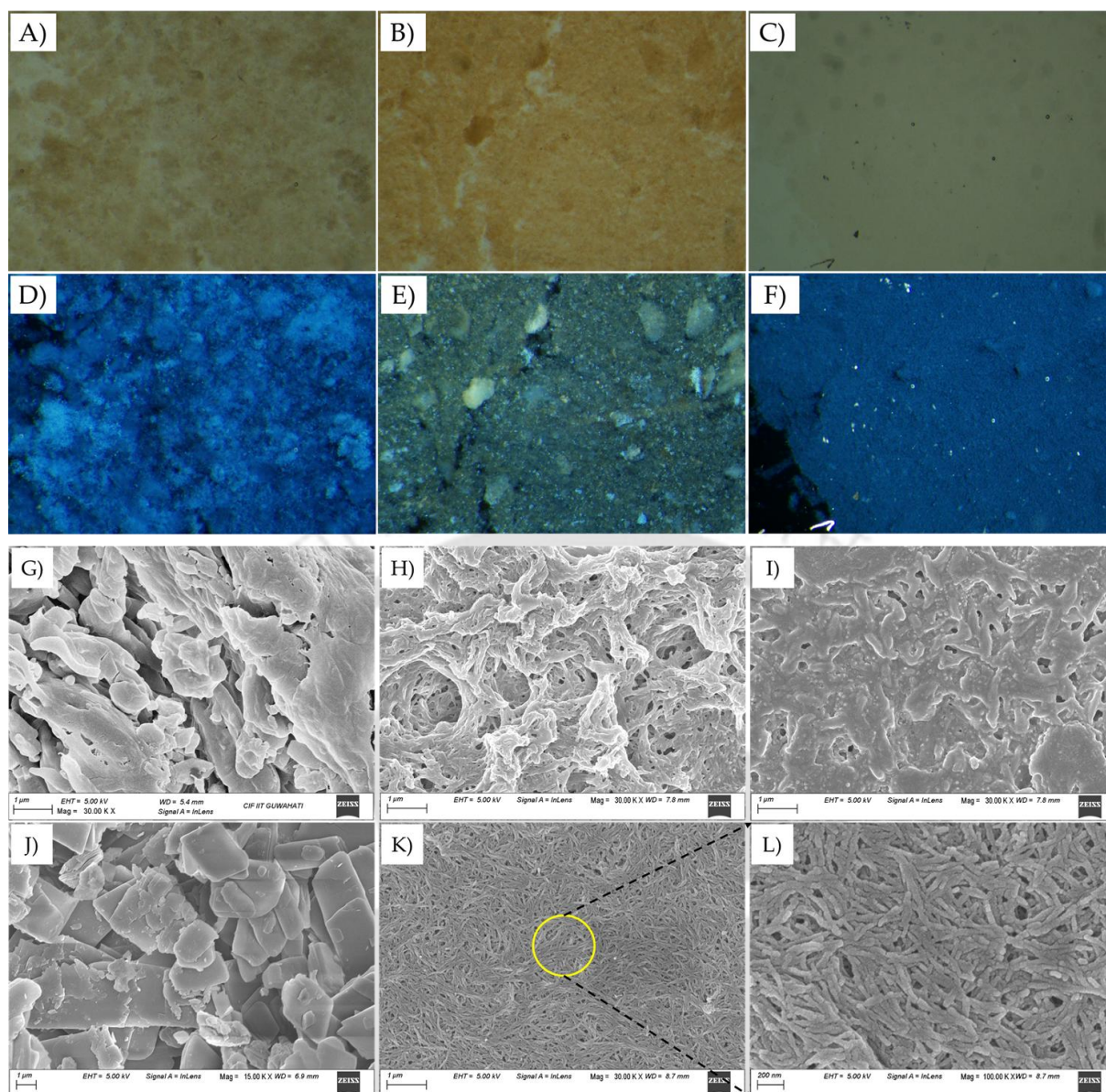


Figure 6.6. Bright field and POM images of **P-Ag-G (A, D)**, **P-Ag-G (B) (B, E)** and **M-Cd-G (C, F)**; FESEM images of **G) ADH-Py-p**, **H) P-Ag-G gel**, **I) P-Ag-G (B) gel**, **J) ADH-Py-m**, **K) M-Cd-G gel** and **L) magnified picture of M-Cd-G gel**.

The fluorescence spectra of both receptors (10 μM) obtained by exciting them at 300 nm in a DMSO: H₂O ratio of 2:3 were compared with the fluorescence spectra of the gels **P-Ag-G** and **M-Cd-G**, excited at the same wavelength. The emission spectra of both the gels showed bathochromic shifts with enhanced emissions, which might be due to chelation-enhanced fluorescence (CHEF) and/or aggregation-induced emission (AIE), arising from the restriction of intramolecular motion (RIM) in the gel states (Figure A6.28, Annexure 6). We also investigated the supramolecular assemblies of **P-Ag-G**, **P-Ag-G (B)** and **M-Cd-G** by bright field (Figure 6.6 A-6.6 C) and polarized optical microscopy (POM). The wet gels showed bright birefringence region (Figure 6.6

D-6.6 F), further indicating the presence of anisotropic assemblies in the supramolecular gel. The morphology of the powder sample of the receptor **ADH-Py-p**, **ADH-Py-m** and vacuum-dried xerogel of **P-Ag-G**, **P-Ag-G (B)** and **M-Cd-G** was assessed using FESEM analysis. As shown in Figure 6.6, the electron microscopy images of the **ADH-Py-p** powder (Figure 6.6 G) showed an agglomerated morphology which transformed into crosslinked dense fibrous networks, suggesting the formation of a much-ordered supramolecular assembly (Figure 6.6 H). Interestingly, in the case of **P-Ag-G (B)**, fibrous structures were disrupted, unlike **P-Ag-G** and some prominent nanospheres of average diameter 20 nm were observed, probably because of the formation of silver nanoparticles (Figure 6.6 I). On the other hand, the lamellar morphology of **ADH-Py-m** (Figure 6.6 J) got transformed to a nanoribbon morphology of average diameter 40 nm (Figure 6.6 K and 6.6 L). EDX analysis of the xerogels was performed to analyze the chemical compositions, which showed the presence of C, N, O, and Ag elements in the case of **ADH-Ag-G (B)** (Figure A6.29, Annexure 6) and C, N, O, and Cd elements in the case of **M-Cd-G** (Figure A6.30, Annexure 6).

6.3.6. Visual Detection of Cadmium in Real Water Samples

Cadmium is a highly toxic heavy metal, and intake of Cd^{2+} via the direct ingestion of contaminated water can exert a multitude of adverse effects on human health. Hence, monitoring the presence of cadmium in different water samples, including drinking water, is of vital importance. Naked eye detection of cadmium, bypassing the use of sophisticated instrumentation will be very advantageous in this regard. Our receptor **ADH-Py-m** could form gel selectively in the presence of cadmium chloride out of all the metal chlorides tested (Figure A6.13, Annexure 6). The idea of selectivity in gelation has been used for naked eye detection of cadmium in the presence of competitive metal ions like Zn^{2+} , Ni^{2+} , Co^{2+} , Mn^{2+} and Al^{3+} in different real water samples. Lake water and river water specimens were brought from a lake (IIT Guwahati Campus) and the Brahmaputra River (near IIT Guwahati Campus, Assam, India). Milli Q and tap water were available in the laboratory. The receptor **ADH-Py-m** (5 mg) was dissolved in DMSO (200 μL) in 5 different glass vials, and Cd^{2+} (2 equivalents of the receptor, 57 mM), along with Zn^{2+} , Ni^{2+} , Co^{2+} , Mn^{2+} and Al^{3+} (2 equivalents of the receptor for all the metal ions), was dissolved in 300 μL of different water samples separately. All the different aqueous solutions with the above-mentioned metal ions dissolved in them were rapidly added separately to different glass vials containing the receptor. Supramolecular metallogelation of **ADH-Py-m** was observed in all the water samples, viz., Milli Q, river, lake, tap and drinking water containing Cd^{2+} along with other competitive metal ions (Figure 6.7). Metallogelation of the receptor was not hampered even when the competitive metal ions were present in equal equivalents to cadmium compared to that of the

receptor. Thus, naked eye detection of the presence of cadmium in real water samples was feasible with the help of the selective metallogelation concept. We performed a control experiment by dissolving the receptor **ADH-Py-m** (5 mg) in DMSO (200 μ L) and then adding 300 μ L Milli-Q water containing Zn^{2+} , Ni^{2+} , Co^{2+} , Mn^{2+} and Al^{3+} , excluding Cd^{2+} . No gelation was observed, confirming Cd^{2+} was solely responsible for metallogelation with **ADH-Py-m**.

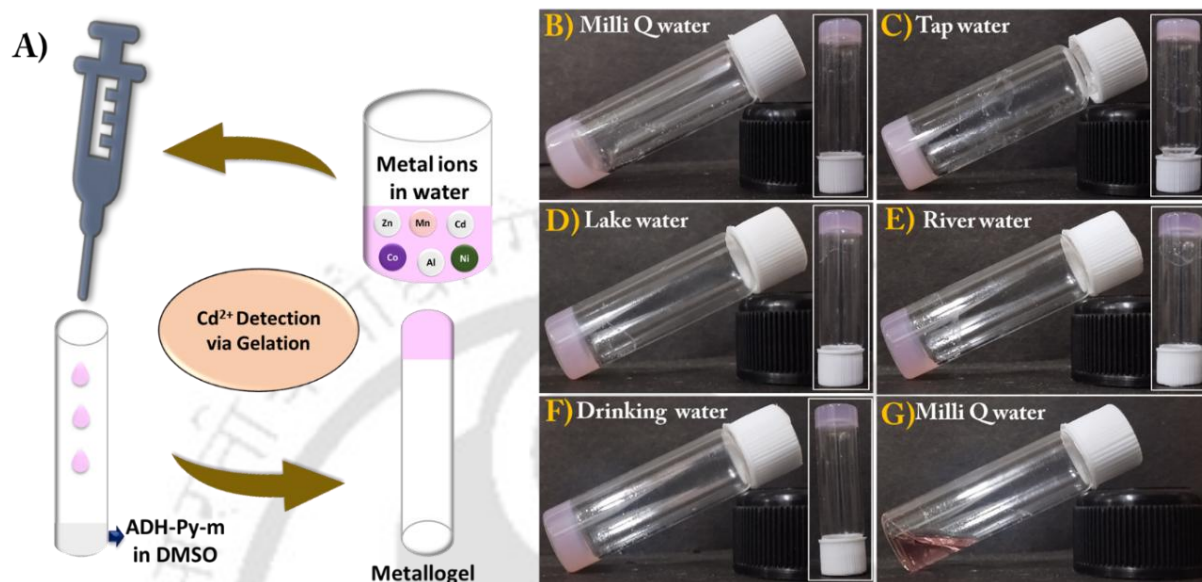


Figure 6.7: A) Metallogelation of **ADH-Py-m** in different water samples B) Milli Q water, C) Tap water, D) Lake water, E) River water, F) Drinking water and G) Milli Q water.

6.4. Conclusion

In conclusion, we have demonstrated the proper relationship between the molecular structures and metallogelation ability of three adipic dihydrazide-based pyridine unit containing positional isomers, viz. **ADH-Py-p**, **ADH-Py-m**, and **ADH-Py-o**. Additionally, **ADH-Ph** was synthesized as a control compound to rationally establish our proposed hypothesis. Out of these four receptors, **ADH-Py-o** and **ADH-Ph** did not show metallogelation property. **ADH-Py-p** could form metallogel **P-Ag-G**, selectively in the presence of Ag^+ , irrespective of the counter anion. The gel matrix eventually facilitated the spontaneous in-situ AgNP formation by reduction of Ag^+ to Ag^0 and formed the metallogel **P-Ag-G (B)**. Both **P-Ag-G** and **P-Ag-G (B)** could show anti-bacterial activity. **ADH-Py-m**, on the other hand, formed metallogel selectively in the presence of $\text{CdCl}_2 \cdot \text{H}_2\text{O}$ and Cl^- was mandatory for the self-assembly formation, as other salts of cadmium, such as, $3\text{CdSO}_4 \cdot 8\text{H}_2\text{O}$, $\text{Cd}(\text{CH}_3\text{COO})_2 \cdot \text{H}_2\text{O}$, $\text{Cd}(\text{ClO}_4)_2 \cdot \text{H}_2\text{O}$ and $\text{Cd}(\text{NO}_3)_2 \cdot 4\text{H}_2\text{O}$ failed to show metallogelation behaviour. The difference in metallogelation behaviour suggested a different underlying mechanism for the gel formation process, which was investigated through IR and NMR spectroscopic techniques. The selectivity of **ADH-Py-m** for metallogelation towards $\text{CdCl}_2 \cdot \text{H}_2\text{O}$

was then exploited for naked-eye detection of the same through gelation process in different real water samples in the presence of other competitive metal chlorides. The investigation of such positional isomeric effect on metallogelation behaviour may help in better understanding towards designing receptors for metallogel formation purposes. Moreover, our proposed idea of heavy metal ion detection by using the concept of selective metallogelation paves a new way of detecting toxic analytes without the need for any sophisticated instrumentation.

References

- [6.1] I. Pal, N. Kumar Pathak, S. Majumdar, G. Lepcha, A. Dey, S. K. Yatirajula, U. Tripathy and B. Dey, *Inorg. Chem.*, 2024, **63**, 26, 12003-12016.
- [6.2] N. Alam, S. Mondal and D. Sarma, *Coord. Chem. Rev.*, 2024, **504**, 215673.
- [6.3] P. L. Scognamiglio, D. Tesauro and G. N. Roviello, *Processes*, 2025, **13**, 11, 3671.
- [6.4] K. Preet, R. Kumar, L. Kaur, S. Roy, S. C. Sahoo and D. B. Salunke, *J. Mol. Struct.*, 2024, **1310**, 138316.
- [6.5] B. Pal, S. Dhibar, R. Mukherjee, S. Bhattacharjee, P. P. Ray and B. Saha, *Mater. Adv.*, 2023, **4**, 3628-3635.
- [6.6] S. Dhibar, H. Dahiya, K. Karmakar, S. Kundu, S. Bhattacharjee, G. C. Nayak, P. Karmakar, G. D. Sharma and B. Saha, *J. Mol. Liq.*, 2023, **370**, 121020.
- [6.7] K. Karmakar, A. Dey, S. Dhibar, R. Sahu, S. Bhattacharjee, P. Karmakar, P. Chatterjee, A. Mondal and B. Saha, *RSC Adv.*, 2023, **13**, 2561-2569.
- [6.8] H. Wu, J. Zheng, A.-L. Kjøniksen, W. Wang, Y. Zhang and J. Ma, *Adv. Mater.*, 2019, **31**, 1806204.
- [6.9] X. Tao, X. Chen, T. Chen, G. Du, Y. Wang and Q. Li, *Colloids Surf. A Physicochem. Eng. Asp.*, 2022, **634**, 127910.
- [6.10] A. Fortunato and M. Mba, *Gels*, 2021, **7**, 3, 85.
- [6.11] M. K. Dixit, C. Mahendar and M. Dubey, *Chem. Asian J.*, 2022, **17**, e201900559.
- [6.12] M. Sharma, P. J. Sarma, M. J. Goswami and K. K. Bania, *J. Colloid Interface Sci.*, 2017, **490**, 529-541.
- [6.13] D. Bairagi, P. Ghosh, P. Roy and A. Banerjee, *ACS Appl. Nano Mater.*, 2023, **6**, 4, 2299-2309.
- [6.14] T. Mondal, S. Patra, B. Mondal, P. Ghosh, I. W. Hamley and A. Banerjee, *ACS Appl. Polym. Mater.*, 2024, **6**, 18, 11383-11391.
- [6.15] S. Husain, A. Nandi, F. Z. Simnani, U. Saha, A. Ghosh, A. Sinha, A. Sahay, S. Kumar Samal, P. K. Panda and S. K. Verma, *J. Funct. Biomater.*, 2023, **14**, 1, 47.
- [6.16] Y. Cheng, F. Sun, Q. Feng, Q. Zhao and Y. Zhou, *Colloids Surf. A: Physicochem. Eng. Asp.*, 2017, **522**, 43-50.
- [6.17] S. Zhang, W. Jiang, G. Liu, S. Liu, H. Chen, G. Lyu, G. Yang, Y. Liu and Y. Ni, *J. Colloid Interface Sci.*, 2023, **629**, 766-777.
- [6.18] A. Bora, R. Munjal, A. Chakraborty, L. Meena, S. N. Chathangad, S. Sadhukhan and S. Mukhopadhyay, *ACS Appl. Bio Mater.*, 2025, **8**, 7, 6159-6176.
- [6.19] A. Sati, T. N. Ranade, S. N. Mali, H. K. A. Yasin and A. Pratap, *ACS Omega*, 2025, **10**, 8, 7549-7582.
- [6.20] A. De and R. Mondal, *ACS Omega*, 2018, **3**, 6, 6022-6030.
- [6.21] B. O. Okesolaa and D. K. Smith, *Chem. Soc. Rev.*, 2016, **45**, 4226-425.
- [6.22] S. Sarkar, S. Dutta, P. Bairi and T. Pal, *Langmuir*, 2014, **30**, 26, 7833-7841.

- [6.23] M. Roy, A. Adhikary, S. Saha and R. Mondal, *Mater. Adv.*, 2022, **3**, 7328-7338.
- [6.24] S. Sengupta and R. Mondal, *Chem. Eur. J.*, 2013, **19**, 5537-5541.
- [6.25] P. S. Gahlaut, D. Gautam, K. Yadav and B. Jana, *J. Mol. Struct.*, 2023, **1272**, 134152.
- [6.26] B. N. Ghosh, S. Bhowmik, P. Mal and K. Rissanen, *Chem. Commun.*, 2014, **50**, 734-736.
- [6.27] V. Tantishaiyakul, S. Dokmaisrijan, T. Sangfai, N. Hirun, L Li, S. Juntarapet and K. Suknuntha, *Colloids Surf. A Physicochem. Eng. Asp.*, 2014, **446**, 118-126.
- [6.28] G. Picci, C. Caltagirone, A. Garau, V. Lippolis, J. Milia, and J. W. Steed, *Coord. Chem. Rev.*, 2023, **492**, 215225.
- [6.29] N. Alam and D. Sarma, *Soft Matter*, 2020, **16**, 10620-10627.
- [6.30] C. Soman, A. Sebastian, M. K. Mahato, U. V. Varadaraju and E. Prasad, *Mater. Adv.*, 2022, **3**, 5458-5467.
- [6.31] A. Tsuge, D. Hashimura, H. Ikenoue and K. Araki, *Chem. Lett.*, 2022, **51**, 870-872.
- [6.32] N. P. Pathak, A. Sengupta and S. Yadav, *Mater. Adv.*, 2022, **3**, 3906-3914.
- [6.33] P. Dastidar, S. Ganguly and K. Sarkar, *Chem. Asian J.*, 2016, **11**, 2484-2498.
- [6.34] K. Sarkar and P. Dastidar, *Chem. Asian J.*, 2019, **14**, 194-204.
- [6.35] T. Tu, W. Fang, X. Bao, X. Li and K. H. Dötz, *Angew. Chem. Int. Ed.*, 2011, **50**, 6601-6605.
- [6.36] A. Y.-Y. Tam, K. M.-C. Wong and V. W.-W. Yam, *J. Am. Chem. Soc.*, 2009, **131**, 17, 6253-6260.
- [6.37] P. Sahoo, D. K. Kumar, D. R. Trivedi and P. Dastidar, *Tetrahedron Lett.*, 2008, **49**, 19, 3052-3055.
- [6.38] O. A. Pegu and G. Das, *Langmuir*, 2024, **40**, 45, 24095-24105.
- [6.39] O. A. Pegu, R. Moral and G. Das, *Chem. Eng. J.*, 2025, 169128.
- [6.40] R. Moral, O. A. Pegu and G. Das, *Nanoscale*, 2025, Advance Article.
- [6.41] R. Kalaivani, M. Maruthupandy, T. Muneeswaran, A. H. Beevi, M. Anand, C.M. Ramakritinan and A.K. Kumaraguru, *Frontiers in Laboratory Medicine*, 2018, **2**, 1, 30-35.
- [6.42] S. Thammawithan, P. Siritongsuk, S. Nasompag, S. Daduang, S. Klaynongsruang, N. Prapasarakul and R. Patramanon, *Vet. Sci.*, 2021, **8**, 177.
- [6.43] M. Zakia, J. M. Koo, D. Kim, K. Ji, P. Huh, J. Yoon and S. I. Yoo, *Green chem. lett. rev.*, 2020, **13**, 1, 34-40.

Annexure 6

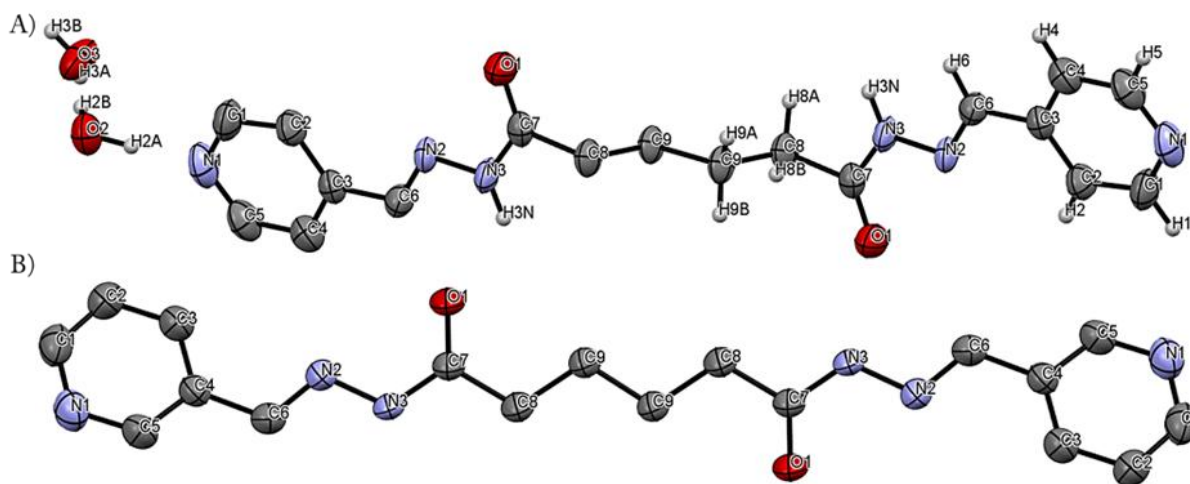


Figure A6.1: ORTEP diagram of ADH-Py-p with 50% occupancy.

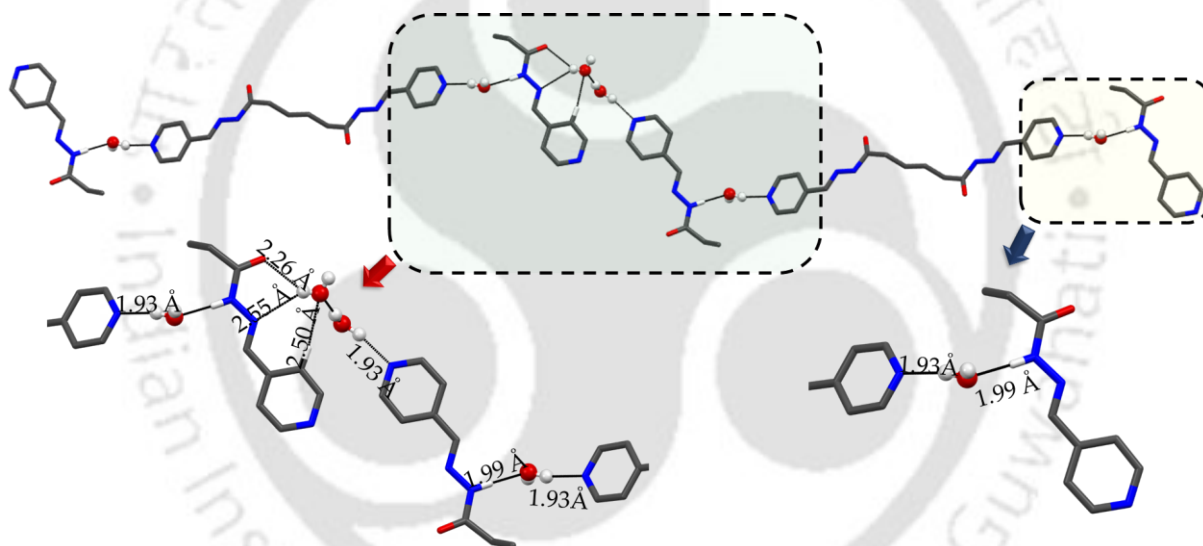


Figure A6.2: Representing labelled ORTEP structures of A) ADH-Py-p, and B) ADH-Py-m with 50% probability level.

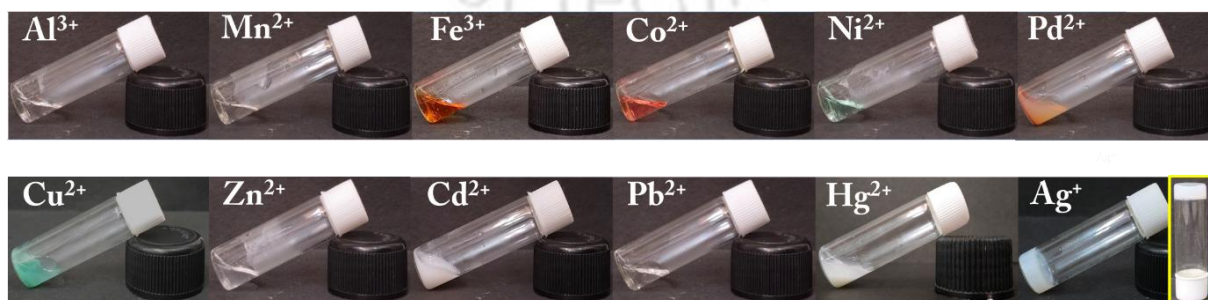


Figure A6.3: Gelation study of ADH-Py-p in presence of different metal salts.

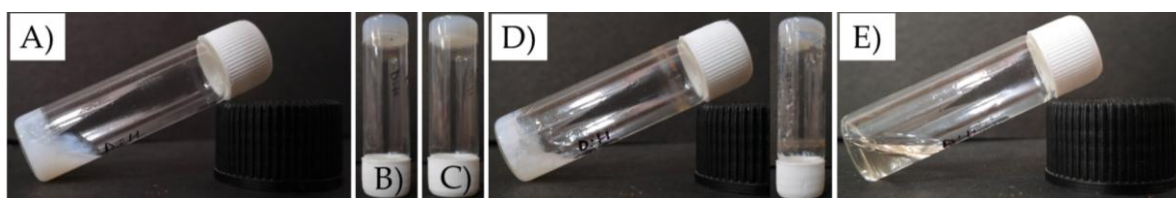


Figure A6.4: Gelation study of ADH-Py-p with AgNO_3 in different ratios of DMSO: H_2O viz. A) 1:4, B) 2:3, C) 1:1, D) 3:2 and E) 4:1.

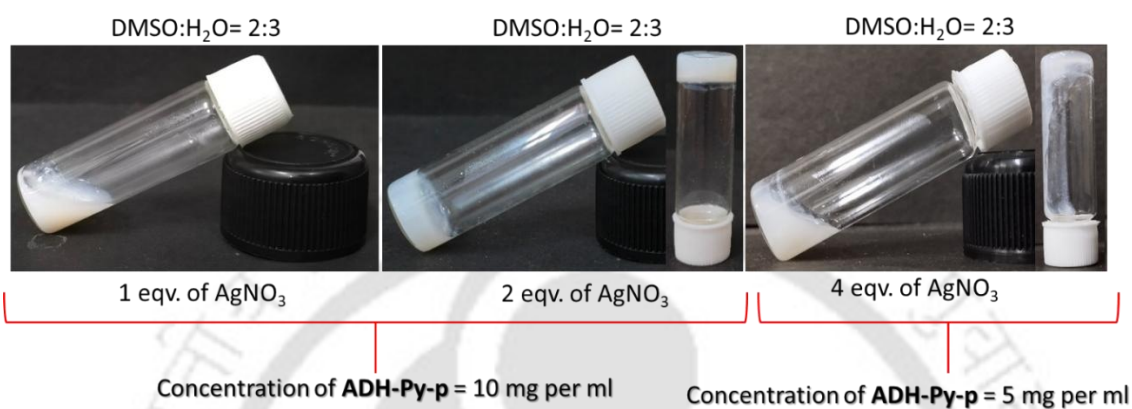


Figure A6.5: Optimization of minimum gelation concentration of ADH-Py-p and AgNO_3 required for metallogel formation.

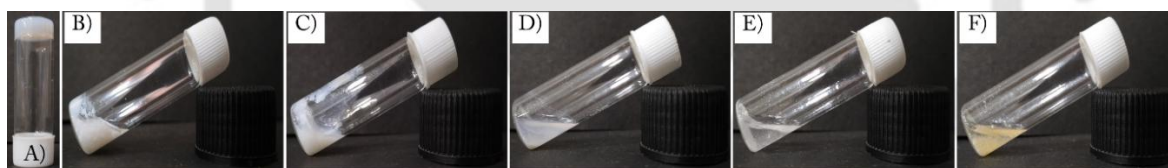


Figure A6.6: Gelation study of ADH-Py-p with AgNO_3 in different solvent mixtures viz. A) DMF- H_2O , B) MeOH- H_2O , C) EtOH- H_2O , D) EA- H_2O , E) ACN- H_2O and F) THF- H_2O .

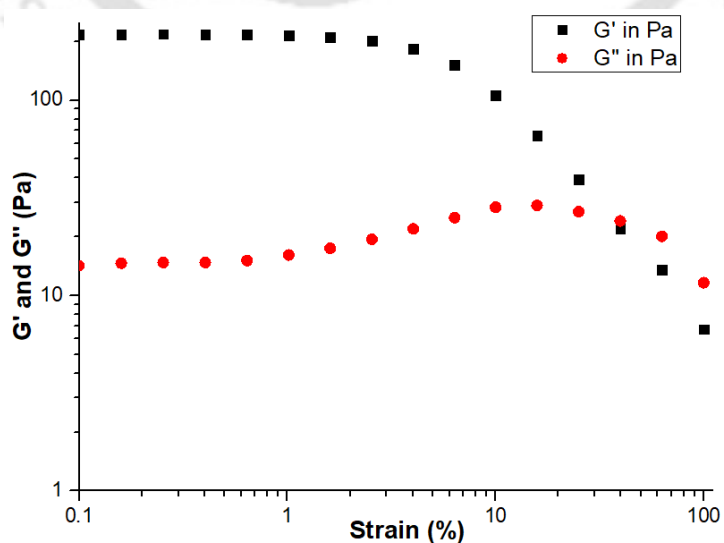


Figure A6.7: Amplitude sweep study of the P-Ag-G organohydrogel.

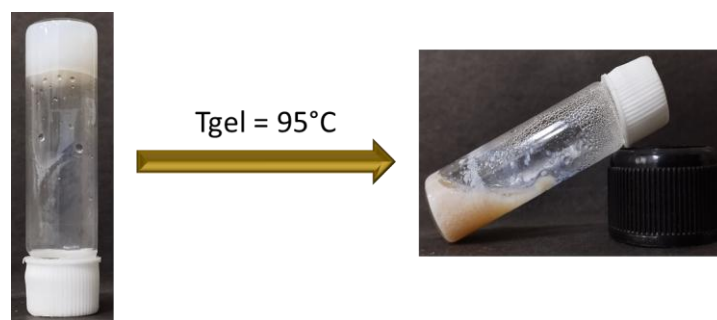


Figure A6.8: Gel-to-sol transition of P-Ag-G gel.

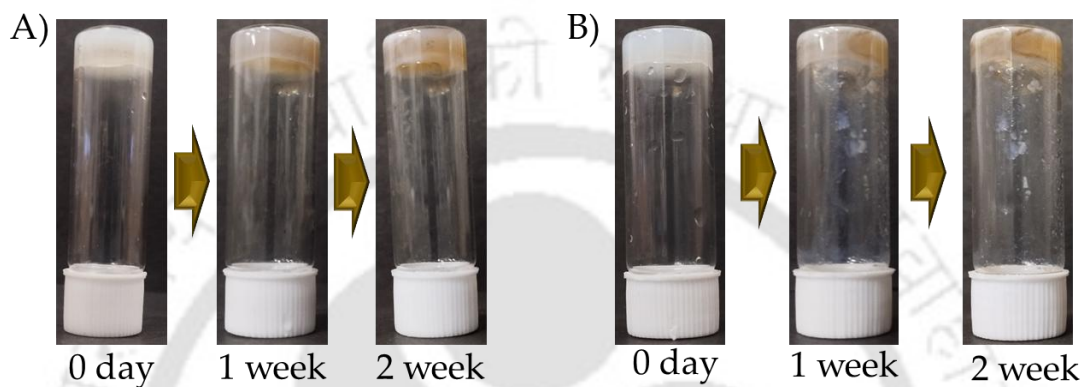


Figure A6.9: Metallogel formed from A) ADH-Py-p and $\text{AgClO}_4 \cdot x\text{H}_2\text{O}$ and B) ADH-Py-p and AgBF_4 .



Figure A6.10: Precipitate formation of ADH-Py-p in presence of AgOAc .

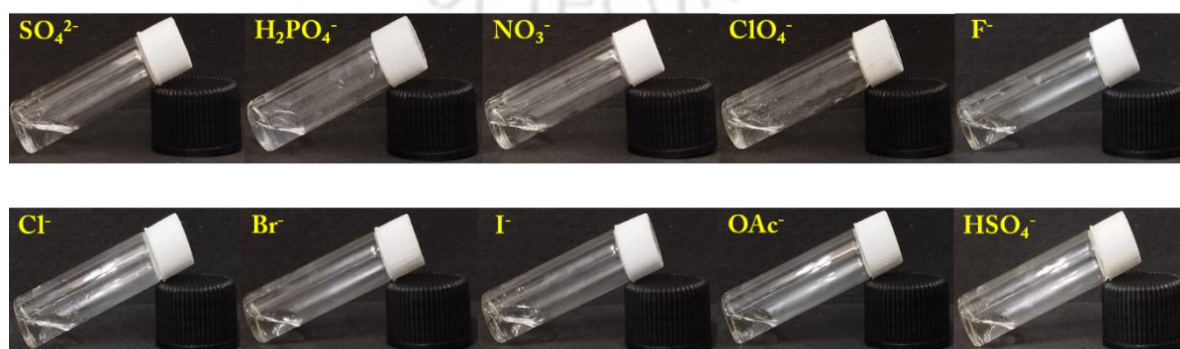


Figure A6.11: Gelation study of ADH-Py-p in presence of TBA salts of different anions.

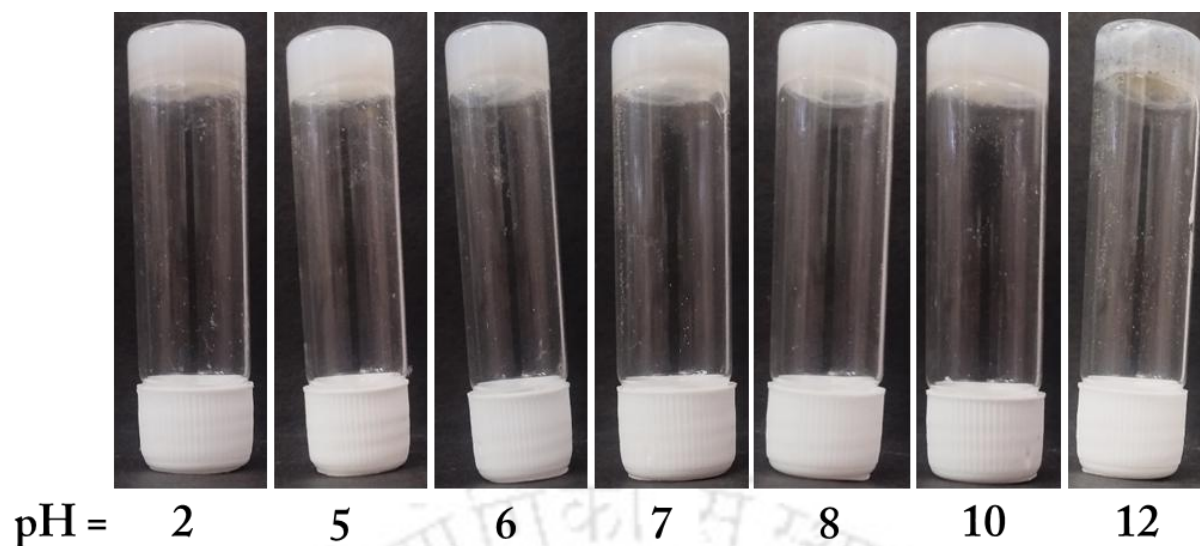


Figure A6.12: Gelation study of ADH-Py-p with AgNO_3 at different pH.

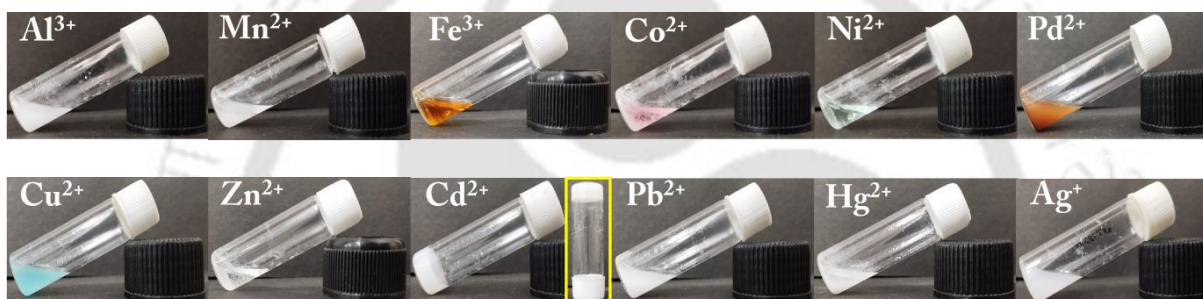


Figure A6.13: Gelation study of ADH-Py-m in presence of different metal salts.

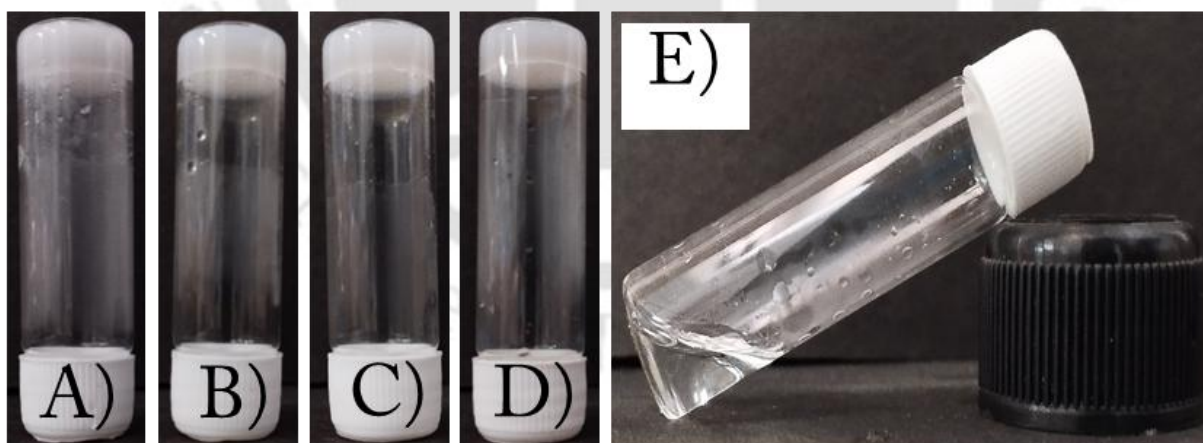


Figure A6.14: Gelation study of ADH-Py-m with $\text{CdCl}_2 \cdot \text{H}_2\text{O}$ in different ratios of DMSO: H_2O viz. A) 1:4, B) 2:3, C) 1:1, D) 3:2 and E) 4:1.

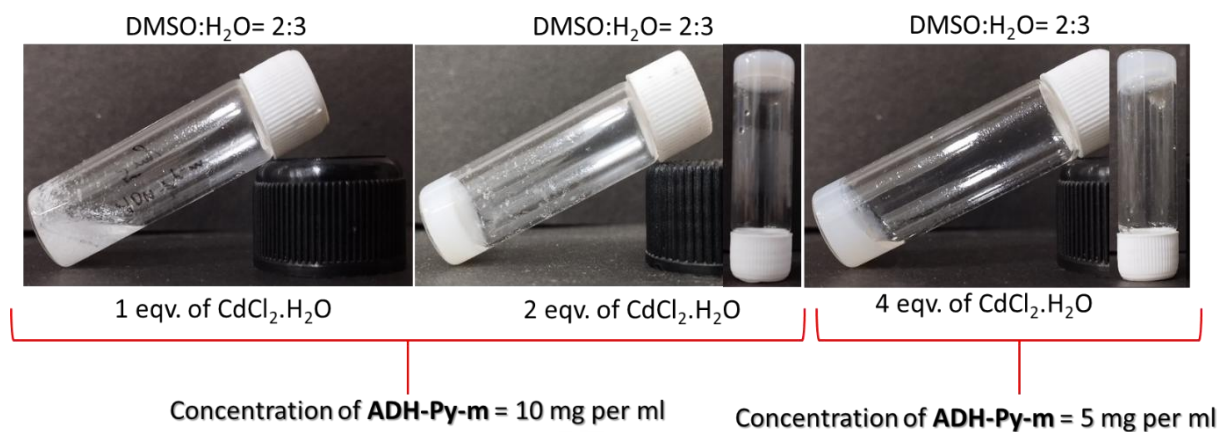


Figure A6.15: Optimization of minimum gelation concentration of ADH-Py-m and CdCl₂.H₂O required for metallogel formation.



Figure A6.16: Gelation study of ADH-Py-m with CdCl₂ in different solvent mixtures viz. A) DMF-H₂O, B) MeOH-H₂O, C) EtOH-H₂O, D) EA-H₂O, E) ACN-H₂O and F) THF-H₂O.

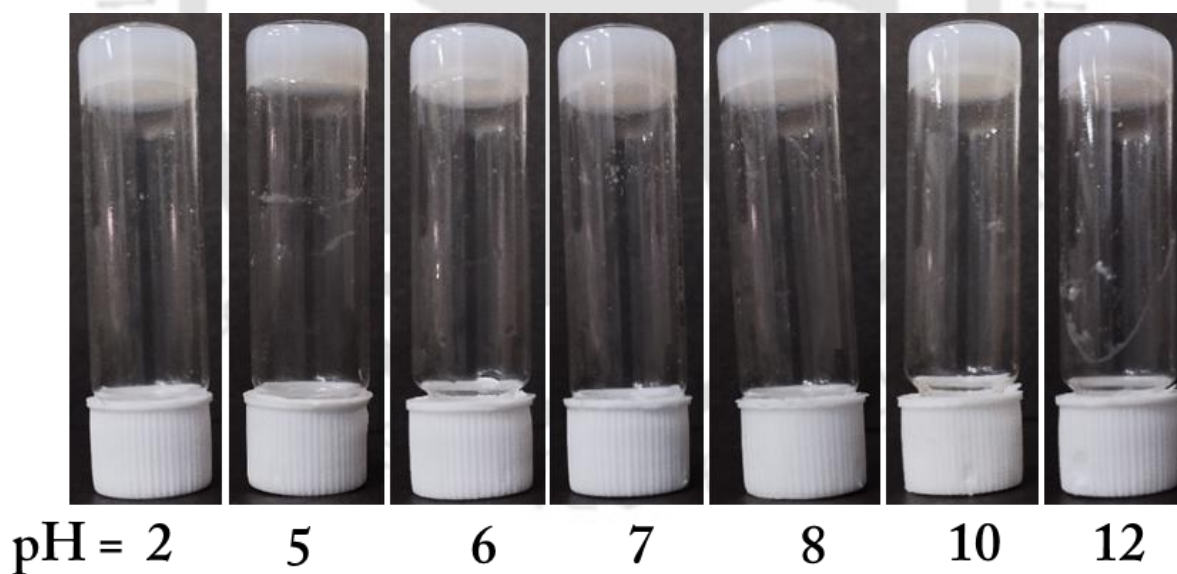


Figure A6.17: Gelation study of ADH-Py-m with CdCl₂.H₂O at different pH.

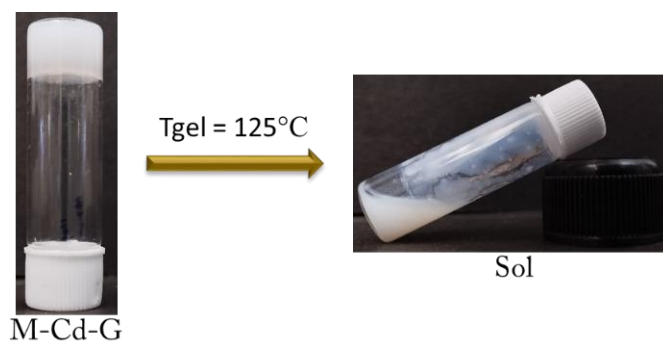


Figure A6.18: Gel-to-sol transition of M-Cd-G gel.

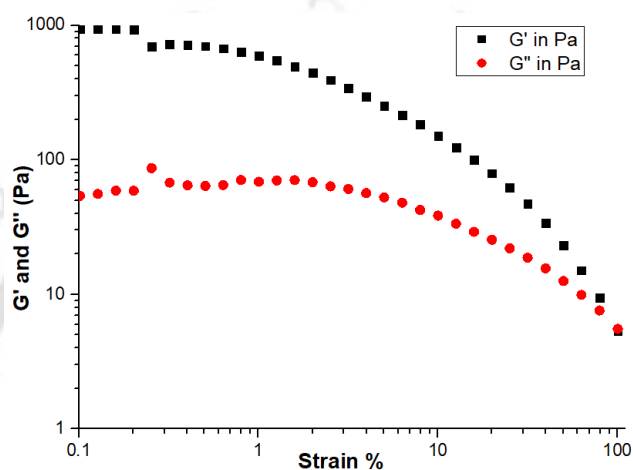


Figure A6.19: Amplitude sweep study of the M-Cd-G organohydrogel.

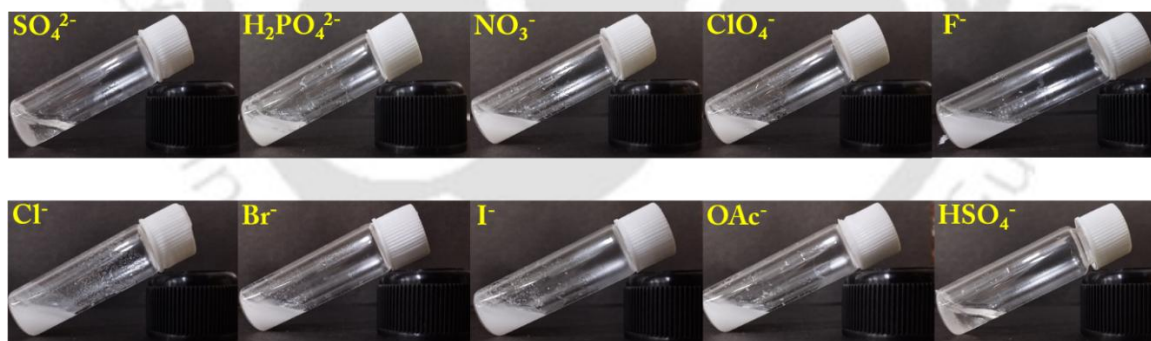


Figure A6.20: Gelation study of ADH-Py-m in presence of TBA salts of different anions.

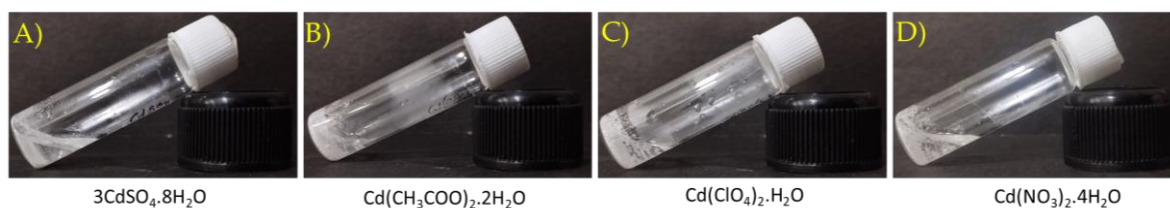
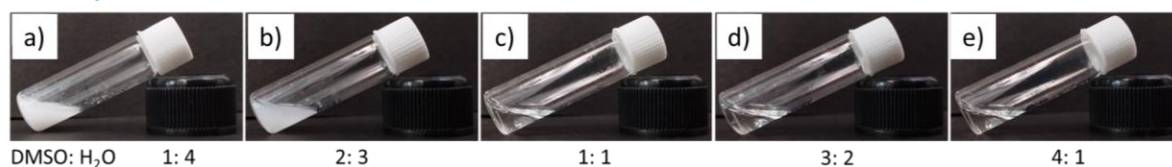
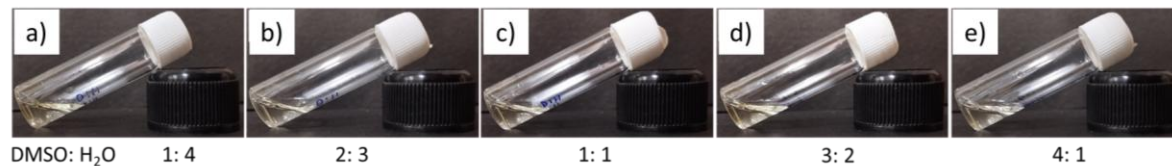


Figure A6.21: Gelation study of ADH-Py-m in presence of A) $3\text{CdSO}_4 \cdot 8\text{H}_2\text{O}$, B) $\text{Cd}(\text{CH}_3\text{COO})_2 \cdot 2\text{H}_2\text{O}$, C) $\text{Cd}(\text{ClO}_4)_2 \cdot \text{H}_2\text{O}$ and D) $\text{Cd}(\text{NO}_3)_2 \cdot 4\text{H}_2\text{O}$.

A) ADH-Py-m



B) ADH-Py-o



C) ADH-Ph

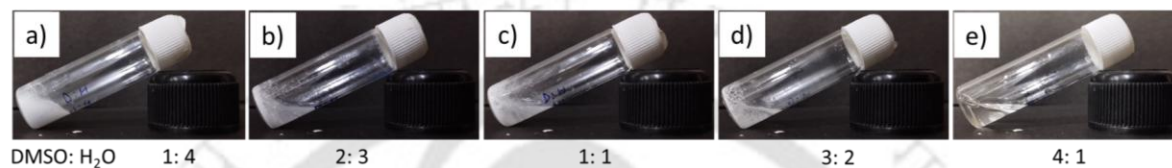
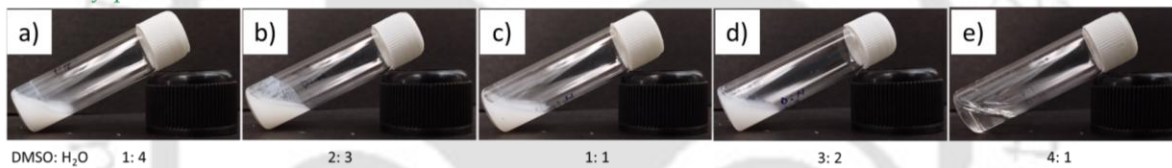
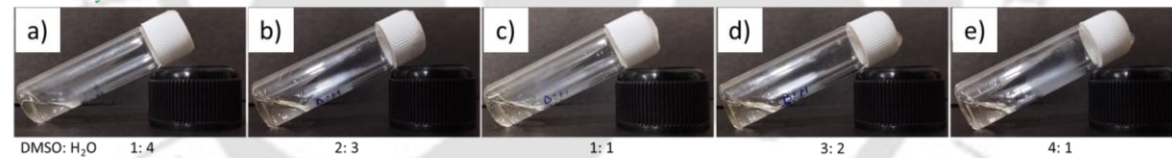


Figure A6.25: Gelation study of A) ADH-Py-m B) ADH-Py-o and C) ADH-Ph in presence of AgNO_3 .

A) ADH-Py-p



B) ADH-Py-o



C) ADH-Ph



Figure A6.26: Gelation study of A) ADH-Py-m B) ADH-Py-o and C) ADH-Ph in presence of $\text{CdCl}_2 \cdot \text{H}_2\text{O}$.

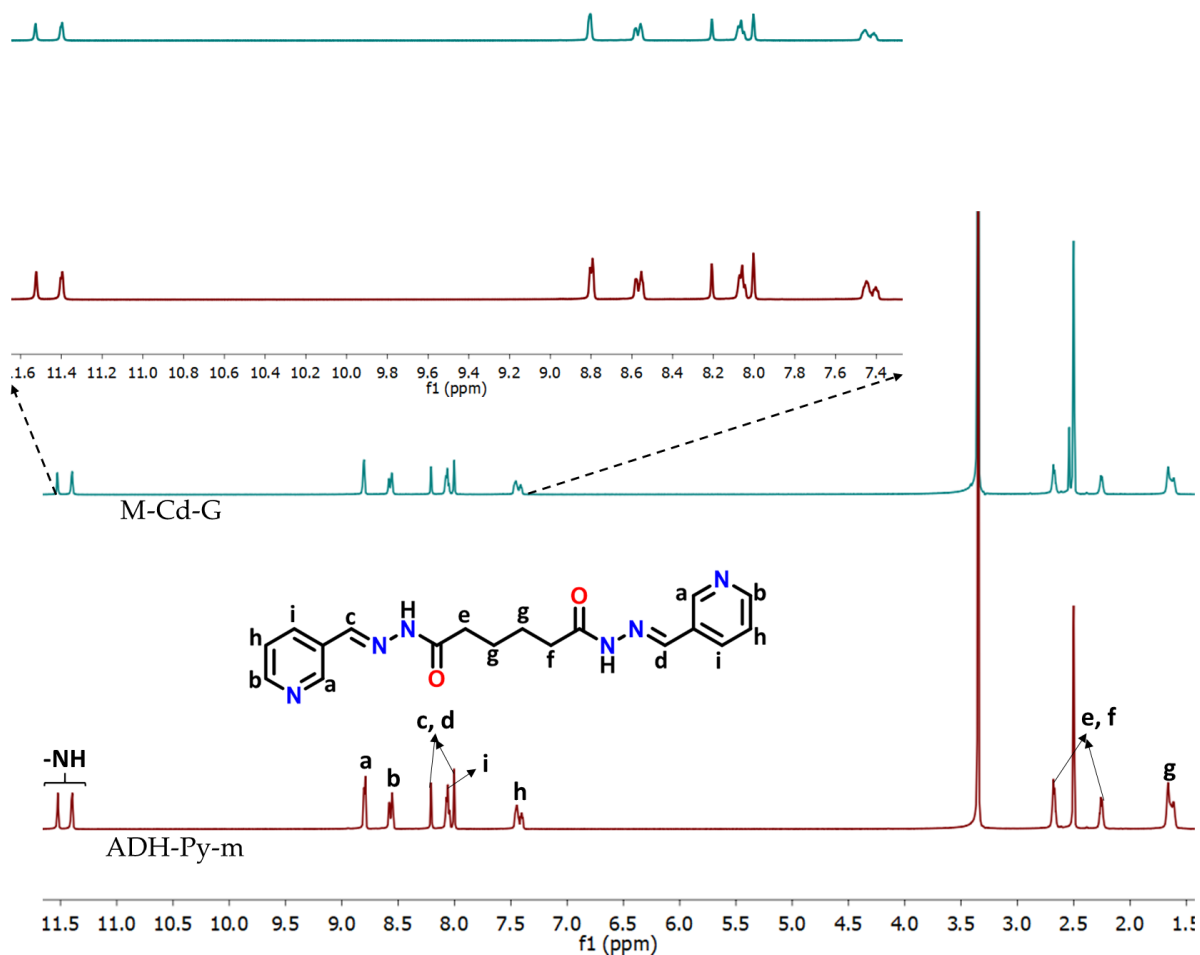


Figure A6.27: Stacked ^1H NMR spectra of the receptor A) ADH-Py-m and xerogel B) M-Cd-G.

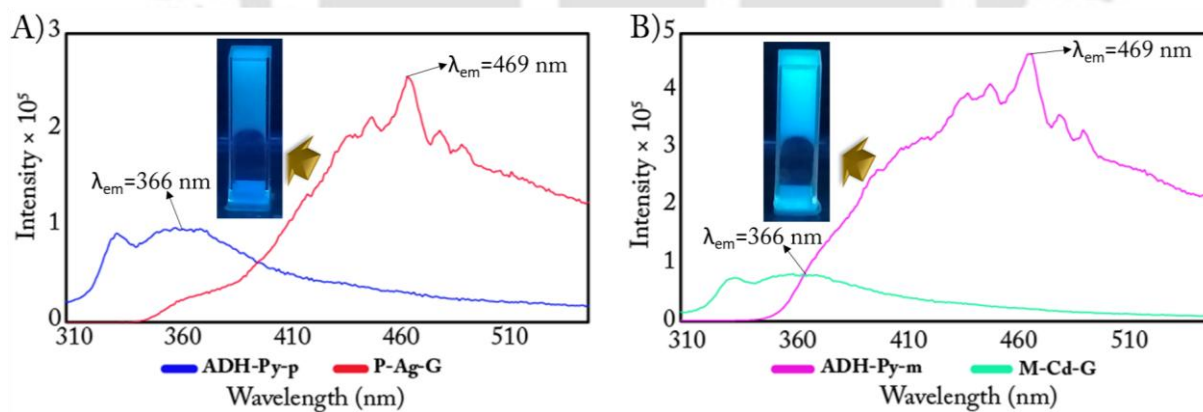


Figure A6.28: Fluorescence spectra of A) ADH-Py-p and P-Ag-G; B) ADH-Py-m and M-Cd-G.

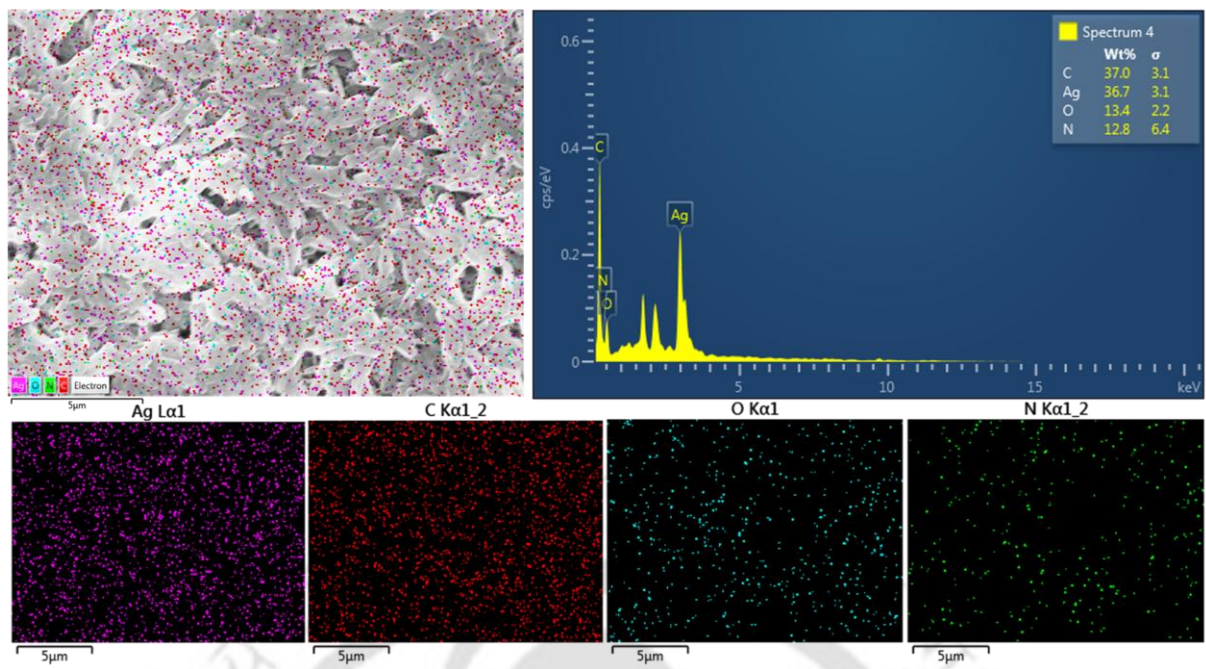


Figure A6.29: EDX analysis of P-Ag-G (B) xerogel.

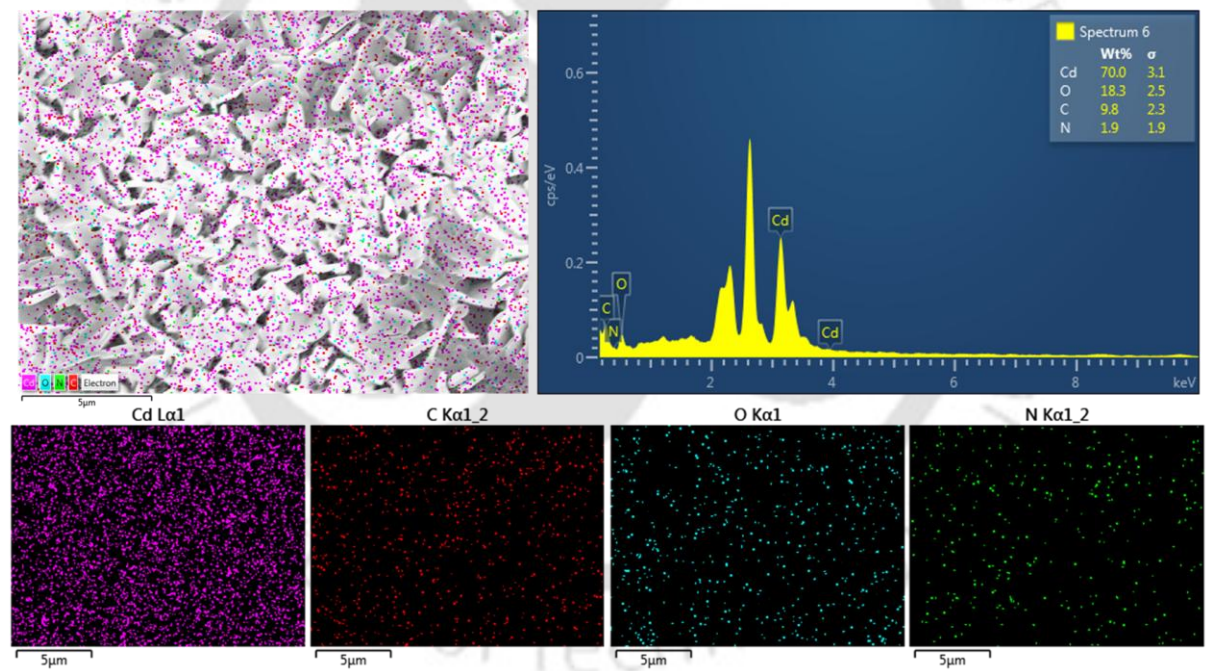


Figure A6.30: EDX analysis of M-Cd-G xerogel.

Table A6.1. Crystallographic parameters and refinement data of ADH-Py-p and ADH-Py-m.

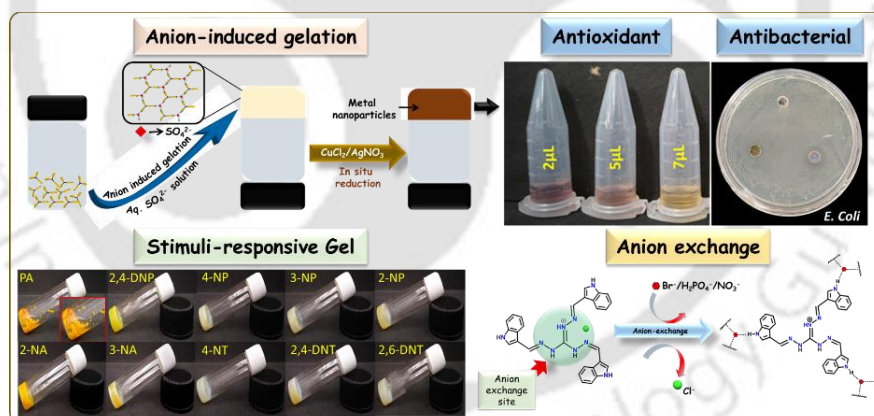
Parameters	ADH-Py-p	ADH-Py-m
formula	C ₁₈ H ₂₈ N ₆ O ₆	C ₁₈ H ₂₀ N ₆ O ₂
fw	424.46	352.40
cryst syst	monoclinic	monoclinic
space group	P 21/n	P 21/c
a (Å)	4.7954(2)	5.1338(5)
b (Å)	18.0963(7)	36.089(3)
c (Å)	12.5479(5)	4.8052(4)
α (deg)	90	90
β (deg)	90.255(1)	103.093(3)
γ (deg)	90	90
V (Å ³)	1088.88(8)	867.13(14)
Z	2	2
DC (g cm ⁻³)	1.295	1.350
μ (Mo Kα) (mm ⁻¹)	0.099	0.093
F (000)	452.0	372.0
T (K)	293 K	298 K
θmax (deg)	24.993	24.994
total no. of rflns	22629	19675
no. of indep rflns	1921	1529
no. of obsd rflns	1418	1193
no. of params refined	156	122
R1, I > 2σ(I)	0.0870(1418)	0.0489(1193)
wR2, I > 2σ(I)	0.2344(1921)	0.1207(1529)
GOF (F ²)	1.227	1.145
CCDC no.	2515769	2515774

Table A6.2. Hydrogen bonding distances (Å) and Bond angles (°) in ADH-Py-p and ADH-Py-m.

Ligand/Complex	D-H...A	d(D...H)/Å	d(H...A)/Å	d(D...A)/Å	<D-H...A/°	Symmetry codes
ADH-Py-p	O2-H2A...N1	0.88 (5)	1.93 (5)	2.788 (5)	166 (5)	-1/2 - x, -1/2 + y, 1/2 - z
	O2-H2B...O3	0.95 (6)	1.79 (6)	2.739 (5)	172 (4)	x, y, z
	O3-H3A...O2	0.82 (7)	2.04 (6)	2.855 (5)	170 (6)	1 + x, y, z
	O3-H3B...O1	0.74 (7)	2.26 (7)	2.916 (5)	148 (6)	1/2 + x, 1/2 - y, -1/2 + z
	O3-H3B...N2	0.74 (7)	2.55 (6)	3.168 (5)	143 (7)	1/2 + x, 1/2 - y, -1/2 + z
	N3-H3N...O2	0.88 (4)	1.99 (5)	2.851 (5)	168 (4)	x, y, z
	C2-H2...O3	0.93	2.50	3.415 (5)	167	-1/2 + x, 1/2 - y, 1/2 + z
ADH-Py-m	N3-H3N...O1	0.87 (3)	2.04 (3)	2.891 (3)	167 (3)	x, y, 1 + z
	C3-H3...N1	0.93	2.57	3.464 (3)	160	-1 + x, y, -1 + z

Chapter 7

Anion Induced Supramolecular Gel for Visual Detection of Picric Acid and in situ Formation of Gel Nanocomposites: Solid-State Anion Exchange of Guanidinium based receptor



7.1. Background and Focus of the Chapter

Anion-responsive gels based on urea are well known in the literature, [7.1] and anions are usually exploited as a means for breaking the gel structure through disturbance of intermolecular hydrogen bonds [7.2]. Recent research has highlighted metal-induced self-assembly to form a gel network, as the incorporation of a metal center can integrate the interesting and unique properties of metal complexes into gelator molecules [7.3]. However, to date, only a handful of examples report the preparation of anion-induced self-assemblies into supramolecular gels, as designing such compounds is tricky and challenging, although the lower toxicity of metal-free systems may be advantageous for both environmental and biological applications. In 2008, Ogden et al. synthesized a proline-functionalized calixarene probe that could form a gel with anions like nitrate, bromide, and chloride with specific cations, where gel formation was most dependent on the anion; however, variations in the cation had a lesser but notable impact [7.4]. In 2010, Zhang and co-workers prepared a melamine-based hydrogel in the presence of PO_4^{3-} , NO_3^- , and SO_4^{2-} at an optimal gelation pH of 2-5 [7.5]. In 2014, Nachtsheim et al. synthesized an N-[(uracil-5-yl)methyl]urea base hydrogelator that formed a gel on adding sodium phosphate buffer [7.6]. However, it is worth mentioning that the cation also appeared to play a crucial role in the self-assembly process, as changing the buffer from sodium to potassium phosphate again disrupted gel formation. In the year 2014, Banerjee et al. synthesized an m-aminopyridine and amino acid-based amphiphile 1, which could selectively form a gel in the presence of HCl [7.7]. Pyridinium hydrochloride was formed in the presence of HCl by utilizing the lone pair electrons of the pyridine nitrogen and the chloride ion, yet again emphasizing the role of cations. Recently, Šindelář et al. designed a macrocyclic bambusuril anion receptor, where selective hydrogelation was evident only in the presence of iodide or perchlorate anions, and further utilized hydrogel materials in the release of model cationic drugs [7.8]. Selectivity remains one of the major challenges regarding anion-triggered gelation reported so far, along with the fact that, in most cases, the role of the cation cannot be neglected. Furthermore, the real-world applicability of these anion-induced supramolecular gels is still to be determined. So far, only a single example has utilized the gel material for further applications [7.8].

Low molecular weight gelators that find applications in detecting toxic ions, chemicals, and hazardous pollutants are of paramount interest in the research area of supramolecular chemistry

[7.9]. The effect of toxic and hazardous pollutants on the environment is a major concern in environmental pollution, and different nitroaromatics are mentionable in this regard [7.10]. Among the nitroaromatics, PA is used as a powerful explosive, and it can cause eye irritation, headache, anaemia, kidney problems, and severe liver and respiratory organ damage [7.11]. Moreover, PA also finds applications in dye industries, pharmaceuticals, rocket fuel manufacturing, and chemical laboratories [7.12]. Thus, there is a need for the detection of these nitroaromatic species. Although solution and vapour phase detection of PA has been achieved utilizing various sensors based on small molecules, nanoparticles, metal-organic frameworks, and polymers, [7.13] in most cases, the sensing mechanisms rely on fluorescence quenching and intermolecular charge transfer processes that demand the utilization of sophisticated spectroscopic and electrochemical tools to carry out the experiments. However, a supramolecular gel matrix as a naked eye sensor for PA involving phase transformation is rarely explored, as per our literature survey [7.9, 7.14-7.16].

The development of hybrid materials resulting from the combination of supramolecular gels with nanoparticles of different origins is another research field that is getting a boost in recent times [7.17]. The synthesis of metal nanoparticles is receiving great attention because of their unique catalytic properties and wide-ranging applications, including anti-bacterial and anti-oxidant activities. However, there are only a few reports of supramolecular LMWGs being employed for generating nanocomposites by the spontaneous in situ reduction of metal salts into nanoparticles [7.18-7.24]. Hence, there is still much scope for improvement in this particular area in terms of achieving greater efficiency, superior designing of the LMWGs, and their real-world applicability. In line with anion-coordination-driven gelation, anion exchange is a promising technology for wastewater treatment to reduce the concentration of ionic impurities [7.25]. Anion exchange is also a ubiquitous feature of metal-halide perovskite nanocrystal chemistry [7.26]. Exchanging anions inside metal-organic frameworks with other anions may lead to changes in their structure and physical properties [7.27]. Wang et al., in 2024, utilised a composite approach combining ion exchange with a redox strategy for achieving the efficient separation of radioactive IO_3^- [7.28]. In this regard, solid-state anion exchange by charged small molecule receptors may be beneficial for the development of materials for the exchange of undesired anions with the more desired ones.

The guanidinium moiety often plays a crucial role in biological systems as it can coordinate with different anionic groups [7.29]. The geometrical Y-shape and planar orientation of the guanidinium moiety can direct the hydrogen bonding, and as such, it can bind oxoanions, such as carboxylates, phosphates, sulfates, chromates, or even pertechnetate [7.30]. On the other hand, indole-based receptors exhibit excellent selectivity in anion binding, sensing, and transport [7.31]. There are a very small number of reports to date that have utilised guanidinium-based receptors

for supramolecular gelation, more specifically for anion-induced gelation purposes, along with their applications as multifunctional smart gelators. In 2013, Schmuck and co-workers presented a quadruple zwitterionic molecule based on a tetrahedral pentaerythritol core containing guanidiniocarbonyl pyrrole cations on the side arms, which forms thermoreversible, transparent gels in DMSO. The gels exhibited dual pH dependence; they transformed into sols by the addition of either an acid or base [7.32]. In the following years, the Schmuck group reported a variety of gels based on the zwitterionic nature of the guanidiniocarbonyl pyrrole unit [7.33-7.34]. In most of these reports, however, the practical applications of these gel materials are still due. Trabolsi et al. prepared a guanidinium-based dynamic covalent gel obtained at room temperature from the imine condensation of a flexible triamino guanidinium hydrochloride salt (TG·Cl) and diformyl pyridine (DFP). The covalent gel functions as a redox-responsive actuator by releasing or adsorbing water molecules depending on the redox state of the guanidinium units [7.35]. Hence, our continuous effort to design probes/receptors capable of forming fascinating self-assembled architectures and employing such self-assembled systems in different applications, along with sensing and recognition [7.36-7.40], led us to prepare a guanidinium-indole-based receptor **GUA-IND** with an indole functional group in the three arms. The receptor exhibited the rarely observed anion-induced supramolecular gelation selectively in the presence of the SO_4^{2-} anion, independent of the counter cation. This is the first report of a simple Schiff base low molecular weight guanidinium-indole-based receptor showing selective anion-induced gelation, as per our extensive literature survey. The supramolecular gelator **GUA-IND**, reported by our group, could selectively respond to PA among different nitro-aromatic compounds by showing a gel-to-sol transition along with a color change. The gel matrix was employed for the in-situ reduction of precious metal salts like Cu^{2+} and Ag^+ into their nanoparticles without using any external reducing agents, and the gel nanocomposite thus formed showed antioxidant and antimicrobial properties. The receptor also showed anion exchange phenomena in the solid state with anions of different sizes and shapes. Besides, we synthesized a previously reported compound, **GUA-NAP**, as a control compound in our study [7.41].

7.2. Objective of the Chapter

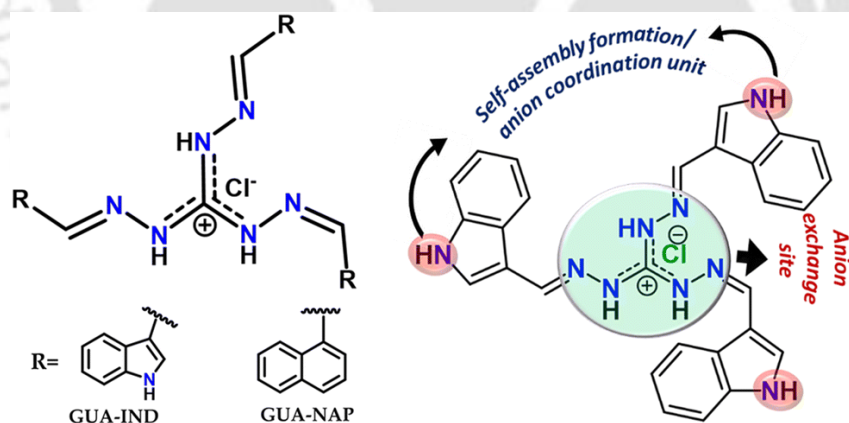
The tripodal receptor **GUA-IND** was synthesized using guanidinium hydrazide as a core, and its three arms were prepared with three indole moieties. This Schiff base receptor formed an organohydrogel (**GI-G**) when triggered by the presence of $\text{SO}_4^{2-}/\text{HSO}_4^-$ anions selectively, thus demonstrating the rarely observed anion-induced supramolecular gelation behaviour. The supramolecular gel (**GI-G**) was found to be stimuli-responsive towards picric acid (PA) among

different nitro-aromatic compounds, enabling completely naked eye sensing of picric acid, circumventing the need for any instruments. Gel nanocomposites (**GI-Cu-G** and **GI-Ag-G**), formed from **GI-G** via in situ reduction of precious metal salts like Cu^{2+} and Ag^+ into their nanoparticles inside the gel matrix without using any external reducing agents, demonstrated antioxidant and antimicrobial activities. Additionally, the receptor facilitated anion exchange in the solid state with diverse anions, emphasizing its versatility and innovative design. This research paves the way for the development of advanced materials with tailored functionalities.

7.3. Results and Discussion

7.3.1. Design rationale of receptor GUA-IND

Receptor **GUA-IND** was synthesized using guanidinium hydrazide as the core, and its three arms were prepared with three indole moieties. It was expected that the receptor would coordinate with anions (especially oxoanions) utilizing the coulombic interactions of the guanidinium core and hydrogen bonding interactions with the indole $-\text{NH}$ groups, which are at the periphery. This self-assembled system, via extended hydrogen bonding between the receptor and anions, may lead to the formation of a supramolecular gel with stimuli-responsive properties. Moreover, owing to the presence of multiple hydrogen bond donors, investigation of the solid-state interactions with anions of different sizes and shapes by replacing the counter anion Cl^- may provide another dimension to the present work (Scheme 7.1).



Scheme 7.1: Structures of **GUA-IND** and **GUA-NAP** and design rationale of **GUA-IND**.

7.3.2. Solid-state self-assembly in GUA-IND

The solid-state self-assembly behavior of **GUA-IND** has been investigated with the help of crystallographic structural analysis. The crystal structure analysis of **GUA-IND** revealed a propeller-shaped structure with Cl^- as a counterion, which did not participate in any kind of interaction (Figure 7.1 A). The **GUA-IND** molecule formed a dimeric assembly with the help of

six C–H $\cdots\pi$ interactions (C–H $\cdots\pi$ = 3.30 Å) originating from the indole ring C–H (Figure 7.1 B). Such dimeric assemblies self-assemble among themselves to create a long three-dimensional helical architecture (Figure 7.1 B). It was interesting to note here that there was no involvement of hydrogen bonding interactions in the overall self-assembly of **GUA-IND**, inferring a very weak self-assembled supramolecular architecture. This particular observation allowed us to further perform architectural tuning of **GUA-IND** for a myriad of fascinating applications, such as gelation and anion exchange, which we have discussed in detail in the subsequent studies performed in this article.

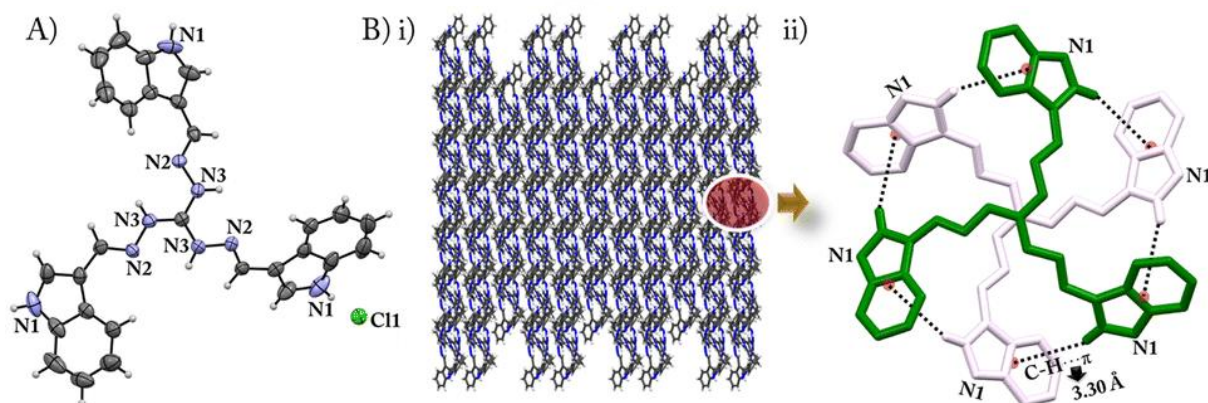


Figure 7.1: (A) ORTEP diagram of the crystal structure of **GUA-IND** (with 50% probability level), (B) (i) solid-state self-assembly formation of **GUA-IND** with the help of various non-covalent interactions, (ii) dimeric self-assembly formation of **GUA-IND** with the help of C–H $\cdots\pi$ interactions.

7.3.3. Anion coordination-induced gelation

The gelation study was performed in the presence of TBA salts of different anions, viz., SO_4^{2-} , HSO_4^- , H_2PO_4^- , ClO_4^- , NO_3^- , OH^- , F^- , Cl^- , Br^- , I^- , OAc^- , and CN^- (Figure 7.2 B) in DMSO– H_2O (1:4, v/v). However, selective gelation was observed only in the presence of SO_4^{2-} and HSO_4^- (Figure 7.2 A). Nonetheless, the gel formed with HSO_4^- remained stable for only 3–4 hours. Partial gelation was observed in the presence of H_2PO_4^- ; however, it disrupted within a few seconds of formation. The gel formed with SO_4^{2-} (**GI-G**) could remain stable up to 48–72 hours. The gelation studies were performed in different ratios of DMSO– H_2O (Figure A7.1, Annexure 7); however, we decided to proceed with the maximum amount of water content (DMSO: H_2O ratio of 1:4 v/v). The minimum gelation concentration of SO_4^{2-} and HSO_4^- required for gelation was 0.5 equivalents of the receptor, below which no gelation was observed (Figure A7.2, Annexure 7). However, we proceeded by taking 1 equivalent of SO_4^{2-} and HSO_4^- concentration compared to that of the receptor, where the receptor concentration was fixed at 5 mg mL^{-1} . However, minimum gelation concentration of the receptor was found to be as low as 1 mg mL^{-1} (Figure A7.3, Annexure 7).

SO_4^{2-} assisted in the formation of a three-dimensional hydrogen bonding network with the $-\text{NH}$ of the indole moiety of the receptor. With the rest of the anions, solution or precipitate formation was observed under the identical conditions. Notably, the receptor alone could not form a gel under the same conditions. The result could be best described as the effect of the Hofmeister series, which explained the salting out of solutes by kosmotropes like SO_4^{2-} anions by increasing the ordering of water molecules [7.42-7.43]. Literature reports showed that the Hofmeister effect could be used to modulate the thermodynamic, rheological, and mechanical properties of gels, and usually, the kosmotropic ions enhanced the mechanical properties [7.44-7.48].

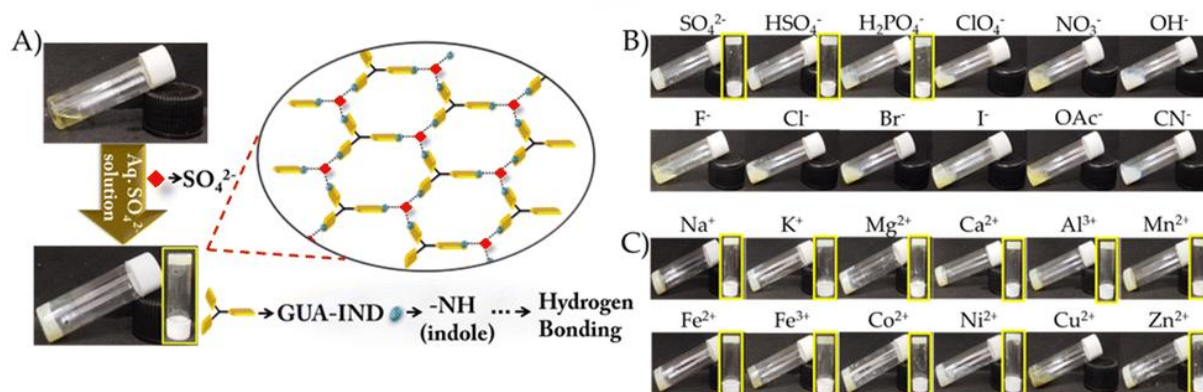


Figure 7.2: (A) Formation of a supramolecular gel by **GUA-IND** in the presence of $(\text{TBA})_2\text{SO}_4$ (schematic of the gel network). Gelation study of **GUA-IND** (B) in the presence of different anions (TBA salts), and (C) various metal sulfate salts, *viz.*, Na^+ , Mg^{2+} , Al^{3+} , K^+ , Ca^{2+} , Mn^{2+} , Fe^{2+} , Fe^{3+} , Co^{2+} , Ni^{2+} , Cu^{2+} and Zn^{2+} .

The **GI-G** gel formation was observed at different pH levels ranging from ~ 2 to ~ 12 (Figure A7.4). Various metal sulfate salts, including Na^+ , Mg^{2+} , Al^{3+} , K^+ , Ca^{2+} , Mn^{2+} , Fe^{2+} , Fe^{3+} , Co^{2+} , Ni^{2+} , and Zn^{2+} , also successfully formed organohydrogels (Figure 7.2 C), validating further that the anion had the predominant role for gel formation irrespective of the cations. However, gelation was barred only with CuSO_4 , followed by colour change from white to greenish black likely due to complexation of the receptor with Cu^{2+} . The UV-Vis spectrum of **GUA-IND** in the presence of $\text{CuSO}_4 \cdot 5\text{H}_2\text{O}$ in DMSO showed a weak charge transfer band at ~ 420 nm along with the absorption band of the receptor at ~ 340 nm (Figure A7.5). The gel-to-sol transition temperature (T_{gel}) of **GI-G** gel formed in DMSO- H_2O (1:4, v/v) was calculated to be ~ 84 °C (Figure A7.6). From the results of T_{gel} , a relatively high temperature (~ 84 °C) was required for the gel to convert into solution, indicating that the prepared gel had good stability in a normal environment. Rheological measurements were employed to investigate the viscoelastic behavior and provide quantitative information about the mechanical strength of the **GI-G** gel. As shown in Figure A7.7, the results of the frequency sweep test of rheology for the organohydrogel indicated that **GI-G** gel exhibited a higher elastic storage modulus (G') and a lower loss modulus (G''), demonstrating the

authenticity of gelation judgment [7.49]. The gel formation was also observed in DMF (dimethylformamide)-H₂O (1:4, v/v) in the presence of SO₄²⁻ and HSO₄⁻ TBA salts (Figure A7.8). However, gel formation was not observed for other binary solvent systems like MeOH (methanol)-H₂O, THF (tetrahydrofuran)-H₂O, ACN (acetonitrile)-H₂O, DCM (dichloromethane)-H₂O, and EA (ethyl acetate)-H₂O under the same conditions (Figure A7.9).

Gelation mechanism

To understand the interaction sites of the receptor with SO₄²⁻, ¹H NMR, FT-IR, PXRD, UV-Vis, and FESEM studies were performed. We recorded the ¹H NMR spectra of **GUA-IND** in DMSO-*d*₆. We then prepared the **GI-G** gel in a DMSO-*d*₆-D₂O (ratio 1:4) mixture and dissolved it in DMSO-*d*₆ to record the ¹H NMR spectra. The full stacked NMR spectra of **GUA-IND** and **GI-G** gel are provided in Figure A7.10, Annexure 7. The comparison of the ¹H NMR spectra of the gelator **GUA-IND** and the **GI-G** gel in DMSO-*d*₆ could provide insight into the self-assembly process. The H_a protons corresponding to the indole -NH moiety and the H_b protons corresponding to the protons of the guanidinium core in the **GI-G** gel disappeared, suggesting extensive hydrogen bonding interactions with SO₄²⁻ anions. Imine protons (H_c) of **GUA-IND** showed an upfield shift ($\Delta\delta$ 0.14 ppm) along with broadening of the peak. This suggested involvement of the above-mentioned protons in the formation of the gel network. Also, protons of the aromatic region of receptor **GUA-IND** showed slight upfield shifting in the gel state, proposing π - π interactions in the gel state (Figure 7.3 A and B). The comparison of the FT-IR spectra of **GUA-IND** and the xerogel of **GI-G** (Figure 7.3 C) revealed severe broadening of the peak at 3514 cm⁻¹ corresponding to indole -NH stretching frequency of **GI-G** in the xerogel, further strengthening the fact that indole -NH was involved in the formation of an extended H-bonding network with the SO₄²⁻ anion. Comparison of PXRD spectra of **GUA-IND** and the **GI-G** xerogel further helped in understanding the self-assembly process for gelation (Figure 7.3 D). The PXRD pattern of the **GI-G** xerogel showed a peak at 10.66° with a d-spacing value of 0.83 nm, which is absent in the **GUA-IND** powder, suggesting diminished intermolecular distances in the **GI-G** gel. Besides, the peaks at $2\theta = 22.22^\circ, 24.83^\circ, 25.86^\circ$ with d-spacings of 0.40 nm, 0.37 nm, and 0.35 nm in **GUA-IND**, respectively, shifted to $2\theta = 23.04^\circ, 25.31^\circ, 26.07^\circ$ with d-spacings of 0.38 nm, 0.35 nm, and 0.33 nm in **GI-G** xerogel, indicating aromatic ring interaction by π - π stacking in the gel state [7.51]. The UV-Vis spectroscopy of the receptor (initial concentration 10 μ M) recorded with increasing concentrations of the SO₄²⁻ anion in DMSO revealed the emergence of a new absorption peak at ~ 385 nm while decreasing the absorbance of the receptor at ~ 340 nm with the formation of an isosbestic point at 365 nm (Figure A7.11, Annexure 7). The absorbance at ~ 385 nm increased up

to 80 μM concentration of the SO_4^{2-} anion, after which the absorbance did not increase even though the $[\text{SO}_4^{2-}]$ concentration increased. The observed changes provide further evidence for the hydrogen bonding interactions between receptor **GUA-IND** and SO_4^{2-} anions. Morphological alterations of **GI-G** in the xerogel form compared to the receptor **GUA-IND** were analyzed via FESEM analysis. Block-shaped morphology was observed for **GUA-IND** (Figure 7.3 E), while gel fibers entangled on the blocks were observed in the **GI-G** xerogel (Figure 7.3 F).

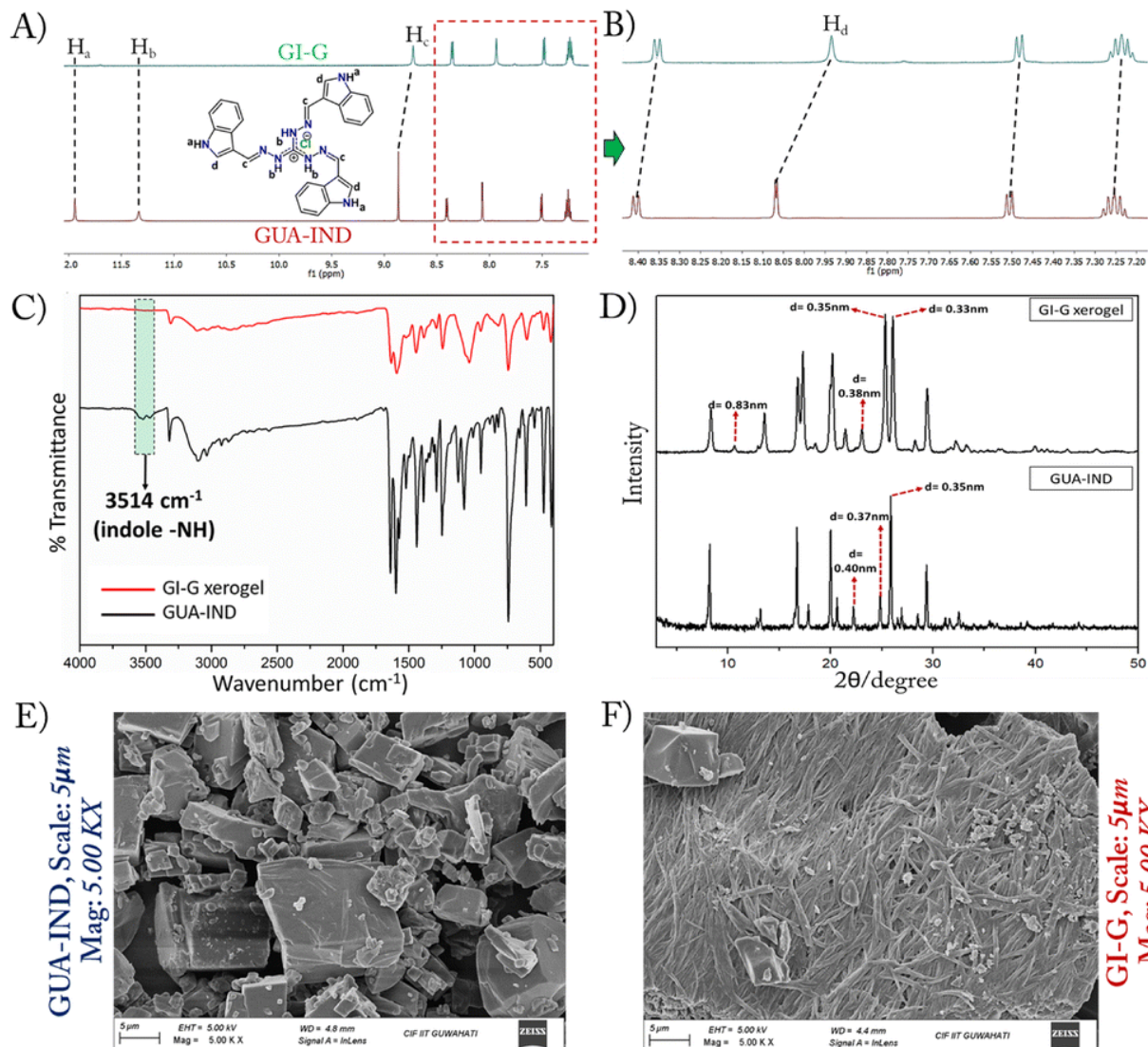


Figure 7.3: (A) Stacked ^1H NMR spectra of **GUA-IND** and **GI-G**. (B) Enlarged aromatic region of the stacked ^1H NMR spectra. (C) Stacked FT-IR spectra of **GUA-IND** and **GI-G** xerogels. (D) Stacked PXRD spectra of **GUA-IND** and **GI-G** xerogels. FESEM analysis of (E) **GUA-IND** and (F) **GI-G** xerogels.

To further confirm the role of indole-NH in anion-induced gel formation, we prepared a control probe, **GUA-NAP**, by keeping the guanidinium core fixed but fabricating the three arms with naphthalene in place of indole. We then checked the gelation behavior of **GUA-NAP** by adding aqueous solutions of different anions (TBA salts) into the DMSO solution (DMSO: H_2O = 1:4,

v/v) of the receptor (Figure A7.12, Annexure 7). However, no gelation was observed; instead, precipitate formation was observed with all the selected anions, further strengthening the role of indole –NH in the gelation process.

7.3.4. Sensing of PA by the GI-G gel

The SO_4^{2-} induced gelation of our receptor **GUA-IND** was majorly driven by H-bonding interactions of the SO_4^{2-} anion with the –NH of the indole moiety and aromatic ring interactions by π – π stacking as established in the mechanism of gelation. Therefore, presence of picric acid might disrupt the already existing well organised H-bonding network thereby leading to rupture of the supramolecular gel network. By utilizing this idea, the stimuli responsive properties of the **GI-G** gel were investigated in the presence of different nitro-aromatic compounds including picric acid (PA) and other nitrophenols (Figure A7.13, Annexure 7), viz. 2,4-dinitrophenol (2,4-DNP), 4-nitrophenol (4-NP), 3-nitrophenol (3-NP), 2-nitrophenol (2-NP), 2-nitroaniline (2-NA), 3-nitroaniline (3-NA), 4-nitrotoluene (4-NT), 2,4-dinitrotoluene (2,4-DNT) and 2,6-dinitrotoluene (2,6-DNT). We prepared the **GI-G** gel and added different nitro-aromatic compounds (3 equiv.) of the receptor on top of the gel. It was observed that after 1.5 hours, the gel containing PA was slowly destroyed into a yellow-colored sol (Figure 7.4). Under identical conditions, the other nitrophenols in the study did not disrupt the gel, although the colour of the gel changed to yellow/yellow-orange with some of the nitro-aromatic compounds like 2,4-DNP and 2-NA, and slightly yellow in the presence of 2-NP, 3-NA, and 2,4-DNT. PA being electron deficient in nature could form charge transfer complex with the indole moiety of our receptor. To find the minimum concentration of PA up to which the disruption of the gel occurred, different concentrations of PA solutions in a minimal volume of DMSO (100 μL) were prepared. For the detailed procedure, refer to section A7.8 of the Annexure 7. The receptor concentration was fixed at 5 mg ml^{-1} to prepare the **GI-G** gel. It was observed that the gel loaded with 3 equivalents of PA solution (28.8 mM), compared to the receptor concentration, was disrupted within 1.5 hours (Figure A7.14, Annexure 7). However, within 24 hours, PA concentrations up to 4.8 mM could disrupt the gel. PA solutions of concentrations lower than 4.8 mM could not disrupt the gel, even after 24 hours of observation, although the colour of the gel turned bright orange from creamy white. Hence, the minimal concentration of PA that could be detected by the phase transformation-based detection method within 24 hours is 4.8 mM. Although the minimal concentration of PA required for gel disruption is not that impressive, the detection limit might improve with an improved design rationale. The significance of this finding lies in the fact that, for the first time, we report an anion-induced gel system for the sensing of PA that can be easily visualised through the naked eye. The UV-Vis

spectra of the receptor **GUA-IND** recorded in aqueous medium in the presence of PA revealed a charge transfer peak at 420 nm along with the absorption peak of the receptor at 340 nm (Figure A7.15, Annexure 7).

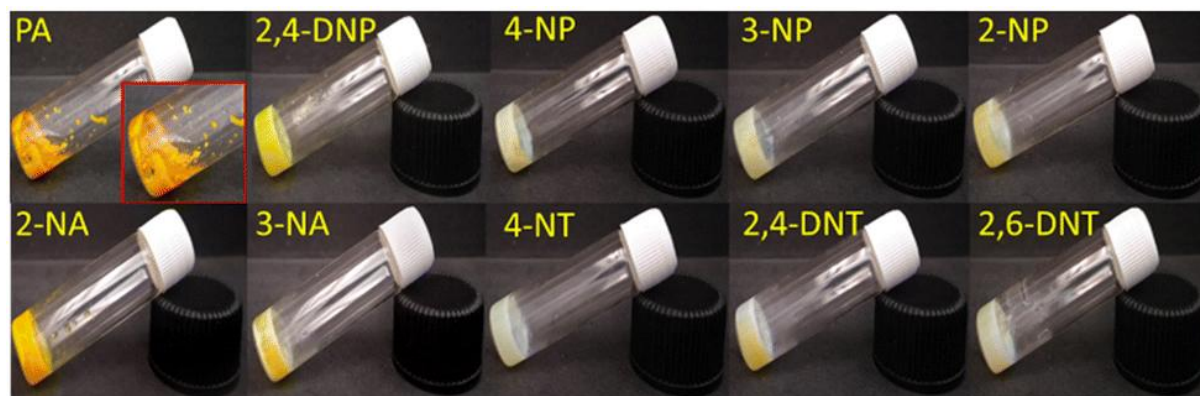


Figure 7.4: Stimuli-responsive behavior of **GI-G** towards PA among different nitro-aromatic compounds after 24 hours.

The charge transfer bands at 420 and 430 nm were also observed for **GUA-IND** in the presence of 2,4-DNP and 2-NA, respectively. To further confirm the underlying mechanism, PA was added to the **GI-G** gel prepared in DMSO- d_6 and D $_2$ O (1:4), and the ^1H NMR spectrum of the resulting partly ruptured gel was recorded in DMSO- d_6 (Figure A7.16, Annexure 7). It was observed that the H_a protons corresponding to the indole $-\text{NH}$ moiety and the H_b protons corresponding to the guanidinium core, which had disappeared in the **GI-G** gel, reappeared in the **GI-G** + PA gel, indicating the breakage of the H-bonded network earlier formed in the presence of the sulfate anion, as sulfate is more prone to undergo H-bonding interactions with the acidic $-\text{OH}$ unit of PA, thus freeing the **GUA-IND** receptor and generating new kinds of interactions with PA. The upfield shift of the aromatic region protons suggested that PA formed π - π stacking interactions with the indole moieties, leading to the rupture of the gel. The disruption of gel fibres was also supported by morphological analysis of **GI-G** and **GI-G** + PA gels *via* FESEM experiment, which revealed that the gel fibers completely collapsed in the presence of PA (Figure A7.17, Annexure 7).

7.3.5. *In situ* reduction of metal salts into nanoparticles within the gel matrix

We investigated the effect of different metal salts on the **GI-G** gel by adding 3 equivalents (with respect to the receptor **GUA-IND**) of different metal salts, viz., AlCl_3 , $\text{MnCl}_2 \cdot 4\text{H}_2\text{O}$, $\text{FeCl}_3 \cdot 6\text{H}_2\text{O}$, $\text{CoCl}_2 \cdot 6\text{H}_2\text{O}$, $\text{NiCl}_2 \cdot 6\text{H}_2\text{O}$, $\text{CuCl}_2 \cdot 2\text{H}_2\text{O}$, ZnCl_2 , $\text{CdCl}_2 \cdot \text{H}_2\text{O}$, PbCl_2 , and AgNO_3 (Figure A7.18, Annexure 7). It was observed that the gel disintegrated before 24 hours in the presence of all the metal salts taken, except $\text{CuCl}_2 \cdot 2\text{H}_2\text{O}$ and AgNO_3 . Additionally, there was a drastic colour change

(Figure A7.19 A and Figure A7.19 B, Annexure 7) from creamy white to greenish black and ash black for the Cu- and Ag-containing **GI-G** gel (**GI-Cu-G** and **GI-Ag-G**, respectively) (Figure 7.5 A and D), which is characteristic of the reduction of metals into metal NPs, capped inside the gel fibers. The colour of the gel turned black in the case of $\text{FeCl}_3 \cdot 6\text{H}_2\text{O}$; however, the gel disrupted completely within 24 hours, and hence we did not investigate it further. Such spontaneous in situ reduction of metals into metal NPs inside a supramolecular gel matrix without using any external reducing agents is very important yet scarce in the literature. The selectivity in metal ion reduction probably stems from the redox potentials of different metal ions, and it was observed that **GUA-IND** could not reduce metal ions with redox potential lower than that of Cu^{2+} . Redox potential values of different metal ions have been included in the supporting document (Table A7.3).

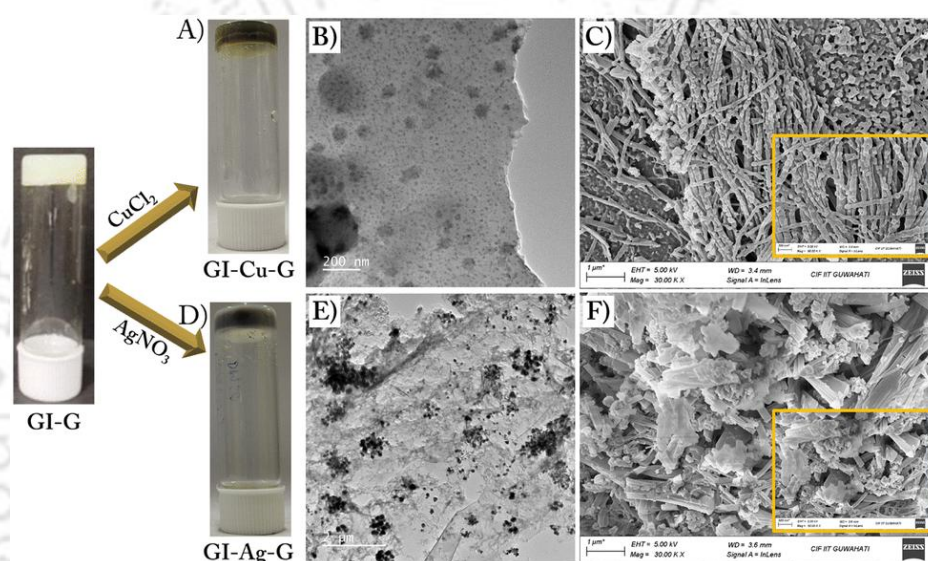


Figure 7.5: Formation of (A) **GI-Cu-G** and (D) **GI-Ag-G** gels from **GI-G** gel by the addition of $\text{CuCl}_2 \cdot 2\text{H}_2\text{O}$ and AgNO_3 , respectively, TEM images of (B) copper and (E) silver nanoparticles. FESEM images of (C) **GI-Cu-G** and (F) **GI-Ag-G** xerogels.

Characterization of nanoparticles

Different spectroscopic methods were employed for a deeper investigation of the NPs residing inside the **GI-G** gel matrix. UV-Vis spectroscopic study of **GI-Cu-G** (**GI-G** + CuCl_2) in DMSO revealed the appearance of a broad absorption band at ~ 550 nm as a shoulder peak along with the characteristic peak of the receptor at ~ 340 nm, corresponding to the surface plasmon resonance (SPR) band of CuNPs [7.52-7.53] as depicted in (Figure A7.20 A, Annexure 7). Similarly, **GI-Ag-G** (**GI-G** + AgNO_3) in DMSO revealed the appearance of a broad absorption band at ~ 500 nm as a shoulder peak along with the characteristic peak of the receptor at 340 nm, corresponding to the surface plasmon resonance (SPR) band of AgNPs [7.54-7.55] (Figure A7.20 B, Annexure

7). Field Emission Scanning Electron Microscopy (FESEM) images of **GI-Cu-G** and **GI-Ag-G** revealed complete alteration of the morphology of **GI-G** gel (Figure 7.5 C and F). EDX analysis of the xerogels of **GI-Cu-G** and **GI-Ag-G** revealed that most of the spherical-shaped CuNPs and AgNPs were localized on the gel network (as depicted in Figure A7.21 A and Figure A7.21 B, Annexure 7). We reasoned that the interaction between the Cu^{2+} and Ag^+ ions, with the gel networks, led to the formation of CuNPs and AgNPs, respectively, which were found to be localized on the gel nanofibers. Field Emission Transmission Electron Microscopy (FETEM) analysis revealed that spherical-shaped CuNPs and AgNPs were observed on the surface of the gel fibers (Figure 7.5 B and E) with sizes of the particles in the range of ~ 6 to ~ 9 nm and ~ 85 to ~ 116 nm, respectively (Figure A7.22, Annexure 7). The size correlates well with the SPR bands observed for both Cu and Ag nanoparticles, as per the literature reports.^{56–58} Although in the case of CuNPs the particle sizes were observed to have an even distribution with a mean diameter of ~ 8 nm, in the case of AgNPs, a broad distribution of particle sizes was observed with a mean diameter of ~ 98 nm. IR spectra of both the nanocomposites (xerogel) did not show any changes in the spectra compared to the spectra of the **GI-G** xerogel (Figure A7.23, Annexure 7). Furthermore, we performed ^1H NMR spectroscopic studies of the **GI-Cu-G** and **GI-Ag-G** gel nanocomposites (xerogels), which revealed downfield shifts of the $-\text{NH}$ peaks corresponding to the indole/guanidinium/imine units of the **GI-G** xerogel, and along with this, a slight downfield shift of the peak near indole $-\text{NH}$ was observed, thus supporting the interaction of Cu^{2+} and Ag^+ ions with the **GI-G** gel fibers (as depicted in Figure A7.24, Annexure 7). However, NOESY spectra recorded for the xerogels of **GI-Cu-G** and **GI-Ag-G** did not show any correlation peaks (Figure A7.25, Annexure 7).

Further investigations were carried out to find the exact oxidation states of the Cu and Ag nanoparticles by XPS analysis (Figure 7.6). The binding energies of Cu 2p_{3/2} and Cu 2p_{1/2} at 933.02 eV and 953.02 eV, respectively, confirmed the presence of zerovalent Cu (Figure 7.6 A and 7.6 B) [7.59-7.60]. On the other hand, the binding energies of Ag 3d_{5/2} and 3d_{3/2} at 368.21 eV and 374.35 eV in XPS confirmed the presence of Ag(0) (Figure 7.6 C and D) [7.61-7.62]. Also, the N 1s peak at 400.3 eV for the receptor **GUA-IND** (peaks of guanidinium as well as that of indole) showed significant changes for both **GI-Cu-G** and **GI-Ag-G**, indicating strong interactions between N and Cu/Ag (Figure A7.26, Annexure 7). Recently, our group has demonstrated such nanoparticle formation as a result of the interactions between metal and the gel nanofibers [7.63].

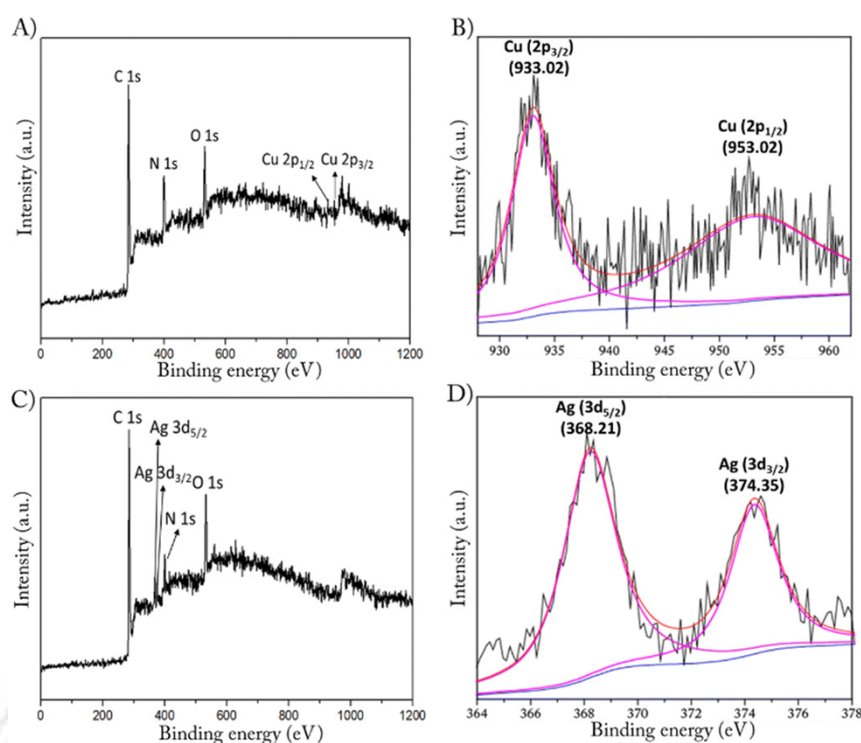


Figure 7.6: Survey XPS spectra of (A) CuNPs and (C) AgNPs; (B) Cu 2p, (D) Ag 3d fine XPS spectra of CuNPs and AgNPs, respectively.

To check the stability of the nanocomposites, **GI-Cu-G** and **GI-Ag-G** gels were washed with water, and then the same gels were washed with EDTA disodium dihydrate solution (50 mM), as shown in Figure A7.27, Annexure 7. The greenish black and ash black colours of the **GI-Cu-G** and **GI-Ag-G** nanocomposite gels, respectively, on the top of the filter papers after the washes did not change, and the water and EDTA disodium dihydrate solutions collected after the respective washes in the conical flask also did not show any colour. These observations suggested that the gel matrix-metal nanoparticle interactions were irreversible owing to the formation of zerovalent Cu and Ag.

7.3.6. Application of GI-G and nanocomposite gels (GI-Cu-G and GI-Ag-G)

Since AgNPs and CuNPs can show outstanding antimicrobial activity [7.64-7.65] and antioxidant properties [7.66-7.67], we investigated the antioxidant and antibacterial activities of the **GI-G** and the nanocomposite gels (**GI-Cu-G** and **GI-Ag-G**).

Antioxidant activity

DPPH (2,2-diphenyl-1-picrylhydrazyl) analysis was performed to investigate the antioxidant properties of the **GI-G** and nanocomposite gels. The DPPH free radical is a long-lived organic

nitrogen radical with a deep purple color, and the reduction of this stable free radical by accepting electrons from an antioxidant leads to a color change from purple to yellow of the corresponding hydrazine [7.68]. After reduction, the DPPH radical is converted to DPPH₂, and the violet color of the solution changes to yellow. This leads to a decrease in the absorption intensity of the solution at 517 nm. The **GI-G**, **GI-Cu-G**, and **GI-Ag-G** gels exhibited concentration-dependent free radical scavenging activities (Figure 7.7 A-7.7 C). We prepared the gel, partially disrupted by shaking, and then pipetted out different amounts of the gel (2 μ L, 5 μ L, and 7 μ L) and dissolved it in methanol. The DPPH radical scavenging activities of the **GI-G**, **GI-Cu-G**, and **GI-Ag-G** gels were observed to be ~53% for **GI-G**, ~90% for **GI-Cu-G**, and ~68% for **GI-Ag-G** at 7 μ L mL⁻¹. Since compounds based on guanidinium and indole moieties can show good antioxidant activities [7.69-7.70], the cumulative effect of both can endow the **GI-G** gel with its antioxidant property.

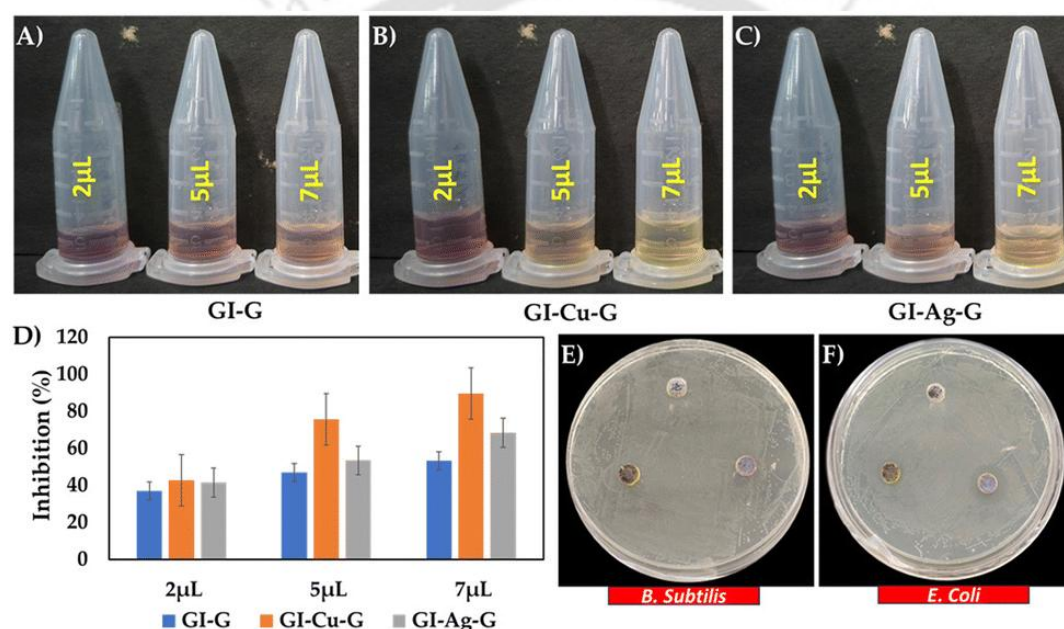


Figure 7.7: DPPH assay pictures of (A) **GI-G**, (B) **GI-Cu-G**, (C) **GI-Ag-G**, (D) antioxidant inhibition effect in percentage, and antimicrobial activity against (E) *E. coli* and (F) *B. subtilis*.

Antibacterial activity

We investigated the antibacterial activity of **GI-G**, **GI-Cu-G**, and **GI-Ag-G** gel against *E. coli* and *B. subtilis*, used as representative Gram-negative and Gram-positive groups of bacteria, by zone of inhibition studies. Among all the gel samples, the **GI-Ag-G** nanocomposite organohydrogel showed the maximum antibacterial inhibition with a zone diameter of 15 mm, while **GI-Cu-G** showed antibacterial inhibition with a zone diameter of 10 mm for *E. coli*. This can be because of the gel matrix decorated with Cu and Ag nanoparticles, which facilitated effective cell membrane

disruption and leakage of ions that made them highly effective against Gram-negative bacteria. However, the gel samples were not effective against the Gram-positive bacterial strain.

7.3.7. Solid-state anion exchange

To study the solid-state anion coordination behaviour of **GUA-IND**, we tried to crystallize different anions with **GUA-IND** (refer to section A7.11 of the Annexure 7 for detailed procedures). In the course of crystallization, the phenomenon of anion exchange was observed, where the counter anion (Cl^-) of **GUA-IND** was exchanged by different anions such as Br^- , NO_3^- , and H_2PO_4^- during the process of crystallization. Such an anion exchange process is very important because of its implications in environmental remediation applications in terms of the removal of toxic anions. It was interesting to note that the said anion exchange phenomenon was accompanied by differential solid state self-assembly behaviour inflicted mainly via hydrogen bonding interaction between the probe and the anions of interest. Crystal structure analysis of the aforementioned anions with **GUA-IND** revealed a very similar anion-coordination-driven self-assembly pattern except for H_2PO_4^- . The $-\text{NH}$ unit of the terminal indole ring extended across the three arms of **GUA-IND** actively participated in hydrogen bonding interactions with all the anions. Each anion coordinated with three nearby **GUA-IND** through hydrogen bonding interactions, thus facilitating the expansion of the cage-like, two-dimensional assembled architectures.

In the complex $[\text{GUA-IND}\cdot\text{Br}]^-$, the Br^- anion formed three hydrogen bonding interactions with three nearby indole $-\text{NH}$ units of three **GUA-IND** molecules (Figure 7.8 C) with an average hydrogen bonding distance of 2.45 Å ($\text{Br1}\cdots\text{H1N} = 2.45$ Å). The trigonal planar NO_3^- anion was observed to be encapsulated via six hydrogen bonding interactions involving three bifurcated hydrogen bonds in the complex $[\text{GUA-IND}\cdot\text{NO}_3]^-$ (average hydrogen bonding distance is 2.13 Å) (Figure 7.8 A). However, in the case of $[\text{GUA-IND}\cdot\text{H}_2\text{PO}_4]^-$ (Figure 7.8 B) apart from having a similar kind of encapsulation process as discussed earlier for the other anions, although different in coordination type (having an average hydrogen bonding distance of 2.22 Å involving $\text{O2}\cdots\text{H4} = 2.06$ Å, $\text{O1}\cdots\text{H4} = 2.63$ Å, $\text{O3}\cdots\text{H7A} = 2.19$ Å, and $\text{O3}\cdots\text{H1} = 2.03$ Å), the H_2PO_4^- anion forms a cyclic dimeric structure with an $R_{22}(8)$ arrangement, which further expands along crystallographic a -axis with the help of hydrogen bonding interactions ($\text{O2}\cdots\text{H1B} = 1.64$ Å, and $\text{O3}\cdots\text{H4B} = 1.70$ Å). Such an expansion of the dimeric assembly facilitates the formation of a three-dimensional network in the $[\text{GUA-IND}\cdot\text{H}_2\text{PO}_4]^-$ -complex, which is not the case in all the other anionic complexes.

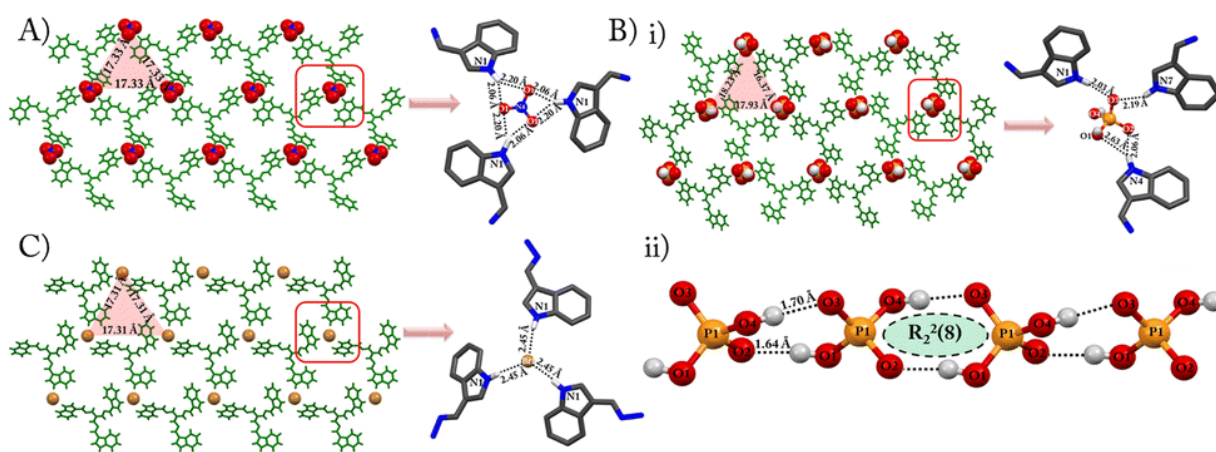


Figure 7.8: Crystal structures of **GUA-IND** with (A) NO_3^- , (B) H_2PO_4^- , and (C) Br^- as counter anions.

The solid-state study was well supported via the solution state study, performed through ^1H NMR titration experiments of Br^- , NO_3^- , and H_2PO_4^- with **GUA-IND** in $\text{DMSO}-d_6$ solvent (Figure A7.28-A7.30, Annexure 7). For both Br^- , and NO_3^- anions, upon addition of aliquots of the respective anions to the solution of **GUA-IND** in $\text{DMSO}-d_6$, very negligible shifts of the peaks corresponding to H_a , H_b , H_c and H_d were observed [$\Delta\delta\text{H}_a(\text{Br}^-) = 0.005$ ppm (upfield), $\Delta\delta\text{H}_a(\text{NO}_3^-) = 0.02$ ppm (upfield), $\Delta\delta\text{H}_b(\text{Br}^-) = 0.002$ ppm (upfield), $\Delta\delta\text{H}_b(\text{NO}_3^-) = 0$, $\Delta\delta\text{H}_c(\text{Br}^-) = 0.006$ ppm (downfield), $\Delta\delta\text{H}_c(\text{NO}_3^-) = 0$, $\Delta\delta\text{H}_d(\text{Br}^-) = 0.001$ ppm (downfield), and $\Delta\delta\text{H}_d(\text{NO}_3^-) = 0.01$ ppm (upfield)] suggesting very weak hydrogen bonding interactions in the solution phase. In contrast, for H_2PO_4^- , a significant upfield shifts of the peaks corresponding to H_a , H_b , H_c , and H_d ($\Delta\delta\text{H}_a = 0.14$ ppm, $\Delta\delta\text{H}_c = 0.25$ ppm, and $\Delta\delta\text{H}_d = 0.23$ ppm) were observed upon the addition of ~ 4 equiv. of H_2PO_4^- , along with this, the disappearance of the peak corresponding to H_b (on addition of ~ 1 equiv. of the anions) was also evident, signifying a strong hydrogen bonding interaction of **GUA-IND** with H_2PO_4^- in the solution phase. All the details of the crystallographic refinement and hydrogen-bonding interactions are furnished in Tables A7.1 and A7.2, respectively.

The crystals obtained after the successful anion exchange were also analysed through ^1H NMR spectroscopy and compared with those of **GUA-IND**. For the crystals of the complexes [**GUA-IND** $\cdot\text{NO}_3$] $^-$ and [**GUA-IND** $\cdot\text{H}_2\text{PO}_4$], shifts of the peaks (Figure A7.31, Annexure 7) corresponding to H_a , H_b , H_c , and H_d were observed, and for [**GUA-IND** $\cdot\text{NO}_3$] $^-$, the shifts were observed to be $\Delta\delta\text{H}_a = 0.098$ ppm (upfield), $\Delta\delta\text{H}_b = 0.017$ ppm (upfield), $\Delta\delta\text{H}_c = 0.021$ ppm (upfield), and $\Delta\delta\text{H}_d = 0.01$ ppm (upfield), and for [**GUA-IND** $\cdot\text{H}_2\text{PO}_4$], $\Delta\delta\text{H}_a = 0.231$ ppm (upfield), $\Delta\delta\text{H}_b = 0.208$ ppm (downfield), $\Delta\delta\text{H}_c = 0.17$ ppm (upfield), and $\Delta\delta\text{H}_d = 0.143$ ppm (upfield). Those peaks shifting firmly supported our claim of an anion exchange process. For the [**GUA-IND** $\cdot\text{Br}$] $^-$ complex, we could not perform the NMR study as the crystallization of the

complex was tough, as it rarely crystallized. Initially, we fortunately obtained the crystals in a very small amount. Furthermore, to confirm whether the crystal structures of $[\text{GUA-IND}\cdot\text{NO}_3]^-$ and $[\text{GUA-IND}\cdot\text{H}_2\text{PO}_4]^-$ were truly representative of the bulk materials, PXRD experiments were performed. The peak positions of the experimental PXRD patterns of both $[\text{GUA-IND}\cdot\text{NO}_3]^-$ (Figure A7.32, Annexure 7) and $[\text{GUA-IND}\cdot\text{H}_2\text{PO}_4]^-$ (Figure A7.33, Annexure 7) corresponded well with the results simulated from the single-crystal data, indicating the high purity of the synthesized samples and complete Cl^- displacement. The variations in the reflection intensities between the simulated and experimental patterns can be attributed to the difference in the preferred orientation of the powder samples during the data collection of the PXRD experiment.

To check the selectivity in the anion exchange process, the receptor **GUA-IND** was dissolved in DMSO in a glass vial, and 3 equivalents (of the receptor) of different TBA anions, viz., Br^- , NO_3^- , H_2PO_4^- , SO_4^{2-} , HSO_4^- , ClO_4^- , and I^- , were added. Within one week, crystals appeared in the glass vial, and after analysing via SCXRD, the crystals were found to be $[\text{GUA-IND}\cdot\text{H}_2\text{PO}_4]^-$. The polarized microscopic image of $[\text{GUA-IND}\cdot\text{H}_2\text{PO}_4]^-$ is shown in the Annexure 7 (Figure A7.34, Annexure 7). The selectivity observed in the anion exchange in the solid state further supports the stronger binding of H_2PO_4^- with the receptor compared to the other anions tested, which was consistent with the earlier observed ^1H NMR titration data, where the maximum chemical shift of the indole $-\text{NH}$ was observed with H_2PO_4^- , while for Br^- and NO_3^- , this shift was found to be minimum. From the ^1H NMR data of the $[\text{GUA-IND}\cdot\text{NO}_3]^-$ and $[\text{GUA-IND}\cdot\text{H}_2\text{PO}_4]^-$ crystals, more prominent chemical shifts for H_a , H_b , H_c , and H_d were observed in the $[\text{GUA-IND}\cdot\text{H}_2\text{PO}_4]^-$ crystal compared to the chemical shifts of the same in the $[\text{GUA-IND}\cdot\text{NO}_3]^-$ crystal.

Reversibility in the anion exchange process was also investigated. Crystals of $[\text{GUA-IND}\cdot\text{NO}_3]^-$ and $[\text{GUA-IND}\cdot\text{H}_2\text{PO}_4]^-$ were dissolved in DMSO (2 mg) in two separate glass vials, and 50 μL of TBACl was added to both vials. Within one week, crystals grew and were analysed *via* SCXRD. The crystals obtained in both cases were identified to be $[\text{GUA-IND}\cdot\text{Cl}]^-$. The PXRD spectra of the crystals obtained after the reversibility experiment matched the spectra of the crystals of the **GUA-IND** receptor (Figure A7.35, Annexure 7), further confirming the reversibility of the anion exchange process.

7.4. Conclusion

In summary, we prepared a guanidinium-based tripodal gelator with indole moieties in the three arms of the receptor. The gelator portrayed the rare anion coordination-induced gelation phenomena selectively in the presence of $\text{SO}_4^{2-}/\text{HSO}_4^-$ anion in a DMSO- H_2O (1: 4, v/v) mixture.

The **GI-G** gel formed in the presence of SO_4^{2-} exhibited excellent stimulus-responsive properties

towards PA among different nitroaromatic compounds. The **GI-G** gel formed nanocomposites, **GI-Cu-G** and **GI-Ag-G**, in the presence of Cu and Ag metal ions *via in situ* reduction of precious metal salts like Cu and Ag into their nanoparticles without using any external reducing agents, which, along with **GI-G**, could exhibit antioxidant and antimicrobial activities. Along with anion coordination-induced gelation, the receptor **GUA-IND** exhibited a phenomenon of anion exchange where the counter anion (Cl^-) of **GUA-IND** was replaced by different anions such as Br^- , NO_3^- , and H_2PO_4^- during the process of crystallization, paving the way for the synthesis of versatile multifunctional low molecular weight receptors.

References

- [7.1] H. Maeda *Chem. – Eur. J.*, 2008, **14**, 11274-11282.
- [7.2] C. A. Offiler, C. D. Jonesa and J. W. Steed, *Chem. Commun.*, 2017, **53**, 2024-2027.
- [7.3] A. Y.-Y. Tama and V. W.-W. Yam, *Chem. Soc. Rev.*, 2013, **42**, 1540-1567.
- [7.4] T. Becker, C. Y. Goh, F. Jones, M. J. McIlldowie, M. Mocerino and M. I. Ogden, *Chem. Commun.*, 2008, 3900-3902
- [7.5] J.-S. Shen, Q.-G. Cai, Y.-B. Jiangb and H.-W. Zhang, *Chem. Commun.*, 2010, **46**, 6786-6788.
- [7.6] A. J. Kleinsmann, N. M. Weckenmann and B. J. Nachtsheim, *Chem. – Eur. J.*, 2014, **20**, 9753-97.
- [7.7] S. Basak, N. Nandia and A. Banerjee, *Chem. Commun.*, 2014, **50**, 6917-6919.
- [7.8] Z. Kokan, M. D. Smrčková and V. Šindelář, *Chem*, 2021, **7**, 2473-2490.
- [7.9] S. Mondal, R. Raza and K. Ghosh, *New J. Chem.*, 2019, **43**, 10509-10516.
- [7.10] J. Shen, J. Zhang, Y. Zuo, L. Wang, X. Sun, J. Li, W. Han and R. He, *J. Hazard. Mater.*, 2009, **163**, 1199-1206.
- [7.11] B. Naskar, A. Bauzá, A. Frontera, D. K. Maiti, C. D. Mukhopadhyay and S. Goswami, *Dalton Trans.*, 2018, **47**, 15907-15916.
- [7.12] R. Moral, O. A. Pegu and G. Das, *Dyes Pigm.*, 2023, **218**, 111502.
- [7.13] M. Fabin, M. Łapkowski and T. Jarosz, *Appl. Sci.*, 2023, **13**, 3991.
- [7.14] R. Dahiwadkar, A. Murugan, D. Johnson, R. Chakraborty, V. Thiruvengatam and S. Kanvah, *J. Photochem. Photobiol., A*, 2023, **434**, 114227.
- [7.15] S. Sarkar, S. Dutta, S. Chakrabarti, P. Bairi and T. Pal, *ACS Appl. Mater. Interfaces*, 2014, **6**, 6308-6316.
- [7.16] S. Mondal and K. Ghosh, *ChemistrySelect*, 2017, **2**, 4800-4806.
- [7.17] D. Das, T. Kara and P. K. Das, *Soft Matter*, 2012, **8**, 2348-2365.
- [7.18] B. O. Okesola, S. K. Suravaram, A. Parkin and D. K. Smith, *Angew. Chem., Int. Ed.*, 2016, **55**, 183-187.
- [7.19] T. Ghosh, A. Biswas, S. Bhowmik and A. K. Das, *Chem. – Asian J.*, 2021, **16**, 215-223.
- [7.20] P. Slavík, D. W. Kurkaa and D. K. Smith, *Chem. Sci.*, 2018, **9**, 8673-8681.
- [7.21] S. Ye, W. Zhang, Z. Zhai, S. Shang, L. Huang, Z. Song and J. Jiang, *Langmuir*, 2024, **40**, 647-656.
- [7.22] R. Jain, G. Khandelwal and S. Roy, *Langmuir*, 2019, **35**, 5878-5889.
- [7.27] S. D. G. Schejtman, P. A. Mercadal, M. L. Picchio, A. V. Veglia and E. A. Coronado, *J. Phys. Chem. C*, 2022, **126**, 9979-9988.
- [7.24] B. Chen, E. H. Fragal, E. Faudry and S. Halila, *ACS Appl. Mater. Interfaces*, 2024, **16**, 70818-70827.

- [7.26] J. Gregory and R. V. Dhond, *Water Res.*, 1972, **6**, 681-684.
- [7.27] S. E. Creutz, E. N. Crites, M. C. D. Siena and D. R. Gamelin, *Chem. Mater.*, 2018, **30**, 4887-4891.
- [7.28] Q. Guo, J. Li, Y. Zhao, L. Li, L. He, F. Zhao, F. Zhai, M. Zhang, L. Chen, Z. Chai and S. Wang, *Angew. Chem., Int. Ed.*, 2024, **63**, e202400849.
- [7.29] P. Blondeau, M. Segura, R. P. Fernández and J. d. Mendoza, *Chem. Soc. Rev.*, 2007, **36**, 198-210.
- [7.30] M. Wenzel, J. Steup, K. Ohto and J. J. Weigand, *Chem. Lett.*, 2022, **51**, 20-29.
- [7.31] G. Picci, M. T. Mulvee, C. Caltagirone, V. Lippolis, A. Frontera, R. M. Gomila and J. W. Steed, *Molecules*, 2022, **27**, 1257.
- [7.32] Y. Hisamatsu, S. Banerjee, M. B. Avinash, T. Govindaraju and C. Schmuck, *Angew. Chem., Int. Ed.*, 2013, **52**, 12550-12554.
- [7.33] M. Externbrink, S. Riebe, C. Schmuck and J. Voskuhl, *Soft Matter*, 2018, **14**, 6166-6170.
- [7.34] P. Jana and C. Schmuck, *Chem. – Eur. J.*, 2017, **23**, 320-326.
- [7.35] G. Das, S. Nagaraja, V. Sridurai, D. B. Shinde, M. Addicoat, T. Prakasam, F. Gándara, F. Ravoux, S. K. Sharma, G. G. Nair, Z. Lai, R. Jagannathan, M. A. Olson and A. Trabolsi, *Chem. Mater.*, 2019, **31**, 4148-4155.
- [7.36] S. De and G. Das, *Langmuir*, 2022, **38**, 6158-6163.
- [7.37] S. De, O. A. Pegu and G. Das, *Langmuir*, 2023, **39**, 2444-2449.
- [7.38] O. A. Pegu, A. Das and G. Das, *J. Mol. Struct.*, 2023, **1294**, 136427.
- [7.39] O. A. Pegu, R. Moral and G. Das, *Cryst. Growth Des.*, 2023, **23**, 8370-8380.
- [7.40] R. Moral and G. Das, *Soft Matter*, 2024, **20**, 7668-7677.
- [7.41] S. Mukherjee, A. V. Desai, A. I. Inamdar, B. Manna and S. K. Ghosh, *Cryst. Growth Des.*, 2015, **15**, 3493-3497.
- [7.42] O. S. Lawal, *Food Chem.*, 2006, **95**, 101-107.
- [7.43] K. Aoki, K. Shiraki and T. Hattori, *Phys. Chem. Chem. Phys.*, 2016, **18**, 15060-15069.
- [7.44] L. Wang, Y. Dong, L. Wang, M. Cui, Y. Zhang, L. Jiang and X. Sui, *Food Hydrocolloids*, 2023, **143**, 108905.
- [7.45] Q. He, Y. Huang and S. Wang, *Adv. Funct. Mater.*, 2018, **28**, 1705069.
- [7.46] X. Wang, C. Qiao, S. Jiang, L. Liu and J. Yao, *Soft Matter*, 2021, **17**, 1558-1565.
- [7.47] J. Zhang, B. Zhang, Q. Chen, B. Zhang and J. Song, *Nanoscale Res. Lett.*, 2019, **14**, 5.
- [7.48] Q. Hu, H. Li, X. Chen, Y. Wang, H. Wu, S. Guo and K. Xu, *Adv. Funct. Mater.*, 2024, **34**, 2406968.
- [7.49] L. Liao, X. Jia, H. Lou, J. Zhong, H. Liu, S. Ding, C. Chen, S. Hong and X. Luo, *RSC Adv.*, 2021, **11**, 11519-11528.
- [7.50] S. Sharma, M. Kumaria and N. Singh, *Soft Matter*, 2020, **16**, 6532-6538.
- [7.51] X. Ma, S. Liu, Z. Zhang, Y. Niua and J. Wu, *Soft Matter*, 2017, **13**, 8882-8885.
- [7.52] R. Hassanién, M. M. Almaky, A. Houltonc and B. R. Horrocks, *RSC Adv.*, 2016, **6**, 99422-99432.
- [7.53] F. LewisOscar, D. MubarakAli, C. Nithya, R. Priyanka, V. Gopinath, N. S. Alharbi and N. Thajuddin, *Biofouling*, 2015, **31**, 379-391.
- [7.53] F. LewisOscar, D. MubarakAli, C. Nithya, R. Priyanka, V. Gopinath, N. S. Alharbi and N. Thajuddin, *Biofouling*, 2015, **31**, 379-391.
- [7.54] D. G. Kumar, R. R. Achar, J. R. Kumar, G. Amala, V. K. Gopalakrishnan, S. Pradeep, A. A. Shati, M. Y. Alfaihi, S. E. I. Elbehairi, E. Silina, V. Stupin, N. Manturova, C. Shivamallu and S. P. Kollur, *BMC Complementary Med. Ther.*, 2023, **23**, 167.

- [7.55] A. K. Alzubaidi, W. J. A. Kaabi, A. A. Ali, S. Albukhaty, H. A. Karagoly, G. M. Sulaiman, M. Asiri and Y. Khane, *Appl. Sci.*, 2023, **13**, 2182.
- [7.56] R. Sierra-Ávila, M. Pérez-Alvarez, G. Cadenas-Pliego, V. C. Padilla, C. Ávila-Orta, O. P. Camacho, E. Jiménez-Regalado, E. Hernández-Hernández and R. M. Jiménez-Barrera, *J. Nanomater.*, 2015, 367341.
- [7.57] M. A. B. Aissa, B. Tremblay, A. Andrieux-Ledier, E. Maisonhaute, N. Raouafi and A. Courty, *Nanoscale*, 2015, **7**, 3189-3195.
- [7.58] B. Mekuye, The Impact of Size on the Optical Properties of Silver Nanoparticles Based on Dielectric Function, ed. Edited by S. Ameen, M. S. Akhtar, A. Jiménez-Suárez and G. Seisedos, Nanotechnology and Nanomaterials Annual Volume 20242023.
- [7.59] D. S. Keerthi, M. M. Vani and B. Krishnamurthy, *Trans. Indian Natl. Acad. Eng.*, 2024, **9**, 867-877.
- [7.60] N. Sarwar, S. H. Choi, G. Dastgeer, U. B. Humayoun, M. Kumar, A. Nawaz, D. I. Jeong, S. F. A. Zaidi and D. H. Yoon, *Appl. Surf. Sci.*, 2021, **542**, 148609.
- [7.61] A. K. Bishoyi, C. R. Sahoo, P. Samal, N. P. Mishra, B. R. Jali, M. S. Khan and R. N. Padhy, *Sci. Rep.*, 2024, **14**, 7513.
- [7.62] X. Liu, D. Gregurec, J. Irigoyen, A. Martinez, S. Moya, R. Ciganda, P. Hermange, J. Ruiz and D. Astruc, *Nat. Commun.*, 2016, **7**, 13152.
- [7.63] O. A. Pegu and G. Das, *Langmuir*, 2024, **40**, 24095-24105.
- [7.64] A. P. Ingle, N. Duran and M. Rai, *Appl. Microbiol. Biotechnol.*, 2014, **98**, 1001-1009.
- [7.65] J. Talapko, T. Matijević, M. Juzbašić, A. Antolović-Požgain and I. Škrlec, *Microorganisms*, 2020, **8**, 1400.
- [7.66] A. V. Samrot, S. P. R. Singh, R. Deenadhayalan, V. V. Rajesh, S. Padmanaban and K. Radhakrishnan, *Oxygen*, 2022, **2**, 591-604.
- [7.67] Z. Bedlovičová, I. Strapáč, M. Baláž and A. Salayová, *Molecules*, 2020, **25**, 3191.
- [7.68] P. Hesamzadeh, A. Seif, K. Mahmoudzadeh, M. G. Koli, A. Mostafazadeh, K. Nayeri, Z. Mirjafary and H. Saeidian, *Sci. Rep.*, 2024, **14**, 6473.
- [7.69] S. Packiaraj, A. Pushpaveni, S. Govindarajan and J. M. Rawson, *CrystEngComm*, 2016, **18**, 7978-7993.
- [7.70] J. Kumar, N. Kumar, N. Satib and P. K. Hota, *New J. Chem.*, 2020, **44**, 8960-8970.

Annexure 7



Figure A7.1: Gelation studies of **GUA-IND** with $(TBA)_2SO_4$ in different ratios of DMSO: H_2O viz. A) 1:4, B) 2:3, C) 1:1, D) 3:2 and E) 4:1.



Figure A7.2: Gelation studies of **GUA-IND** with $(TBA)_2SO_4$ in different ratios of DMSO: H_2O viz. A) 1:4, B) 2:3, C) 1:1, D) 3:2 and E) 4:1.



Figure A7.3: The minimum gelation concentration of **GUA-IND** required for gelation with $(TBA)_2SO_4$.

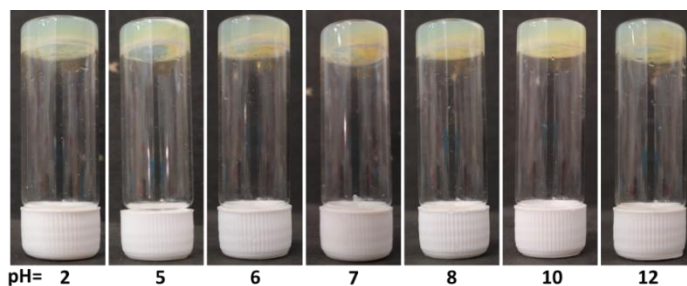


Figure A7.4: The minimum gelation concentration of GUA-IND required for gelation with $(TBA)_2SO_4$.

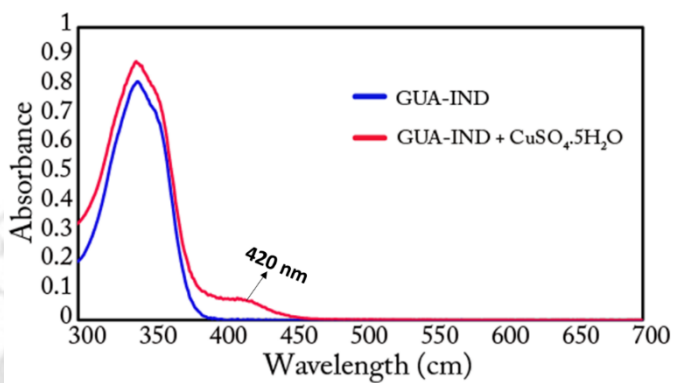


Figure A7.5: Absorption spectra of GUA-IND in presence and absence of $CuSO_4 \cdot 5H_2O$.

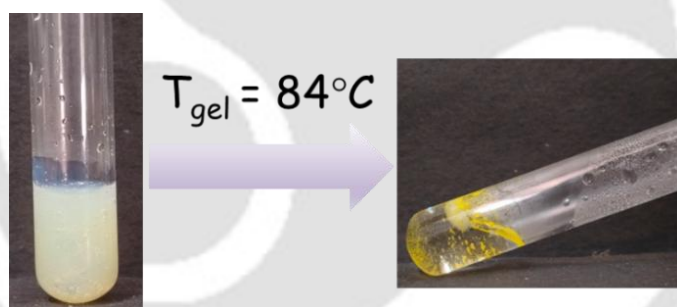


Figure A7.6: Gel-to-sol transition of GI-G gel.

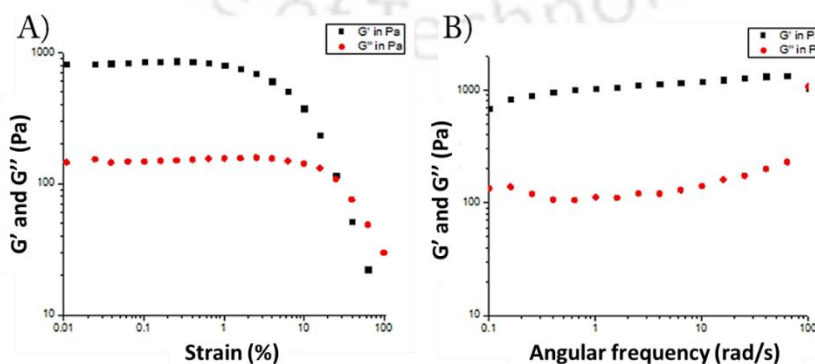


Figure A7.7: A) Amplitude sweep and B) frequency sweep of the GI-G gel.

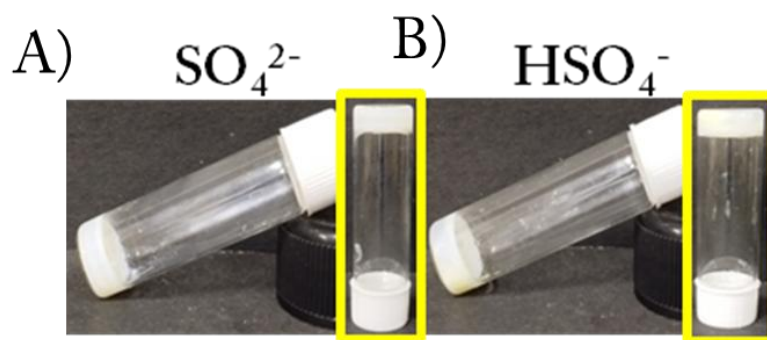


Figure A7.8: Gelation study of GUA-IND in DMF: H₂O (1:4, v/v) in the presence of A) SO₄²⁻ and B) HSO₄⁻.

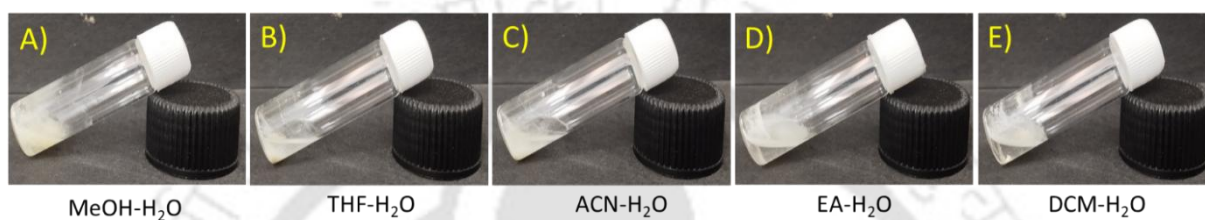


Figure A7.9: Gelation study of GUA-IND with SO₄²⁻ in A) MeOH (methanol)-H₂O, B) THF (tetrahydrofuran)-H₂O, C) ACN (acetonitrile)-H₂O, D) DCM (dichloromethane)-H₂O, E) EA (ethylacetate)-H₂O.

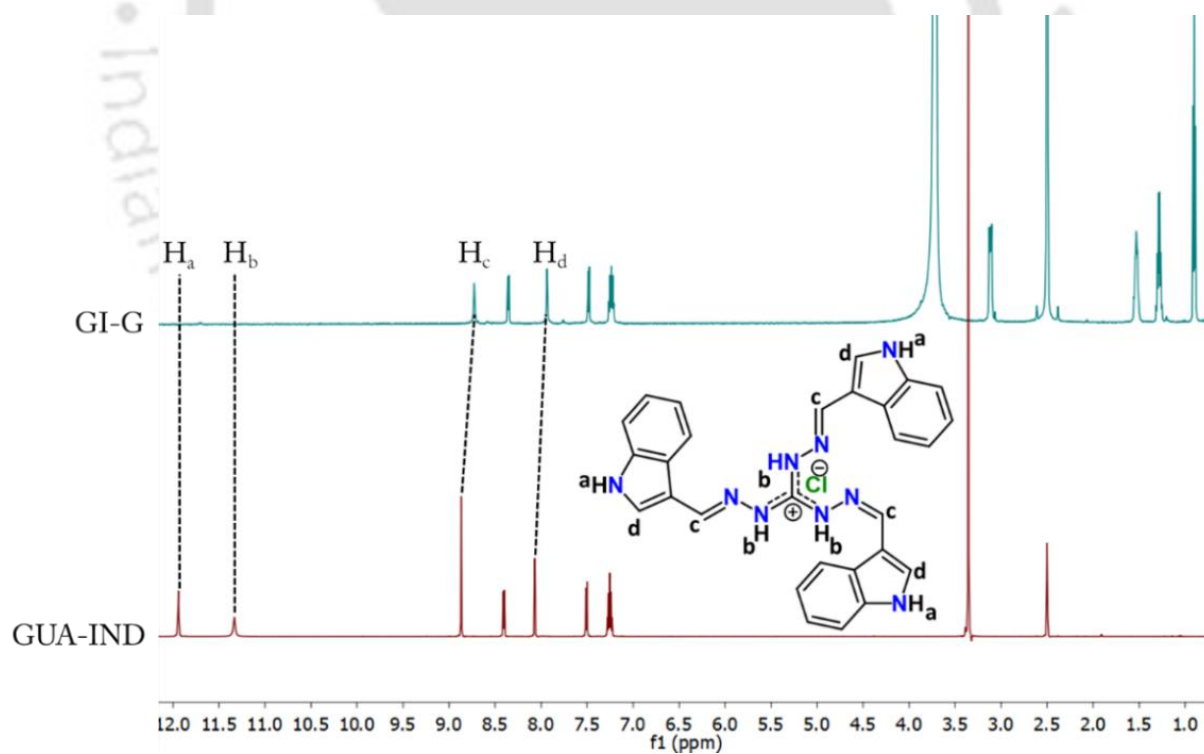


Figure A7.10: Stacked ¹H NMR spectra of GUA-IND and GI-G.

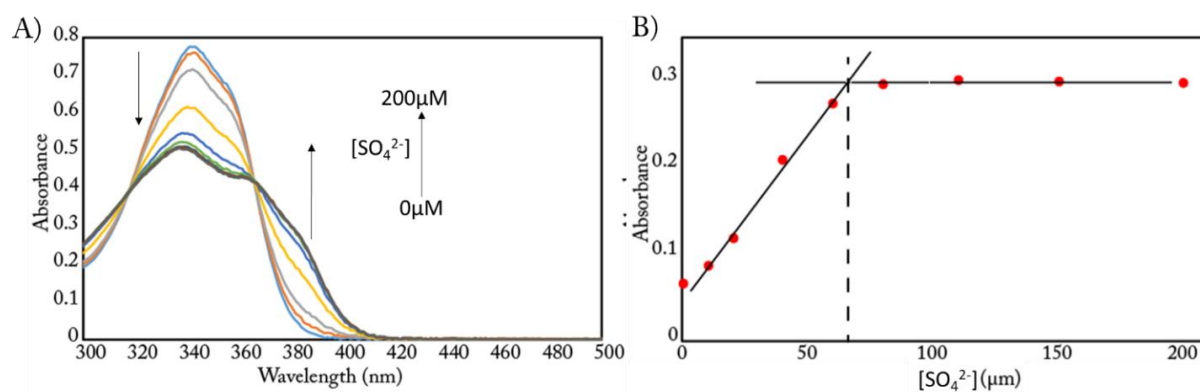


Figure A7.11: A) UV-Vis spectra of GUA-IND with increasing concentration of SO_4^{2-} anion, B) plot of absorbance vs. $[\text{SO}_4^{2-}]$ anion at 385 nm wavelength.

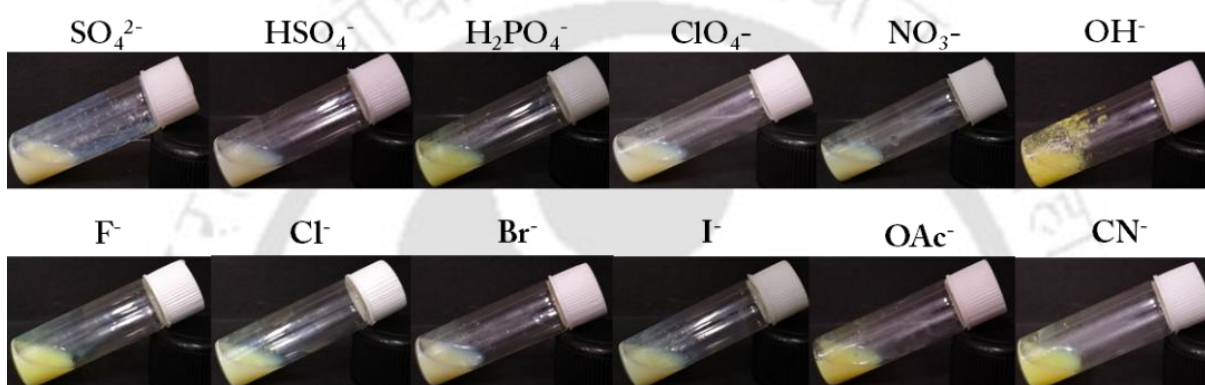


Figure A7.12: Gelation study of GUA-NAP in DMSO-H₂O (1: 4, v/v) in the presence of different anions of TBA salts.

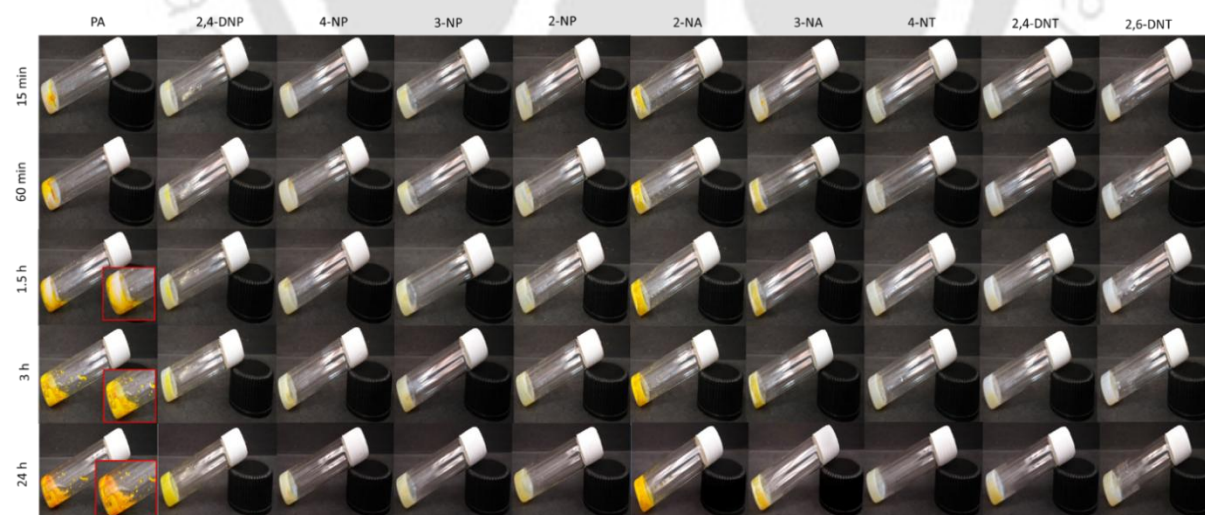


Figure A7.13: Stimuli responsive behaviour of GUA-IND towards different nitro-aromatic compounds at different time-intervals.

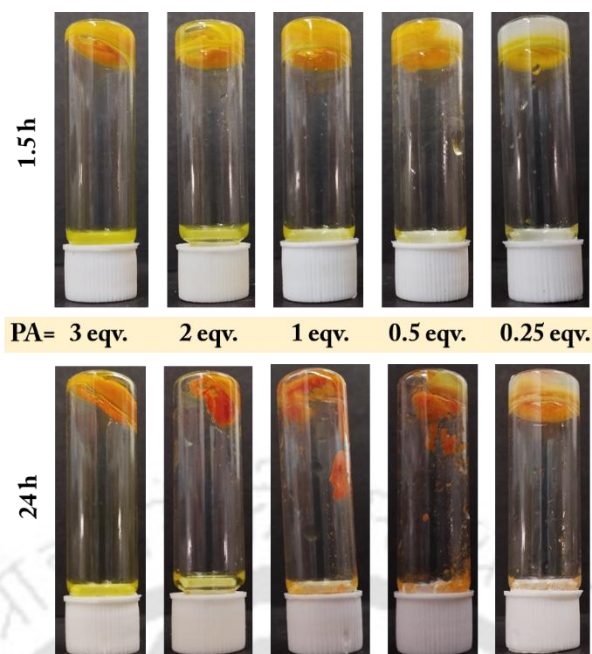


Figure A7.14: GI-G gel after addition of different equivalents of PA.

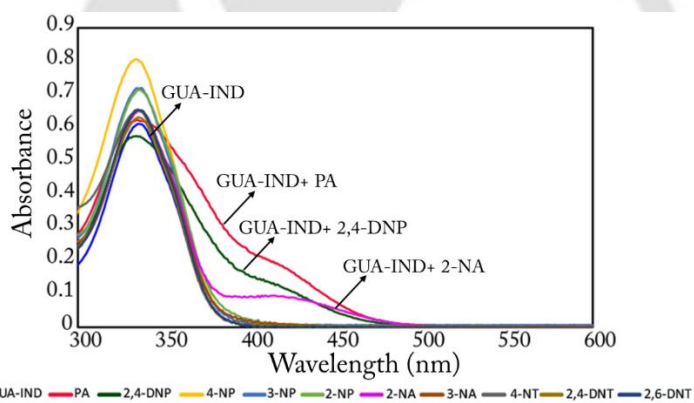


Figure A7.15: UV-Vis spectra of GUA-IND in presence of different nitro-aromatic compounds in H₂O.

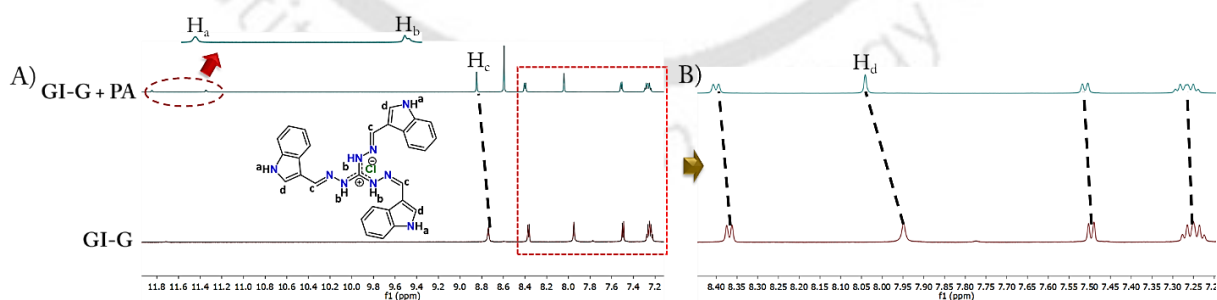


Figure A7.16: ¹H NMR spectra of A) GI-G and B) GI-G + PA in DMSO-*d*₆.

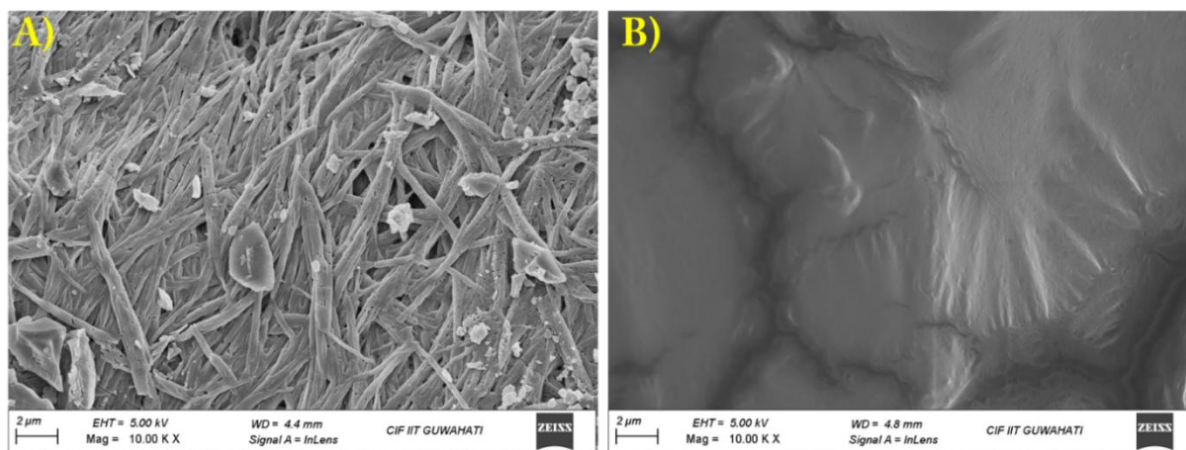


Figure A7.17: FESEM images of A) GI-G xerogel and B) GI-G + PA xerogel.

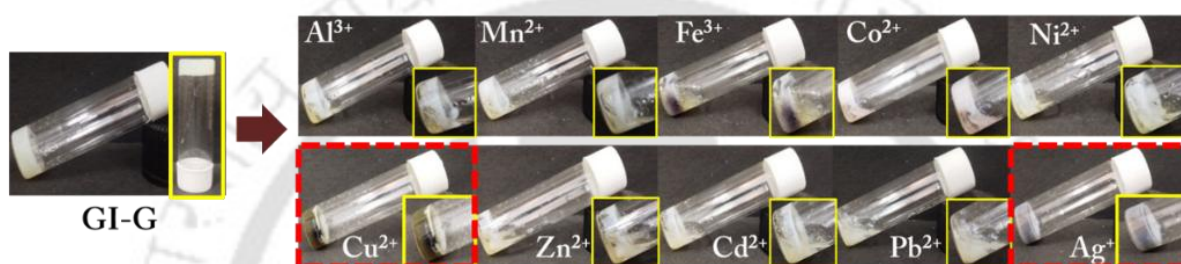


Figure A7.18: Effect of different metal salts on GI-G gel.

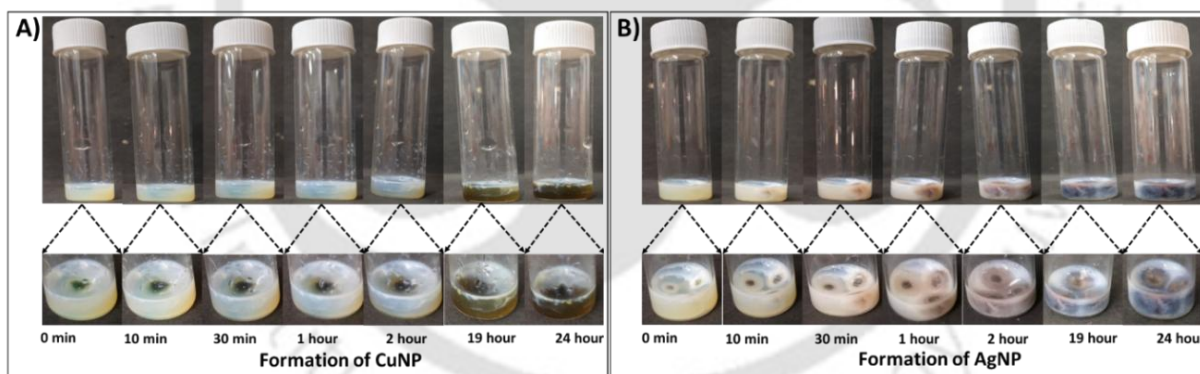


Figure A7.19: Formation of A) CuNPs and B) AgNPs.

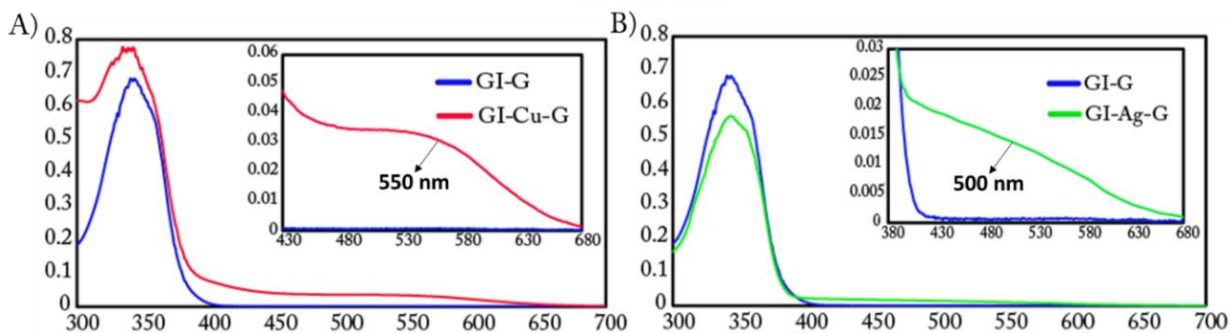


Figure A7.20: UV-Vis spectra of A) GI-Cu-G and B) GI-Ag-G gel nanocomposites dissolved in DMSO.

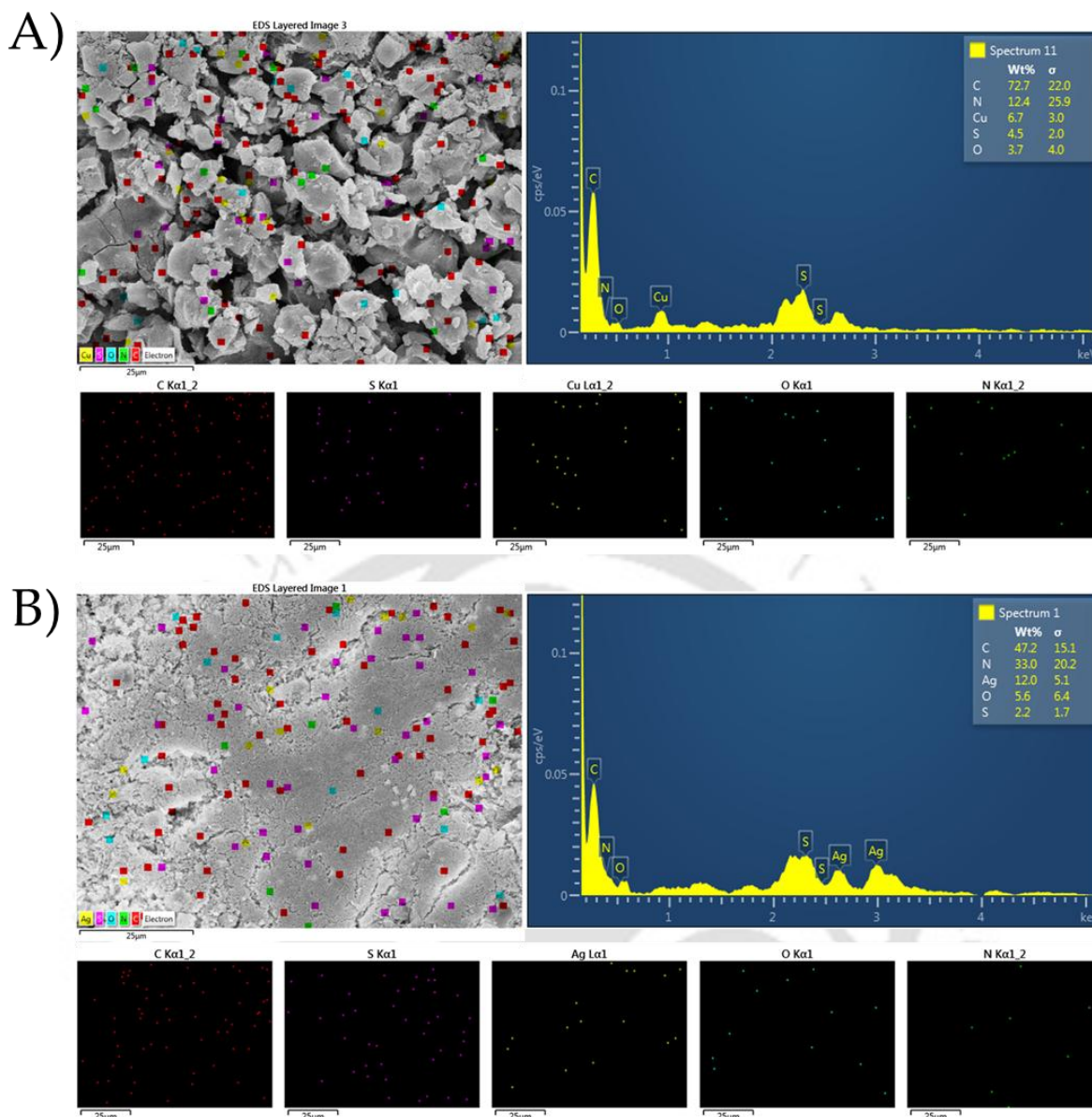


Figure A7.21: Energy dispersive X-ray (EDX) spectrum analysis of A) GI-Cu-G and B) GI-Ag-G xerogel. C: carbon, N: nitrogen; S: sulphur; O: oxygen; Cu: copper, Ag: silver.

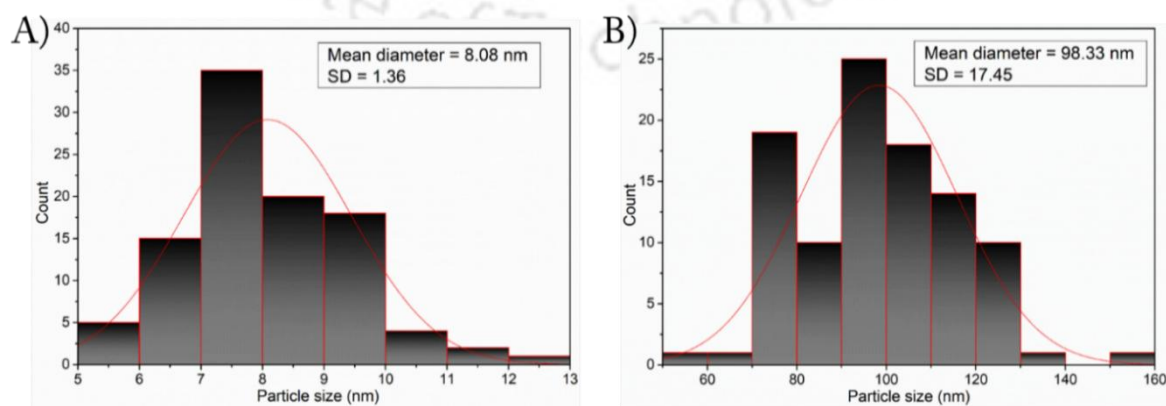


Figure A7.22: Histogram of the particle size distribution of A) GI-Cu-G and B) GI-Ag-G.

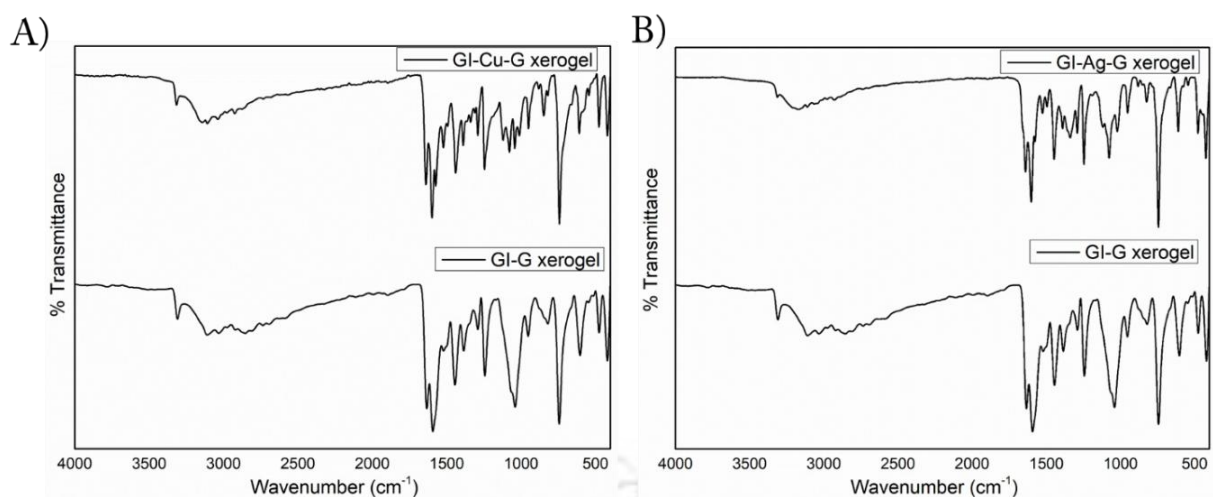


Figure A7.23: Stacked IR spectra of A) GI-Cu-G and GI-G and B) GI-Ag-G and GI-G xerogel in DMSO- d_6 .

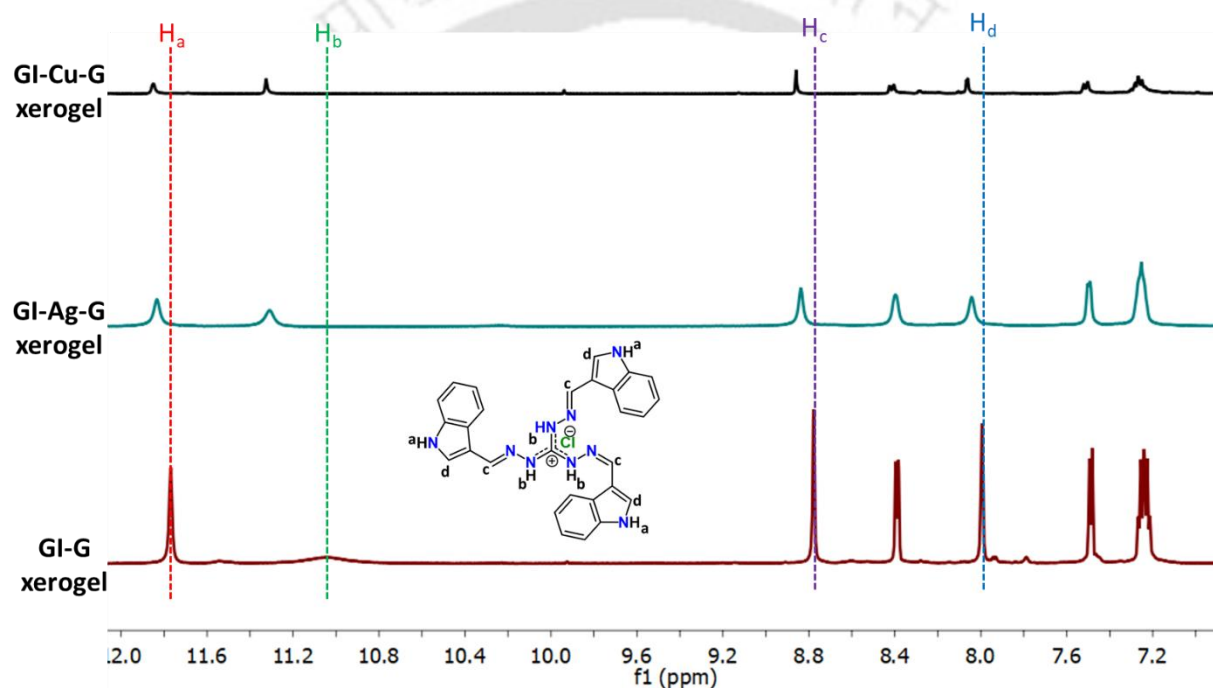


Figure A7.24: Stacked ^1H NMR spectra of GI-G, GI-Cu-G and GI-Ag-G xerogel in DMSO- d_6 .

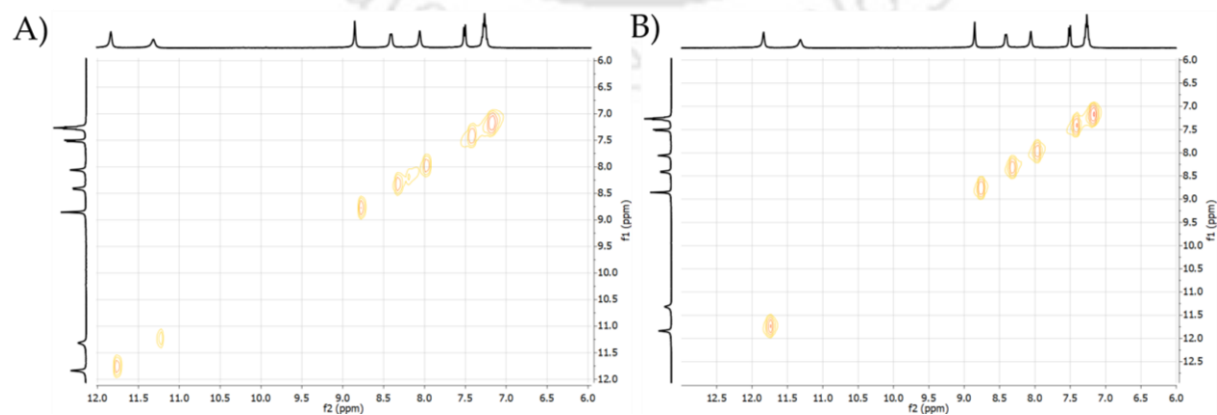


Figure A7.25: NOESY spectra of A) GI-Cu-G and B) GI-Ag-G xerogel in DMSO- d_6 .

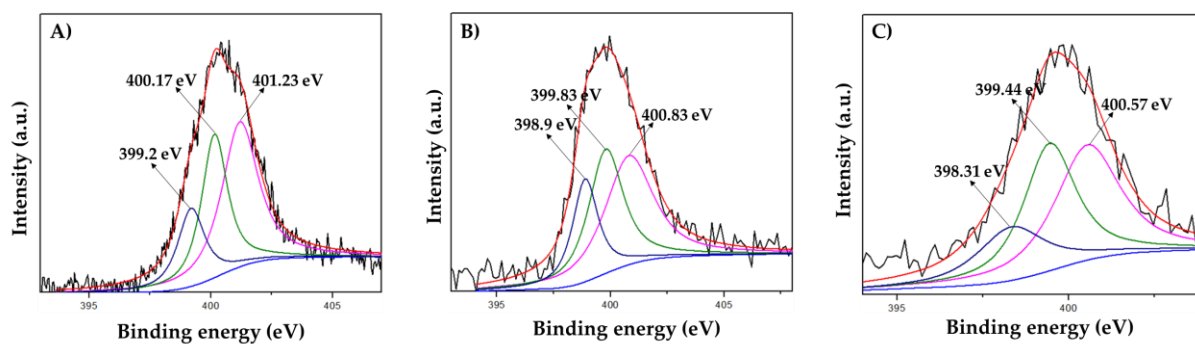


Figure A7.26: XPS spectra of N1s of A) GI-G, B) GI-Cu-G and A) GI-Ag-G xerogel.

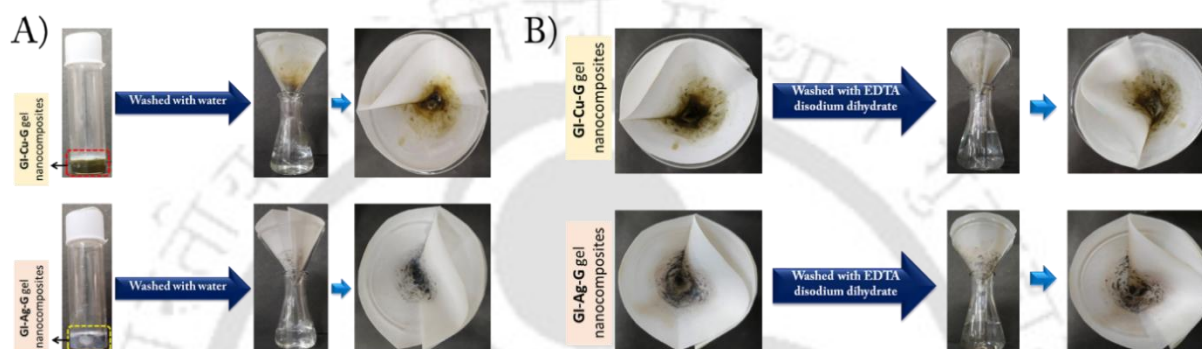


Figure A7.27: Images of GI-Cu-G and GI-Ag-G gels A) washed with water B) washed with EDTA disodium dihydrate.

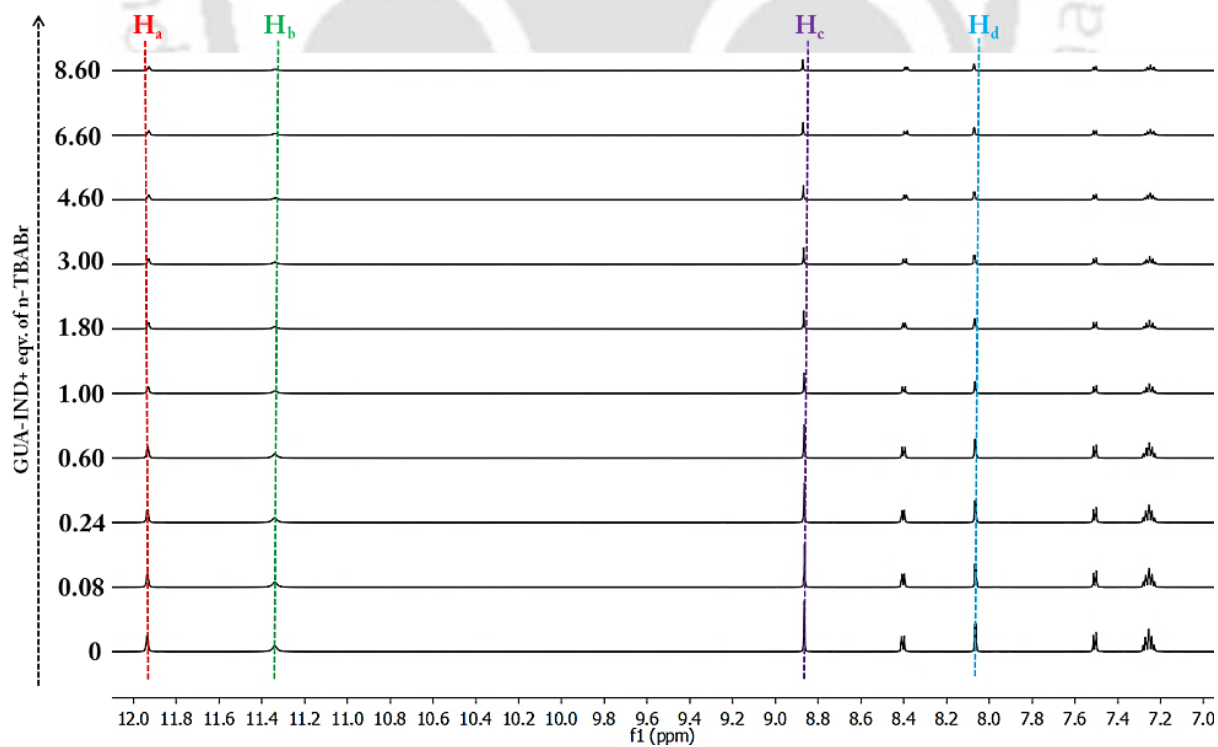


Figure A7.28: ^1H NMR titration of GUA-IND in $\text{DMSO-}d_6$ with increasing concentration of Br^- .

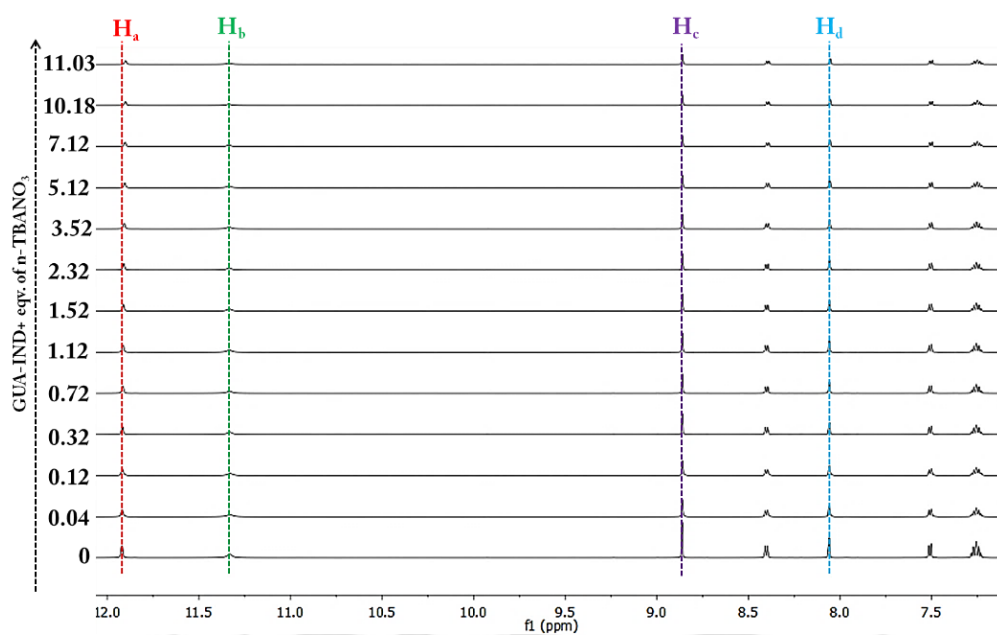


Figure A7.29: ^1H NMR titration of GUA-IND in $\text{DMSO-}d_6$ with increasing concentration of Br^- .

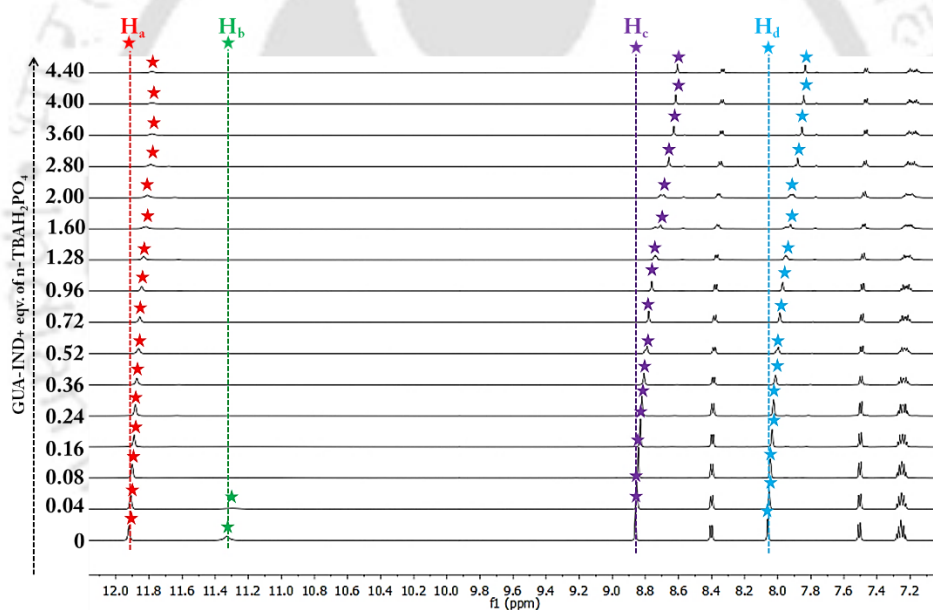


Figure A7.30: ^1H NMR titration of GUA-IND in $\text{DMSO-}d_6$ with increasing concentration of H_2PO_4^- .

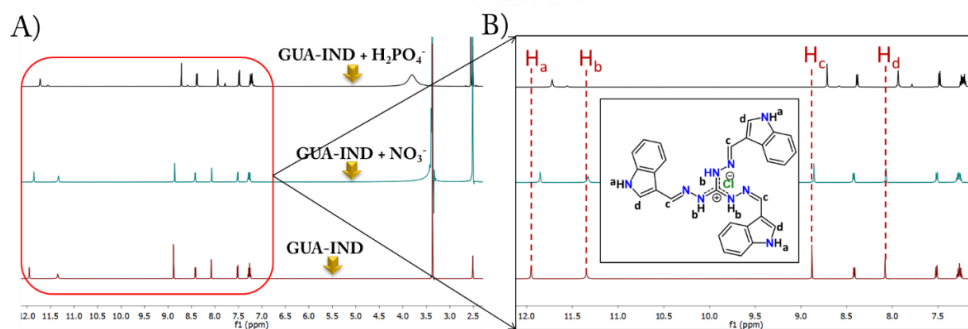


Figure A7.31: Stacked ^1H NMR spectra of GUA-IND, GUA-IND + NO_3^- , GUA-IND + H_2PO_4^- in $\text{DMSO-}d_6$.

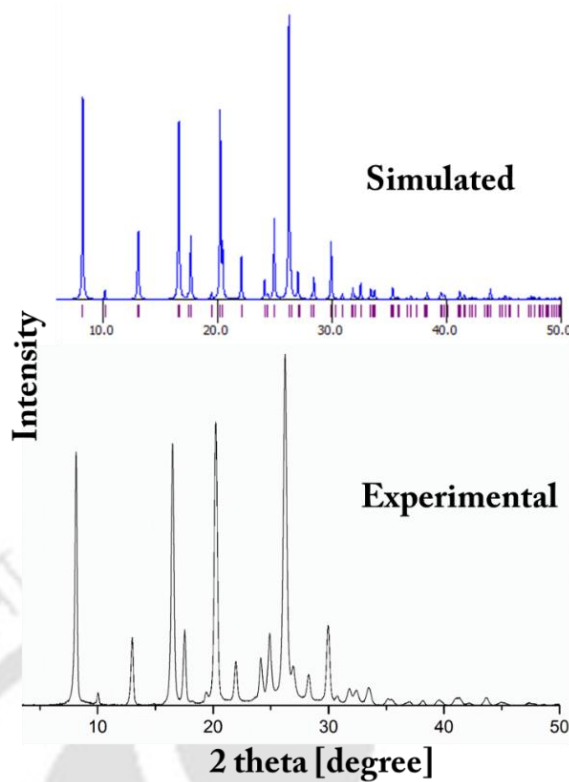


Figure A7.32: Powder X-ray diffraction: simulated pattern from the single-crystal X-ray of [GUA-IND.NO₃]⁻ (blue), experimental pattern from the crystalline solid of [GUA-IND.NO₃]⁻ (black).

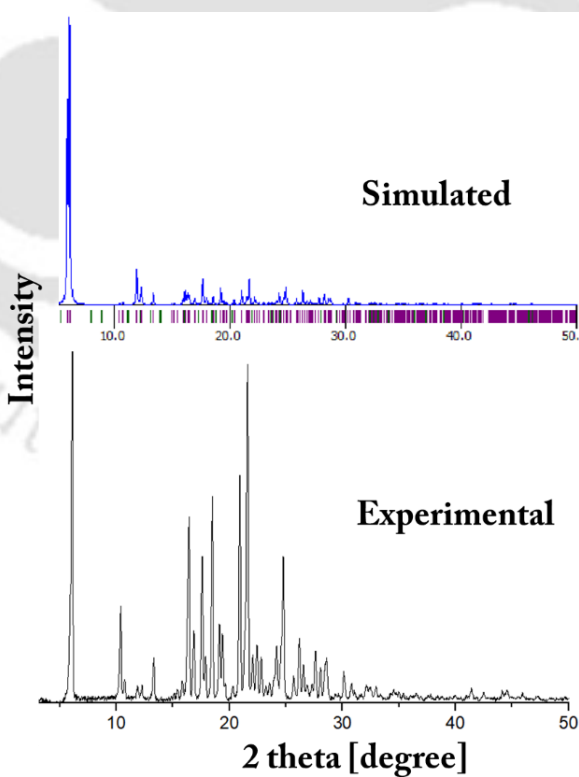


Figure A7.33: Powder X-ray diffraction: simulated pattern from the single-crystal X-ray of [GUA-IND.H₂PO₄]⁻ (blue), experimental pattern from the crystalline solid of [GUA-IND.H₂PO₄]⁻ (black).

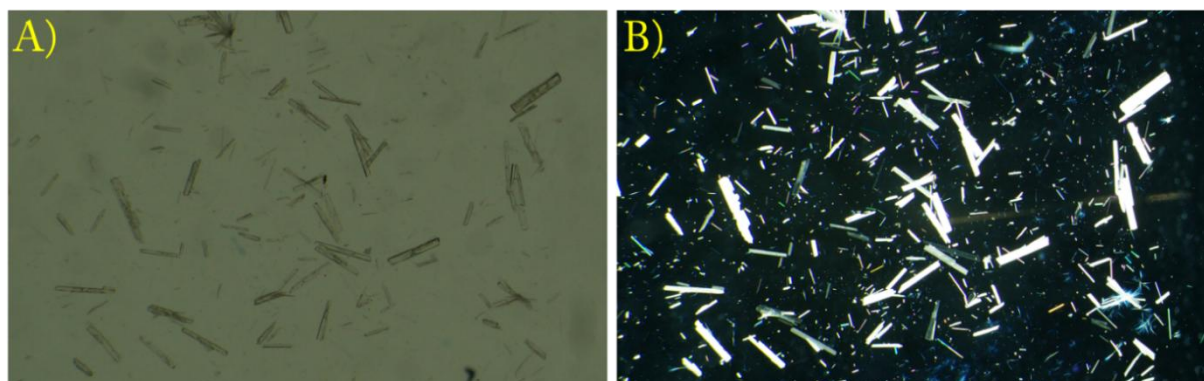


Figure A7.34: A) Bright field and B) Polarised microscopic image of $[\text{GUA-IND.H}_2\text{PO}_4]^-$ crystals.

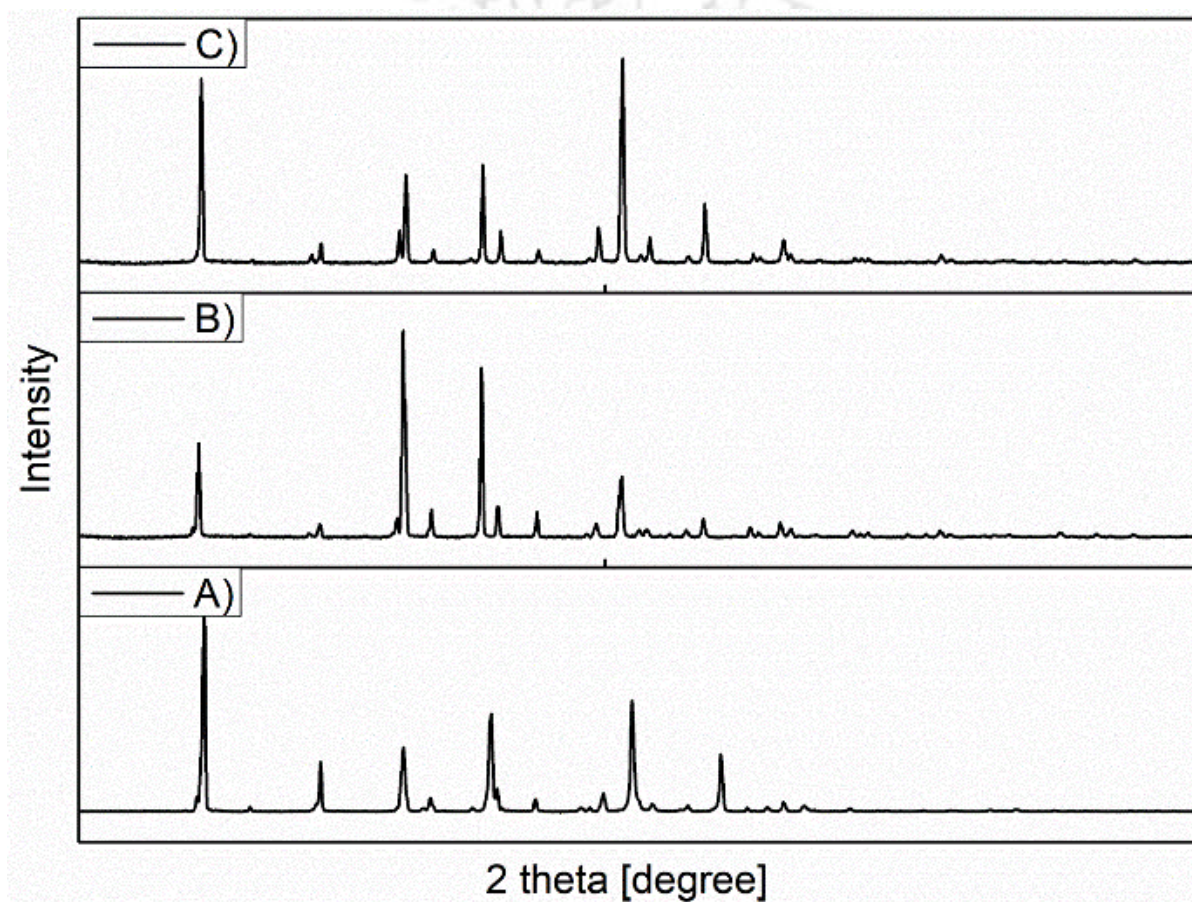


Figure A7.35: Stacked PXRD spectra of A) crystals of **GUA-IND** obtained from crystallisation of **GUA-IND** in DMSO, B) crystals of **GUA-IND** obtained after reversible anion exchange of Cl^- with $[\text{GUA-IND.NO}_3]^-$ and C) crystals of **GUA-IND** obtained after reversible anion exchange of Cl^- with $[\text{GUA-IND.H}_2\text{PO}_4]^-$.

Table A7.1. Crystallographic parameters and refinement data of the receptors and anionic complex of GUA-IND.

Parameters	Gua-IND	[GUA-IND.Br] ⁻	[GUA-IND.NO ₃] ⁻	[GUA-IND.H ₂ PO ₄] ⁻
formula	C ₅₆ H ₄₈ Cl N ₁₈	C ₂₈ H ₂₄ Br N ₉	C ₂₈ H ₂₄ N ₁₀ O ₃	C ₃₀ H ₃₂ N ₉ O ₅ P S
fw	1008.57	566.47	548.57	661.67
cryst syst	trigonal	trigonal	trigonal	orthorhombic
space group	R -3 :H	R -3 :H	R -3 :H	P n a 21
a (Å)	16.4700(6)	17.310(2)	17.333(3)	8.2595(4)
b (Å)	16.4700(6)	17.310(2)	17.333(3)	16.3723(8)
c (Å)	15.5495(8)	15.538(4)	15.209(3)	29.5080(14)
α (deg)	90	90	90	90
β (deg)	90	90	90	90
γ (deg)	120	120	120	90
V (Å ³)	3652.9(3)	4031.8(15)	3957.1(15)	3990.3(3)
Z	3	6	6	4
DC (g cm ⁻³)	1.375	1.400	1.381	1.101
μ (Mo Kα) (mm ⁻¹)	0.140	1.565	0.096	0.165
F (000)	1581.0	1740.0	1716.0	1384.0
T (K)	298 K	295 K	297 K	295 K
θmax (deg)	24.973	24.984	26.406	26.379
total no. of rflns	27090	32366	33633	61785
no. of indep rflns	1396	1577	1800	8088
no. of obsd rflns	1250	1362	1354	4958
no. of params refined	114	115	132	419
R1, I > 2σ(I)	0.1393(1250)	0.0872(1362)	0.0529(1354)	0.0923(4958)
wR2, I > 2σ(I)	0.4276(1396)	0.2595(1577)	0.1762(1800)	0.1907(8088)
GOF (F ²)	2.177	1.096	1.056	1.059
CCDC no.	2419337	2419425	2419339	2419341

Table A7.2. Hydrogen bonding distances (Å) and Bond angles (°) in the neutral receptors and their anionic complexes.

Ligand/Complex	D-H...A	d(D...H)/Å	d(H...A)/Å	d(D...A)/Å	<D-H...A/°	Symmetry codes
GUA-IND	N3-H3N...N2	0.86	2.36	2.665 (5)	101	-x+y, 1-x, z
[GUA-IND.Br]⁻	N1- H1N...Br1	0.86	2.45	3.264 (5)	158	x, y, z
	N3-H3N...N2	0.86	2.35	2.657 (7)	102	-x+y, 1-x, z
[GUA-IND.NO₃]⁻	N1-H1N...O1	0.95 (3)	2.20 (3)	3.039 (3)	147 (3)	x, y, z
	N1-H1N...O1	0.95 (3)	2.08 (3)	2.957 (5)	154 (3)	-y, x-y, z
	N3-H3N...N2	0.88 (3)	2.30 (3)	2.655 (3)	104.2 (19)	-x+y, 1-x, z
[GUA-IND.H₂PO₄]⁻	N1-H1...O3	0.86	2.03	2.860 (10)	162	1/2-x, -1/2+y, 1/2+z
	O1-H1B...O2	0.82	1.65	2.450 (9)	166	1/2+x, 1/2-y, z
	N3-H3...N8	0.86	2.20	2.561 (9)	105	x, y, z
	N4-H4...O2	0.86	2.06	2.900 (11)	164	-1/2+x, 1/2-y, z
	O4-H4B...O3	0.82	1.70	2.516 (8)	171	-1/2+x, 1/2-y, z
	N6-H6...N2	0.86	2.38	2.696 (9)	102	x, y, z
	N6-H6...O5	0.86	2.56	3.194 (10)	132	-1/2+x, 1/2-y, z
	N7-H7A...O3	0.86	2.19	2.927 (11)	143	1/2-x, 1/2+y, ½+z
	N9-H9...O5	0.86	2.42	2.810 (9)	108	x, y, z

Table A7.3. Standard reduction potential of different metal ions [A7.1-A7.3].

Half reaction	Reduction potential (V)
Al^{3+}/Al	-1.66
Mn^{2+}/Mn	-1.18
Zn^{2+}/Zn	-0.76
Cd^{2+}/Cd	-0.40
Ni^{2+}/Ni	-0.25
Pb^{2+}/Pb	-0.13
Cu^{2+}/Cu	+0.34
Ag^{+}/Ag	+0.80
$\text{Fe}^{3+}/\text{Fe}^{2+}$	+0.77
Co^{2+}/Co	-0.29

[A7.1] K. Shimuraa and H. Yoshida, *Energy Environ. Sci.*, 2011, **4**, 2467-2481.

[A7.2] A. Šulčius, *J. Sci. Educ.*, 2008.

[A7.3] L. Rocchetti, A. Amato and F. Beolchini, *J. Clean. Prod.*, 2016, **116**, 299-305.

CONCLUSION & FUTURE PERSPECTIVES

In summary, this thesis elucidates some significant results regarding solution state self-assembly behaviour of small molecular probes/receptors and their stimuli responsiveness towards environmentally and biologically relevant analytes. The design rationales of these receptors were further improved so that they enabled the supramolecular gel formation which could find various material applications along with detection of important analytes. The studies were majorly performed in a comparative mode by designing molecules with same skeleton but differing in peripheral substitutions for better understanding of aggregation as well as sensing mechanism.

During this perceptive chemical expedition, firstly in chapter 3, we prepared three 4-(dimethylamino)cinnamaldehyde-based Schiff base receptors (**L1-3**) having different fluorophore molecules to have a comparative study regarding the effect of changing aromatic core (naphthalene in **L1**, anthracene in **L2**, and pyrene in **L3**) towards aggregation and recognition potential. The probes were furnished with donor-acceptor groups and could demonstrate solvent polarity induced self-assembly patterns as investigated through FESEM analysis. The solution state aggregation behaviour of these receptors were investigated through UV-Vis spectroscopy. The π electron-rich and strongly emissive nature of the self-assembled receptors were then exploited for studying the interaction with different nitro phenols including picric acid (PA) in the aqueous medium via fluorescence spectroscopy. PA being the most electron-deficient among different nitro phenols caused highest quenching in the fluorescence intensity of the receptors **L1**, **L2**, and **L3**, thus giving selective sensing of PA. The highest selectivity was observed with **L3**, as it was the most electron-rich among the three. The analytical utility of the receptors was also established via the detection of PA in various real water samples as well as through paper strips. Moreover, all three receptors **L1**, **L2**, and **L3** could recognize picric acid in the solid state.

In chapter 4, two unsymmetrical benzimidazole based urea receptors **R1** and **R2** were designed, varying the terminal substituents. **R1** was fabricated with a naphthyl group while **R2** contained 3-cyanophenyl group. Modulation in the peripheral substitution led to changes in aggregation as well as chemosensing properties. While **R1** displayed aggregation induced emission (AIE) property, **R2** on the other hand showed typical ACQ behaviour. **R1** exhibited excellent optical sensing properties towards only SO_4^{2-} and HSO_4^- , **R2** on the other contrary was not that selective towards SO_4^{2-} and HSO_4^- . Encapsulation of HSO_4^- inside the cation-sealed cavity of receptor **R1** and n-TBA was reported via SCXRD analysis. The easily synthesized model paper strips were employed to show real-life applications of the receptors via the detection of $\text{SO}_4^{2-}/\text{HSO}_4^-$. In line with the

previous study, this chapter also suggested that tailoring functional groups within the molecular framework could modulate aggregation as well as sensing behaviour.

In chapter 5, along with detailing the facets of solution state aggregation and chemosensing, we also focused on designing of receptors capable of showing supramolecular self-assembly phenomena in terms of supramolecular gelation. We synthesized two C_3 -symmetric acylhydrazone-based probes, **TRI-QUI** and **TRI-NAP** with different peripheral substituents. Both compounds had the same skeleton; however, the three arms of **TRI-QUI** were fabricated with quinoline groups while **TRI-NAP** contained naphthalene groups at the periphery to investigate their difference in response to aggregation as well as sensing phenomena. Both the probes showed AIE property. Also, **TRI-QUI** could display selective turn-on response towards Zn^{2+} in 0.1 M HEPES buffer (0.2% DMSO) due to chelation-induced enhanced fluorescence (CHEF) effect. The real-world applicability of **TRI-QUI** was demonstrated via Zn^{2+} sensing in real water samples as well as via paper strip experiments. In contrast, no sensing phenomena was observed by the probe **TRI-NAP** in aqueous medium. Furthermore, **TRI-QUI** self-assembled to form a supramolecular gel in a DMSO:H₂O (2:3, v/v) mixture and could interact with metal ions/anions in the gel phase with alteration in morphological behavior as evident from FESEM studies. The gel could adsorb small molecules like methyl orange and bromophenol blue, with an uptake efficiency of 63% and 60%, respectively, making it supramolecular gel-based multi-functional smart material.

In chapter 6, we designed four adipic dihydrazide based receptor molecules for metallogelation purpose. **ADH-Py-o**, **ADH-Py-m**, **ADH-Py-p** were positional isomers where the two arms of the adipic dihydrazide were fabricated with -o, -m, -p amino pyridine respectively while **ADH-Ph** contained phenyl groups at the terminal positions. We explored the effect of positional isomerism on metallogelation behaviours. It was interesting to observe that only **ADH-Py-p** and **ADH-Py-m** could show selective metallogelation behaviour with $AgNO_3$ (**P-Ag-G**) and $CdCl_2 \cdot H_2O$ (**M-Cd-G**) respectively. **P-Ag-G** facilitated the in-situ formation of AgNPs inside the gel matrix. The gel nanocomposite showed antibacterial activity against the bacterial strains *B. subtilis* and *E. Coli*. Nevertheless, the idea of selective metallogelation of **ADH-Py-m** only in presence of $CdCl_2 \cdot H_2O$ was further exploited for visual detection of Cd^{2+} through gelation process in different real water samples in presence of various competitive metal chloride salts. Important to mention here is **ADH-Py-o** and **ADH-Ph** did not show metallogelation behaviour with any of the metal ions studied for our work under the identical conditions. This study clearly stated the importance of presence and proper positioning of pyridine -N to form a polymeric network through coordination of metal ion.

After preparing receptors for metallogel formation, we paid attention for designing of receptor for anion coordination driven supramolecular gelation, as lower toxicity of metal-free systems may be advantageous for both environmental and biological applications. **GUA-IND** was synthesized using guanidinium hydrazide as the core, and its three arms were functionalized with three indole moieties. **GUA-IND** displayed selective gelation only in the presence of SO_4^{2-} and HSO_4^- (**GI-G**) and partial gelation in the presence of H_2PO_4^- . The **GI-G** gel exhibited excellent stimulus-responsive properties towards PA among different nitroaromatic compounds, where the sensing of PA could be easily visualised through the naked eye as gel to sol transition occurred in presence of PA. Besides, **GI-G** gel formed nanocomposites, **GI-Cu-G** and **GI-Ag-G**, in the presence of Cu and Ag metal ions, which, along with **GI-G**, could exhibit antioxidant and antimicrobial activities. Moreover, **GUA-IND** exhibited a phenomenon of anion exchange where the counter anion (Cl^-) of **GUA-IND** was replaced by different anions such as Br^- , NO_3^- , and H_2PO_4^- during the process of crystallization. This research work paves the way for advanced materials with tailored functionalities.

In brief, small molecule-based probes/receptors can be very advantageous in sensing of important analytes because their easy chemical modification to interact selectively with specific analytes. Subsequently these small molecular probes can form bigger supramolecular species, which can improve both the sensitivity and selectivity of the sensor for detection of the target analyte. The thesis discusses intriguing photophysical properties of the developed small molecular receptors as well as their ability for sensing of cationic, anionic as well as neutral species. Moreover, the thesis emphasizes on improved design rationale for formation of low molecular weight supramolecular gels/metallogels/anion-driven gels derived from the self-assembly of small molecules. The supramolecular gels very attractive as they find application in various fields and this thesis explores some applications like removal of harmful analytes through adsorption, gel-sol transition based visual detection of analytes, facilitation of in situ formation of metal nanoparticles etc. These gels are very fascinating, however, there are still substantial gaps in the understanding and challenges for designing of such systems. The thesis is also intended to provide investigations regarding structure-function relationships for designing of low molecular weight gelators for supramolecular metallogelation purpose. The thesis also sheds lights on rare anion-induced supramolecular gelation giving a future prospective for rational designing of more such gelator molecules for real-life applications. Thus, the thesis lays a strong foundation for the development of small molecule with aggregative nature and hence, contributing significantly towards supramolecular chemistry to cultivate understanding and advancement in this research area.



Rubi Moral
Research Scholar

CONTACT

Department of chemistry
IIT Guwahati, Assam-781039
Email: rubi.moral@iitg.ac.in /
rubimoral96@gmail.com
Phone no.: 9435198247/
9706907434

EDUCATION

INDIAN INSTITUTE OF TECHNOLOGY GUWAHATI, ASSAM, INDIA

Research scholar, PMRF
Department of chemistry
(July 2021-current)

Thesis: *Supramolecular Self-assembly of Low Molecular Weight Receptors: Aggregation, Chemosensing and Gelation Study*

Supervisor: Prof. Gopal Das

TEZPUR UNIVERSITY, TEZPUR, ASSAM, INDIA

Department of chemistry
MSc. in chemistry
(2018-2020)

COTTON UNIVERSITY, GUWAHATI, ASSAM, INDIA

Department of chemistry
BSc. in chemistry
(2013-2015)

COTTON COLLEGE, GUWAHATI, ASSAM, INDIA

Higher Secondary (2015)

ASSAM JATIYA BIDYALAYA, GUWAHATI, ASSAM, INDIA

HSLC (2013)

PROFESSIONAL EXPERIENCE

- ❖ Served as a trained operator of 600MHz Nuclear Magnetic Resonance (NMR) Spectrometer instrument at IIT Guwahati (2022-2026).

ACHIEVEMENTS

- ❖ Gold medalist in BSc. (2015-2018), Cotton University (Chemistry honours).
- ❖ CSIR-UGC NET JRF June 2020 (AIR 72) in CHEMICAL SCIENCES.
- ❖ Qualified GATE 2021.
- ❖ Recipient of DST-INSPIRE scholarship.

❖ Recipient of prestigious PMRF fellowship.

JOURNAL PUBLICATIONS

1. Probing the Potential of Hitherto Unexplored Base-Stabilised Borylenes in Dinitrogen Binding. F. Fantuzzi, **R. Moral**, R. D. Dewhurst, H. Braunschweig and A. K. Phukan, *Chemistry-A European Journal*, 2022, 28, e20210412.
2. Probing the aggregation potential and picric acid recognition aptitude by altering aromatic core substitution in a series of cinnamaldehyde-based receptors, **R. Moral**, O. A. Pegu, and G. Das, *Dyes and Pigments*, 2023, 218, 111502.
3. Terminal substituent induced differential aggregation and sensing properties: A case study of neutral benzimidazole based urea receptors. **R. Moral**, O. A. Pegu, and G. Das, *New Journal of Chemistry*, 2023, 47, 19625-19632.
4. Exploring the gelation and AIE property of tripodal acylhydrazone-based probe: Turn-on Zn(II) sensing in HEPES buffer. **R. Moral** and G. Das, *Soft Matter*, 2024, 20, 7668-7677.
5. Anion-driven supramolecular gel: naked-eye detection of picric acid, facilitating in situ formation of gel nanocomposites and enabling solid-state anion exchange. **R. Moral**, O. A. Pegu and G. Das, *Nanoscale*, 2025, 17, 26845-26854.
6. Positional Isomerism Influencing Differential Supramolecular Metallogelation: Biological Applications and Heavy Metal Ion Detection. **R. Moral**, O. A. Pegu and G. Das, manuscript submitted.
7. An expedition towards designing of luminescent supramolecular metallogels for chemosensing applications. **R. Moral**, and G. Das, *Inorganica Chimica Acta*, 2025, 581, 122635.
8. Anion Coordination Chemistry: An Expedition Towards Designing of Functional Materials. O. A. Pegu, **R. Moral** and G. Das, *Chemistry: An Asian Journal*, 2025, 20, e202401236.
9. Oil spill remediation: Recent developments of Phase Selective Organogelators (PSOGs). **R. Moral** and G. Das, manuscript submitted.
10. Anion Induced Intramolecular Cyclisation of Urea-Based Receptors: Entrapment of Cyclic $[\text{SO}_4(\text{H}_2\text{O})_4]^{2-}$ Cluster and Encapsulation of Anions with varied Dimensionality. O. A. Pegu, **R. Moral** and G. Das, *Crystal Growth and Design*, 2023, 23, 8370-8380.
11. PSOG for selective thixotropic/thermo-reversible gelation in oil: Oil spill recovery and fuel-adulteration detection. **O. A. Pegu**, R. Moral and G. Das, *Chemical Engineering Journal*, 2025, 169128 (In Press).

CONFERENCES ATTENDED

1. Poster presentation in *North East Research Conclave (NERC 2022)*, IIT Guwahati, India May, 2022.
 2. Attended *Frontiers in Chemical Sciences (FICS-2022)*, IIT Guwahati, India on December, 2022.
 3. Poster presentation in *Modern Trends in Inorganic Chemistry (MTIC-2023)*, IISc Bangalore, India on December, 2023.
 4. Oral presentation in *Frontiers in Chemical Sciences (FICS-2024)*, IIT Guwahati, India on December, 2024.
 5. Poster presentation in *National Conference on Polymers and Advanced Functional Materials (NCPAFM-2024)*, IAAST, Guwahati, India on December, 2024. (**1st Prize**)
 6. Poster presented in the *36th CRSI National Symposium in Chemistry (CRSI-NSC-36) and CRSI-RSC Symposium*, Dibrugarh University, Dibrugarh, India, on February, 2026.
-

TEACHING EXPERIENCE

1. Teaching Assistantship under PMRF scheme at Cotton University, Course: Inorganic Chemistry (tutorial) for M.Sc. and B.Sc. students (2022-2026).
2. Co-guided two projects of three M.Sc. final year student (2023, 2024 and 2026).
3. Co-guided internship project of three students (2024 and 2025), NEP FYUG Program. (DBT sponsored Project).

PROJECT EXPERIENCE

1. Successfully completed M. Sc. project entitled as “*Dinitrogen Binding and Activation by Base Stabilised Borylenes: A Theoretical Study*” at Tezpur University, 2020, under the guidance of Prof. Ashwini Kumar Phukan, Tezpur University.
-

EXPERTISE

Instruments handled: 600MHz Nuclear Magnetic Resonance (NMR) Spectrometer (trained operator), Spectroscopic Techniques (UV-Vis, Fluorescence, FTIR), Dynamic light scattering (DLS), and Fluorescence Microscopy.

Software handling: Origin, Adobe Illustrator, MestreNova, ChemDraw, ImageJ, XPSPEAK41, etc.

I hereby declare that, all the aforementioned information is true to the best of my knowledge.


Rubi Moral